

ABSTRACT

WELLS, KAYLEE ANEJA. Excited State Dynamics in Rhenium(I) Bichromophores. (Under the direction of Dr. Felix N. Castellano).

A brief introduction into the photophysical concepts pertinent to the projects discussed in this document are provided in **Chapter 1**. This includes fundamental theory of light absorption, excited state deactivation pathways, energy transfer, and electron transfer. In addition to photophysical concepts, the experimental designs of the instrumentation used in these studies are also presented.

Chapter 2 begins the bichromophoric story of the transient absorption dynamics from the sub-picosecond to supra-nanosecond time domain in a series of Re(I) metal-organic bichromophores of the general motif, $[\text{Re}(\text{5-R-phen})(\text{CO})_3(\text{dmap})](\text{PF}_6)$, where R is a naphthalimide (NI), phen = 1,10-phenanthroline, and dmap is 4-dimethylaminopyridine are reported. The ligand centered (LC) excited states of this series were varied by systematically modifying the 4-position of the NI with -H (**NI**), -Br (**BrNI**), phenoxy (**PONI**), thiobenzene (**PSNI**), and piperidine (**PNI**), rendering a series of metal-organic bichromophores (**Re1-Re5**, respectively). To model the photophysical properties of the bichromophores, five closely related organic chromophores as well as $[\text{Re}(\text{phen})(\text{CO})_3(\text{dmap})](\text{PF}_6)$ (**Re6**) were investigated in parallel. In addition to transient absorption, the energy transfer processes were studied with time-resolved photoluminescence (PL) spectroscopy and electronic structure calculations. A thermal equilibrium between the triplet LC and triplet metal-to-ligand-charge-transfer (MLCT) excited states was established between three of the five bichromophores.

In **Chapter 3**, I present the synthesis, structural characterization, electronic structure calculations, and the ultrafast and supra-nanosecond photophysical properties of a series of five Re(I) bichromophores exhibiting metal-to-ligand charge transfer (MLCT) excited states based on the general formula $fac\text{-}[\text{Re}(\text{N}^{\wedge}\text{N})(\text{CO})_3(\text{PNI-py})]\text{PF}_6$, where PNI-py is 4-piperidinyl-1,8-

naphthalimidepyridine and N^N is a diimine ligand (**Re1-5**), along with their corresponding model chromophores where 4-ethylpyridine was substituted for PNI-py (**Mod1-5**). The diimine ligands used include 1,10-phenanthroline (phen, **1**), 2,9-dimethyl-4,7-diphenyl-1,10-phenanthroline (bcp, **2**), 4,4'-di-*tert*-butyl-2,2'-bipyridine (dtbb, **3**), 4,4'-diethylester-2,2'-bipyridine (deeb, **4**), and 2,2'-biquinoline (biq, **5**). In these metal-organic bichromophores, structural modification of the diimine ligand resulted in substantial changes to the observed energy transfer efficiencies between the two chromophores as a result of the variation in ³MLCT excited state energies. The photophysical properties and energetic pathways of the model chromophores were investigated in parallel to accurately track the changes that arose from introduction of the organic chromophore pendant on the ancillary ligand. All relevant photophysical and energy transfer processes were probed and characterized using time-resolved photoluminescence spectroscopy, ultrafast and nanosecond transient absorption spectroscopy, and time-dependent density functional theory calculations. Of the five bichromophores in this study, four (**Re1-4**) exhibited a thermal equilibrium between the ³PNI-py and the triplet ³MLCT excited state, drastically extending the lifetimes of the parent model chromophores.

Chapter 4 concludes the rhenium(I) bichromophore saga with the steady-state and ultrafast to suprananosecond excited state dynamics of fac-[Re(**NBI-phen**)(CO)₃(L)](PF₆) (**NBI-phen** = 16H-benzo[4',5']isoquinolino[2',1':1,2]imidazo[4,5-f][1,10]phenanthroline-16-one) as well as their respective models of the general molecular formula [Re(phen)(CO)₃(L)](PF₆) (L = PPh₃ and CH₃CN) were investigated using transient absorption and time-gated photoluminescence spectroscopy. The **NBI-phen** containing molecules exhibited enhanced visible light absorption with respect to their models and rapid formation (< 6 ns) of the triplet ligand-centred (LC) excited

state of the organic ligand, **NBI-phen**. These triplet states exhibit an extended excited state lifetime that enable the energized molecules to readily engage in triplet-triplet annihilation photochemistry.

© Copyright 2021 by Kaylee Wells

All Rights Reserved

Excited State Dynamics in Rhenium(I) Bichromophores

by
Kaylee Aneja Wells

A dissertation submitted to the Graduate Faculty of
North Carolina State University
in partial fulfillment of the
requirements for the degree of
Doctor of Philosophy

Chemistry

Raleigh, North Carolina
2021

APPROVED BY:

Felix N. Castellano
Committee Chair

Elena Jakubikova

David A. Shultz

Reza Ghiladi

DEDICATION

To all the wrong the decisions that led me to the right places.

BIOGRAPHY

Kaylee Wells was born in Kenansville, North Carolina to Louise René Wells and Raymond Mack Wells, 30 August 1995. She is the younger sister to Nikki and Melissa, and aunt to Preston and Kyttalia. She attended the University of Mount Olive graduating Suma Cum Laude with a Bachelor of Science in Chemistry in 2017, with a double minor in Religion and Physics. Growing interested in physical and inorganic chemistry during her tenure at Mount Olive, she decided to join the Castellano group in the summer of 2017 at North Carolina State University. In 2021 she received her Doctor of Philosophy under the direction of Professor Felix N. Castellano and will begin an industrial career at Intel.

ACKNOWLEDGMENTS

There are countless people I would love to thank for getting me to the position I am in to be writing this section. I would first like to thank Kyle Swartz for his support, love, and never-ending patience. I am not sure who endured more during my tenure at NCSU, but I would wager good money that it is a tossup. I am forever grateful to my parents for their unwavering faith in me and loving me unconditionally. My family and friends I would like to thank as well, for continuous support and understanding. To all my previous teachers and professors, I would not be here were it not for you. To Venus, my overly clingy kitty. Thank you for not deleting my entire dissertation, though you have tried countless times. And thank you for trying to help me write this. I may have had to delete all of your input, but your efforts are acknowledged.

I would also like to thank my advisor, Prof. Phil Castellano, for allowing me to start early and jump out of the frying pan into the fire. His guidance and support these past five(ish) years have been resolute. To Dr. James Yarnell, who was not only an excellent mentor while at NCSU but has supported me even after he graduated. Drs. Sofia Garakyaraghi, Chelsea Taliaferro, Christopher Papa, and Evgeny Danilov have bestowed upon me instrumental wisdom that has honestly carried me through some of the toughest times of my PhD career. Other group members Daniel T. Yonemoto, who just defended his PhD literally two hours before me,¹ are coming up on their prelim's, Michael Rosko, our super dope post-docs Drs. Maggie Hudson and Tia Lee, and finally our amazing team of undergrads (past and present), Jon Palmer, Megan Griffin, Adrienne Faulkner, and Ben Masters have made work fun, exciting, and worth-while.

¹ Which I am totally not salty about.

TABLE OF CONTENTS

LIST OF TABLES	viii
LIST OF FIGURES, SCHEMES, AND CHARTS	x
Chapter 1: Chapter 1 An Introduction to the Fundamentals of Molecular Photoprocesses	1
1.1 Photochemistry vs. Photophysics	1
1.2 Photophysical Processes	1
1.2.1 Light Absorption	1
1.2.2 The Franck-Condon Principle	5
1.3 Excited State Decay	7
1.3.1 Non-radiative Decay Processes	7
1.3.2 Radiative Decay Processes	8
1.3.3 Quantum Yield and Excited State Lifetime	12
1.3.4 Bimolecular Quenching Processes	11
1.4 Spectroscopic Instrumentation	15
1.4.1 UV-vis	15
1.4.2 Transient Absorption (TA) Spectroscopy: nsTA and fsTA	18
1.4.3 Photoluminescence, Time-Resolved Photoluminescence, and Time-Resolved Intensity Decay Measurements.....	22
1.5 References	26
Chapter 2: Chapter 2 Excited-State Triplet Equilibria in a Series of Re(I)-Naphthalimide Bichromophores	28
2.1 Abstract	28
2.2 Introduction	29
2.3 Experimental	32
2.3.1 Reagents and Chemicals.....	32
2.3.2 Characterization Data for the Studied Complexes	33
2.3.3 General Techniques	36
2.3.4 Nanosecond Transient Absorption Spectroscopy.....	37
2.3.5 Femtosecond Transient Absorption Spectroscopy	37
2.3.6 Time-Resolved Emission Intensity Decay Measurements	37
2.3.7 Density Functional Theory (DFT) Calculations.....	38
2.4 Results and Discussion	39
2.4.1 Syntheses	39
2.4.2 UV-vis Electronic Spectra.....	41
2.4.3 Electronic Structure Calculations.....	43
2.4.4 Static and Dynamic PL Spectroscopy	45
2.4.5 Transient Absorption Spectroscopy	53
2.4.6 Excited State Equilibrium	62
2.4.7 Excited State Evolution and Decay Kinetics.....	66

2.5 Conclusions	69
2.6 Acknowledgements	70
2.7 References	71
Chapter 3: Energy transfer Processes in Next-Generation Metal-Organic Bichromophores	79
3.1 Abstract	79
3.2 Introduction	80
3.3 Experimental	84
3.3.1 Reagents and Chemical	84
3.3.2 General	84
3.3.3 Electrochemistry	85
3.3.4 Femtosecond Transient Absorption Spectroscopy	85
3.3.5 Nanosecond Transient Absorption Spectroscopy	86
3.3.6 Time-Resolved Photoluminescence (TR-PL) Intensity Decay Measurements	86
3.3.7 Density Functional Theory (DFT) Calculations	87
3.3.8 Time-Dependent DFT (TD-DFT) Calculations	88
3.4 Results and Discussion	88
3.4.1 Synthesis	88
3.4.2 Electronic Structure Calculations	90
3.4.3 Steady-State Absorption and Photoluminescence Spectroscopy	92
3.4.4 Nanosecond Transient Absorption Spectroscopy	98
3.4.5 Femtosecond Transient Absorption	102
3.4.6 Excited State Equilibrium	106
3.4.7 Excited State Evolution and Decay	108
3.5 Conclusions	109
3.6 Acknowledgements	110
3.7 References	111
Chapter 4: Accessing the Triplet Manifold of Naphthalenebenzimidazole- Phenanthroline in Rhenium(I) Bichromophores	118
4.1 Abstract	118
4.2 Introduction	118
4.3 Experimental	121
4.3.1 Reagents and Chemicals	121
4.3.2 General Techniques	121
4.3.3 Characterization Data for Studied Molecules	122
4.3.4 Ultrafast Transient Absorption Spectroscopy	123
4.3.5 Nanosecond Transient Absorption and Time-Resolved Photoluminescence Spectroscopy	124

4.3.6 Density Functional Theory (DFT) and Time-Dependent DFT (TD-DFT) Calculations	124
4.4 Results and Discussion	125
4.4.1 Syntheses	125
4.4.2 Electronic Structure Calculations	126
4.4.3 Electronic Absorption and Photoluminescence Spectroscopy	129
4.4.4 Transient Absorption and Time-Resolved Spectroscopy	133
4.5 Conclusions	139
4.6 Acknowledgements	139
4.7 References	141
Appendices	147
Appendix A	148
A.1 Synthetic Details and Structural Characterization	148
A.2 Additional Optical Spectra	181
A.3 Additional Transient Absorption Spectra	191
A.4 Additional DFT Results	220
Appendix B	234
B.1 Synthetic Details and Structural Characterizations	234
B.2 Electronic Structure Calculations	257
B.3 Additional Spectroscopic Information	279
B.4 References	295
Appendix C	296
C.1 Synthetic Details and Structural Characterizations	296
C.2 Additional Computational Data	317
C.3 Additional Spectroscopic Data	331
C.4 References	340

LIST OF TABLES

Table 2.1	Static photophysical properties of the NI , BrNI , PONI , PSNI , PNI model compounds and Re1-Re6 measured in acetonitrile (black) and THF (blue)	43
Table 2.2	Time-resolved PL and TA data recorded for Re1-Re6 in acetonitrile.....	51
Table 2.3	Calculated triplet energy gap of Re1-Re5 using different methodologies.....	64
Table 3.1	Steady-state photophysical data of Mod1-5 , PNI-py, PNI, and Re1-5	97
Table 3.2	Time-resolved TA and PL data recorded for Mod1-Mod5 and Re1-Re5 in THF	102
Table 4.1	Electronic absorbance and photoluminescence data of studied molecules in THF	130
Table A1	Summary of time constants from UFTA global fit analysis	209
Table A2	Wavelength, energies, and oscillator strength (<i>f</i>) for selected $S_0 \rightarrow S_n$ excitations as determined via TDDFT at the level of theory specified below. Experimental UV/Vis data obtained in acetonitrile at room temperature.....	220
Table A3	Wavelength and energies for selected $S_0 \rightarrow T_n$ excitations as determined via TDDFT at the level of theory specified below. Experimental photoluminescence data obtained in 2-methyltetrahydrofuran at 77 K	221
Table A4	Wavelength, energies, and oscillator strength (<i>f</i>) for selected $S_0 \rightarrow S_n$ excitations as determined via TDDFT at the level of theory specified below. Experimental UV/Vis data obtained in acetonitrile at room temperature.....	227
Table A5	Wavelength and energies for selected $S_0 \rightarrow T_n$ excitations as determined via TDDFT at the level of theory specified below. Experimental photoluminescence data obtained in 2-methyltetrahydrofuran at 77 K	228
Table B1	Reduction potentials of Mod1-5 obtained from DPV experiments using a platinum disk as the working electrode, a platinum wire as the counter electrode, and Ag/AgNO ₃ as the reference electrode	257
Table B2	Optimized Singlet Geometries of Re1-5 and Mod1-5	258
Table B3	Experimental UV/Vis data obtained in THF at room temperature. Wavelength, energies, and oscillator strength (<i>f</i>) for selected $S_0 \rightarrow S_n$ excitations as determined via TDDFT at the level of theory specified below	278
Table B4	Energies of the LUMO's of Re-CDI complexes with both ancillary ligands	279

Table C1	Selected electronic excitation energies (nm) and corresponding oscillator strengths (f) of the low-lying singlet excited states of complexes Mod1-2 and Re1-2	323
Table C2	Optimized singlet geometries of Re1-2 and Mod1-2	325
Table C3	Data table of Re1 rate constants and beta values after fitting using the TTA fitting equation from Deng et. al. Experiments were carried out in deaerated THF ($\lambda_{\text{ex}} = 415$ nm).....	334
Table C4	Data table of Re2 rate constants and beta values after fitting using the TTA fitting equation from Deng et. al. Experiments were carried out in deaerated THF ($\lambda_{\text{ex}} = 415$ nm).....	335

LIST OF FIGURES, SCHEMES, AND CHARTS

Figure 1.1	Illustration of the Franck-Condon principle where the excited state PES is distorted more along the nuclear coordinates (Q) and its effect on the absorption band. This figure was adapted from the literature.....	6
Figure 1.2	Normalized absorption and fluorescence spectra of anthracene in ethanol	10
Figure 1.3	Jablonski (energy) diagram portraying absorption and the various excited state decay processes that follow. Figure adapted from Edinburgh Instruments (https://www.edinst.com/blog/jablonski-diagram/).....	10
Figure 1.4	Photoinduced reductive and oxidative bimolecular electron transfer quenching mechanisms	13
Figure 1.5	Schematic of the FRET mechanism between two singlet states where the dashed lines represent the non-radiative energy transfer from donor to acceptor (dipole-dipole interaction).....	14
Figure 1.6	Dexter exchange mechanisms. The top is a schematic of EnT between an excited donor in the triplet state and a singlet acceptor in the ground state. The bottom is a schematic of DET occurring between two singlet states	15
Figure 1.7	Representative electronic transition types found in octahedral transition metal complexes.....	17
Figure 1.8	Generalized nsTA apparatus	19
Figure 1.9	Generalized schematic of the fsTA setup.....	20
Figure 1.10	Schematic of a spectrofluorometer. Diagram adapted from the literature	23
Figure 2.1	Naphthalimide chromophores evaluated in this study	31
Scheme 2.1	Synthetic procedures for the preparation of NI , BrNI , PONI , PSNI and Re1-Re6	40
Figure 2.2	(A) Electronic spectra of NI , BrNI , PONI , PSNI , and PNI recorded in acetonitrile. (B) Electronic spectra of Re1-Re6 recorded in acetonitrile.....	42
Figure 2.3	Room temperature emission spectra of (A) NI ($\lambda_{ex} = 325$ nm), BrNI ($\lambda_{ex} = 325$ nm), PONI ($\lambda_{ex} = 355$ nm), PSNI ($\lambda_{ex} = 395$), and PNI ($\lambda_{ex} = 395$) recorded in aerated acetonitrile and of (B) Re1-Re6 ($\lambda_{ex} = 385$) recorded in deaerated acetonitrile	48

Figure 2.4	Time-resolved 77 K PL emission spectra of Re1-Re6 at the specified delay times following a 7 ns fwhm, 350 nm (Re1-Re3) or 400 nm (Re4-Re6) laser pulse in 2-MeTHF	52
Figure 2.5	Excited-state absorption difference spectra of Re1 in ACN during short delay times (A) and long delay times (B) following 350 nm pulsed excitation (105 fs fwhm)	54
Figure 2.6	Excited-state absorption difference spectra of Re3 measured in acetonitrile across short (A) and long (B) delay times following 350 nm pulsed laser excitation (105 fs fwhm)	56
Figure 2.7	Excited-state absorption difference spectra of Re4 measured in acetonitrile during short (A) intermediate (B) and long (C) delay times following 400 nm pulsed laser excitation (105 fs fwhm)	58
Figure 2.8	Excited-state absorption difference spectra of Re5 measured in acetonitrile during short (A) and long (B) delay times following 400 nm pulsed laser excitation (105 fs fwhm)	59
Figure 2.9	Excited-state absorption difference spectra of Re1 (A), Re2 (B), Re3 (C), Re4 (D), and Re5 (E) measured in acetonitrile following 350 nm pulsed laser excitation (2.5 mJ/pulse, 7 ns fwhm) or 400 nm pulsed laser excitation (3.0 mJ/pulse, 7 ns fwhm). Samples were deaerated using the freeze-pump-thaw degas method.....	61
Figure 2.10	Qualitative energy level diagrams of the photophysical processes occurring in Re1-Re3 (A), Re4 (B), and Re5 (C) in acetonitrile at room temperature	68
Figure 3.1	Qualitative energy level diagram describing ‘ping-pong’ energy transfer process between the Re(I) MLCT and PNI excited states.....	82
Figure 3.2	The Re(I) chromophores and Re(I)-PNI bichromophores investigated in this study	84
Scheme 3.1	Synthesis of PNI-py, the Re1-5 bichromophores, and the Mod1-5 model chromophores	89
Figure 3.3	Representative schematic diagram of the HOMO, LUMO, and LUMO+1 of the model complexes (Mod3 above) and rhenium bichromophores (Re3 below)	91
Figure 3.4	(A) Electronic absorption spectra of Mod1-5 recorded in THF. (B) Electronic absorption spectra of Re1-5 and PNI-py recorded in THF	94
Figure 3.5	Static photoluminescence spectra of (A) Mod1-5 and (B) Re1-5 and PNI measured in deaerated THF excited at 408 nm	95

Figure 3.6	Transient absorption difference spectra with the corresponding ground state absorption spectrum (dashed line) of Re5 (45.4 μM) measured in THF with 355 nm laser pulses (5.0 mJ/pulse)	99
Figure 3.7	(A) Transient absorption difference spectra with the corresponding ground state absorption spectrum (dashed line) of Re2 (44.3 μM) recorded in THF with 355 nm laser pulses (5.0 mJ/pulse). (B) The concentration dependent study of Re2 illustrating self-quenching behavior with single wavelength transient absorption kinetics detected at 465 nm ($\lambda_{\text{ex}} = 410$ nm, 2.0 mJ/pulse). Samples were deaerated using the freeze-pump-thaw method.....	101
Figure 3.8	Excited state absorption difference spectra of Re2 in THF excited following 400 nm pulsed laser excitation (105 fs fwhm, 0.3 μJ /pulse).....	103
Figure 3.9	Excited state absorption difference spectra of Re5 in THF excited following 400 nm pulsed laser excitation (105 fs fwhm, 0.3 μJ /pulse).....	104
Figure 3.10	Representative (Re1-4) time-resolved photoluminescence data showing Re4 early times (left) and delayed time (right) depicting the delayed phosphorescence from the $^3\text{MLCT}^*$ excited state	108
Figure 3.11	Qualitative energy level diagrams of the photophysical processes occurring in Re1-4 (A) and Re5 (B).....	109
Chart 4.1	The bichromophores Re1 , Re2 , and relevant model complexes Mod1 and Mod2 investigated here.....	120
Scheme 4.1	Synthetic pathways leading to NBI-phen , Re1 and Re2	126
Figure 4.1	Representative frontier molecular orbital diagrams of the Mod1 and corresponding NBI-phen complex Re1 , where L = PPh_3	127
Figure 4.2	Electronic absorption spectra of (A) Re1 and Re2 and (B) Mod1 and Mod2 measured in THF.....	130
Figure 4.3	Static photoluminescence spectra of (A) Re1 and Re2 ($\lambda_{\text{ex}} = 415$ nm) and (B) Mod1 and Mod2 ($\lambda_{\text{ex}} = 355$ nm) in deaerated THF.....	132
Figure 4.4	UFTA of (A) Re2 in THF following 400 nm pulsed laser excitation (105 fs fwhm, 0.3 mJ/pulse) and (B) nsTA of Re2 in deaerated THF following 415 nm excitation (1.8 mJ/pulse)	134
Figure 4.5	Representative (Mod1 and Mod2) transient absorption spectra of (A) UFTA of Mod2 following 350 nm excitation (105 fs fwhm, 50 μJ /pulse) in THF and (B) nsTA of Mod2 following 355 nm excitation (1.8 mJ/pulse) in deaerated THF	136

Figure 4.6	Representative (Re1 and Re2) time-resolved photoluminescence data of Re2 at (A) room temperature in deaerated THF and (B) 77 K in 2-MeTHF following 415 nm excitation (1.8 mJ/pulse)	138
Figure A1	¹ H NMR spectrum of NI in CD ₂ Cl ₂ (400 MHz)	148
Figure A2	¹ H NMR spectrum of NI in CD ₂ Cl ₂ (400 MHz) with zoomed in aromatic region.....	149
Figure A3	HRMS of NI	149
Figure A4	¹ H NMR spectrum of [Re(NI-phen)(CO) ₃ (dmap)](PF ₆) (Re1) in CD ₂ Cl ₂ (400 MHz)	151
Figure A5	¹ H NMR spectrum of [Re(NI-phen)(CO) ₃ (dmap)](PF ₆) (Re1) in CD ₂ Cl ₂ (400 MHz) with zoomed in aromatic region	152
Figure A6	¹ H- ¹ H COSY NMR spectrum of [Re(NI-phen)(CO) ₃ (dmap)](PF ₆) (Re1) in CD ₂ Cl ₂ (400 MHz)	153
Figure A7	HRMS of [Re(NI-phen)(CO) ₃ (dmap)](PF ₆) (Re1)	154
Figure A8	¹ H NMR spectrum of BrNI in CD ₂ Cl ₂ (400 MHz).....	155
Figure A9	¹ H NMR spectrum of BrNI in CD ₂ Cl ₂ (400 MHz) with zoomed in aromatic region.....	155
Figure A10	HRMS of BrNI	156
Figure A11	¹ H NMR spectrum of [Re(BrNI-phen)(CO) ₃ (dmap)](PF ₆) (Re2) in CD ₂ Cl ₂ (400 MHz)	158
Figure A12	¹ H NMR spectrum of [Re(BrNI-phen)(CO) ₃ (dmap)](PF ₆) (Re2) in CD ₂ Cl ₂ (400 MHz) with zoomed in aromatic region	158
Figure A13	¹ H- ¹ H COSY NMR spectrum of [Re(BrNI-phen)(CO) ₃ (dmap)](PF ₆) (Re2) in CD ₂ Cl ₂ (400 MHz)	159
Figure A14	HRMS of [Re(BrNI-phen)(CO) ₃ (dmap)](PF ₆) (Re2)	160
Figure A15	¹ H NMR spectrum of PONI in CD ₂ Cl ₂ (400 MHz).....	161
Figure A16	¹ H NMR spectrum of PONI in CD ₂ Cl ₂ (400 MHz) with zoomed in aromatic region.....	161
Figure A17	HRMS of PONI	162

Figure A18 ^1H NMR spectrum of $[\text{Re}(\text{PONI-phen})(\text{CO})_3(\text{dmap})](\text{PF}_6)$ (Re3) in CD_2Cl_2 (400 MHz)	164
Figure A19 ^1H NMR spectrum of $[\text{Re}(\text{PONI-phen})(\text{CO})_3(\text{dmap})](\text{PF}_6)$ (Re3) in CD_2Cl_2 (400 MHz) with zoomed in aromatic region	164
Figure A20 ^1H - ^1H COSY NMR spectrum of $[\text{Re}(\text{PONI-phen})(\text{CO})_3(\text{dmap})](\text{PF}_6)$ (Re3) in CD_2Cl_2 (400 MHz)	165
Figure A21 HRMS of $[\text{Re}(\text{PONI-phen})(\text{CO})_3(\text{dmap})](\text{PF}_6)$ (Re3)	166
Figure A22 ^1H NMR spectrum of PSNI in CD_2Cl_2 (400 MHz).....	167
Figure A23 ^1H NMR spectrum of PSNI in CD_2Cl_2 (400 MHz) with zoomed in aromatic region.....	167
Figure A24 HRMS of PSNI	168
Figure A25 ^1H NMR spectrum of $[\text{Re}(\text{PSNI-phen})(\text{CO})_3(\text{dmap})](\text{PF}_6)$ (Re4) in CD_2Cl_2 (400 MHz)	170
Figure A26 ^1H NMR spectrum of $[\text{Re}(\text{PSNI-phen})(\text{CO})_3(\text{dmap})](\text{PF}_6)$ (Re4) in CD_2Cl_2 (400 MHz) with zoomed in aromatic region	170
Figure A27 ^1H - ^1H COSY NMR spectrum of $[\text{Re}(\text{PSNI-phen})(\text{CO})_3(\text{dmap})](\text{PF}_6)$ (Re4) in CD_2Cl_2 (400 MHz)	171
Figure A28 HRMS of $[\text{Re}(\text{PSNI-phen})(\text{CO})_3(\text{dmap})](\text{PF}_6)$ (Re4).....	172
Figure A29 ^1H NMR spectrum of $[\text{Re}(\text{PNI-phen})(\text{CO})_3(\text{dmap})](\text{PF}_6)$ (Re5) in CD_2Cl_2 (400 MHz)	173
Figure A30 ^1H NMR spectrum of $[\text{Re}(\text{PNI-phen})(\text{CO})_3(\text{dmap})](\text{PF}_6)$ (Re5) in CD_2Cl_2 (400 MHz) with zoomed in aromatic region	174
Figure A31 ^1H NMR spectrum of $[\text{Re}(\text{PNI-phen})(\text{CO})_3(\text{dmap})](\text{PF}_6)$ (Re5) in CD_2Cl_2 (400 MHz) with zoomed in aliphatic region.....	174
Figure A32 ^1H - ^1H COSY NMR spectrum of $[\text{Re}(\text{PNI-phen})(\text{CO})_3(\text{dmap})](\text{PF}_6)$ (Re5) in CD_2Cl_2 (400 MHz)	175
Figure A33 HRMS of $[\text{Re}(\text{PNI-phen})(\text{CO})_3(\text{dmap})](\text{PF}_6)$ (Re5)	176
Figure A34 ^1H NMR spectrum of $[\text{Re}(\text{phen})(\text{CO})_3(\text{dmap})](\text{PF}_6)$ (Re6) in CD_2Cl_2 (400 MHz) with zoomed in aromatic region	177

Figure A35 ^1H NMR spectrum of $[\text{Re}(\text{phen})(\text{CO})_3(\text{dmap})](\text{PF}_6)$ (Re6) in CD_2Cl_2 (400 MHz) with zoomed in aromatic region.....	177
Figure A36 HRMS of $[\text{Re}(\text{phen})(\text{CO})_3(\text{dmap})](\text{PF}_6)$ (Re6).....	178
Figure A37 ATR-FTIR spectra of NI , BrNI , PONI , PSNI , and PNI	179
Figure A38 ATR-FTIR spectra of Re1-Re6	180
Figure A39 (a) Electronic spectra of NI , BrNI , PONI , PSNI , and PNI in THF. (b) Electronic spectra of Re1-Re6 in THF.....	181
Figure A40 (a) Additive combination of electronic spectra between organic chromophore model and Re(I) model in ACN. (b) Electronic spectra of Re1-Re6 in ACN.....	182
Figure A41 (a) Additive combination of electronic spectra between organic chromophore model and Re(I) model in THF. (b) Electronic spectra of Re1-Re6 in THF.....	183
Figure A42 Photoluminescence spectra of NI , BrNI , PONI , PSNI , PNI , and Re1-Re6 in THF.....	184
Figure A43 Excitation spectra of NI in ACN monitored at shortwave (left) and longwave (right) emission maxima.....	185
Figure A44 Excitation spectra of BrNI in ACN monitored at shortwave (left) and longwave (right) emission maxima.....	185
Figure A45 Photoluminescence decay of Re1 at 600 nm in ACN (left) and THF (right). Excited at 355 nm (3 mJ/pulse).....	186
Figure A46 Photoluminescence decay of Re2 at 600 nm in ACN (left) and THF (right). Excited at 355 nm (3 mJ/pulse).....	186
Figure A47 Photoluminescence Decay of Re3 at 600 nm in ACN (top) and 590 nm in THF (bottom). Excited at 355 nm (3 mJ/pulse).....	187
Figure A48 Photoluminescence decay of Re6 at 600 nm in ACN (top) and THF (bottom). Excited at 410 nm (3 mJ/pulse).....	188
Figure A49 Time-resolved photoluminescence emission spectra of Re1 (A), Re2 (B), Re3 (C), Re4 (D), and Re5 (E) at specified times after a 7 ns, 350 nm (Re1-Re3) and 400 nm (Re4 and Re5) laser pulse in deaerated ACN.....	189
Figure A50 Time-resolved 77 K photoluminescence emission spectra of NI , BrNI , PONI , PSNI , and PNI at 25 ms after a 7 ns, 400 nm laser pulse in 2-methyl THF with 10% ethyl iodide.....	190

Figure A51 Excited-state absorption difference spectra of NI in ACN during short delay times (A) and long delay times (B) following 350 nm pulsed excitation (105 fs fwhm)	191
Figure A52 Excited-state absorption difference spectra of BrNI in ACN during short delay times (A) and long delay times (B) following 350 nm pulsed excitation (105 fs fwhm)	192
Figure A53 Excited-state absorption difference spectra of Re1 in ACN during short delay times (A) and long delay times (B) following 400 nm pulsed excitation (105 fs fwhm)	193
Figure A54 Ultrafast transient absorption kinetic data of Re1 in ACN following 350 nm pulsed excitation. (A) Single wavelength kinetic analysis at 470 nm. (B) Single wavelength kinetic analysis at 370 nm. (C) Single wavelength kinetic analysis at 470 nm	194
Figure A55 Global fit spectral analysis of ultrafast transient absorption data of Re(NI-phen)(CO) ₃ Cl in THF (A), Re1 in THF (B), and Re1 in ACN (C) following 350 nm pulsed excitation.....	195
Figure A56 Excited-state absorption difference spectra of Re2 in ACN during short delay times (A) and long delay times (B) following 350 nm pulsed excitation (105 fs fwhm)	196
Figure A57 Ultrafast transient absorption kinetic data of Re2 in ACN following 350 nm pulsed excitation. (A) Single wavelength kinetic analysis at 485 nm. (B) Single wavelength kinetic analysis at 375 nm. (C) Single wavelength kinetic analysis at 485 nm	197
Figure A58 Global fit spectral analysis of ultrafast transient absorption data Re(BrNI-phen)(CO) ₃ Cl in THF (A), Re2 in THF (B), and Re2 in ACN (C) following 350 nm pulsed excitation.....	198
Figure A59 Excited-state absorption difference spectra of PONI in ACN during short delay times (A) and long delay times (B) following 350 nm pulsed excitation (105 fs fwhm)	199
Figure A60 Ultrafast transient absorption kinetic data of Re3 in ACN following 350 nm pulsed excitation. (A) Single wavelength kinetic analysis at 370 nm. (B) Single wavelength kinetic analysis at 425 nm. (C) Single wavelength kinetic analysis at 500 nm. (D) Single wavelength kinetic analysis at 475 nm	200
Figure A61 Global fit spectral analysis of ultrafast transient absorption data of Re(PONI-phen)(CO) ₃ Cl in THF (A), Re3 in THF (B), and Re3 in ACN (C) following 350 nm pulsed excitation.....	201

Figure A62 Excited-state absorption difference spectra of PSNI in ACN during short delay times (A) and long delay times (B) following 400 nm pulsed excitation (105 fs fwhm)	202
Figure A63 Ultrafast transient absorption kinetic data of Re4 in ACN following 400 nm pulsed excitation. Single wavelength kinetic analysis at 450 nm (A), 520 nm (B), and 615 (C) at short time after the laser pulse. Single wavelength kinetic analysis at 390 nm (D), 430 nm (E), and 650 (F) at longer time after the laser pulse	203
Figure A64 Global fit spectral analysis of ultrafast transient absorption data of Re(PSNI-phen)(CO) ₃ Cl in THF (A), Re4 in THF (B), and Re4 in ACN (C) following 400 nm pulsed excitation.....	204
Figure A65 Excited-state absorption difference spectra of PNI in ACN during short delay times (A) and long delay times (B) following 400 nm pulsed excitation (105 fs fwhm)	205
Figure A66 Ultrafast transient absorption kinetic data of Re5 in ACN following 400 nm pulsed excitation. Single wavelength kinetic analysis at 425 nm (A) and 550 nm (B) at short time after the laser pulse. Single wavelength kinetic analysis at 415 nm (C) and 475 nm (D) at longer time after the laser pulse.....	206
Figure A67 Global fit spectral analysis of ultrafast transient absorption data of Re(PNI-phen)(CO) ₃ Cl in THF (A), Re5 in THF (B), and Re5 in ACN (C) following 400 nm pulsed excitation.....	207
Figure A68 Excited-state absorption difference spectra of Re6 in ACN following 400 nm pulsed excitation (105 fs fwhm).....	208
Figure A69 Ultrafast transient absorption kinetic data of Re6 in ACN following 400 nm pulsed excitation.....	208
Figure A70 Excited-state absorption difference spectra of NI (A), BrNI (B), PONI (C), and PSNI (D) in ACN following 350 nm pulsed excitation (3 mJ/pulse, 7 ns fwhm)	210
Figure A71 Transient absorption decay of NI in ACN. Excited at 355 nm (3 mJ/pulse)	211
Figure A72 Transient absorption decay of BrNI in ACN. Excited at 355 nm (3 mJ/pulse).....	211
Figure A73 Transient absorption decay of PONI in ACN. Excited at 355 nm (3 mJ/pulse)....	211
Figure A74 Transient absorption decay of PSNI in ACN. Excited at 355 nm (3 mJ/pulse).....	212
Figure A75 Excited-state absorption difference spectra of Re1 (A), Re2 (B), Re3 (C), Re4 (D), and Re5 (E) in THF. Re1-3 were excited using a Continuum Minilite with	

355 nm pulsed excitation (3.4 mJ/pulse, 5 ns fwhm). Re4-5 were excited using the OPOTEK with 410 nm pulsed excitation (3 mJ/pulse, 7 ns fwhm)	213
Figure A76 Transient absorption decay of Re1 in ACN (top) and THF (bottom). Excited at 355 nm (3 mJ/pulse)	214
Figure A77 Transient absorption decay of Re2 in ACN (top) and THF (bottom). Excited at 355 nm (3 mJ/pulse)	215
Figure A78 Transient absorption decay of Re3 in ACN (top) and THF (bottom). Excited at 355 nm (3 mJ/pulse)	216
Figure A79 Transient absorption decay of Re4 in ACN (top) and THF (bottom). Excited at 410 nm (3 mJ/pulse)	217
Figure A80 Transient absorption decay of Re5 in ACN (top) and THF (bottom). Excited at 410 nm (3 mJ/pulse)	218
Figure A81 Transient absorption decay of Re6 in ACN (top) and THF (bottom). Excited at 410 nm (3 mJ/pulse)	219
Figure A82 Natural transition orbitals for selected $S_0 \rightarrow S_n$ and $S_0 \rightarrow T_n$ excitations of NI determined at the M06/Def2-SVP (left) and CAM-B3LYP/Def2-SVP (right) levels of theory; λ is the fraction of the hole-particle contribution to the excitation	222
Figure A83 Natural transition orbitals for selected $S_0 \rightarrow S_n$ and $S_0 \rightarrow T_n$ excitations of BrNI determined at the M06/Def2-SVP (left) and CAM-B3LYP/Def2-SVP (right) levels of theory; λ is the fraction of the hole-particle contribution to the excitation	223
Figure A84 Natural transition orbitals for selected $S_0 \rightarrow S_n$ and $S_0 \rightarrow T_n$ excitations of PONI determined at the M06/Def2-SVP (left) and CAM-B3LYP/Def2-SVP (right) levels of theory; λ is the fraction of the hole-particle contribution to the excitation	224
Figure A85 Natural transition orbitals for selected $S_0 \rightarrow S_n$ and $S_0 \rightarrow T_n$ excitations of PSNI determined at the M06/Def2-SVP (left) and CAM-B3LYP/Def2-SVP (right) levels of theory; λ is the fraction of the hole-particle contribution to the excitation	225
Figure A86 Natural transition orbitals for selected $S_0 \rightarrow S_n$ and $S_0 \rightarrow T_n$ excitations of PNI determined at the M06/Def2-SVP (left) and CAM-B3LYP/Def2-SVP (right) levels of theory; λ is the fraction of the hole-particle contribution to the excitation	226

Figure A87 Natural transition orbitals for selected $S_0 \rightarrow S_n$ and $S_0 \rightarrow T_n$ excitations of Re1 determined at the M06/Def2-SVP (left) and CAM-B3LYP/Def2-SVP (right) levels of theory; λ is the fraction of the hole-particle contribution to the excitation	229
Figure A88 Natural transition orbitals for selected $S_0 \rightarrow S_n$ and $S_0 \rightarrow T_n$ excitations of Re2 determined at the M06/Def2-SVP (left) and CAM-B3LYP/Def2-SVP (right) levels of theory; λ is the fraction of the hole-particle contribution to the excitation	230
Figure A89 Natural transition orbitals for selected $S_0 \rightarrow S_n$ and $S_0 \rightarrow T_n$ excitations of Re3 determined at the M06/Def2-SVP (left) and CAM-B3LYP/Def2-SVP (right) levels of theory; λ is the fraction of the hole-particle contribution to the excitation	231
Figure A90 Natural transition orbitals for selected $S_0 \rightarrow S_n$ and $S_0 \rightarrow T_n$ excitations of Re4 determined at the M06/Def2-SVP (left) and CAM-B3LYP/Def2-SVP (right) levels of theory; λ is the fraction of the hole-particle contribution to the excitation	232
Figure A91 Natural transition orbitals for selected $S_0 \rightarrow S_n$ and $S_0 \rightarrow T_n$ excitations of Re5 determined at the M06/Def2-SVP (left) and CAM-B3LYP/Def2-SVP (right) levels of theory; λ is the fraction of the hole-particle contribution to the excitation	233
Figure A92 Natural transition orbitals for selected $S_0 \rightarrow S_n$ and $S_0 \rightarrow T_n$ excitations of Re6 determined at the M06/Def2-SVP (left) and CAM-B3LYP/Def2-SVP (right) levels of theory; λ is the fraction of the hole-particle contribution to the excitation	233
Figure B1 ^1H NMR spectrum of NNI-py in in CD_2Cl_2 (400 MHz). (A) Full spectrum and (B) Zoomed in aromatic region	235
Figure B2 ^1H NMR spectrum of PNI-py in in CD_2Cl_2 (400 MHz)	236
Figure B3 ^1H NMR spectrum of <i>fac</i> -[Re(phen)(CO) ₃ (PNI-py)](PF ₆) (Re1) in CD_2Cl_2 (400 MHz)	237
Figure B4 HRMS of <i>fac</i> -[Re(phen)(CO) ₃ (PNI-py)](PF ₆) (Re1)	238
Figure B5 ^1H NMR spectrum of <i>fac</i> -[Re(bcp)(CO) ₃ (PNI-py)](PF ₆) (Re2) in CD_2Cl_2 (400 MHz). Due to overlapping signals from the 10 protons of the phenyl rings on the bcp ligand and the single proton on the naphthalene ring in PNI that yields a triplet at 7.74-7.57 ppm, the program integrated that region to 12 when it should be 11	239

Figure B6	HRMS of <i>fac</i> -[Re(bcp)(CO) ₃ (PNI-py)](PF ₆) (Re2)	240
Figure B7	¹ H NMR spectrum of <i>fac</i> -[Re(dtbb)(CO) ₃ (PNI-py)](PF ₆) (Re3) in CD ₂ Cl ₂ (400 MHz)	241
Figure B8	HRMS of <i>fac</i> -[Re(dtbb)(CO) ₃ (PNI-py)](PF ₆) (Re3).....	242
Figure B9	¹ H NMR spectrum of <i>fac</i> -[Re(deeb)(CO) ₃ (PNI-py)](PF ₆) (Re4) in CD ₂ Cl ₂ (400 MHz)	243
Figure B10	HRMS of <i>fac</i> -[Re(deeb)(CO) ₃ (PNI-py)](PF ₆) (Re4)	244
Figure B11	¹ H NMR spectrum of <i>fac</i> -[Re(biq)(CO) ₃ (PNI-py)](PF ₆) (Re5) in CD ₂ Cl ₂ (400 MHz)	245
Figure B12	HRMS of <i>fac</i> -[Re(biq)(CO) ₃ (PNI-py)](PF ₆) (Re5).....	246
Figure B13	¹ H NMR spectrum of <i>fac</i> -[Re(phen)(CO) ₃ (4-etry)](PF ₆) (Mod1) in CD ₂ Cl ₂ (400 MHz)	247
Figure B14	HRMS of <i>fac</i> -[Re(phen)(CO) ₃ (4-etry)](PF ₆) (Mod1)	248
Figure B15	¹ H NMR spectrum of <i>fac</i> -[Re(bcp)(CO) ₃ (4-etry)](PF ₆) (Mod2) in CD ₂ Cl ₂ (400 MHz)	249
Figure B16	HRMS of <i>fac</i> -[Re(bcp)(CO) ₃ (4-etry)](PF ₆) (Mod2)	250
Figure B17	¹ H NMR spectrum of <i>fac</i> -[Re(dtbb)(CO) ₃ (4-etry)](PF ₆) (Mod3) in CD ₂ Cl ₂ (400 MHz)	251
Figure B18	HRMS of <i>fac</i> -[Re(dtbb)(CO) ₃ (4-etry)](PF ₆) (Mod3).....	252
Figure B19	¹ H NMR spectrum of <i>fac</i> -[Re(deeb)(CO) ₃ (4-etry)](PF ₆) (Mod4) in CD ₂ Cl ₂ (400 MHz)	253
Figure B20	HRMS of <i>fac</i> -[Re(deeb)(CO) ₃ (4-etry)](PF ₆) (Mod4).....	254
Figure B21	¹ H NMR spectrum of <i>fac</i> -[Re(biq)(CO) ₃ (4-etry)](PF ₆) (Mod5) in CD ₂ Cl ₂ (400 MHz)	255
Figure B22	HRMS of <i>fac</i> -[Re(biq)(CO) ₃ (4-etry)](PF ₆) (Mod5).....	256
Figure B23	ATR-FTIR spectra of Re1-5 , Mod1-5 , and PNI-py overlaid.....	257
Figure B24	HOMO, LUMO, and LUMO + 1 of Mod1-5 . M06//Def2-SVP/SDD PCM: THF	275

Figure B25 HOMO, LUMO, and LUMO + 1 of Re1-5 . M06//Def2-SVP/SDD PCM: THF ...	275
Figure B26 LUMO + 2 of Re1 . M06//Def2-SVP/SDD PCM: THF	277
Figure B27 Triplet spin densities of Mod1-5 and Re1-5 . M06//Def2-SVP/SDD PCM: THF	279
Figure B28 Additive combination of electronic spectra between PNI , Re(I) model and Re(I) complex in THF.....	280
Figure B29 77 K of PNI-py triplet sensitized using 10% EtI. Blue shoulder is residual fluorescence. Energy estimated by converting to wavenumbers and taking the peak maximum	281
Figure B30 Excited-state absorption difference spectra of Mod1 (A), Mod2 (B), Mod3 (C), Mod4 (D), and Mod5 (E) in THF. Mod1-5 were excited using a Continuum Minilite with 355 nm pulsed excitation (5.0 mJ/pulse, 5 ns fwhm).....	282
Figure B31 Time-resolved photoluminescence spectra of Mod1 (A), Mod2 (B), Mod3 (C), Mod4 (D), and Mod5 (E) in THF. Mod1-5 were excited using a Continuum Minilite with 355 nm pulsed excitation (5.0 mJ/pulse, 5 ns fwhm).....	283
Figure B32 nsTA (left, 450 nm) and photoluminescence (right, 557 nm) decays of Mod1 . Excited at 410 nm (2.0 mJ/pulse).....	284
Figure B33 nsTA (left, 520 nm) and photoluminescence (right, 556 nm) decays of Mod2 . Excited at 410 nm (2.0 mJ/pulse).....	284
Figure B34 nsTA (left, 455 nm) and photoluminescence (right, 556 nm) decays of Mod3 . Excited at 410 nm (2.0 mJ/pulse).....	284
Figure B35 nsTA (left, 475 nm) and photoluminescence (right, 627 nm) decays of Mod4 . Excited at 410 nm (2.0 mJ/pulse).....	285
Figure B36 nsTA (left, 403 nm) and photoluminescence (right, 660 nm) decays of Mod5 . Excited at 410 nm (2.0 mJ/pulse).....	285
Figure B37 Excited-state absorption difference spectra of Re1 (92.3 μ M) in THF excited using a Continuum Minilite with 355 nm pulsed excitation (5.0 mJ/pulse, 5 ns fwhm)	285
Figure B38 Excited-state absorption difference spectra of Re3 (90.7 μ M) in THF excited using a Continuum Minilite with 355 nm pulsed excitation (5.0 mJ/pulse, 5 ns fwhm)	286

Figure B39 Excited-state absorption difference spectra of Re4 (93.0 μM) in THF excited using a Continuum Minilite with 355 nm pulsed excitation (5.0 mJ/pulse, 5 ns fwhm)	286
Figure B40 Time-resolved photoluminescence spectra of Re1 at early times (left) and later times (right) after excitation using a Continuum Minilite with 355 nm pulsed excitation (5.0 mJ/pulse, 5 ns fwhm)	286
Figure B41 Time-resolved photoluminescence spectra of Re2 at early times (left) and later times (right) after excitation using a Continuum Minilite with 355 nm pulsed excitation (5.0 mJ/pulse, 5 ns fwhm)	287
Figure B42 Time-resolved photoluminescence spectra of Re3 at early times (left) and later times (right) after excitation using a Continuum Minilite with 355 nm pulsed excitation (5.0 mJ/pulse, 5 ns fwhm)	287
Figure B43 Time-resolved photoluminescence emission spectra of Re5 at specified times after excitation using a Continuum Minilite with 355 nm pulsed excitation (5.0 mJ/pulse, 5 ns fwhm).....	288
Figure B44 The concentration dependent study of Re1 showing self-quenching behavior using the LP 920 laser flash photolysis system (Edinburgh Instruments) with a Vibrant 355 Nd:YAG/OPO system (OPOTEK) for pulsed laser excitation for single wavelength kinetics detection at 465 nm ($\lambda_{\text{ex}} = 410$ nm, 2.0 mJ/pulse).....	288
Figure B45 The concentration dependent study of Re3 showing self-quenching behavior using the LP 920 laser flash photolysis system (Edinburgh Instruments) with a Vibrant 355 Nd:YAG/OPO system (OPOTEK) for pulsed laser excitation for single wavelength kinetics detection at 465 nm ($\lambda_{\text{ex}} = 410$ nm, 2.0 mJ/pulse).....	288
Figure B46 The concentration dependent study of Re4 showing self-quenching behavior using the LP 920 laser flash photolysis system (Edinburgh Instruments) with a Vibrant 355 Nd:YAG/OPO system (OPOTEK) for pulsed laser excitation for single wavelength kinetics detection at 465 nm ($\lambda_{\text{ex}} = 410$ nm, 2.0 mJ/pulse).....	289
Figure B47 nsTA decay at 400 nm of Re5 . Excited at 410 nm (2.0 mJ/pulse).....	289
Figure B48 Excited-state absorption difference spectra of Mod1 (A), Mod2 (B), Mod3 (C), Mod4 (D), and Mod5 (E) in THF following 400 nm pulsed excitation (105 fs fwhm, 0.7 μJ /pulse).....	290
Figure B49 Ultrafast transient absorption kinetic data of Mod1 in THF following 400 nm pulsed excitation. Single wavelength kinetic analysis at 460 nm	291
Figure B50 Ultrafast transient absorption kinetic data of Mod2 in THF following 400 nm pulsed excitation. Single wavelength kinetic analysis at 520 nm	291

Figure B51 Ultrafast transient absorption kinetic data of Mod3 in THF following 400 nm pulsed excitation. Single wavelength kinetic analysis at 455 nm	291
Figure B52 Ultrafast transient absorption kinetic data of Mod4 in THF following 400 nm pulsed excitation. Single wavelength kinetic analysis at 550 nm	292
Figure B53 Ultrafast transient absorption kinetic data of Mod5 in THF following 400 nm pulsed excitation. Single wavelength kinetic analysis at 550 nm	292
Figure B54 Excited-state absorption difference spectra of Re1 in THF following 400 nm pulsed excitation (105 fs fwhm).....	292
Figure B55 Excited-state absorption difference spectra of Re3 in THF following 400 nm pulsed excitation (105 fs fwhm).....	293
Figure B56 Excited state absorption difference spectra of Re4 in THF excited following 400 nm pulsed laser excitation (105 fs fwhm)	293
Figure B57 Ultrafast transient absorption kinetic data of Re1 in THF following 400 nm pulsed excitation. Single wavelength kinetic analysis at 430 nm	293
Figure B58 Ultrafast transient absorption kinetic data of Re2 in THF following 400 nm pulsed excitation. Single wavelength kinetic analysis at 430 nm	294
Figure B59 Ultrafast transient absorption kinetic data of Re3 in THF following 400 nm pulsed excitation. Single wavelength kinetic analysis at 430 nm	294
Figure B60 Ultrafast transient absorption kinetic data of Re4 in THF following 400 nm pulsed excitation. Single wavelength kinetic analysis at 430 nm	294
Figure B61 Ultrafast transient absorption kinetic data of Re5 in THF following 400 nm pulsed excitation. Single wavelength kinetic analysis at 435 nm	295
Figure B62 Energy level diagram of Mod1-5 . The mixed ³ MLCT and LC is for Mod1-2 only	295
Figure C1 700 MHz ¹ HNMR of 16H-benzo[4',5']isoquinolino[2',1':1,2]imidazo[4,5-f][1,10]phenanthrolin-16-one (NBI-phen) in CDCl ₃ at 300K.....	303
Figure C2 176 MHz ¹³ CNMR of 16H-benzo[4',5']isoquinolino[2',1':1,2]imidazo[4,5-f][1,10]phenanthrolin-16-one (NBI-phen) in CDCl ₃ at 300K.....	304
Figure C3 HR-ESIMS of 16H-benzo[4',5']isoquinolino[2',1':1,2]imidazo[4,5-f][1,10]phenanthrolin-16-one (NBI-phen)	305

Figure C4	700 MHz ^1H NMR of fac-[Re(NBI-phen)(CO) $_3$ (PPh $_3$)](PF $_6$) (Re1) in DMSO at 300K	306
Figure C5	176 MHz ^{13}C NMR of fac-[Re(NBI-phen)(CO) $_3$ (PPh $_3$)](PF $_6$) (Re1) in DMSO at 300K	307
Figure C6	HR-ESIMS of fac-[Re(NBI-phen)(CO) $_3$ (PPh $_3$)](PF $_6$) (Re1)	308
Figure C7	700 MHz ^1H NMR of fac-[Re(NBI-phen)(CO) $_3$ (CH $_3$ CN)](PF $_6$) (Re2) in CD $_3$ CN at 300K	309
Figure C8	176 MHz ^{13}C NMR of fac-[Re(NBI-phen)(CO) $_3$ (CH $_3$ CN)](PF $_6$) (Re2) in CH $_3$ CN at 300K	310
Figure C9	HR-ESIMS of fac-[Re(NBI-phen)(CO) $_3$ (CH $_3$ CN)](PF $_6$) (Re2).....	311
Figure C10	700 MHz ^1H NMR of fac-[Re(phen)(CO) $_3$ (PPh $_3$)](PF $_6$) (Mod1) in CD $_3$ CN at 300K	312
Figure C11	176 MHz ^{13}C NMR of fac-[Re(phen)(CO) $_3$ (PPh $_3$)](PF $_6$) (Mod1) in CD $_3$ CN at 300K	313
Figure C12	HR-ESIMS of fac-[Re(phen)(CO) $_3$ (PPh $_3$)](PF $_6$) (Mod1)	314
Figure C13	700 MHz ^1H NMR of fac-[Re(phen)(CO) $_3$ (CH $_3$ CN)](PF $_6$) (Mod2) in CD $_2$ Cl $_2$ at 300K	315
Figure C14	176 MHz ^{13}C NMR of fac-[Re(phen)(CO) $_3$ (CH $_3$ CN)](PF $_6$) (Mod2) in CD $_2$ Cl $_2$ at 300K	316
Figure C15	HR-ESIMS of fac-[Re(phen)(CO) $_3$ (CH $_3$ CN)](PF $_6$) (Mod2)	317
Figure C16	Frontier molecular orbital diagrams of the model Re(I)-CDI complex Mod2 and corresponding NBI-phen complex Re2 , where L = CH $_3$ CN.....	318
Figure C17	Experimental electronic absorption spectra overlay of Mod1 with calculated singlet excited states	318
Figure C18	Experimental electronic absorption spectra overlay of Re1 with calculated singlet excited states	319
Figure C19	Experimental electronic absorption spectra overlay of Mod2 with calculated singlet excited states	319
Figure C20	Experimental electronic absorption spectra overlay of Re2 with calculated singlet excited states	320

Figure C21	Natural transition orbitals for the three lowest transitions of Mod1 predicted via TD-DFT at the PBE0-D3/Def2-SVP level of theory; λ is the fraction of the hole–particle contribution to the excitation.....	320
Figure C22	Natural transition orbitals for the three lowest transitions of Re1 predicted via TD-DFT at the PBE0-D3/Def2-SVP level of theory; λ is the fraction of the hole–particle contribution to the excitation.....	321
Figure C23	Natural transition orbitals for the three lowest transitions of Mod2 predicted via TD-DFT at the PBE0-D3/Def2-SVP level of theory; λ is the fraction of the hole–particle contribution to the excitation.....	322
Figure C24	Natural transition orbitals for the three lowest transitions of Re2 predicted via TD-DFT at the PBE0-D3/Def2-SVP level of theory PCM: THF; λ is the fraction of the hole–particle contribution to the excitation.....	323
Figure C25	Natural orbitals of Re1 . PBE0-D3/Def2-SVP level of theory PCM: THF	324
Figure C26	Natural orbitals of Re2 . PBE0-D3/Def2-SVP level of theory PCM: THF	324
Figure C27	Triplet spin densities of (A) Re1 and (B) Re2 . PBE0-D3/Def2-SVP level of theory PCM: THF.....	325
Figure C28	Natural transition orbitals for the three lowest transitions of NBI-phen predicted via TD-DFT at the PBE0-D3/Def2-SVP level of theory PCM: THF; λ is the fraction of the hole–particle contribution to the excitation	325
Figure C29	Electronic absorption spectra and PL of NBI in THF.....	332
Figure C30	Aerated PL of Re1 (left) and Re2 (right). Feature at 473 nm is Raman band of THF excited at 415 nm.....	332
Figure C31	Excitation scans of Re1 , Mod1 (left) and Re2 , Mod2 (right). Monitored PL peak is denoted in the legend.....	333
Figure C32	UFTA of (A) Re1 in THF following 400 nm pulsed laser excitation (105 fs fwhm, 0.3 mJ/pulse) and (B) nsTA of Re1 in deaerated THF following 415 nm excitation (1.8 mJ/pulse)	333
Figure C33	Ultrafast transient absorption kinetic data of Re1 in THF following 400 nm pulsed excitation. Single wavelength kinetic analysis at 460 nm	334
Figure C34	Ultrafast transient absorption kinetic data of Re1 in THF following 400 nm pulsed excitation. Single wavelength kinetic analysis at 460 nm	334

Figure C35 Kinetic traces and fits of Re1 at 2.0 (A), 1.6 (B), 1.2 (C), and 0.8 (D) mJ/pulse in deaerated THF ($\lambda_{\text{ex}} = 415 \text{ nm}$).....	336
Figure C36 Kinetic traces and fits of Re2 at 2.0 (A), 1.7 (B), 1.4 (C), and 1.0 (D) mJ/pulse in deaerated THF ($\lambda_{\text{ex}} = 415 \text{ nm}$).....	336
Figure C37 UFTA of NBI in THF following 400 nm pulsed laser excitation (105 fs fwhm, 0.5 mJ/pulse)	336
Figure C38 Nanosecond transient absorption spectra of (A) UFTA of Mod1 following 350 nm excitation (105 fs fwhm, 50 $\mu\text{J/pulse}$) in THF and (B) nsTA of Mod1 following 355 nm excitation (1.8 mJ/pulse) in deaerated THF.....	337
Figure C39 Ultrafast transient absorption kinetic data of Mod1 following 350 nm excitation (105 fs fwhm, 50 $\mu\text{J/pulse}$) in THF. Single wavelength kinetic analysis at 500 nm.....	337
Figure C40 Ultrafast transient absorption kinetic data of Mod2 following 350 nm excitation (105 fs fwhm, 50 $\mu\text{J/pulse}$) in THF. Single wavelength kinetic analysis at 500 nm.....	338
Figure C41 Time-resolved photoluminescence data of Re1 at (A) room temperature in deaerated THF and (B) 77 K in 2-MeTHF following 415 nm excitation (1.8 mJ/pulse)	338
Figure C42 Time-resolved photoluminescence spectra of Mod1 after excitation using a Continuum Minilite with 355 nm pulsed excitation (2.0 mJ/pulse, 5 ns fwhm)....	339
Figure C43 Time-resolved photoluminescence spectra of Mod2 after excitation using a Continuum Minilite with 355 nm pulsed excitation (2.0 mJ/pulse, 5 ns fwhm)....	339
Figure C44 nsTA kinetics (left) and PL kinetics (right) of Mod1 in THF after excitation using a Continuum Minilite with 355 nm pulsed excitation (2.0 mJ/pulse, 5 ns fwhm). Intense noise on nsTA kinetics due to a ND filter being placed in front of Xe arc lamp to reduce amount of decomposition of sample.....	340
Figure C45 nsTA kinetics (left) and PL kinetics (right) of Mod2 in THF after excitation using a Continuum Minilite with 355 nm pulsed excitation (2.0 mJ/pulse, 5 ns fwhm)	340

Chapter 1: An Introduction to the Fundamentals of Molecular Photoprocesses

1.1. Photochemistry vs. Photophysics

Photochemical and photophysical processes have been closely linked to the development of life on this planet. These processes, photochemistry and photophysics are terms commonly taught together in classes. However, these two words are not interchangeable despite their shared prefix and they differ in the processes that they describe. *Photochemistry* refers to the chemical changes induced by the absorption of a photon and eventuates in the formation of an isolated photoproduct. *Photophysics* refers to the competing physical processes that deactivate an electronically excited state (referred to from hereon as excited state and denoted by an asterisk) and result in the regeneration of the original ground state species. The processes that deactivate an excited state include radiative (r) and nonradiative (nr) decay processes.¹ While the molecules discussed in detail later in this document are capable of fueling photochemical reactions, the focus of this work is to follow the radiative and nonradiative decay pathways from the initially prepared excited state species back to the original ground state.

1.2. Photophysical Processes

1.2.1. Light Absorption

The principle interaction between light and matter occurs when a molecule absorbs a photon of frequency that matches an allowed energy change within the molecule, i.e. the Bohr equation,

$$h\nu = E_f - E_i \quad (\text{Eq. 1.1})$$

Where E_f and E_i are the energies of the excited state wavefunction (Ψ_f) and the ground state wavefunction (Ψ_i) respectively. Not only must the energies match, there has to be a direct interaction with the electromagnetic field of the photon and the molecule. Since the effect of the

magnetic field is so weak on the molecule, the electric vector of the exciting photon and the electric dipole of the molecule are only considered during the light absorption process.¹

The process of absorbing light can be further discussed in terms of the time-dependent perturbation theory in which the initial state of the molecule's wavefunction can be described by the Schrödinger equation,

$$\hat{H}_0 \Psi_i = E \Psi_i \quad (\text{Eq. 1.2})$$

Once exposed to light, the Hamiltonian operator, \hat{H}_0 , is no longer able to describe the energy of the system due to the change in dipole moment of the molecule induced by the absorption of light. Therefore, the perturbation operator, \hat{H}' , must be added to the Hamiltonian to describe the new effects on the molecule resulting from the irradiation process. The eigenfunctions of $(\hat{H}_0 + \hat{H}')$ will be different than Ψ_i and will also be functions of time:

$$(\hat{H}_0 + \hat{H}') \Psi(x, t) = E \Psi(x, t) \quad (\text{Eq. 1.3})$$

where Ψ is the total wavefunction. The perturbation effect can be thought of as a time-dependent mixing of the initial wavefunction with all other possible wavefunctions. Once the perturbation is removed at time t , there is a finite probability that the molecule will be found in the final wavefunction, Ψ_f , distinctively different than the initial wavefunction. This probability is proportional to the square of the *transition dipole moment* (TM). In bra-ket notation (Eq. 1.4), the TM is written in shorthand as

$$\langle \Psi_i | \hat{\mu} | \Psi_f \rangle \quad (\text{Eq. 1.4})$$

which is shorthand for writing the TM in integral notation ($\int \Psi_i \hat{\mu} \Psi_f d\tau$) and $\hat{\mu}$ is the *dipole-moment operator*.¹

If the probability of a transition is proportional to the square of the transition moment, then the probability of a given transition can be calculated from the absorption spectra through its relation with the

oscillator strength f , which is a measure of the integrated intensity of the absorption over the band (Eq. 1.5).¹

$$f = 4.315 \times 10^{-9} \int \epsilon d\nu = \frac{8\pi^2 \nu_{if} m_e}{3he^2} \langle \Psi_i | \hat{\mu} | \Psi_f \rangle^2 \quad (\text{Eq. 1.5})$$

Using the Born—Oppenheimer approximation, we can separate the total wavefunction, Ψ into an electronic wavefunction, ψ , and a vibrational wavefunction, θ (Eq. 1.6) due to light absorption processes occurring on a much shorter time scale with respect to nuclear motions (vibrations).

$$\text{TM} = \int \psi_f \theta_f \hat{\mu} \psi_i \theta_i d\tau \quad (\text{Eq. 1.6})$$

Using the Born—Oppenheimer approximation, the dipole-moment operator does not affect nuclear coordinates and Eq. 1.5 can be separated into two parts which consists of an electronic and nuclear (vibrational) component (θ). Upon further approximation of the electronic wavefunction, it can be separated into one electron wavefunction, ϕ , and the corresponding spin wavefunction, S (Eq. 1.7)

$$\text{TM} = \int \phi_i \hat{\mu} \phi_f d\tau_e \int S_i S_f d\tau_S \int \theta_i \theta_f d\tau_N \quad (\text{Eq. 1.7})$$

where ϕ_i and ϕ_f are the initial and final orbitals of the excited electron, S_i and S_f are the corresponding spin functions and θ_i and θ_f are the initial and final vibrational wavefunctions. The first term of Eq 1.7 corresponds to the orbital or electronic transition moment and depends on the orbital (spatial) overlap and symmetry of the initial and final wavefunctions. This gives rise to the symmetry selection rule where the direct product of the irreducible representations of the initial and final states must transform as one of the dipole operators (x, y, or z) as found in the character table of a molecule's point group for a transition to be considered orbitally allowed. The second term is called the spin overlap integral and depends on the initial and final spin states of the excited

electron. This term gives rise to the spin selection rule where the initial and final spin of the excited electron must be the same for a transition to be spin allowed. The final term is referred to as the overlap of the vibrational wavefunctions or Franck-Condon factors and is the quantum mechanical basis of the Franck-Condon principle. This factor can modulate the intensity of transitions, i.e. how much of the excited state potential energy surface overlaps with the ground state potential energy surface (Figure 1.1).¹⁻³

When considering the selection rules above and Eq. 1.7, it can be inferred that when any one of these terms is zero, i.e. the initial spin is a triplet and the final spin is a singlet, the total transition moment will also be zero and the transition is said to be *forbidden*. Also, if the initial and final wavefunctions are orthogonal, there will be no electronic transition even if the direct product transforms as x, y, or z. With that said, some transitions that are formally forbidden can still be observed in an absorption envelope due to exceptions to the spin selection rule. For example, an electronic transition can be coupled with an asymmetric vibration that breaks the symmetry of a system, relaxing the symmetry selection rule giving rise to a vibronically allowed transition. When this happens, the electronic and vibrational components of Ψ are no longer separable and the direct product of the orbital and vibrational irreducible representations govern their selection rules. The spin selection rule is fairly rigid but may be relaxed in the presence of a heavy atom to give rise to spin-orbit coupling (SOC) allowing a transition to occur between a singlet and triplet state.¹⁻³

1.2.2 The Franck-Condon Principle

The last term in the transition moment integral (Eq. 1.7), called the Franck-Condon term, is important in determining the shape of the absorption band. Since electronic motion is much quicker than nuclear motion, it is assumed that electronic transitions are *vertical* (i.e there is no change in nuclear coordinates during the electronic transition). Resting ground state electrons are most likely to be located in the lowest vibrational level ($v = 0$) at the ground state equilibrium geometry ($Q = 0$ where Q represents the nuclear coordinates). When the excited state potential energy surface (PES) is not displaced or distorted with respect to the ground state, there is maximum overlap between the $v = 0$ level of the ground state and $v = 0$ level of the excited state, leading to a 0-0 transition that reveals itself as a sharp and narrow absorption band (Figure 1.1a). When the excited state is geometrically distorted relative to the ground state, the instantaneous promotion of an electron results in population of a higher energy vibrational level ($v > 0$) with a nuclear geometry that most closely resembles that of the ground state. To determine the intensity distribution of the absorption band, the values of the vibrational overlap integrals for the various 0- v transitions need to be evaluated. The most intense portion of the band will appear where the maximum vibrational overlap occurs with the excited state vibrational level that intercepts the excited state potential energy surface (PES) at the equilibrium geometry (Figure 1.1b). The rest of the absorption band decreases in intensity as you go higher and lower in energy across the excited state PES vibrational levels as the overlap decreases between the excited state PES and the ground state equilibrium. Sometimes an excitation can lead to formation of the excited state at energies higher than the dissociation energy and the band shape will appear to be structured on the low energy side and featureless on the high energy side (Figure 1.1c).¹⁻³

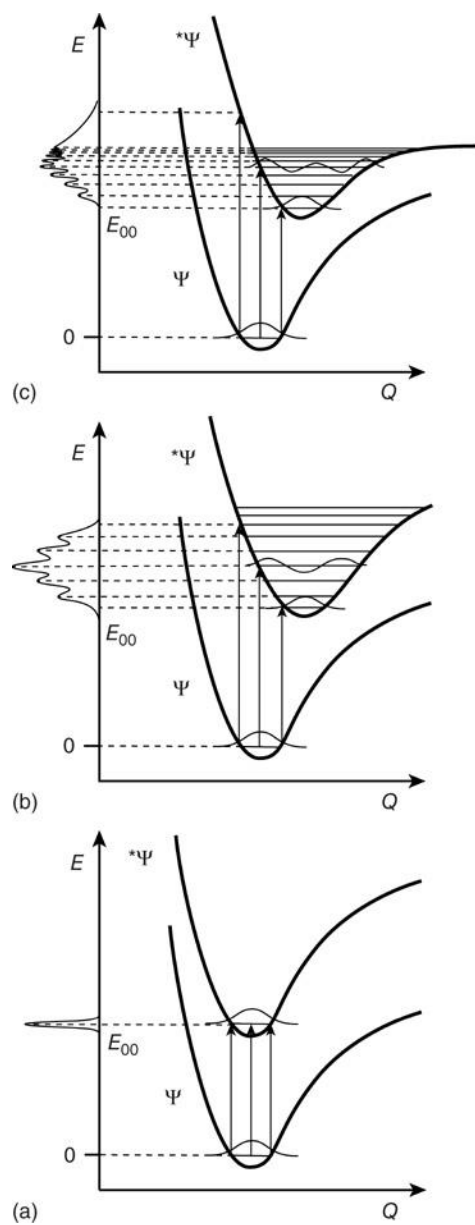


Figure 1.1. Illustration of the Franck-Condon principle where the excited state PES is distorted more along the nuclear coordinates (Q) and its effect on the absorption band. This figure was adapted from the literature.¹

When absorption profiles are obtained in the gas-phase or in a rigid glass, vibronic information can be elucidated as the absorption bands have structure and definition in the visible and ultraviolet regions. When absorption is obtained in solution however, most of that information is lost due to the interactions with solvent molecules and the superposition of different vibrational

progressions. On Jablonski diagrams, excitations are represented as vertical, solid arrows (Figure 1.3).¹⁻³

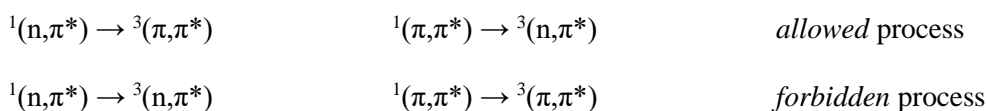
1.3. Excited State Decay

1.3.1. Non-radiative Decay Processes

Upon absorption of a quantum of light, a molecule promotes an electron from the ground state potential energy surface to an excited state potential energy surface. However, as discussed in Section 1.2.2, the newly formed excited state is generally not at the lowest vibrational level of the excited state surface. When an electron populates a higher vibrational level of a surface, it is regarded as “hot”, leading to the first type of non-radiative decay: vibrational relaxation. The molecule prefers to be at the zero vibrational level (i.e. the Boltzmann equilibrium) of the excited state surface and will release excess energy via collisions with nearby molecules. In solution, molecules vibrationally relax via collision with the solvent matrix. This type of non-radiative relaxation is among the fastest deactivation processes (10^{-13} s timescale). Therefore, all physical and chemical processes that occur from the excited state are assumed to take place from the thermally equilibrated excited state.^{1, 2}

Other non-radiative decay processes include internal conversion (IC) and intersystem crossing (ISC). Internal conversion is a radiationless transition that takes place between two excited states of the *same* multiplicity (e.g. singlet→singlet). When the energy gap between the two singlet states is small (corresponding to less than visible energy), the rate of IC is typically on the time scale of picoseconds (ps, 10^{-12} s). These transitions, similar to vibrational relaxation, are incredibly fast and therefore occur prior to any radiative processes. As a consequence, Kasha’s rule was formulated, which states that any photon emission comes from the lowest excited state of a specified multiplicity (i.e. S_1 not S_4).⁴ Intersystem crossing is similar to IC but is instead a

transition that takes place between two excited states of *different* multiplicity (e.g. singlet \rightarrow triplet). This procedure is formally spin forbidden (see Section 1.4.1) but can occur when the spin selection rule is sufficiently relaxed. For example, when the singlet-triplet gap is close enough that it can thermally populate the other, or with spin-orbit coupling induced by a heavy atom (heavy atom effect). Additionally, when ISC is observed in the absence of heavy atoms, it is often due to the interaction of excited states of different symmetry through spin-orbit coupling (El-Sayed Rules⁵). Because this is a forbidden process with respect to multiplicity, the process is generally slow but can become more efficient if the transition involves a change of orbital type:^{1, 2, 5}



Vibrational relaxation, both IC and ISC are represented as wavy, horizontal lines on a Jablonski diagram (Figure 1.3).

1.3.2. Radiative Decay Processes

As the name suggests, radiative decay processes involve a photon emitting from an excited state as the molecule relaxes back to the ground state. Most molecules conform to Kasha's rule where the emission takes place from the lowest excited state of a given spin multiplicity. However, there are notable exceptions to this rule, such as with porphyrins and azulene dye derivatives where radiative processes from S_2 are observed.⁶ With that said, for an excited state to radiatively decay, it must follow the same spin and symmetry selection rules as to which it was first promoted to an excited state. When a photon emits from a state of same spin as the ground state, it is called *fluorescence*. When a photon emits from a state of different spin (i.e. after ISC occurs), that emissive event is termed *phosphorescence*. Fluorescence has rate constants on the order of 10^9 s^{-1} due to their spin allowedness and phosphorescence has rate constants up to 1 s^{-1} due to it being a formally spin forbidden process. The extremely long rate constants are generally reserved to the long lived spin forbidden excited states

of organic molecules and can be much shorter once a heavy atom, such as ruthenium, is added to the system due to enhanced spin-orbit coupling; e.g. $\text{Ru}(\text{bpy})_3^{2+}$ has a $^3\text{MLCT}^*$ rate constant of $1.67 \times 10^6 \text{ s}^{-1}$ ($\tau = 600 \text{ ns}$) in water.⁷

As stated earlier, the Franck-Condon factor determines the band shape of the emissive event. When the PES of the excited state involves no change in nuclear coordinates with respect to the ground state (nested) the emission will appear to be narrow and sharp as if it were almost an atomic line spectrum (Figure 1a). The peak maximum will correspond to the 0-0 transition. When the PES of the excited state is not nested with respect to the ground state (highly distorted in the case of MLCT transitions), the emissions will be broad and Gaussian-shaped with a peak maximum at energies higher than the 0-0 transition. This effect is called the Stokes shift and corresponds to the shift in peak maximum of the absorption and emission bands. The greater the geometric distortion, the greater the Stokes shift. When the ground and excited states are considered identical harmonic oscillators, the absorption and emission envelope will be the mirror images of each other (Figure 1.2). As with the absorption of a photon, the emission of a photon is portrayed as a solid vertical arrow on a Jablonski diagram (Figure 1.3).^{1, 2, 8}

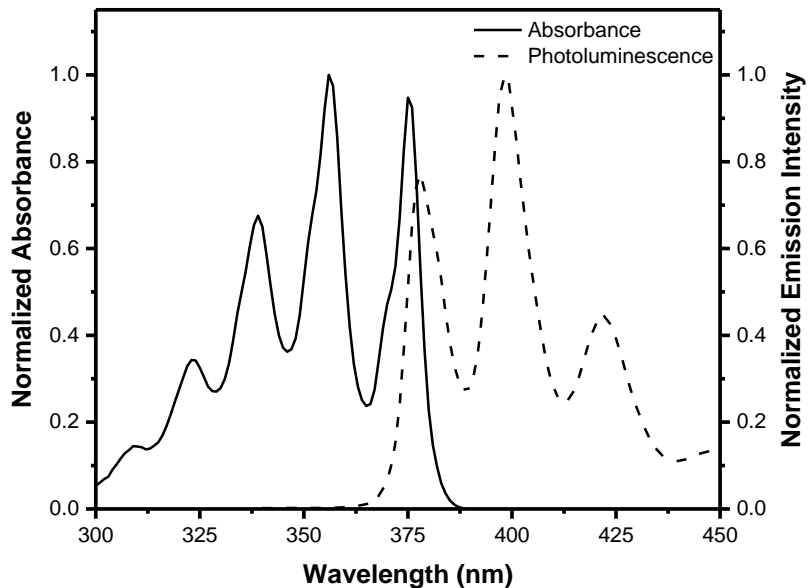


Figure 1.2. Normalized absorption and fluorescence spectra of anthracene in ethanol.

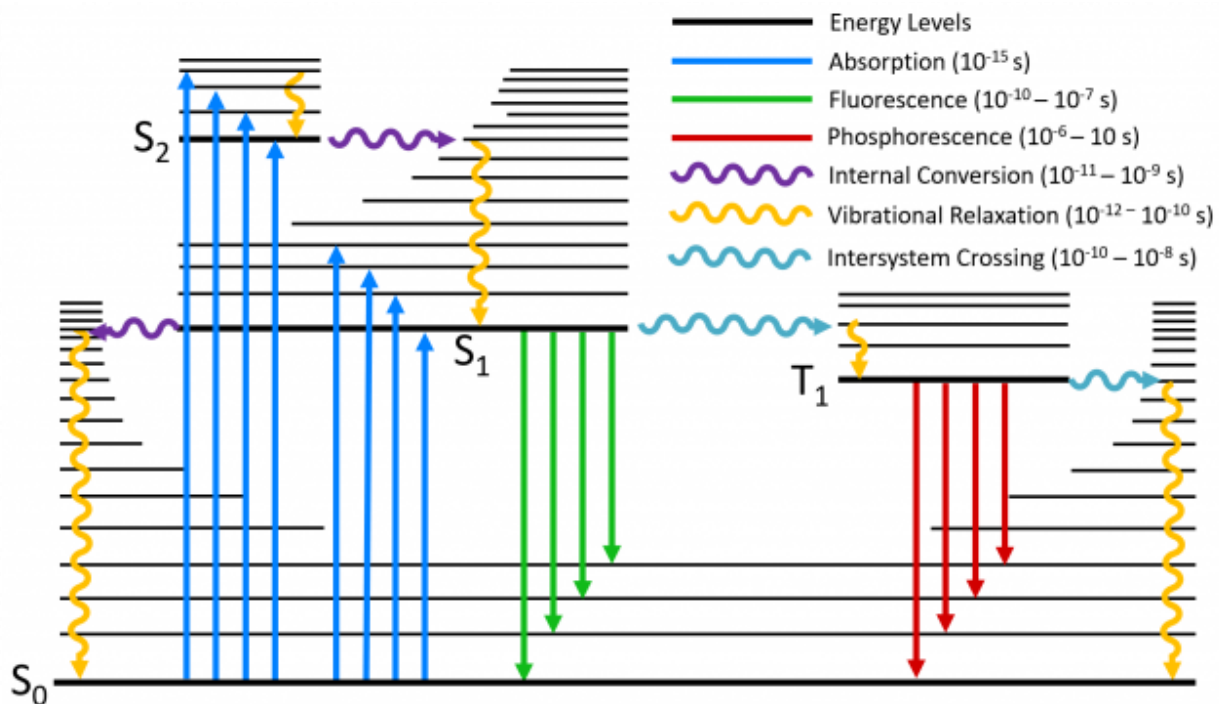


Figure 1.3. Jablonski (energy) diagram portraying absorption and the various excited state decay processes that follow. Figure adapted from Edinburgh Instruments (<https://www.edinst.com/blog/jablonski-diagram/>).

1.3.3. Quantum Yield and Excited State Lifetime

From the quantification of various radiative properties, valuable photophysical information can be obtained to glean insight into the dynamics of the excited state processes occurring after the initial absorption event has taken place. Two important pieces of information that can be obtained from the emission of a molecule are quantum yield (Φ) and lifetime (τ). The quantum yield of photoluminescence is the ratio of emitted photons to absorbed photons (Eq. 1.8). When a molecule is considered extremely emissive, its quantum yield is close to unity (100%) (e.g. rhodamines).⁸ Inspection of Eq 1.8 reveals that the underlying factors that determine the intensity of emission are the radiative rate constant (k_r) and non-radiative rate constant (k_{nr}) (IC, ISC, quenching, etc.).

$$\Phi_{PL} = \frac{\# \text{ photon emitted}}{\# \text{ photon absorbed}} = \frac{k_r}{k_r + k_{nr}} \quad (\text{Eq. 1.8})$$

The k_r and k_{nr} values are the factors that control the longevity of the excited state lifetime. The lifetime refers to the amount of time it takes for 1/e of the excited state molecules to return to the ground state and is equal to the inverse of $k_r + k_{nr}$ (Eq. 1.9).^{8,9}

$$\tau = \frac{1}{k_r + k_{nr}} \quad (\text{Eq. 1.9})$$

Combing Eqs. 1.8 and 1.9 allow for the exact values of k_r and k_{nr} to be determined, as shown in Eqs. 1.10 and 1.11.

$$\Phi_{PL} \times \tau = k_r \quad (\text{Eq. 1.10})$$

$$\frac{1}{\tau} - k_r = k_{nr} \quad (\text{Eq. 1.11})$$

Further details on how to measure the quantum yield and lifetime will be discussed later in the instrumentation section (1.4 Spectroscopic Instrumentation).

1.3.4. Bimolecular Quenching Processes

Once in the excited state, a molecule is energy-rich and will deactivate via radiative, non-radiative, and/or a variety of bimolecular chemical quenching processes to achieve a lower-energy, stable configuration. The molecule can undergo many bimolecular pathways to quench the excited state. One of the quenching processes is for the molecule to form the solvato complex with the solvent, called an exciplex, an excited state complex. An exciplex can also form between the excited state species and another molecule that is different than the original species. An excited molecule can also associate to a ground state molecule of the same species forming an excimer (an excited state dimer). These quenching pathways are generally undesirable and synthetic and experimental design is usually employed to prevent these species from forming.^{1,2}

Electron transfer (ET) and energy transfer (EnT) on the other hand are two quenching pathways that are usually desired, and molecules are synthesized with these processes in mind. Once in the excited state, a molecule becomes a better electron donor and a better electron acceptor than the respective ground state. This effect occurs because when an electron is promoted to a higher molecular orbital, it reduces its ionization potential, rendering the molecule more easily oxidized. When the electron is promoted to a higher molecular orbital, it leaves a hole behind in the energetically lower molecular orbital making the electron affinity for the excited state species greater than its ground state counterpart (i.e. more easily reduced). There are two pathways in which electron transfer can occur in the excited state: reductive and oxidative quenching. Reductive quenching describes the mechanism in which the acceptor is the excited state species and accepts an electron from a ground state donor. Oxidative quenching describes the mechanism in which the donor is the excited state species and donates an electron to a ground state acceptor (Figure 1.4). When using transition metal complexes, the complex itself can be both the donor and the acceptor due to redox sites present on the metal and

ligand.^{1, 2, 9} Electron transfer has been extensively studied since the late 60s and multiple examples can be found in the literature by Weller, Rhem, Marcus, and others.¹⁰⁻¹⁵

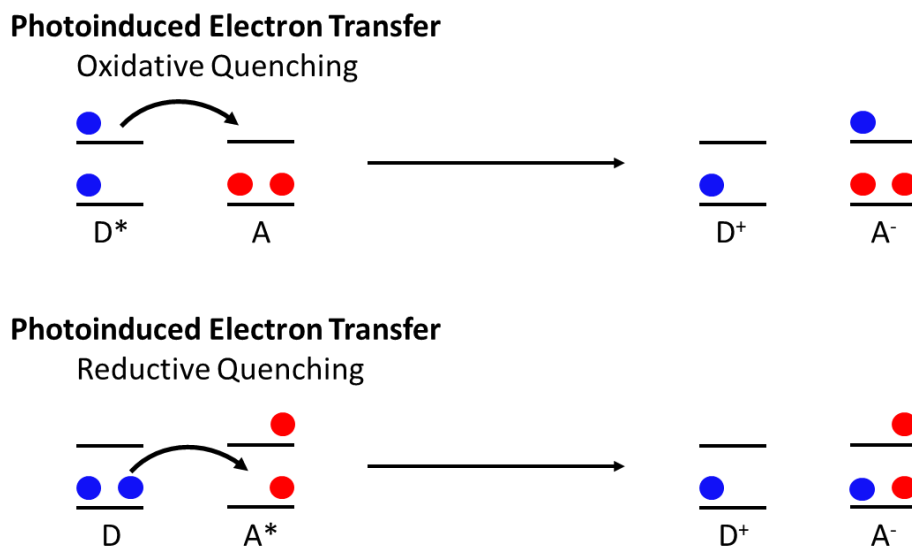


Figure 1.4. Photoinduced reductive and oxidative bimolecular electron transfer quenching mechanisms.

In order for either of these electron transfer quenching mechanisms to occur, an electron donor-acceptor system must meet these three criteria: sufficiently long lifetime, orbital overlap of participating orbitals, and thermodynamically favorable electron transfer. To transfer an electron, the donor orbital must be higher in energy than the acceptor so that the process is a downhill reaction. The donor and acceptor orbitals must overlap via close bonding proximity, or more likely, via collisions. For these collisions to occur, the lifetime of the excited state must be long enough to allow the donor and acceptor to diffuse through solution and collide. For this reason, it is primarily triplet excited states that participate in electron transfer due to their nanosecond to microsecond lifetimes.^{1, 2, 9}

Energy transfer has also been studied extensively but predates ET by a few decades, with pivotal contributions by Cairo,¹⁶ Franck,¹⁷ Cairo and Franck,¹⁸ Perrin F., and Perrin J.,¹⁹⁻²¹ Förster,^{22,}²³ Dexter,²⁴ and many others.²⁵⁻²⁷ There are two energy transfer processes that are of particular interest to this work and the photophysical world on the whole: Förster Resonance Energy Transfer (FRET or the Coulombic mechanism) (Figure 1.5) and Dexter Energy Transfer (DET or the electron exchange

mechanism) (Figure 1.6). FRET is a long-range mechanism that does not require physical contact between donor and acceptor. For this mechanism to occur, it requires the distance between donor and acceptor to be less than 10 nm, have substantial spectral overlap between the emission band of the donor and the absorption band of the acceptor, and non-orthogonal orientation between the donor and acceptor. This non-radiative energy transfer process proceeds via dipole-dipole coupling of the donor and acceptor. Given that the photoluminescence of the donor and absorption of the acceptor must spectrally overlap, the greater the quantum yield, absorption oscillator strengths, and spectral overlap integral, the stronger the FRET interaction. From the spectral overlap, the Förster distance (R_0^6) can be calculated, which is the distance in which EnT has 50% efficiency. This means that anything less than that distance has EnT efficiencies approaching unity.

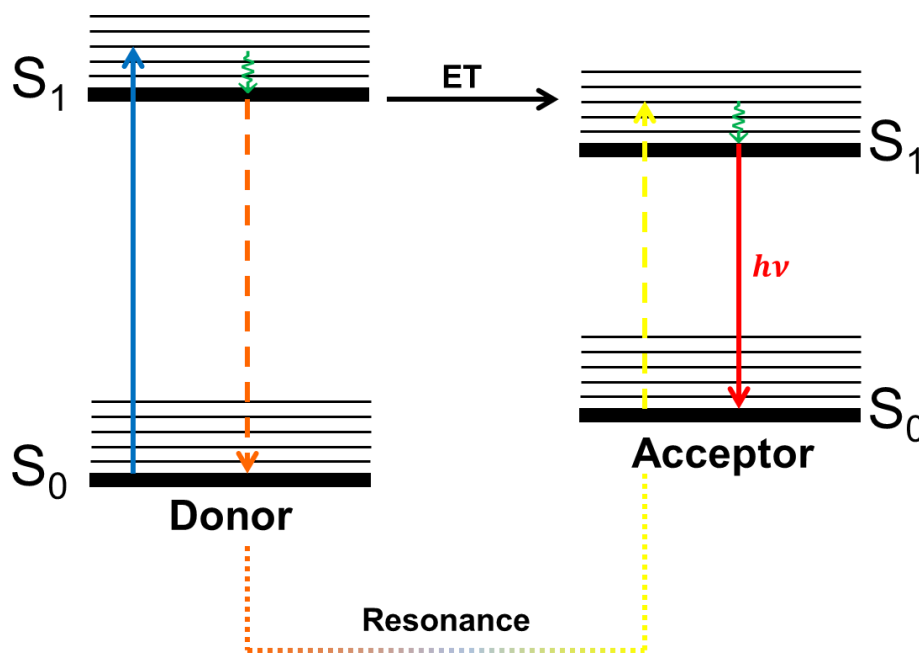


Figure 1.5. Schematic of the FRET mechanism between two singlet states where the dashed lines represent the non-radiative energy transfer from donor to acceptor (dipole-dipole interaction).

The Dexter mechanism, unlike FRET, requires close distances between donor and acceptor and is therefore termed short-range EnT. Additionally, DET proceeds via the *exchange* of electrons as opposed to the dipole coupling mechanism observed with FRET and is rate independent of

oscillator strength. The exchange mechanism requires both spectral and wavefunction overlap; the donor and acceptor need to be closer than 10 \AA . The exchange of electrons can either be intermolecular (collisions) or intramolecular (direct bonding) and the rate exponentially decreases as you separate donor and acceptor pairs. Because this mechanism involves the exchange of an electron from an excited donor, once the exchange happens, the donor will be in the ground state and the acceptor in the excited. This EnT mechanism can occur between different states of multiplicity as well as states of same multiplicity (Figure 1.6).^{1, 2, 9}

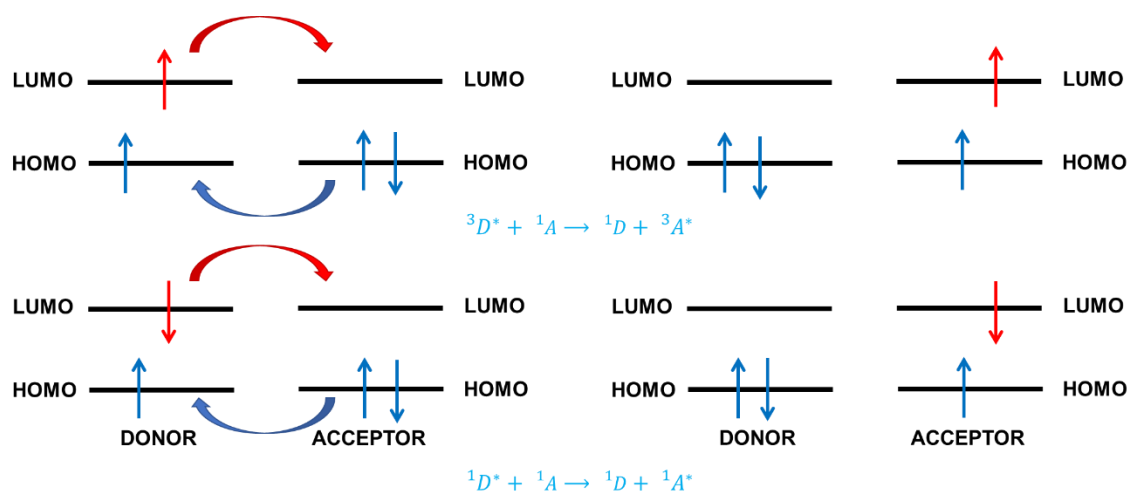


Figure 1.6. Dexter exchange mechanisms. The top is a schematic of EnT between an excited donor in the triplet state and a singlet acceptor in the ground state. The bottom is a schematic of DET occurring between two singlet states.

1.4. Spectroscopic Instrumentation

1.4.1. UV-vis

As stated earlier, matter, or more specifically, molecules absorb light. What energy (and to what degree) a particular molecule absorbs light is of interest when the end goal of a project is to understand how the excited electronic states of a molecule evolve and decay over time. Before interpretation of the excited states under investigation can begin, it is imperative to first know how an electron in the ground electronic state of a molecule is promoted to those excited states. This is

accomplished by obtaining the ultraviolet-visible (UV-vis) spectrum of a molecule. UV-vis spectroscopy is established on the measurement of transmittance (T , a.u.) or absorbance (A , a.u.) of a solution in a cell of path length b (cm).²⁸ Transmittance is the amount of light that a solution allows through and absorbance is the negative logarithm of T (Eq. 1.12). Aside from obtaining information about the excited states that can be formed, UV-vis spectroscopy is also a quantitative measurement that can be used to determine the concentration of an analyte in solution from its absorption profile due to its linear relationship as seen in Beer's Law:

$$A = -\log(T) = \epsilon bc \quad (\text{Eq. 1.12})$$

where ϵ is molar absorptivity ($\text{M}^{-1} \text{cm}^{-1}$), and c is concentration (M).³

In inorganic chemistry, there are three main types of electronic transitions: charge transfer (CT), dd (ligand field or crystal field), and ligand centered (LC) (Figure 1.7). Charge transfer transitions involve the shifting of charge from one moiety on a molecule to another. Because of this, the energy gap between these transitions is smaller than transitions that share spatial overlap (e.g. $\pi \rightarrow \pi^*$) and manifest in the visible region of the electromagnetic spectrum. These CT transitions can be further classified regarding their origin; ligand to metal charge transfer (LMCT) and metal to ligand charge transfer (MLCT). These bands are intense with molar absorptivities around $10^4 \text{ M}^{-1} \text{cm}^{-1}$. Charge transfer bands are generally broad and featureless in their absorption profiles. Transitions that occur within the d-orbitals (dd transitions) are considered to be forbidden due to their symmetry being gerade (inversion through the center of symmetry results in no sign changes) while the dipole operator is always ungerade ((inversion through the center of symmetry results in sign changes) (see Section 1.2.1 for discussion of symmetry selection rules). These transitions are *Laporte forbidden* but can be vibronically allowed and are considered to be weakly absorbing transitions with molar absorptivities from 1-100 $\text{M}^{-1} \text{cm}^{-1}$. Ligand centered transitions

involve only the ligand and are usually $\pi \rightarrow \pi^*$ or $n \rightarrow \pi^*$. The $\pi \rightarrow \pi^*$ transitions are very intense with molar absorptivities of $10^5 \text{ M}^{-1}\text{cm}^{-1}$ and are high in energy due to their much larger energy gap when compared to CT or dd transitions. (The $n \rightarrow \pi^*$ transitions are generally, much weaker than $\pi \rightarrow \pi^*$ due to the small orbital overlap between n and π^* orbitals.) The absorption profiles of LC transitions can exhibit little to a lot of structure in the UV region of the spectrum.

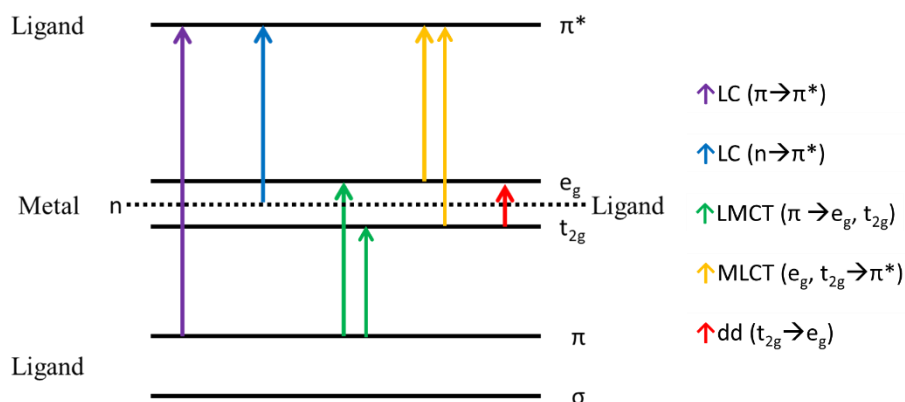


Figure 1.7. Representative electronic transition types found in octahedral transition metal complexes.

A UV-visible absorption spectrum is obtained from a UV-visible spectrophotometer and is commercially available in a variety of configurations. Two of the most common types are single-beam and double-beam instruments. Single-beam instruments have four main components: a light source, typically a tungsten or deuterium lamp, a monochromator for wavelength selection, a sample holder, and a detector. A detector for this setup could be a photomultiplier tube (PMT) which are particularly good at absorbance measurements at a signal wavelength and, are therefore exceptionally good for analytical and kinetic studies. Since there is only a single beam, a blank must be inserted prior to sample data collection and a stable voltage supply is necessary to avoid any light intensity fluctuations from the lamp source.^{1, 28}

An alternative setup for single-beam instruments is when the detector is a diode array. The instrumental setup for these spectrophotometers is as follows: a light source, the sample, a grating,

and finally, the diode array detector. Some advantages of this setup over other single-beam instruments equipped with a PMT is the speed at which an entire UV-vis spectrum can be obtained. Rather than a monochromator moving for selection of each wavelength in a range, the transmitted light from a sample hits a grating which allows for each diode of the array to detect a narrow band of the spectrum across the complete UV-vis spectrum.^{1, 28}

Double-beam instruments are more common as it allows for correction of radiation fluctuations and wavelength intensity as these instruments can measure both the blank and the sample simultaneously as well as allowing for continuous recording of absorption spectra. The instrumental setup involves the light beam to be split into two parts after passing through the monochromator which is how it is able to measure both the blank and sample at the same time.^{1,}

28

1.4.2. Transient Absorption (TA) Spectroscopy: nsTA and fsTA

UV-vis spectroscopy yields insightful information about various excited states that originate from the ground state. However, a typical UV-vis ground state spectrum does not show any excited state features. To visualize the transient species that are too short lived to be viewed under conventional instrumentation, transient absorption spectroscopy is necessary due to its shorter detection times. This technique is called flash photolysis. Flash photolysis involves an intense light pulse that perturbs the equilibrium of the system. The light pulse must be intense enough to create a large enough concentration of transient species. This technique allows for the two types of measurement methods. The first is to collect a transient absorption spectrum at a specified time after an excitation pulse collected using a charge coupled device (CCD) camera. CCD cameras can collect a spectrum over a range of wavelengths at once. The second is to measure the kinetics of an absorbance feature (excited state feature or ground state bleach) at a single

wavelength as a function of time. The duration of the light pulse determines the time-resolution of the measurement.^{1,2}

For light pulses that are nanoseconds (ns) long, TA systems can cover time windows that range from 10^{-9} to 10^{-2} s long and can measure all transient and intermediate species longer than a few ns. The nsTA system used in the Castellano lab apparatus is depicted in Figure 1.8.

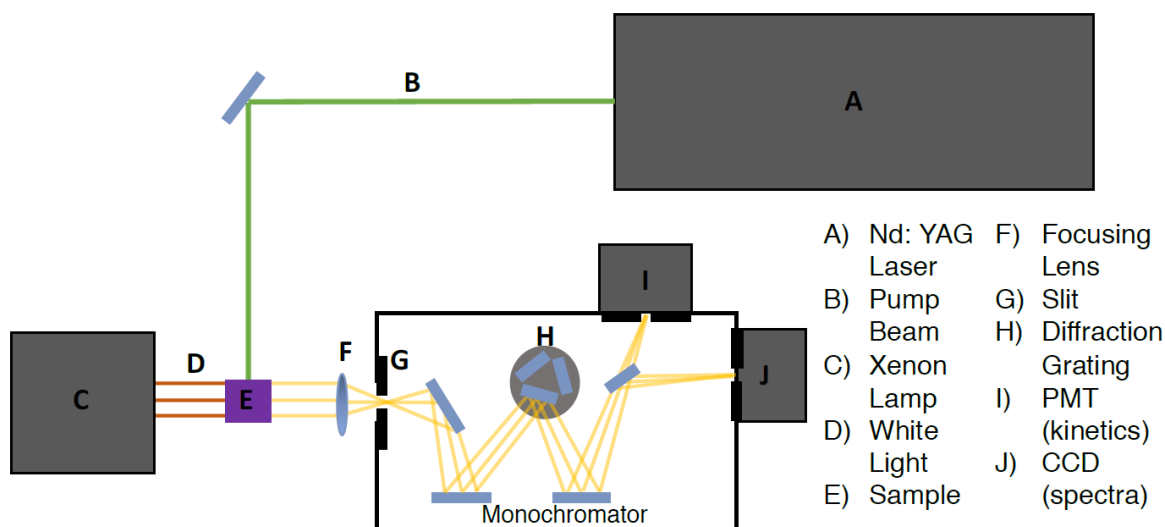


Figure 1.8. Generalized nsTA apparatus.

To collect an excited state difference spectrum, the xenon lamp (C), probes the sample (E) and the iCCD camera (J) obtains a ground state spectrum. Then, the Nd:YAG (A), produces a monochromatic light pump (B) that is directed into the sample and is overlapped in space with the probe. The sample is then probed again with the xenon lamp after a specified time and the camera captures the excited state spectrum. To protect the sample from degradation from the xenon lamp, a computer-controlled shutter blocks the probe beam exposing the sample to the probe at specified time intervals. The computer then converts the transmitted data before and after the excitation pump to ΔOD (change in optical density). To collect single-wavelength kinetics, the process is repeated except the transmitted light is collected in the PMT (I) instead.

A similar concept to the nsTA, fsTA also yields insight into the excited states of molecules but on a different time scale. Since the time resolution of these experiments is so much shorter than that of the previous set up, electronics alone cannot be used to control the delay between the pump and probe beams. Figure 1.9 shows a generalized schematic of the fsTA system used in the Castellano lab.

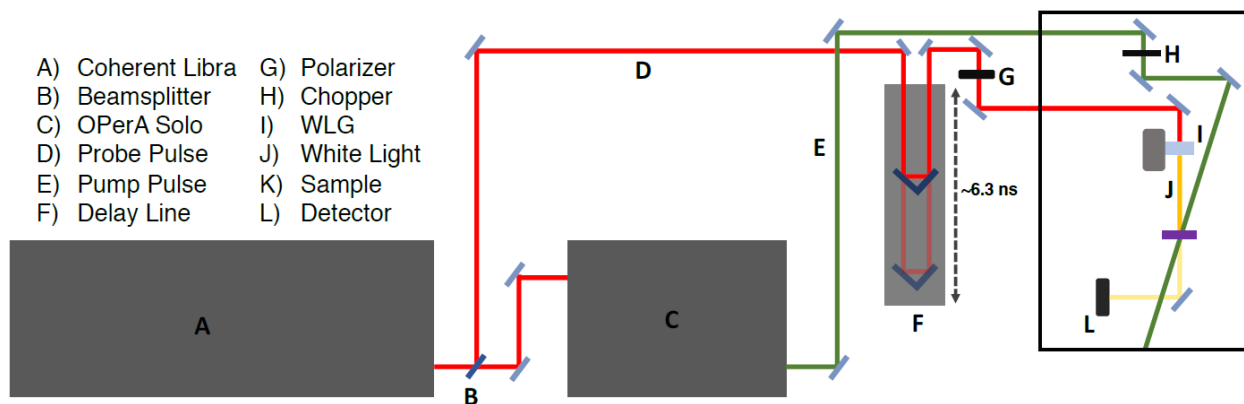


Figure 1.9. Generalized schematic of the fsTA setup.

Inside the Coherent Libra (A) is a Ti:Sapphire regenerative amplifier which produces 800 nm pulses (100 fs at 1 kHz of 4 mJ). From the Libra, the beam hits a beam splitter that transmits 50% of the beam into an optical parametric amplifier (OperA Solo) (C). The OperA Solo then generates the desired excitation wavelength (300 nm – 3 μ m) (pump) and then exits hitting mirrors until it is directed into the TA chamber. Inside the chamber, the pump passes through a chopper (H) that blocks every other pulse of the pump by operating at 500 Hz. By going through the chopper and blocking every other pulse, this will allow for measurements to be taken with the pump beam and without the pump beam so that the computer can calculate Δ OD. After the chopper, the pump beams that pass through are then focused onto the sample and are then the probe is dumped at the back of the chamber. The remaining 50% of the Libra output beam is reflected and is directed to the delay stage (F) to be used as the probe. The delay stage is comprised of a set

of mirrors placed on a moving stage that is controlled by a computer to physically alter the distance in which the probe beam travels to get the sub-picosecond time resolution. After exiting the delay stage, the probe beam goes through a polarizer (G) which selects polarization of the probe to the magic angle (54.7°) relative to pump polarization. The probe beam is then directed through a white light generating (WLG) crystal. The pump and probe beam are then overlapped in space on the sample and the transmitted light is then recorded at the detector (L, a fiber optic cable linked to the CCD camera) which collects difference spectra and kinetics simultaneously.

The iCCD camera on the nsTA and the fiber optic cable that is linked to a CCD camera on the fsTA reports the difference spectra as a function of wavelength. Using equation 1.15 and 1.16, the computer converts the signals obtained from the sample into the familiar difference spectra with positive features indicating excited state features and negative features corresponding to ground state bleaches (or stimulated emission in the fsTA).

$$\Delta OD = OD_{\text{pump}} - OD_{\text{probe}} \quad (\text{Eq. 1.15})$$

$$\Delta OD = -\log \left(\frac{T_{\text{pump}}}{T_{\text{probe}}} \right) \quad (\text{Eq. 1.16})$$

The instrument first probes the sample without the pump to obtain a ground state absorption spectrum of the sample and is treated as the baseline. This is taken before each pump pulse because during the excitation of the sample, on a fraction of the sample is excited; i.e. the majority of the sample remains in the ground state so it is imperative for the instrument to have a baseline that includes experimental artifacts and the absorption profile of the sample prior to any excitation. When the sample is pumped, the ground state population is depleted and creates a population in the excited state. This leaves less molecules in the ground state that can absorb the probe light leading to the negative signal in the difference spectra; i.e the ground state bleach. When the excited state absorbs more than the ground state, a positive feature will exist in the difference

spectrum. It is important to note that the detector is recording all light reaching it. On the nsTA, to avoid any photoluminescence from the sample, the instrument will collect a fluorescence background (obtained by exciting the sample and then recording the light emitted from it without the probe) and subtract that from the final difference spectrum. On the fsTA, the emissive event is recorded and is called stimulated emission and appears where the sample emits. This appears as a negative feature because more light is hitting the detector than initially recorded and is translated as less absorbance.^{1,9}

Kinetics of an excited state or ground state evolution is elucidated from single-wavelength analysis of the feature of interest. This information is essential to understanding the features seen in a difference spectrum and how they change over time. Kinetic traces are analyzed by fitting the traces with sums of exponential terms (Eq 1.17) which provide the time constants associated with the excited state decay processes.

$$y(t) = y_0 + A_1 e^{-t/\tau_1} + A_2 e^{-t/\tau_2} + \dots \quad (\text{Eq. 1.17})$$

In Eq 1.17, A_n is the amplitude of the components and τ_n are the decay time constants of the event(s) of interest at that wavelength. The first term of the equation, y_0 is an offset parameter equal to the terminating y-value. This is necessary when the signal does not decay to the baseline in the time span that it is being fit.^{1,9}

1.4.3. Photoluminescence, Time-Resolved Photoluminescence, and Time-Resolved Intensity Decay Measurements

After an absorptive event, a molecule can emit light. This process is called photoluminescence (PL) and can be monitored in steady-state and time-resolved instruments. Photoluminescence measurements provide crucial information about the excited state(s) just as the

absorption events (electronic and vibrational) do. Steady-state measurements are performed on spectrofluorometers (Figure 1.10).

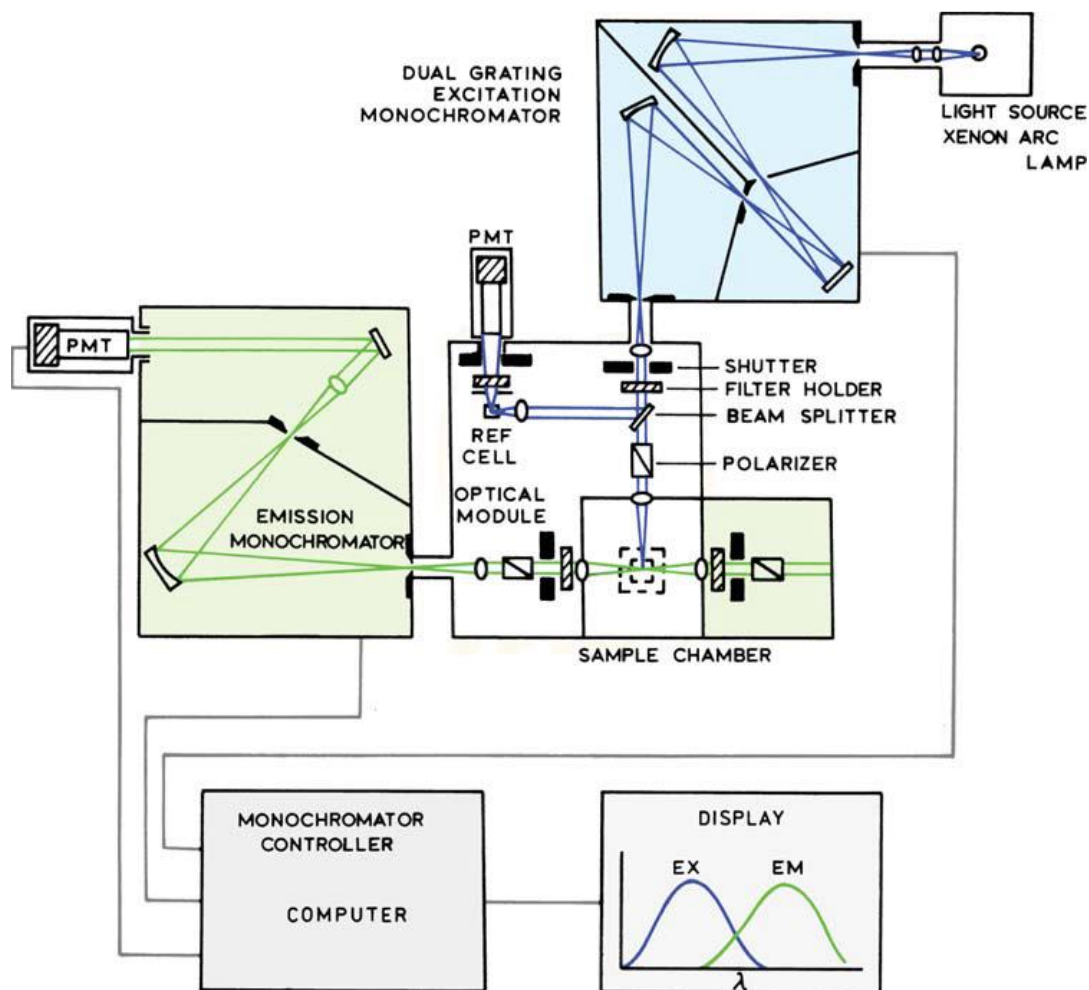


Figure 1.10. Schematic of a spectrofluorometer. Diagram adapted from the literature.⁸

The lamp source, generally a xenon arc lamp, is passed through a monochromator to select the excitation wavelength. Part of the beam is split and sent into a reference to measure the intensity of white light going into the sample. The other portion of the beam goes through the sample. At a right angle to the excitation beam, the PL from the sample is focused into the emission monochromator. The PL is collected 90° with respect to the excitation beam to reduce the amount

of excitation light from hitting the detector. After passing through the emission monochromator, the PL is sent into the detector. To obtain an emission spectrum, the excitation monochromator is set to a wavelength value from the absorption profile (usually the lowest energy band) and the emission monochromator scans a spectral range at where the PL may occur. Excitation spectra may also be obtained from spectrofluorometers. To perform an excitation measurement, first the emission profile must be known since the emission monochromator will be fixed at a wavelength within the emission envelope. The excitation monochromator will scan a range of the absorption profile. Excitation spectra are important when there are multiple bands in the emission profile. If all the bands produce the absorption profile, then all the bands are emissive events from the same ground state molecule. On the other hand, this technique can identify if there are any emissive impurities in the sample if the excitation spectra vary greatly from the absorption profile. When performing both emission and excitation measurements, it is important to use optically dilute samples. This is to reduce the inner filter effects that arise from loss of linearity (the linear relationship between luminescence intensity and concentration of the sample) when optically dense solutions are used.^{1,2,8}

Use of the steady-state instruments can be used to obtain the emission quantum yield (QY). (Section 1.3.3). One method to measure QY is based on the comparison with a standard species of known QY. This method requires the same spectral region of the sample and reference to be scanned, i.e. the emission profiles need to be in the same wavelength range, and both need to be corrected for instrumental response. When the same excitation wavelength is used, then the unknown QY can be calculated using Eq. 1.18.

$$\Phi = \Phi_R \frac{S}{S_R} \frac{A_R}{A} \frac{\eta^2}{\eta_R^2} \quad (\text{Eq. 1.18})$$

In Eq 1.18, Φ is the PL QY, S is the area under the emission spectrum, A is the absorbance at the excitation wavelength, and η is the refractive index of the solvent. The R subscript denotes the reference quantities.^{1, 2, 8, 9}

Time-resolved emission spectra are collected using a pulsed excitation source, such as a Nd:YAG laser. In the Castellano lab, the nsTA system can also be used to obtain time-resolved emission spectra. Like the steady-state instrumentation set up, the excitation source is 90° to the iCCD camera (Figure 1.9). The emitted photons are focused into a slit prior to entering the camera which can collect photons at specific times after excitation (time-gate). This technique allows for observations of emissive events that are darker or slower (phosphorescence) than the initial primary event that is only seen in the steady-state instrument. Alternatively, this can be used to show that there is only one emissive event present. This set up can also be used for single-wavelength analysis when the lifetime is ns to μ s long via single-wavelength analysis and using the PMT instead of the iCCD camera.

1.5. References

1. Balzani, V.; Ceroni, P.; Juris, A., *Photochemistry and Photophysics Concepts, Research, Applications*. First ed.; Wiley-VCH Verlag GmbH & Co. KGaA: Weinheim, Germany, 2014.
2. Montalti, M.; Credi, A.; Prodi, L.; Gandolfi, M. T., *Handbook of Photochemistry*. Third ed.; CRC Press: Taylor & Francis Group: New York, 2006.
3. Wertz, D. W.; Shultz, D. A., *Advanced Inorganic Chemistry II: Applications of Group Theory to Bonding and Spectroscopy* North Carolina State University: North Carolina, 2018.
4. Kasha, M., Characterization of electronic transitions in complex molecules. *Discuss. Faraday Soc.* **1950**, 9, 14.
5. El-Sayed, M. A., Spin—Orbit Coupling and the Radiationless Processes in Nitrogen Heterocyclics. *J. Chem. Phys.* **1963**, 38 (12), 2834-2838.
6. Demchenko, A. P.; Tomin, V. I.; Chou, P.-T., Breaking the Kasha Rule for More Efficient Photochemistry. *Chem. Rev.* **2017**, 117 (21), 13353-13381.
7. Juris, A.; Balzani, V.; Barigelletti, F.; Campagna, S.; Belser, P.; Von Zelewsky, A., Ru(II) polypyridine complexes: photophysics, photochemistry, electrochemistry, and chemiluminescence. *Coord. Chem. Rev.* **1988**, 84, 85-277.
8. Lakowicz, J. R., *Principles of Fluorescence Spectroscopy*. 3rd ed.; Springer Science+Business Media, LLC: New York, 2006.
9. Kalyanasundaram, K., *Photochemistry of Polypyridine and Porphyrin Complexes*. Academic Press Limited London, 1992.
10. Knibbe, H.; Rehm, D.; Weller, A., Intermediates and Kinetics of Fluorescence Quenching by Electron Transfer. *Ber. Buns. Phys. Chem.* **1968**, 72 (2), 257-263.
11. Taube, H., Electron Transfer between Metal Complexes— A Retrospective View (Nobel Lecture). *Angew. Chem. Int. Eng.* **1984**, 23 (5), 329-339.
12. Weller, A., Electron-Transfer and Complex Formation in the Excited State. *Pure Appl. Chem.* **1968**, 16 (1), 115-124.
13. Marcus, R. A., Exchange reactions and electron transfer reactions including isotopic exchange. Theory of oxidation-reduction reactions involving electron transfer. Part 4.—A statistical-mechanical basis for treating contributions from solvent, ligands, and inert salt. *Discuss. Faraday Soc.* **1960**, 29 (0), 21-31.
14. Marcus, R. A., On the Theory of Electron-Transfer Reactions. VI. Unified Treatment for Homogeneous and Electrode Reactions. *J. Chem. Phys.* **1965**, 43 (2), 679-701.

15. Meyer, T. J., Optical and thermal electron transfer in metal complexes. *Acc. Chem. Res.* **1978**, *11* (3), 94-100.
16. Cairo, G., Über Entstehung wahrer Lichtabsorption und scheinbare Koppelung von Quantensprungen. *Z. Phys.* **1922**, *10*, 185-199.
17. Franck, J., Einige aus der Theorie von Klein und Rosseland zu ziehende Folgerungen über Fluorescence, photochemische Prozesse und die Elektronenemission glühender Körper. *Z. Phys.* **192**, *9*, 259-266.
18. Cairo, G.; Franck, J., Über Zerlegung von Wasserstoffmolekülen durch angeregte Quecksilberatome. *Z. Phys.* **1922**, *11*, 161-166.
19. Perrin, J., Fluorescence et induction moléculaire par résonance. *C. R. Acad. Sci.* **1927**, *184*, 1097-1100.
20. Perrin, F., La fluorescence des solutions. *Ann. Phys.* **1929**, *12*, 169-275.
21. Perrin, F., Théorie quantique des transferts d'activation entre molécules de même espèce. Cas des solutions fluorescents. *Ann. Phys.* **1932**, *17*, 283-314.
22. Förster, T., Energiewanderung und Fluoreszenz. *Naturwissenschaften* **1946**, *33*, 166-175.
23. Förster, T., Zwischenmolekulare Energiewanderung und Fluoreszenz. *Ann. Phys.* **1948**, *2*, 55-75.
24. Dexter, D. L., A Theory of Sensitized Luminescence in Solids. *J. Chem. Phys.* **1953**, *21* (5), 836-850.
25. Gaviola, E.; Pringsheim, P., Über den einfluss der konzentration auf die polarisation der fluoreszenz von farbstofflösungen. *Z. Phys.* **1924**, *24*, 24-36.
26. Kallman, H.; London, F., Über quantenmechanische Energieübertragung zwischen atomaren Systemen. *Z. Phys. Chem. B.* **1928**, *2*, 207-243.
27. Andrews, D. L., *Encyclopedia of Applied Spectroscopy*. WILEY-VCH Verlag GmbH & Co. KGaA: Weinheim, Germany, 2009.
28. Skoog, D. A.; Holler, F. J.; Crouch, S. R., *Principles of Instrumental Analysis*. Sixth ed.; Thomson Brooks/Cole: Canada, 2007.

Chapter 2: Excited-State Triplet Equilibria in a Series of Re(I)-Naphthalimide Bichromophores

Portions of this chapter have been previously published in *Journal of Physical Chemistry B*, **2019**, *123* (35), 7611-7627. DOI: 10.1021/acs.jpcc.9b05688. My contributions to this paper include the ns transient absorption spectra and kinetics and the quantum yield data for the rhenium(I) complexes in acetonitrile and tetrahydrofuran. The entire paper is presented to provide the full story.

2.1. Abstract

We present the synthesis, structural characterization, electronic structure calculations, and the ultrafast and supra-nanosecond photophysical properties of a series of five bichromophores of the general structural formula $[\text{Re}(5\text{-R-phen})(\text{CO})_3(\text{dmap})](\text{PF}_6)$, where R is a naphthalimide (NI), phen = 1,10-phenanthroline, and dmap is 4-dimethylaminopyridine. The NI chromophore was systematically modified at their 4-positions with -H (**NI**), -Br (**BrNI**), phenoxy (**PONI**), thiobenzene (**PSNI**), and piperidine (**PNI**), rendering a series of metal-organic bichromophores (**Re1-Re5**, respectively) featuring variability in the singlet and triplet energies in the pendant NI subunit. Five closely related organic chromophores as well as $[\text{Re}(\text{phen})(\text{CO})_3(\text{dmap})](\text{PF}_6)$ (**Re6**) were investigated in parallel to appropriately model the photophysical properties exhibited in the bichromophores. The excited state processes of all molecules in this study were elucidated using a combination of transient absorption spectroscopy and time-resolved photoluminescence (PL) spectroscopy, revealing the kinetics of the energy transfer processes occurring between the appended chromophores. The spectroscopic analysis was further supported by electronic structure calculations which identified the origin of many of the experimentally observed electronic transitions.

2.2. Introduction

Rhenium(I) carbonyl-diimine (Re-CDI) complexes have been studied for many decades because of their desirable photophysical and redox properties, chemical robustness, and synthetic flexibility;¹ making them useful in fields such as photochemical molecular devices,^{2,3} solar energy conversion,^{4,5} luminescence sensing,⁶⁻¹⁴ and biotechnology,^{15,16} among others.¹⁷⁻¹⁹ More recently, these types of molecules have garnered interest as photocatalysts in carbon dioxide reduction,¹⁹⁻²⁴ as the increase of atmospheric CO₂ has steadily risen across the world with no tangible solutions in sight.^{25,26} In these systems, the Re-CDI is used in conjunction with a sacrificial electron donor and light to catalytically drive the reduction of CO₂ to CO. The most efficient photocatalyst to date, [Re(bpy)(CO)₃(P(OEt)₃)]⁺, was found to have a photocatalytic CO₂ reduction quantum yield of 0.38,²⁷ demonstrating the utility of these types of complexes in atmospheric CO₂ mitigation. Unfortunately, the drawback to many Re-CDI complexes used in CO₂ reduction is their inability to absorb strongly in the visible region. To counter this, highly absorbing ruthenium(II) complexes have been covalently linked to the Re-CDI CO₂ reduction catalyst, resulting in greatly improved photocatalytic activity attributed to intermolecular electron transfer between the Ru(II) and Re(I) species.²⁸⁻³⁰

In many Re-CDI complexes, the observed photoluminescence (PL) originates from the triplet metal-to-ligand charge transfer (MLCT) excited state.³¹⁻³³ Since these molecules have the general molecular formulae Re(L-L)(CO)₃X or [Re(L-L)(CO)₃L]⁺, the MLCT excited state can be energetically tuned through modification of the ancillary ligands (X or L) which coarsely modulates the Re(I) d-orbital energies, and thus the HOMO energy.³⁴ Additionally, the π* energies of the chromophoric ligand (L-L), can also be modified, resulting in predictable changes to the LUMO energy.³⁵ Other types of excited states, such as ligand-centered (LC) excited states, can

also be observed in the triplet manifold of Re-CDI complexes if conjugated aryl systems or organic chromophores are appended to either the ancillary or chromophoric ligands.³⁶⁻⁴⁰ Many of the synergistic benefits of polychromophoric systems (i.e. excited state lifetime extension, increase in absorption cross section, etc.) have been documented by our research group,^{33, 41-48} in addition to many others.⁴⁹⁻⁶⁰

The attachment of the organic chromophore 4-piperidinyl-naphthalenimide (**PNI**) to a Re-CDI complex was previously investigated, revealing profound changes in the resultant photophysical properties with respect to the two isolated molecules.³³ The Re(I) and **PNI** chromophores were purposefully selected in that study for their characteristic spectroscopic infrared handles that enabled transient vibrational spectroscopic interrogation of the energy transfer processes occurring between these moieties. The comprehensive utilization of time-resolved PL emission, transient absorption, and time-resolved infrared spectroscopies from the femtosecond to microsecond time regimes, revealed “ping-pong” energy transfer occurring between the **PNI** and Re-CDI complex. The initial ligand-centered singlet excited state was localized on the **PNI** chromophore (¹PNI) and underwent Förster-type resonance energy transfer (FRET) to the Re-CDI chromophore ($\tau_{FRET} = 43.5$ ps) forming the ³MLCT excited state. After approximately 20 ns, the excited state returned to the **PNI** chromophore through a Dexter-like triplet–triplet energy transfer (TTET) process, finally populating the long-lived triplet excited state localized on the **PNI** chromophore (³PNI). Due to the energetic proximity between the ³MLCT and ³PNI excited states ($\Delta E = 1680$ cm⁻¹) and rapid forward and reverse triplet-triplet energy transfer (rTTET) reactions with respect to the other deactivation pathways, a thermal excited state equilibrium became established between these two triplets resulting in a 3000-fold increase in the observed ³MLCT lifetime; this radiative process is termed thermally-activated delayed PL. At the

conclusion of that study, two questions remained unanswered. First, if weakly emissive organic chromophores were used instead of **PNI** whose quantum yield for fluorescence approaches unity,⁶¹⁻⁶⁴ would singlet energy transfer to the Re-CDI moiety still take place? Second, what ³MLCT/³NI energy gap is sufficient for sustaining the equilibrium between these two excited states at room temperature. To address these questions, a series of five Re(I) bichromophores (**Re1-Re5**) were synthesized by substituting the 4-position of the NI subunit pendant to the 5-position of the phenanthroline ligand with various substituents: -H (**NI, Re1**), -Br (**BrNI, Re2**), phenoxy (**PONI, Re3**), thiobenzene (**PSNI, Re4**), or piperidine (**PNI, Re5**) (see Figure 2.1) while conserving the Re-CDI complex's ³MLCT excited state energetics across all molecules. The naphthalimide substitutions modulated many of the observed photophysical properties, including the energies of the associated NI excited states and fluorescence quantum yields, as observed in the appropriate model chromophores.

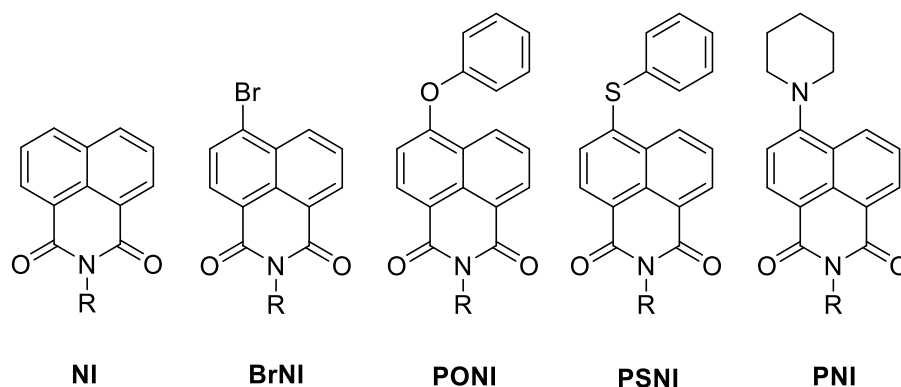


Figure 2.1. Naphthalimide chromophores evaluated in this study.

One objective was to investigate how the substitution of the naphthalimide subunit modulated the efficiency of the energy transfer processes that occurs in the bichromophore. Ultrafast transient absorption spectroscopy was used to compare the bichromophore to the appropriate model systems to assign the observed excited state features. Despite being weakly

fluorescent, there was still energy transfer observed to the Re-CDI chromophore in the **NI** and **BrNI** containing bichromophores **Re1** and **Re2**. Of the five bichromophores interrogated, four were shown to exhibit “ping-pong” energy transfer characteristics, whereas the **PSNI** containing molecule (**Re4**) had photophysical properties echoing those of its model compound.

Another objective was to determine the energy gap between the low-lying triplet states on the Re-CDI complex ($^3\text{MLCT}$) and the naphthalimide chromophore (^3NI) where the excited state equilibrium would no longer be established at room temperature. To increase the energy gap with respect to that observed in the Re-PNI complex, the new molecules here replaced the chloride ligand with dimethylaminopyridine (dmap), resulting in a higher energy $^3\text{MLCT}$ excited state. Additionally, this generated an ionic complex that was more soluble in spectroscopic friendly solvents including acetonitrile. Structural modification of the naphthalimides resulted in a 0.25 eV (2000 cm^{-1}) variation of the ^3NI excited state energy across the series, with the **NI** being the highest and the **PNI** being the lowest in energy. The change in ^3NI excited state energies resulted in triplet excited state equilibrium and characteristic $^3\text{MLCT}$ delayed PL being observed in the three naphthalimides with the highest energy ^3NI excited states (**NI**, **BrNI**, and **PONI**), whereas **PSNI** and **PNI** exclusively featured ligand-localized photophysics with no observed $^3\text{MLCT}$ emission.

2.3. Experimental

2.3.1. Reagents and Chemicals

All synthetic manipulations were performed under an inert and dry nitrogen atmosphere using standard techniques. All reagents were purchased from VWR and used as received. The precursors NNI, NNI-phen, PNI-phen, and $\text{Re}(\text{PNI-phen})(\text{CO})_3\text{Cl}$, as well as **PNI**, were synthesized according to their published procedures.^{33, 44, 46} The synthetic procedures used to make all the chromophores are outlined in Scheme 1. The identity and purity of all compounds studied

were confirmed using ^1H NMR, ATR-FTIR, high-resolution mass spectrometry, and elemental analysis. Synthetic details for all precursors and products in this study are included in Appendix A. Spectroscopic samples were prepared using spectroscopic grade tetrahydrofuran or acetonitrile and were degassed using the freeze-pump-thaw technique.⁶⁵

2.3.2. Characterization Data for the Studied Complexes

2-(p-tolyl)-1H-benzo[de]isoquinoline-1,3(2H)-dione (**NI**). ^1H NMR (400 MHz, CD_2Cl_2), δ 8.60 (dd, $J = 7.2, 1.1$ Hz, 2H), 8.31 (dd, $J = 8.1, 1.2$ Hz, 2H), 7.81 (dd, $J = 8.3, 7.3$ Hz, 2H), 7.37 (d, $J = 8.0$ Hz, 2H), 7.18 (d, $J = 8.2$ Hz, 2H), 2.46 (s, 3H). MS [HR-ESI (CH_2Cl_2) m/z] 288.1027 $[\text{M}+\text{H}]^+$, calcd ($\text{C}_{19}\text{H}_{14}\text{NO}_2$) 288.1025. Anal. Calcd (found) for $\text{C}_{19}\text{H}_{13}\text{NO}_2$: C, 79.43 (79.14); H, 4.56 (4.81); N, 4.88 (4.87). ATR-FTIR: 490, 516, 538, 781, 812, 1185, 1234, 1352, 1373, 1514, 1587, 1656, 1673, 1699 cm^{-1} .

$[\text{Re}(\text{NI-phen})(\text{CO})_3(\text{dmap})](\text{PF}_6)$ (**Re1**). ^1H NMR (400 MHz, CD_2Cl_2), δ 9.58 (ddd, $J = 12.8, 5.2, 1.4$ Hz, 2H), 8.82 (dd, $J = 8.4, 1.4$ Hz, 1H), 8.66 (ddd, $J = 16.2, 7.3, 1.2$ Hz, 2H), 8.51 (dd, $J = 8.5, 1.4$ Hz, 1H), 8.48 – 8.43 (m, 2H), 8.25 (s, 1H), 8.16 (dd, $J = 8.3, 5.2$ Hz, 1H), 8.04 (dd, $J = 8.5, 5.1$ Hz, 1H), 7.90 (ddd, $J = 8.3, 7.3, 4.6$ Hz, 2H), 7.65 (d, $J = 7.4$ Hz, 2H), 6.27 (d, $J = 7.4$ Hz, 2H), 2.91 (s, 6H). MS [HR-ESI (CH_2Cl_2) m/z] 766.1224 $[\text{M}-\text{PF}_6]^+$, calcd ($\text{C}_{34}\text{H}_{23}\text{N}_5\text{O}_5^{185}\text{Re}$) 766.1229. Anal. Calcd (found) for $\text{C}_{34}\text{H}_{23}\text{F}_6\text{N}_5\text{O}_5\text{PRe}\cdot 0.5\text{H}_2\text{O}$: C, 44.30 (44.15); H, 2.62 (2.40); N, 7.60 (7.46). ATR-FTIR: 557, 730, 779, 838, 1234, 1350, 1587, 1626, 1673, 1709, 1903, 2058 cm^{-1} .

6-bromo-2-(p-tolyl)-1H-benzo[de]isoquinoline-1,3(2H)-dione (**BrNI**). ^1H NMR (400 MHz, CD_2Cl_2), δ 8.69 – 8.62 (m, 2H), 8.42 (d, $J = 7.9$ Hz, 1H), 8.10 (d, $J = 7.8$ Hz, 1H), 7.90 (dd, $J = 8.5, 7.3$ Hz, 1H), 7.37 (d, $J = 7.9$ Hz, 2H), 7.18 (d, $J = 8.2$ Hz, 2H), 2.46 (s, 3H). MS [HR-ESI (CH_2Cl_2) m/z] 366.0134 $[\text{M}+\text{H}]^+$, calcd ($\text{C}_{19}\text{H}_{13}\text{NO}_2^{79}\text{Br}$) 366.0130. Anal. Calcd (found) for

C₁₉H₁₂BrNO₂: C, 62.32 (62.04); H, 3.30 (3.27); N, 3.82 (3.81). ATR-FTIR: 422, 500, 518, 730, 781, 814, 1193, 1238, 1344, 1365, 1589, 1656, 1707 cm⁻¹.

[Re(BrNI-phen)(CO)₃(dmap)](PF₆) (**Re2**). ¹H NMR (400 MHz, CD₂Cl₂), δ 9.58 (ddd, J = 12.1, 5.1, 1.3 Hz, 2H), 8.81 (ddd, J = 9.3, 8.6, 1.2 Hz, 2H), 8.72 (ddd, J = 15.2, 7.3, 1.2 Hz, 1H), 8.52 – 8.43 (m, 2H), 8.26 (s, 1H), 8.23 – 8.13 (m, 2H), 8.08 – 7.96 (m, 2H), 7.65 (d, J = 7.4 Hz, 2H), 6.27 (d, J = 7.4 Hz, 2H), 2.91 (d, J = 0.5 Hz, 6H). MS [HR-ESI (CH₂Cl₂) m/z] 844.0316 [M–PF₆]⁺, calcd (C₃₄H₂₂N₅O₅¹⁸⁵Re⁷⁹Br) 844.0334. Anal. Calcd (found) for C₃₄H₂₂BrF₆N₅O₅Pre·0.5H₂O: C, 40.81 (40.58); H, 2.32 (2.17); N, 7.00 (6.72). ATR-FTIR: 418, 477, 514, 543, 557, 726, 781, 838, 1234, 1364, 1363, 1589, 1626, 1673, 1713, 1905, 2028 cm⁻¹.

6-phenoxy-2-(p-tolyl)-1H-benzo[de]isoquinoline-1,3(2H)-dione (**PONI**). ¹H NMR (400 MHz, CD₂Cl₂), δ 8.78 (dd, J = 8.4, 1.2 Hz, 1H), 8.66 (dd, J = 7.3, 1.2 Hz, 1H), 8.45 (d, J = 8.3 Hz, 1H), 7.84 (dd, J = 8.4, 7.3 Hz, 1H), 7.55 – 7.47 (m, 2H), 7.39 – 7.30 (m, 3H), 7.27 – 7.22 (m, 2H), 7.18 (d, J = 8.2 Hz, 2H), 6.96 (d, J = 8.3 Hz, 1H), 2.46 (s, 3H). MS [HR-ESI (CH₂Cl₂) m/z] 380.1289 [M+H]⁺, calcd (C₂₅H₁₈NO₃) 380.1287. Anal. Calcd (found) for C₂₅H₁₇NO₃·0.1H₂O: C, 78.77 (78.84); H, 4.55 (4.73); N, 3.67 (3.67). ATR-FTIR: 485, 696, 753, 779, 804, 1136, 1177, 1201, 1236, 1356, 1575, 1660, 1699 cm⁻¹.

[Re(PONI-phen)(CO)₃(dmap)](PF₆) (**Re3**). ¹H NMR (400 MHz, CD₂Cl₂), 9.58 (ddd, J = 11.6, 5.2, 1.4 Hz, 2H), 8.94 (dd, J = 8.5, 1.2 Hz, 1H), 8.82 (dd, J = 8.4, 1.4 Hz, 1H), 8.71 (ddd, J = 15.9, 7.3, 1.2 Hz, 1H), 8.56 – 8.44 (m, 2H), 8.24 (s, 1H), 8.16 (dd, J = 8.3, 5.2 Hz, 1H), 8.08 – 8.01 (m, 1H), 7.93 (ddd, J = 8.4, 7.3, 4.5 Hz, 1H), 7.65 (dd, J = 7.4, 2.2 Hz, 2H), 7.59 – 7.50 (m, 2H), 7.38 (td, J = 7.4, 1.2 Hz, 1H), 7.29 (dd, J = 7.5, 1.2 Hz, 2H), 7.01 (dd, J = 8.3, 4.4 Hz, 1H), 6.26 (dd, J = 7.3, 5.2 Hz, 2H), 2.91 (s, 3H), 2.90 (s, 3H). MS [HR-ESI (CH₂Cl₂) m/z] 858.1478 [M–PF₆]⁺, calcd (C₄₀H₂₇N₅O₆¹⁸⁵Re) 858.1491. Anal. Calcd (found) for C₄₀H₂₇F₆N₅O₆Pre·H₂O:

C, 46.97 (47.06); H, 2.86 (2.68); N, 6.85 (6.79). ATR-FTIR: 557, 781, 840, 1206, 1236, 1254, 1356, 1579, 1626, 1671, 1707, 1907, 2028 cm^{-1} .

6-(phenylthio)-2-(p-tolyl)-1H-benzo[de]isoquinoline-1,3(2H)-dione (**PSNI**). ^1H NMR (400 MHz, CD_2Cl_2), δ 8.73 (dd, $J = 8.5, 1.1$ Hz, 1H), 8.64 (dd, $J = 7.3, 1.1$ Hz, 1H), 8.35 (d, $J = 7.9$ Hz, 1H), 7.84 (dd, $J = 8.5, 7.3$ Hz, 1H), 7.61 – 7.53 (m, 2H), 7.51 – 7.45 (m, 3H), 7.39 – 7.32 (m, 3H), 7.16 (d, $J = 8.1$ Hz, 2H), 2.45 (s, 3H). MS [HR-ESI (CH_2Cl_2) m/z] 396.1058 [$\text{M}+\text{H}$] $^+$, calcd ($\text{C}_{25}\text{H}_{18}\text{NO}_2\text{S}$) 396.1058. Anal. Calcd (found) for $\text{C}_{25}\text{H}_{17}\text{NO}_2\text{S}$: C, 75.93 (75.66); H, 4.33 (4.56); N, 3.54 (3.54). ATR-FTIR: 445, 516, 685, 747, 777, 810, 904, 1134, 1175, 1185, 1230, 1346, 1361, 1507, 1562, 1581, 1656, 1697 cm^{-1} .

$[\text{Re}(\text{PSNI-phen})(\text{CO})_3(\text{dmap})](\text{PF}_6)$ (**Re4**). ^1H NMR (400 MHz, CD_2Cl_2), δ 9.57 (ddd, $J = 12.6, 5.1, 1.4$ Hz, 2H), 8.84 (ddd, $J = 24.3, 8.5, 1.3$ Hz, 2H), 8.70 (ddd, $J = 16.3, 7.3, 1.1$ Hz, 1H), 8.48 (dd, $J = 8.5, 1.3$ Hz, 1H), 8.36 (dd, $J = 15.7, 8.0$ Hz, 1H), 8.23 (s, 1H), 8.16 (dd, $J = 8.3, 5.2$ Hz, 1H), 8.04 (dd, $J = 8.5, 5.1$ Hz, 1H), 7.93 (ddd, $J = 8.5, 7.4, 4.7$ Hz, 1H), 7.67 – 7.62 (m, 4H), 7.56 – 7.52 (m, 3H), 7.31 (dd, $J = 8.0, 5.0$ Hz, 1H), 6.26 (td, $J = 5.5, 1.6$ Hz, 2H), 2.91 (s, 3H), 2.89 (s, 3H). MS [HR-ESI (CH_2Cl_2) m/z] 874.1242 [$\text{M}-\text{PF}_6$] $^+$, calcd ($\text{C}_{40}\text{H}_{27}\text{N}_5\text{O}_5\text{S}^{185}\text{Re}$) 874.1262. Anal. Calcd (found) for $\text{C}_{40}\text{H}_{27}\text{F}_6\text{N}_5\text{O}_5\text{PReS}$: C, 47.06 (46.98); H, 2.67 (2.68); N, 6.86 (6.78). ATR-FTIR: 557, 728, 751, 779, 838, 1234, 1363, 1585, 1626, 1671, 1709, 1905, 2028 cm^{-1} .

$[\text{Re}(\text{PNI-phen})(\text{CO})_3(\text{dmap})](\text{PF}_6)$ (**Re5**). ^1H NMR (400 MHz, CD_2Cl_2), δ 9.56 (ddd, $J = 13.1, 5.1, 1.4$ Hz, 2H), 8.80 (dd, $J = 8.3, 1.4$ Hz, 1H), 8.66 – 8.44 (m, 4H), 8.22 (s, 1H), 8.14 (dd, $J = 8.3, 5.2$ Hz, 1H), 8.02 (dd, $J = 8.5, 5.1$ Hz, 1H), 7.79 (ddd, $J = 8.5, 7.3, 5.3$ Hz, 1H), 7.64 (d, $J = 7.4$ Hz, 2H), 7.27 (dd, $J = 8.2, 6.1$ Hz, 1H), 6.26 (d, $J = 7.4$ Hz, 2H), 3.36 (m, $J = 5.4$ Hz, 4H), 2.91 (s, 6H), 1.92 (m, $J = 10.7$ Hz, 4H), 1.78 (m, 2H). MS [HR-ESI (CH_2Cl_2) m/z] 849.1945

$[M-PF_6]^+$, calcd ($C_{39}H_{32}N_6O_5^{185}Re$) 849.1964. Anal. Calcd (found) for $C_{39}H_{32}F_6N_6O_5PRE \cdot H_2O$: C, 46.20 (46.17); H, 3.38 (3.16); N, 8.29 (8.10). ATR-FTIR: 557, 781, 840, 1232, 1365, 1583, 1626, 1664, 1701, 1909, 2028 cm^{-1} .

$[Re(phen)(CO)_3(dmap)](PF_6)$ (**Re6**). 1H NMR (400 MHz, CD_2Cl_2), δ 9.51 (dd, $J = 5.1, 1.4$ Hz, 2H), 8.79 (dd, $J = 8.3, 1.4$ Hz, 2H), 8.17 (s, 2H), 8.10 (dd, $J = 8.3, 5.1$ Hz, 2H), 7.53 (d, $J = 7.4$ Hz, 2H), 6.19 (d, $J = 7.4$ Hz, 2H), 2.86 (s, 6H). MS [HR-ESI (CH_2Cl_2) m/z] 571.0909 $[M-PF_6]^+$, calcd ($C_{22}H_{18}N_4O_3^{185}Re$) 571.0908. Anal. Calcd (found) for $C_{22}H_{18}F_6N_4O_3PRE \cdot 0.5H_2O$: C, 36.37 (36.52); H, 2.64 (2.42); N, 7.71 (7.59). ATR-FTIR: 557, 724, 836, 1626, 1897, 1919, 2025 cm^{-1} .

2.3.3. General Techniques

1H and ^{13}C NMR spectra were recorded on a Varian Inova 400 NMR operating at a working frequency of 400 MHz for 1H . All chemical shifts were referenced to residual solvent signals. High-resolution electron spray ionization mass spectrometry (ESI-MS) were performed at Michigan State University Mass Spectrometry Facility. Elemental analysis data was measured by Atlantic Microlab, Inc., Norcross, GA. Attenuated total reflectance Fourier-transform infrared (ATR-FTIR) spectroscopy was performed using the Bruker Alpha Platinum ATR. Optical absorption spectra were measured on a Shimadzu UV-3600 spectrometer. Steady-state luminescence spectra were obtained from an Edinburgh FS 920. Quantum yield measurements were performed on **NI** and **BrNI** using anthracene in aerated ethanol as the standard ($\Phi_{PL} = 0.28$),⁶⁶ **PONI** using 9,10-diphenylanthracene in aerated cyclohexane as the standard ($\Phi_{PL} = 0.97$),⁶⁶ **PSNI** and **Re1-Re6** using $[Ru(bpy)_3](PF_6)_2$ in aerated acetonitrile as the standard ($\Phi_{PL} = 0.018$),⁶⁶ and **PNI** in acetonitrile using **PNI** in aerated toluene as the standard ($\Phi_{PL} = 0.91$).⁶⁴

2.3.4. Nanosecond Transient Absorption Spectroscopy

Transient absorption measurements were collected using a LP920 laser flash photolysis system (Edinburgh Instruments) described previously.⁶⁷ Samples were prepared to have a 25 μM concentration (3.0 mJ/pulse) in a 1 cm path length quartz optical cell and degassed using the freeze-pump-thaw technique. All transient absorption experiments were performed at room temperature. The reported difference spectra and kinetic data are the average of 50 laser shots. The ground state absorption spectra were taken before and after each experiment to ensure there was no sample degradation. The transient kinetic data was evaluated using the fitting routines available in OriginPro 2016.

2.3.5. Femtosecond Transient Absorption Spectroscopy.

The transient absorption measurements were performed at the NCSU Imaging and Kinetic Spectroscopy (IMAKS) Laboratory using a mode-locked Ti:sapphire laser (Coherent Libra) as described previously.⁶⁸ The pump beam was directed into a parametric amplifier (Coherent OPerA Solo) to generate the 350 and 400 nm excitation. The probe beam was focused onto a calcium fluoride crystal to generate a white light continuum between 350 to 775 nm. The pump beam was focused and overlapped with the probe beam through a 2 mm path length cuvette. The ground-state absorption spectra were taken before and after each experiment to ensure there was no sample photo-degradation during the experiment. The transient kinetic data at specific wavelengths was evaluated using the fitting routines available in OriginPro 2016. The global fit analysis was performed using Surface Explorer available from Ultrafast Systems.

2.3.6. Time-Resolved Emission Intensity Decay Measurements

Single wavelength emission intensity decays at 77 K and room temperature were acquired with an LP920 laser flash photolysis system (Edinburgh Instruments) using the Vibrant 355 LD

Nd:YAG/OPO system (OPOTEK) as the excitation source ($\lambda_{\text{ex}} = 355/410$ nm, ~ 3.0 mJ/pulse). Spectroscopic samples were prepared to have a 25 μM concentration and PL transients were collected at emission maximums for most experiments, with all exceptions noted in text. Time-gated emission spectra were collected using the same system. Emission spectra and PL transients were collected with an iStar ICCD camera (Andor Technology), which was controlled by the L900 software program (Edinburgh Instruments). Reported time-gated emission spectra are the average of 50 laser flashes.

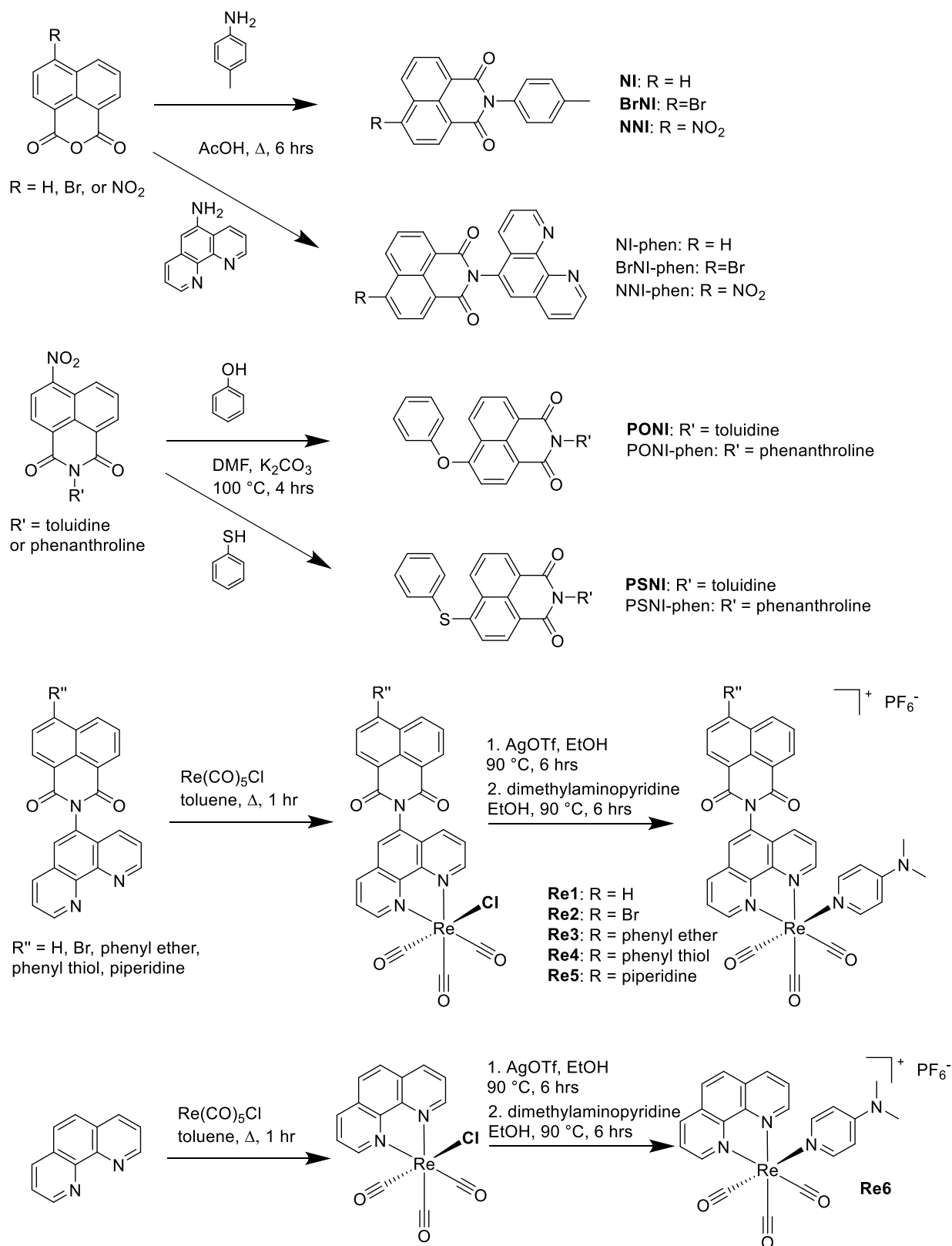
2.3.7. Density Functional Theory (DFT) Calculations

The calculations utilized in this study were performed using the Gaussian 09 software package (revision D.01)⁶⁹ and the computation resources of the North Carolina State University High Performance Computing Center. Ground state and triplet state geometry optimizations were performed using the B3LYP,^{70, 71} M06,⁷² and CAM-B3LYP functionals,⁷³ along with the def2-SVP basis set of the Alrichs group as implemented in Gaussian 09.⁷⁴ The Stuttgart–Dresden effective core potentials (ECPs)⁷⁵ were used to replace the core electrons in rhenium for all calculations. The polarizable continuum model was used to simulate the acetonitrile solvent environment for all calculations.⁷⁶ Frequency calculations were performed on all optimized structures and no imaginary frequencies were obtained. The TD-DFT calculations were performed using the same conditions as described for the geometry optimizations.⁷⁷⁻⁷⁹ The energy and oscillator strengths were computed for each of the 50 lowest singlet excitations. The natural transition orbitals of the low-lying singlet and triplet transitions were generated using GaussView 5.0.⁸⁰

2.4. Results and Discussion

2.4.1. Syntheses

The schemes used to synthesize all the chromophores in this study are collected in Scheme 2.1. Briefly, the naphthalimide chromophores were prepared by departing from the corresponding naphthalene anhydride (either unsubstituted or substituted with Br or NO₂ in the 4- position) and reacting with a primary amine (*p*-toluidine or 5-amino-1,10-phenanthroline) using published protocols to generate the **NI** and **BrNI** model chromophores and ligands (NI-phen and BrNI-phen), along with the nitronaphthalimide intermediates (**NNI** and NNI-phen).⁴⁶ The nitro group was substituted by refluxing the nitronaphthalimide in DMF with a phenol or thiolbenzene under basic conditions or piperidine to yield the other three naphthalimide chromophores and ligands (**PONI**, **PSNI**, **PNI**, PONI-phen, PSNI-phen, and PNI-phen).^{33, 44, 81, 82} The 5-substituted phenanthroline ligands were coordinated to Re(CO)₅Cl using published protocols.³⁴ The chloride ligand was subsequently removed by refluxing *fac*-Re(L-L)(CO)₃Cl with silver triflate in ethanol, forming the solvato-complex. The silver chloride precipitate was removed by filtration over Celite. The dmap ligand was finally added to the isolated solvato-complex and refluxed in ethanol to yield the desired product (**Re1-Re6**). The final isolated products (facial isomers) were structurally characterized using ¹H NMR spectroscopy, high resolution mass spectroscopy, elemental analysis, and FT-IR spectroscopy. Furthermore, the molecular structures of the bichromophores **Re1** to **Re5** were confirmed using ¹H-¹H COSY NMR spectroscopy.



Scheme 2.1. Synthetic procedures for the preparation of NI, BrNI, PONI, PSNI and Re1-Re6.

2.4.2. UV-vis Electronic Spectra

The electronic spectra for the model compounds and bichromophores measured in acetonitrile are presented in Figure 2.2, with additional spectroscopic data collected in Table 2.1. The **NI** and **BrNI** chromophores both have structured lowest energy electronic transitions with a maximum absorbance corresponding to a $\pi \rightarrow \pi^*$ transition at 332 and 340 nm, respectively (Figure 2.2a). In **PONI**, **PSNI**, and **PNI**, the low energy transition, which is now broad and featureless, red shifts progressively (359, 384, and 407 nm, respectively) and is consistent with possessing significant charge transfer character as demonstrated in prior work, Figure 2.2a.^{33, 44, 46} All five naphthalimide model chromophores possess relatively intense low energy transitions with molar extinction coefficients ranging from 11300 to 17100 $M^{-1}cm^{-1}$, Figure 2.2a. The model Re(I) compound (**Re6**) has a broad and featureless absorption band centered at 368 nm which is assigned to the $d\pi(Re) \rightarrow \pi^*(phen)$ MLCT transitions and a higher energy band at 276 nm which corresponds to the $\pi \rightarrow \pi^*$ transitions localized on the phen ligand, Figure 2b. As also illustrated in Figure 2.2b, the low energy electronic transitions observed in each of the bichromophores (**Re1-Re5**) emulates that expected for a simple mixture of the composing molecules. This is illustrated in Figures A40-S41, where the absorption spectrum of **Re6** is added to that of the appropriate NI model compound's absorption spectrum. In all cases, the additive and measured spectra of the five bichromophores were found to be in good quantitative agreement, illustrating that there is no significant electronic communication between the respective subunits.

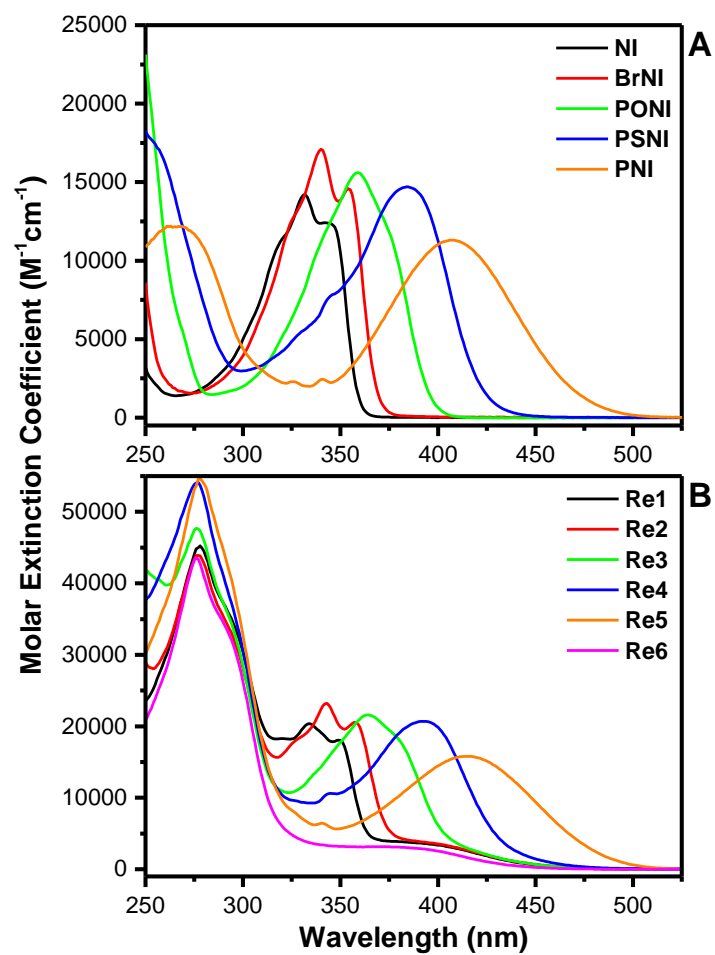


Figure 2.2. (A) Electronic spectra of NI, BrNI, PONI, PSNI, and PNI recorded in acetonitrile. (B) Electronic spectra of Re1-Re6 recorded in acetonitrile.

Table 2.1. Static photophysical properties of the **NI**, **BrNI**, **PONI**, **PSNI**, **PNI** model compounds and **Re1-Re6** measured in acetonitrile (black) and THF (blue).

Molecule	$\lambda_{\text{abs max/nm}}$ ($\epsilon/\text{M}^{-1}\text{cm}^{-1}$) ^[a]	$\lambda_{\text{em max/nm}}$ (RT) ^[a]	$\lambda_{\text{em max/nm}}$ (77 K) ^[b,c]	Φ_{em} in air ^[a]	Φ_{em} deaerated ^[a,d]
NI	332 (14200) 330 (12500)	374, 506 375, 486	538	0.0005 ^[e] 0.0004 ^[e]	---
BrNI	340 (17100) 339 (16300)	387, 537 379, 514	553	0.0005 ^[e] 0.0005 ^[e]	---
PONI	359 (15601) 357 (14300)	431 422	416, ^[f] 547	0.18 ^[g] 0.038 ^[g]	---
PSNI	384 (14700) 382 (13900)	518 500	450, ^[f] 579	0.004 ^[h] 0.006 ^[h]	---
PNI	407 (11300) 398 (11300)	539 516	492, ^[f] 605	0.084 ^[i] 0.81 ^[i]	---
Re1	334 (20400) 334 (20200)	630 ^[d] 614 ^[d]	536, 512	0.0030 ^[h] 0.0028 ^[h]	0.014 ^[h] 0.020 ^[h]
Re2	343 (23200) 343 (23900)	626 ^[d] 617 ^[d]	555, 516	0.0014 ^[h] 0.0014 ^[h]	0.011 ^[h] 0.015 ^[h]
Re3	364 (21600) 363 (24000)	435, 628 ^[d] 611 ^[d]	546, 514	0.0023 ^[h] 0.0014 ^[h]	0.014 ^[h] 0.018 ^[h]
Re4	392 (20700) 393 (20700)	613 ^[d] 613, 645 ^[d]	577, 516	0.0011 ^[h] 0.0010 ^[h]	0.0035 ^[h] 0.0082 ^[h]
Re5	415 (15800) 410 (15400)	548 ^[d] 523 ^[d]	595, 512	0.0032 ^[h] 0.0087 ^[h]	0.0031 ^[h] 0.011 ^[h]
Re6	368 (3160) 372 (3600)	602 ^[d] 601 ^[d]	507	0.011 ^[h] 0.016 ^[h]	0.024 ^[h] 0.029 ^[h]

^[a] Room temperature measurements were made with ACN or THF as a solvent. ^[b] 77 K measurements were made with 2-methyl-THF. ^[c] Emission maximum determined from time-gated PL spectra using the LP 920. ^[d] Samples deaerated using freeze-pump-thaw method. ^[e] Quantum yields were measured using anthracene in aerated ethanol as the standard ($\Phi_{\text{PL}} = 0.28$).⁶⁶ ^[f] Emission maximum determined from steady-state PL spectra using the FS 920. ^[g] Quantum yields were measured using 9,10-diphenylanthracene in aerated cyclohexane as the standard ($\Phi_{\text{PL}} = 0.97$).⁶⁶ ^[h] Quantum yields were measured using $[\text{Ru}(\text{bpy})_3](\text{PF}_6)_2$ in aerated acetonitrile as the standard ($\Phi_{\text{PL}} = 0.018$).⁶⁶ ^[i] Quantum yields were measured using **PNI** in aerated toluene as the standard ($\Phi_{\text{PL}} = 0.91$).⁶⁴

2.4.3. Electronic Structure Calculations

Time-dependent density functional theory (TD-DFT) calculations were performed on all the molecules to glean insight into the nature of the lowest energy electronic transitions observed experimentally. The B3LYP, M06, and CAM-B3LYP functionals were used to perform the ground state geometric optimization and the corresponding TD-DFT calculations, Table A2. Across the

series of naphthalimide model chromophores, the M06 functional yielded the best quantitative modeling of the transition energies, whereas the B3LYP functional was consistently lower in energy and the CAM-B3LYP functional was consistently higher in energy. Unfortunately, both the B3LYP and M06 functionals did not adequately model the **PSNI** chromophore, as both predicted a low energy transition with significant oscillator strength that was not observed experimentally. By using the long-range corrected functional, CAM-B3LYP, the energies of the calculated low energy transitions were all overcorrected (rendered too high in energy), however the trend in relative energies observed in the experimental data were revealed in the low energy transitions using this functional. Natural transition orbital analysis for the $S_0 \rightarrow S_1$ and $S_0 \rightarrow S_2$ transitions using the M06 and CAM-B3LYP functionals was performed on the naphthalimide chromophores, Figures A82-S86. The $S_0 \rightarrow S_1$ transition across the series can be best described as being $\pi \rightarrow \pi^*$ in character, with a small amount of charge transfer observed in **PONI** and a significant amount observed in both **PSNI** and **PNI**. The $S_0 \rightarrow S_2$ transition varied a greater amount across the series and its value was functional dependent. This transition is considerably weaker than the $S_0 \rightarrow S_1$ transition (**PSNI** is the only exception) and was not observed experimentally.

The same TD-DFT analysis was performed on the rhenium chromophores (**Re1-Re6**) with the calculated transitions available in Appendix A, Table A4. Using both the B3LYP and M06 functionals, the calculated charge transfer transition for the Re(I) model (**Re6**) was predicted as too low in energy when compared to the experimental data (0.54 and 0.31 eV lower in energy for the B3LYP and M06 functionals, respectively). Moreover, many new charge transfer transitions in the bichromophores were calculated that were simply not observed experimentally. As with the naphthalimide model compounds, the CAM-B3LYP functional gave the best quantitative match to experimental data based on the trends observed experimentally. Natural transition orbital

analysis for the $S_0 \rightarrow S_1$, $S_0 \rightarrow S_2$, and $S_0 \rightarrow S_n$ transitions using the M06 and CAM-B3LYP functionals were performed on **Re1-Re6**, see Figures A87-S92. In the model MLCT chromophore **Re6**, the $S_0 \rightarrow S_1$ transition can best be described as charge transfer with electronic density originating from the metal and dmap ligands and transitioning to the phenanthroline ligand. This type of transition was observed in all the bichromophores near 3.66 eV (using the CAM-B3LYP functional) and represents the $S_0 \rightarrow S_1$ transition in **Re1-Re3** and the $S_0 \rightarrow S_2$ transition in **Re4-Re5**. The ligand-centered transition localized on the naphthalimide chromophore was also clearly observed in all instances (based on energy and oscillator strength). Using the CAM-B3LYP functional, the NI-localized LC transition is the $S_0 \rightarrow S_4$ transition in **Re1**, the $S_0 \rightarrow S_3$ transition in **Re2** and **Re3**, and the $S_0 \rightarrow S_1$ transition in **Re4** and **Re5**.

2.4.4. Static and Dynamic PL Spectroscopy

The static PL spectra recorded for the model chromophores and Re(I) bichromophores in acetonitrile are presented in Figure 2.3, with additional spectroscopic data collected in Table 2.1. The **NI** and **BrNI** molecules have two observable emission bands in aerated acetonitrile at room temperature, Figure 2.3a. The high energy band in both molecules was structured with emission maxima at 374 and 387 nm, respectively, consistent with fluorescence from the $S_1 \pi \rightarrow \pi^*$ excited state. The low energy PL observed was broad, featureless, and sensitive to solvent polarity, with emission maxima at 506 and 537 nm, respectively. Additionally, excitation spectra were measured in acetonitrile at the high and low energy emission maxima for both dual-emitting chromophores. Regardless of the monitored wavelength, the recorded spectra mimic the low energy transition observed in the electronic spectra of **NI** and **BrNI**, supporting the assignment as dual emission (Figures A43-44). The low-energy emission bands likely originate from a conformational change of the molecule and the formation of planar-intramolecular charge transfer (PICT) excited states.

This dual emission phenomenon has been documented by multiple research groups and demonstrated to occur when the *N*-aryl group of the 1,8-naphthalimide is substituted with an electronically donating substituent.^{63, 83-85} First documented by Bérces and coworkers, a series of 1,8-naphthalimides were prepared using an unsubstituted phenyl ring as the model and adding electron donating or withdrawing substituents to the para position of the *N*-aryl group (among many other NI derivatives). In their model system, only the short-wave fluorescence emission (386 nm in ACN) originating from the $S_1 \pi \rightarrow \pi^*$ excited state was observed. By adding an electron donating group (*p*-MeO) to the *N*-aryl group, the two low-lying excited states undergo pseudo-Jahn-Teller coupling which allows the excited state to cross to the nearly isoenergetic S_2 potential energy surface. Once on this surface, the *N*-aryl group rotates to nearly a coplanar geometry with the naphthalimide and stabilizes the charge transfer excited state. In the *p*-MeO substituted molecule, the long-wave fluorescence (603 nm in ACN) originating from the S_2 CT excited state is observed almost exclusively.⁸⁵ In the case of **NI** and **BrNI**, the *p*-methyl on the *N*-aryl group is electronically more donating than hydrogen but less so than a *p*-MeO so it is probable that some degree of pseudo-Jahn-Teller coupling takes place, therefore supporting the observation of both short-wave and long-wave fluorescence bands in **NI** and **BrNI**.

The **PONI**, **PSNI**, and **PNI** molecules all have broad and featureless fluorescence spectra, with maxima at 431, 518, and 539 nm, respectively, Figure 2.3a. When **PONI**, **PSNI**, and **PNI** are dissolved in lower polarity solvents such as THF or toluene, they experience positive solvatochromism whereas the corresponding PL spectra shift to lower energy with increasing medium polarity. The combination of the broad featureless emission spectra and solvatochromic nature of this PL are both indicative of charge transfer character in the emissive state of these three molecules. In acetonitrile, the emission quantum yield of **PONI** is substantial ($\Phi_F = 0.18$),

followed by **PNI** and **PSNI** ($\Phi_F = 0.084$ and 0.004 , respectively). When dissolved in a lower polarity solvent, such as THF, the **PNI** becomes the most emissive ($\Phi_F = 0.81$), followed by **PONI** and **PSNI** ($\Phi_F = 0.038$ and 0.006 , respectively). In the case of **NI**, **BrNI**, **PSNI**, the low fluorescence quantum yields are likely due to efficient intersystem crossing (ISC) from the S_1 excited state to the triplet manifold.⁶¹ The **PONI** chromophore has a substantially larger fluorescence quantum yield and likely has less efficient ISC. The emission intensity of **PNI** is extremely solvent dependent where fluorescence quantum yields greater than 90% persist in nonpolar solvents such as toluene. In this case, the fluorescence is likely quenched through another mechanism, such as twisted intermolecular charge transfer (TICT) states as the solvent polarity plays a large role in TICT excited state decay.⁸⁶⁻⁸⁸

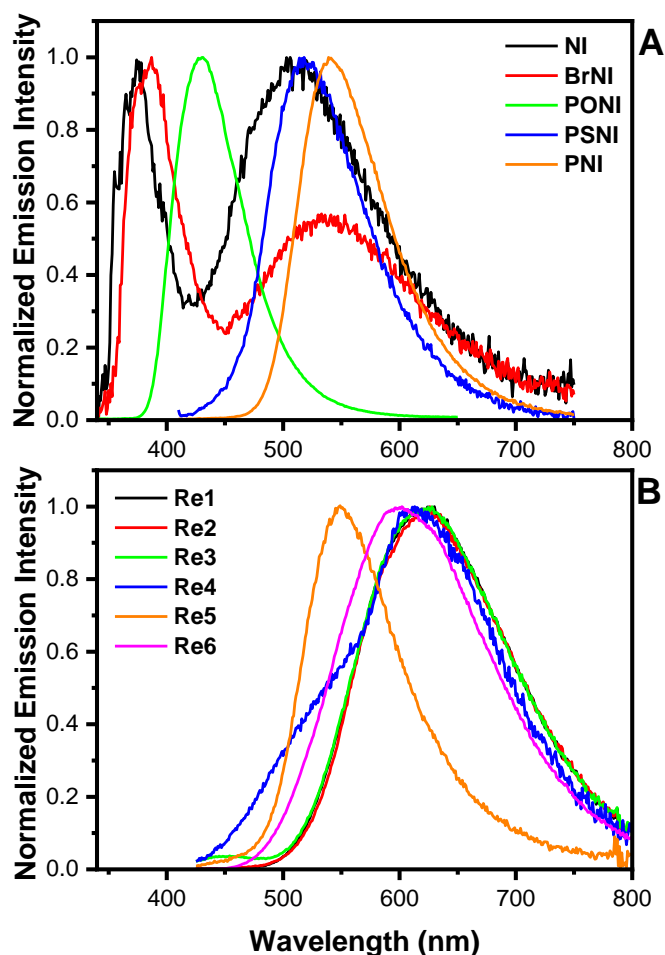


Figure 2.3. Room temperature emission spectra of (A) **NI** ($\lambda_{\text{ex}} = 325$ nm), **BrNI** ($\lambda_{\text{ex}} = 325$ nm), **PONI** ($\lambda_{\text{ex}} = 355$ nm), **PSNI** ($\lambda_{\text{ex}} = 395$), and **PNI** ($\lambda_{\text{ex}} = 395$) recorded in aerated acetonitrile and of (B) **Re1-Re6** ($\lambda_{\text{ex}} = 385$) recorded in deaerated acetonitrile.

The Re(I) model complex (**Re6**) displays a broad, featureless PL emission band centered at 602 nm, which originates from the $^3\text{MLCT}$ excited state, Figure 2.3b. The light emission of **Re6** is quenched by molecular oxygen and possesses a lifetime of 176 ns in deaerated acetonitrile (Figure A48), consistent with the lowest excited state being triplet in origin. Similarly, $^3\text{MLCT}$ PL was observed in **Re1-Re4**, however the spectral profiles are slightly red-shifted to 628 nm in these molecules, Figure 2.3b. Furthermore, the naphthalimide fluorescence is quantitatively quenched in **Re1** and **Re2** (not shown), predominantly quenched in **Re3**, appears as a shoulder in **Re4**, and

is the PL spectrum primarily observed in **Re5**, Figure 2.3b. Since prior studies have demonstrated that Förster-like energy transfer is the primary quenching pathway of the naphthalimide fluorescence in related metal-organic chromophores,^{33, 44} this implies that the energy transfer efficiency is decreasing as the fluorescence of the appended naphthalimide red-shifts. The fact that there is less spectral overlap between the singlet fluorescence donor emission (naphthalimide) and the acceptor absorbance (Re-CDI) as the naphthalimide red-shifts supports these experimental observations being consistent with resonance energy transfer quenching across the series. The PL quantum yields of the bichromophores are smaller than that of **Re6** with **Re1-Re3** having about half the efficiency when compared to the model chromophore ($\Phi_{PL} = 0.013, 0.009, \text{ and } 0.011$, respectively). The other two bichromophores (**Re4** and **Re5**) have substantially less MLCT-based PL and in the case of **Re5**, the observed spectrum is composed of predominately unquenched fluorescence from the **PNI** moiety. As demonstrated in our previous study, the MLCT phosphorescence in the bichromophores is mostly derived from the triplet excited state equilibrium formed between the ³MLCT and ³LC states, with the population of the higher energy ³MLCT excited state based on a Boltzmann distribution.³³ Therefore, the lower the energy of the ³NI excited state (as in **Re4** and **Re5**), the lower the relative population of the ³MLCT excited state and therefore less PL emanating from that state.

PL intensity decays of the metal-organic bichromophores were collected at 600 nm to investigate the population decay kinetics of the ³MLCT state whose data are collected in Table 2.2. In **Re1-Re3**, the emission intensity decays were adequately fit to biexponential functions whose average lifetimes were much longer lived with respect to the Re-CDI model complex, suggesting that equilibrium is indeed operative between the ³MLCT and ³NI excited states.^{33, 44} The biexponential nature of these decays have been previously observed and attributed to

concentration-dependent self-quenching.^{33, 44, 46, 61} To simplify comparisons between molecules, average lifetimes were used and it was determined that **Re1** possessed the shortest lifetime when compared to **Re2** and **Re3** measured at matched concentrations under identical experimental conditions. Furthermore, time-gated PL spectra acquired at numerous delay times confirmed that the emission originated from the ³MLCT excited state in all instances, Figure A49. There was no evidence of any delayed ³MLCT PL in **Re4** and **Re5**, instead only prompt emission from a combination of the naphthalimide fluorescence and strongly quenched MLCT PL was observed. Time-gated PL spectra confirmed these findings as there was little delayed emission observed beyond those prompt signals seen in **Re4** and **Re5**. Since these molecules have the lowest ³NI energies, it is likely that the energy gap is too large to enable thermal population of the higher lying ³MLCT excited state at room temperature and therefore no delayed PL could be observed.

Since phosphorescence was not observed from the ³LC excited state in any of the metal-organic bichromophores at room temperature, each molecule was dissolved in 2-methyltetrahydrofuran (2-MeTHF) and frozen at 77 K by immersion in liquid N₂. At this temperature, the distinct phosphorescence from the ³NI excited states in each instance (**Re1-Re5**) was experimentally distinguished from the ¹NI and ³MLCT states using time-gated PL, Figure 2.4. The PL spectra measured at 1 μs was broad and featureless, with a maximum near 515 nm for all bichromophores (**Re1-Re5**), very closely matching that of the model MLCT complex **Re6**. We conclude that the origin of the emission observed at this time delay emanates from the ³MLCT state resident on the Re-CDI complex. Extending the observation onset to 25 ms after the laser pulse, the observed PL was red-shifted with respect to the ³MLCT PL spectrum, and is vibronically structured, suggesting that the emission now originates from the ³NI excited state. To confirm these assignments, the naphthalimide models were also measured at 77 K under identical

conditions, revealing emission spectra that were very close in energy and spectral features to those of the bichromophores measured at 25 ms delay, Figure A50. The PL decays at 77 K were well modeled using biexponential kinetics for the bichromophores where the first component corresponded to the decay of the $^3\text{MLCT}$ excited state ($\tau \sim 11 \mu\text{s}$) and the second component corresponded to the decay of the extremely long-lived ^3NI excited state ($\tau \geq 10 \text{ ms}$). Since both the $^3\text{MLCT}$ and ^3NI excited states decay independently at 77 K, the excited state equilibrium observed at room temperature in **Re1-Re3** no longer takes place, thereby eliminating any observation of delayed $^3\text{MLCT}$ PL.

Table 2.2. Time-resolved PL and TA data recorded for **Re1-Re6** in acetonitrile.

Molecule	τ_{PL} (298 K) ^[a]	$\tau_{PL\text{ ave}}$ (298 K) ^[b]	τ_{TA} (298 K) ^[c]	$\tau_{TA\text{ ave}}$ (298 K) ^[d]	τ_{PL} (77 K) ^[e]
Re1	6.5 μs , 27.0 μs	14.5 μs	6.6 μs , 19.6 μs	11.9 μs	11.1 μs , 544 ms
Re2	9.5 μs , 60.7 μs	56.6 μs	21.9 μs , 81.3 μs	53.7 μs	10.6 μs , 8.6 ms
Re3	16 μs , 64.6 μs	54.7 μs	18.8 μs , 70.0 μs	42.2 μs	12.6 μs , 612 ms
Re4	< 15 ns	---	34.2 μs , 186 μs	116 μs	10.6 μs , 102 ms
Re5	< 15 ns	---	43.9 μs , 177 μs	136 μs	9.2 μs , 288 ms
Re6	176 ns	---	182 ns	---	13.6 μs

^[a] PL decay of **Re1-Re6** ($25 \pm 2 \mu\text{M}$) measured at 600 nm in deaerated acetonitrile at room temperature. ^[b] Average time constant determined from a weighted average of biexponential components measured in deaerated acetonitrile at room temperature. ^[c] Transient absorption intensity decay of **Re1-Re6** ($25 \pm 2 \mu\text{M}$) measured at 470 nm (**Re1**), 480 nm (**Re2**), 480 nm (**Re3**), 670 nm (**Re4**), 480 nm (**Re5**), 475 nm (**Re6**) in deaerated acetonitrile at room temperature. ^[d] Average time constant determined from a weighted average of biexponential components measured in deaerated acetonitrile at room temperature. ^[e] PL decay of **Re1-Re6** measured at 535 nm (**Re1**), 555 nm (**Re2**), 550 nm (**Re3**), 575 nm (**Re4**), 600 nm (**Re5**), 500 nm (**Re6**) in 2-MeTHF at 77 K.

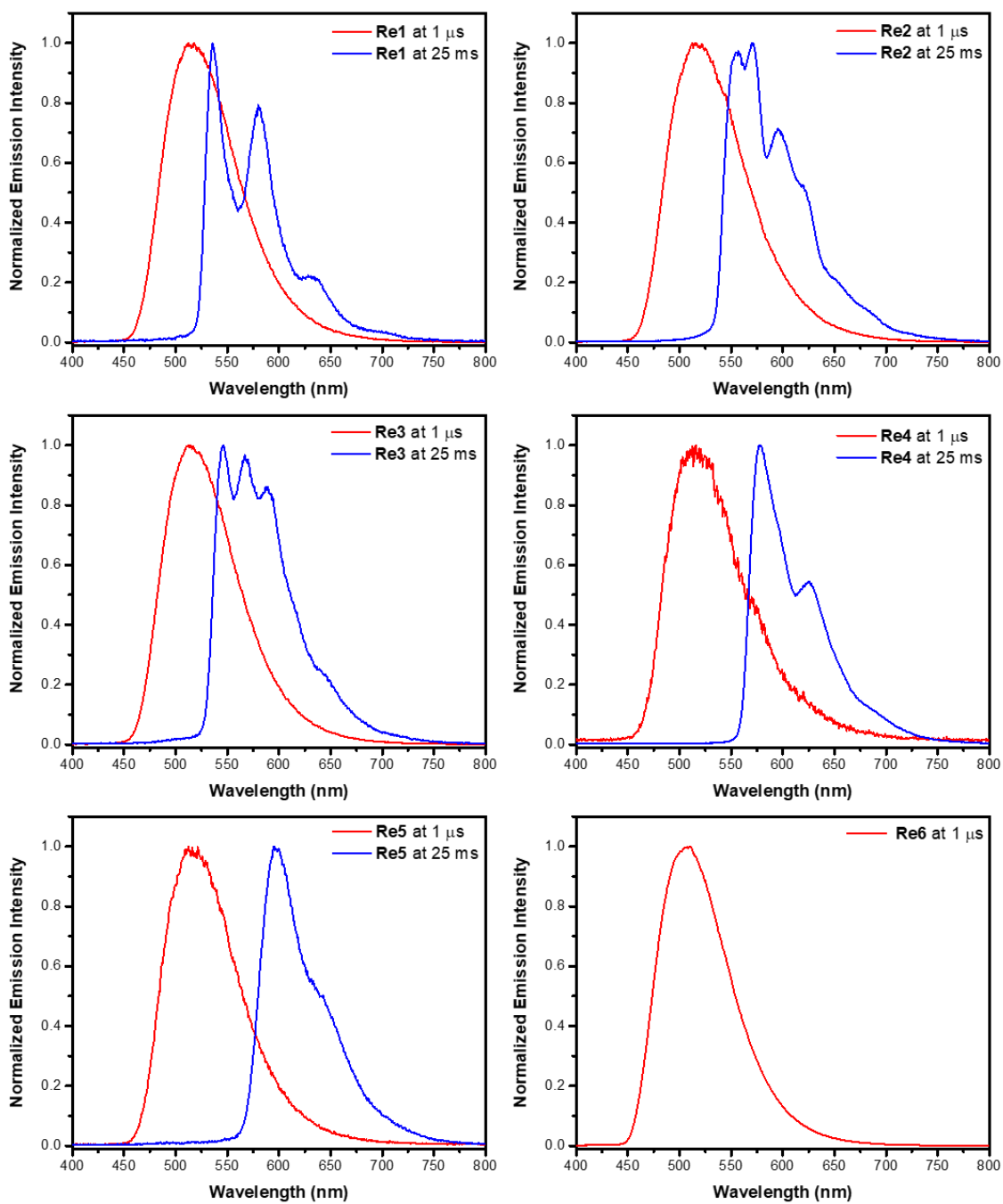


Figure 2.4. Time-resolved 77 K PL emission spectra of **Re1-Re6** at the specified delay times following a 7 ns fwhm, 350 nm (**Re1-Re3**) or 400 nm (**Re4-Re6**) laser pulse in 2-MeTHF.

2.4.5. Transient Absorption Spectroscopy

When attaching the **NI** or **BrNI** structural motif to the Re(I) chromophore, as in the case for **Re1** and **Re2**, the observed excited state processes are consistent with energy transfer occurring between the chromophores. As presented in Figure 2.5, following 350 nm excitation, a transient absorption feature near 475 nm is promptly observed and quantitatively matches that of the S_1 excited state absorptions observed in the **NI** moiety, Figure A51. Unlike the model chromophore, this transient feature in **Re1** decays rapidly ($\tau = 400$ fs) with a new absorption appearing at 370 nm ($\tau = 315$ fs) along with a broad feature near 525 nm that spans into the NIR region. This excited state transient is completely formed by 5 ps and is assigned as the $^3\text{MLCT}$ state of the Re(I) chromophore as it matches the excited state features observed in the Re(I) model (**Re6**) measured under the same experimental conditions, Figure A68. The transition from the $^1\text{LC}, \pi, \pi^*$ state localized on the NI chromophore to the $^3\text{MLCT}$ state was found to have a time constant of 400 fs as this matches the decay of the 470 nm transient feature and the subsequent growth of the 370 nm feature, Figure A54. Going from 5 ps through the end of the delay stage on the nanosecond timescale, the broad excited state absorbance from 500 nm to the NIR decreases in intensity whereas the transient feature at 470 nm grows in; the latter has been previously assigned to the ^3LC triplet excited state localized on the NI chromophore. The kinetic transition from the $^3\text{MLCT}$ excited state to the ^3LC excited state was tracked by analyzing the growth of the 470 nm transient feature, which corresponded to a time constant of 4.1 ± 0.2 ns. Since **NI** has its major low energy absorption band positioned well into the UV, the MLCT state could be selectively excited in **Re1**, Figure A53. Using 400 nm as the excitation source, the initially observed features at 510 fs revealed the presence of the $^3\text{MLCT}$ state with a concomitant growth of the ^3LC feature (470 nm) occurring with a similar time constant as measured with 350 nm laser pulses, $\tau = 4.0$ ns. **Re2**

displays similar excited state features and kinetics to that measured in **Re1**, demonstrating that the addition of the bromo substituent to the naphthalimide does not drastically alter the cascade of excited states or their relative time constants, Figures A56-S58.

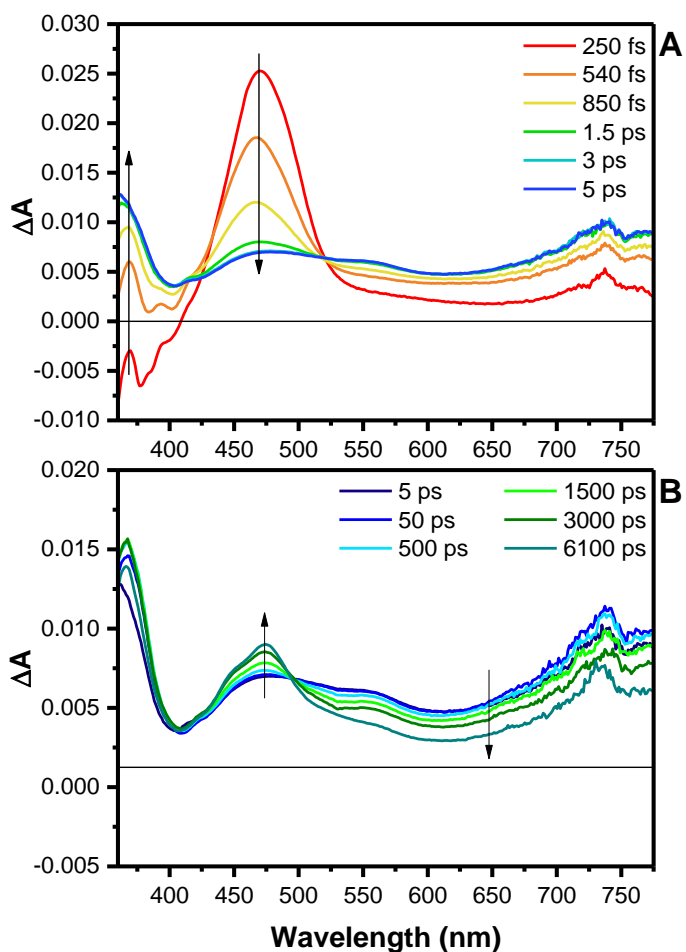


Figure 2.5. Excited-state absorption difference spectra of **Re1** in ACN during short delay times (A) and long delay times (B) following 350 nm pulsed excitation (105 fs fwhm).

When the **PONI** chromophore is attached to the Re(I) subunit, as in **Re3**, the effects of energy transfer between chromophores are also clearly delineated. When using 350 nm laser pulses, the excited state difference spectrum of **Re3** at 250 fs quantitatively matches that of the **PONI** model, suggesting that the initial excited state is indeed localized on the **PONI**

chromophore, Figure 2.6. The excited state absorbance at 450 nm undergoes a similar thermalization process observed with the **PONI** model, except now when the blue-shifted excited state absorbance at 425 nm decays, a new excited state feature at 360 nm grows in and matches that of the ³MLCT excited state of the Re(I) model **Re6**. The change in these absorption features suggests vibrational relaxation from the initially populated Franck-Condon state localized on the **PONI** moiety ($\tau = 170$ fs) is followed by resonance energy transfer to the Re(I) chromophore ($\tau = 1.5$ ps) with subsequent ultrafast intersystem crossing to the ³MLCT excited state. When examining the kinetics at 370 nm, the data is best fit to a sum of three exponentials yielding one time constant ($\tau = 26$ ps) matching that observed in **Re6** measured under the same conditions, Figure A69. Towards the end of the delay stage, the excited state absorbance at 360 nm and at 725 nm decrease in intensity as the excited state feature at 475 nm, assigned as the triplet localized on the **PONI**, gains intensity. The growth of this 475 nm feature is best fit to a single exponential function with a time constant of 4.4 ns, nearly matching what was observed in **Re1** and **Re2**, Figure A60. The change in these spectral features suggest a triplet-triplet energy transfer process returning the excited state density from the ³MLCT state back to the ³LC state on the **PONI** ligand.

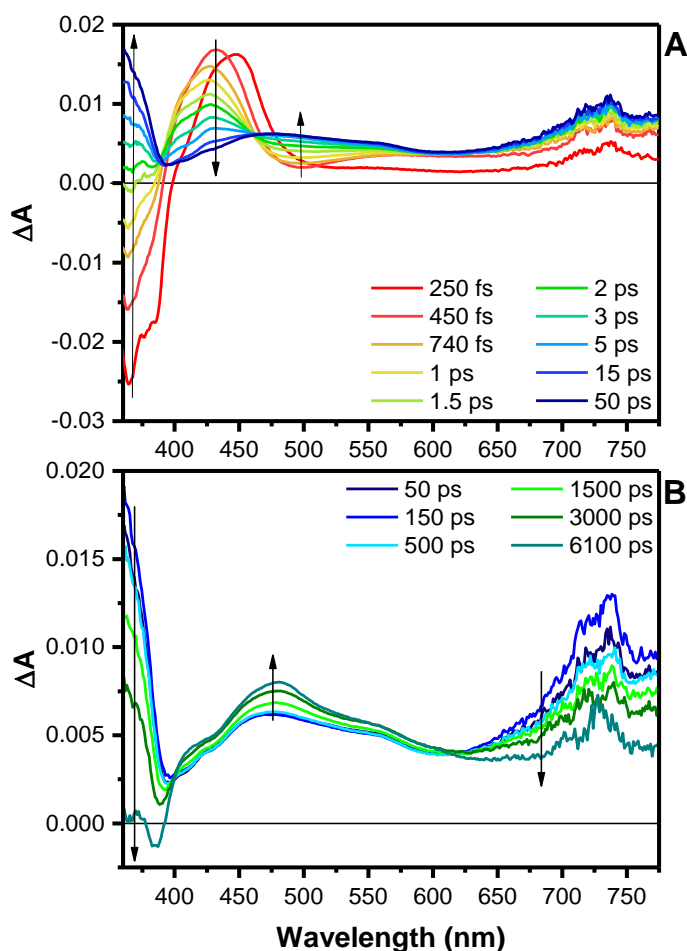


Figure 2.6. Excited-state absorption difference spectra of **Re3** measured in acetonitrile across short (A) and long (B) delay times following 350 nm pulsed laser excitation (105 fs fwhm).

Unlike **Re1-Re3**, when coupling the **PSNI** subunit to the Re(I) complex to yield **Re4**, there were no significant changes in terms of the transient absorption difference spectra and kinetics in comparison to the **PSNI** model chromophore. As displayed in Figure 2.7, the excited state absorption features for the short and intermediate time ranges in **Re4** nearly match those observed in **PSNI**, suggesting that the ^3LC formation does not proceed through the $^3\text{MLCT}$ excited state as was observed in **Re1-Re3**. Following the first relaxation process at 450 nm, the kinetics in **Re4** are best modeled using a biexponential function recovering time constants consistent to those of the **PSNI** model ($\tau_1 = 100$ fs; $\tau_2 = 3.3$ ps; see Figure A63). As stated earlier, the initial time

constant is assigned to vibrational relaxation of the initially prepared “hot” excited state whereas the second component is associated with the rotation of the *N*-phenanthroline and/or thiobenzene groups leading to the relaxed geometry of the ¹PSNI charge transfer excited state. Since the fluorescence of the **PSNI** and the absorbance of the Re(I) complex have minimal spectral overlap, any possible FRET occurring between the two covalently linked molecules is likely inefficient and slow. To benchmark representative efficient and rapid FRET in a related molecule, a 45 ps time constant was observed for this process in a Re(I)-PNI bichromophore.³³ Since internal conversion to a non-fluorescent excited state on the **PSNI** moiety is markedly faster ($\tau = 3.3$ ps) with respect to an efficient FRET process, energy transfer to the Re(I) chromophore is no longer possible and excited state density remains fixed on the **PSNI** subunit in **Re4**. Following the decay of the excited state features in the intermediate time regime, subsequent formation of the long-lived ³NI excited state occurred with a time constant of 73 ps. The minor variation in the excited state difference spectra at long delay times are attributed to a minor fraction of ³MLCT excited state being generated as a result of non-selective sample excitation. When using 400 nm laser pulses in **Re4**, the ¹NI excited state is predominately populated, however there is a small fraction of the ¹MLCT excited state being generated in this experiment. Since population of the ¹MLCT excited state will almost immediately intersystem cross to the ³MLCT excited state, the observed changes at long delay times are likely due to triplet-triplet energy transfer from the minor ³MLCT excited state population converting into the long-lived ³LC **PSNI** excited state. The time constant for this process was determined to be 2.9 ns in acetonitrile using global fit analysis, Figure A64.

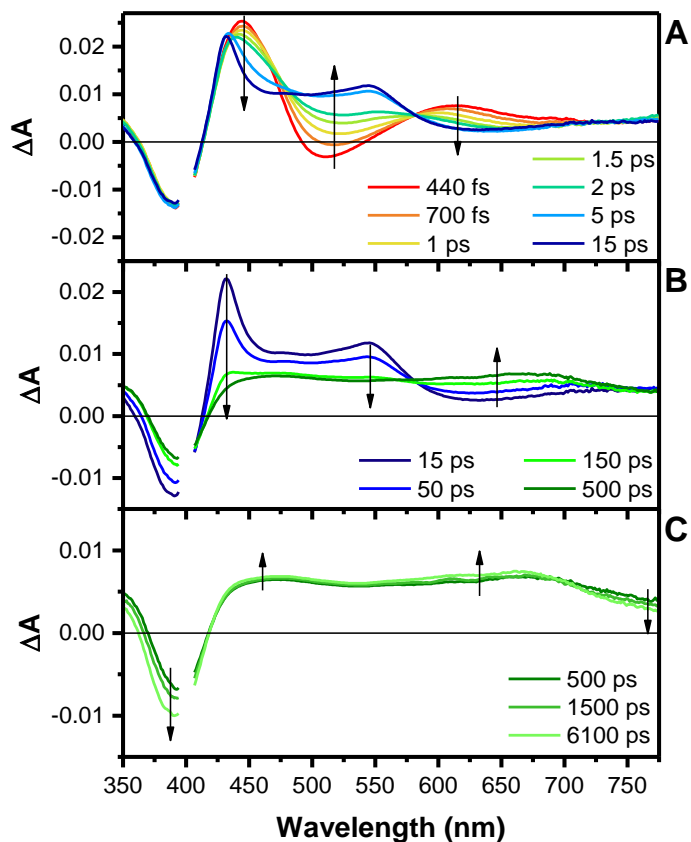


Figure 2.7. Excited-state absorption difference spectra of **Re4** measured in acetonitrile during short (A) intermediate (B) and long (C) delay times following 400 nm pulsed laser excitation (105 fs fwhm).

The excited state difference spectra recorded for the **Re5** species is shown in Figure 2.8. At 300 fs, the excited state features quantitatively match those previously measured for the ^1NI excited state localized on **PNI**. By kinetically tracking the excited state absorbance at 430 nm, the decay can best be fit to two time constants where the fast component ($\tau = 900$ fs) is assigned to vibrational relaxation and the slower component ($\tau = 42$ ps) corresponds to energy transfer to the **Re(I)** chromophore through the FRET mechanism as observed in the previous investigated **Re(I)-PNI** bichromophore.³³ Translating towards the end of the delay stage, the ground state bleach recovers as the excited state features at 470 and 750 nm increase, which are characteristic

signatures of the ^3NI excited state, indicating the final triplet-triplet energy transfer process from the $^3\text{MLCT}$ to the ^3NI excited state. Following the kinetics of the transient features at 415 or 475 nm reveal a single exponential time constant of 2.1 ns for this TTET process, Figure A66.

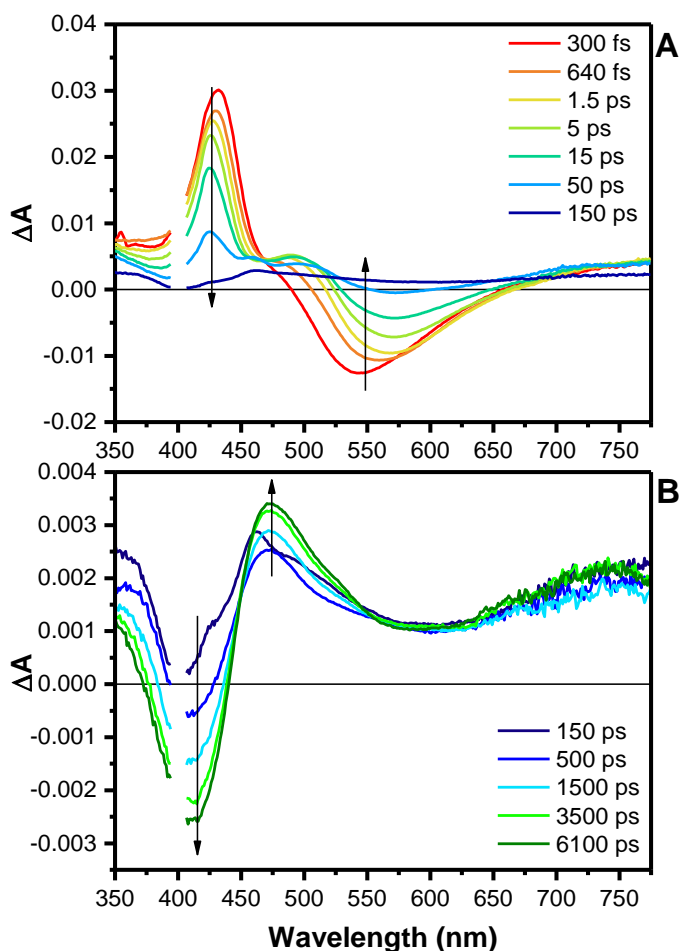


Figure 2.8. Excited-state absorption difference spectra of **Re5** measured in acetonitrile during short (A) and long (B) delay times following 400 nm pulsed laser excitation (105 fs fwhm).

The excited state absorption difference spectra measured in the microsecond time domain for the five **Re1-Re5** bichromophores are presented in Figure 2.9. In each case, the observed excited state difference spectra were consistent with the ultrafast excited state difference spectra obtained at 6.1 ns, implying that the identical excited state was observed throughout the time scales of these two experiments. These excited state features continue to persist for tens to hundreds of

microseconds (Table 2.2), suggesting that the absorption features originate from a long-lived ^3LC excited state in each instance. Since each naphthalimide model chromophore forms the corresponding triplet excited state independently (except in the case of **PNI**), the same transient absorption experiments were performed on the model molecules in order to compare the excited state difference spectra directly, Figure A70. The excited state difference spectra for **NI** and **Re1**, include two excited state absorptions at 370 and 475 nm, Figure 2.9a. The difference spectra for **BrNI** and **Re2** are very similar to that of **NI** and **Re1**, where the two characteristic excited state absorptions were red-shifted to 380 and 490 nm, Figure 2.9b. The excited state difference spectra for **PONI** and **Re3** have a broad excited state absorbance centered at 470 nm and a ground state bleach located at 365 nm (Figure 2.9c) while **PSNI** and **Re4** have a broad excited state absorbance centered at 675 nm and a ground state bleach located at 390 nm, Figure 2.9d. The excited state difference spectrum for **Re5** has a broad excited state absorbance with two peaks at 480 and 725 nm and a ground state bleach located at 410 nm, Figure 2.9e. Previous experiments using thioxanthone sensitized the triplet excited state in **PNI** which is in qualitatively good agreement to the excited state difference spectra presented for **Re5** in Figure 2.9e.⁴⁴ The transient absorption decay kinetics were also collected for each of the NI models and presented in Appendix A (Figures A71-74).

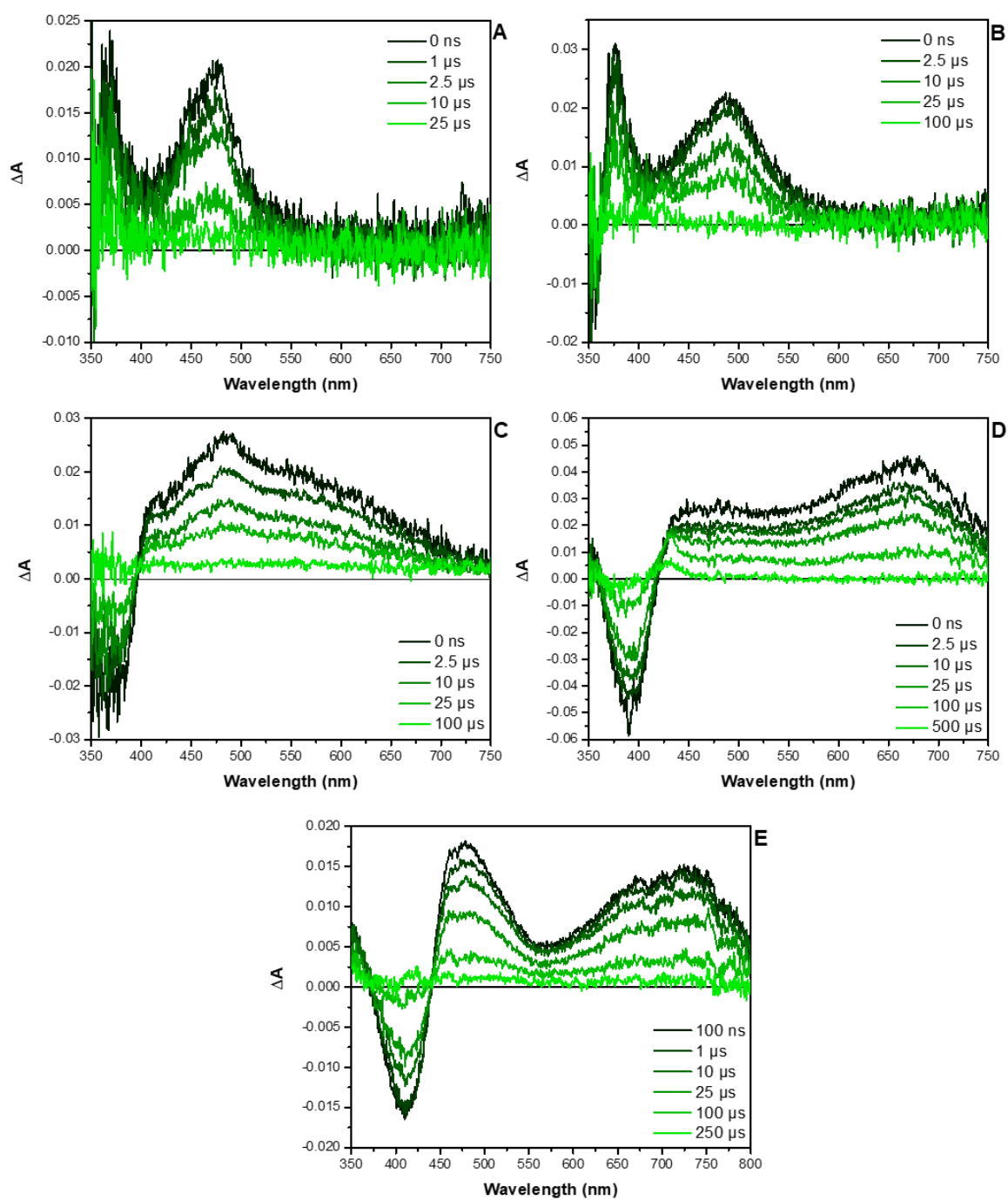


Figure 2.9. Excited-state absorption difference spectra of **Re1** (A), **Re2** (B), **Re3** (C), **Re4** (D), and **Re5** (E) measured in acetonitrile following 350 nm pulsed laser excitation (2.5 mJ/pulse, 7 ns fwhm) or 400 nm pulsed laser excitation (3.0 mJ/pulse, 7 ns fwhm). Samples were deaerated using the freeze-pump-thaw degas method.

2.4.6. Excited State Equilibrium

The decay kinetics of the delayed $^3\text{MLCT}$ PL and the ^3LC excited state absorptions measured in **Re1-Re3** at room temperature are very similar, suggesting that the two excited states in these molecules are indeed in thermal equilibrium. As observed previously, the time constant measured from both experiments was found to lie in between that of the anticipated $^3\text{MLCT}$ decay (174 ns) and ^3NI decay time constants ($> 500 \mu\text{s}$), indicative of a thermal equilibrium process occurring between the two triplet excited states.^{33, 44, 46} The excited state lifetime was shortest in **Re1** and this is likely due to the energy gap between the two triplet excited states being smallest and therefore more rapid population of the shorter-lived $^3\text{MLCT}$ excited state. As the energy gap between the triplet excited states increase across the series (based on ^3LC phosphorescence data), the population of the higher energy $^3\text{MLCT}$ excited state is anticipated to systematically decrease, resulting in excited state lifetime properties more characteristic of the organic chromophore. Once this energy gap becomes too large for sufficient population of the higher energy excited state at room temperature, the bichromophore photophysics in **Re4** and **Re5** then strongly resembles those of the **PSNI** and **PNI** models, respectively. The long-lived ^3LC excited state absorption was also observed in **Re4** and **Re5**, however, there was no significant evidence of delayed $^3\text{MLCT}$ PL observed on similar time-scales and therefore no evidence for a triplet excited state equilibrium.

The triplet energy gap between the ^3NI and $^3\text{MLCT}$ excited states in **Re1-Re5** was estimated using several different experimental and electronic structure calculation-based methodologies as summarized in Table 2.3. The simplest method for estimating the energy gap between the two excited states is to compare the phosphorescence energies of the two emitting states using time-gated PL spectroscopy. Since the phosphorescence of the ^3NI excited state was not observed at room temperature in any of the molecules under investigation, the 77 K PL spectra

(Figure 2.4) originating from the two excited states were resolved. From this spectral information, the energy gap was found to range from 2430 to 3900 cm^{-1} with **Re1** having the smallest energy gap and **Re5** having the largest energy gap. Unfortunately, this particular method cannot be considered reliable since the state energies of charge transfer states substantially shift when measured as 77 K glasses due to a combination of a pronounced thermally-induced Stokes shift and the rigidochromic effect. Since the naphthalimide chromophores have little to no charge character in their triplet excited states when compared to the parent Re(I) MLCT complex, the resulting phosphorescence of the naphthalimides shift insignificantly upon cooling to 77 K. Therefore, the calculated triplet energy gaps using this methodology are substantially overestimated with respect to room temperature. The $^3\text{MLCT}/^3\text{NI}$ energy gap for the five bichromophores were also estimated by taking the difference between the experimental room temperature MLCT PL tangent (using the highest energy side of the emission band and intersecting this with the x-axis) and the 77 K NI tangent to circumvent the temperature-dependent shift of the MLCT excited state energy. In this case, the energy gaps were determined to be much smaller, ranging from 600 to 2120 cm^{-1} with the energetic ordering following the respective compound numbering scheme, **Re1** to **Re5**. The energy gaps calculated in this manner are likely more accurate to the true room temperature triplet separation but are believed to be slightly underestimated due to the $< 500 \text{ cm}^{-1}$ blue shift expected for the nonpolar naphthalimide triplet excited states resident in these metal-organic bichromophores.^{67, 89}

Table 2.3. Calculated triplet energy gap of **Re1-Re5** using different methodologies.

Molecule	Emission $\Delta E_{\text{MLCT-NI}}$ (cm^{-1}) ^[a,b]	Emission $\Delta E_{\text{MLCT-NI}}$ (cm^{-1}) ^[a,c]	Equilibrium ΔE (cm^{-1}) ^[d]	ΔSCF $\Delta E_{\text{Re6-NI}}$ (cm^{-1}) ^[e]	TD-DFT $\Delta E_{\text{T2-T1}}$ (cm^{-1}) ^[f]
Re1	2430	600	880	1740	2860
Re2	2800	1070	1280	2430	3580
Re3	2680	860	1180	2140	2860
Re4	3650	1870	2000	2980	4060
Re5	3900	2120	1860 ^[g]	4020	4340

^[a] The $E_{0,0}$ emission energies were estimated using highest energy side of the emission band and intersecting this with the x-axis. ^[b] The $^3\text{MLCT}$ and ^3NI emission measured at 77 K in 2-MeTHF. ^[c] The $^3\text{MLCT}$ emission taken at room temperature (in THF) with the ^3NI emission measured at 77 K in 2-MeTHF. ^[d] The energy gap was calculated using equations 1-3 based on prior studies.^{33, 44} ^[e] The energy gap was calculated by subtracting the ΔSCF (TS-GS) energy of NI models from the ΔSCF (TS-GS) energy of the **Re6** using DFT//CAM-B3LYP/Def2-SVP/SDD level of theory. ^[f] The energy gap was calculated by subtracting the $S_0 \rightarrow T_2$ energy from the $S_0 \rightarrow T_1$ energy of **Re1-Re5** using TD-DFT//B3LYP/Def2-SVP/SDD level of theory.^[g] The ^3NI rate constant was approximated to 6670 s^{-1} ($\tau \approx 150 \mu\text{s}$) since ^3NI formation was not observed in **PNI**; estimated from previous triplet sensitization efforts using thioxanthone.

The third method for estimating the energy gap was identical to our prior studies,^{33, 44} where the energy separation between the two triplet excited states can be approximated using the measured rate constants in Eqs. 2.1-2.3. The bimolecular nature of the $^3\text{MLCT}$ emission of the bichromophores were simplified using a weighted average of the two components. Using **Re1** as a representative example, the time constants obtained from transient absorption decays for **NI**, **Re1**, and **Re6** were converted to rate constants ($5.80 \times 10^3 \text{ s}^{-1}$, $8.40 \times 10^4 \text{ s}^{-1}$ and $5.50 \times 10^6 \text{ s}^{-1}$, respectively) and inserted into Eq. 2.1 to determine the relative population of each excited state. The relative population (α) is then used to determine the equilibrium constant (K_{eq}) in Eq. 2.2, which was determined to be 69.2 in this instance. Finally, the equilibrium constant was substituted into the Arrhenius equation (Eq. 2.3) to determine the energy difference between the two excited states. Using this method, energy gaps of 880, 1280, 1180, 2000, and 1860 cm^{-1} were determined for **Re1**, **Re2**, **Re3**, **Re4**, and **Re5** respectively. Please note that the model **PNI** chromophore does

not populate a triplet excited state without being photosensitized by a triplet donor such as thioxanthone. The resulting kinetics from this sensitization process are complicated (in addition to being concentration dependent) so the time constant for the triplet excited state decay was estimated as $\tau \approx 150 \mu\text{s}$. The energy gaps calculated in this manner agree well with the differences in the phosphorescence energies detailed above.

$$k_{obs} = \alpha[k_{LC}] + (1 - \alpha)[k_{MLCT}] \quad (\text{Eq. 2.1})$$

$$K_{eq} = \frac{{}^3LC}{{}^3MLCT} = \frac{\alpha}{1 - \alpha} \quad (\text{Eq. 2.2})$$

$$\Delta E = -RT \ln(K_{eq}) \quad (\text{Eq. 2.3})$$

The remaining approaches for estimating the energy gap between the two triplet excited states in **Re1-Re5** was through DFT calculations. For the delta self-consistent field (ΔSCF) method, the optimized ground state and triplet state geometries of the model chromophores (**NI**, **BrNI**, **PONI**, **PSNI**, **PNI** and **Re6**) were used to estimate their energies. The estimated energy of the ${}^3\text{NI}$ and ${}^3\text{MLCT}$ excited states (depending on the functionals used) were calculated by taking the difference in the respective triplet state and ground state energies. Finally, the ${}^3\text{NI}$ energy of the five naphthalimide model compounds were subtracted from the ${}^3\text{MLCT}$ energy of **Re6** to determine the energy gap. Using this approach, the trend in energy gaps correlate well with the other three experimental methods with values ranging from 1740 to 4020 cm^{-1} . When comparing energy gaps obtained from the equilibrium method, there appears to be a systematic error of approximately 900 cm^{-1} where the ΔSCF approach overestimates the triplet gap. The TD-DFT method calculates the energies of the $S_0 \rightarrow T_1$ and $S_0 \rightarrow T_2$ transitions from the optimized ground state and takes the difference in energy between the two states. Using natural transition orbital (NTO) analysis, the ${}^3\text{NI}$ and ${}^3\text{MLCT}$ excited states can be clearly delineated for the $S_0 \rightarrow T_1$ and

$S_0 \rightarrow T_2$ transitions, respectively for **Re1-Re5**, Figures A87-S91. The same trend is observed here as was determined in the Δ SCF method, but now there appears to be a larger systematic error as the energy gaps using the NTOs range from 2860 to 4340 cm^{-1} .

Overall, the five approaches consistently varied with the anticipated trends in the energy gaps but had a larger variance when it came to the absolute values. The equilibrium method was likely the most accurate when estimating the energy gap but exact triplet excited state decay kinetics are needed for both model chromophores in order to be useful. The largest energy gaps previously reported for similar excited state equilibria between 2 triplet excited states in a metal-organic bichromophores were 1680 cm^{-1} and 1740 cm^{-1} ,^{33, 41} so the energy gap in **Re4** is sufficiently large for the ^3NI decay kinetics to outcompete thermal activation of the $^3\text{MLCT}$ excited state, thereby shunting the triplet equilibrium process.

2.4.7. Excited State Evolution and Decay Kinetics

The relevant energy level diagrams summarizing the observed photophysical processes of **Re1-Re5** are displayed in Figure 2.10. **Re1-Re3** follow the “ping-pong” energy transfer mechanism described previously,³³ where the initially populated ^1NI excited state localized on the naphthalimide subunit first transfers its energy to the $^1\text{MLCT}$ excited state localized on the Re(I) chromophore. These three bichromophores feature significantly faster singlet energy transfer time constants ($\tau = 360$ fs to $\tau = 1.5$ ps) compared to the previous bichromophore containing PNI ($\tau = 45$ ps),³³ due to greater spectral overlaps between the naphthalimide emission and Re(I) MLCT absorption. The second energy transfer process takes place once the $^3\text{MLCT}$ excited state is formed, this time returning the excited state energy back to the naphthalimide chromophore yielding its long-lived ^3NI excited state. While the ^3NI is the lowest energy excited state, in **Re1-Re3** the $^3\text{MLCT}$ is in sufficient energetic proximity enabling thermally activated reverse TTET

facilitating a triplet excited state equilibrium. This results in the generation of markedly extended lifetimes for the $^3\text{MLCT}$ excited state, manifested through the observation of delayed MLCT-based PL.

Re4 breaks the trend observed in the first three bichromophores by maintaining the excited state density localized predominately on the naphthalimide chromophore, following near identical excited state decay as that observed in the **PSNI** model. This occurs since the singlet energy transfer efficiency to the Re(I) chromophore is extremely slow (poor spectral overlap) and efficient internal conversion/intersystem crossing rapidly takes place within the **PSNI** subunit. Once the long-lived ^3NI excited state is formed, it is also too low in energy with respect to the $^3\text{MLCT}$ excited state to yield any excited state equilibrium, so subsequently no delayed MLCT PL is observed. Since intersystem crossing was not observed in the **PNI** chromophore, **Re5** still relies on inefficient singlet energy transfer to the Re(I) chromophore in order to access the triplet manifold (despite the poor spectral overlap) resulting in another example of “ping-pong” energy transfer leading to the generation of the lowest excited state. However, unlike **Re1-Re3**, the energy gap between the $^3\text{MLCT}$ and ^3NI excited states in **Re5** is simply too large for excited state equilibrium to become established at room temperature so this excited state dissipates non-radiatively exclusively through the ^3NI excited state.

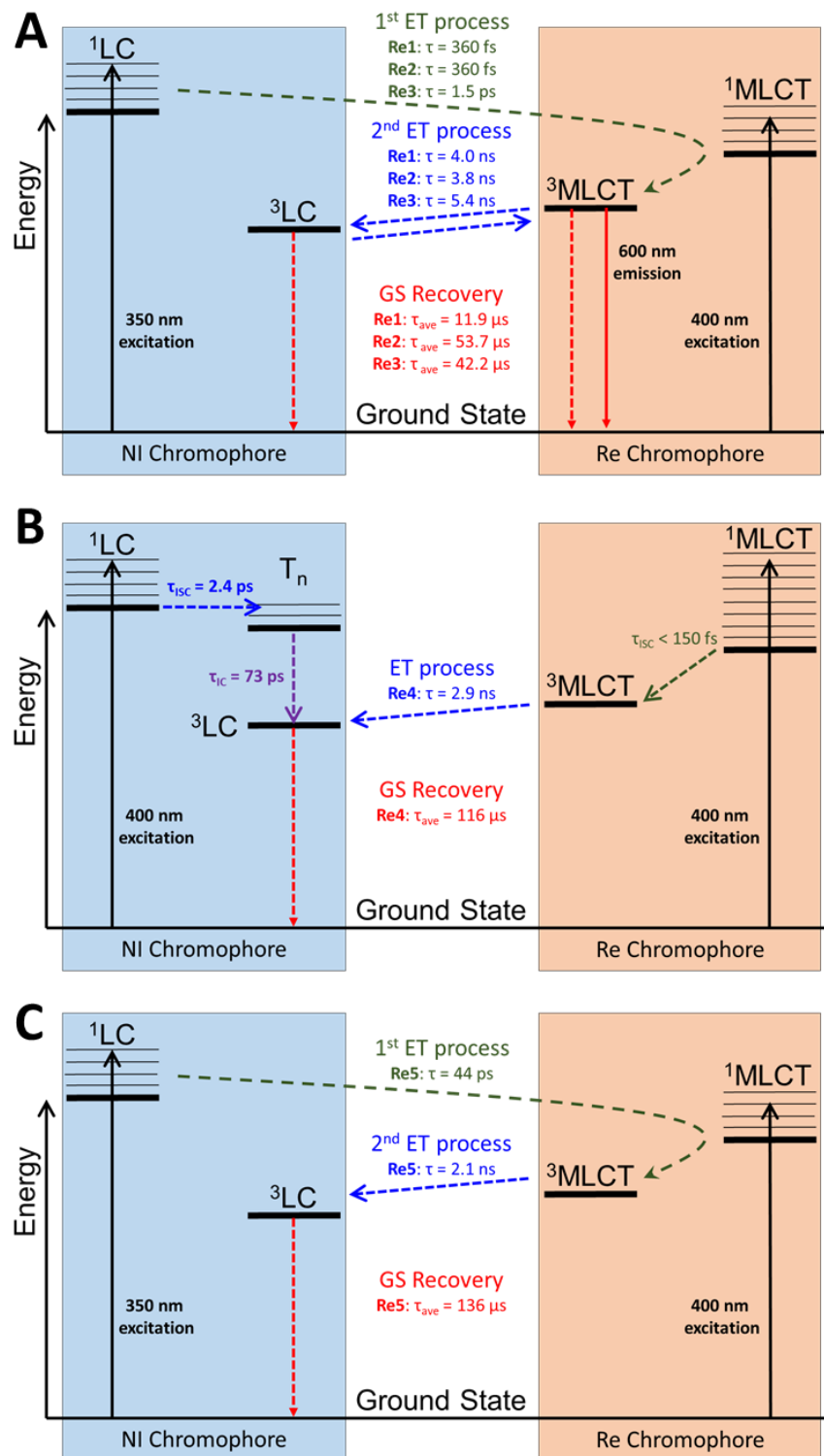


Figure 2.10. Qualitative energy level diagrams of the photophysical processes occurring in **Re1-Re3** (A), **Re4** (B), and **Re5** (C) in acetonitrile at room temperature.

2.5. Conclusions

In this investigation, the excited state processes and the associated kinetics of a series of five distinct NI chromophores along with five Re(I)-NI bichromophores were elucidated using a combination of transient absorption spectroscopy and time-resolved PL spectroscopy. Additionally, the spectroscopic analysis was supported by electronic structure calculations to identify the origin of many of the observed electronic transitions. The series of naphthalimides were synthesized by substituting the 4-position of the naphthalimide with various substituents (hydrogen, bromine, phenoxy, thiobenzene, piperidine), resulting in changes to many of the requisite photophysical properties, including energies of the ^1NI and ^3NI states and fluorescence quantum yields. By covalently attaching these newly synthesized naphthalimide ligands to a Re(I) MLCT complex, a series of bichromophores were created to evaluate the energy transfer processes occurring between the two chromophores and the subsequent excited state equilibrium formed between the low energy $^3\text{MLCT}$ and ^3NI excited states. Four of the five bichromophores demonstrated “ping-pong” energy transfer where the initially excited naphthalimide chromophore was found to rapidly transfer its energy to the Re(I) chromophore. Following fast intersystem crossing and the formation of the $^3\text{MLCT}$ excited state localized on the Re(I) chromophore, the excited state energy was back transferred to the naphthalimide chromophore and the formation of the ^3NI state was observed. Excited state triplet equilibrium was observed in the three bichromophores featuring the highest energy ^3NI excited states (**Re1-Re3**), resulting in the observation of delayed $^3\text{MLCT}$ PL with lifetimes extending well into the microsecond time regime. The two bichromophores with the lowest energy ^3NI excited states (**Re4** and **Re5**) did not thermally populate the higher energy $^3\text{MLCT}$ level. In these instances, ^3NI ligand-centered

deactivation dominated the photophysical processes, decaying with lifetimes exceeding 100 μ s at room temperature.

2.6. Acknowledgments

This work was supported by the U.S. Department of Energy, Office of Science, Office of Basic Energy Sciences, under Award No. DE-SC0011979. J.E.Y. was supported by the Air Force Institute of Technology (AFIT). I would also like to thank the co-authors, James E. Yarnell, Jonathan R. Palmer, Josué M. Breaux, and Felix N. Castellano.

2.7. References

1. Balzani, V.; Campagna, S., *Photochemistry and Photophysics of Coordination Compounds II*. Springer-Verlag: Berlin, Germany, 2007.
2. Patrocínio, A. O. T.; Frin, K. P. M.; Murakami Iha, N. Y., Solid State Molecular Device Based on a Rhenium(I) Polypyridyl Complex Immobilized on TiO₂ Films. *Inorg. Chem.* **2013**, *52* (10), 5889-5896.
3. Zanoni, K. P. S.; Murakami Iha, N. Y., Reversible trans [right left harpoons] cis photoisomerizations of [Re(CO)₃(ph₂phen)(stpyCN)]⁺ towards molecular machines. *Dalton Trans.* **2017**, *46* (30), 9951-9958.
4. O'Regan, B.; Graetzel, M., A low-cost, high-efficiency solar cell based on dye-sensitized colloidal titanium dioxide films. *Nature* **1991**, *353* (6346), 737-740.
5. Photosensitization and Photocatalysis Using Inorganic and Organometallic Compounds. Kalyanasundaram, K.; Grätzel, M., Eds. Kluwer: Dordrecht, Netherlands, 1993.
6. Szymanski, H.; Lakowicz, J. R., Fluorescence lifetime-based sensing and imaging. *Sens. Actuators, B* **1995**, *29* (1-3), 16-24.
7. de Silva, A. P.; Gunaratne, H. Q. N.; Gunnlaugsson, T.; Huxley, A. J. M.; McCoy, C. P.; Rademacher, J. T.; Rice, T. E., Signaling recognition events with fluorescent sensors and switches. *Chem. Rev.* **1997**, *97* (5), 1515-1566.
8. Beer, P. D., Transition-Metal Receptor Systems for the Selective Recognition and Sensing of Anionic Guest Species. *Acc. Chem. Res.* **1998**, *31* (2), 71-80.
9. Castellano, F. N.; Lakowicz, J. R., A water-soluble luminescence oxygen sensor. *Photochem. Photobiol.* **1998**, *67* (2), 179-183.
10. Lakowicz, J. R.; Castellano, F. N.; Dattelbaum, J. D.; Tolosa, L.; Rao, G.; Gryczynski, I., Low-Frequency Modulation Sensors Using Nanosecond Fluorophores. *Anal. Chem.* **1998**, *70* (24), 5115-5121.
11. Slone, R. V.; Benkstein, K. D.; Belanger, S.; Hupp, J. T.; Guzei, I. A.; Rheingold, A. L., Luminescent transition-metal-containing cyclophanes ("molecular squares"): covalent self-assembly, host-guest studies and preliminary nanoporous materials applications. *Coord. Chem. Rev.* **1998**, *171*, 221-243.
12. Lakowicz, J. R., *Principles of Fluorescence Spectroscopy*. 3rd ed.; Springer: New York, NY, 2006.
13. Sun, S.-S.; Lees, A. J., Anion recognition through hydrogen bonding: a simple, yet highly sensitive, luminescent metal-complex receptor. *Chem. Commun.* **2000**, (17), 1687-1688.

14. Demas, J. N.; DeGraff, B. A., Applications of luminescent transition platinum group metal complexes to sensor technology and molecular probes. *Coord. Chem. Rev.* **2001**, *211*, 317-351.
15. Terpetschnig, E.; Szmecinski, H.; Malak, H.; Lakowicz, J. R., Metal-ligand complexes as a new class of long-lived fluorophores for protein hydrodynamics. *Biophys. J.* **1995**, *68* (1), 342-350.
16. Guo, X.-Q.; Castellano, F. N.; Li, L.; Lakowicz, J. R., Use of a Long-Lifetime Re(I) Complex in Fluorescence Polarization Immunoassays of High-Molecular-Weight Analytes. *Anal. Chem.* **1998**, *70* (3), 632-637.
17. Probst, B.; Kolano, C.; Hamm, P.; Alberto, R., An Efficient Homogeneous Intermolecular Rhenium-Based Photocatalytic System for the Production of H₂. *Inorg. Chem.* **2009**, *48* (5), 1836-1843.
18. Probst, B.; Rodenberg, A.; Guttentag, M.; Hamm, P.; Alberto, R., A Highly Stable Rhenium-Cobalt System for Photocatalytic H₂ Production: Unraveling the Performance-Limiting Steps. *Inorg. Chem.* **2010**, *49* (14), 6453-6460.
19. Yi, X.; Zhao, J.; Wu, W.; Huang, D.; Ji, S.; Sun, J., Rhenium(I) tricarbonyl polypyridine complexes showing strong absorption of visible light and long-lived triplet excited states as a triplet photosensitizer for triplet-triplet annihilation upconversion. *Dalton Trans.* **2012**, *41* (29), 8931-8940.
20. Hayashi, Y.; Kita, S.; Brunschwig, B. S.; Fujita, E., Involvement of a Binuclear Species with the Re-C(O)O-Re Moiety in CO₂ Reduction Catalyzed by Tricarbonyl Rhenium(I) Complexes with Diimine Ligands: Strikingly Slow Formation of the Re-Re and Re-C(O)O-Re Species from Re(dmb)(CO)₃S (dmb = 4,4'-Dimethyl-2,2'-bipyridine, S = Solvent). *J. Am. Chem. Soc.* **2003**, *125* (39), 11976-11987.
21. Takeda, H.; Koike, K.; Inoue, H.; Ishitani, O., Development of an Efficient Photocatalytic System for CO₂ Reduction Using Rhenium(I) Complexes Based on Mechanistic Studies. *J. Am. Chem. Soc.* **2008**, *130* (6), 2023-2031.
22. Smieja, J. M.; Kubiak, C. P., Re(bipy-tBu)(CO)₃Cl-improved Catalytic Activity for Reduction of Carbon Dioxide: IR-Spectroelectrochemical and Mechanistic Studies. *Inorg. Chem.* **2010**, *49* (20), 9283-9289.
23. Cokoja, M.; Bruckmeier, C.; Rieger, B.; Herrmann, W. A.; Kühn, F. E., Transformation of Carbon Dioxide with Homogeneous Transition-Metal Catalysts: A Molecular Solution to a Global Challenge? *Angew. Chem. Int. Ed.* **2011**, *50* (37), 8510-8537.
24. Eynat, H.; W., S. L. J.; Ronny, N., Photochemical Reduction of CO₂ with Visible Light Using a Polyoxometalate as Photoreductant. *Chem. Eur. J.* **2017**, *23* (1), 92-95.

25. Raynaud, D.; Barnola, J. M., An Antarctic ice core reveals atmospheric CO₂ variations over the past few centuries. *Nature* **1985**, *315*, 309.
26. Canadell, J. G.; Le Quéré, C.; Raupach, M. R.; Field, C. B.; Buitenhuis, E. T.; Ciais, P.; Conway, T. J.; Gillett, N. P.; Houghton, R. A.; Marland, G., Contributions to accelerating atmospheric CO₂ growth from economic activity, carbon intensity, and efficiency of natural sinks. *Proc. Natl. Acad. Sci.* **2007**, *104* (47), 18866-18870.
27. Hori, H.; Johnson, F. P. A.; Koike, K.; Ishitani, O.; Ibusuki, T., Efficient photocatalytic CO₂ reduction using [Re(bpy)(CO)₃{P(OEt)₃}]⁺. *J. Photochem. Photobiol. A: Chemistry* **1996**, *96* (1), 171-174.
28. Gholamkhash, B.; Mametsuka, H.; Koike, K.; Tanabe, T.; Furue, M.; Ishitani, O., Architecture of Supramolecular Metal Complexes for Photocatalytic CO₂ Reduction: Ruthenium–Rhenium Bi- and Tetranuclear Complexes. *Inorg. Chem.* **2005**, *44* (7), 2326-2336.
29. Sato, S.; Koike, K.; Inoue, H.; Ishitani, O., Highly efficient supramolecular photocatalysts for CO₂ reduction using visible light. *Photochem. Photobiol. Sci.* **2007**, *6* (4), 454-461.
30. Koike, K.; Naito, S.; Sato, S.; Tamaki, Y.; Ishitani, O., Architecture of supramolecular metal complexes for photocatalytic CO₂ reduction: III: Effects of length of alkyl chain connecting photosensitizer to catalyst. *J. Photochem. Photobiol. A: Chemistry* **2009**, *207* (1), 109-114.
31. Demas, J. N.; DeGraff, B. A., Design and applications of highly luminescent transition metal complexes. *Anal. Chem.* **1991**, *63* (17), 829-837.
32. Kalyanasundaram, K., *Photochemistry of Polypyridine and Porphyrin Complexes*. Academic Press: London, UK, 1991.
33. Yarnell, J. E.; Deaton, J. C.; McCusker, C. E.; Castellano, F. N., Bidirectional "ping-pong" energy transfer and 3000-fold lifetime enhancement in a Re(I) charge transfer complex. *Inorg. Chem.* **2011**, *50* (16), 7820-7830.
34. Caspar, J. V.; Meyer, T. J., Application of the energy gap law to nonradiative, excited-state decay. *J. Phys. Chem.* **1983**, *87* (6), 952-957.
35. Wrighton, M.; Morse, D. L., Nature of the lowest excited state in tricarbonylchloro-1,10-phenanthroline-rhenium(I) and related complexes. *J. Amer. Chem. Soc.* **1974**, *96* (4), 998-1003.
36. Larsen, C. B.; van der Salm, H.; Clark, C. A.; Elliott, A. B. S.; Fraser, M. G.; Horvath, R.; Lucas, N. T.; Sun, X.-Z.; George, M. W.; Gordon, K. C., Intraligand Charge-Transfer Excited States in Re(I) Complexes with Donor-Substituted Dipyridophenazine Ligands. *Inorg. Chem.* **2014**, *53* (3), 1339-1354.

37. Shillito, G. E.; Hall, T. B. J.; Preston, D.; Traber, P.; Wu, L.; Reynolds, K. E. A.; Horvath, R.; Sun, X. Z.; Lucas, N. T.; Crowley, J. D.; George, M. W.; Kupfer, S.; Gordon, K. C., Dramatic Alteration of $^3\text{ILCT}$ Lifetimes Using Ancillary Ligands in $[\text{Re}(\text{L})(\text{CO})_3(\text{phen-TPA})]^{n+}$ Complexes: An Integrated Spectroscopic and Theoretical Study. *J. Am. Chem. Soc.* **2018**, *140* (13), 4534-4542.
38. Langdon-Jones, E. E.; Williams, C. F.; Hayes, A. J.; Lloyd, D.; Coles, S. J.; Horton, P. N.; Groves, L. M.; Pope, S. J. A., Luminescent 1,8-Naphthalimide-Derived ReI Complexes: Syntheses, Spectroscopy, X-ray Structure and Preliminary Bioimaging in Fission Yeast Cells. *Eur. J. Inorg. Chem.* **2017**, *2017* (44), 5279-5287.
39. Franco, F.; Cometto, C.; Garino, C.; Minero, C.; Sordello, F.; Nervi, C.; Gobetto, R., Photo- and Electrocatalytic Reduction of CO_2 by $[\text{Re}(\text{CO})_3\{\alpha,\alpha'\text{-Diimine-(4-piperidinyl-1,8-naphthalimide)}\}\text{Cl}]$ Complexes. *Eur. J. Inorg. Chem.* **2015**, *2015* (2), 296-304.
40. Adams, B. S.; Shillito, G. E.; van der Salm, H.; Horvath, R.; Larsen, C. B.; Sun, X.-Z.; Lucas, N. T.; George, M. W.; Gordon, K. C., Alteration of Intraligand Donor–Acceptor Interactions Through Torsional Connectivity in Substituted Re-dppz Complexes. *Inorg. Chem.* **2017**, *56* (21), 12967-12977.
41. McCusker, C. E.; Chakraborty, A.; Castellano, F. N., Excited State Equilibrium Induced Lifetime Extension in a Dinuclear Platinum(II) Complex. *J. Phys. Chem. A* **2014**, *118* (45), 10391-10399.
42. Tyson, D. S.; Castellano, F. N., Intramolecular Singlet and Triplet Energy Transfer in a Ruthenium(II) Diimine Complex Containing Multiple Pyrenyl Chromophores. *J. Phys. Chem. A* **1999**, *103* (50), 10955-10960.
43. Tyson, D. S.; Bialecki, J.; Castellano, F. N., Ruthenium(II) complex with a notably long excited state lifetime. *Chem. Commun.* **2000**, (23), 2355-2356.
44. Tyson, D. S.; Luman, C. R.; Zhou, X.; Castellano, F. N., New Ru(II) Chromophores with Extended Excited-State Lifetimes. *Inorg. Chem.* **2001**, *40* (16), 4063-4071.
45. Tyson, D. S.; Henbest, K. B.; Bialecki, J.; Castellano, F. N., Excited State Processes in Ruthenium(II)/Pyrenyl Complexes Displaying Extended Lifetimes. *J. Phys. Chem. A* **2001**, *105* (35), 8154-8161.
46. Yarnell, J. E.; McCusker, C. E.; Leeds, A. J.; Breaux, J. M.; Castellano, F. N., Exposing the excited-state equilibrium in an Ir(III) bichromophore: a combined time resolved spectroscopy and computational study. *Eur. J. Inorg. Chem.* **2016**, *2016* (12), 1808-1818.
47. Castellano, F. N., Transition metal complexes meet the rylenes. *Dalton Trans.* **2012**, *41* (28), 8493.

48. Castellano, F. N., Altering Molecular Photophysics by Merging Organic and Inorganic Chromophores. *Acc. Chem. Res.* **2015**, *48* (3), 828-839.
49. Leydet, Y.; Bassani, D. M.; Jonusauskas, G.; McClenaghan, N. D., Equilibration between Three Different Excited States in a Bichromophoric Copper(I) Polypyridine Complex. *J. Am. Chem. Soc.* **2007**, *129* (28), 8688-8689.
50. Laine, P. P.; Bedioui, F.; Loiseau, F.; Chiorboli, C.; Campagna, S., Conformationally Gated Photoinduced Processes within Photosensitizer-Acceptor Dyads Based on Osmium(II) Complexes with Triarylpyridinio-Functionalized Terpyridyl Ligands: Insights from Experimental Study. *J. Am. Chem. Soc.* **2006**, *128* (23), 7510-7521.
51. Michalec, J. F.; Bejune, S. A.; McMillin, D. R., Multiple Ligand-Based Emissions from a Platinum(II) Terpyridine Complex Attached to Pyrene. *Inorg. Chem.* **2000**, *39* (13), 2708-2709.
52. Whited, M. T.; Djurovich, P. I.; Roberts, S. T.; Durrell, A. C.; Schlenker, C. W.; Bradforth, S. E.; Thompson, M. E., Singlet and triplet excitation management in a bichromophoric near-infrared-phosphorescent BODIPY-benzoporphyrin platinum complex. *J. Am. Chem. Soc.* **2011**, *133* (1), 88-96.
53. Simon, J. A.; Curry, S. L.; Schmehl, R. H.; Schatz, T. R.; Piotrowiak, P.; Jin, X.; Thummel, R. P., Intramolecular Electronic Energy Transfer in Ruthenium(II) Diimine Donor/Pyrene Acceptor Complexes Linked by a Single C-C Bond. *J. Am. Chem. Soc.* **1997**, *119* (45), 11012-11022.
54. Wilson, G. J.; Launikonis, A.; Sasse, W. H. F.; Mau, A. W. H., Excited-State Processes in Ruthenium(II) Bipyridine Complexes Containing Covalently Bound Arenes. *J. Phys. Chem. A* **1997**, *101* (27), 4860-4866.
55. Wilson, G. J.; Launikonis, A.; Sasse, W. H. F.; Mau, A. W. H., Chromophore-Specific Quenching of Ruthenium Trisbipyridine-Arene Bichromophores by Methyl Viologen. *J. Phys. Chem. A* **1998**, *102* (26), 5150-5156.
56. Harriman, A.; Hissler, M.; Khatyr, A.; Ziessel, R., A ruthenium(II) tris(2,2'-bipyridine) derivative possessing a triplet lifetime of 42 μ s. *Chem. Commun.* **1999**, (8), 735-736.
57. McClenaghan, N. D.; Barigelletti, F.; Maubert, B.; Campagna, S., Towards ruthenium(II) polypyridine complexes with prolonged and predetermined excited state lifetimes. *Chem. Commun.* **2002**, (6), 602-603.
58. Passalacqua, R.; Loiseau, F.; Campagna, S.; Fang, Y.-Q.; Hanan, G. S., In search of ruthenium(II) complexes based on tridentate polypyridine ligands that feature long-lived room-temperature luminescence: The multichromophore approach. *Angew. Chem., Int. Ed.* **2003**, *42* (14), 1608-1611.

59. Cohen, B. W.; Lovaasen, B. M.; Simpson, C. K.; Cummings, S. D.; Dallinger, R. F.; Hopkins, M. D., 1000-Fold Enhancement of Luminescence Lifetimes via Energy-Transfer Equilibration with the T₁ State of Zn(TPP). *Inorg. Chem.* **2010**, *49* (13), 5777-5779.
60. Lavie-Cambot, A.; Lincheneau, C.; Cantuel, M.; Leydet, Y.; McClenaghan, N. D., Reversible electronic energy transfer: a means to govern excited-state properties of supramolecular systems. *Chem. Soc. Rev.* **2010**, *39* (2), 506-515.
61. Aveline, B. M.; Matsugo, S.; Redmond, R. W., Photochemical Mechanisms Responsible for the Versatile Application of Naphthalimides and Naphthalaldimides in Biological Systems. *J. Am. Chem. Soc.* **1997**, *119* (49), 11785-11795.
62. Kolosov, D.; Adamovich, V.; Djurovich, P.; Thompson, M. E.; Adachi, C., 1, 8-naphthalimides in phosphorescent organic LEDs: the interplay between dopant, exciplex, and host emission. *J. Am. Chem. Soc.* **2002**, *124* (33), 9945-9954.
63. Cao, H.; Chang, V.; Hernandez, R.; Heagy, M. D., Matrix screening of substituted N-aryl-1, 8-naphthalimides reveals new dual fluorescent dyes and unusually bright pyridine derivatives. *J. Org. Chem.* **2005**, *70* (13), 4929-4934.
64. Greenfield, S. R.; Svec, W. A.; Gosztola, D.; Wasielewski, M. R., Multistep Photochemical Charge Separation in Rod-like Molecules Based on Aromatic Imides and Diimides. *J. Am. Chem. Soc.* **1996**, *118* (28), 6767-6777.
65. Barboy, N.; Feitelson, J., Deoxygenation of solutions for transient studies. *Anal. Biochem.* **1989**, *180* (2), 384-386.
66. Suzuki, K.; Kobayashi, A.; Kaneko, S.; Takehira, K.; Yoshihara, T.; Ishida, H.; Shiina, Y.; Oishi, S.; Tobita, S., Reevaluation of absolute luminescence quantum yields of standard solutions using a spectrometer with an integrating sphere and a back-thinned CCD detector. *Phys. Chem. Chem. Phys.* **2009**, *11* (42), 9850.
67. Yarnell, J. E.; De La Torre, P.; Castellano, F. N., Efficient phosphorescence from naphthalenebenzimidazole coordinated iridium(III) chromophores. *Eur. J. Inorg. Chem.* **2017**, *2017* (44), 5238-5245.
68. Garakyaraghi, S.; Danilov, E. O.; McCusker, C. E.; Castellano, F. N., Transient Absorption Dynamics of Sterically Congested Cu(I) MLCT Excited States. *J. Phys. Chem. A* **2015**, *119* (13), 3181-3193.
69. Frisch, M.; Trucks, G.; Schlegel, H.; Scuseria, G.; Robb, M.; Cheeseman, J.; Scalmani, G.; Barone, V.; Mennucci, B.; Petersson, G.; Nakatsuji, H.; Caricato, M.; Li, X.; Hratchian, H. P.; Izmaylov, A. F.; Bloino, J.; Zheng, G.; Sonnenberg, J. L.; Hada, M.; Ehara, M.; Toyota, K.; Fukuda, R.; Hasegawa, J.; Ishida, M.; Nakajima, T.; Honda, Y.; Kitao, O.; Nakai, H.; Vreven, T.; Montgomery, J. A., Jr.; Peralta, J. E.; Ogliaro, F.; Bearpark, M.; Heyd, J. J.; Brothers, E.; Kudin, K. N.; Staroverov, V. N.; Kobayashi, R.; Normand, J.; Raghavachari, K.; Rendell, A.; Burant, J. C.; Iyengar, S. S.; Tomasi, J.;

- Cossi, M.; Rega, N.; Millam, J. M.; Klene, M.; Knox, J. E.; Cross, J. B.; Bakken, V.; Adamo, C.; Jaramillo, J.; Gomperts, R.; Stratmann, R. E.; Yazyev, O.; Austin, A. J.; Cammi, R.; Pomelli, C.; Ochterski, J. W.; Martin, R. L.; Morokuma, K.; Zakrzewski, V. G.; Voth, G. A.; Salvador, P.; Dannenberg, J. J.; Dapprich, S.; Daniels, A. D.; Farkas, Ö.; Foresman, J. B.; Ortiz, J. V.; Cioslowski, J.; Fox, D. J. *Gaussian 09, Revision D.01*, Gaussian, Inc., Wallingford CT: 2009.
70. Becke, A. D., A new mixing of Hartree-Fock and local-density-functional theories. *J. Chem. Phys.* **1993**, *98* (2), 1372-1377.
71. Becke, A. D., Density-functional thermochemistry. III. The role of exact exchange. *J. Chem. Phys.* **1993**, *98* (7), 5648-5652.
72. Zhao, Y.; Truhlar, D. G., The M06 suite of density functionals for main group thermochemistry, thermochemical kinetics, noncovalent interactions, excited states, and transition elements: two new functionals and systematic testing of four M06-class functionals and 12 other functionals. *Theor. Chem. Acc.* **2008**, *120* (1-3), 215-241.
73. Yanai, T.; Tew, D. P.; Handy, N. C., A new hybrid exchange–correlation functional using the Coulomb-attenuating method (CAM-B3LYP). *Chem. Phys. Lett.* **2004**, *393* (1), 51-57.
74. Weigend, F.; Ahlrichs, R., Balanced basis sets of split valence, triple zeta valence and quadruple zeta valence quality for H to Rn: Design and assessment of accuracy. *Phys. Chem. Chem. Phys.* **2005**, *7* (18), 3297-3305.
75. Andrae, D.; Haeussermann, U.; Dolg, M.; Stoll, H.; Preuss, H., Energy-adjusted ab initio pseudopotentials for the second and third row transition elements. *Theor. Chim. Acta* **1990**, *77* (2), 123-141.
76. Cossi, M.; Scalmani, G.; Rega, N.; Barone, V., New developments in the polarizable continuum model for quantum mechanical and classical calculations on molecules in solution. *J. Chem. Phys.* **2002**, *117* (1), 43.
77. Stratmann, R. E.; Scuseria, G. E.; Frisch, M. J., An efficient implementation of time-dependent density-functional theory for the calculation of excitation energies of large molecules. *J. Chem. Phys.* **1998**, *109* (19), 8218-8224.
78. Bauernschmitt, R.; Ahlrichs, R., Treatment of electronic excitations within the adiabatic approximation of time dependent density functional theory. *Chem. Phys. Lett.* **1996**, *256* (4,5), 454-464.
79. Casida, M. E.; Jamorski, C.; Casida, K. C.; Salahub, D. R., Molecular excitation energies to high-lying bound states from time-dependent density-functional response theory: characterization and correction of the time-dependent local density approximation ionization threshold. *J. Chem. Phys.* **1998**, *108* (11), 4439-4449.

80. Dennington, R.; Keith, T.; Millam, J. *GaussView, Version 5*, Semichem Inc.: Shawnee Mission, Kansas, 2009.
81. Mukherjee, S.; Thilagar, P., Molecular flexibility tuned emission in "V" shaped naphthalimides: Hg(II) detection and aggregation-induced emission enhancement (AIEE). *Chem. Commun.* **2013**, 49 (66), 7292-7294.
82. Zhou, P.; Yao, J.; Hu, G.; Fang, J., Naphthalimide Scaffold Provides Versatile Platform for Selective Thiol Sensing and Protein Labeling. *ACS Chem. Biol.* **2016**, 11 (4), 1098-1105.
83. Nandhikonda, P.; Begaye, M. P.; Cao, Z.; Heagy, M. D., Discovery of dual fluorescent 1, 8-naphthalimide dyes based on balanced seesaw photophysical model. *Chem. Commun.* **2009**, (33), 4941-4943.
84. Nandhikonda, P.; Begaye, M. P.; Cao, Z.; Heagy, M. D., Frontier molecular orbital analysis of dual fluorescent dyes: predicting two-color emission in N-aryl-1, 8-naphthalimides. *Org. Biomol. Chem.* **2010**, 8 (14), 3195-3201.
85. Demeter, A.; Bérces, T.; Biczók, L.; Wintgens, V.; Valat, P.; Kossanyi, J., Comprehensive model of the photophysics of N-phenylnaphthalimides: The role of solvent and rotational relaxation. *J. Phys. Chem.* **1996**, 100 (6), 2001-2011.
86. Kucheryavy, P.; Li, G.; Vyas, S.; Hadad, C.; Glusac, K. D., Electronic properties of 4-substituted naphthalimides. *J. Phys. Chem. A* **2009**, 113 (23), 6453-6461.
87. Liu, X.; Qiao, Q.; Tian, W.; Liu, W.; Chen, J.; Lang, M. J.; Xu, Z., Aziridinyl fluorophores demonstrate bright fluorescence and superior photostability by effectively inhibiting twisted intramolecular charge transfer. *J. Am. Chem. Soc.* **2016**, 138 (22), 6960-6963.
88. Mednykh, Y. A.; Manaev, Y. A.; Volchkov, V. V.; Uzhinov, B. M., Influence of the configuration of the amine nitrogen atom on the efficiency of fluorescence of 4-aminonaphthalimide derivatives. *Russ. J. Gen. Chem.* **2004**, 74 (11), 1728-1733.
89. Ventura, B.; Bertocco, A.; Braga, D.; Catalano, L.; d'Agostino, S.; Grepioni, F.; Taddei, P., Luminescence properties of 1, 8-naphthalimide derivatives in solution, in their crystals, and in co-crystals: toward room-temperature phosphorescence from organic materials. *J. Phys. Chem. C* **2014**, 118 (32), 18646-18658.

Chapter 3: Energy Transfer Processes in Next-Generation Metal-Organic Bichromophores

Portions of this chapter have been previously published in *Inorganic Chemistry*, **2020**, 59 (12), 8259-8271. DOI: <https://doi.org/10.1021/acs.inorgchem.0c00644>

3.1. Abstract

We present the synthesis, structural characterization, electronic structure calculations, and the ultrafast and supra-nanosecond photophysical properties of a series of five Re(I) bichromophores exhibiting metal-to-ligand charge transfer (MLCT) excited states based on the general formula $fac-[Re(N^N)(CO)_3(PNI-py)]PF_6$, where PNI-py is 4-piperidinyl-1,8-naphthalimidepyridine and N^N is a diimine ligand (**Re1-5**), along with their corresponding model chromophores where 4-ethylpyridine was substituted for PNI-py (**Mod1-5**). The diimine ligands used include 1,10-phenanthroline (phen, **1**), 2,9-dimethyl-4,7-diphenyl-1,10-phenanthroline (bcp, **2**), 4,4'-di-*tert*-butyl-2,2'-bipyridine (dtbb, **3**), 4,4'-diethylester-2,2'-bipyridine (deeb, **4**), and 2,2'-biquinoline (biq, **5**). In these metal-organic bichromophores, structural modification of the diimine ligand resulted in substantial changes to the observed energy transfer efficiencies between the two chromophores as a result of the variation in ³MLCT excited state energies. The photophysical properties and energetic pathways of the model chromophores were investigated in parallel to accurately track the changes that arose from introduction of the organic chromophore pendant on the ancillary ligand. All relevant photophysical and energy transfer processes were probed and characterized using time-resolved photoluminescence spectroscopy, ultrafast and nanosecond transient absorption spectroscopy, and time-dependent density functional theory calculations. Of the five bichromophores in this study, four (**Re1-4**) exhibited a thermal equilibrium between the ³PNI-py and the triplet ³MLCT excited state, drastically extending the lifetimes of the parent model chromophores.

3.2. Introduction

Rhenium(I) carbonyl diimine (Re-CDI) complexes of the generic form *fac*-[Re(N[^]N)(CO)₃(L)]⁺ (where N[^]N is a bidentate diimine ligand and L is a neutral ligand or anion) have been of interest to researchers since the first publication by Wrighton and coworkers in the 1970s due to their diverse photophysical behavior.¹ These molecules are thermally and photochemically stable, exhibit expansive photophysical tunability, and are relatively easy to synthesize.² Since Wrighton and coworkers first reported a comprehensive investigation into Re(I)-CDI complexes, these molecules have become pivotal to the study of excited state electron transfer (ET) and energy transfer (EnT) processes. Applications that utilize such excited state chemistry include photochemical molecular devices, solar energy conversion, photovoltaics, chemical sensing, photoredox catalysis, biotechnology applications such as DNA intercalation, along with many others.³⁻¹¹

The myriad applications of Re-CDI complexes directly results from their low energy, visible absorption bands and their long-lived, solvent sensitive, lowest energy triplet metal-to-ligand-charge-transfer (MLCT) excited states that are strongly photoluminescent.^{2, 3, 5, 8} The structure of these molecules enables facile synthetic manipulation of the diimine or ancillary ligands resulting in deterministic changes to the triplet MLCT photoluminescence (PL). Variation of the ancillary ligand modulates the energy levels of the Re(I) dπ-orbitals and therefore the HOMO energies.^{1, 12, 13} In contrast, modification of the diimine ligand affects the first reduction potential of the Re-CDI, altering the charge transfer energy via changes in the LUMO energy. When the HOMO and LUMO gap is changed through ligand modification, the MLCT energy correspondingly changes.^{1, 12, 13} Moreover, extension of the π-conjugation or addition of an organic chromophore to either the diimine ligand or ancillary ligand generates ligand-centered (LC)

excited states in these molecules. Strategic adjustments in the ligand moieties can increase the visible absorption cross-sections and may rigidify the molecular framework to decrease non-radiative decay in the resultant metal complexes which improves their effectiveness towards ET and EnT processes. Previously, reversible energy transfer at room temperature has been reported when energetically proximate inorganic and organic chromophores were fused together in the same MLCT complex.¹⁴ These polychromophoric systems can be designed to access synergetic properties of the composite chromophores, including lifetime extension which is imperative to many applications for a number of research groups¹⁴⁻²⁵ including our own.²⁶⁻³¹

We have extensively investigated the intriguing photophysical properties that arise after linking 4-piperidinyl-naphthalimide (PNI) and other naphthalimide (NI) derivatives to transition metal complexes.^{4, 32-34} In 2011, Yarnell and coworkers demonstrated that when PNI was covalently linked to the 5-position of 1,10-phenanthroline on a Re-CDI, the molecule exhibited “ping-pong” energy transfer between the MLCT and PNI excited states, Figure 3.1. In that study, time-resolved PL and transient absorption (TA) spectroscopies from sub-picosecond to the microsecond time domain were utilized to monitor the excited state dynamics of the complex. These spectroscopic measurements revealed energy transfer from ¹PNI to the ¹MLCT excited state through Förster resonance energy transfer (FRET) featuring a time constant of 43 ps, ultimately yielding the ³MLCT excited state. Furthermore, the ³MLCT state participated in back energy transfer (reverse triplet-triplet energy transfer, rTTET) to the triplet manifold of the PNI subunit within 20 ns through a Dexter-like process. Due to the energetic proximity ($\Delta E = 1680 \text{ cm}^{-1}$) and the rapid rate of energy transfer occurring between the two triplet excited states, the thermal equilibrium process extended the excited state lifetime of the parent Re-CDI from 197 ns to 651 μs .⁴

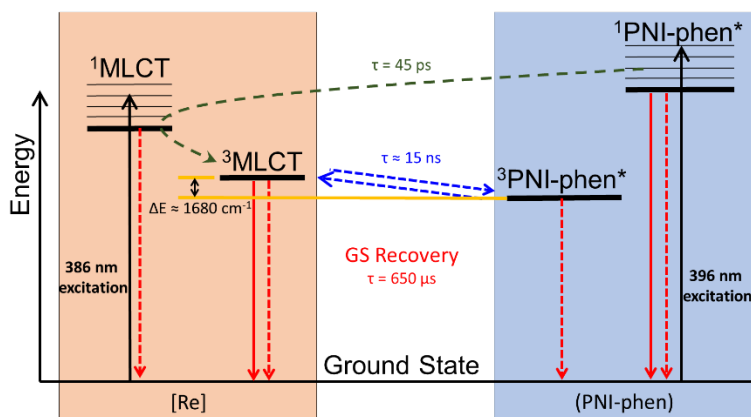


Figure 3.1. Qualitative energy level diagram describing ‘ping-pong’ energy transfer process between the Re(I) MLCT and PNI excited states.⁴

Although this initial study established the precedence for lifetime extension and increased visible absorption cross sections resulting from the fusion of inorganic and organic chromophores, there were a few remaining questions that could not be addressed. If low fluorescence quantum yield organic chromophores were used instead of the highly emissive PNI chromophore, could singlet energy transfer still occur? Additionally, what energy gap between the ³MLCT and ³LC excited states is sufficient for rTTET to occur effectively at room temperature? To address these concerns, we studied the effects of five weakly emissive NIs on the rate of FRET from NI to Re-CDI while investigating the effects of varying the energy levels of the NI fragment on the resulting thermal equilibrium between the NI and Re-CDI subunits. In these instances, four of the five bichromophores studied still exhibited “ping-pong” energy transfer behavior.³¹

While we have examined the influence of NI donor ligands on the resultant energy transfer processes, the influence of the MLCT energetics on these processes has never been addressed. In particular, what happens when the MLCT energy levels are altered without changing those of the ligand centered excited state? To significantly modify the energy levels of the MLCT excited states in Re-CDI complexes, the diimine ligand must be changed; therefore, the previous approach where the NI subunit was covalently linked to the backbone of 1,10-phenanthroline can no longer be

used. Instead the PNI chromophore for the current series was appended onto the Re(I) core through the 4-position of the ancillary pyridine ligand freeing up the diimine ligand for systematic alteration. Here, five newly conceived Re(I) bichromophores, *fac*-[Re(phen)(CO)₃(PNI-py)](PF₆) (phen = 1,10-phenanthroline, **1**), *fac*-[Re(bcp)(CO)₃(PNI-py)](PF₆) (bcp = 2,9-dimethyl-4,7-diphenyl-1,10-phenanthroline, **2**), *fac*-[Re(dtbb)(CO)₃(PNI-py)](PF₆) (dtbb = 4,4'-di-*tert*-butyl-2,2'-bipyridine, **3**), *fac*-[Re(deeb)(CO)₃(PNI-py)](PF₆) (deeb = 4,4'-di-ethyl-2,2'-bipyridine, **4**), and *fac*-[Re(biq)(CO)₃(PNI-py)](PF₆) (biq = 2,2'-biquinoline, **5**), (**Re1-5**, respectively) along with five Re(I) model MLCT chromophores, *fac*-[Re(N[^]N)(CO)₃(4-ety)](PF₆) (where N[^]N = phen, bcp, dtbb, deeb, biq and 4-ety is 4-ethylpyridine), (**Mod1-5**, respectively, Figure 3.2) were synthesized and investigated using steady-state and time-resolved PL and electronic spectroscopy as well as computational modeling to determine the effects of varying the MLCT energy levels on the energy transfer processes in the Re(I) bichromophores. It is interesting to note that in addition to determining what energy gaps are necessary to enable the various energy transfer processes in **Re1-5**, the proposed architecture of these bichromophores enables examination of the effect of the physical separation between the two constituents on the rate of respective photophysical processes and whether these processes can be partially or completely attenuated in the spatial separation achieved across these conserved molecular geometries.

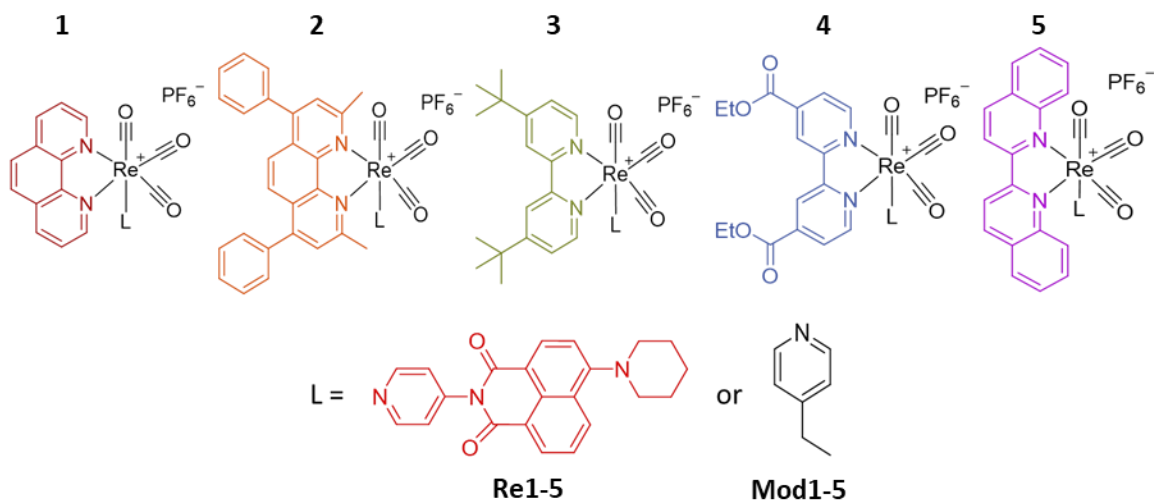


Figure 3.2. The Re(I) chromophores and Re(I)-PNI bichromophores investigated in this study.

3.3. Experimental

3.3.1. Reagents and Chemicals

All syntheses were performed under an inert, dry nitrogen atmosphere using standard techniques. All reagents were purchased from Sigma—Aldrich or Alfa Aesar and used as received. Spectroscopic samples were prepared using spectroscopic-grade tetrahydrofuran and were degassed using the freeze—pump—thaw technique for at least four cycles. The diimine ligand, deeb, was synthesized according to literature procedures and used without any additional purification.³⁵ Complete synthesis and structural characterization details for all molecules investigated here are provided in Appendix B.

3.3.2. General

¹H NMR spectra were recorded with a Varian Innova 400 instrument operating at a working frequency of 400 MHz. Electronic absorption spectra were measured with a Shimadzu UV-3600 and Cary 60 UV/Vis spectrophotometer. Steady-state photoluminescence spectra were measured on an Edinburgh FLS 980 or an Edinburgh FS920 fluorimeter. Quantum yield measurements were performed using degassed samples with [Ru(bpy)₃](PF₆)₂ in acetonitrile as a

standard (λ_{em} 621 nm, $\Phi_p = 0.095$)³⁶ for both the PNI-py and model complexes. The PNI-py complexes (**Re1-5**) were referenced to an additional standard, PNI in toluene (λ_{em} 498 nm, $\Phi_f = 0.91$)³⁷. Attenuated total reflectance Fourier-transform infrared (ATR-FTIR) spectroscopy on solid samples was conducted using a Bruker Alpha Platinum ATR. High-resolution electrospray mass spectrometry was carried out by the Michigan State University Mass Spectrometry Core, East Lansing, MI. Elemental analyses were determined by Atlantic Microlab, Inc., Norcross, GA.

3.3.3. Electrochemistry

Differential-pulse voltammetry (DPV) measurements were performed using CH Instruments model 600E series potentiostat. The measurements were carried out under an inert and dry atmosphere of nitrogen in a glovebox (MBraun). Reduction potentials were recorded in tetrahydrofuran containing 0.1 M tetrabutylammonium hexafluorophosphate (TBAPF₆) as the supporting electrolyte. A platinum disk was used as the working electrode (1.6 mm), a platinum wire as the counter electrode, and Ag/AgNO₃ as the reference electrode.

3.3.4. Femtosecond Transient Absorption Spectroscopy

The transient absorption measurements were performed at the NCSU Imaging and Kinetic Spectroscopy (IMAKS) Laboratory using a mode-locked Ti:sapphire laser (Coherent Libra) as described previously.³⁸ The pump beam was directed into a parametric amplifier (Coherent OPerA Solo) to generate the 400 nm excitation. The probe beam was focused onto a calcium fluoride crystal to generate a white light continuum between 350 and 775 nm. The pump beam (~700 μ m) was focused and overlapped with the probe beam through a 2 mm path length cuvette to allow for a stir bar to be used. The ground-state absorption spectra were taken before and after each experiment to ensure there was no sample photo-degradation during the experiment. The transient

kinetic data at specific wavelengths was evaluated using the fitting routines available in OriginPro 2018b (v 9.55).

3.3.5. Nanosecond Transient Absorption Spectroscopy

Nanosecond transient absorption measurements were collected with a LP920 laser flash photolysis system from Edinburgh Instruments. A Vibrant 355 Nd:YAG/OPO system (OPOTEK) was used for pulsed laser excitation for single wavelength kinetics. A Continuum Minilite Nd:YAG laser with 355 nm excitation was used to obtain the transient absorption difference spectra. To collect the transient absorption difference spectra in the visible portion of the spectrum, an iStar ICCD camera (Andor Technology), controlled by the LP920 software program was used. Samples were degassed using the freeze-pump-thaw technique for at least four cycles in a 10 mm path-length quartz optical cell. Samples were prepared to have optical densities between 0.2 and 0.8 at the excitation wavelength ($\lambda_{\text{ex}} = 355$ nm for difference spectra and $\lambda_{\text{ex}} = 410$ nm for single-wavelength kinetics). All flash-photolysis experiments were performed at room temperature unless otherwise noted. The reported difference spectra and kinetic data are the average of 100 laser pulses. The ground-state electronic absorption spectra were recorded before and after each experiment to ensure no sample photo-degradation. The transient kinetic data was evaluated using the fitting routines available in Origin Student 2018b (v. 9.55).

3.3.6. Time-Resolved Photoluminescence (TR-PL) Intensity Decay Measurements

Single-wavelength photoluminescence emission intensity decays for the model complexes (**Mod1-5**) and **Re5** were acquired with an LP920 laser flash photolysis system (Edinburgh Instruments) using the Vibrant 355 Nd:YAG/OPO system (OPOTEK) as the excitation source ($\lambda_{\text{ex}} = 410$ nm). Photoluminescence decays were collected at their respective emission maxima. Time-gated emission spectra were collected using the same apparatus, except the 355 nm Minilite

Nd:YAG laser was used for the excitation source instead.. Emission spectra were collected using an iStar ICCD camera (Andor Technology), controlled by the LP920 software program. The reported time-gated emission spectra are the average of 100 laser pulses. For **Re1-4**, the single-wavelength emission intensity decays could not be obtained using the LP920 laser flash photolysis system or on a nitrogen-pumped broadband dye laser (2-3 nm fwhm) from PTI (GL-3300 N₂ laser, GL-301 dye laser), using an apparatus that has been previously described.²⁶ Due to the significant amount of unquenched fluorescence from the PNI-py ligand, reliable decays of the phosphorescence could not be recorded even when probing the red edge of the MLCT emission band and is therefore not reported in this study.

3.3.7. Density Functional Theory (DFT) Calculations

The calculations utilized in this work were performed using the Gaussian 16 software package (Revision A.03)³⁹ and the computational resources of the North Carolina State University High Performance Computing Center. Ground state and lowest energy triplet state geometry optimizations were performed using the M06 functional,⁴⁰ along with the Def2-SVP basis set of the Alrichs group as implemented in Gaussian 16 for all nonmetal atoms.⁴¹ The Stuttgart-Dresden effective core potentials (ECP) were used to replace the core electrons in rhenium for all calculations.⁴² An f-polarization function was also added to the rhenium.⁴³ The polarizable continuum model (PCM) was used to simulate the tetrahydrofuran solvent environment for all calculations except the ground state geometry optimizations in which the optimization was performed in vacuum followed by a single point energy calculation with the PCM correction.⁴⁴ Frequency calculations were performed on all optimized structures and no imaginary frequencies were found. An ultrafine grid was used in all calculations. The molecular orbitals involved in the

low-lying singlet transitions as well as the triplet spin density surfaces were generated using GaussView 6.0.⁴⁵

3.3.8. Time-Dependent DFT (TD-DFT) Calculations

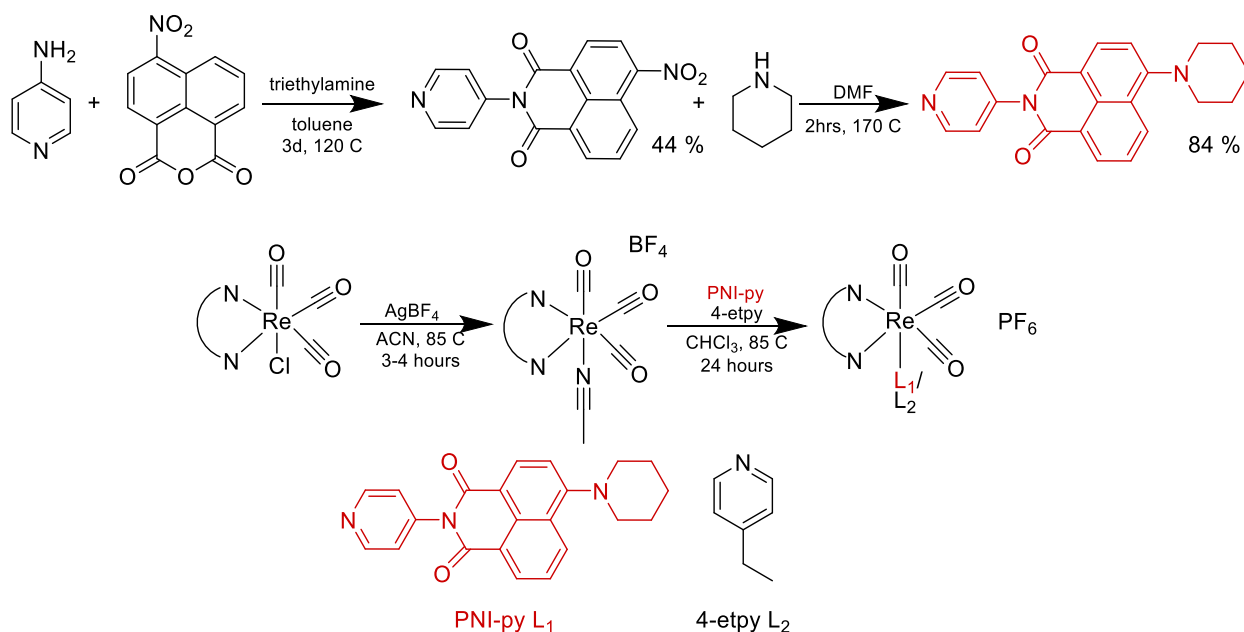
Time-dependent calculations were performed on each respective optimized ground-state geometry using the Gaussian 16 software package (Revision A.03)^{39, 46-48} and the computation resources of the North Carolina State University High Performance Computing Center. The calculations were performed using the same level of theory as in the DFT calculations described above. The polarizable continuum model (PCM) correction was used to simulate the tetrahydrofuran solvent environment for all calculations.⁴⁴ The energy and oscillator strength were computed for each of the 50 lowest singlet excitations. The UV/Vis spectra were generated from the singlet excitations using GaussView 6.0.⁴⁵

3.4. Results and Discussion

3.4.1. Synthesis

The PNI-py ligand and *fac*-[Re(N[^]N)(CO)₃(PNI-py)](PF₆) (**Re1-5**) and *fac*-[Re(N[^]N)(CO)₃(4-etpy)](PF₆) (**Mod1-5**) (where N[^]N = phen (**1**), bcp (**2**), dtbb (**3**), deeb (**4**), biq (**5**)) were synthesized as outlined in Scheme 1 using modified procedures available from the literature.^{49, 50} The PNI-py ligand was prepared by refluxing 4-nitro-1,8-naphthalic anhydride with an excess of 4-aminopyridine in toluene containing triethylamine for three days at 120°C to generate the 4-pyridyl-4-nitro-1,8-naphthalimide (NNI-py) intermediate. The isolated NNI-py species was then refluxed with an excess of piperidine in DMF for 2 hours at 170°C to obtain the pure final product, PNI-py, in 84% yield. The Re(I) complexes were prepared by departing from the analogous Re(N[^]N)(CO)₃Cl⁵¹ precursor that was treated with 1.02 equivalents of AgBF₄ for 3 hours in acetonitrile at 85°C shielded from light. The reaction solution was filtered through Celite

and the residue washed with acetonitrile. The acetonitrile filtrate was removed via rotary evaporation and the ancillary ligand of choice was added in 1.2 equivalents (PNI-py) or in large excess (4-etpy) and refluxed for 24 hours at 85°C in chloroform. Once isolated, the final product underwent a metathesis precipitation reaction to exchange the BF_4^- anion for the PF_6^- anion using NH_4PF_6 (concentrated NH_4PF_6 solution added to a 1:1 methanol/acetone mixture). The isolated molecules were then recrystallized as necessary in dichloromethane and hexanes to obtain each product in acceptable yield. The final products (**Re1-5** and **Mod1-5**) were characterized using ^1H NMR spectroscopy, high-resolution electrospray mass spectrometry, elemental analysis, ATR-FTIR, and electrochemistry (**Mod1-5** only) (Figures B3-23, Table B1). These molecules are all thermally and photochemically stable in a range of organic solvents and in the solid state.



Scheme 3.1. Synthesis of PNI-py, the **Re1-5** bichromophores, and the **Mod1-5** model chromophores.^{49, 50}

3.4.2. Electronic Structure Calculations

Density function theory (DFT) calculations at the M06//Def2-SVP/SDD level of theory in THF (PCM) were performed on all molecules in this study to obtain the geometry optimized ground state (S_0) (Table B2). For **Mod1-5**, the HOMO consisted of primarily d -orbitals and the LUMO consisted of primarily diimine π^* -antibonding orbitals (Figure B24). **Re1-5** have a HOMO that consists of a π -bonding interaction on the PNI-py ligand in which the electron density resides over the naphthalimide and piperidine units. The LUMO consists of diimine π^* -antibonding orbitals and the LUMO+1 (LUMO+2 for **Re1**) consists of a π^* -antibonding interaction localized on the PNI-py ligand where the electron density migrates away from the piperidine and localizes more extensively on the naphthalimide subunit (Figures B25-26). Time-dependent DFT (TD-DFT) calculations at the same level of theory were performed to demonstrate which electronic transitions occurred upon ~400 nm excitation (Table B3). All model complexes exhibited intense MLCT ($d\pi(\text{Re}) \rightarrow \pi^*(\text{N}^{\wedge}\text{N})$) transitions resulting from HOMO to LUMO excitation except **Mod5** in which the most intense transition was HOMO-1 to LUMO. The electron density in the HOMO resides primarily on the t_{2g} orbitals of the Re(I) center with little contribution from the pyridine ring and the electron density resides on the diimine ligand in the LUMO in **Mod1-5**, Figure 3.3. The HOMOs of **Re1-5** feature electron density centralized on the naphthalimide moiety in a bonding interaction. The LUMOs are centralized on the Re(I) $d\pi$ orbitals and the respective diimine ligand. The LUMO + 1 is centralized on the naphthalimide in an antibonding interaction except for **Re1** where the LUMO + 1 has electron density on the $\pi^*(\text{phen})$ and LUMO + 2 is similar to the LUMO + 1 of **Re2-5**. The HOMOs located on the PNI-py ligand have identical energies in **Re1-5** (-6.55 ± 0.01 eV) while the corresponding LUMO + 1 (LUMO + 2 in **Re1**) energies are also the same (-2.74 ± 0.01 eV). The energies of the LUMOs (electron density on the diimine

ligand) in **Mod1-5** are comparable to the energies of the LUMOs (electron density of the diimine ligand) calculated in **Re1-5** (Table B4). These combined data illustrate that the MLCT transition ($d\pi(\text{Re}) \rightarrow \pi^*(\text{N}^{\wedge}\text{N})$) energy remains the same irrespective of the nature of the ancillary ligand, indicating that there is no major change in the electronic transitions between **Mod1-5** and **Re1-5**. Triplet spin density calculations also aided in the determination of the lowest excited state configuration in all molecules, Figure B27. In **Mod1-5**, the triplet spin character was indicative of a $^3\text{MLCT}^*$ ($d\pi(\text{Re}) \rightarrow \pi^*(\text{N}^{\wedge}\text{N})$) excited state as the spin density was distributed over the Re atom and diimine ligands. For **Re1-3**, the triplet spin density rested entirely within the PNI-py ligand, **Re4** had triplet spin density on the Re atom and the deeb and PNI-py ligand fragments, and **Re5** had triplet spin resembling that of **Mod5** in which it resides on the Re atom and biq ligand.

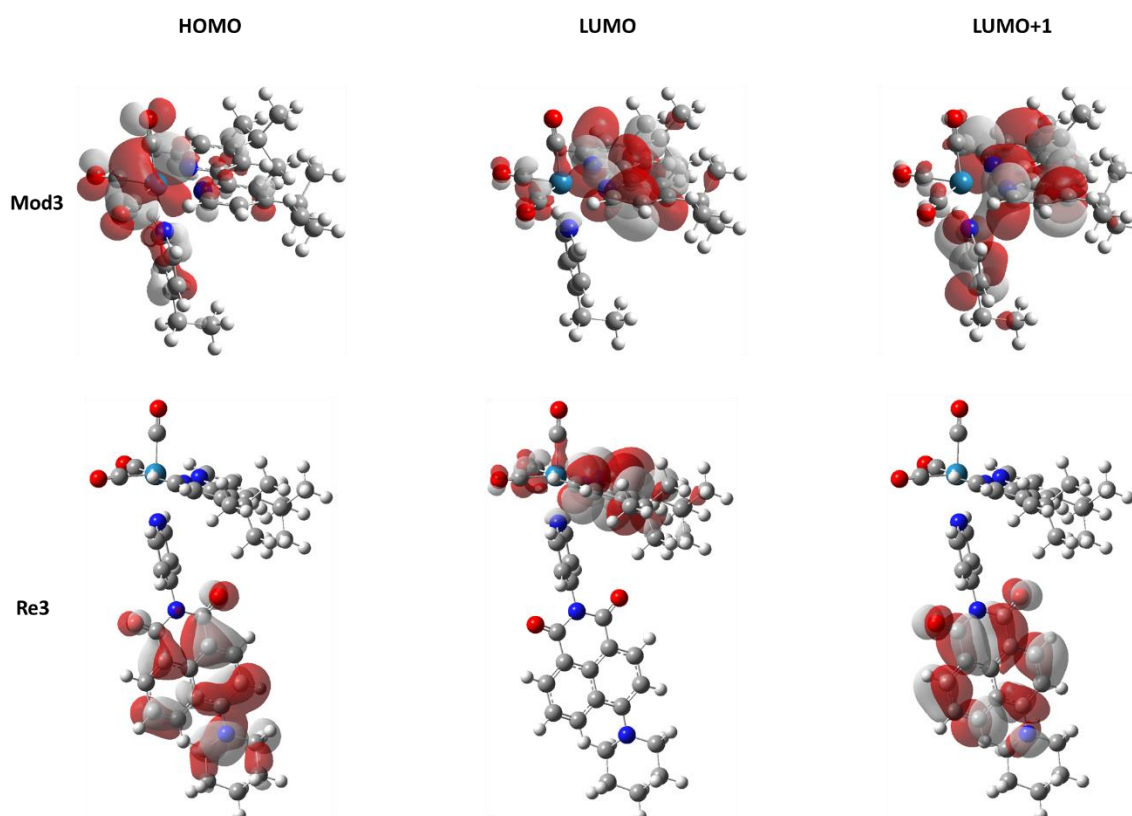


Figure 3.3. Representative schematic diagram of the HOMO, LUMO, and LUMO+1 of the model complexes (**Mod3** above) and rhenium bichromophores (**Re3** below).

3.4.3 Steady-State Absorption and Photoluminescence Spectroscopy

The PNI-py chromophore used in this study is similar to another naphthalimide, PNI-tol which has been extensively studied, where they differ only in the substituent on the imide nitrogen (pyridine and toluene, respectively).^{4, 15, 28, 32, 33, 37} The combination of the absorption spectra of the Re(I) MLCT model chromophores (**Mod1-5**) in concert with PNI-py effectively reproduces the authentic electronic spectra of the Re(I) bichromophores **Re1-5**, Figure B28. This indicates that the addition of the PNI subunit to the pyridine bound to the Re(I) CDI core does not significantly alter the electronics of the resultant complexes. During preliminary photoluminescence studies, it was evident that the free PNI-py ligand interacted with the THF solvent, requiring us to identify an alternative model chromophore for the free ligand. Therefore, PNI was used as a free-ligand surrogate due to their similar photophysical characteristics.^{37, 52}

The UV-Vis absorption spectra were collected in aerated THF and the corresponding photoluminescence spectra were measured in deaerated THF. The steady state absorption and photoluminescence spectra for **Mod1-5** and **Re1-5** are presented in Figures 3.4 and 3.5, respectively. Additional spectroscopic results are summarized in Table 3.1. The lowest energy absorption bands of **Mod1-5** (Figure 3.4a) are assigned to MLCT transitions, analogous to related molecules.^{12, 13, 53-55} The higher energy absorption bands (>350 nm) of **Mod1-5** and **Re1-5** are assigned to the $\pi \rightarrow \pi^*$ transitions localized in the respective diimine ligand. The photoluminescence emission bands measured in **Mod1-5** (Figure 3.5a) are assigned to ³MLCT based PL due to their overall broad and featureless shape, large Stokes' shift, and excited state lifetimes (discussed below), all being characteristic of ³MLCT phosphorescence, Figure 3.5a. Additionally, molecules of similar structure have also been assigned as to having ³MLCT photoluminescence.^{12, 13, 53, 54} However, the unusual photoluminescence, where the observed

emission bands are coincident with **Mod1-3**, warranted further investigation as to whether the lowest excited state of **Mod1-3** is indeed of $^3\text{MLCT}$ character. Since the excited state lifetime and nanosecond transient absorption spectra (discussed below) of **Mod3** was consistent with the photophysical properties expected from MLCT transition, further investigation was needed for **Mod1** and **Mod2**. Electronic structure calculations suggested (discussed above) that the absorption transition arises from primarily $d\pi(\text{Re})$ and $\pi^*(\text{phen/bcp})$ orbitals. Triplet spin density modeling of **Mod1** and **Mod2** predict that the spin density resides on the $d\pi(\text{Re})$ and the π^* orbitals of the diimine ligand present, suggesting that the transition is almost exclusively MLCT in nature. Moreover, there is literature precedence concerning the mixing of MLCT and LC transitions in Re-CDI molecules.⁵⁶⁻⁶⁰ Furthermore, recent studies from our group on a similar Re-CDI containing 1,10-phenanthroline (phen) have shown that when a stronger field ligand was incorporated as the ancillary ligand, the π^* orbitals of the phen moiety readily mixed with the $d\pi(\text{Re})$ state. This mixing results in the lowest excited state being composed of LC and MLCT character, which markedly increased the excited state lifetime.⁵ In a related study, we constructed a Re-CDI with phen and dimethylaminopyridine (dmap). This molecule possessed significant MLCT character in its lowest excited state,¹² and was effectively used as a model for the bichromophores in that study despite there being some ^3LC contributions.³¹ Therefore, we decided to use **Mod1** and **Mod2** as MLCT model molecules for comparison to their respective bichromophores, despite these complexes presenting a negligible amount of LC character, in subsequent sections of this manuscript, as the lowest excited states of **Mod1** and **Mod2** display predominantly MLCT character. The emission bands of **Mod4** and **Mod5** are red shifted with respect to **Mod3** (Figure 3.5a), consistent with the bathochromic shift observed in their respective electronic absorption spectra in Figure 3.4a.

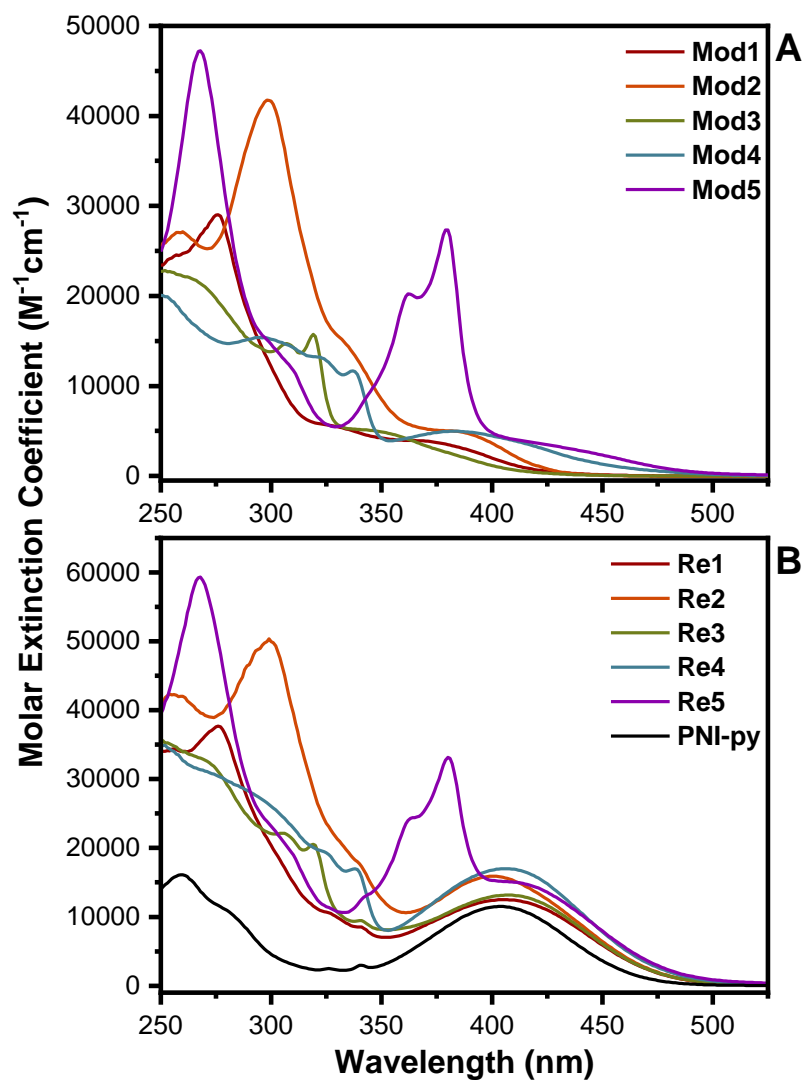


Figure 3.4. (A) Electronic absorption spectra of **Mod1-5** recorded in THF. (B) Electronic absorption spectra of **Re1-5** and PNI-py recorded in THF.

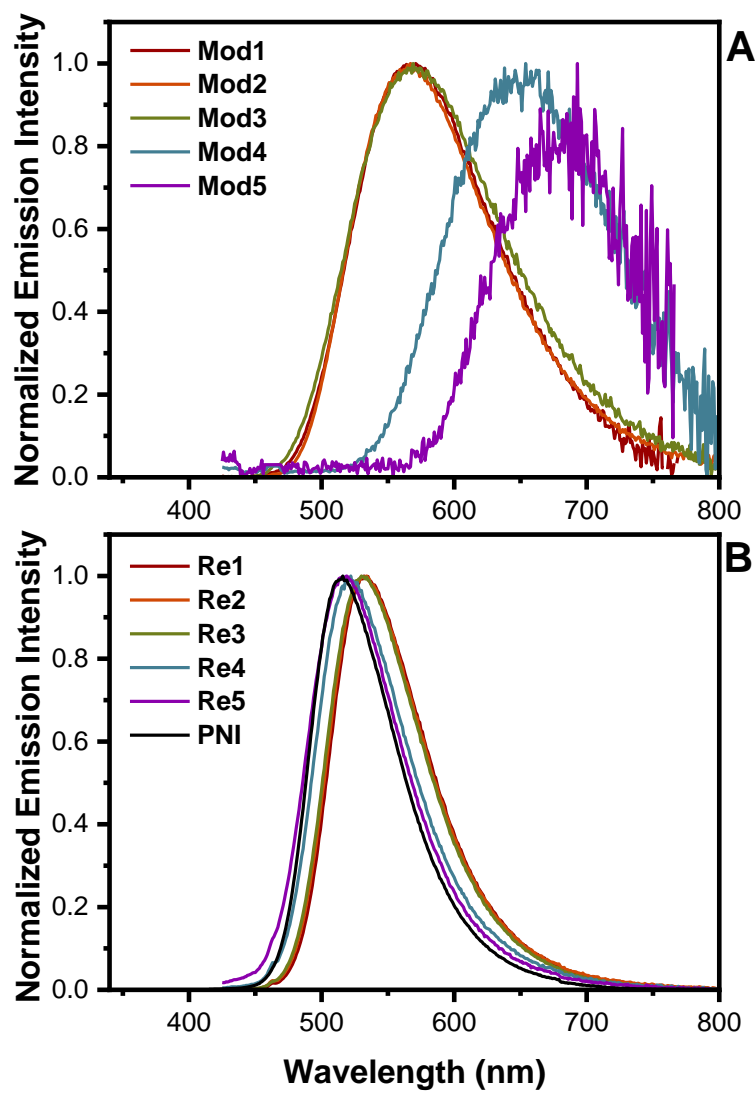


Figure 3.5. Static photoluminescence spectra of (A) **Mod1-5** and (B) **Re1-5** and PNI measured in deaerated THF excited at 408 nm.

The lowest energy absorption band of **Re1-5** is primarily composed of the intraligand CT band from PNI-py, Figure 3.4b. The addition of the PNI-py chromophore does not completely obscure the MLCT transition observed in the model complexes, instead adds to the molar absorptivity of that wavelength region. Due to the overlap of the PNI-py localized absorptions with those of the MLCT transitions, excitation of the low energy band does not selectively excite the PNI-py ligand exclusively; however, PNI-py absorbs the majority of the excitation light due to its

significantly higher molar extinction coefficient compared to that of the MLCT transitions, Table 3.1.

In the photoluminescence spectra of **Re1-5** (Figure 3.5b), it is evident that prevailing emission originates largely from the PNI moiety, analogous to the characteristic fluorescence observed in PNI itself, which is the black line displayed in Figure 3.5b. Therefore, the emission spectra measured in **Re1-5** (Figure 3.5b) is assigned as singlet ¹PNI fluorescence. Incidentally, these experimental observations are largely consequence of the nature of the experiment wherein low energy excitation primarily promotes the ¹PNI-py ligand centered excited state. Since there is incomplete energy transfer (discussed immediately below) occurring between the PNI-py ligand and the Re-CDI unit (Table 3.1) and only the brightest and fastest emission events are easily measured in static photoluminescence spectroscopy, all other lower yielding light emission processes are effectively masked. However, some of the fluorescence of the PNI ligand is quenched (Table 3.1) suggesting that energy transfer is occurring via the FRET mechanism. The efficiency of the energy transfer processes occurring through FRET was calculated using Equation 3.1 where QY_{ReX} and QY_{PNI} denote the quantum yields measured for the PNI-py fluorescence emanating from **Re1-5** and PNI, respectively.⁶¹

$$\text{EnT} = 1 - \frac{\text{QY}_{\text{ReX}}}{\text{QY}_{\text{PNI}}} \quad (3.1)$$

The most efficient Förster energy transfer was measured in **Re4** at 94% and all of the **Re1-5** bichromophores featured FRET values > 78%, Table 3.1. The residual fluorescence from the PNI-py subunit in **Re4** was sufficient to conceal all other emission events from the MLCT ($d\pi(\text{Re}) \rightarrow \pi^*(\text{N}^{\wedge}\text{N})$) excited state that was observed in **Mod1-5**, Figure 3.5a. In Re(PNI-phen)(CO)₃Cl, where the PNI subunit was covalently linked to the diimine subunit, the FRET efficiency was greater than 99% and photoluminescence was observed from both the ¹PNI and ³MLCT excited states in

static PL experiments.⁴ Clearly, the relocation of the PNI subunit to the tail end of the ancillary pyridine ligand in the present investigation significantly impacted the efficiency of the distance-dependent FRET processes in **Re1-5**.

Table 3.1. Steady-state photophysical data of **Mod1-5**, PNI-py, PNI, and **Re1-5**.

	$\lambda_{\text{abs max}}$ (nm) (ϵ , $\text{M}^{-1} \text{cm}^{-1}$) ^a	$\lambda_{\text{em max}}$ (nm)	Φ_{em} ^d	EnT (%) ^e	${}^3\text{E}_{\text{em}}$ (cm^{-1}) ^f
Mod1	364 (3950)	567	0.24	--	19500
Mod2	377 (5000)	567	0.27	--	20000
Mod3	339 (5000)	569	0.093	--	19900
Mod4	385 (5000)	650	0.013	--	16200
Mod5	407 (4200)	689	0.0024	--	14900
PNI	403 (11500) ^b	516 ^c	0.80 ^c	--	16200 ^g
Re1	407 (12500)	533	0.13	84	--
Re2	400 (15900)	536	0.091	89	--
Re3	407 (13200)	533	0.18	78	--
Re4	406 (15400)	525	0.049	94	--
Re5	403 (15200)	516	0.061	92	--

^aPeak maximum given is of the lowest energy band (shoulder for Mod1-5). ^bPeak maximum and molar extinction coefficient used are for PNI-py. ^cFluorescence data is for PNI. ^dQuantum yield of Mod1-5 and PNI was measured using $[\text{Ru}(\text{bpy})_3](\text{PF}_6)_2$ as the standard.⁶² Quantum yield of Re1-5 were measured using $[\text{Ru}(\text{bpy})_3](\text{PF}_6)_2$ as the standard as well as PNI in toluene.^{37, 62} Samples for quantum yield studies were prepared at 0.1 OD at 408 nm (excitation) and were deaerated using the freeze-pump-thaw method with a 10 % error. ^eEnT efficiency was calculated using Equation 1. ^fTriplet energies estimated from the emission profiles of Mod1-5 and taking the tangent on the high energy side of the band. ^gTriplet energy of PNI-py was obtained from sensitizing the triplet excited state by using 10% ethyl iodide as an additive and obtaining the phosphorescence spectrum of PNI-py at 77 K in a 2-MeTHF glass.

Using the photoluminescence emission spectra of **Mod1-5**, the energies of the corresponding triplet excited states can be readily estimated. As expected, the three complexes that coincide, **Mod1-3**, have nearly identical triplet energies ($\sim 20000 \text{ cm}^{-1}$) and the two red shifted molecules, **Mod4** (16200 cm^{-1}) and **Mod5** (14900 cm^{-1}), have significantly lower energies. The triplet energy of PNI-py (16200 cm^{-1}) was obtained from triplet sensitization of the free ligand at 77 K using 10 % ethyl iodide in 2-MeTHF (Figure B29). A summary of the triplet state energies

of **Mod1-5** and PNI-py are collected in Table 3.1. The triplet states in the **Mod1-5** are assumed to correspond to the triplet energies of the $^3\text{MLCT}$ ($(d\pi(\text{Re}) \rightarrow \pi^*(\text{N}^{\wedge}\text{N}))$) excited state levels in **Re1-5**. The triplet energy of PNI-py recorded at 77K in the presence of ethyl iodide is assumed to appropriately estimate the triplet energy of the PNI subunit. Given this combined experimental information, we can readily approximate the energy gap between the two chromophoric units in the **Re1-5** title molecules.

3.4.4. Nanosecond Transient Absorption Spectroscopy

Upon excitation using 355 nm nanosecond laser pulses (5 ns fwhm), **Mod1-5** (Figure B30) in deaerated THF display positive absorption features across the entire visible region. The excited state features ranging between 350-400 nm are somewhat distorted due to overlap with the high molar absorptivity ground state absorptions in this region. **Mod5** (Figures B30) features a structureless bleaching signal below 400 nm. **Mod3** and **Mod4** exhibited transient excited state absorption features consistent with the $^3\text{MLCT}$ excited state, being comparable to the respective radical anion of the diimine unit resident in the structure, Figure B30. Single-wavelength kinetic analysis of these transient features yielded excited state lifetimes consistent with $^3\text{MLCT}$ excited states, 301 and 65.1 ns for **Mod3** and **Mod4** respectively (Table 3.2, Figures B34-35).⁶³ **Mod5** and **Re5** featured similar excited state spectral features that corresponded to the same excited state lifetime, 38.9 and 39.5 ns for **Mod5** and **Re5**, respectively (Table 3.2, Figures 3.6, B30, B36, and B47). **Mod1** and **Mod2** possess excited state spectral features that are similar due to their shared phenanthroline core but feature extended lifetimes that do not suggest pure $^3\text{MLCT}^*$ behavior, $\tau = 1.50 \mu\text{s}$ for **Mod1** and $\tau = 8.24 \mu\text{s}$ for **Mod2** (Table 3.2, Figures B30, B32-33).

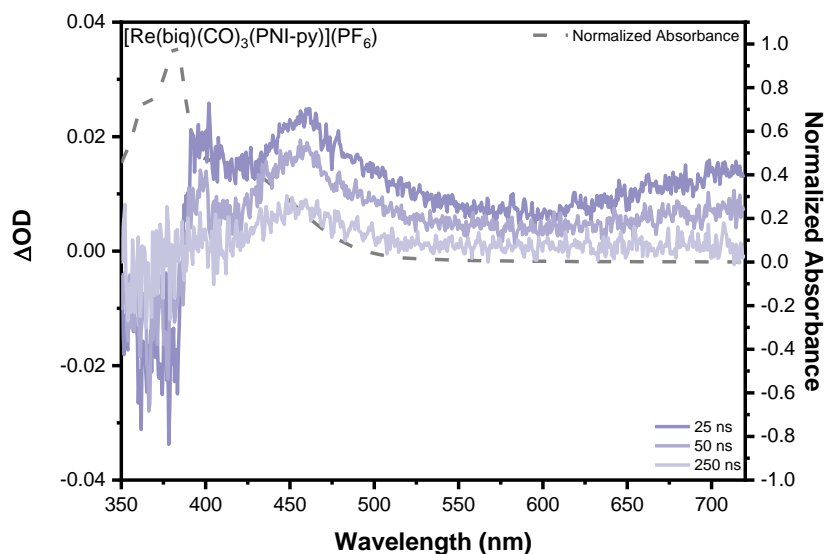


Figure 3.6. Transient absorption difference spectra with the corresponding ground state absorption spectrum (dashed line) of **Re5** (45.4 μ M) measured in THF with 355 nm laser pulses (5.0 mJ/pulse).

When **Re1-5** are excited with 355 nm light, the five Re(I) complexes fall under two distinguishing categories: (1) the TA difference spectra are indicative of the $^3\text{PNI}^*$ excited state or (2) the TA difference spectra are qualitatively identical to those recorded for the respective model chromophores **Mod1-5**. **Re1-4** fall into category 1 whereas **Re5** falls into category 2. Beginning with **Re5** (Figure 3.6), it is safe to postulate that the lowest excited state is of $^3\text{MLCT}^*$ ($d\pi(\text{Re}) \rightarrow \pi^*(\text{biq})$) character. Evidence of this is clear-cut as the profile of the transient absorption features are similar between **Re5** and **Mod5** (Figures 3.6, B30), and both have a ground state bleach below 400 nm. Additionally, the lifetime obtained from single-wavelength analysis of the transient excited state features of **Re5** (Figure B47) and **Mod 5** (Figure B36) are both single exponential, both equaling 40 ns, leaving little doubt that the nature of the excited state in both molecules is conserved.

Looking into category one, **Re1-3** have qualitatively identical TA difference spectra. There is a ground state bleach centered near 400 nm and an excited state absorption feature centered at 465 nm (Figures 3.7a and B37-38). **Re4** has an excited state absorbance centered at 461 nm with a ground state bleach located at 400 nm (Figure B39). These difference spectra are all consistent with $^3\text{PNI}^*$ as measured in previous studies.^{4, 32-34} One notable difference between the signal observed here and the signal observed in previous work is that there is not a second broad feature in the visible region spanning into the NIR. That second feature apparently results from the PNI moiety being covalently linked to the diimine ligand and is therefore absent in the current investigation. Another clear indicator that we are populating the $^3\text{PNI}^*$ excited state in **Re1-4** is the biexponential, concentration dependent lifetimes^{4, 32, 33} which is, in general, a characteristic of triplet naphthalimides.⁶⁴⁻⁶⁶ This biexponential behavior is due to $^3\text{PNI}^*$ self-quenching and was quantified by measuring the excited state decay kinetics as a function of concentration, which yielded the theoretical lifetimes at infinite dilution (lifetime in the absence of self-quenching): $\tau_\infty = 5110 \mu\text{s}$ in **Re1**, $\tau_\infty = 918 \mu\text{s}$ in **Re2**, $\tau_\infty = 1170 \mu\text{s}$ in **Re3**, and $\tau_\infty = 1.17 \mu\text{s}$ in **Re4** (Figure 3.7b, Figures B44-46, and Table 3.2) all of which are significantly longer than their respective model complex.

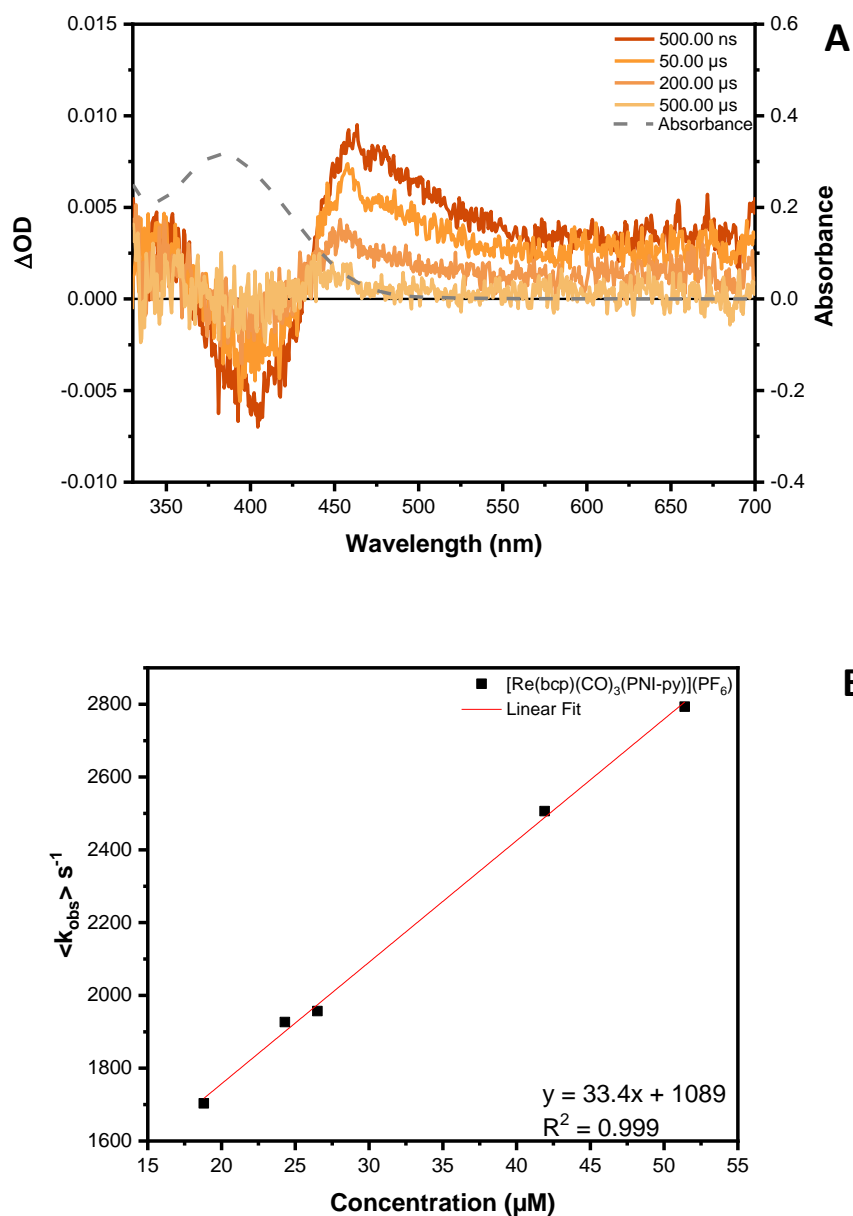


Figure 3.7. (A) Transient absorption difference spectra with the corresponding ground state absorption spectrum (dashed line) of **Re2** (44.3 μM) recorded in THF with 355 nm laser pulses (5.0 mJ/pulse). (B) The concentration dependent study of **Re2** illustrating self-quenching behavior with single wavelength transient absorption kinetics detected at 465 nm ($\lambda_{\text{ex}} = 410$ nm, 2.0 mJ/pulse). Samples were deaerated using the freeze-pump-thaw method.

Table 3.2. Time-resolved TA and PL data recorded for **Mod1-Mod5** and **Re1-Re5** in THF.

	τ_{TA} (ns)	τ_{PL} (ns)	τ_{TA} (μ s) ^a
Mod1	1500	1480	--
Mod2	8240	7600	--
Mod3	301	296	--
Mod4	65.1	68.1	--
Mod5	38.9	39.5	--
Re1	--	--	5110
Re2	--	--	918
Re3	--	--	1170
Re4	--	--	1.17
Re5	39.5	9.97	--

All kinetics measured using the LP 920 laser flash photolysis system (Edinburgh Instruments) with a Vibrant 355 Nd:YAG/OPO system (OPOTEK) for pulsed laser excitation for single wavelength kinetics detection at peak excited state features (410 nm, 2.0 mJ/pulse). Samples were deaerated using the freeze-pump-thaw method. ^aLifetime at theoretical infinite dilution.

3.4.5.

Femtosecond Transient Absorption Spectroscopy

The ultrafast excited state absorption difference spectra of **Mod1-5** are presented in Figure B48 while those of **Re2** and **Re5** are shown in Figures 3.8 and 3.9 (λ_{ex} = 400 nm, 105 fs fwhm, 0.3 μ J/pulse); the corresponding data for **Re1**, **Re3**, and **Re4** are provided in Figures B54-56. In **Mod1-4**, the positive transient absorption features are indicative of MLCT excited state absorptions that dominate across the visible region.^{63, 67} **Mod5** displays a ground state bleach between 350 – 400 nm, coinciding with its ground state absorption spectrum, Figure 3.4a. Across the visible and extending into the NIR spectral region, only excited state absorptions are present in each of these molecules, Figure B48. **Re1-4** display stimulated emission peaks centered near 550 nm over the initial delay times and have excited state absorption features centered at 430 nm that evolve over the time course of the experiment, eventually peaking at 460 nm (Figures 3.8, and B54-56). **Re5** (Figure 3.9) possesses similar initial excited state absorption features at 430 nm as well as a stimulated emission band near 550 nm. However, the 430 nm excited state feature evolves

into a structured absorption band with a peak centered at 400 nm and a shoulder near 500 nm extending into the NIR. There is also a ground state bleach that echoes what was observed over the same wavelength region (350 – 400 nm) in **Mod5** (Figure B48).

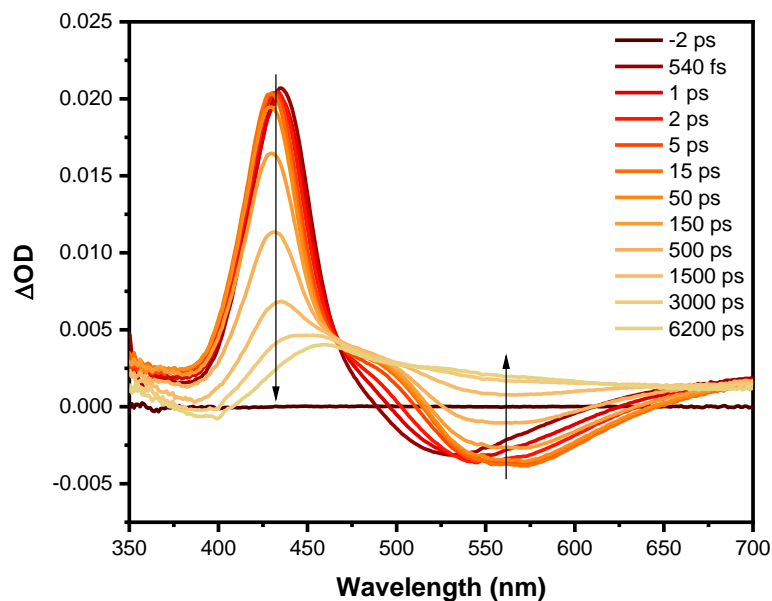


Figure 3.8. Excited state absorption difference spectra of **Re2** in THF excited following 400 nm pulsed laser excitation (105 fs fwhm, 0.3 $\mu\text{J}/\text{pulse}$).

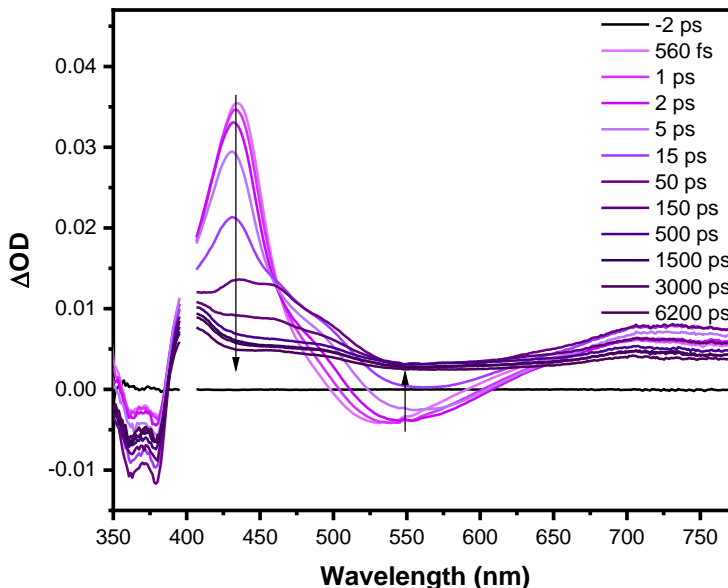


Figure 3.9. Excited state absorption difference spectra of **Re5** in THF excited following 400 nm pulsed laser excitation (105 fs fwhm, 0.3 μ J/pulse).

All of the model complexes (**Mod1-5**) exhibit ultrafast excited state absorption features and associated time constants (Figures B49-53) that are significantly different than their PNI-containing counterparts (**Re1-5**). For **Mod1-3**, the fastest time constants recorded ($\tau = 120$, 170 and 140 fs respectively) arise from intersystem crossing and the formation of the radical anion on the diimine ligand. **Mod1-5** universally possessed a second time constant corresponding to vibrational relaxation ($\tau = 2.7$ to 16 ps).^{5, 68} In addition to vibrational relaxation, **Mod4** and **Mod5** had an additional time constant on the order of 100s of ps ($\tau = 107$ and 120 ps). This slow time constant was also observed in the nanoseconds time domain, hence, is attributed to the onset of the triplet MLCT excited state decay process. In **Mod1-5**, the line shape of the relaxed excited-state spectral feature persists into the nanosecond TA time scale, indicating that there are no additional excited states observed between the picosecond and nanosecond time domains.

The femtosecond transient absorption difference spectra of **Re1-Re4** (Figures 3.8 and B54-56) follow a similar energy migration trajectory, eventually resulting in $^3\text{PNI}^*$ formation. Additionally, stimulated emission is present as a peak centered at 550 nm as seen in previous papers for metal-organic chromophores containing a PNI subunit.^{4, 32, 33} Over time, this feature red shifts due to distortions caused by overlap of excited state features. Across all four molecules, immediately upon excitation at 400 nm, the signal that promptly appears corresponds to $^1\text{PNI}^*$, having a maximum at 430 nm. The $^1\text{PNI}^*$ excited state decays, forming intermediate $^1\text{MLCT}^*$ and $^3\text{MLCT}^*$ states, eventually producing $^3\text{PNI}^*$ over the course of 6 ns which has a peak maximum at 460 nm. **Re1-Re3** each exhibit three similar time constants (Figures B57-59) following predominant excitation of $^1\text{PNI}^*$. The first decay component corresponds to the initial vibrational relaxation of “hot” $^1\text{PNI}^*$ to form relaxed $^1\text{PNI}^*$ ($\tau = 3.8, 2.1, \text{ and } 3.5$ ps for **Re1**, **Re2**, and **Re3**, respectively). From $^1\text{PNI}^*$, the molecules undergo energy transfer through the FRET mechanism, preparing the $^1\text{MLCT}^*$ state which then immediately undergoes intersystem crossing (ISC) to the $^3\text{MLCT}^*$ state ($\tau = 261, 260, \text{ and } 256$ ps for **Re1**, **Re2**, and **Re3**, respectively). The FRET process ($^1\text{PNI}^*$ to $^1\text{MLCT}^*$) in the title molecules is occurring with much slower rate constants and lower efficiencies with respect to the related systems reported previously,^{4, 31} likely a consequence of the distance and orientation of the respective chromophores. Finally, the $^3\text{MLCT}^*$ state engages in intramolecular triplet-triplet energy transfer (TTET) from the MLCT state on the rhenium complex to the PNI ligand having time constants of $\tau = 1.88, 1.79, \text{ and } 2.3$ ns for **Re1**, **Re2**, and **Re3**, respectively. The corresponding time constant assigned to the intramolecular TTET process in **Re4** (Figure B60) is 701 ps and at the present time we do not have a good explanation of why this time constant is significantly smaller than those measured in **Re1-Re3**. The remaining ultrafast processes in these molecules appear to be self-consistent. Vibrational relaxation of “hot” $^1\text{PNI}^*$

followed by FRET to form the $^1\text{MLCT}^*$ state and ISC to the $^3\text{MLCT}^*$ state have time constants that are the same order of magnitude in **Re1-Re4** (2-4 ps for vibrational relaxation, 104-261 ps for FRET followed by ISC in **Re1-Re4**).

In stark contrast to **Re1-Re4**, **Re5** (Figure 3.9, B61) does not exhibit any evidence of $^3\text{PNI}^*$ in its lowest excited state. However, evidence for $^3\text{PNI}^*$ in the excited state decay of **Re5** is clearly present during picosecond delay times. Additionally, the peak maximum of the “hot” $^1\text{PNI}^*$ state in **Re5** is slightly red shifted (5 nm) due to the contributions of the $^1\text{MLCT}^*$ ($d\pi(\text{Re}) \rightarrow \pi^*(\text{biq})$) state, in part believed to be a consequence of non-selective excitation. The time constant associated with this process is assigned to vibrational relaxation of “hot” $^1\text{PNI}^*$ to $^1\text{PNI}^*$ ($\tau = 9.6$ ps). A potential explanation for the magnitude of this time constant is the greater contribution from the $^1\text{MLCT}^*$ ($d\pi(\text{Re}) \rightarrow \pi^*(\text{biq})$) state which is distinct with respect to the other molecules. The FRET and ISC processes in **Re5** ultimately lead to the $^3\text{MLCT}^*$ ($d\pi(\text{Re}) \rightarrow \pi^*(\text{biq}, \text{PNI})$) state formation with a time constant of 76 ps, which persists throughout the duration of the experiment. **Re5** features a lowest $^3\text{MLCT}^*$ excited state, distinct with respect to the remaining PNI-containing molecules since the $^3\text{MLCT}^*$ ($d\pi(\text{Re}) \rightarrow \pi^*(\text{biq})$) state energy is significantly lower than that of $^3\text{PNI}^*$ (Table 3.1), thereby inhibiting any repopulation of the latter. This is also why the nanosecond transient absorption excited state lifetime of **Re5** quantitatively matches that of **Mod5**, as they are both derived from a similar $^3\text{MLCT}$ excited state configuration.

3.4.6. Excited State Equilibrium

The decay kinetics of the $^3\text{PNI}^*$ excited state absorption of **Re1-3** are similar, suggesting that the energy migration between the bichromophores are comparable. Correlation between the excited state absorption and delayed $^3\text{MLCT}^*$ PL kinetics was not applicable to this study as in previous work⁴ due to the unquenched fluorescence of the $^1\text{PNI}^*$ moiety. Attempted collection of

the red edge of the $^3\text{MLCT}^*$ PL (655 nm) led to saturation of the detector even with smallest possible slit widths. However, time-resolved PL data featured delayed phosphorescence from the $^3\text{MLCT}^*$ ($d\pi(\text{Re}) \rightarrow \pi^*(\text{N}^{\wedge}\text{N})$) state (Figures B40-42). Additionally, the lifetimes at infinite dilution (918 – 5110 μs , Table 3.2) of these molecules suggest thermal equilibrium between the two triplet states occurs due to the lifetimes being intermediate between pure $^3\text{MLCT}^*$ ($d\pi(\text{Re}) \rightarrow \pi^*(\text{N}^{\wedge}\text{N})$) (300 ns – 8 μs) and $^3\text{PNI}^*$ (270 ms).⁴ The lifetime is shortest in **Re2**, most likely since the $^3\text{MLCT}^*$ ($d\pi(\text{Re}) \rightarrow \pi^*(\text{bcp})$) state is closest in energy to $^3\text{PNI}^*$, despite the PL data suggesting that all three complexes have virtually the same $^3\text{MLCT}^*$ energy. The longer lifetimes are a consequence of the larger energy gaps between the two triplet states, i.e. the intramolecular rTTET process becomes less efficient with increasing energy gap. **Re4** also displays evidence of thermal equilibrium as well through its lifetime at infinite dilution (1.17 μs) being intermediate between the $^3\text{MLCT}^*$ ($d\pi(\text{Re}) \rightarrow \pi^*(\text{deeb})$) (70 ns) and $^3\text{PNI}^*$ (270 ms). Time-resolved PL intensity decays also feature delayed $^3\text{MLCT}^*$ ($d\pi(\text{Re}) \rightarrow \pi^*(\text{deeb})$) PL (Figure 3.10). The decay of **Re4** being so much faster than **Re1-3** is likely a direct result of the triplet states in **Re4** having nearly isoenergetic levels, Table 3.1. Unlike **Re1-4**, **Re5** displays no evidence of thermal equilibrium between the $^3\text{MLCT}^*$ ($d\pi(\text{Re}) \rightarrow \pi^*(\text{biq})$) and $^3\text{PNI}^*$ excited states. The lifetime of the excited state absorption of **Re5** matches the lifetime of the excited state absorption of **Mod5** and there is no concrete evidence of delayed $^3\text{MLCT}^*$ ($d\pi(\text{Re}) \rightarrow \pi^*(\text{biq})$) PL in this molecule, Figure B43.

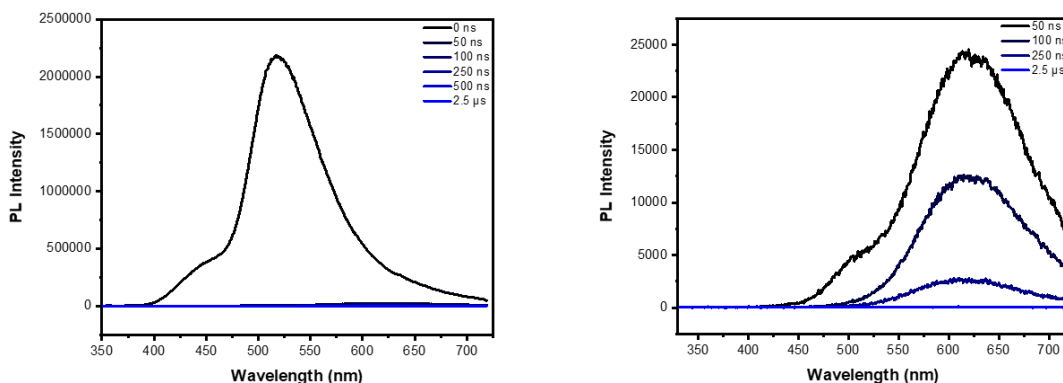


Figure 3.10. Representative (**Re1-4**) time-resolved photoluminescence data showing **Re4** early times (left) and delayed time (right) depicting the delayed phosphorescence from the $^3\text{MLCT}^*$ excited state.

3.4.7. Excited State Evolution and Decay

The proposed energy level diagrams summarizing the energy migration pathways of **Re1-5** are presented in Figure 3.11 (**Mod1-5** Figure B62). Upon initial excitation from the pump beam, **Re1-4** exhibit “ping-pong” like energy transfer as seen in previous work.^{4, 31} In these molecules, the initial excited state is localized on the PNI ($\tau = 2.1 - 4.0$ ps) unit which then transfers to the $^3\text{MLCT}^*$ ($\tau = 104 - 261$ ps) and then finally back to the PNI unit ($\tau = 0.70 - 2.3$ ns) in its triplet manifold. Due to the rapid rates for forward and reverse TTET in **Re1-Re4**, the composite excited state lifetimes are dictated by the energy gap between the two triplet states in equilibrium, i.e. $^3\text{MLCT}$ and ^3PNI .

Re5 is the only bichromophore in this study that does not display a thermal equilibrium between the $^3\text{MLCT}$ ($d\pi(\text{Re}) \rightarrow \pi^*(\text{biq}))$ and ^3PNI excited states. In the picosecond time domain, **Re5** promptly forms an excited state that is primarily localized on the PNI subunit ($\tau = 9.6$ ps), which then transfers this energy to the $^3\text{MLCT}^*$ ($d\pi\text{Re} \rightarrow \pi^*(\text{biq}))$ manifold ($\tau = 76$ ps). However, there is also evidence of some population of the ^3PNI excited state on the same time scale. From this time point forward, the remaining excited state features decay most consistent with the $^3\text{MLCT}$

state returning to the ground state with a time constant of 40 ns, echoing the latter decay process occurring in **Mod5**.

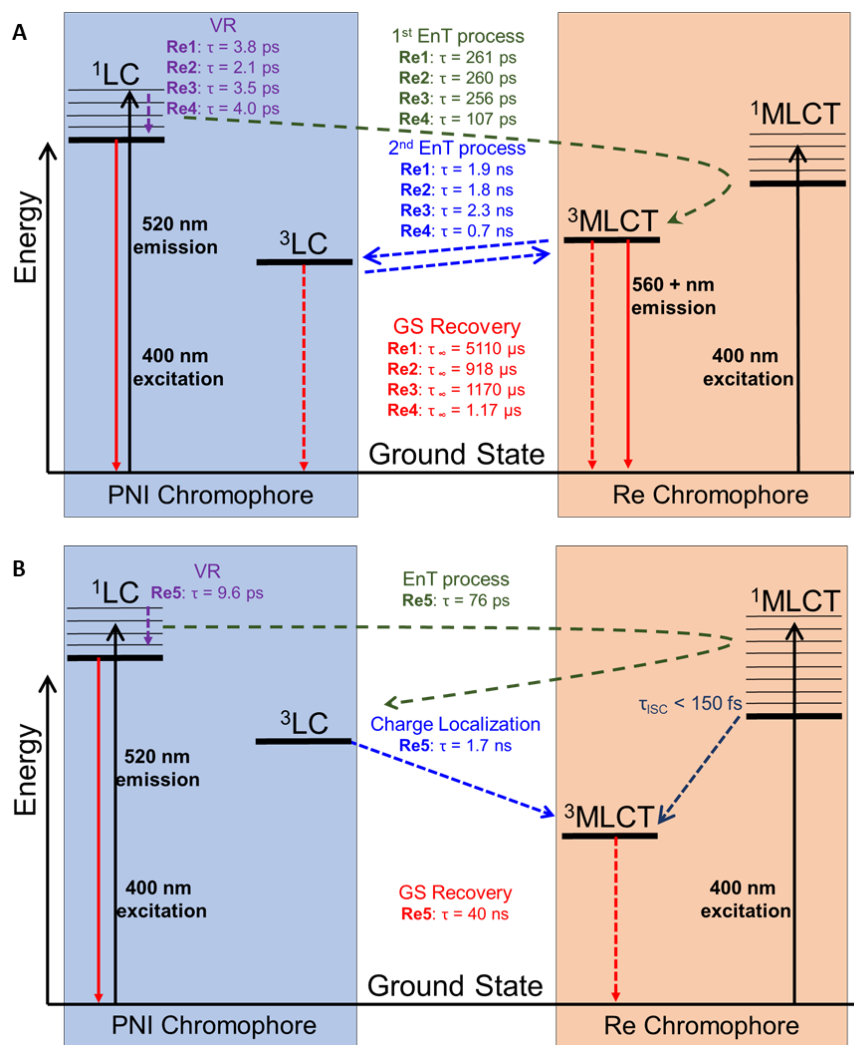


Figure 3.11. Qualitative energy level diagrams of the photophysical processes occurring in **Re1-4** (A) and **Re5** (B).

3.5. Conclusions

In this study, the excited state processes and associated energetic pathways of a series of five Re(I)-PNI bichromophores have been elucidated using a combination of transient absorption spectroscopies, time-resolved PL spectroscopy, and electronic structure calculations. These bichromophoric molecules and their respective models were synthesized by preparing the parent

Re-CDI moiety with a series of five diimine ligands and substituting PNI-py or 4-ety into the ancillary position following published procedures.⁵⁰ The unique diimine ligands yielded profound changes in the resultant molecular photophysical properties. Placement of the PNI subunit in an ancillary ligand position, the various energy transfer processes occurring between the relevant MLCT and PNI excited states were able to be quantitatively assessed. From the battery of static and time-resolved spectroscopic techniques utilized as described above, the data suggest that four of the five bichromophores in this study (**Re1-Re4**) display energetic pathways indicative of “ping-pong” energy transfer as observed in previous work.^{4,31} In **Re1-Re4**, the initially populated ¹PNI* excited state transfers energy to the Re(I) MLCT complex, producing the ³MLCT* state, which thermally equilibrates with ³PNI* state. These four molecules decay to their ground states with lifetimes markedly exceeding those observed in their respective model MLCT chromophores, **Mod1-4**. **Re5**, which possesses the lowest energy MLCT excited state in the series, is initially populated through the ¹PNI* excited state whose energy rapidly transfers to the MLCT manifold, although there is some evidence for ³PNI character as well. This molecule ultimately decays back to its ground state with a transient absorption determined excited state lifetime equivalent to **Mod5**.

3.6. Acknowledgments

This work was supported by the U.S. Department of Energy, Office of Science, Office of Basic Energy Sciences, under Award No. DE-SC0011979. Some personnel were supported by the National Science Foundation (CHE-1665033, K.A.W), the Air Force Institute of Technology (AFIT, J.E.Y), and the Air Force Office of Scientific Research (FA9550-18-1-0331, T.S.L). I would also like to thank my co-workers James E. Yarnell, Jonathan R. Palmer, Tia S. Lee, Christopher M. Papa, and Felix N. Castellano.

3.7. References

1. Wrighton, M.; Morse, D. L., Nature of the lowest excited state in tricarbonylchloro-1,10-phenanthroline-rhenium(I) and related complexes. *J. Am. Chem. Soc.* **1974**, *96* (4), 998-1003.
2. Vlček, A., Ultrafast Excited-State Processes in Re(I) Carbonyl-Diimine Complexes: From Excitation to Photochemistry. In *Photophysics of Organometallics*, Lees, A. J., Ed. Springer Berlin Heidelberg: Berlin, Heidelberg, 2010; pp 115-158.
3. Kumar, A.; Sun, S.-S.; Lees, A. J., Photophysics and Photochemistry of Organometallic Rhenium Diimine Complexes. In *Photophysics of Organometallics*, Lees, A. J., Ed. Springer Berlin Heidelberg: Berlin, Heidelberg, 2010; pp 37-71.
4. Yarnell, J. E.; Deaton, J. C.; McCusker, C. E.; Castellano, F. N., Bidirectional “Ping-Pong” Energy Transfer and 3000-Fold Lifetime Enhancement in a Re(I) Charge Transfer Complex. *Inorg. Chem.* **2011**, *50* (16), 7820-7830.
5. Favale, J. M.; Danilov, E. O.; Yarnell, J. E.; Castellano, F. N., Photophysical Processes in Rhenium(I) Diiminetricarbonyl Arylisocyanides Featuring Three Interacting Triplet Excited States. *Inorg. Chem.* **2019**, *58* (13), 8750-8762.
6. Patrocínio, A. O. T.; Murakami Iha, N. Y., Photoswitches and Luminescent Rigidity Sensors Based on *fac*-[Re(CO)₃(Me₄phen)(L)]⁺. *Inorg. Chem.* **2008**, *47* (23), 10851-10857.
7. Schanze, K. S.; Brent Macqueen, D.; Perkins, T. A.; Cabana, L. A., Studies of intramolecular electron and energy transfer using the *fac*-(diimine)ReI(CO)₃ chromophore. *Coord. Chem. Rev.* **1993**, *122* (1-2), 63-89.
8. Lo, K. K.-W., Exploitation of Luminescent Organometallic Rhenium(I) and Iridium(III) Complexes in Biological Studies. In *Photophysics of Organometallics*, Lees, A. J., Ed. Springer Berlin Heidelberg: Berlin, Heidelberg, 2010; pp 73-114.
9. Chakraborty, I.; Jimenez, J.; Sameera, W. M. C.; Kato, M.; Mascharak, P. K., Luminescent Re(I) Carbonyl Complexes as Trackable PhotoCORMs for CO delivery to Cellular Targets. *Inorg. Chem.* **2017**, *56* (5), 2863-2873.
10. Kuramochi, Y.; Fujisawa, Y.; Satake, A., Photocatalytic CO₂ Reduction Mediated by Electron Transfer via the Excited Triplet State of Zn(II) Porphyrin. *J. Am. Chem. Soc.* **2020**, *142* (2), 705-709.
11. Bruch, Q. J.; Connor, G. P.; Chen, C.-H.; Holland, P. L.; Mayer, J. M.; Hasanayn, F.; Miller, A. J. M., Dinitrogen Reduction to Ammonium at Rhenium Utilizing Light and Proton-Coupled Electron Transfer. *J. Am. Chem. Soc.* **2019**, *141* (51), 20198-20208.
12. Caspar, J. V.; Meyer, T. J., Application of the energy gap law to nonradiative, excited-state decay. *J. Phys. Chem.* **1983**, *87* (6), 952-957.

13. Sacksteder, L.; Zipp, A. P.; Brown, E. A.; Streich, J.; Demas, J. N.; DeGraff, B. A., Luminescence studies of pyridine .alpha.-diimine rhenium(I) tricarbonyl complexes. *Inorg. Chem.* **1990**, *29* (21), 4335-4340.
14. Lavie-Cambot, A.; Lincheneau, C.; Cantuel, M.; Leydet, Y.; McClenaghan, N. D., Reversible electronic energy transfer: a means to govern excited-state properties of supramolecular systems. *Chem. Soc. Rev.* **2010**, *39* (2), 506-515.
15. Franco, F.; Cometto, C.; Garino, C.; Minero, C.; Sordello, F.; Nervi, C.; Gobetto, R., Photo- and Electrocatalytic Reduction of CO₂ by [Re(CO)₃{ α,α' -Diimine-(4-piperidinyl-1,8-naphthalimide)}Cl] Complexes. *Eur. J. Inorg. Chem.* **2015**, *2015* (2), 296-304.
16. Lainé, P. P.; Bedioui, F.; Loiseau, F.; Chiorboli, C.; Campagna, S., Conformationally Gated Photoinduced Processes within PhotosensitizerAcceptor Dyads Based on Osmium(II) Complexes with Triarylpyridinio-Functionalized Terpyridyl Ligands: Insights from Experimental Study. *J. Am. Chem. Soc.* **2006**, *128* (23), 7510-7521.
17. Leydet, Y.; Bassani, D. M.; Jonusauskas, G.; McClenaghan, N. D., Equilibration between Three Different Excited States in a Bichromophoric Copper(I) Polypyridine Complex. *J. Am. Chem. Soc.* **2007**, *129* (28), 8688-8689.
18. Cohen, B. W.; Lovaasen, B. M.; Simpson, C. K.; Cummings, S. D.; Dallinger, R. F.; Hopkins, M. D., 1000-Fold Enhancement of Luminescence Lifetimes via Energy-Transfer Equilibration with the T₁ State of Zn(TPP). *Inorg. Chem.* **2010**, *49* (13), 5777-5779.
19. Wilson, G. J.; Launikonis, A.; Sasse, W. H. F.; Mau, A. W. H., Excited-State Processes in Ruthenium(II) Bipyridine Complexes Containing Covalently Bound Arenes. *J. Phys. Chem. A* **1997**, *101* (27), 4860-4866.
20. Wilson, G. J.; Launikonis, A.; Sasse, W. H. F.; Mau, A. W. H., Chromophore-Specific Quenching of Ruthenium Trisbipyridine–Arene Bichromophores by Methyl Viologen. *J. Phys. Chem. A* **1998**, *102* (26), 5150-5156.
21. Michalec, J. F.; Bejune, S. A.; McMillin, D. R., Multiple Ligand-Based Emissions from a Platinum(II) Terpyridine Complex Attached to Pyrene. *Inorg. Chem.* **2000**, *39* (13), 2708-2709.
22. McClenaghan, N. D.; Barigelletti, F.; Maubert, B.; Campagna, S., Towards ruthenium(II) polypyridine complexes with prolonged and predetermined excited state lifetimes. *Chem. Comm.* **2002**, (6), 602-603.
23. Passalacqua, R.; Loiseau, F.; Campagna, S.; Fang, Y.-Q.; Hanan, G. S., In Search of Ruthenium(II) Complexes Based on Tridentate Polypyridine Ligands that Feature Long-lived Room-Temperature Luminescence: The Multichromophore Approach. *Angew. Chem. Int.* **2003**, *42* (14), 1608-1611.

24. Whited, M. T.; Djurovich, P. I.; Roberts, S. T.; Durrell, A. C.; Schlenker, C. W.; Bradforth, S. E.; Thompson, M. E., Singlet and Triplet Excitation Management in a Bichromophoric Near-Infrared-Phosphorescent BODIPY-Benzoporphyrin Platinum Complex. *J. Am. Chem. Soc.* **2011**, *133* (1), 88-96.
25. Simon, J. A.; Curry, S. L.; Schmehl, R. H.; Schatz, T. R.; Piotrowiak, P.; Jin, X.; Thummel, R. P., Intramolecular Electronic Energy Transfer in Ruthenium(II) Diimine Donor/Pyrene Acceptor Complexes Linked by a Single C–C Bond. *J. Am. Chem. Soc.* **1997**, *119* (45), 11012-11022.
26. Tyson, D. S.; Castellano, F. N., Intramolecular Singlet and Triplet Energy Transfer in a Ruthenium(II) Diimine Complex Containing Multiple Pyrenyl Chromophores. *J. Phys. Chem. A* **1999**, *103*, 10955-10960.
27. Castellano, F. N., Altering Molecular Photophysics by Merging Organic and Inorganic Chromophores. *Acc. Chem. Res.* **2015**, *48* (3), 828-839.
28. Castellano, F. N., Transition metal complexes meet the rylenes. *Dalton Trans.* **2012**, *41* (28), 8493.
29. Tyson, D. S.; Bialecki, J.; Castellano, F. N., Ruthenium(II) complex with a notably long excited state lifetime. *Chem. Comm.* **2000**, (23), 2355-2356.
30. Tyson, D. S.; Henbest, K. B.; Bialecki, J.; Castellano, F. N., Excited State Processes in Ruthenium(II)/Pyrenyl Complexes Displaying Extended Lifetimes. *J. Phys. Chem. A* **2001**, *105* (35), 8154-8161.
31. Yarnell, J. E.; Wells, K. A.; Palmer, J. R.; Breaux, J. M.; Castellano, F. N., Excited-State Triplet Equilibria in a Series of Re(I)-Naphthalimide Bichromophores. *J. Phys. Chem. B* **2019**, *123* (35), 7611-7627.
32. Yarnell, J. E.; McCusker, C. E.; Leeds, A. J.; Breaux, J. M.; Castellano, F. N., Exposing the Excited-State Equilibrium in an Ir(III) Bichromophore: A Combined Time Resolved Spectroscopy and Computational Study. *Eur. J. Inorg. Chem. A* **2016**, *2016* (12), 1808-1818.
33. Tyson, D. S.; Luman, C. R.; Zhou, X.; Castellano, F. N., New Ru(II) Chromophores with Extended Excited-State Lifetimes. *Inorg. Chem.* **2001**, *40* (16), 4063-4071.
34. McCusker, C. E.; Chakraborty, A.; Castellano, F. N., Excited State Equilibrium Induced Lifetime Extension in a Dinuclear Platinum(II) Complex. *J. Phys. Chem. A* **2014**, *118* (45), 10391-10399.
35. Chandrasekharam, M.; Srinivasarao, C.; Suresh, T.; Reddy, M. A.; Raghavender, M.; Rajkumar, G.; Srinivasu, M.; Reddy, P. Y., High spectral response heteroleptic ruthenium (II) complexes as sensitizers for dye sensitized solar cells. *J. Chem. Sci.* **2011**, *123* (1), 37-46.

36. Suzuki, K.; Kobayashi, A.; Kaneko, S.; Takehira, K.; Yoshihara, T.; Ishida, H.; Shiina, Y.; Oishi, S.; Tobita, S., Reevaluation of absolute luminescence quantum yields of standard solutions using a spectrometer with an integrating sphere and a back-thinned CCD detector. *Phys. Chem. Chem. Phys.* **2009**, *11* (42), 9850-9860.
37. Greenfield, S. R.; Svec, W. A.; Gosztola, D.; Wasielewski, M. R., Multistep Photochemical Charge Separation in Rod-like Molecules Based on Aromatic Imides and Diimides. *J. Am. Chem. Soc.* **1996**, *118* (28), 6767-6777.
38. Garakyaraghi, S.; Danilov, E. O.; McCusker, C. E.; Castellano, F. N., Transient Absorption Dynamics of Sterically Congested Cu(I) MLCT Excited States. *J. Phys. Chem. A* **2015**, *119* (13), 3181-3193.
39. Frisch, M. J.; Trucks, G. W.; Schlegel, H. B.; Scuseria, G. E.; Robb, M. A.; Cheeseman, J. R.; Scalmani, G.; Barone, V.; Petersson, G. A.; Nakatsuji, H.; Li, X.; Caricato, M.; Marenich, A. V.; Bloino, J.; Janesko, B. G.; Gomperts, R.; Mennucci, B.; Hratchian, H. P.; Ortiz, J. V.; Izmaylov, A. F.; Sonnenberg, J. L.; Williams; Ding, F.; Lipparini, F.; Egidi, F.; Goings, J.; Peng, B.; Petrone, A.; Henderson, T.; Ranasinghe, D.; Zakrzewski, V. G.; Gao, J.; Rega, N.; Zheng, G.; Liang, W.; Hada, M.; Ehara, M.; Toyota, K.; Fukuda, R.; Hasegawa, J.; Ishida, M.; Nakajima, T.; Honda, Y.; Kitao, O.; Nakai, H.; Vreven, T.; Throssell, K.; Montgomery Jr., J. A.; Peralta, J. E.; Ogliaro, F.; Bearpark, M. J.; Heyd, J. J.; Brothers, E. N.; Kudin, K. N.; Staroverov, V. N.; Keith, T. A.; Kobayashi, R.; Normand, J.; Raghavachari, K.; Rendell, A. P.; Burant, J. C.; Iyengar, S. S.; Tomasi, J.; Cossi, M.; Millam, J. M.; Klene, M.; Adamo, C.; Cammi, R.; Ochterski, J. W.; Martin, R. L.; Morokuma, K.; Farkas, O.; Foresman, J. B.; Fox, D. J. *Gaussian 16 Rev. A.03*, Wallingford, CT, 2016.
40. Zhao, Y.; Truhlar, D. G., The M06 suite of density functionals for main group thermochemistry, thermochemical kinetics, noncovalent interactions, excited states, and transition elements: two new functionals and systematic testing of four M06-class functionals and 12 other functionals. *Theor. Chem. Acc.* **2008**, *120* (1), 215-241.
41. Weigend, F.; Ahlrichs, R., Balanced basis sets of split valence, triple zeta valence and quadruple zeta valence quality for H to Rn: Design and assessment of accuracy. *Phys. Chem. Chem. Phys.* **2005**, *7* (18), 3297-3305.
42. Andrae, D.; Häußermann, U.; Dolg, M.; Stoll, H.; Preuß, H., Energy-adjusted ab initio pseudopotentials for the second and third row transition elements. *Theor. Chim. Acta* **1990**, *77* (2), 123-141.
43. Ehlers, A. W.; Böhme, M.; Dapprich, S.; Gobbi, A.; Höllwarth, A.; Jonas, V.; Köhler, K. F.; Stegmann, R.; Veldkamp, A.; Frenking, G., A set of f-polarization functions for pseudo-potential basis sets of the transition metals Sc-Cu, Y-Ag and La-Au. *Chem. Phys. Lett.* **1993**, *208* (1-2), 111-114.

44. Cossi, M.; Scalmani, G.; Rega, N.; Barone, V., New developments in the polarizable continuum model for quantum mechanical and classical calculations on molecules in solution. *J. Chem. Phys.* **2002**, *117* (1), 43.
45. Dennington, R.; Keith, T. A.; Millam, J. M. *GaussView, Version 6*, Semichem Inc.: Shawnee Mission, KS, 2016.
46. Stratmann, R. E.; Scuseria, G. E.; Frisch, M. J., An efficient implementation of time-dependent density-functional theory for the calculation of excitation energies of large molecules. *J. Chem. Phys.* **1998**, *109* (19), 8218.
47. Bauernschmitt, R.; Ahlrichs, R., Treatment of electronic excitations within the adiabatic approximation of time dependent density functional theory. *Chem. Phys. Lett.* **1996**, *256* (4-5), 454-464.
48. Casida, M. E.; Jamorski, C.; Casida, K. C.; Salahub, D. R., Molecular excitation energies to high-lying bound states from time-dependent density-functional response theory: Characterization and correction of the time-dependent local density approximation ionization threshold. *J. Chem. Phys.* **1998**, *108* (11), 4439.
49. Kitchen, J. A.; Martinho, P. N.; Morgan, G. G.; Gunnlaugsson, T., Synthesis, crystal structure and EPR spectroscopic analysis of novel copper complexes formed from N-pyridyl-4-nitro-1,8-naphthalimide ligands. *Dalton Trans.* **2014**, *43* (17), 6468.
50. Langdon-Jones, E. E.; Williams, C. F.; Hayes, A. J.; Lloyd, D.; Coles, S. J.; Horton, P. N.; Groves, L. M.; Pope, S. J. A., Luminescent 1,8-Naphthalimide-Derived ReI Complexes: Syntheses, Spectroscopy, X-ray Structure and Preliminary Bioimaging in Fission Yeast Cells. *Eur. J. Inorg. Chem.* **2017**, *2017* (44), 5279-5287.
51. Worl, L. A.; Duesing, R.; Chen, P.; Ciana, L. D.; Meyer, T. J., Photophysical properties of polypyridyl carbonyl complexes of rhenium(I). *J. Chem. Soc., Dalton Trans.* **1991**, 849.
52. Kucheryavy, P.; Li, G.; Vyas, S.; Hadad, C.; Glusac, K. D., Electronic Properties of 4-Substituted Naphthalimides. *J. Phys. Chem. A* **2009**, *113* (23), 6453-6461.
53. Zipp, A. P.; Sacksteder, L.; Streich, J.; Cook, A.; Demas, J. N.; Degraff, B. A., Luminescence of rhenium(I) complexes with highly sterically hindered .alpha.-diimine ligands. *Inorg. Chem.* **1993**, *32* (24), 5629-5632.
54. Wallace, L.; Rillema, D. P., Photophysical properties of rhenium(I) tricarbonyl complexes containing alkyl- and aryl-substituted phenanthrolines as ligands. *Inorg. Chem.* **1993**, *32* (18), 3836-3843.
55. Moya, S. A.; Guerrero, J.; Pastene, R.; Sartori, R.; Schmidt, R.; Sariego, R.; Sanz-Aparicio, J.; Fonseca, I.; Martinez-Ripoll, M., Metallic Carbonyl Complexes Containing

Heterocycle Nitrogen Ligands. 2. Tricarbonylbromo(3,3'-R-2,2'-biquinoline)Rhenium(I) Compounds. *Inorg. Chem.* **1994**, *33* (11), 2341-2346.

56. Striplin, D. R.; Crosby, G. A., Photophysical investigations of rhenium(I)Cl(CO)₃(phenanthroline) complexes. *Coord. Chem. Rev.* **2001**, *211* (1), 163-175.
57. Striplin, D. R.; Crosby, G. A., Nature of the emitting ³MLCT manifold of rhenium(I) (diimine) (CO)₃Cl complexes. *Chem. Phys. Lett.* **1994**, *221* (5), 426-430.
58. Mai, S.; Gattuso, H.; Fumanal, M.; Muñoz-Losa, A.; Monari, A.; Daniel, C.; González, L., Excited-states of a rhenium carbonyl diimine complex: solvation models, spin-orbit coupling, and vibrational sampling effects. *Phys. Chem. Chem. Phys.* **2017**, *19* (40), 27240-27250.
59. Yang, L.; Ren, A.-M.; Feng, J.-K.; Liu, X.-J.; Ma, Y.-G.; Zhang, M.; Liu, X.-D.; Shen, J.-C.; Zhang, H.-X., Theoretical Studies of Ground and Excited Electronic States in a Series of Halide Rhenium(I) Bipyridine Complexes. *J. Phys. Chem. A* **2004**, *108* (32), 6797-6808.
60. Vlček, A.; Záliš, S., Comments on “Theoretical Studies of Ground and Excited Electronic States in a Series of Halide Rhenium(I) Bipyridine Complexes”. *J. Phys. Chem. A* **2005**, *109* (12), 2991-2992.
61. Lakowicz, J. R., *Principles of Fluorescence Spectroscopy*. 3rd ed.; Springer Science+Business Media, LLC: New York, 2006.
62. Suzuki, K.; Kobayashi, A.; Kaneko, S.; Takehira, K.; Yoshihara, T.; Ishida, H.; Shiina, Y.; Oishi, S.; Tobita, S., Reevaluation of absolute luminescence quantum yields of standard solutions using a spectrometer with an integrating sphere and a back-thinned CCD detector. *Phys. Chem. Chem. Phys.* **2009**, *11* (42), 9850.
63. Kalyanasundaram, K., Luminescence and redox reactions of the metal-to-ligand charge-transfer excited state of tricarbonylchloro-(polypyridyl)rhenium(I) complexes. *J. Chem. Soc., Faraday Trans. 2* **1986**, *82* (12), 2401.
64. Aveline, B. M.; Matsugo, S.; Redmond, R. W., Photochemical Mechanisms Responsible for the Versatile Application of Naphthalimides and Naphthalidiimides in Biological Systems. *J. Am. Chem. Soc.* **1997**, *119* (49), 11785-11795.
65. Rogers, J. E.; Kelly, L. A., Nucleic Acid Oxidation Mediated by Naphthalene and Benzophenone Imide and Diimide Derivatives: Consequences for DNA Redox Chemistry. *J. Am. Chem. Soc.* **1999**, *121* (16), 3854-3861.
66. Rogers, J. E.; Weiss, S. J.; Kelly, L. A., Photoprocesses of Naphthalene Imide and Diimide Derivatives in Aqueous Solutions of DNA. *J. Am. Chem. Soc.* **2000**, *122* (3), 427-436.

67. El Nahhas, A.; Consani, C.; Blanco-Rodríguez, A. M. A.; Lancaster, K. M.; Braem, O.; Cannizzo, A.; Towrie, M.; Clark, I. P.; Zálaiš, S.; Chergui, M.; Vlček, A. N., Ultrafast Excited-State Dynamics of Rhenium(I) Photosensitizers $[\text{Re}(\text{Cl})(\text{CO})_3(\text{N},\text{N})]$ and $[\text{Re}(\text{imidazole})(\text{CO})_3(\text{N},\text{N})]^+$: Diimine Effects. *Inorg. Chem.* **2011**, *50* (7), 2932-2943.
68. Liard, D. J.; Busby, M.; Matousek, P.; Towrie, M.; Vlček, A., Picosecond Relaxation of $^3\text{MLCT}$ Excited States of $[\text{Re}(\text{Etpy})(\text{CO})_3(\text{dmb})]^+$ and $[\text{Re}(\text{Cl})(\text{CO})_3(\text{bpy})]$ as Revealed by Time-Resolved Resonance Raman, UV-vis, and IR Absorption Spectroscopy. *J. Phys. Chem. A* **2004**, *108* (13), 2363-2369.

Chapter 4: Accessing the Triplet Manifold of Naphthalenebenzimidazole-Phenanthroline in Rhenium(I) Bichromophores

Portions of this chapter has been previously published in *Dalton Transactions*, **2021**. DOI: 10.1039/D1DT02329B

4.1. Abstract

The steady-state and ultrafast to suprananosecond excited state dynamics of *fac*-[Re(NBI-phen)(CO)₃(L)](PF₆) (**NBI-phen** = 16H-benzo[4',5']isoquinolino[2',1':1,2]imidazo[4,5-f][1,10]phenanthroline-16-one) as well as their respective models of the general molecular formula [Re(phen)(CO)₃(L)](PF₆) (L = PPh₃ and CH₃CN) were investigated using transient absorption and time-gated photoluminescence spectroscopy. The **NBI-phen** containing molecules exhibited enhanced visible light absorption with respect to their models and rapid formation (< 6 ns) of the triplet ligand-centered (LC) excited state of the organic ligand, NBI-phen. These triplet states exhibit an extended excited state lifetime that enable the energized molecules to readily engage in triplet-triplet annihilation photochemistry.

4.2. Introduction

Since Wrighton and co-workers original study,¹ rhenium(I) carbonyl diimine (Re-CDI) molecules have remained popular due to their thermal and photochemical stability, expansive photophysical properties, and ease of synthesis.²⁻⁹ The synthetic flexibility of this class of chromophores allows for the molecule to be incorporated into polymers and supramolecular structures enabling a myriad of applications.¹⁰⁻¹⁴ In fact, Re-CDI molecules are currently utilized in CO₂ reduction photochemistry, photochemical molecular devices, solar energy conversion, biological applications, and as sensors and photosensitizers.¹⁵⁻²⁴

A significant drawback to many Re-CDI complexes is that they typically exhibit poor visible absorption properties and short triplet metal-to-ligand-charge-transfer (MLCT) lifetimes

on the order of 100s of nanoseconds.²⁵ However, fine-tuning the electronic structure, and thus the corresponding electronic transitions, may be achieved through facile synthetic manipulations. The Re(I) $d\pi$ orbital energies are easily modified by varying the π -accepting and π -donating strength of the ancillary ligand, which are typically associated with the HOMO energy in these complexes.²⁶ Additionally, the π^* orbital energies, the orbitals typically associated with the LUMO energy of the chromophoric diimine ligand, may also be adjusted by adding substituents on the diimine aromatic rings.¹ Thus, modification of both the ancillary and diimine ligands causes variations in the Re(I) $d\pi$ and diimine π^* orbital energies, thereby modulating the MLCT excited state properties.

Our research group has conducted numerous studies monitoring changes in the excited state dynamics in Re-CDIs.²⁷⁻²⁹ In these studies, we focused on appending additional organic chromophores within the ligand framework, which leads to excited state lifetime extension via a thermal equilibrium between the triplet ligand-centred (^3LC) and $^3\text{MLCT}$ excited states.³⁰⁻³⁸ After extensively studying the photophysical interactions in these systems by modulation of both LC and MLCT excited state energies, we became interested in exploring new families of organic chromophores to determine what changes in their excited state dynamics might occur while testing their utility as light-harvesters and other potentially bespoke photophysical processes.

Most recently, we have investigated a series of thionated perinones³⁹ that exhibit efficient triplet excited state formation, building off work by Anzenbacher and co-workers on the oxygenated analogues.⁴⁰ Their work on polycyclic benzimidazoles inspired us to incorporate the perinone unit into rhenium(I) MLCT chromophores to increase their visible-absorption cross-sections and determine if the perinone triplet could be sensitized through the heavy-atom effect. Perinones are polycyclic aromatic hydrocarbons that belong to a class of organic dyes that have

found extensive use in the automotive industry and in organic n-type semiconductor materials.⁴⁰⁻
⁴⁴ Considering their relatively high fluorescence quantum yields and significant visible absorption cross-sections, we postulated that this class of molecules would be of interest to construct newly conceived metal-organic bichromophores. Using the synthesis provided by Yang et al⁴⁵ to synthesize a perinone that is nested within a chelating ligand, we were able to successfully synthesize and photophysically characterize two new rhenium(I) bichromophores (**Chart 1**), *fac*-[Re(NBI-phen)(CO)₃(PPh₃)](PF₆) (**Re1**) and *fac*-[Re(NBI-phen)(CO)₃(CH₃CN)](PF₆) (**Re2**) (NBI-phen = naphthalene benzimidazole phenanthroline) as well as two model rhenium(I) chromophores *fac*-[Re(phen)(CO)₃(PPh₃)](PF₆) (**Mod1**) and *fac*-[Re(phen)(CO)₃(CH₃CN)](PF₆) (**Mod2**) which serve as control/model molecules to make direct comparisons to the bichromophores. The CH₃CN and PPh₃ moieties were purposefully selected as strong ancillary ligands to promote the formation of ligand-centered triplet excited states. Using a combination of steady-state and time-resolved techniques supported with computational modelling, we determined the **NBI-phen** ligand establishes the necessary energetics to serve as a visible light harvester featuring rapid formation of the long-lived ³LC excited state.

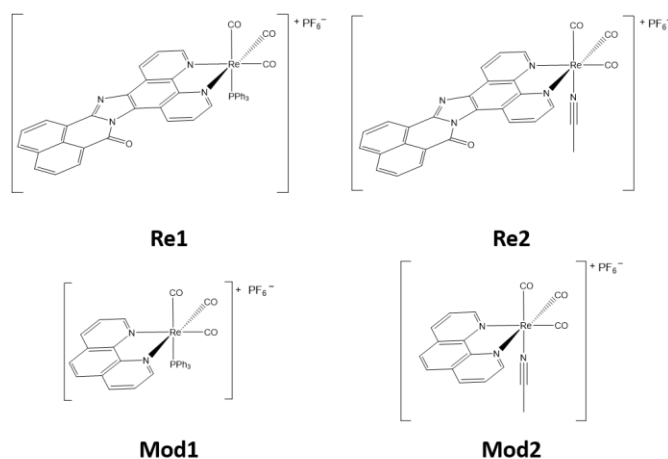


Chart 4.1. The bichromophores **Re1**, **Re2**, and relevant model complexes **Mod1** and **Mod2** investigated here.

4.3. Experimental

4.3.1. Reagents and Chemicals

All reagents and chemicals were purchased from Sigma—Aldrich or VWR and used as received. All syntheses were performed under an inert nitrogen atmosphere using standard techniques for the rigorous exclusion of air and water. Spectroscopic samples were prepared using spectroscopic-grade tetrahydrofuran and were prepared under an inert and dry atmosphere of nitrogen in a glovebox (MBraun). Complete synthesis and structural characterization details for all molecules investigated here are provided in Appendix C.

4.3.2. General Techniques

All chemicals and solvents were analytical grade, and they were used without further purification. Nuclear magnetic resonance (NMR) spectra were measured at 298 K with a Bruker® Avance NEO 700 MHz (^1H) and 176 MHz (^{13}C) and processed with MestreNova software (version 10.0.2), with the chemical shifts referenced to residual solvent signals. The chemical shifts (δ ppm) are referenced to the respective solvent, and splitting patterns are designated as s (singlet), d (doublet), t (triplet), m (multiplet). High resolution electrospray ionization mass spectrometry (HR-ESI-MS) was measured by the Michigan State University Mass Spectrometry Core, East Lansing, MI. MS values are given as m/z . Electronic absorption spectra was measured with a Shimadzu UV-3600 and Cary 60 UV/Vis spectrophotometer. Steady-state photoluminescence (PL) spectra and quantum yield measurements were measured on an Edinburgh FS 5 fluorimeter equipped with an integrating sphere (absolute). Excitation scans were performed on an Edinburgh FS 920 fluorimeter. All spectral PL measurements were performed using optically dilute samples at ($0.1 \geq \text{OD}$) at excitation wavelength.

4.3.3. Characterization Data for Studied Molecules

16H-benzo[4',5']isoquinolino[2',1':1,2]imidazo[4,5-f][1,10]phenanthroline-16-one (**NBI-phen**). (64 %). ^1H NMR (700 MHz, CDCl_3) δ 10.80 (d, $J = 8.7$ Hz, 1H), 9.56 (d, $J = 8.2$ Hz, 1H), 9.36 (t, $J = 5.3$ Hz, 2H), 9.23 (d, $J = 7.4$ Hz, 1H), 9.17 (d, $J = 7.4$ Hz, 1H), 8.66 (d, $J = 8.1$ Hz, 1H), 8.59 (d, $J = 8.2$ Hz, 1H), 8.45 – 8.42 (m, 1H), 8.33 – 8.30 (m, 1H), 8.14 (dd, $J = 11.4, 4.0$ Hz, 1H), 8.11 (t, $J = 7.8$ Hz, 1H) ppm. ^{13}C NMR (176 MHz, CDCl_3) δ 159.93, 151.64, 150.36, 144.93, 144.89, 139.16, 137.70, 137.44, 136.74, 135.76, 132.63, 132.25, 131.90, 129.08, 128.83, 128.02, 126.77, 126.29, 123.99, 121.76, 121.09, 120.94, 77.34, 77.16, 76.98, 21.26 ppm. MS [HR-ESI]: m/z calcd for $\text{C}_{24}\text{H}_{12}\text{N}_4\text{OH}$ $[\text{M}+\text{H}]^+$ 373.1089, found 373.1094. (**Fig. C1-3**).

fac-[Re(NBI-phen)(CO)₃(PPh₃)](PF₆) (**Re1**). (96 %). ^1H NMR (700 MHz, DMSO) δ 10.16 (d, $J = 8.6$ Hz, 1H), 9.41 (d, $J = 5.0$ Hz, 1H), 9.31 (t, $J = 7.0$ Hz, 2H), 8.97 (d, $J = 7.1$ Hz, 1H), 8.93 (d, $J = 7.2$ Hz, 1H), 8.69 (d, $J = 8.0$ Hz, 1H), 8.53 (d, $J = 8.1$ Hz, 1H), 8.09 (t, $J = 7.6$ Hz, 1H), 8.07 – 8.00 (m, 3H), 7.35 (t, $J = 7.4$ Hz, 3H), 7.25 (t, $J = 6.7$ Hz, 6H), 7.01 – 6.97 (m, 6H) ppm. ^{13}C NMR (176 MHz, DMSO) δ 194.95, 160.86, 155.04, 153.32, 152.42, 144.99, 144.44, 138.65, 138.32, 136.42, 134.14, 132.98, 132.86, 132.26, 132.20, 131.67, 131.05, 129.93, 129.13, 129.07, 128.08, 128.00, 127.82, 127.59, 127.50, 126.12, 125.99, 124.97, 124.47, 122.94, 122.59, 120.12, 40.02, 39.88, 39.76, 39.64, 39.52, 39.40, 39.28, 39.16 ppm. MS [HR-ESI]: m/z calcd for $\text{C}_{45}\text{H}_{27}\text{N}_4\text{O}_4\text{PRe}$ $[\text{M}]^+$ 903.1299, found 903.1307. (**Fig. C4-6**).

fac-[Re(NBI-phen)(CO)₃(CH₃CN)](PF₆) (**Re2**). (71 %). ^1H NMR (700 MHz, CD_3CN) δ 10.48 (d, $J = 8.6$ Hz, 1H), 9.51 (t, $J = 5.8$ Hz, 2H), 9.47 (d, $J = 4.8$ Hz, 1H), 9.01 (d, $J = 7.2$ Hz, 1H), 8.96 (d, $J = 7.2$ Hz, 1H), 8.57 (d, $J = 8.0$ Hz, 1H), 8.42 (d, $J = 8.1$ Hz, 1H), 8.20 (ddd, $J = 18.7, 8.4, 4.9$ Hz, 2H), 8.01 (dt, $J = 15.5, 7.7$ Hz, 2H) ppm. ^{13}C NMR (176 MHz, CD_3CN) δ 155.38, 153.88, 146.88, 140.41, 140.10, 137.58, 135.93, 134.30, 133.87, 132.96, 128.94, 128.82, 128.67,

128.11, 127.30, 127.00, 126.49, 126.28, 124.40, 123.87, 123.48, 121.29, 120.71, 118.26, 68.24, 26.20, 1.27, 1.15. MS [HR-ESI]: m/z calcd for $C_{29}H_{15}N_5O_4Re$ $[M]^+$ 682.0654, found 682.0661.

(Fig. C7-9).

fac-[Re(phen)(CO)₃(PPh₃)](PF₆) (**Mod1**). (98 %). ¹H NMR (700 MHz, CD₃CN) δ 9.11 (dd, $J = 5.1, 0.6$ Hz, 2H), 8.62 (d, $J = 8.2$ Hz, 2H), 8.05 (s, 2H), 7.73 (dd, $J = 8.2, 5.1$ Hz, 2H), 7.33 (dt, $J = 7.4, 3.7$ Hz, 3H), 7.20 (td, $J = 7.7, 2.1$ Hz, 6H), 7.04 – 7.00 (m, 6H) ppm. ¹³C NMR (176 MHz, CD₃CN) δ 155.79, 147.18, 140.24, 133.51, 133.45, 131.95, 131.93, 129.94, 129.88, 129.65, 129.38, 128.87, 127.56, 118.26, 1.27 ppm. MS [HR-ESI]: m/z calcd for $C_{33}H_{23}N_2O_3PRe$ $[M]^+$ 711.0976, found 711.0970. (Fig. C10-12).

fac-[Re(phen)(CO)₃(CH₃CN)](PF₆) (**Mod2**). (91 %). ¹H NMR (400 MHz, CD₂Cl₂) δ 9.38 (dd, $J = 5.1, 1.3$ Hz, 2H), 8.80 (dd, $J = 8.3, 1.3$ Hz, 2H), 8.21 (s, 2H), 8.05 (dd, $J = 8.3, 5.1$ Hz, 2H), 2.06 (s, 3H), 1.54 (s, 3H) ppm. ¹³C NMR (176 MHz, CD₂Cl₂) δ 154.46, 147.24, 140.55, 131.72, 128.63, 127.13, 54.15, 54.00, 53.84, 53.69, 53.53, 3.70 ppm. MS [HR-ESI]: m/z calcd for $C_{17}H_{11}N_3O_3Re$ $[M]^+$ 490.0330, found 490.0339. (Fig. C13-15).

4.3.4. Ultrafast Transient Absorption Spectroscopy

The transient absorption measurements were performed at the NCSU Imaging and Kinetic Spectroscopy (IMAKS) Laboratory using a mode-locked Ti:sapphire laser (Coherent Libra) as described previously.⁴⁶ The pump beam was directed into a parametric amplifier (Coherent OPerA Solo) to generate the 400 nm excitation. The probe beam was focused onto a calcium fluoride crystal to generate a white light continuum between 350 and 750 nm. The pump beam (~700 μ m) was focused and overlapped with the probe beam through a 2 mm path length cuvette to allow for a stir bar to be used. The ground-state absorption spectra were taken before and after each experiment to ensure there was no sample photo-degradation during the experiment. The transient

kinetic data at specific wavelengths was evaluated using the fitting routines available in OriginPro 2018b (v 9.55).

4.3.5. Nanosecond Transient Absorption and Time-Resolved Photoluminescence

Spectroscopy

Nanosecond transient absorption (nsTA) and time—resolved photoluminescence (TR—PL) measurements were collected with a LP920 laser flash photolysis system from Edinburgh Instruments controlled by L900 software program (Edinburgh Instruments). A Vibrant 355 Nd:YAG/OPO system (OPOTEK) was used for pulsed laser excitation for **Re1** and **Re2**. A Continuum Minilite Nd:YAG laser with 355 nm excitation was used for pulsed laser excitation for **Mod1** and **Mod2**. To collect the transient absorption difference spectra and time—gated PL spectra in the visible portion of the spectrum, an iStar ICCD camera (Andor Technology), controlled by L900 was used. Single—wavelength kinetic analysis for absorption and PL were collected using a R2658P PMT detector (Hamamatsu) also controlled by L900. Samples were prepared under an inert and dry atmosphere of nitrogen in a glovebox (MBraun) in a 10 mm path-length quartz optical cell. Samples were prepared to have optical densities between 0.3 and 0.6 at the excitation wavelength ($\lambda_{\text{ex}} = 410$ nm for **Re1** and **Re2** and $\lambda_{\text{ex}} = 355$ nm for **Mod1** and **Mod2**). All flash-photolysis experiments were performed at room temperature unless otherwise noted. The ground-state electronic absorption spectra were recorded before and after each experiment to ensure no sample photo-degradation. The transient kinetic data was evaluated using the fitting routines available in Origin Student 2018b (v. 9.55).

4.3.6. Density Functional Theory (DFT) and Time-Dependent DFT (TD-DFT) Calculations

Density functional theory (DFT) and time-dependent DFT (TD-DFT) calculations were performed on all complexes using the Gaussian 16 software package (revision A.03)⁴⁷ and the

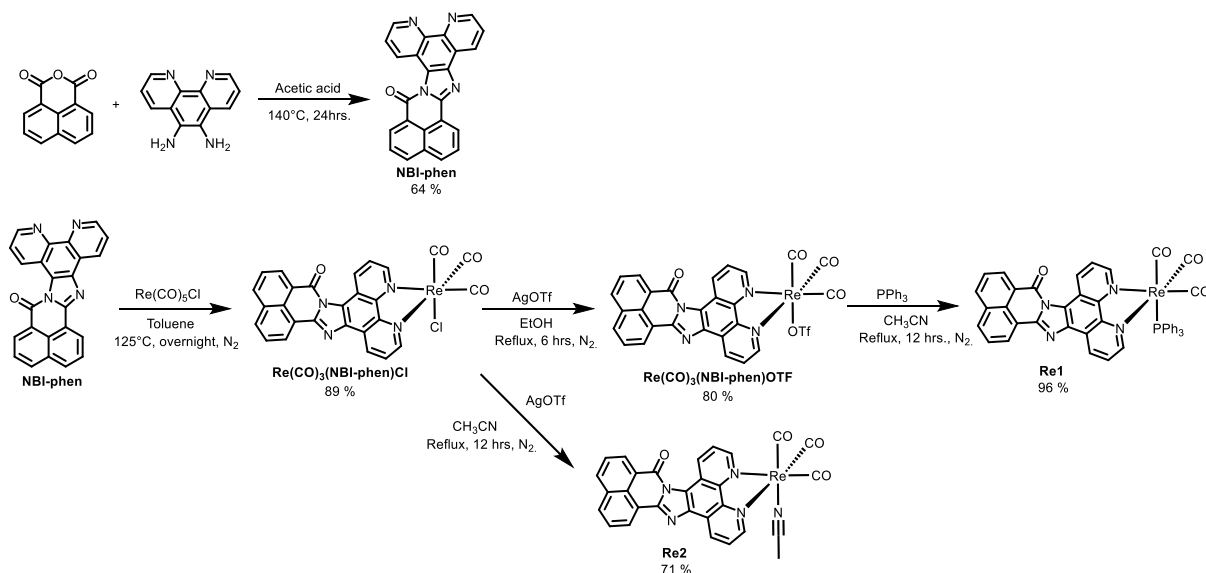
computational resources of the North Carolina State University High Performance Computing Center. Geometry optimizations and TD-DFT calculations were performed using the PBE1PBE (PBE0) functional⁴⁸ and the Def2-SVP basis set of the Alrichs group on all atoms.⁴⁹ The Stuttgart-Dresden effective core potentials (ECP) were used to replace the core electrons in rhenium for all calculations.⁵⁰ The polarizable continuum model (PCM)⁵¹ was used to simulate the effects of the tetrahydrofuran (THF) solvent environment for all calculations, and the GD3 dispersion correction⁵² was used for all ground and excited state geometry optimizations. Frequency calculations were performed on all optimized structures and no imaginary frequencies were obtained. TD-DFT calculations were used to obtain the energy, oscillator strength, and related molecular orbital contributions for the 50 lowest singlet-singlet vertical transitions for all molecules studied. The natural transition orbitals (NTOs)⁵³ of the low-lying singlet-singlet transitions were generated and visualized using GaussView 6.0.⁵⁴ Triplet spin density surfaces and natural orbitals (NOs) were generated from the optimized T₁ excited states and were also visualized with GaussView 6.0.

4.4. Results and Discussion

4.4.1. Syntheses

All syntheses were performed under an inert and dry nitrogen atmosphere using standard techniques. All reagents were purchased from VWR or Sigma-Aldrich and used as received. The synthetic procedures used to make all the chromophores are outlined in Scheme 4.1. The identity and purity of all compounds studied were confirmed using ¹H NMR, ¹³C NMR, and high-resolution mass spectrometry. Synthetic details for all precursors and products in this study are included in the Supporting Information. Briefly, 1,8-naphthalic anhydride, 5,6-diamino-1,10-phenanthroline, and acetic acid were added to a pressure vessel and heated to 140 °C for 24 hours

to synthesize the **NBI-phen** ligand.⁴⁵ Synthesis of **Re1** and **Re2** began with **NBI-phen** and $\text{Re}(\text{CO})_5\text{Cl}$ refluxing in toluene to make the chloride intermediate. **Re1** was then treated with AgOTf in EtOH to remove the chloride which was then reacted with PPh_3 in CH_3CN to synthesize the final product. **Re2** also began with the chloride intermediate as with **Re1** but was treated with AgOTf in CH_3CN to synthesize the final product. **Mod1** and **Mod2** were synthesized according to previous literature precedence.^{55, 56}



Scheme 4.1. Synthetic pathways leading to **NBI-phen**, **Re1** and **Re2**.

4.4.2. Electronic Structure Calculations

Ground state geometry optimizations were initially performed on both the model complexes (**Mod1** and **Mod2**) and the bichromophores (**Re1** and **Re2**) to establish how the frontier molecular orbitals are altered by interchanging 1,10-phenanthroline with **NBI-phen** as the diimine ligand. Representative frontier orbital diagrams are shown below in Figure 4.1 for **Mod1** and **Re1**. Corresponding diagrams are reported in Figure C16 for **Mod2** and **Re2**. The frontier orbitals for **Mod1** depict the three highest occupied molecular orbitals to be the $\text{Re}(\text{I})$ $d\pi$ orbitals, while the LUMO corresponds to the π^* orbital on the diimine. This suggests that the lowest energy transitions in the UV-Vis of this complex are MLCT in nature. Similar conclusions can be drawn

from Figure C16 for **Mod2**. Conversely, the frontier orbitals for **Re1** reveal the emergence of a diimine-based π molecular orbital as the HOMO, while the LUMO is lowered in energy and maintained as the π^* orbital on the diimine. Additionally, the HOMO-LUMO gap is calculated to be much smaller in **Re1** than in **Mod1** (~ 0.6 eV). As a result, it is expected that the lowest energy transition in **Re1** is ligand-centered and the complex will exhibit superior visible light absorption than its corresponding model complex, **Mod1**. Similarly, this trend is also observed when comparing **Mod2** to **Re2**.

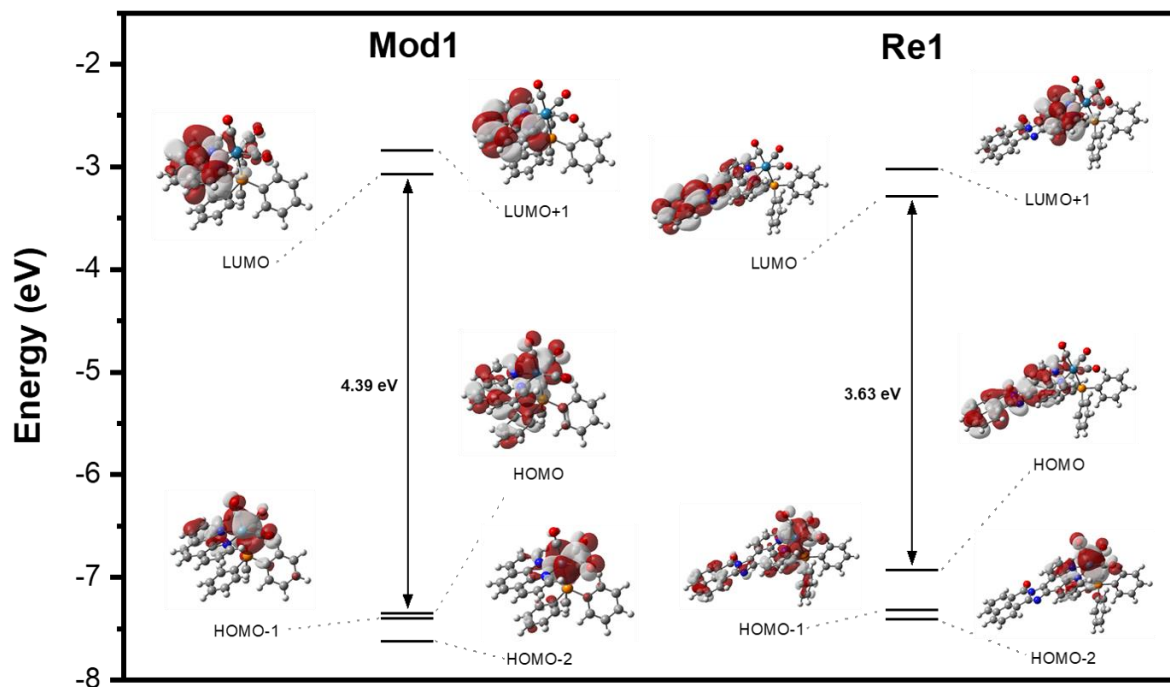


Figure 4.1. Representative frontier molecular orbital diagrams of the **Mod1** and corresponding NBI-phen complex **Re1**, where L = PPh₃.

Using the optimized ground state geometries, the electronic absorption spectrum of each complex was simulated by calculating the 50 lowest singlet transitions for each complex. The calculated electronic absorption spectra of **Mod1** and **Re1** are presented in Figures C17 and C18, respectively, and are overlaid with their experimental spectra. For **Mod1**, the calculated spectrum

is in good agreement with experimental data, with the lowest energy absorption maximum being slightly overestimated in energy. The calculated electronic absorption spectrum of **Re1** is also in good agreement with experimental data, with the lowest energy absorption maximum being slightly underestimated in energy. Natural transition orbitals were calculated for the three lowest-lying vertical excitations of **Mod1** and **Re1** to elucidate the character of the transitions making up the majority of the lowest energy absorption bands. The resultant hole-particle pairs are displayed in Figure C21 for **Mod1** and Figure C22 for **Re1**. The energies and oscillator strengths for these transitions are compiled in Table C1. The three lowest energy singlet transitions for **Mod1** are all MLCT in nature with low oscillator strength. The hole corresponds to a Re(I) $d\pi$ orbital in each case and the particle corresponds to a π^* orbital on the diimine. Conversely, the lowest energy singlet transition for **Re1** is LC in nature with significant oscillator strength. The hole corresponds to a π orbital on the diimine and the particle corresponds to a π^* orbital on the diimine. The pure MLCT transition for **Re1** is not observed until the $S_0 \rightarrow S_3$ transition, which is significantly higher in energy with much lower oscillator strength than the LC transition (see Table C1). These results are consistent with those predicted from the change in frontier molecular orbitals shown in Figure 4.1 when interchanging 1,10-phenanthroline with **NBI-phen** as the diimine, and is also observed in **Mod2** and **Re2** (Figures C23-24).

The character of the lowest energy triplet excited state in the bichromophores were assigned by calculating natural orbitals from the optimized geometry of the lowest energy triplet state. Using **Re1** as a representative example, the singly-occupied natural orbitals display the unpaired spins to be located on the diimine ligand in orbitals of π -symmetry (Figure C25). It should be noted that the natural orbitals depict a significant degree of intra-ligand charge transfer in this triplet excited state, which is not observed in the lowest energy singlet vertical LC transition

predicted using TD-DFT. Additionally, the Re(I) $d\pi$ natural orbitals are observed to all be doubly occupied, further confirming there is no MLCT character in this lowest energy triplet excited state. The natural orbital analysis for **Re2** depicted in Figure C26 gives the same results. Finally, the spin density surfaces generated from the lowest energy triplet state of **Re1** and **Re2** both depict spin density to be localized solely on the **NBI-phen** ligand (Figure C27), corroborating that the lowest energy triplet excited state in these complexes are ^3LC .

4.4.3. Electronic Absorption and Photoluminescence Spectroscopy

The electronic absorption spectra of **Re1-2** and **Mod1-2** are presented in Figure 4.2, with additional spectroscopic results in Table 4.1. **Mod1** and **Mod2** are the model inorganic chromophores for this study and **NBI** (Figure C29) is used as a model organic chromophore. **NBI-phen** is not used as the organic model due to its insolubility in many organic solvents. During photophysical study of the two bichromophores (discussed below), **Re1** and **Re2**, it became clear that these molecules shared remarkably similar characteristics with the features seen in an Ir(III) chromophore featuring the **NBI** ligand.⁵⁷ While the photophysical data for **NBI** will be used in lieu of **NBI-phen**, it is important to note that due to the extended π system of **NBI-phen** a bathochromic shift in its absorption and photoluminescence features is expected.

Molecule	λ_{abs} , nm (ϵ , $\text{M}^{-1} \text{cm}^{-1}$)	λ_{em} , nm RT ^a (77 K) ^b	Φ_{em} ^c (%)
Re1	292 (31200) 406 (18700)	535, 624, 688 (540, 614, 675)	< 1
Re2	294 (37700) 404 (21200)	506, 633, 689 (532, 615, 672)	< 1
Mod1	275 (24700) 374 (3340)	524	46.8
Mod2	277 (25800) 365 (3180)	548	11.7

^aRoom temperature PL maxima are corrected and were performed in deaerated THF. ^b77 K measurements were made with 2-MeTHF and PL maxima are uncorrected. ^cAbsolute quantum yields.

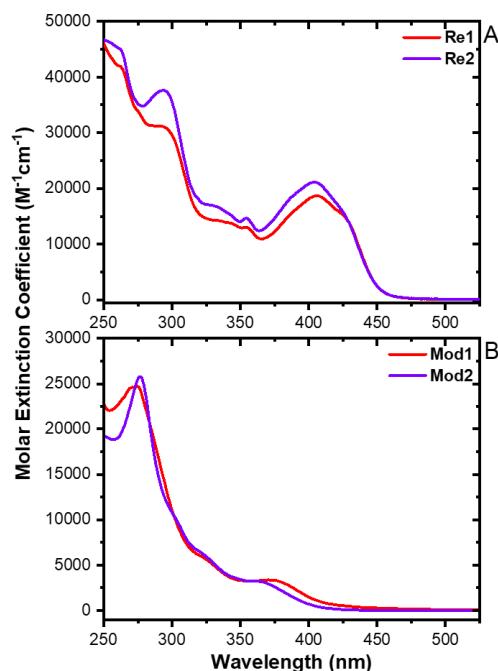


Figure 4.2. Electronic absorption spectra of (A) **Re1** and **Re2** and (B) **Mod1** and **Mod2** measured in THF.

From Figure 4.2A, the visible absorption cross-section was observed to be markedly enhanced for **Re1** and **Re2** as compared to their respective model chromophores, Figure 4.2B. This increase in visible light absorptivity is a direct consequence of the **NBI** being fused to the 1,10-phenanthroline ligand. The higher energy transitions of both **Re1** and **Re2** in the UV, < 300 nm, are of higher energy $\pi \rightarrow \pi^*$ transitions on the diimine ligand. The generally broad and slightly featured low energy band has a peak maximum at 406 nm with a shoulder at 425 nm for **Re1** and 404 nm with a shoulder at 425 nm for **Re2**. TD-DFT calculations of both **Re1** and **Re2** indicate

the lowest energy transition, $S_0 \rightarrow S_1$, is a $\pi \rightarrow \pi^*$ transition localized on the **NBI-phen**. It is not until the $S_0 \rightarrow S_3$ transition that MLCT character is observed at much higher energy. **NBI**, Figure C29, has a largely broad and featureless low energy band. Computations show that the two lowest energy transitions are comprised of a charge transfer band where the electron density is localized along the π system of the entire ligand and then shifts towards the naphthalene end of the ligand ($S_0 \rightarrow S_1$) and a $\pi \rightarrow \pi^*$ transition ($S_0 \rightarrow S_2$).³⁹ This behaviour is mirrored in the **NBI-phen** ligand as seen in the computations (Figure C28).

The static PL spectra of **Re1** and **Re2** share similar features (Figure 4.3A) after being excited with 415 nm. **Re1** has three peak maximums at 535, 624, and 688 nm. The peak maximums of **Re2** are 506, 633, and 689 nm. The slight shoulder at 477 nm in both complexes is from the Raman band of THF which is noticeable due to the low quantum yield values for both bichromophoric complexes (< 1%). For both molecules, the highest energy peak is assigned to the singlet fluorescence of the organic chromophore due to their similar peak positions and because the peak remains even after being exposed to molecular dioxygen (Figure C30). The two lower energy features are therefore designated to be the triplet PL emission of the **NBI-phen** ligand, which were completely quenched by exposure to molecular dioxygen (Figure C30). Further evidence of these peaks triplet character is the triplet sensitized spectrum of **NBI** recorded by Yarnell and co-workers.⁵⁷ In their study, they found the triplet state of **NBI** to emit at 607 and 664 nm in 2-MeTHF. Excitation scans (Figure C31) monitoring emission intensity at all three observed PL peaks for both **Re1** and **Re2** reproduced the lowest energy band of the absorbance spectra that we characterize as exclusively **NBI-phen** electronic transitions. These combined data all suggest that not only do these molecules obey Kasha's rule, the lowest emitting state of these two bichromophores consists of triplet **NBI-phen** with residual singlet fluorescence of the same unit.

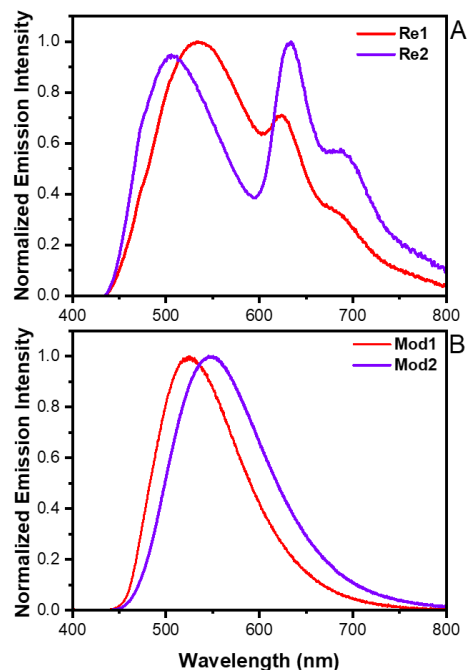


Figure 4.3. Static photoluminescence spectra of (A) **Re1** and **Re2** ($\lambda_{\text{ex}} = 415$ nm) and (B) **Mod1** and **Mod2** ($\lambda_{\text{ex}} = 355$ nm) in deaerated THF.

Mod1 and **Mod2** electronic absorption spectra are presented in Figure 4.2B and their steady-state PL in Figure 4.3B. The absorbance and photoluminescence spectra of both model compounds are analogous to previously synthesized rhenium(I) tricarbonyl diimines of similar structure.^{2, 28, 29, 55, 56, 58} **Mod1** and **Mod2** absorption spectrum is characterized by strong UV absorption < 300 nm correlating to $\pi \rightarrow \pi^*$ transitions of the phenanthroline ligand. The lower energy band of the model complexes with peak maximums at 374 and 365 nm for **Mod1** and **Mod2** respectively are attributed to the MLCT transition, consistent with previously reported data of similarly constructed molecules and agree with the TD-DFT calculations performed (discussed above). The PL of both models (Figure 4.3B) are assigned to the $^3\text{MLCT}$ excited state due to their large stokes shift (524 nm, **Mod1**, and 548 nm, **Mod2**), broad and featureless profile, and excited state lifetime (discussed below). Additionally, previous molecules of a similar structural motif have their PL assigned to being $^3\text{MLCT}$ character.^{2, 28, 29, 55, 56, 58}

4.4.4. Transient Absorption and Time-Resolved PL Spectroscopy

The ultrafast excited state absorption difference spectra of **Re2** are presented in Figure 4.4A, and **Mod2** in Figure 4.5A, while those of **Re1** and **Mod1** are presented in Figures C32A and C38A, respectively. **Re2** ultrafast excited state difference spectra (Figure 4.4A) is used as representative data for both bichromophores as the UFTA of **Re1** is nearly identical. The UFTA of **Re2** shares similar features at early time scales with **NBI** (Figure C37). The prompt signal shows that there are excited state features that align well with **NBI** at 363, 460, and 698 nm. The dip in the excited state between 460 and 698 nm is due to stimulated emission that is not quite intense enough to be a negative feature but still distorts the excited state features at early time delays. Additionally, there is a ground state bleach centered at 406 nm, in good agreement with the low energy absorption band already assigned to ^1LC transitions within the **NBI-phen** unit (Figure 4.2A). Over the course of the experiment, the excited state features evolve into a state where there is no stimulated emission; the excited state features in the visible region peak at 460 nm and span out into the NIR. This behaviour is in stark contrast to **NBI** where no new features are seen after 6 ns (Figure C37).

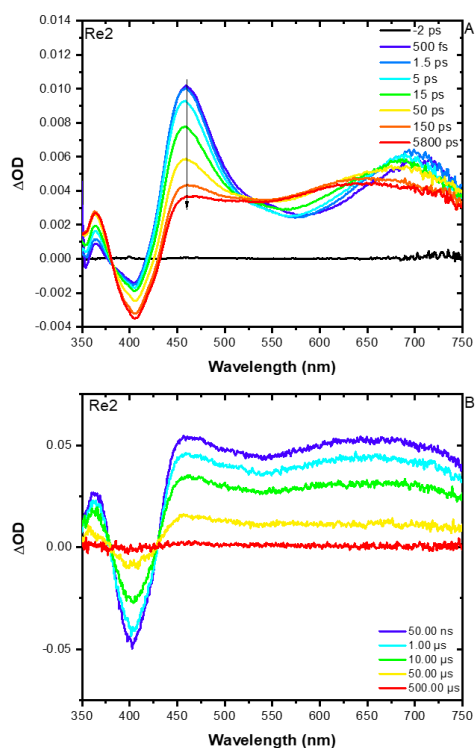


Figure 4.4. UFTA of (A) **Re2** in THF following 400 nm pulsed laser excitation (105 fs fwhm, 0.3 mJ/pulse) and (B) nsTA of **Re2** in deaerated THF following 415 nm excitation (1.8 mJ/pulse).

Single wavelength analysis at 460 nm of **Re2** yields a biexponential decay where the faster time constant is 10.5 ps and the second is 74.2 ps (**Re1** $\tau_1 = 7.6$ and $\tau_2 = 39.1$ ps) (Figures C33-34). Due to the similar features between the prompt signal of the bichromophores and the **NBI**, we have attributed the first time constant to the singlet decay of the organic ligand on the bichromophores. The second time constant we are assigning to the ISC rate from the singlet manifold to the triplet manifold of the **NBI-phen** ligand. These two time constants are consistent with the work done by Blanco-Rodríguez et al where ISC from the singlet state to the triplet state is possible due to the close proximity of a heavy atom, rhenium.^{59, 60} There is no spectroscopic or kinetic evidence that the MLCT-based electronic transitions play an active role in the ultrafast time domain of these molecules as seen in previous bichromophoric studies. However, there is spectroscopic evidence that the **NBI-phen** is entering its triplet excited state. The final trace at 6 ns

in Figure 4.4A mimics the initial trace in the nsTA spectra in Figure 4.4B. Lack of new spectroscopic features between the two experiments implies that the final excited state is formed in the ultrafast and then decays back to ground state. Further evidence that supports assignment of ^3LC character of the **NBI-phen** as the final excited state is discussed immediately below.

Representative ultrafast excited state difference spectra of the models are of **Mod2** are presented in Figure 4.5A (**Mod1** Figure C38A). After 350 nm excitation (105 fs fwhm, 50 $\mu\text{J}/\text{pulse}$), the compound displays only excited state features that develop a more refined shape over the course of the experiment with peak maxima at 400 and 450 nm. These absorption features are vastly different than their respective bichromophoric molecule (Figure 4.4A, C32A). The associated short time constants observed in **Mod1** and **Mod2** are significantly different (< 150 fs) than those measured in **Re1** and **Re2**. Additionally, the longer time decay components observed in the model complexes, 8.84 and 9.35 ps for **Mod2** and **Mod1** respectively, (Figures C39-40) are unique with respect to the kinetics observed in the title chromophores. The faster time constant measured for both models are assigned to intersystem crossing and formation of the radical anion on the diimine ligand. The longer time components are believed to correspond to vibrational cooling on the triplet surface. Both time constants are in good agreement with previously studied Re-CDI molecules featuring MLCT excited states.^{5, 8, 28, 29}

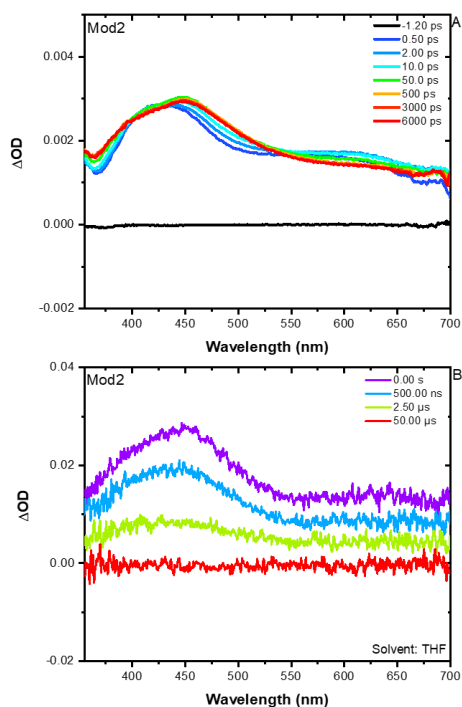


Figure 4.5. Representative (**Mod1** and **Mod2**) transient absorption spectra of (A) UFTA of **Mod2** following 350 nm excitation (105 fs fwhm, 50 $\mu\text{J}/\text{pulse}$) in THF and (B) nsTA of **Mod2** following 355 nm excitation (1.8 mJ/pulse) in deaerated THF.

The nsTA excited state difference spectra of **Re2** is displayed in Figure 4.4B as representative data for both bichromophores of this study. From the trace, we see that the features are consistent with the final trace from the UFTA data indicating that the same excited state is observed at the end of the UFTA experiment and throughout the nsTA experiment. There are two excited state features, one in the UV ca. 375 nm and one that peaks in the visible near 460 nm that broadens out to the NIR. These two features sandwich a ground state bleach at 400 nm. Because both **Re1** and **Re2** have nearly identical excited state features and ground state bleaches, this suggests that the excited state observed in the ns time domain is of $^3\text{NBI-phen}$ as it is the shared ligand between the two compounds. Additionally, these features persist for hundreds of microseconds suggesting that the associated excited state observed is of ^3LC character. Further support that the excited state observed is $^3\text{NBI-phen}$ is the triplet sensitized nsTA spectrum of

³**NBI** presented by Yarnell et. al where there is an excited state feature ca. 450 nm that spans out to the NIR.⁵⁷ This slight blue shift in the excited state difference spectrum is expected as the ligand is structured differently and is a free ligand in solution. Single-wavelength kinetic analysis at 460 nm yielded a kinetic trace that could not be fit to a mono-exponential decay and was found to be power dependent in nature. Observing this phenomenon, we fit the data using eq. 1

$$\Delta A = \frac{\Delta A_0(1-\beta)}{\exp(k_T t) - \beta} \quad \text{eq. 1}$$

where β equates to the initial fraction of triplet decay occurring through TTA.⁶¹

From this fitting equation and multiple experimental pulse energies (Figures C35-36, Tables C3-4), we were able to ascertain that these molecules, **Re1** and **Re2**, undergo triplet-triplet annihilation (TTA) with themselves and have an experimental triplet decay rate constant on the order of 10^3 s^{-1} .

Room temperature and 77 K TR-PL spectra of **Re2** are displayed in Figure 4.6 with relevant peak maximums in Table 4.1. In the RT experiment (Figure 4.6A) with a long gate (10.00 μs), we were able to resolve one feature at 515 with two red shoulders at 623, and 684 nm. Under similar experimental conditions **Re1** displayed a feature at 532 nm but only one shoulder at 622 nm (Figure C41A). In a frozen glass at 77 K, the red features became more pronounced, appearing much more like the features seen in the static PL spectra (Figure 4.3A). As such, we confidently assign the features as ¹LC and ³LC in nature. Additionally, we were able to watch the RT PL decay over the same time range as the transient absorption (Figure 4.4B) experiment discussed above. The incredibly long-lived excited state, excited state spectral features, TR-PL, and calculations all lend significant support in assigning ³**NBI-phen** as the final excited state.

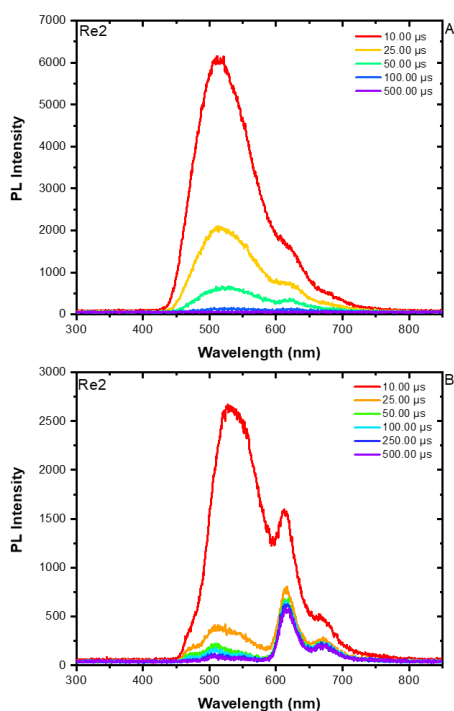


Figure 4.6. Representative (**Re1** and **Re2**) time-resolved photoluminescence data of **Re2** at (A) room temperature in deaerated THF and (B) 77 K in 2-MeTHF following 415 nm excitation (1.8 mJ/pulse).

Mod2 nsTA is displayed in Figure 4.5B and is representative of **Mod1** (Figure C38B). Upon 355 nm excitation, prompt signal shows positive absorption features across the entire visible region, similar to its UFTA, Figure 4.5A. The excited state features of both model complexes resemble the $^3\text{MLCT}$ transition in Re-CDI molecules featuring a phenanthroline ligand.^{27-29, 62} Additionally, the lifetimes of the two models are consistent with $[\text{Re}(\text{phen})(\text{CO})_3(\text{L})]^+$ (L = neutral ligand) molecules featuring a $^3\text{MLCT}$ with lifetimes of 2.2 and 2.3 μs for **Mod1** and **Mod2** respectively (Figure C44-45).^{2, 28, 56} The TR-PL and their PL lifetimes of both models are presented in Figure C42-45. Like their steady-state PL, the TR-PL spectra of the models are broad and featureless with peak maxima at 516 nm and 540 nm for **Mod1** and **Mod2**, respectively. Over the course of the experiment, no new features are noted, and the experimental lifetime of their PL

($\tau = 2.5 \mu\text{s}$ for both **Mod1** and **Mod2**) matches their nsTA lifetime indicating that the final excited state is also the emitting state.

4.5. Conclusions

In this study, we have successfully integrated a perinone, **NBI-phen**, onto two Re(I) carbonyl diimine complexes and have fully characterized the excited state processes from prompt excitation to ground state and compared them to their respective model compounds. Additionally, we have used electronic structure calculations to provide theoretical relevance and support for our experimental findings. This study has revealed that by integrating the **NBI-phen** ligand into the framework of the Re-CDI, we obtain higher visible light absorptivity and extended excited state lifetimes that are capable of self-quenching via TTA in solution. However, the incorporation of the perinone onto the Re(I) centre dramatically decreased the quantum yield. We conclude that upon excitation, the ^1LC band of the **NBI-phen** undergoes ISC to the ^3LC due to the heavy-atom effect presented by Re(I), where it then decays back to the ground state. Lastly, while a thermal equilibrium between the organic ligand and Re-CDI was not formed in these two systems due to the large energy gap between the $^3\text{MLCT}$ and ^3LC states, the long-lived nature of the **NBI-phen** ^3LC state makes these materials an ideal candidate as a low-lying triplet reservoir. As such, if an inorganic chromophore of appropriate MLCT energy is introduced in place of our present Re-CDI complexes, a strong thermal equilibrium is likely to establish.²⁷⁻³⁸ However, these materials are well suited for light harvesting applications and readily sensitize the organic triplet making them good candidates for a variety of applications.^{11, 13, 15-17, 24}

4.6 Acknowledgments

This work was supported by the U.S. Department of Energy, Office of Science, Office of Basic Energy Sciences, under Award No. DE-SC0011979. Some personnel were supported by the National Science Foundation (CHE-1955795, K.A.W.), the Air Force Institute of Technology (AFIT, J.E.Y.), the

Air Force Office of Scientific Research (FA9550-18-1-0331, D.T.Y.). I would like to also thank my co-authors, James E. Yarnell, Sara Sheykhi, Jonathan R. Palmer, Daniel T. Yonemoto, Rosalynd Joyce, Sofia Garakyaraghi, and Felix N. Castellano.

4.7. References

1. Wrighton, M.; Morse, D. L., Nature of the lowest excited state in tricarbonylchloro-1,10-phenanthroline-rhenium(I) and related complexes. *J. Am. Chem. Soc.* **1974**, *96* (4), 998-1003.
2. Wallace, L.; Rillema, D. P., Photophysical properties of rhenium(I) tricarbonyl complexes containing alkyl- and aryl-substituted phenanthrolines as ligands. *Inorg. Chem.* **1993**, *32* (18), 3836-3843.
3. Moya, S. A.; Guerrero, J.; Pastene, R.; Sartori, R.; Schmidt, R.; Sariego, R.; Sanz-Aparicio, J.; Fonseca, I.; Martinez-Ripoll, M., Metallic Carbonyl Complexes Containing Heterocycle Nitrogen Ligands. 2. Tricarbonylbromo(3,3'-R-2,2'-biquinoline)Rhenium(I) Compounds. *Inorg. Chem.* **1994**, *33* (11), 2341-2346.
4. Shillito, G. E.; Hall, T. B. J.; Preston, D.; Traber, P.; Wu, L.; Reynolds, K. E. A.; Horvath, R.; Sun, X. Z.; Lucas, N. T.; Crowley, J. D.; George, M. W.; Kupfer, S.; Gordon, K. C., Dramatic Alteration of 3ILCT Lifetimes Using Ancillary Ligands in $[\text{Re}(\text{L})(\text{CO})_3(\text{phen-TPA})]^{n+}$ Complexes: An Integrated Spectroscopic and Theoretical Study. *J. Am. Chem. Soc.* **2018**, *140* (13), 4534-4542.
5. El Nahhas, A.; Consani, C.; Blanco-Rodríguez, A. M.; Lancaster, K. M.; Braem, O.; Cannizzo, A.; Towrie, M.; Clark, I. P.; Zálíš, S.; Chergui, M.; Vlček, A., Ultrafast Excited-State Dynamics of Rhenium(I) Photosensitizers $[\text{Re}(\text{Cl})(\text{CO})_3(\text{N,N})]$ and $[\text{Re}(\text{imidazole})(\text{CO})_3(\text{N,N})]^+$: Diimine Effects. *Inorg. Chem.* **2011**, *50* (7), 2932-2943.
6. Villegas, J. M.; Stoyanov, S. R.; Huang, W.; Rillema, D. P., Photophysical, Spectroscopic, and Computational Studies of a Series of Re(I) Tricarbonyl Complexes Containing 2,6-Dimethylphenylisocyanide and 5- and 6-Derivatized Phenanthroline Ligands. *Inorg. Chem.* **2005**, *44* (7), 2297-2309.
7. Smithback, J. L.; Helms, J. B.; Schutte, E.; Woessner, S. M.; Sullivan, B. P., Preparative Routes to Luminescent Mixed-Ligand Rhenium(I) Dicarbonyl Complexes. *Inorg. Chem.* **2006**, *45* (5), 2163-2174.
8. Atallah, H.; Taliaferro, C. M.; Wells, K. A.; Castellano, F. N., Photophysics and ultrafast processes in rhenium(i) diimine dicarbonyls. *Dalton Trans.* **2020**, *49* (33), 11565-11576.
9. Vlček, A., Ultrafast Excited-State Processes in Re(I) Carbonyl-Diimine Complexes: From Excitation to Photochemistry. In *Photophysics of Organometallics*, Lees, A. J., Ed. Springer Berlin Heidelberg: Berlin, Heidelberg, 2010; pp 115-158.
10. North, A. J.; Karas, J. A.; Ma, M. T.; Blower, P. J.; Ackermann, U.; White, J. M.; Donnelly, P. S., Rhenium and Technetium-oxo Complexes with Thioamide Derivatives of Pyridylhydrazine Bifunctional Chelators Conjugated to the Tumour Targeting Peptides Octreotate and Cyclic-RGDfK. *Inorg. Chem.* **2017**, *56* (16), 9725-9741.

11. Orchanian, N. M.; Hong, L. E.; Skrainka, J. A.; Esterhuizen, J. A.; Popov, D. A.; Marinescu, S. C., Surface-Immobilized Conjugated Polymers Incorporating Rhenium Bipyridine Motifs for Electrocatalytic and Photocatalytic CO₂ Reduction. *ACS Appl. Energy Mater.* **2019**, *2* (1), 110-123.
12. Shestopalov, M. A.; Mironov, Y. V.; Brylev, K. A.; Kozlova, S. G.; Fedorov, V. E.; Spies, H.; Pietzsch, H.-J.; Stephan, H.; Geipel, G.; Bernhard, G., Cluster Core Controlled Reactions of Substitution of Terminal Bromide Ligands by Triphenylphosphine in Octahedral Rhenium Chalcobromide Complexes. *J. Am. Chem. Soc.* **2007**, *129* (12), 3714-3721.
13. Toganoh, M.; Ikeda, S.; Furuta, H., Synthesis, Reactivity, and Properties of N-Fused Porphyrin Rhenium(I) Tricarbonyl Complexes. *Inorg. Chem.* **2007**, *46* (23), 10003-10015.
14. Nikonova, O. A.; Jansson, K.; Kessler, V. G.; Sundberg, M.; Baranov, A. I.; Shevelkov, A. V.; Drobot, D. V.; Seisenbaeva, G. A., Electrochemical Synthesis, Structural Characterization, and Decomposition of Rhenium Oxoethoxide, Re₄O₄(OEt)₁₂. Ligand Influence on the Structure and Bonding in the High-Valent Tetranuclear Planar Rhenium Alkoxide Clusters. *Inorg. Chem.* **2008**, *47* (4), 1295-1300.
15. Franco, F.; Cometto, C.; Garino, C.; Minero, C.; Sordello, F.; Nervi, C.; Gobetto, R., Photo- and Electrocatalytic Reduction of CO₂ by [Re(CO)₃{ α,α' -Diimine-(4-piperidinyl-1,8-naphthalimide)}Cl] Complexes. *Eur. J. Inorg. Chem.* **2015**, *2015* (2), 296-304.
16. Agarwal, J.; Fujita, E.; Schaefer, H. F.; Muckerman, J. T., Mechanisms for CO Production from CO₂ Using Reduced Rhenium Tricarbonyl Catalysts. *J. Am. Chem. Soc.* **2012**, *134* (11), 5180-5186.
17. Takeda, H.; Koike, K.; Inoue, H.; Ishitani, O., Development of an Efficient Photocatalytic System for CO₂ Reduction Using Rhenium(I) Complexes Based on Mechanistic Studies. *J. Am. Chem. Soc.* **2008**, *130* (6), 2023-2031.
18. Zanoni, K. P. S.; Murakami Iha, N. Y., Reversible trans \rightleftharpoons cis photoisomerizations of [Re(CO)₃(ph₂phen)(stpyCN)]⁺ towards molecular machines. *Dalton Trans.* **2017**, *46* (30), 9951-9958.
19. Patrocínio, A. O. T.; Frin, K. P. M.; Murakami Iha, N. Y., Solid State Molecular Device Based on a Rhenium(I) Polypyridyl Complex Immobilized on TiO₂ Films. *Inorg. Chem.* **2013**, *52* (10), 5889-5896.
20. Knopf, K. M.; Murphy, B. L.; MacMillan, S. N.; Baskin, J. M.; Barr, M. P.; Boros, E.; Wilson, J. J., In Vitro Anticancer Activity and in Vivo Biodistribution of Rhenium(I) Tricarbonyl Aqua Complexes. *J. Am. Chem. Soc.* **2017**, *139* (40), 14302-14314.
21. Klenner, M. A.; Zhang, B.; Ciancaleoni, G.; Howard, J. K.; Maynard-Casely, H. E.; Clegg, J. K.; Massi, M.; Fraser, B. H.; Pascali, G., Rhenium(i) complexation–dissociation

- strategy for synthesising fluorine-18 labelled pyridine bidentate radiotracers. *RSC Advances* **2020**, *10* (15), 8853-8865.
22. Lee, L. C.-C.; Leung, K.-K.; Lo, K. K.-W., Recent development of luminescent rhenium(i) tricarbonyl polypyridine complexes as cellular imaging reagents, anticancer drugs, and antibacterial agents. *Dalton Trans.* **2017**, *46* (47), 16357-16380.
 23. R. Dilworth, J.; J. Parrott, S., The biomedical chemistry of technetium and rhenium. *Chem. Soc. Rev.* **1998**, *27* (1), 43-55.
 24. Manav, N.; Kesavan, P. E.; Ishida, M.; Mori, S.; Yasutake, Y.; Fukatsu, S.; Furuta, H.; Gupta, I., Phosphorescent rhenium-dipyrrinates: efficient photosensitizers for singlet oxygen generation. *Dalton Trans.* **2019**, *48* (7), 2467-2478.
 25. Balzani, V.; Campagna, S.; Barbieri, A.; Ebrary, I., *Photochemistry and Photophysics of Coordination Compounds II*. Springer-Verlag: Berlin, Germany, 2007.
 26. Caspar, J. V.; Kober, E. M.; Sullivan, B. P.; Meyer, T. J., Application of the energy gap law to the decay of charge-transfer excited states. *J. Am. Chem. Soc.* **1982**, *104* (2), 630-632.
 27. Yarnell, J. E.; Deaton, J. C.; McCusker, C. E.; Castellano, F. N., Bidirectional "Ping-Pong" Energy Transfer and 3000-Fold Lifetime Enhancement in a Re(I) Charge Transfer Complex. *Inorg. Chem.* **2011**, *50* (16), 7820-7830.
 28. Wells, K. A.; Yarnell, J. E.; Palmer, J. R.; Lee, T. S.; Papa, C. M.; Castellano, F. N., Energy Migration Processes in Re(I) MLCT Complexes Featuring a Chromophoric Ancillary Ligand. *Inorg. Chem.* **2020**, *59* (12), 8259-8271.
 29. Yarnell, J. E.; Wells, K. A.; Palmer, J. R.; Breaux, J. M.; Castellano, F. N., Excited-State Triplet Equilibria in a Series of Re(I)-Naphthalimide Bichromophores. *J. Phys. Chem. B* **2019**, *123* (35), 7611-7627.
 30. Tyson, D. S.; Bialecki, J.; Castellano, F. N., Ruthenium(II) complex with a notably long excited state lifetime. *Chem. Comm.* **2000**, (23), 2355-2356.
 31. Castellano, F. N., Altering Molecular Photophysics by Merging Organic and Inorganic Chromophores. *Acc. Chem. Res.* **2015**, *48* (3), 828-839.
 32. Castellano, F. N., Transition metal complexes meet the rylenes. *Dalton Trans.* **2012**, *41* (28), 8493.
 33. Tyson, D. S.; Castellano, F. N., Intramolecular Singlet and Triplet Energy Transfer in a Ruthenium(II) Diimine Complex Containing Multiple Pyrenyl Chromophores. *J. Phys. Chem. A* **1999**, *103*, 10955-10960.

34. Tyson, D. S.; Henbest, K. B.; Bialecki, J.; Castellano, F. N., Excited State Processes in Ruthenium(II)/Pyrenyl Complexes Displaying Extended Lifetimes. *J. Phys. Chem. A* **2001**, *105* (35), 8154-8161.
35. McCusker, C. E.; Chakraborty, A.; Castellano, F. N., Excited State Equilibrium Induced Lifetime Extension in a Dinuclear Platinum(II) Complex. *J. Phys. Chem. A* **2014**, *118* (45), 10391-10399.
36. Yarnell, J. E.; McCusker, C. E.; Leeds, A. J.; Breaux, J. M.; Castellano, F. N., Exposing the Excited-State Equilibrium in an Ir(III) Bichromophore: A Combined Time Resolved Spectroscopy and Computational Study. *Eur. J. Inorg. Chem. A* **2016**, *2016* (12), 1808-1818.
37. Tyson, D. S.; Luman, C. R.; Zhou, X.; Castellano, F. N., New Ru(II) Chromophores with Extended Excited-State Lifetimes. *Inorg. Chem.* **2001**, *40* (16), 4063-4071.
38. Yonemoto, D. T.; Papa, C. M.; Mongin, C.; Castellano, F. N., Thermally Activated Delayed Photoluminescence: Deterministic Control of Excited-State Decay. *J. Am. Chem. Soc.* **2020**, *142* (25), 10883-10893.
39. Palmer, J. R.; Wells, K. A.; Yarnell, J. E.; Favale, J. M.; Castellano, F. N., Visible-Light-Driven Triplet Sensitization of Polycyclic Aromatic Hydrocarbons Using Thionated Perinones. *J. Phys. Chem. Lett.* **2020**, *11* (13), 5092-5099.
40. Mamada, M.; Pérez-Bolívar, C.; Kumaki, D.; Esipenko, N. A.; Tokito, S.; Anzenbacher Jr, P., Benzimidazole Derivatives: Synthesis, Physical Properties, and n-Type Semiconducting Properties. *Chem. Eur. J.* **2014**, *20* (37), 11835-11846.
41. Mizuguchi, J., Crystal Structure and Electronic Characterization of trans- and cis-Perinone Pigments. *J. Phys. Chem. B* **2004**, *108* (26), 8926-8930.
42. Debije, M. G.; Verbunt, P. P. C.; Nadkarni, P. J.; Velate, S.; Bhaumik, K.; Nedumbamana, S.; Rowan, B. C.; Richards, B. S.; Hoeks, T. L., Promising fluorescent dye for solar energy conversion based on a perylene perinone. *Appl. Opt.* **2011**, *50* (2), 163-169.
43. Kobrakov, K. I.; Zubkova, N. S.; Stankevich, G. S.; Shestakova, Y. S.; Stroganov, V. S.; Adrov, O. I., New aroyleneimidazoles as dyes for thermoplastic polymeric materials. *Fibre Chem.* **2006**, *38* (3), 183-187.
44. Loutfy, R. O.; Hor, A. M.; Kazmaier, P. M.; Burt, R. A.; Hamer, G. K., Organic photoconductive (OPC) devices incorporating bisarylimidazole perinone pigments. *Dyes Pig.* **1991**, *15* (2), 139-156.
45. Yang, Y.; Brückmann, J.; Frey, W.; Rau, S.; Karnahl, M.; Tschierlei, S., Electron storage capability and singlet oxygen productivity of a Ru(II) photosensitizer containing a fused naphthaloylenebenzene moiety at the 1,10-phenanthroline ligand. *Chem. Eur. J.* **2020**, *26*, 17027-17034.

46. Garakyaraghi, S.; Danilov, E. O.; McCusker, C. E.; Castellano, F. N., Transient Absorption Dynamics of Sterically Congested Cu(I) MLCT Excited States. *J. Phys. Chem. A* **2015**, *119* (13), 3181-3193.
47. Frisch, M. J.; Trucks, G. W.; Schlegel, H. B.; Scuseria, G. E.; Robb, M. A.; Cheeseman, J. R.; Scalmani, G.; Barone, V.; Petersson, G. A.; Nakatsuji, H.; Li, X.; Caricato, M.; Marenich, A. V.; Bloino, J.; Janesko, B. G.; Gomperts, R.; Mennucci, B.; Hratchian, H. P.; Ortiz, J. V.; Izmaylov, A. F.; Sonnenberg, J. L.; Williams; Ding, F.; Lipparini, F.; Egidi, F.; Goings, J.; Peng, B.; Petrone, A.; Henderson, T.; Ranasinghe, D.; Zakrzewski, V. G.; Gao, J.; Rega, N.; Zheng, G.; Liang, W.; Hada, M.; Ehara, M.; Toyota, K.; Fukuda, R.; Hasegawa, J.; Ishida, M.; Nakajima, T.; Honda, Y.; Kitao, O.; Nakai, H.; Vreven, T.; Throssell, K.; Montgomery Jr., J. A.; Peralta, J. E.; Ogliaro, F.; Bearpark, M. J.; Heyd, J. J.; Brothers, E. N.; Kudin, K. N.; Staroverov, V. N.; Keith, T. A.; Kobayashi, R.; Normand, J.; Raghavachari, K.; Rendell, A. P.; Burant, J. C.; Iyengar, S. S.; Tomasi, J.; Cossi, M.; Millam, J. M.; Klene, M.; Adamo, C.; Cammi, R.; Ochterski, J. W.; Martin, R. L.; Morokuma, K.; Farkas, O.; Foresman, J. B.; Fox, D. J. *Gaussian 16 Rev. A.03*, Wallingford, CT, 2016.
48. Adamo, C.; Barone, V., Toward reliable density functional methods without adjustable parameters: The PBE0 model. *J. Chem. Phys.* **1999**, *110* (13), 6158-6170.
49. Weigend, F.; Ahlrichs, R., Balanced basis sets of split valence, triple zeta valence and quadruple zeta valence quality for H to Rn: Design and assessment of accuracy. *Phys. Chem. Chem. Phys.* **2005**, *7* (18), 3297-3305.
50. Andrae, D.; Häußermann, U.; Dolg, M.; Stoll, H.; Preuß, H., Energy-adjusted ab initio pseudopotentials for the second and third row transition elements. *Theor. Chim. Acta* **1990**, *77* (2), 123-141.
51. Cossi, M.; Scalmani, G.; Rega, N.; Barone, V., New developments in the polarizable continuum model for quantum mechanical and classical calculations on molecules in solution. *J. Chem. Phys.* **2002**, *117* (1), 43.
52. Grimme, S.; Antony, J.; Ehrlich, S.; Krieg, H., A consistent and accurate ab initio parametrization of density functional dispersion correction (DFT-D) for the 94 elements H-Pu. *J. Chem. Phys.* **2010**, *132* (15), 154104.
53. Martin, R. L., Natural transition orbitals. *J. Chem. Phys.* **2003**, *118* (11), 4775-4777.
54. Dennington, R.; Keith, T. A.; Millam, J. M. *GaussView, Version 6*, SemicheM Inc.: Shawnee Mission, KS, 2016.
55. Caspar, J. V.; Meyer, T. J., Application of the energy gap law to nonradiative, excited-state decay. *J. Phys. Chem.* **1983**, *87* (6), 952-957.

56. Gonçalves, M. R.; Frin, K. P. M., Synthesis, characterization, photophysical and electrochemical properties of rhenium(I) tricarbonyl diimine complexes with triphenylphosphine ligand. *Polyhedron* **2017**.
57. Yarnell, J. E.; De La Torre, P.; Castellano, F. N., Efficient Phosphorescence from Naphthalenebenzimidazole-Coordinated Iridium(III) Chromophores. *Eur. J. Inorg. Chem.* **2017**, *2017* (44), 5238-5245.
58. Chakraborty, I.; Jimenez, J.; Sameera, W. M. C.; Kato, M.; Mascharak, P. K., Luminescent Re(I) Carbonyl Complexes as Trackable PhotoCORMs for CO delivery to Cellular Targets. *Inorg. Chem.* **2017**, *56* (5), 2863-2873.
59. *IUPAC Compendium of Chemical Terminology "Gold Book"*. 2nd ed.; Blackwell Scientific Publications: Oxford.
60. Blanco-Rodríguez, A. M.; Kvapilová, H.; Sýkora, J.; Towrie, M.; Nervi, C.; Volpi, G.; Zálíš, S.; Vlček, A., Photophysics of Singlet and Triplet Intraligand Excited States in [ReCl(CO)₃(1-(2-pyridyl)-imidazo[1,5- α]pyridine)] Complexes. *J. Am. Chem. Soc.* **2014**, *136* (16), 5963-5973.
61. Deng, F.; Blumhoff, J.; Castellano, F. N., Annihilation Limit of a Visible-to-UV Photon Upconversion Composition Ascertained from Transient Absorption Kinetics. *J. Phys. Chem. A* **2013**, *117* (21), 4412-4419.
62. Kalyanasundaram, K., Luminescence and redox reactions of the metal-to-ligand charge-transfer excited state of tricarbonylchloro-(polypyridyl)rhenium(I) complexes. *J. Chem. Soc., Faraday Trans. 2* **1986**, *82* (12), 2401.

APPENDICES

Appendix A

A.1. Synthetic Details and Structural Characterization

Synthesis of 2-(p-tolyl)-1H-benzo[de]isoquinoline-1,3(2H)-dione (**NI**). p-Toluidine (10.16 mmol, 1.09 g), 1,8-naphthalic anhydride (9.24 mmol, 1.82 g), and 50 mL of glacial acetic acid were added to a 150 mL pressure vessel and heated to 140 °C for 6 hours. Once cool, 25 mL of distilled water was added to the solution and the white precipitate was filtered on a glass frit. The solid was washed with 200 mL of water and dried overnight under vacuum. The crude solid was filtered using the isolera automated flash column with a silica column and eluted with dichloromethane/hexanes in a 3:1 ratio. The solvent was removed and the white solid was obtained in 60% yield. ¹H NMR (400 MHz, CD₂Cl₂), δ 8.60 (dd, J = 7.2, 1.1 Hz, 2H), 8.31 (dd, J = 8.1, 1.2 Hz, 2H), 7.81 (dd, J = 8.3, 7.3 Hz, 2H), 7.37 (d, J = 8.0 Hz, 2H), 7.18 (d, J = 8.2 Hz, 2H), 2.46 (s, 3H). MS [HR-ESI (CH₂Cl₂) m/z] 288.1027 [M+H]⁺, calcd (C₁₉H₁₄NO₂) 288.1025. Anal. Calcd (found) for C₁₉H₁₃NO₂: C, 79.43 (79.14); H, 4.56 (4.81); N, 4.88 (4.87). ATR-FTIR: 490, 516, 538, 781, 812, 1185, 1234, 1352, 1373, 1514, 1587, 1656, 1673, 1699 cm⁻¹.

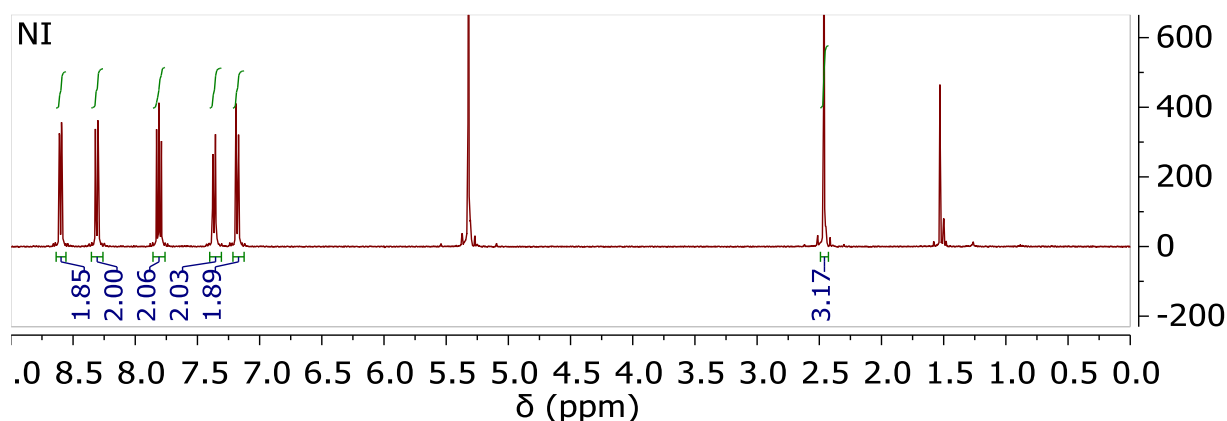


Figure A1. ¹H NMR spectrum of **NI** in CD₂Cl₂ (400 MHz).

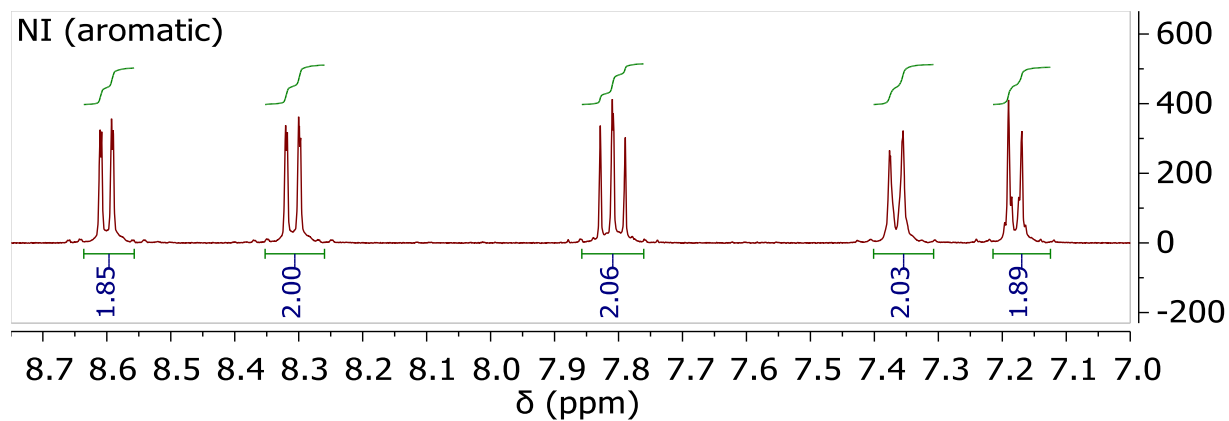


Figure A2. ^1H NMR spectrum of **NI** in CD_2Cl_2 (400 MHz) with zoomed in aromatic region.

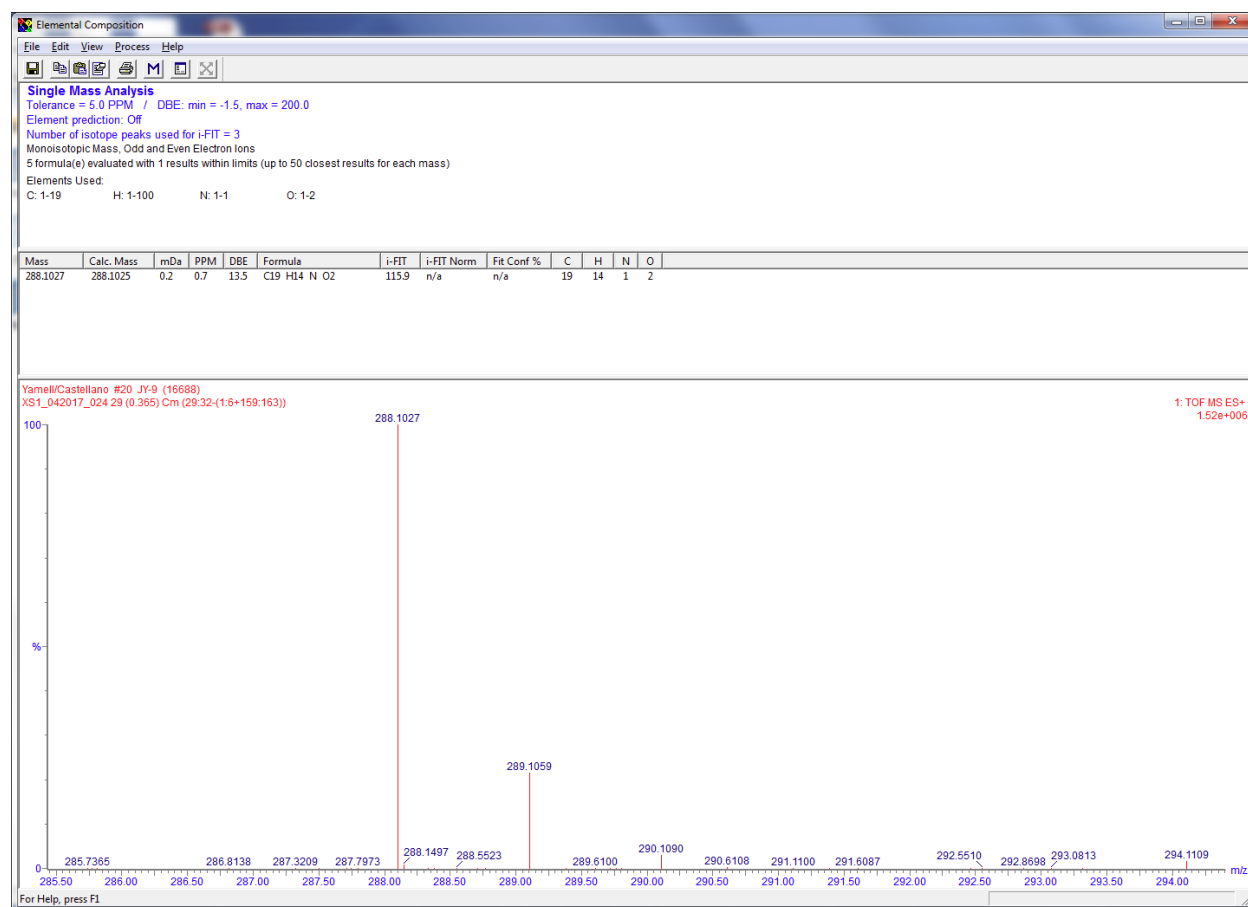


Figure A3. HRMS of **NI**.

Synthesis of 2-(1,10-phenanthroline-5-yl)-1H-benzo[de]isoquinoline-1,3(2H)-dione (**NI-phen**). 5-Amino-1,10-phenanthroline (4.4 mmol, 859 mg), 1,8-naphthalic anhydride (4 mmol, 793 mg), and

20 mL of glacial acetic acid were added to a 75 mL pressure vessel and heated to 145 °C for 24 hours. Once cool, 15 mL of distilled water was added to the solution and the tan precipitate was filtered on a glass frit. The solid was washed with 250 mL of water and dried overnight under vacuum. The off-white solid was obtained in 52% yield (785 mg). ¹H NMR (400 MHz, CDCl₃), δ 9.31 – 9.22 (m, 2H), 8.71 (dd, J = 7.3, 1.1 Hz, 2H), 8.38 (dd, J = 8.4, 1.1 Hz, 2H), 8.31 (dd, J = 8.2, 1.8 Hz, 1H), 8.06 (dd, J = 8.3, 1.7 Hz, 1H), 7.91 – 7.84 (m, 3H), 7.71 (dd, J = 8.0, 4.4 Hz, 1H), 7.59 (dd, J = 8.3, 4.3 Hz, 1H).

Synthesis of Re(NI-phen)(CO)₃Cl. Pentacarbonylchlororhenium(I) (1 mmol, 363 mg) was added to one equivalent of NI-phen (1 mmol, 374 mg) and 20 mL of toluene in a 50 mL round bottom flask. The solution was degassed, put under N₂, and refluxed while mixing for 1 hour. After cooling, the yellow precipitate was filtered out on a glass frit and washed with 200 mL of toluene. The yellow solid was dried under vacuum overnight and was obtained in 98% yield (671 mg). ¹H NMR (400 MHz, CD₂Cl₂), δ 9.47 – 9.39 (m, 2H), 8.70 (ddd, J = 13.4, 7.3, 1.2 Hz, 2H), 8.65 (dd, J = 8.3, 1.4 Hz, 1H), 8.44 (dt, J = 8.3, 1.3 Hz, 2H), 8.37 (dd, J = 8.5, 1.4 Hz, 1H), 8.18 (s, 1H), 7.95 (dd, J = 8.2, 5.1 Hz, 1H), 7.90 (ddd, J = 8.5, 7.3, 1.6 Hz, 2H), 7.83 (dd, J = 8.5, 5.1 Hz, 1H).

Synthesis of [Re(NI-phen)(CO)₃(dmap)](PF₆) (**Re1**). Re(NI-phen)(CO)₃Cl (0.25 mmol, 170 mg) and silver triflate (0.26 mmol, 67 mg) were added to 100 mL round bottom flask along with 50 mL of absolute ethanol. The solution was covered (dark), deaerated, put under N₂, and refluxed for 6 hours. Once cool, the solution was filtered through celite on a glass frit to remove AgCl from solution. The yellow filtrate was added to an excess of dimethylaminopyridine (2.5 mmol, 305 mg) and the solution was then refluxed for an additional 3 hours. The solvent volume was reduced

to approximately 10 mL, followed by a dropwise addition of an ammonium hexafluorophosphate solution in water (1.0 g in 10 mL) to precipitate the product. The solid was collected on a glass frit and washed with 200 mL of distilled water. The solid was recrystallized by dissolving in hot methanol and slowly precipitating the solid with a slow addition of ammonium hexafluorophosphate solution in water. The yellow solid was dried under vacuum overnight and was obtained in 99% yield (226 mg). ^1H NMR (400 MHz, CD_2Cl_2), δ 9.58 (ddd, $J = 12.8, 5.2, 1.4$ Hz, 2H), 8.82 (dd, $J = 8.4, 1.4$ Hz, 1H), 8.66 (ddd, $J = 16.2, 7.3, 1.2$ Hz, 2H), 8.51 (dd, $J = 8.5, 1.4$ Hz, 1H), 8.48 – 8.43 (m, 2H), 8.25 (s, 1H), 8.16 (dd, $J = 8.3, 5.2$ Hz, 1H), 8.04 (dd, $J = 8.5, 5.1$ Hz, 1H), 7.90 (ddd, $J = 8.3, 7.3, 4.6$ Hz, 2H), 7.65 (d, $J = 7.4$ Hz, 2H), 6.27 (d, $J = 7.4$ Hz, 2H), 2.91 (s, 6H). MS [HR-ESI (CH_2Cl_2) m/z] 766.1224 [M-PF_6] $^+$, calcd ($\text{C}_{34}\text{H}_{23}\text{N}_5\text{O}_5^{185}\text{Re}$) 766.1229. Anal. Calcd (found) for $\text{C}_{34}\text{H}_{23}\text{F}_6\text{N}_5\text{O}_5\text{PRe}\cdot 0.5\text{H}_2\text{O}$: C, 44.30 (44.15); H, 2.62 (2.40); N, 7.60 (7.46). ATR-FTIR: 557, 730, 779, 838, 1234, 1350, 1587, 1626, 1673, 1709, 1903, 2058 cm^{-1} .

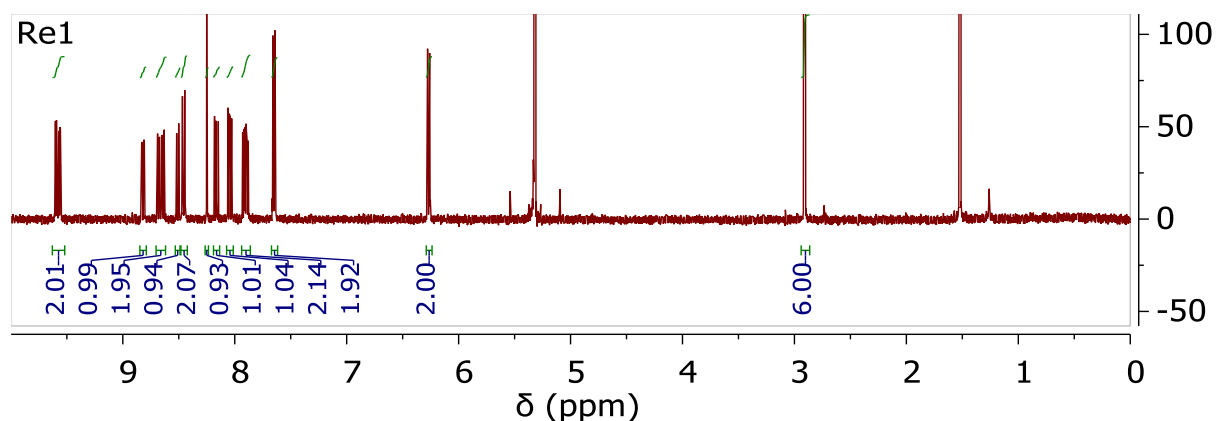


Figure A4. ^1H NMR spectrum of $[\text{Re}(\text{NI-phen})(\text{CO})_3(\text{dmap})](\text{PF}_6)$ (**Re1**) in CD_2Cl_2 (400 MHz).

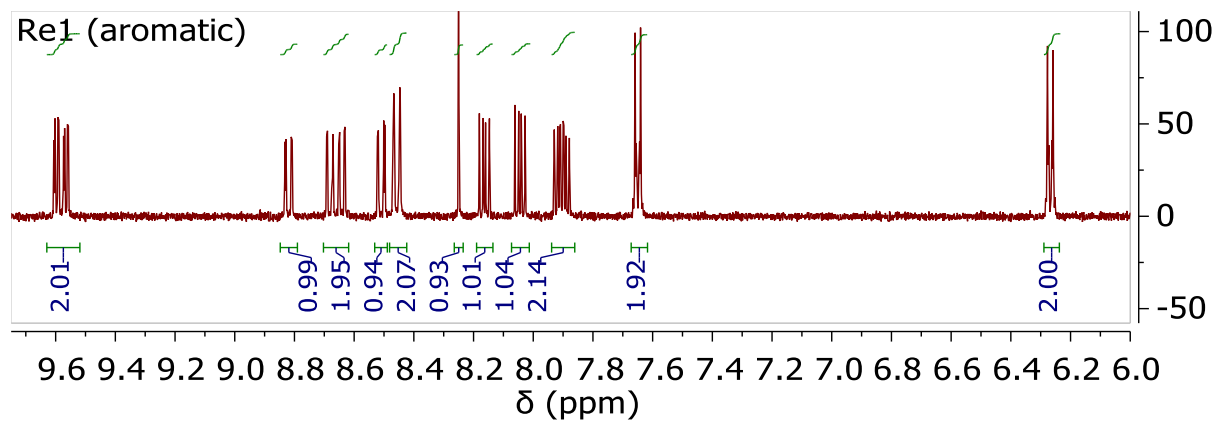


Figure A5. ¹H NMR spectrum of [Re(NI-phen)(CO)₃(dmap)](PF₆) (**Re1**) in CD₂Cl₂ (400 MHz) with zoomed in aromatic region.

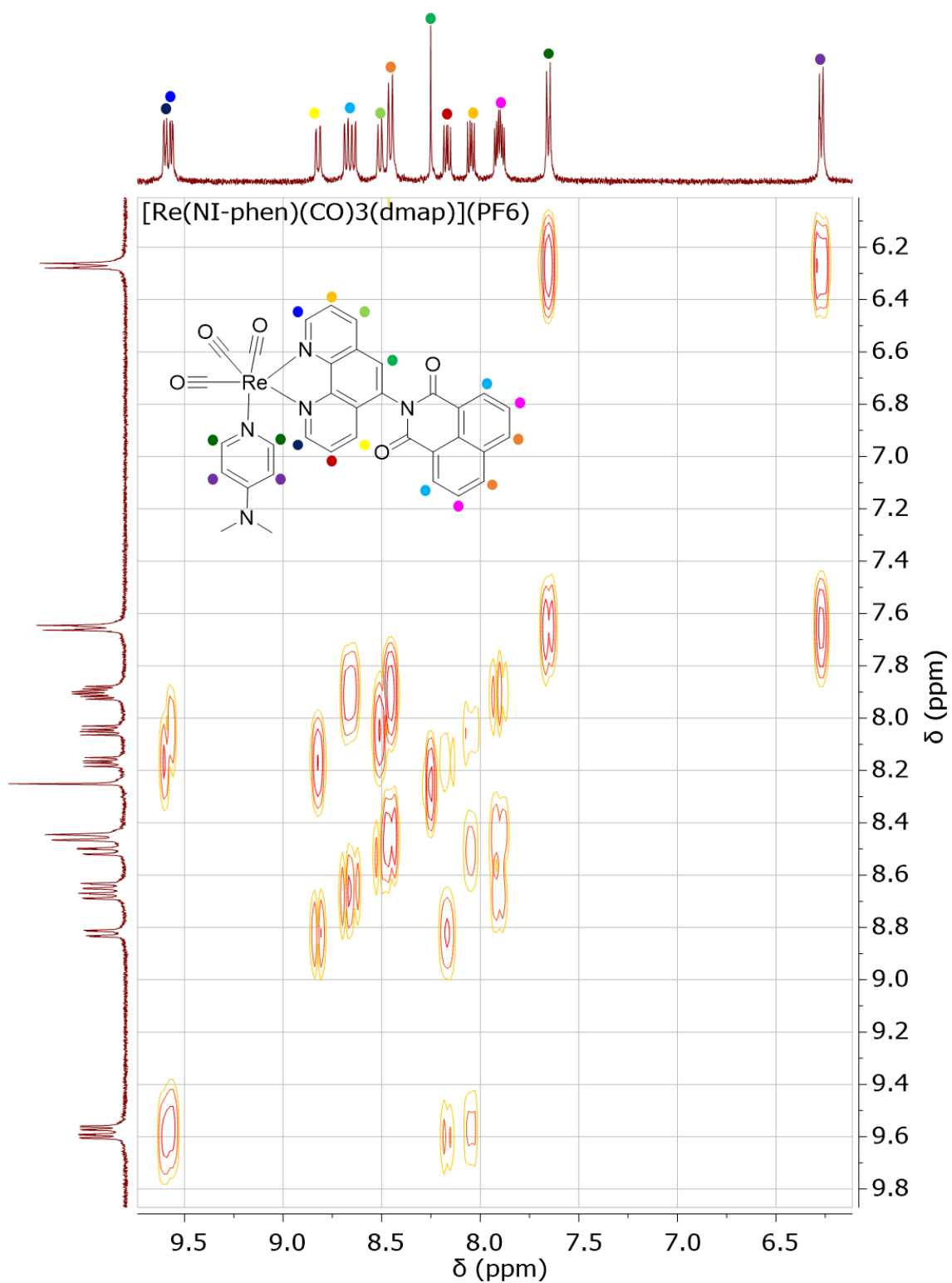


Figure A6. ^1H - ^1H COSY NMR spectrum of $[\text{Re}(\text{NI-phen})(\text{CO})_3(\text{dmap})](\text{PF}_6)$ (**Re1**) in CD_2Cl_2 (400 MHz).

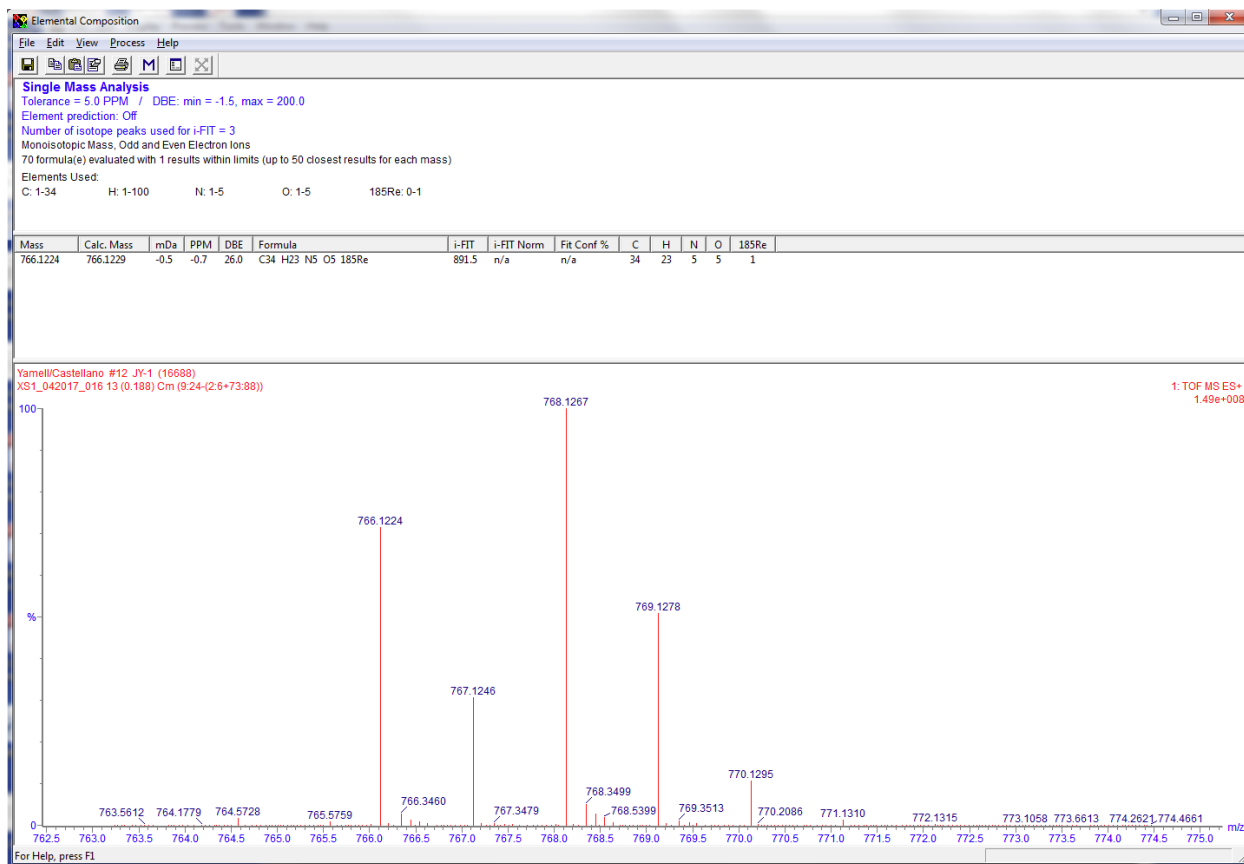


Figure A7. HRMS of $[\text{Re}(\text{NI-phen})(\text{CO})_3(\text{dmap})](\text{PF}_6)$ (**Re1**).

Synthesis of 6-bromo-2-(p-tolyl)-1H-benzo[de]isoquinoline-1,3(2H)-dione (**BrNI**). p-Toluidine (10.16 mmol, 1.09 g), 4-bromo-1,8-naphthalic anhydride (9.24 mmol, 2.56 g), and 50 mL of glacial acetic acid were added to a 150 mL pressure vessel and heated to 140 °C for 6 hours. Once cool, 25 mL of distilled water was added to the solution and the white precipitate was filtered on a glass frit. The solid was washed with 200 mL of water and dried overnight under vacuum. The crude solid was filtered using the isolera automated flash column with a silica column and eluted with dichloromethane/hexanes in a 3:1 ratio. The solvent was removed, and the off-white solid was obtained in 60% yield. ^1H NMR (400 MHz, CD_2Cl_2), δ 8.69 – 8.62 (m, 2H), 8.42 (d, $J = 7.9$ Hz, 1H), 8.10 (d, $J = 7.8$ Hz, 1H), 7.90 (dd, $J = 8.5, 7.3$ Hz, 1H), 7.37 (d, $J = 7.9$ Hz, 2H), 7.18 (d, $J = 8.2$ Hz, 2H), 2.46 (s, 3H). MS [HR-ESI (CH_2Cl_2) m/z] 366.0134 $[\text{M}+\text{H}]^+$, calcd ($\text{C}_{19}\text{H}_{13}\text{NO}_2^{\text{79}}\text{Br}$)

366.0130. Anal. Calcd (found) for C₁₉H₁₂BrNO₂: C, 62.32 (62.04); H, 3.30 (3.27); N, 3.82 (3.81).

ATR-FTIR: 422, 500, 518, 730, 781, 814, 1193, 1238, 1344, 1365, 1589, 1656, 1707 cm⁻¹.

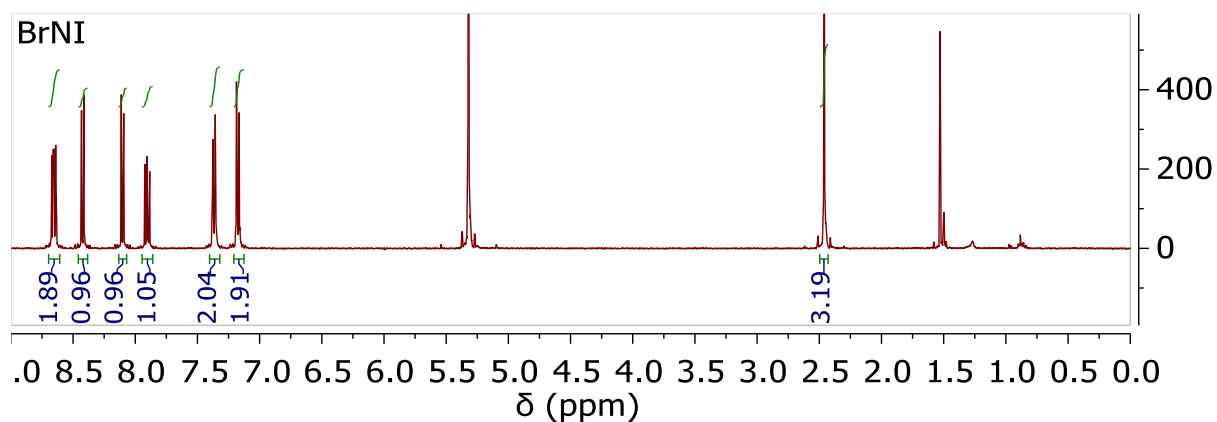


Figure A8. ¹H NMR spectrum of **BrNI** in CD₂Cl₂ (400 MHz).

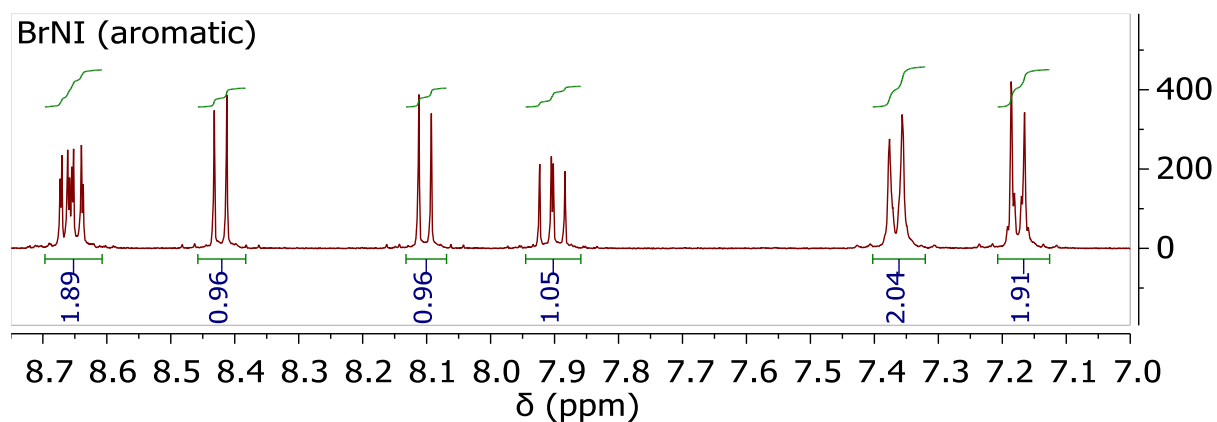


Figure A9. ¹H NMR spectrum of **BrNI** in CD₂Cl₂ (400 MHz) with zoomed in aromatic region.



Figure A10. HRMS of BrNI.

Synthesis of 6-bromo-2-(1,10-phenanthroline-5-yl)-1H-benzo[de]isoquinoline-1,3(2H)-dione (*BrNI-phen*). 5-Amino-1,10-phenanthroline (2.03 mmol, 396 mg), 4-bromo-1,8-naphthalic anhydride (1.85 mmol, 512 mg), and 10 mL of glacial acetic acid were added to a 75 mL pressure vessel and heated to 145 °C for 5 hours. Once cool, 5 mL of distilled water was added to the solution and the tan precipitate was filtered on a glass frit. The solid was washed with 250 mL of water and dried overnight under vacuum. The light brown solid was obtained in 59% yield (498 mg). ¹H NMR (400 MHz, CD₂Cl₂), δ 7.32 (dd, J = 17.8, 4.6 Hz, 2H), 6.81 (t, J = 7.6 Hz, 2H), 6.57 (d, J = 7.8 Hz, 1H), 6.35 (d, J = 8.1 Hz, 1H), 6.22 (d, J = 7.8 Hz, 1H), 6.08 (d, J = 8.3 Hz, 1H), 6.02 (t, J = 8.0 Hz, 1H), 5.95 (s, 1H), 5.80 – 5.59 (m, 2H).

Synthesis of $\text{Re}(\text{BrNI-phen})(\text{CO})_3\text{Cl}$. Pentacarbonylchlororhenium(I) (0.5 mmol, 181 mg) was added to one equivalent of BrNI-phen (0.5 mmol, 227 mg) and 20 mL of toluene in a 50 mL round bottom flask. The solution was degassed, put under N_2 , and refluxed while mixing for 1 hour. After cooling, the yellow precipitate was filtered out on a glass frit and washed with 200 mL of toluene. The yellow solid was dried under vacuum overnight and was obtained in 93% yield (353 mg). ^1H NMR (400 MHz, CDCl_3), δ 9.46 (ddd, $J = 15.3, 5.1, 1.4$ Hz, 2H), 8.82 – 8.74 (m, 2H), 8.60 – 8.49 (m, 2H), 8.29 (dd, $J = 8.5, 1.4$ Hz, 1H), 8.19 (dd, $J = 7.8, 3.2$ Hz, 1H), 8.12 (s, 1H), 7.99 (ddd, $J = 8.6, 7.3, 2.7$ Hz, 1H), 7.92 (dd, $J = 8.2, 5.2$ Hz, 1H), 7.81 (dd, $J = 8.5, 5.0$ Hz, 1H).

Synthesis of $[\text{Re}(\text{BrNI-phen})(\text{CO})_3(\text{dmap})](\text{PF}_6)$ (**Re2**). $\text{Re}(\text{BrNI-phen})(\text{CO})_3\text{Cl}$ (0.25 mmol, 190 mg) and silver triflate (0.26 mmol, 67 mg) were added to 100 mL round bottom flask along with 50 mL of absolute ethanol. The solution was covered (dark), deaerated, put under N_2 , and refluxed for 6 hours. Once cool, the solution was filtered through celite on a glass frit to remove AgCl from solution. The yellow filtrate was added to an excess of dimethylaminopyridine (0.375 mmol, 46 mg) and the solution was then refluxed for an additional 6 hours. The solvent volume was reduced to approximately 10 mL, followed by a dropwise addition of an ammonium hexafluorophosphate solution in water (1.0 g in 10 mL) to precipitate the product. The solid was collected on a glass frit and washed with 250 mL of distilled water. The solid was recrystallized by dissolving in hot methanol and slowly precipitating the solid with a slow addition of ammonium hexafluorophosphate solution in water. The yellow solid was dried under vacuum overnight and was obtained in 90% yield (223 mg). ^1H NMR (400 MHz, CD_2Cl_2), δ 9.58 (ddd, $J = 12.1, 5.1, 1.3$ Hz, 2H), 8.81 (ddd, $J = 9.3, 8.6, 1.2$ Hz, 2H), 8.72 (ddd, $J = 15.2, 7.3, 1.2$ Hz, 1H), 8.52 – 8.43 (m, 2H), 8.26 (s, 1H), 8.23 – 8.13 (m, 2H), 8.08 – 7.96 (m, 2H), 7.65 (d, $J = 7.4$ Hz, 2H), 6.27 (d, $J =$

7.4 Hz, 2H), 2.91 (d, $J = 0.5$ Hz, 6H). MS [HR-ESI (CH_2Cl_2) m/z] 844.0316 $[\text{M-PF}_6]^+$, calcd ($\text{C}_{34}\text{H}_{22}\text{N}_5\text{O}_5^{185}\text{Re}^{79}\text{Br}$) 844.0334. Anal. Calcd (found) for $\text{C}_{34}\text{H}_{22}\text{BrF}_6\text{N}_5\text{O}_5\text{PRe}\cdot 0.5\text{H}_2\text{O}$: C, 40.81 (40.58); H, 2.32 (2.17); N, 7.00 (6.72). ATR-FTIR: 418, 477, 514, 543, 557, 726, 781, 838, 1234, 1364, 1363, 1589, 1626, 1673, 1713, 1905, 2028 cm^{-1} .

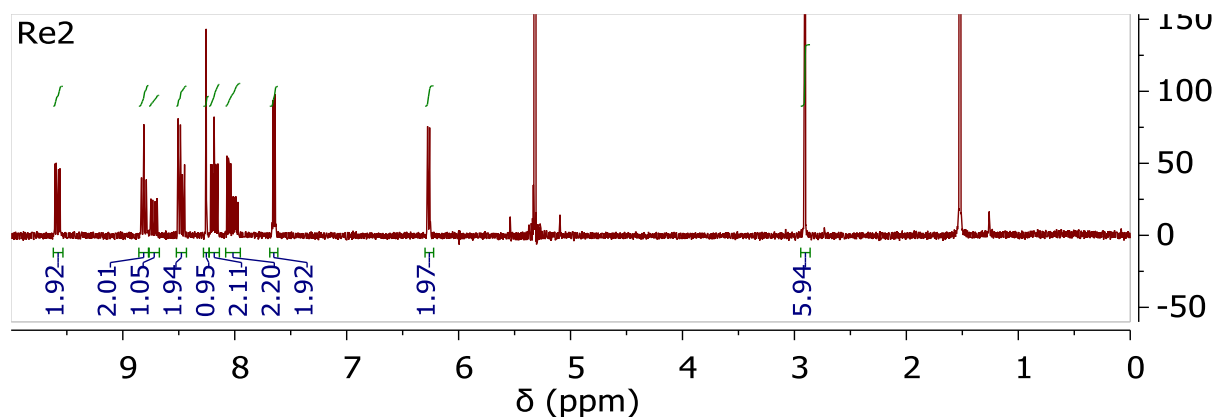


Figure A11. ^1H NMR spectrum of $[\text{Re}(\text{BrNI-phen})(\text{CO})_3(\text{dmap})](\text{PF}_6)$ (**Re2**) in CD_2Cl_2 (400 MHz).

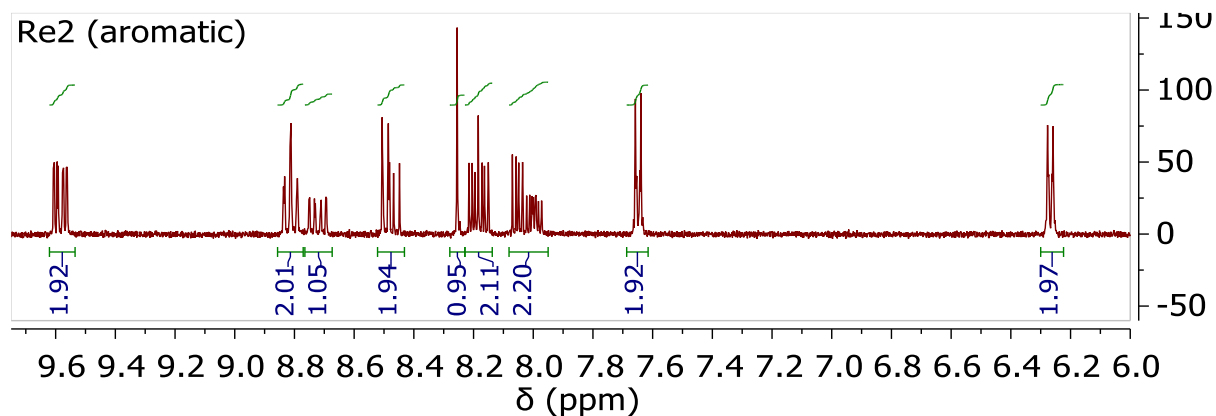


Figure A12. ^1H NMR spectrum of $[\text{Re}(\text{BrNI-phen})(\text{CO})_3(\text{dmap})](\text{PF}_6)$ (**Re2**) in CD_2Cl_2 (400 MHz) with zoomed in aromatic region.

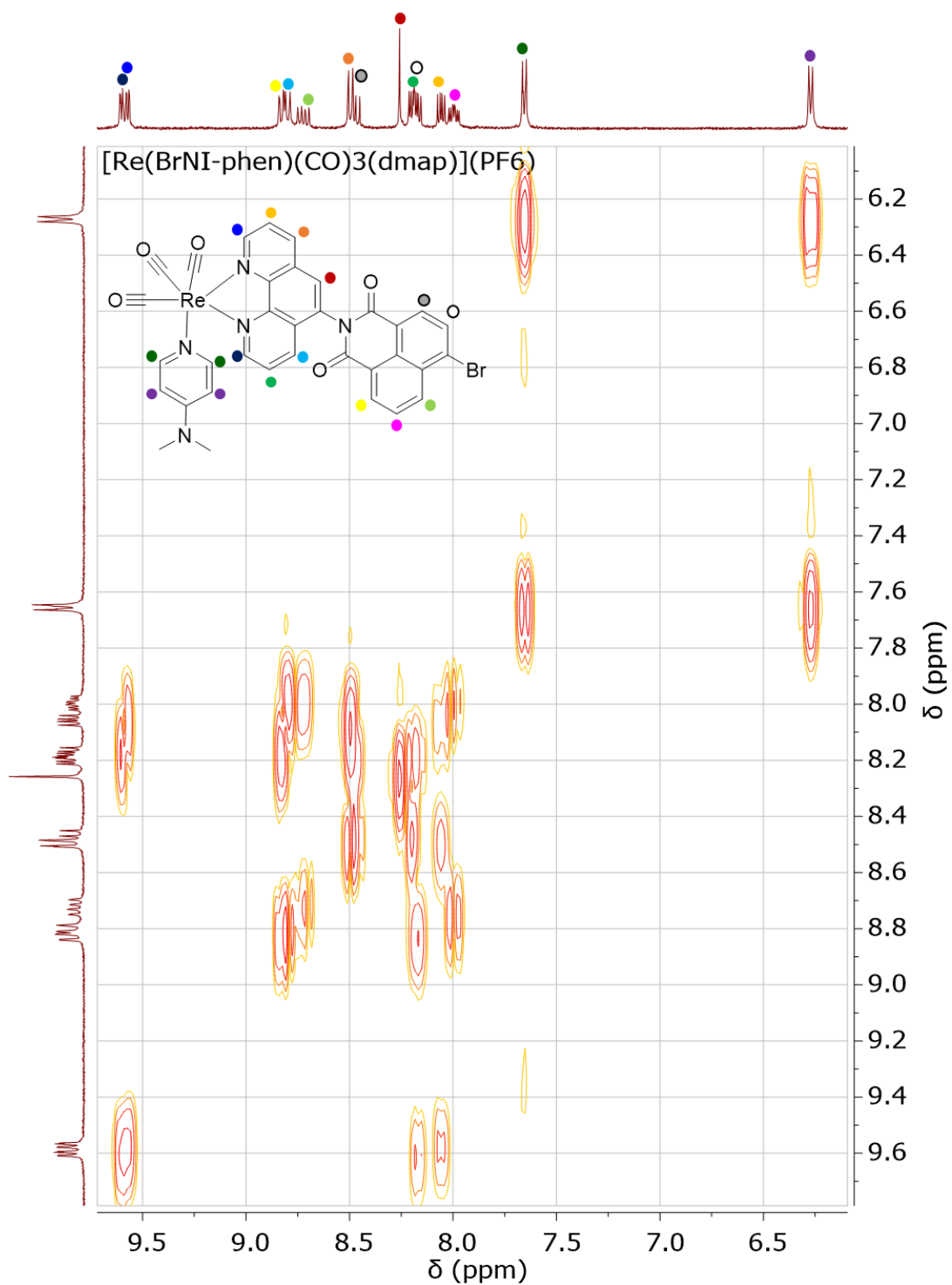


Figure A13. ^1H - ^1H COSY NMR spectrum of $[\text{Re}(\text{BrNI-phen})(\text{CO})_3(\text{dmap})](\text{PF}_6)$ (**Re2**) in CD_2Cl_2 (400 MHz).

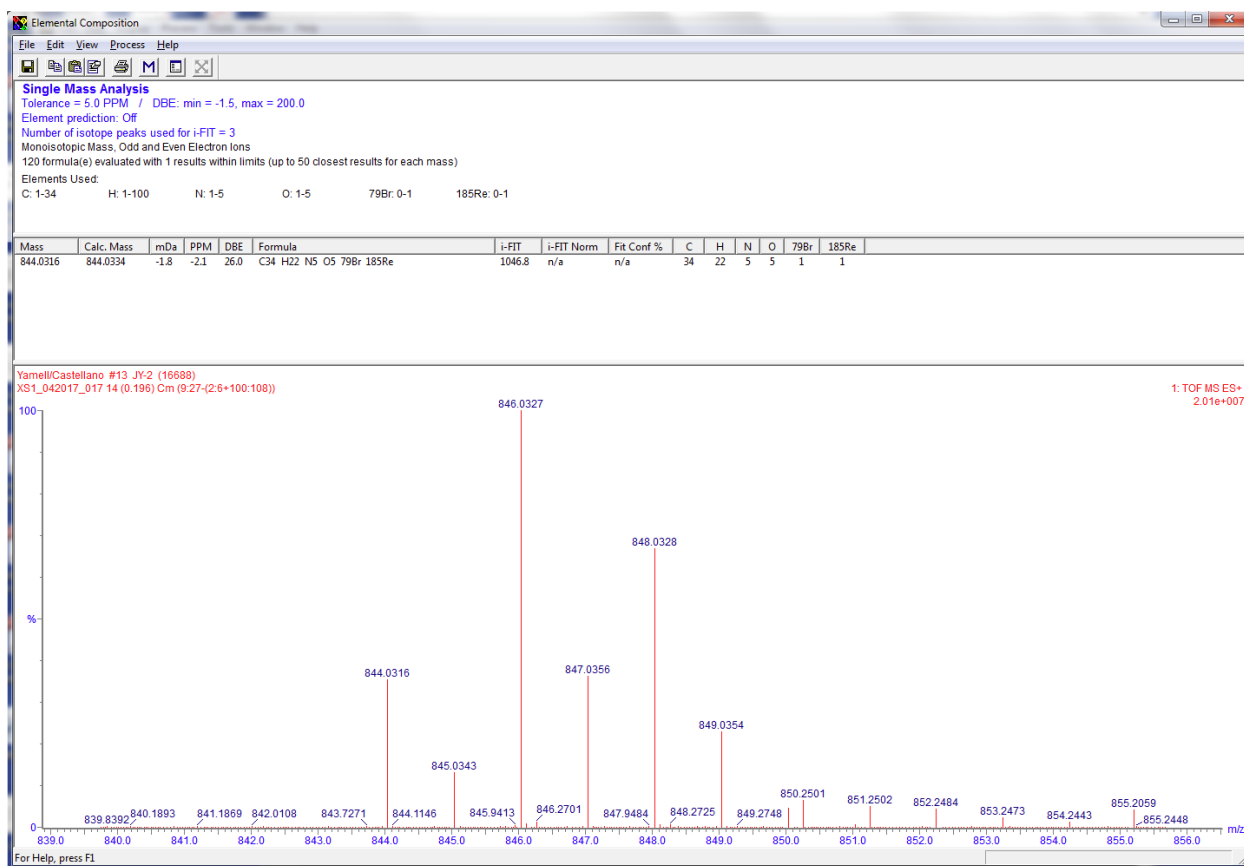


Figure A14. HRMS of $[\text{Re}(\text{BrNI-phen})(\text{CO})_3(\text{dmap})](\text{PF}_6)$ (**Re2**).

Synthesis of 6-phenoxy-2-(p-tolyl)-1H-benzo[de]isoquinoline-1,3(2H)-dione (**PONI**). NNI (1 mmol, 332 mg), phenol (5 mmol, 471 mg), and anhydrous potassium carbonate (5 mmol, 675 mg) were heated at 100 °C in anhydrous dimethylformamide (40 mL) for 4 h. Once cool, 40 mL of distilled water was added to solution to precipitate product. The solid was collected on a glass frit and washed with 200 mL of water. The solid was recrystallized by dissolving in hot ethanol and cooling in a freezer. The off-white product was dried under vacuum overnight and was obtained in 86% yield (326 mg). ^1H NMR (400 MHz, CD_2Cl_2), δ 8.78 (dd, $J = 8.4, 1.2$ Hz, 1H), 8.66 (dd, $J = 7.3, 1.2$ Hz, 1H), 8.45 (d, $J = 8.3$ Hz, 1H), 7.84 (dd, $J = 8.4, 7.3$ Hz, 1H), 7.55 – 7.47 (m, 2H), 7.39 – 7.30 (m, 3H), 7.27 – 7.22 (m, 2H), 7.18 (d, $J = 8.2$ Hz, 2H), 6.96 (d, $J = 8.3$ Hz, 1H), 2.46 (s, 3H). MS [HR-ESI (CH_2Cl_2) m/z] 380.1289 $[\text{M}+\text{H}]^+$, calcd ($\text{C}_{25}\text{H}_{18}\text{NO}_3$) 380.1287. Anal. Calcd

(found) for $C_{25}H_{17}NO_3 \cdot 0.1H_2O$: C, 78.77 (78.84); H, 4.55 (4.73); N, 3.67 (3.67). ATR-FTIR: 485, 696, 753, 779, 804, 1136, 1177, 1201, 1236, 1356, 1575, 1660, 1699 cm^{-1} .

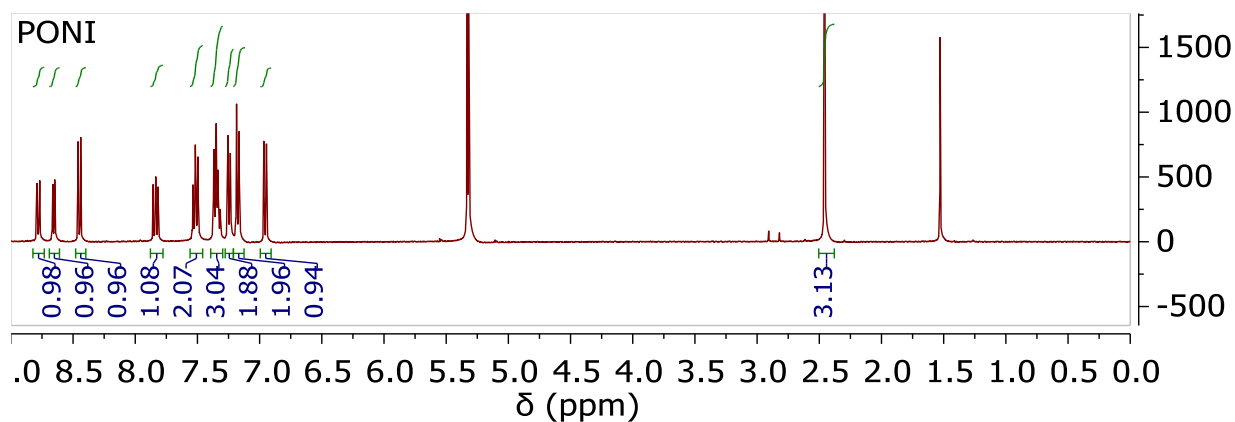


Figure A15. 1H NMR spectrum of **PONI** in CD_2Cl_2 (400 MHz).

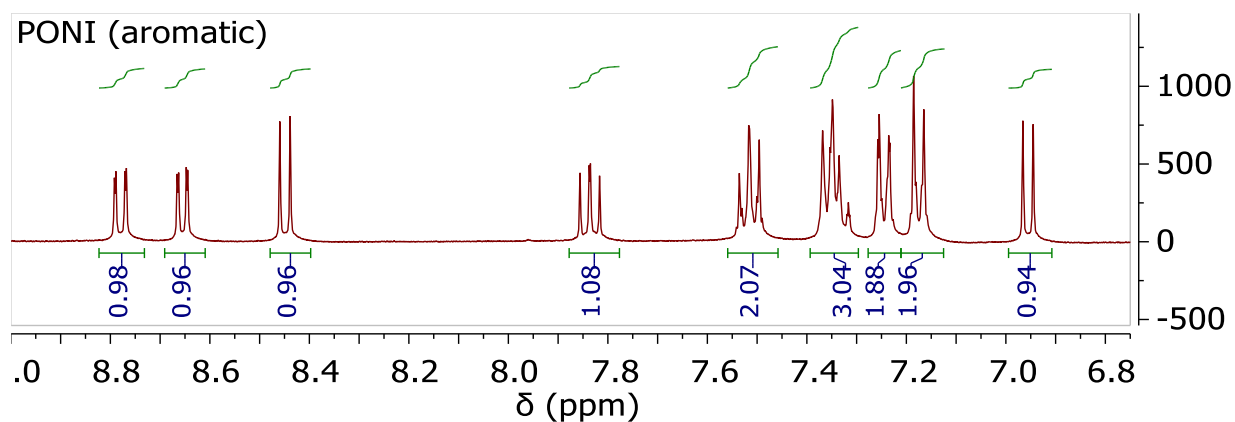


Figure A16. 1H NMR spectrum of **PONI** in CD_2Cl_2 (400 MHz) with zoomed in aromatic region.

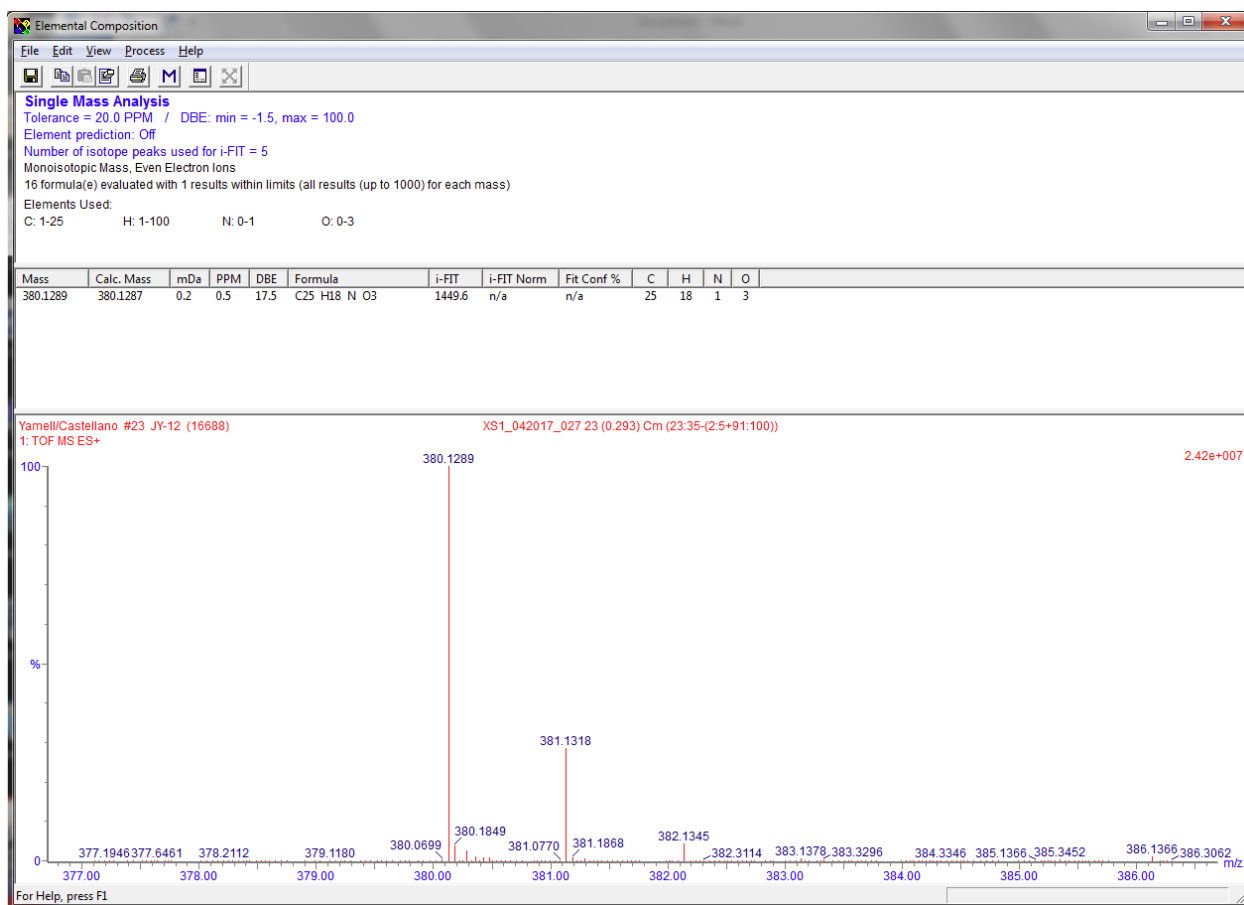


Figure A17. HRMS of PONI.

Synthesis of 2-(1,10-phenanthroline-5-yl)-6-phenoxy-1H-benzo[de]isoquinoline-1,3(2H)-dione (PONI-phen). NNI-phen (1 mmol, 420 mg), phenol (5 mmol, 471 mg), and anhydrous potassium carbonate (5 mmol, 675 mg) were heated at 100 °C in anhydrous dimethylformamide (40 mL) for 4 h. Once cool, 40 mL of distilled water was added to solution to precipitate product. The solid was collected on a glass frit and washed with 200 mL of water. The tan product was dried under vacuum overnight and was obtained in 90% yield (460 mg). ¹H NMR (400 MHz, CD₂Cl₂), δ 9.20 (ddd, J = 17.8, 4.3, 1.7 Hz, 2H), 8.88 (dd, J = 8.4, 1.2 Hz, 1H), 8.73 (dd, J = 7.3, 1.2 Hz, 1H), 8.52 (d, J = 8.3 Hz, 1H), 8.36 – 8.31 (m, 1H), 8.06 (dd, J = 8.3, 1.7 Hz, 1H), 7.95 – 7.87 (m, 2H), 7.71 (dd, J = 8.1, 4.3 Hz, 1H), 7.62 – 7.51 (m, 3H), 7.40 – 7.33 (m, 1H), 7.28 (dd, J = 8.7, 1.1 Hz, 2H), 7.01 (d, J = 8.3 Hz, 1H).

Synthesis of $\text{Re}(\text{PONI-phen})(\text{CO})_3\text{Cl}$. Pentacarbonylchlororhenium(I) (0.4 mmol, 145 mg) was added to one equivalent of PONI-phen (0.4 mmol, 187 mg) and 20 mL of toluene in a 50 mL round bottom flask. The solution was degassed, put under N_2 , and refluxed while mixing for 1 hour. After cooling, the yellow precipitate was filtered out on a glass frit and washed with 200 mL of toluene. The yellow solid was dried under vacuum overnight and was obtained in 92% yield (284 mg). ^1H NMR (400 MHz, CD_2Cl_2), δ 9.43 (ddd, $J = 13.2, 5.1, 1.4$ Hz, 2H), 8.92 (d, $J = 8.5$ Hz, 1H), 8.75 (ddd, $J = 13.8, 7.2, 1.2$ Hz, 1H), 8.64 (d, $J = 8.4$ Hz, 1H), 8.53 (dd, $J = 13.7, 8.3$ Hz, 1H), 8.37 (dd, $J = 8.5, 1.3$ Hz, 1H), 8.17 (s, 1H), 7.99 – 7.88 (m, 2H), 7.83 (dd, $J = 8.5, 5.0$ Hz, 1H), 7.55 (dd, $J = 8.5, 7.4$ Hz, 2H), 7.38 (t, $J = 7.5$ Hz, 1H), 7.31 – 7.26 (m, 2H), 7.01 (dd, $J = 8.2, 1.9$ Hz, 1H).

Synthesis of $[\text{Re}(\text{PONI-phen})(\text{CO})_3(\text{dmap})](\text{PF}_6)$ (**Re3**). $\text{Re}(\text{PONI-phen})(\text{CO})_3\text{Cl}$ (0.25 mmol, 193 mg) and silver triflate (0.26 mmol, 67 mg) were added to 100 mL round bottom flask along with 50 mL of absolute ethanol. The solution was covered (dark), deaerated, put under N_2 , and refluxed for 6 hours. Once cool, the solution was filtered through celite on a glass frit to remove AgCl from solution. The yellow filtrate was added to an excess of dimethylaminopyridine (2.5 mmol, 305 mg) and the solution was then refluxed for an additional 3 hours. The solvent volume was reduced to approximately 10 mL, followed by a dropwise addition of an ammonium hexafluorophosphate solution in water (1.0 g in 10 mL) to precipitate the product. The solid was collected on a glass frit and washed with 250 mL of distilled water. The solid was recrystallized by dissolving in hot methanol and slowly precipitating the solid with a slow addition of ammonium hexafluorophosphate solution in water. The yellow solid was dried under vacuum overnight and was obtained in 90% yield (226 mg). ^1H NMR (400 MHz, CD_2Cl_2), 9.58 (ddd, $J = 11.6, 5.2, 1.4$

Hz, 2H), 8.94 (dd, $J = 8.5, 1.2$ Hz, 1H), 8.82 (dd, $J = 8.4, 1.4$ Hz, 1H), 8.71 (ddd, $J = 15.9, 7.3, 1.2$ Hz, 1H), 8.56 – 8.44 (m, 2H), 8.24 (s, 1H), 8.16 (dd, $J = 8.3, 5.2$ Hz, 1H), 8.08 – 8.01 (m, 1H), 7.93 (ddd, $J = 8.4, 7.3, 4.5$ Hz, 1H), 7.65 (dd, $J = 7.4, 2.2$ Hz, 2H), 7.59 – 7.50 (m, 2H), 7.38 (td, $J = 7.4, 1.2$ Hz, 1H), 7.29 (dd, $J = 7.5, 1.2$ Hz, 2H), 7.01 (dd, $J = 8.3, 4.4$ Hz, 1H), 6.26 (dd, $J = 7.3, 5.2$ Hz, 2H), 2.91 (s, 3H), 2.90 (s, 3H). MS [HR-ESI (CH_2Cl_2) m/z] 858.1478 $[\text{M}-\text{PF}_6]^+$, calcd ($\text{C}_{40}\text{H}_{27}\text{N}_5\text{O}_6^{185}\text{Re}$) 858.1491. Anal. Calcd (found) for $\text{C}_{40}\text{H}_{27}\text{F}_6\text{N}_5\text{O}_6\text{PRe}\cdot\text{H}_2\text{O}$: C, 46.97 (47.06); H, 2.86 (2.68); N, 6.85 (6.79). ATR-FTIR: 557, 781, 840, 1206, 1236, 1254, 1356, 1579, 1626, 1671, 1707, 1907, 2028 cm^{-1} .

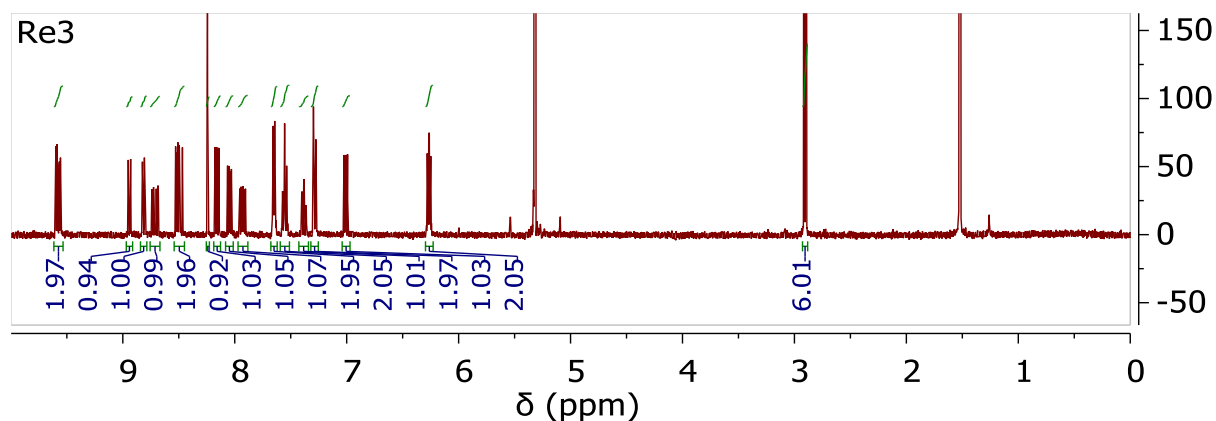


Figure A18. ^1H NMR spectrum of $[\text{Re}(\text{PONI-phen})(\text{CO})_3(\text{dmap})](\text{PF}_6)$ (**Re3**) in CD_2Cl_2 (400 MHz).

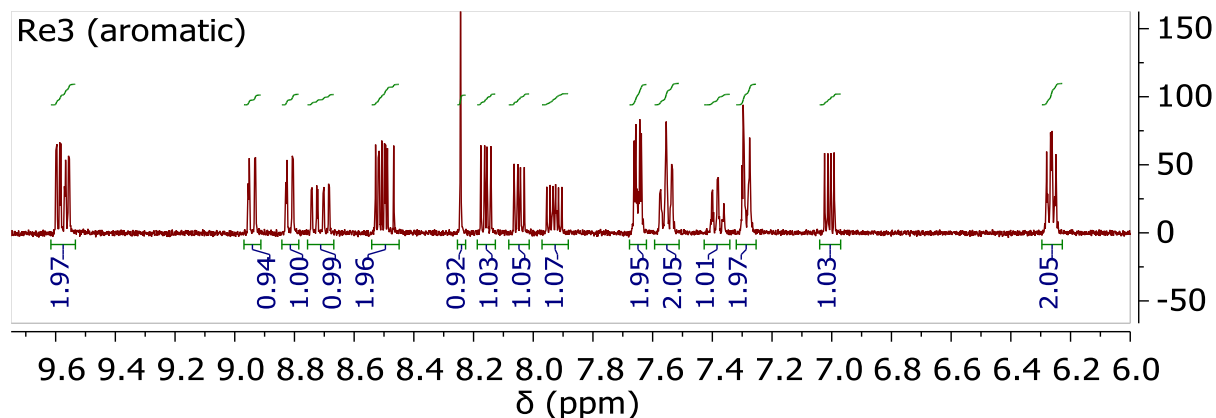


Figure A19. ^1H NMR spectrum of $[\text{Re}(\text{PONI-phen})(\text{CO})_3(\text{dmap})](\text{PF}_6)$ (**Re3**) in CD_2Cl_2 (400 MHz) with zoomed in aromatic region.

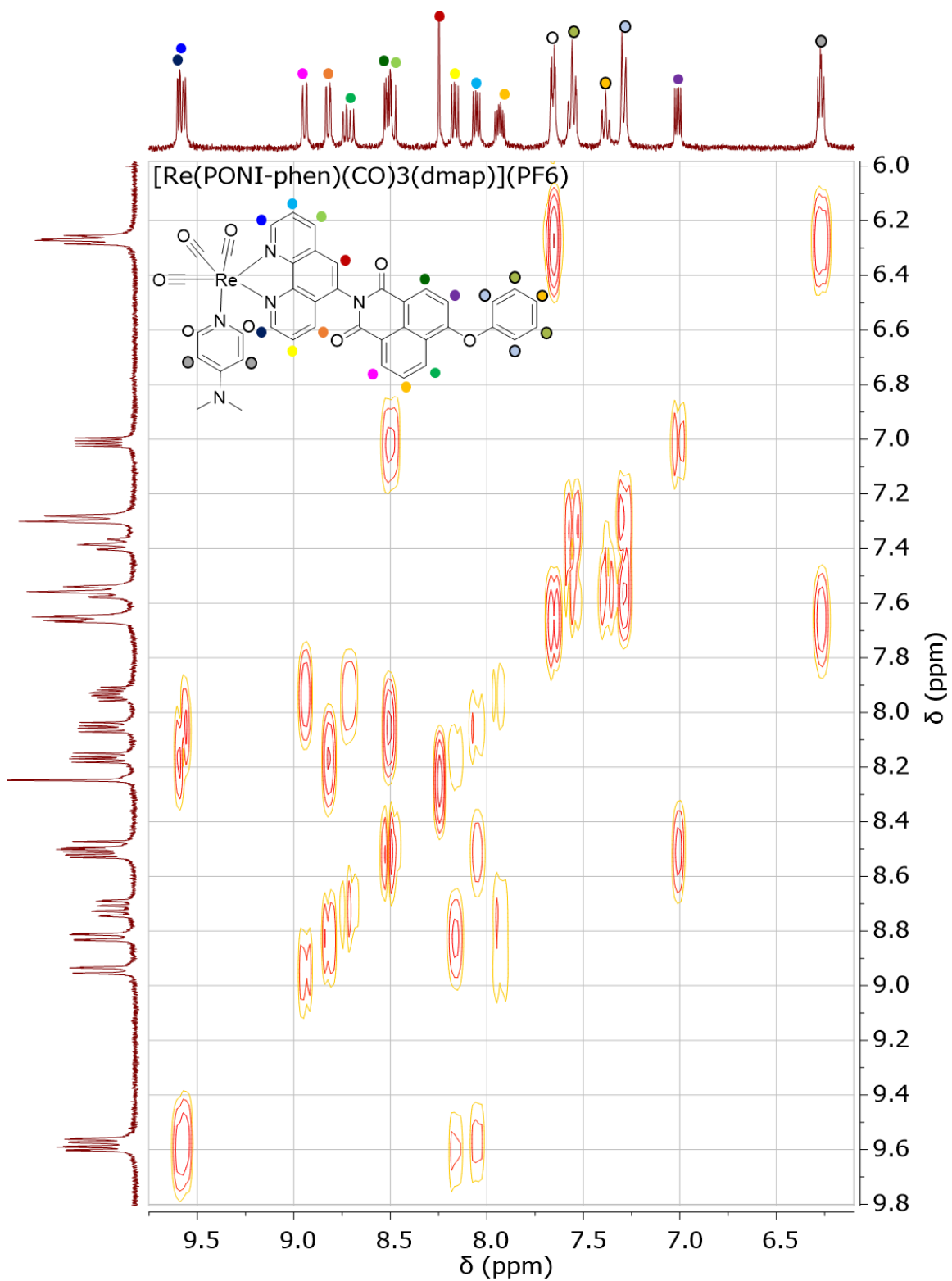


Figure A20. ^1H - ^1H COSY NMR spectrum of $[\text{Re}(\text{PONI-phen})(\text{CO})_3(\text{dmap})](\text{PF}_6)$ (**Re3**) in CD_2Cl_2 (400 MHz).

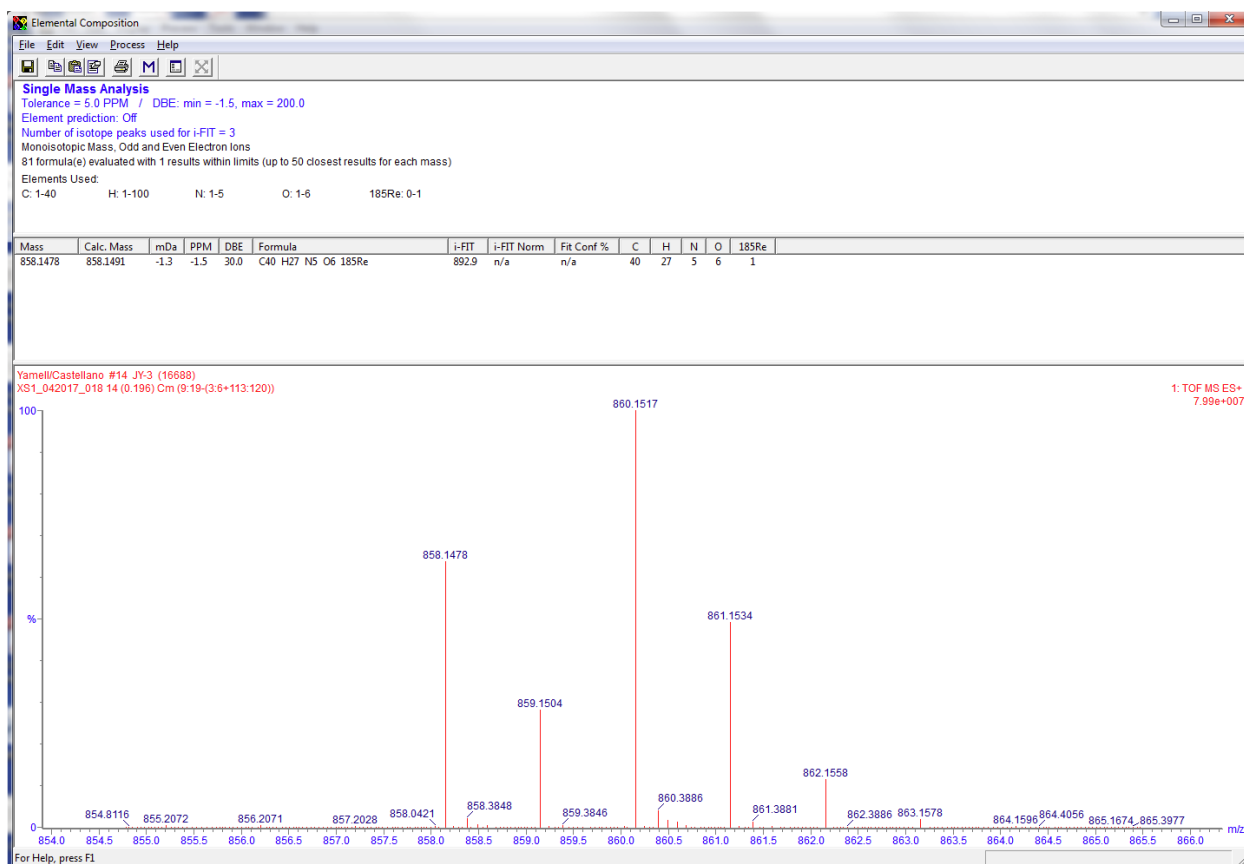


Figure A21. HRMS of $[\text{Re}(\text{PONI-phen})(\text{CO})_3(\text{dmap})](\text{PF}_6)$ (**Re3**).

Synthesis of 6-(phenylthio)-2-(p-tolyl)-1H-benzo[de]isoquinoline-1,3(2H)-dione (**PSNI**). NNI (1 mmol, 332 mg), benzenethiol (5 mmol, 563 μL), and anhydrous potassium carbonate (5 mmol, 675 mg) were heated at 100 $^\circ\text{C}$ in anhydrous dimethylformamide (40 mL) for 4 h. Once cool, 40 mL of distilled water was added to solution to precipitate product. The solid was collected on a glass frit and washed with 200 mL of water. The solid was recrystallized by dissolving in hot ethanol and cooling in a freezer. The yellow product was dried under vacuum overnight and was obtained in 80% yield (317 mg). ^1H NMR (400 MHz, CD_2Cl_2), δ 8.73 (dd, $J = 8.5, 1.1$ Hz, 1H), 8.64 (dd, $J = 7.3, 1.1$ Hz, 1H), 8.35 (d, $J = 7.9$ Hz, 1H), 7.84 (dd, $J = 8.5, 7.3$ Hz, 1H), 7.61 – 7.53 (m, 2H), 7.51 – 7.45 (m, 3H), 7.39 – 7.32 (m, 3H), 7.16 (d, $J = 8.1$ Hz, 2H), 2.45 (s, 3H). MS [HR-ESI (CH_2Cl_2) m/z] 396.1058 $[\text{M}+\text{H}]^+$, calcd ($\text{C}_{25}\text{H}_{18}\text{NO}_2\text{S}$) 396.1058. Anal. Calcd (found) for

C₂₅H₁₇NO₂S: C, 75.93 (75.66); H, 4.33 (4.56); N, 3.54 (3.54). ATR-FTIR: 445, 516, 685, 747, 777, 810, 904, 1134, 1175, 1185, 1230, 1346, 1361, 1507, 1562, 1581, 1656, 1697 cm⁻¹.

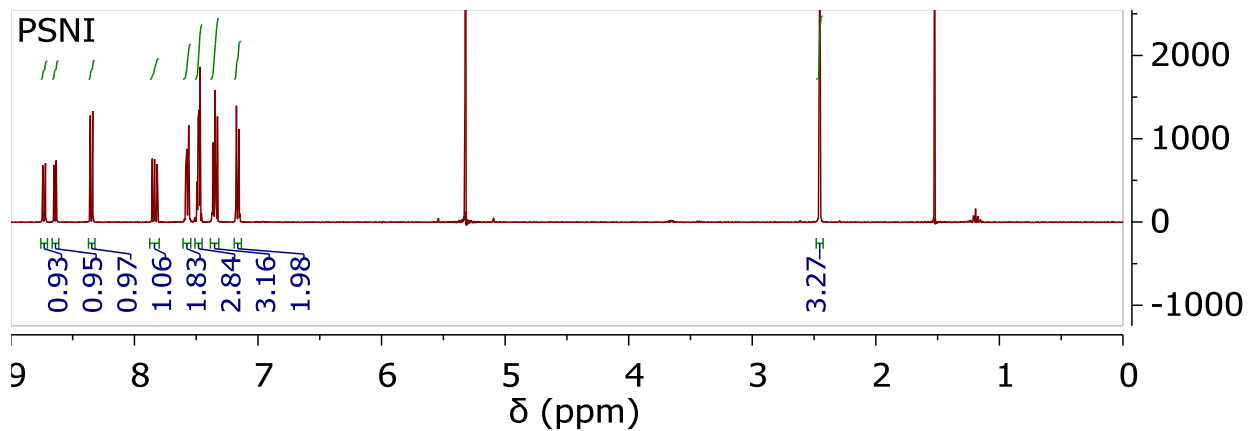


Figure A22. ¹H NMR spectrum of PSNI in CD₂Cl₂ (400 MHz).

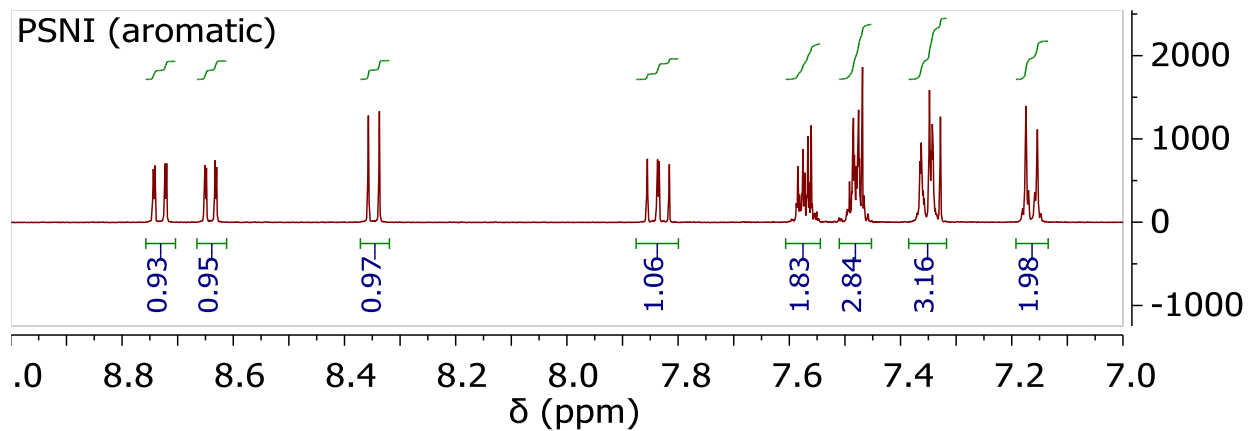


Figure A23. ¹H NMR spectrum of PSNI in CD₂Cl₂ (400 MHz) with zoomed in aromatic region.

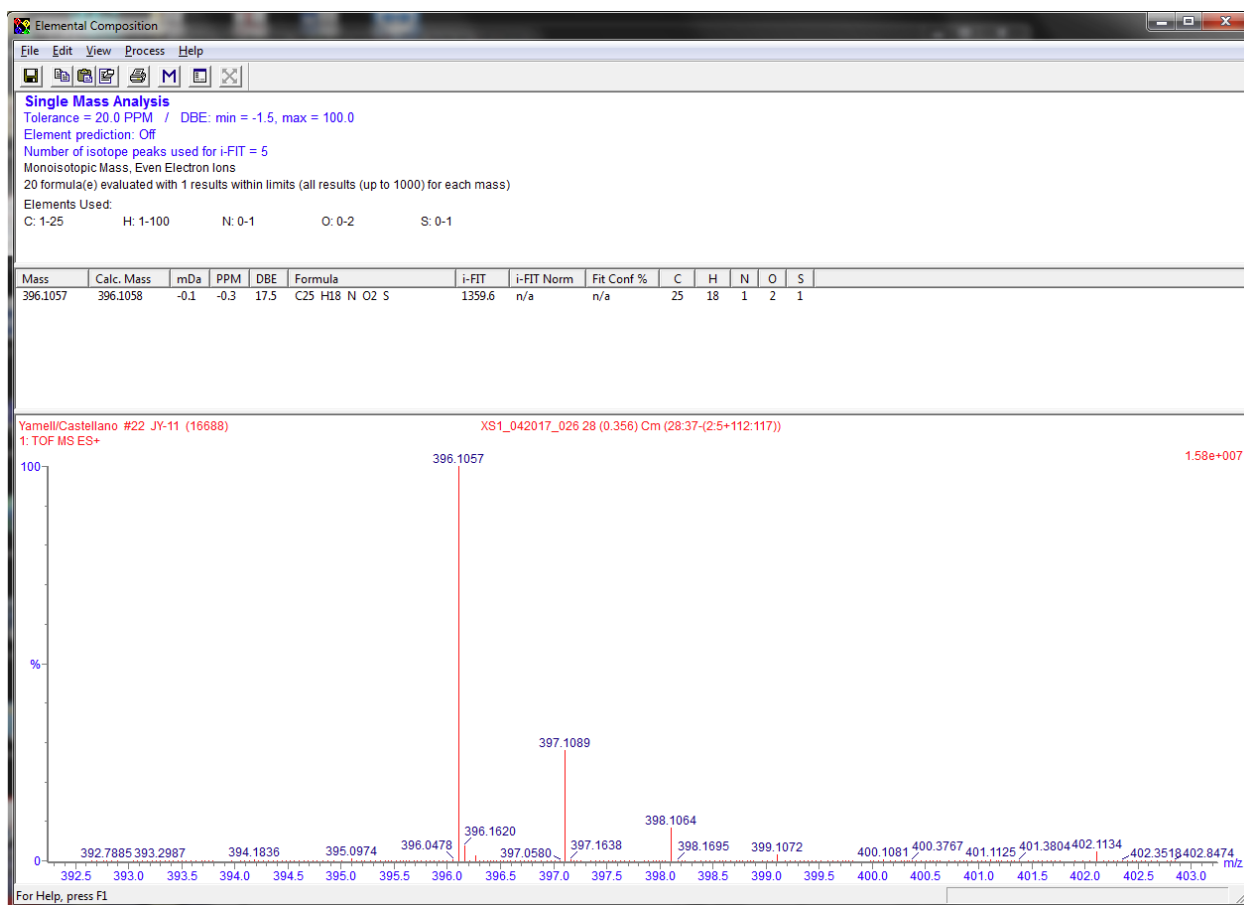


Figure A24. HRMS of PSNI.

Synthesis of 2-(1,10-phenanthroline-5-yl)-6-(phenylthio)-1H-benzo[de]isoquinoline-1,3(2H)-dione (PSNI-phen). NNI-phen (1 mmol, 420 mg), phenol (5 mmol, 563 μ L), and anhydrous potassium carbonate (5 mmol, 675 mg) were heated at 100 $^{\circ}$ C in anhydrous dimethylformamide (40 mL) for 4 h. Once cool, 40 mL of distilled water was added to solution to precipitate product. The solid was collected on a glass frit and washed with 500 mL of water. The tan product was dried under vacuum overnight and was obtained in 66% yield (321 mg). 1 H NMR (400 MHz, CD_2Cl_2), δ 9.22 (dd, $J = 4.4, 1.8$ Hz, 1H), 9.18 (dd, $J = 4.3, 1.7$ Hz, 1H), 8.83 (dd, $J = 8.5, 1.1$ Hz, 1H), 8.71 (dd, $J = 7.3, 1.1$ Hz, 1H), 8.40 (d, $J = 7.9$ Hz, 1H), 8.36 – 8.30 (m, 1H), 8.04 (dd, $J = 8.3, 1.7$ Hz, 1H), 7.95 – 7.86 (m, 2H), 7.71 (dd, $J = 8.0, 4.4$ Hz, 1H), 7.65 – 7.56 (m, 3H), 7.55 – 7.48 (m, 3H), 7.36 (d, $J = 7.9$ Hz, 1H).

Synthesis of $\text{Re}(\text{PSNI-phen})(\text{CO})_3\text{Cl}$. Pentacarbonylchlororhenium(I) (0.5 mmol, 181 mg) was added to one equivalent of PSNI-phen (0.5 mmol, 242 mg) and 20 mL of toluene in a 50 mL round bottom flask. The solution was degassed, put under N_2 , and refluxed while mixing for 1 hour. After cooling, the yellow precipitate was filtered out on a glass frit and washed with 200 mL of toluene. The yellow solid was dried under vacuum overnight and was obtained in 94% yield (369 mg). ^1H NMR (400 MHz, CDCl_3), δ 9.44 (ddd, $J = 14.3, 5.1, 1.4$ Hz, 2H), 8.84 (ddd, $J = 8.5, 3.4, 1.1$ Hz, 1H), 8.75 (ddd, $J = 12.0, 7.3, 1.1$ Hz, 1H), 8.56 (dd, $J = 8.2, 1.4$ Hz, 1H), 8.43 (dd, $J = 10.4, 8.0$ Hz, 1H), 8.28 (dd, $J = 8.5, 1.3$ Hz, 1H), 8.10 (s, 1H), 7.96 – 7.86 (m, 2H), 7.78 (dd, $J = 8.4, 5.1$ Hz, 1H), 7.66 – 7.61 (m, 2H), 7.56 – 7.50 (m, 3H), 7.28 (dd, $J = 8.0, 2.6$ Hz, 1H).

Synthesis of $[\text{Re}(\text{PSNI-phen})(\text{CO})_3(\text{dmap})](\text{PF}_6)$ (**Re4**). $\text{Re}(\text{PSNI-phen})(\text{CO})_3\text{Cl}$ (0.25 mmol, 197 mg) and silver triflate (0.26 mmol, 67 mg) were added to 100 mL round bottom flask along with 50 mL of absolute ethanol. The solution was covered (dark), deaerated, put under N_2 , and refluxed for 6 hours. Once cool, the solution was filtered through celite on a glass frit to remove AgCl from solution. The yellow filtrate was added to an excess of dimethylaminopyridine (2.5 mmol, 305 mg) and the solution was then refluxed for an additional 5 hours. The solvent volume was reduced to approximately 10 mL, followed by a dropwise addition of an ammonium hexafluorophosphate solution in water (1.0 g in 10 mL) to precipitate the product. The solid was collected on a glass frit and washed with 250 mL of distilled water. The solid was recrystallized by dissolving in hot methanol and slowly precipitating the solid with a slow addition of ammonium hexafluorophosphate solution in water. The yellow solid was dried under vacuum overnight and was obtained in 96% yield (245 mg). ^1H NMR (400 MHz, CD_2Cl_2), δ 9.57 (ddd, $J = 12.6, 5.1, 1.4$

Hz, 2H), 8.84 (ddd, $J = 24.3, 8.5, 1.3$ Hz, 2H), 8.70 (ddd, $J = 16.3, 7.3, 1.1$ Hz, 1H), 8.48 (dd, $J = 8.5, 1.3$ Hz, 1H), 8.36 (dd, $J = 15.7, 8.0$ Hz, 1H), 8.23 (s, 1H), 8.16 (dd, $J = 8.3, 5.2$ Hz, 1H), 8.04 (dd, $J = 8.5, 5.1$ Hz, 1H), 7.93 (ddd, $J = 8.5, 7.4, 4.7$ Hz, 1H), 7.67 – 7.62 (m, 4H), 7.56 – 7.52 (m, 3H), 7.31 (dd, $J = 8.0, 5.0$ Hz, 1H), 6.26 (td, $J = 5.5, 1.6$ Hz, 2H), 2.91 (s, 3H), 2.89 (s, 3H). MS [HR-ESI (CH_2Cl_2) m/z] 874.1242 $[\text{M-PF}_6]^+$, calcd ($\text{C}_{40}\text{H}_{27}\text{N}_5\text{O}_5\text{S}^{185}\text{Re}$) 874.1262. Anal. Calcd (found) for $\text{C}_{40}\text{H}_{27}\text{F}_6\text{N}_5\text{O}_5\text{PReS}$: C, 47.06 (46.98); H, 2.67 (2.68); N, 6.86 (6.78). ATR-FTIR: 557, 728, 751, 779, 838, 1234, 1363, 1585, 1626, 1671, 1709, 1905, 2028 cm^{-1} .

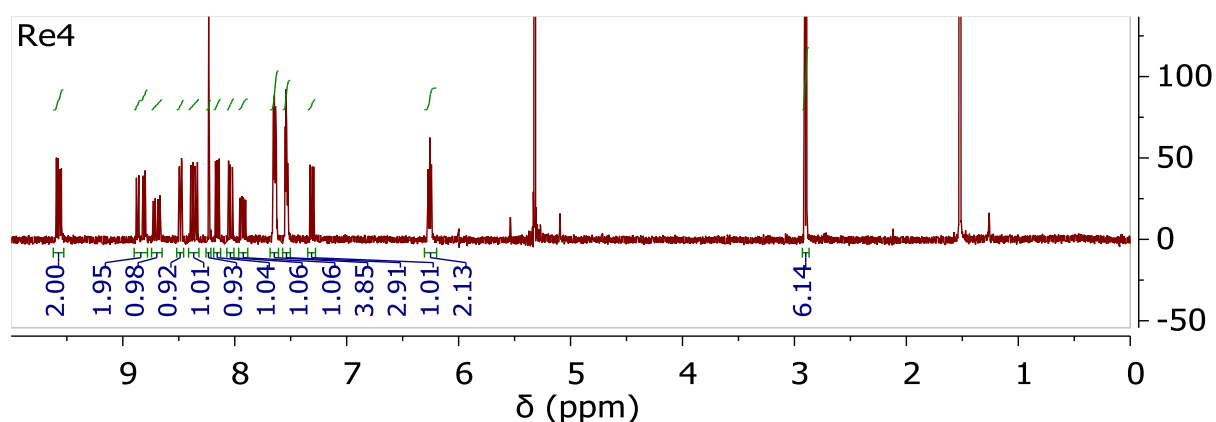


Figure A25. ^1H NMR spectrum of $[\text{Re}(\text{PSNI-phen})(\text{CO})_3(\text{dmap})](\text{PF}_6)$ (**Re4**) in CD_2Cl_2 (400 MHz).

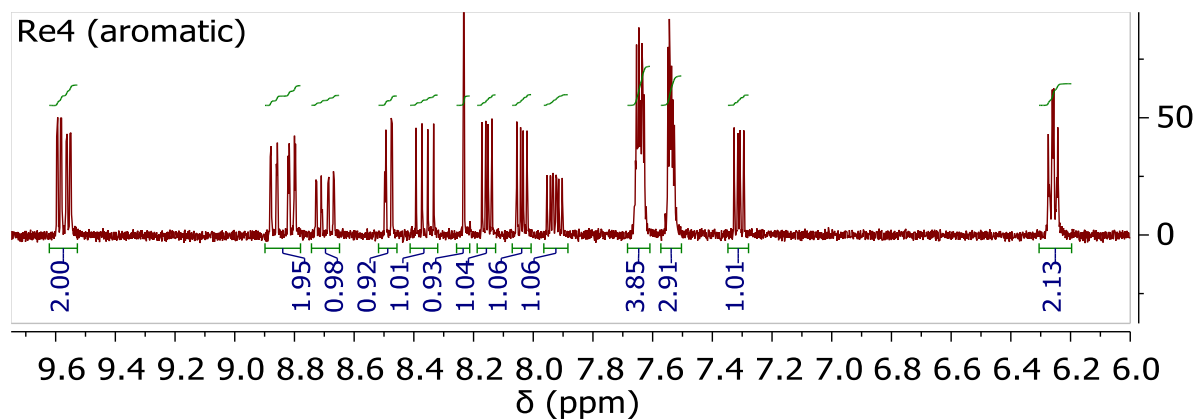


Figure A26. ^1H NMR spectrum of $[\text{Re}(\text{PSNI-phen})(\text{CO})_3(\text{dmap})](\text{PF}_6)$ (**Re4**) in CD_2Cl_2 (400 MHz) with zoomed in aromatic region.

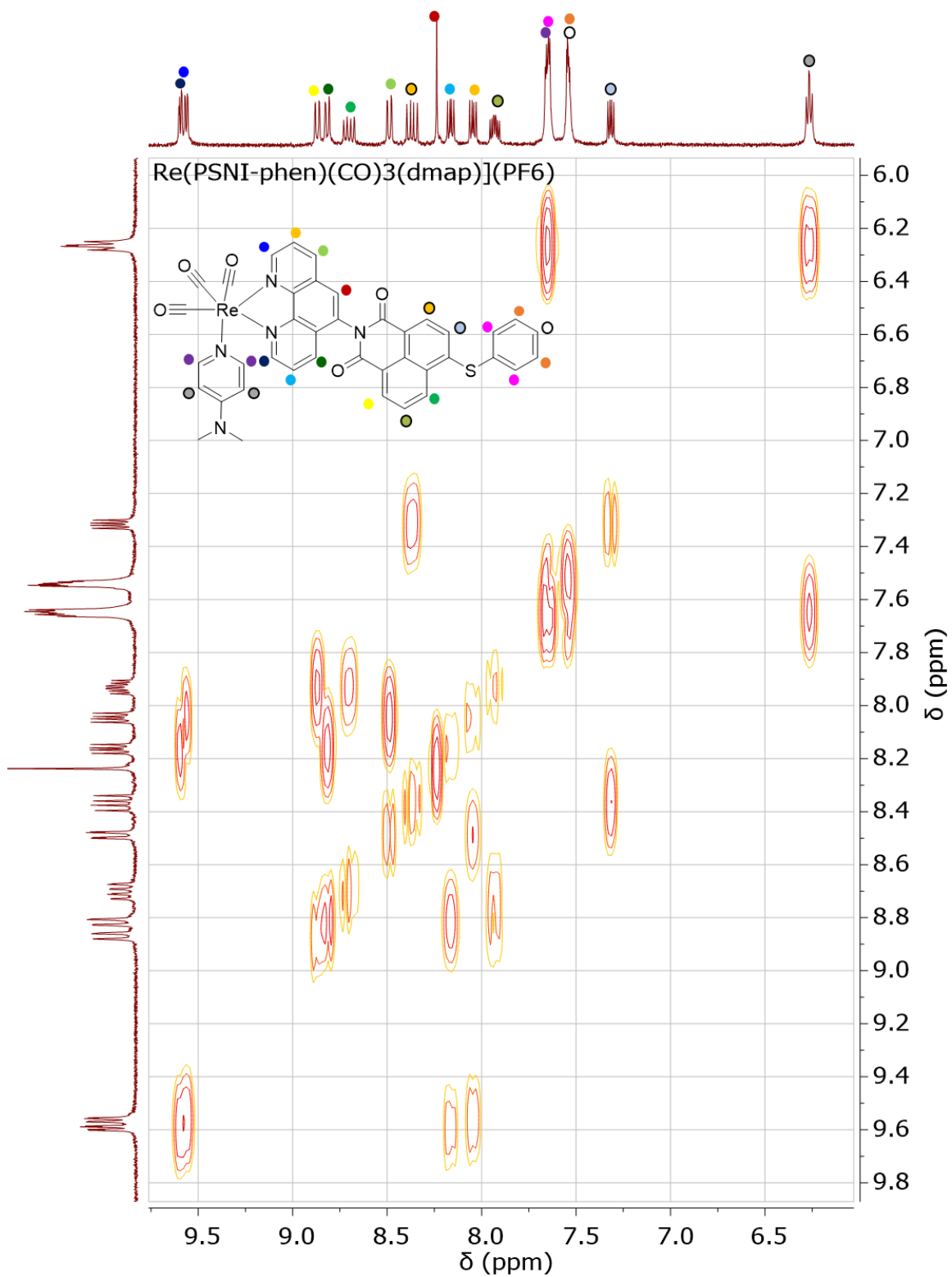


Figure A27. ¹H-¹H COSY NMR spectrum of [Re(PSNI-phen)(CO)₃(dmap)](PF₆) (**Re4**) in CD₂Cl₂ (400 MHz).



Figure A28. HRMS of $[\text{Re}(\text{PSNI-phen})(\text{CO})_3(\text{dmap})](\text{PF}_6)$ (**Re4**).

Synthesis of $[\text{Re}(\text{PNI-phen})(\text{CO})_3(\text{dmap})](\text{PF}_6)$ (**Re5**). $\text{Re}(\text{PNI-phen})(\text{CO})_3\text{Cl}$ (0.25 mmol, 191 mg) and silver triflate (0.26 mmol, 67 mg) were added to 100 mL round bottom flask along with 50 mL of absolute ethanol. The solution was covered (dark), deaerated, put under N_2 , and refluxed for 6 hours. Once cool, the solution was filtered through celite on a glass frit to remove AgCl from solution. The orange filtrate was added to an excess of dimethylaminopyridine (2.5 mmol, 305 mg) and the solution was then refluxed for an additional 3 hours. The solvent volume was reduced to approximately 10 mL, followed by a dropwise addition of an ammonium hexafluorophosphate solution in water (1.0 g in 10 mL) to precipitate the product. The solid was collected on a glass frit and washed with 250 mL of distilled water. The solid was recrystallized by dissolving in hot methanol and slowly precipitating the solid with a slow addition of ammonium

hexafluorophosphate solution in water. The orange solid was dried under vacuum overnight and was obtained in 96% yield (240 mg). ^1H NMR (400 MHz, CD_2Cl_2), δ 9.56 (ddd, $J = 13.1, 5.1, 1.4$ Hz, 2H), 8.80 (dd, $J = 8.3, 1.4$ Hz, 1H), 8.66 – 8.44 (m, 4H), 8.22 (s, 1H), 8.14 (dd, $J = 8.3, 5.2$ Hz, 1H), 8.02 (dd, $J = 8.5, 5.1$ Hz, 1H), 7.79 (ddd, $J = 8.5, 7.3, 5.3$ Hz, 1H), 7.64 (d, $J = 7.4$ Hz, 2H), 7.27 (dd, $J = 8.2, 6.1$ Hz, 1H), 6.26 (d, $J = 7.4$ Hz, 2H), 3.36 (m, $J = 5.4$ Hz, 4H), 2.91 (s, 6H), 1.92 (m, $J = 10.7$ Hz, 4H), 1.78 (m, 2H). MS [HR-ESI (CH_2Cl_2) m/z] 849.1945 [M-PF_6] $^+$, calcd ($\text{C}_{39}\text{H}_{32}\text{N}_6\text{O}_5^{185}\text{Re}$) 849.1964. Anal. Calcd (found) for $\text{C}_{39}\text{H}_{32}\text{F}_6\text{N}_6\text{O}_5\text{PRe}\cdot\text{H}_2\text{O}$: C, 46.20 (46.17); H, 3.38 (3.16); N, 8.29 (8.10). ATR-FTIR: 557, 781, 840, 1232, 1365, 1583, 1626, 1664, 1701, 1909, 2028 cm^{-1} .

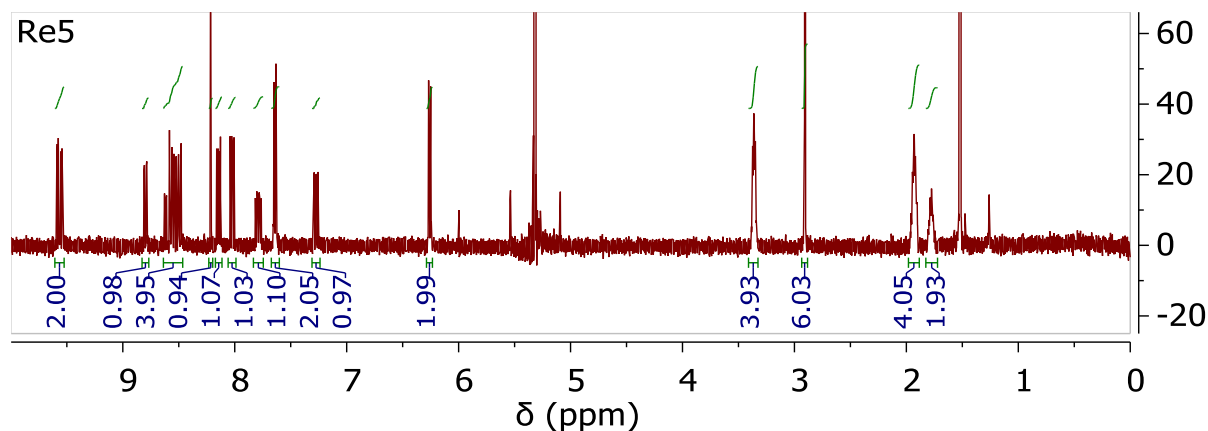


Figure A29. ^1H NMR spectrum of $[\text{Re}(\text{PNI-phen})(\text{CO})_3(\text{dmap})](\text{PF}_6)$ (**Re5**) in CD_2Cl_2 (400 MHz).

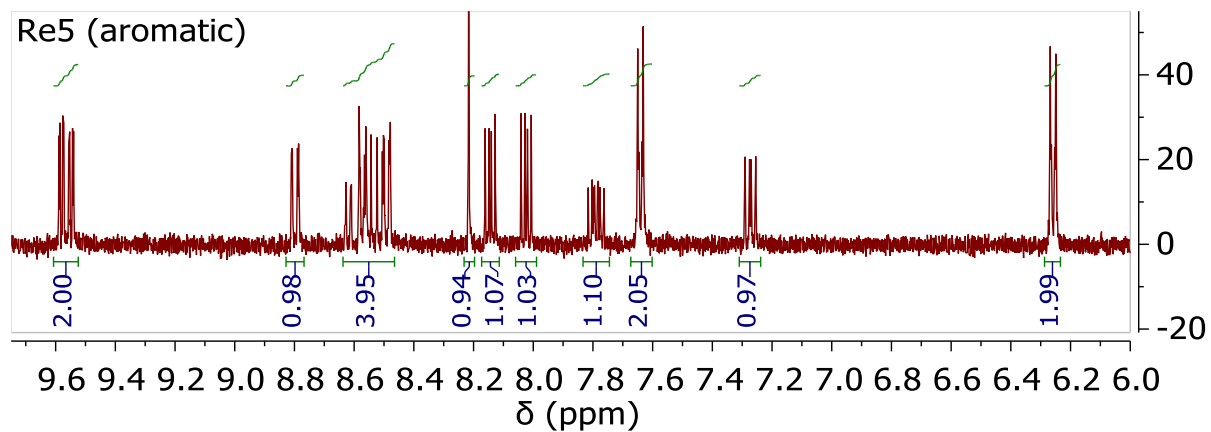


Figure A30. ^1H NMR spectrum of $[\text{Re}(\text{PNI-phen})(\text{CO})_3(\text{dmap})](\text{PF}_6)$ (**Re5**) in CD_2Cl_2 (400 MHz) with zoomed in aromatic region.

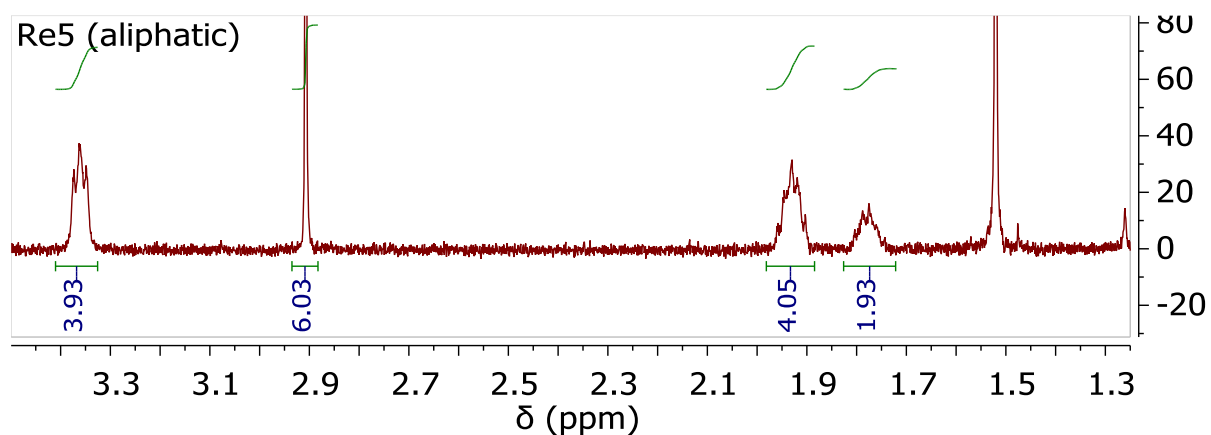


Figure A31. ^1H NMR spectrum of $[\text{Re}(\text{PNI-phen})(\text{CO})_3(\text{dmap})](\text{PF}_6)$ (**Re5**) in CD_2Cl_2 (400 MHz) with zoomed in aliphatic region.

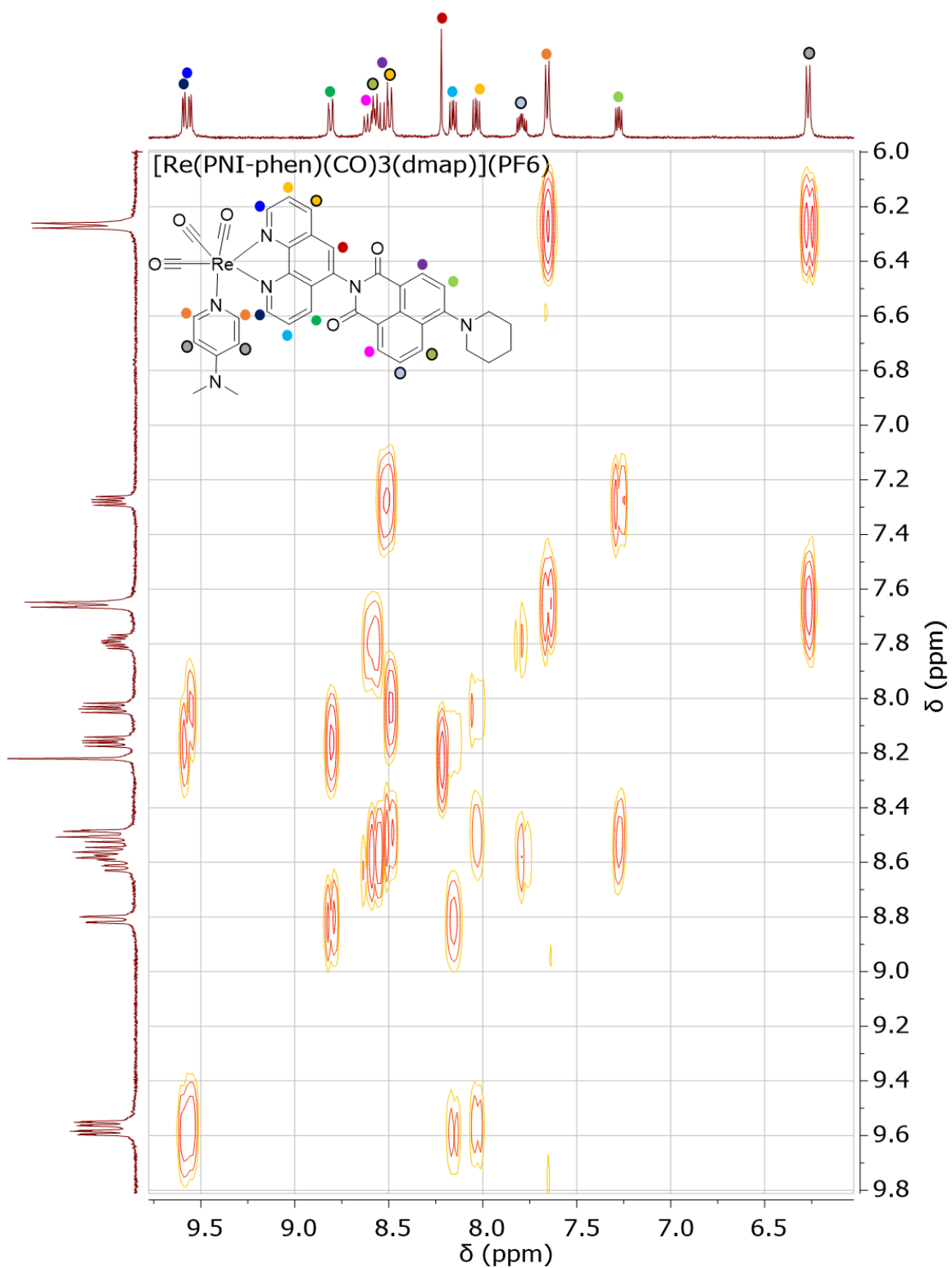


Figure A32. ^1H - ^1H COSY NMR spectrum of $[\text{Re}(\text{PNI-phen})(\text{CO})_3(\text{dmap})](\text{PF}_6)$ (**Re5**) in CD_2Cl_2 (400 MHz).

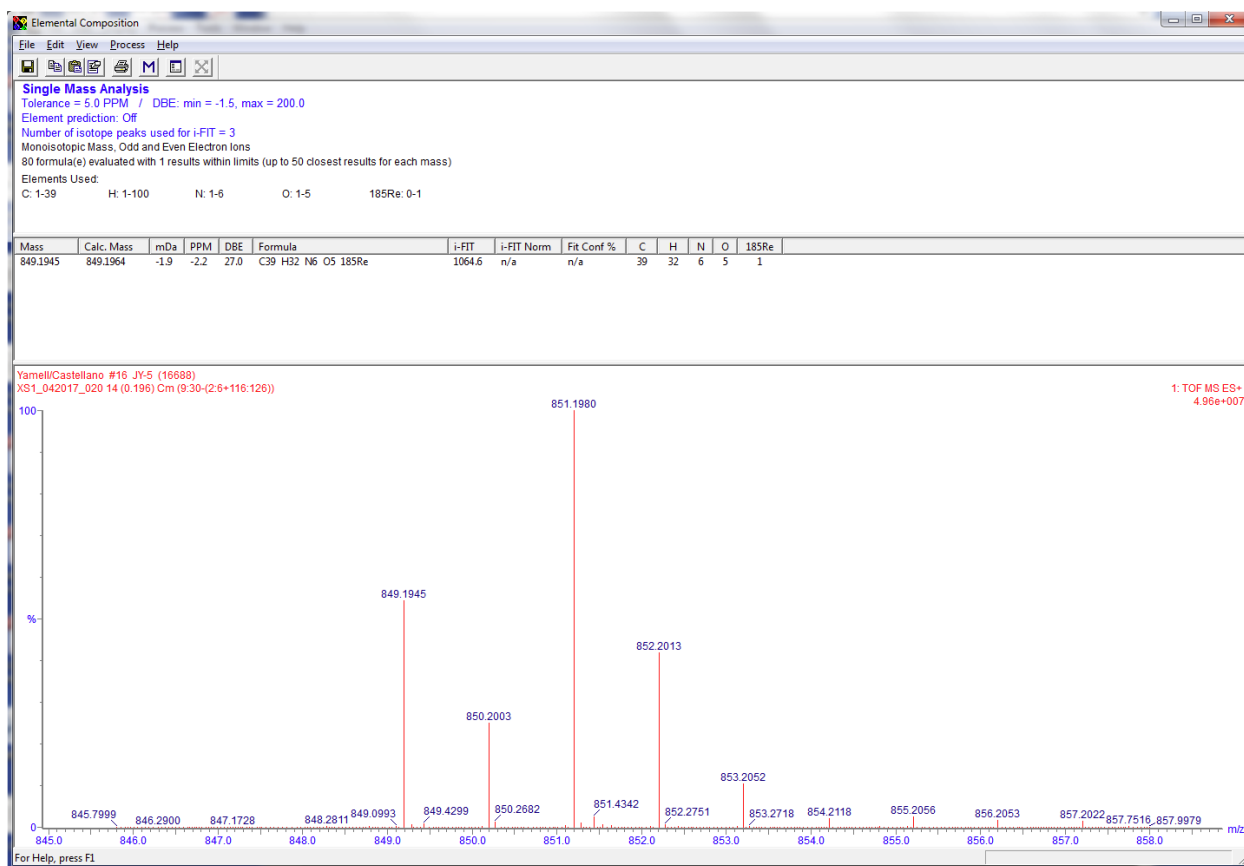


Figure A33. HRMS of $[\text{Re}(\text{PNI-phen})(\text{CO})_3(\text{dmap})](\text{PF}_6)$ (**Re5**).

Synthesis of $[\text{Re}(\text{phen})(\text{CO})_3(\text{dmap})](\text{PF}_6)$ (**Re6**). $\text{Re}(\text{phen})(\text{CO})_3\text{Cl}$ (0.25 mmol, 122 mg) and silver triflate (0.26 mmol, 67 mg) were added to 100 mL round bottom flask along with 50 mL of absolute ethanol. The solution was covered (dark), deaerated, put under N_2 , and refluxed for 6 hours. Once cool, the solution was filtered through celite on a glass frit to remove AgCl from solution. The yellow filtrate was added to an excess of dimethylaminopyridine (2.5 mmol, 305 mg) and the solution was then refluxed for an additional 3 hours. The solvent volume was reduced to approximately 10 mL, followed by a dropwise addition of an ammonium hexafluorophosphate solution in water (1.0 g in 10 mL) to precipitate the product. The solid was collected on a glass frit and washed with 250 mL of distilled water. The solid was recrystallized by dissolving in hot methanol and slowly precipitating the solid with a slow addition of ammonium

hexafluorophosphate solution in water. The orange solid was dried under vacuum overnight and was obtained in 83% yield (148 mg). ^1H NMR (400 MHz, CD_2Cl_2), δ 9.51 (dd, $J = 5.1, 1.4$ Hz, 2H), 8.79 (dd, $J = 8.3, 1.4$ Hz, 2H), 8.17 (s, 2H), 8.10 (dd, $J = 8.3, 5.1$ Hz, 2H), 7.53 (d, $J = 7.4$ Hz, 2H), 6.19 (d, $J = 7.4$ Hz, 2H), 2.86 (s, 6H). MS [HR-ESI (CH_2Cl_2) m/z] 571.0909 $[\text{M}-\text{PF}_6]^+$, calcd ($\text{C}_{22}\text{H}_{18}\text{N}_4\text{O}_3^{185}\text{Re}$) 571.0908. Anal. Calcd (found) for $\text{C}_{22}\text{H}_{18}\text{F}_6\text{N}_4\text{O}_3\text{PRe}\cdot 0.5\text{H}_2\text{O}$: C, 36.37 (36.52); H, 2.64 (2.42); N, 7.71 (7.59). ATR-FTIR: 557, 724, 836, 1626, 1897, 1919, 2025 cm^{-1} .

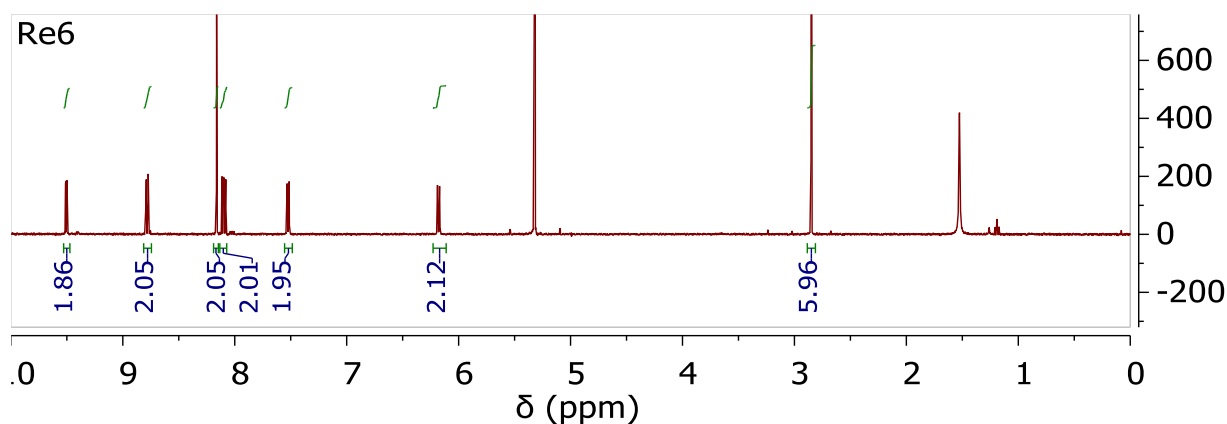


Figure A34. ^1H NMR spectrum of $[\text{Re}(\text{phen})(\text{CO})_3(\text{dmap})](\text{PF}_6)$ (**Re6**) in CD_2Cl_2 (400 MHz) with zoomed in aromatic region.

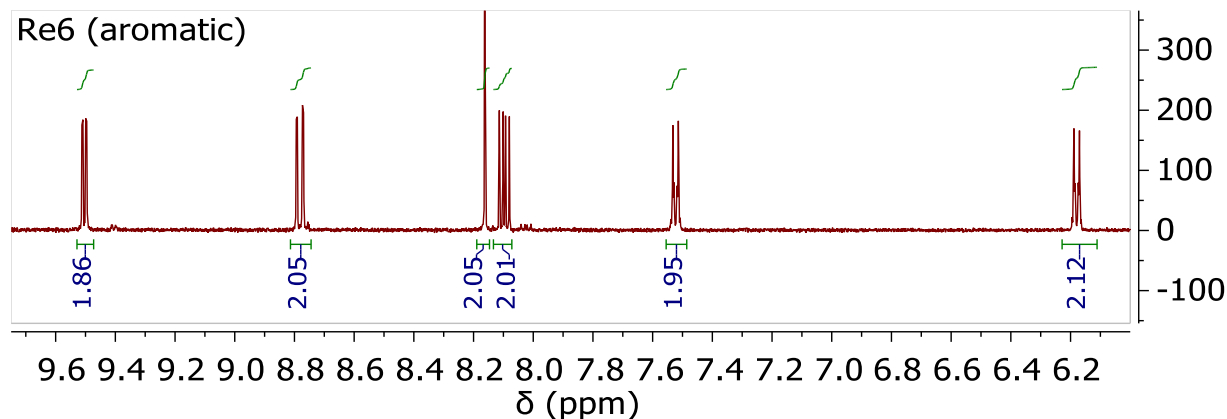


Figure A35. ^1H NMR spectrum of $[\text{Re}(\text{phen})(\text{CO})_3(\text{dmap})](\text{PF}_6)$ (**Re6**) in CD_2Cl_2 (400 MHz) with zoomed in aromatic region.

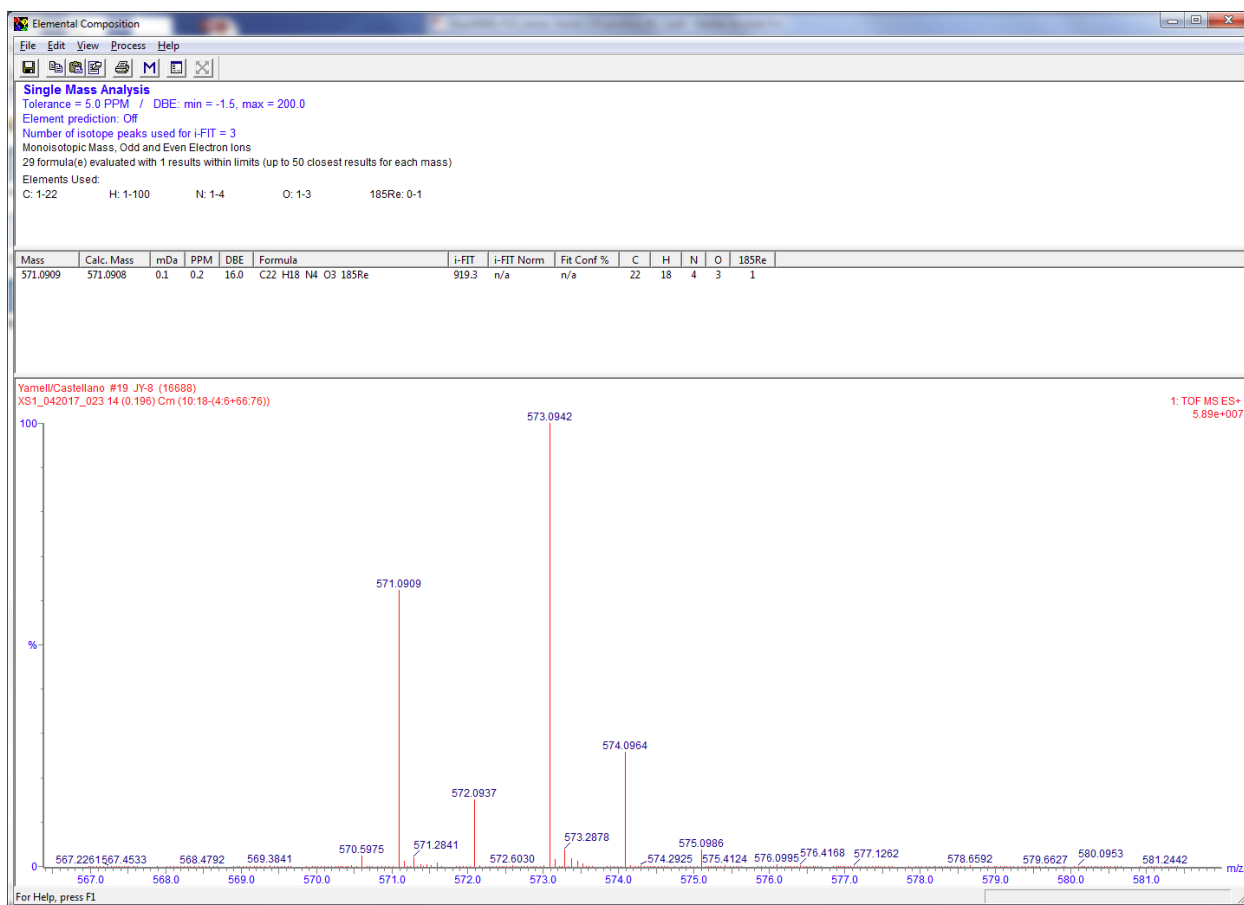


Figure A36. HRMS of $[\text{Re}(\text{phen})(\text{CO})_3(\text{dmap})](\text{PF}_6)$ (**Re6**).

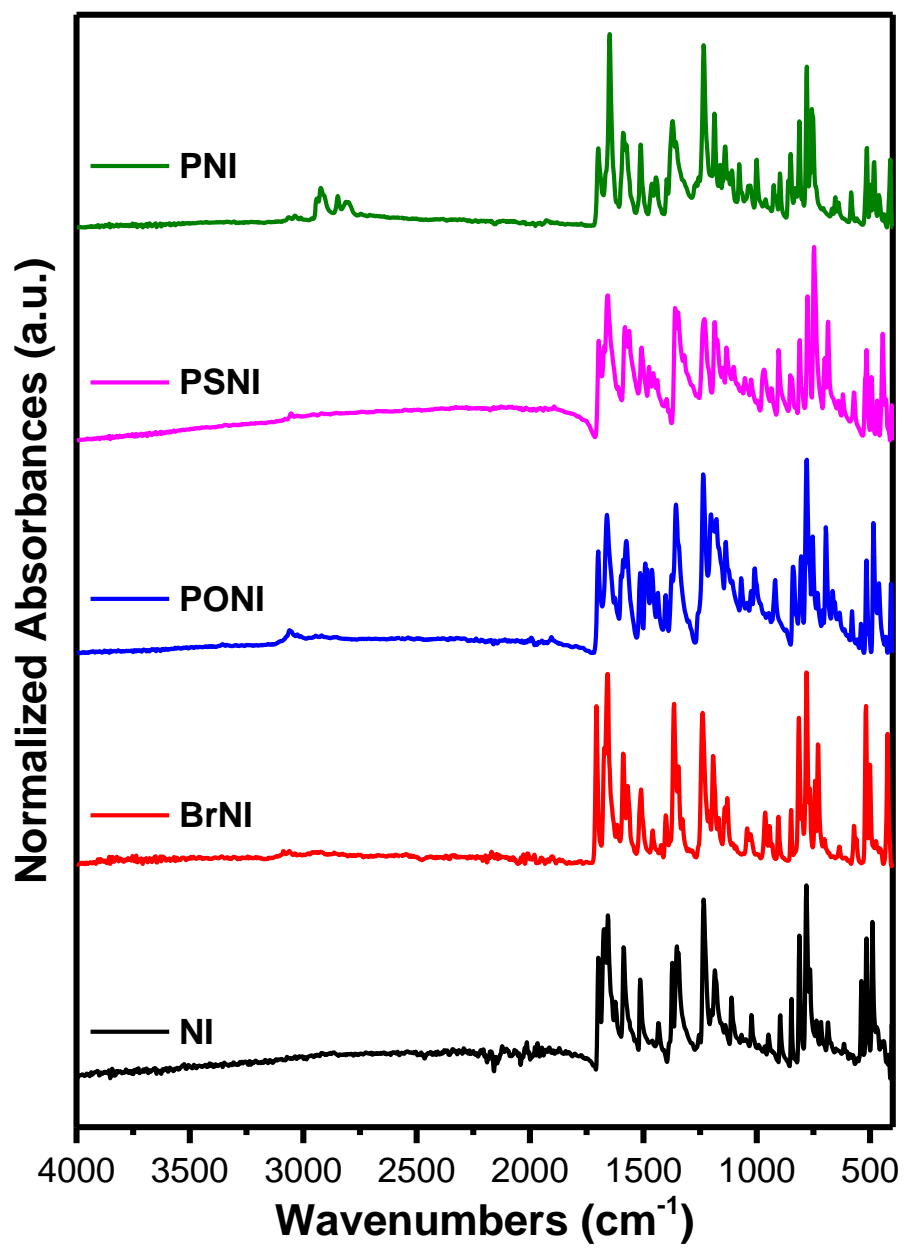


Figure A37. ATR-FTIR spectra of NI, BrNI, PONI, PSNI, and PNI.

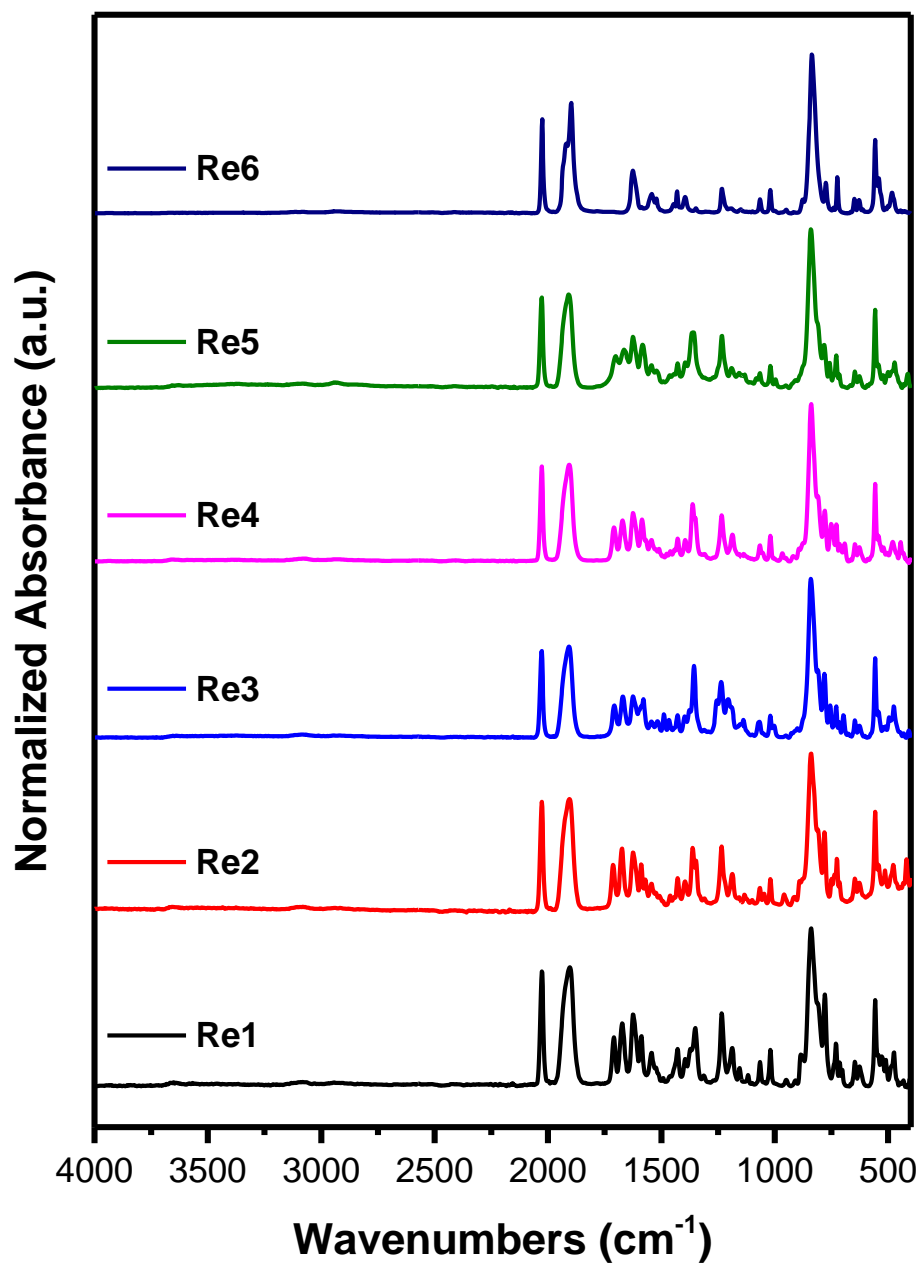


Figure A38. ATR-FTIR spectra of **Re1-Re6**.

A.2. Additional Optical Spectra

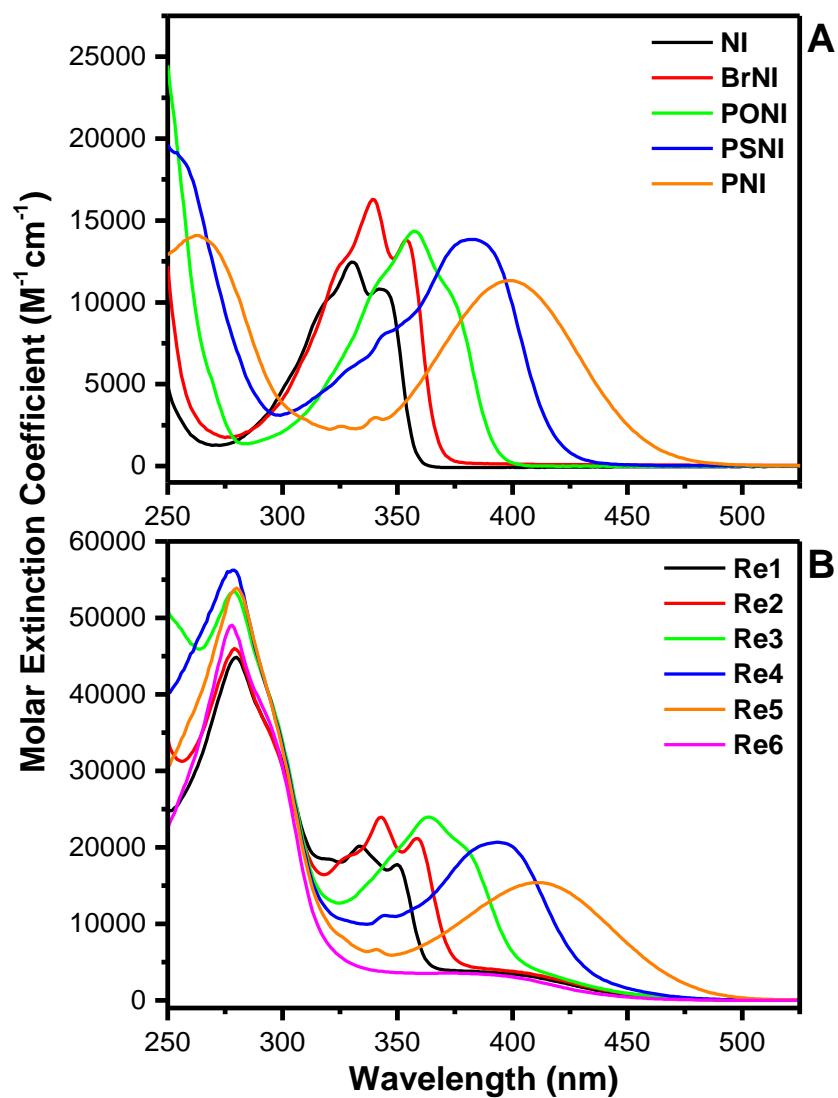


Figure A39. (a) Electronic spectra of NI, BrNI, PONI, PSNI, and PNI in THF. (b) Electronic spectra of Re1-Re6 in THF.

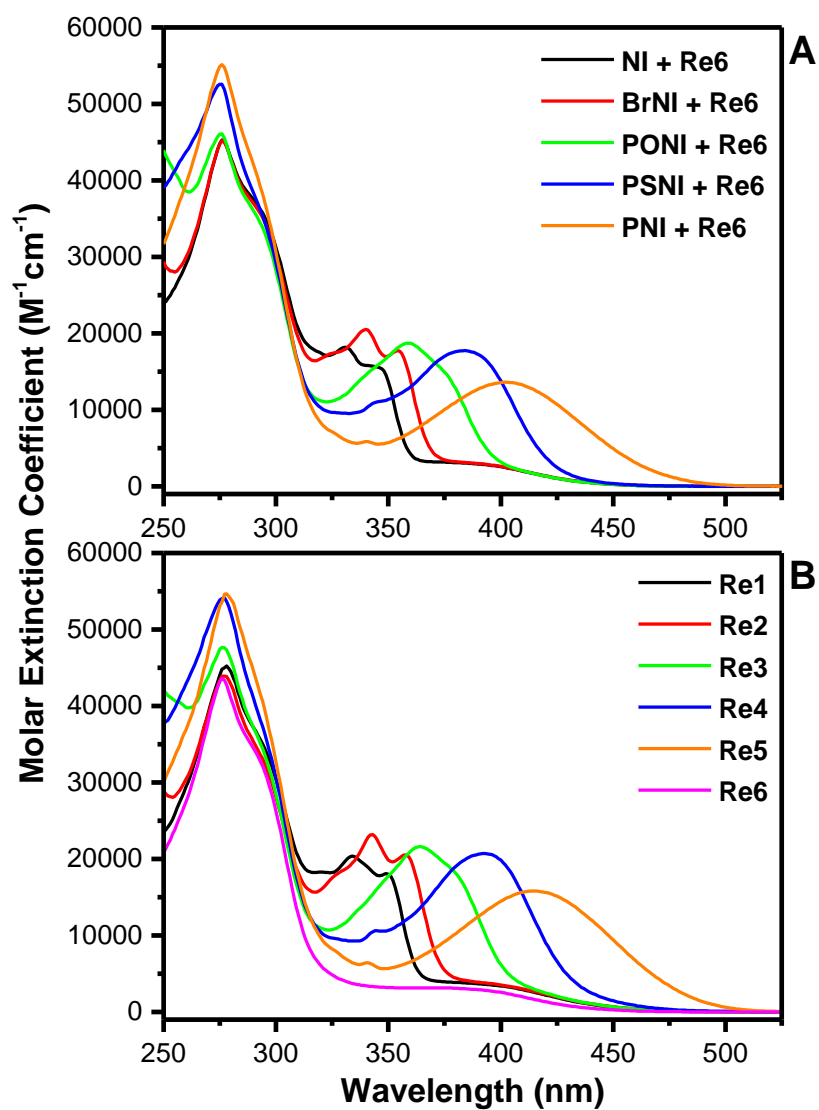


Figure A40. (a) Additive combination of electronic spectra between organic chromophore model and Re(I) model in ACN. (b) Electronic spectra of **Re1-Re6** in ACN.

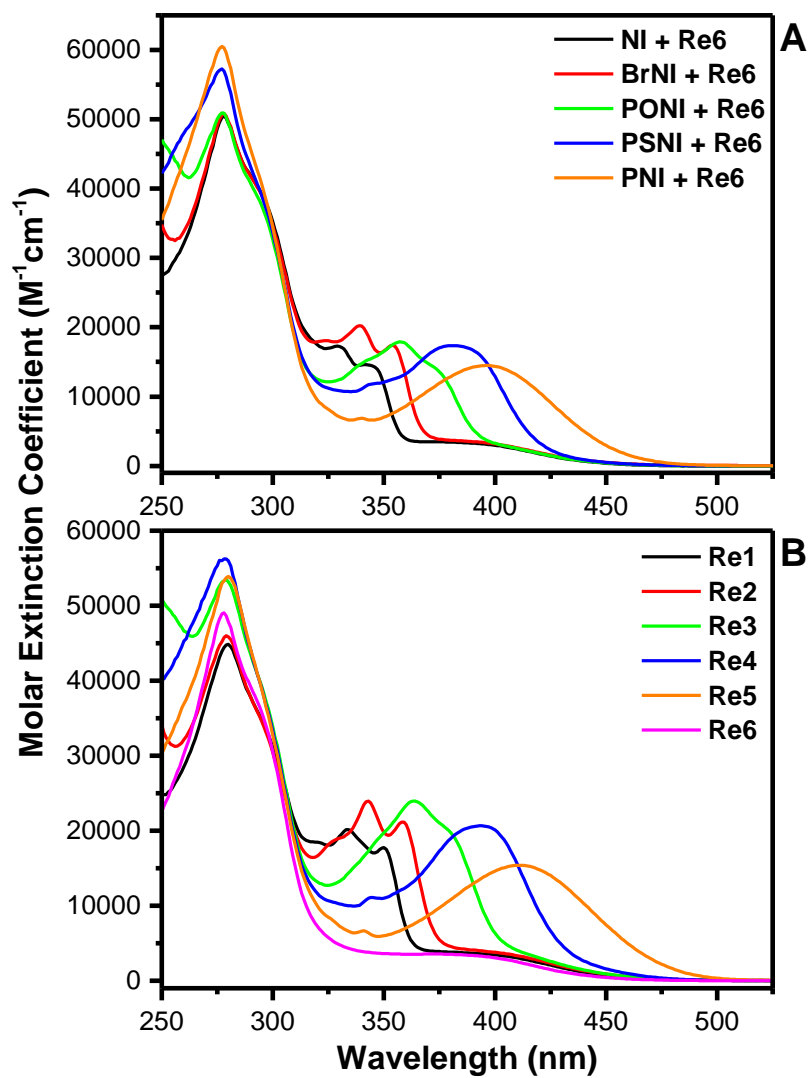


Figure A41. (a) Additive combination of electronic spectra between organic chromophore model and Re(I) model in THF. (b) Electronic spectra of **Re1-Re6** in THF.

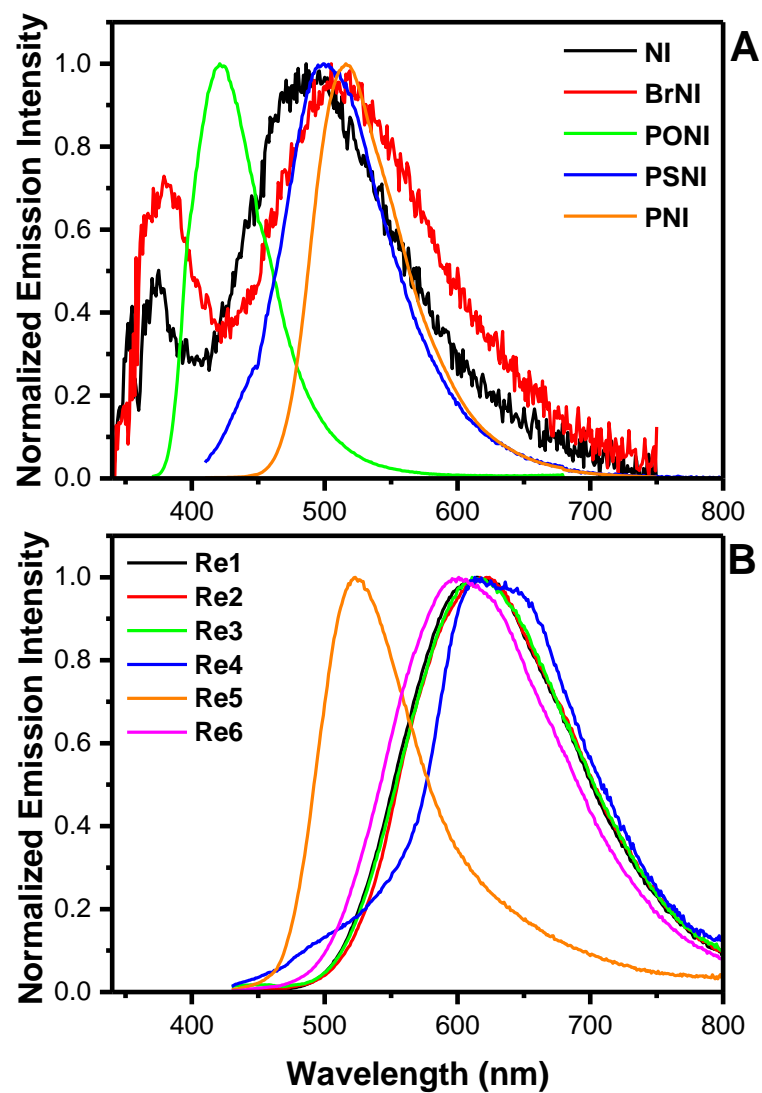


Figure A42. Photoluminescence spectra of NI, BrNI, PONI, PSNI, PNI, and Re1-Re6 in THF.

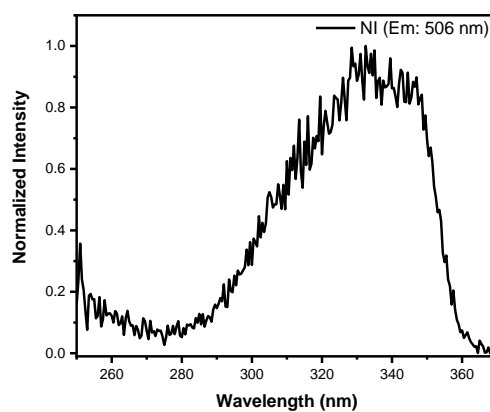
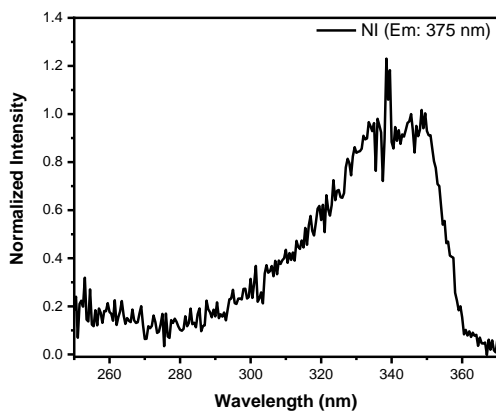


Figure A43. Excitation spectra of NI in ACN monitored at shortwave (left) and longwave (right) emission maxima.

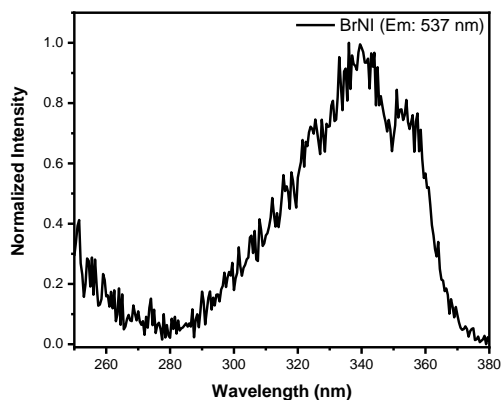
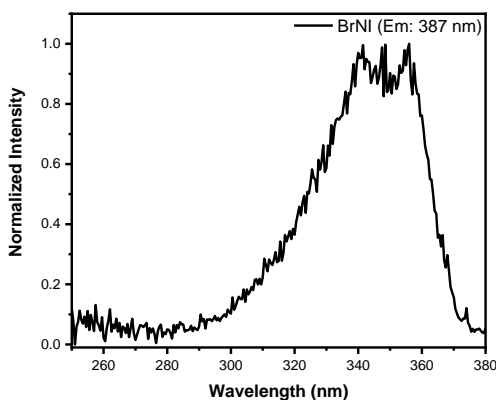


Figure A44. Excitation spectra of BrNI in ACN monitored at shortwave (left) and longwave (right) emission maxima.

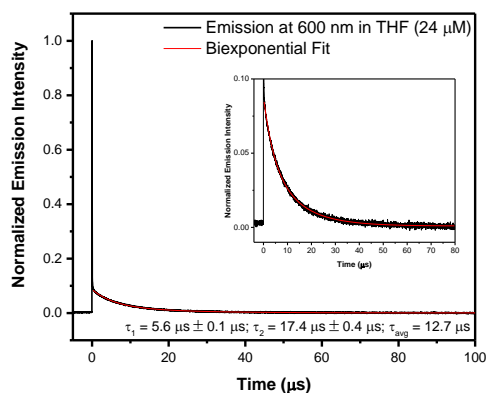
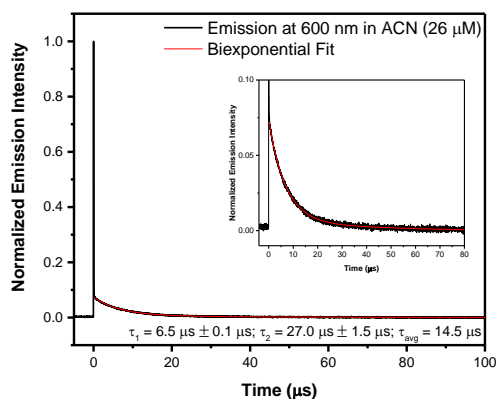


Figure A45. Photoluminescence decay of **Re1** at 600 nm in ACN (left) and THF (right). Excited at 355 nm (3 mJ/pulse).

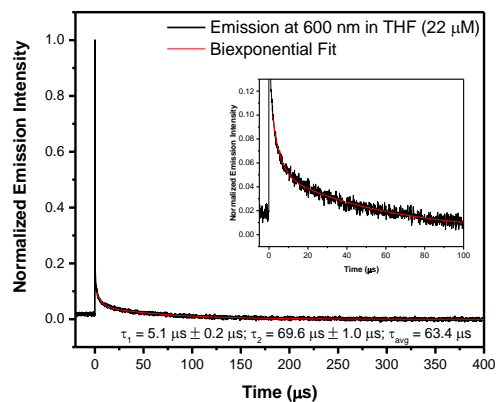
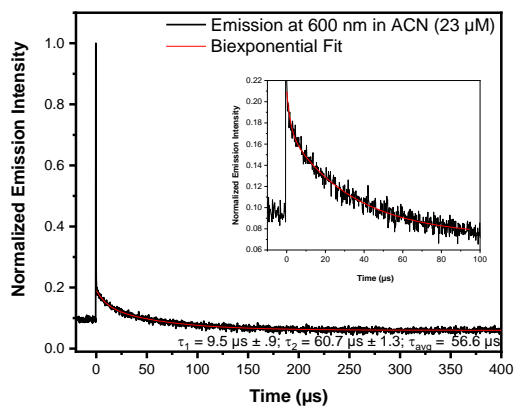


Figure A46. Photoluminescence decay of **Re2** at 600 nm in ACN (left) and THF (right). Excited at 355 nm (3 mJ/pulse).

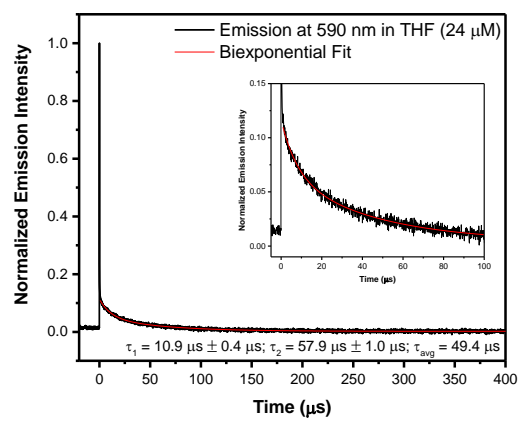
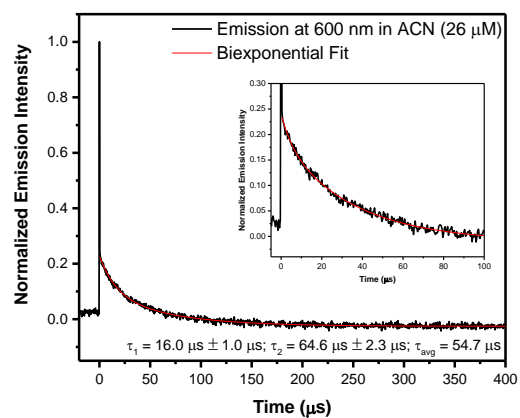


Figure A47. Photoluminescence Decay of **Re3** at 600 nm in ACN (top) and 590 nm in THF (bottom). Excited at 355 nm (3 mJ/pulse).

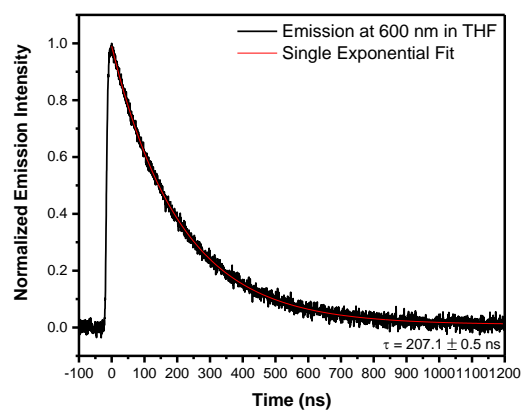
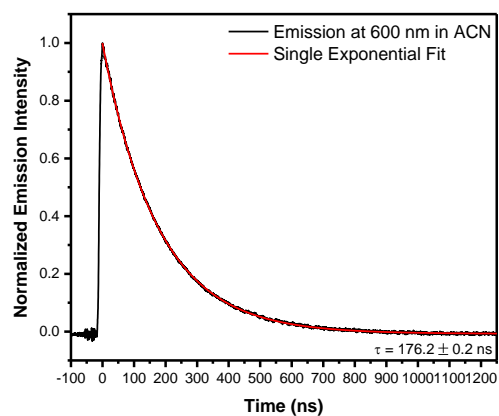


Figure A48. Photoluminescence decay of **Re6** at 600 nm in ACN (top) and THF (bottom). Excited at 410 nm (3 mJ/pulse).

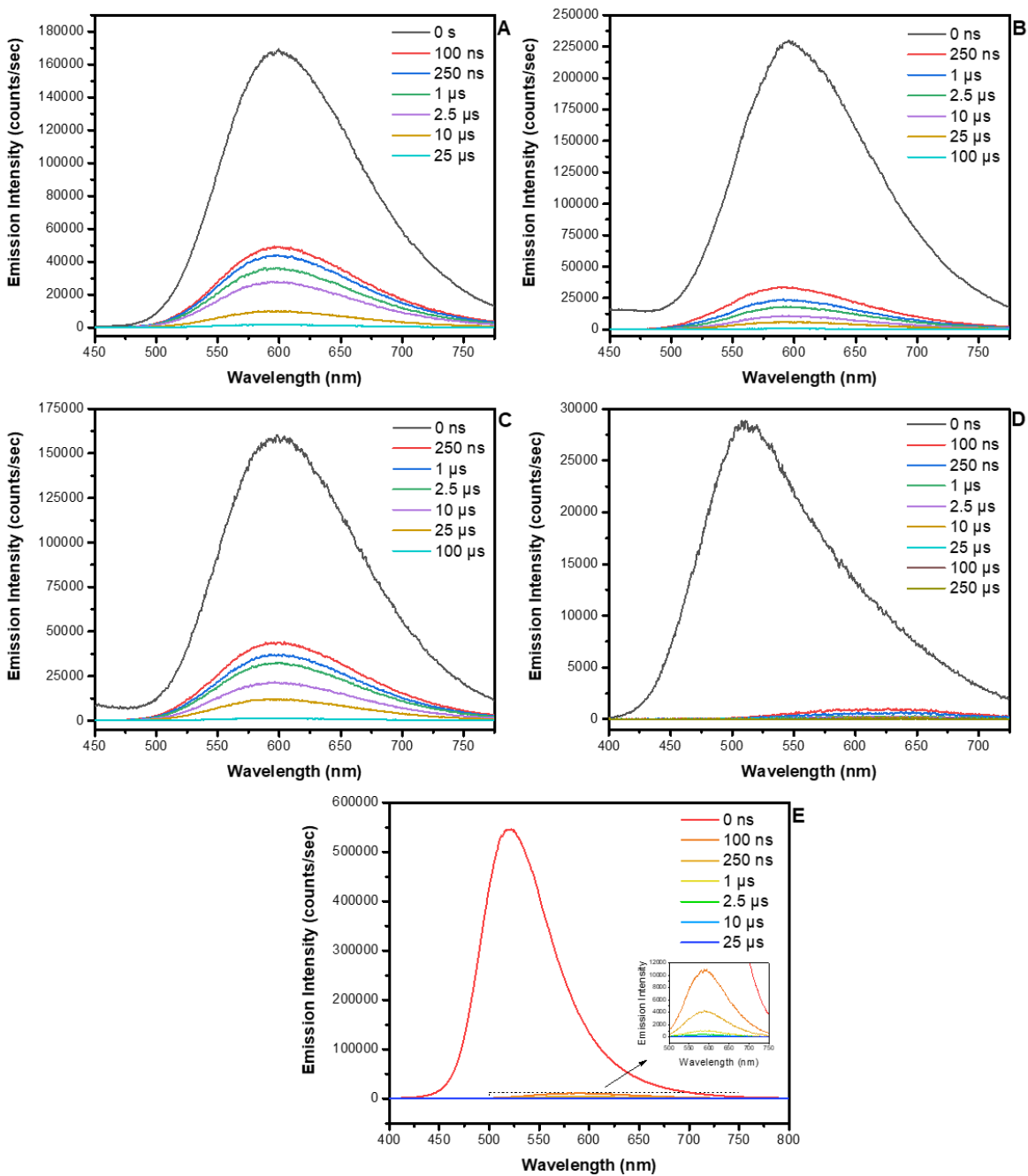


Figure A49. Time-resolved photoluminescence emission spectra of **Re1** (A), **Re2** (B), **Re3** (C), **Re4** (D), and **Re5** (E) at specified times after a 7 ns, 350 nm (**Re1-Re3**) and 400 nm (**Re4** and **Re5**) laser pulse in deaerated ACN.

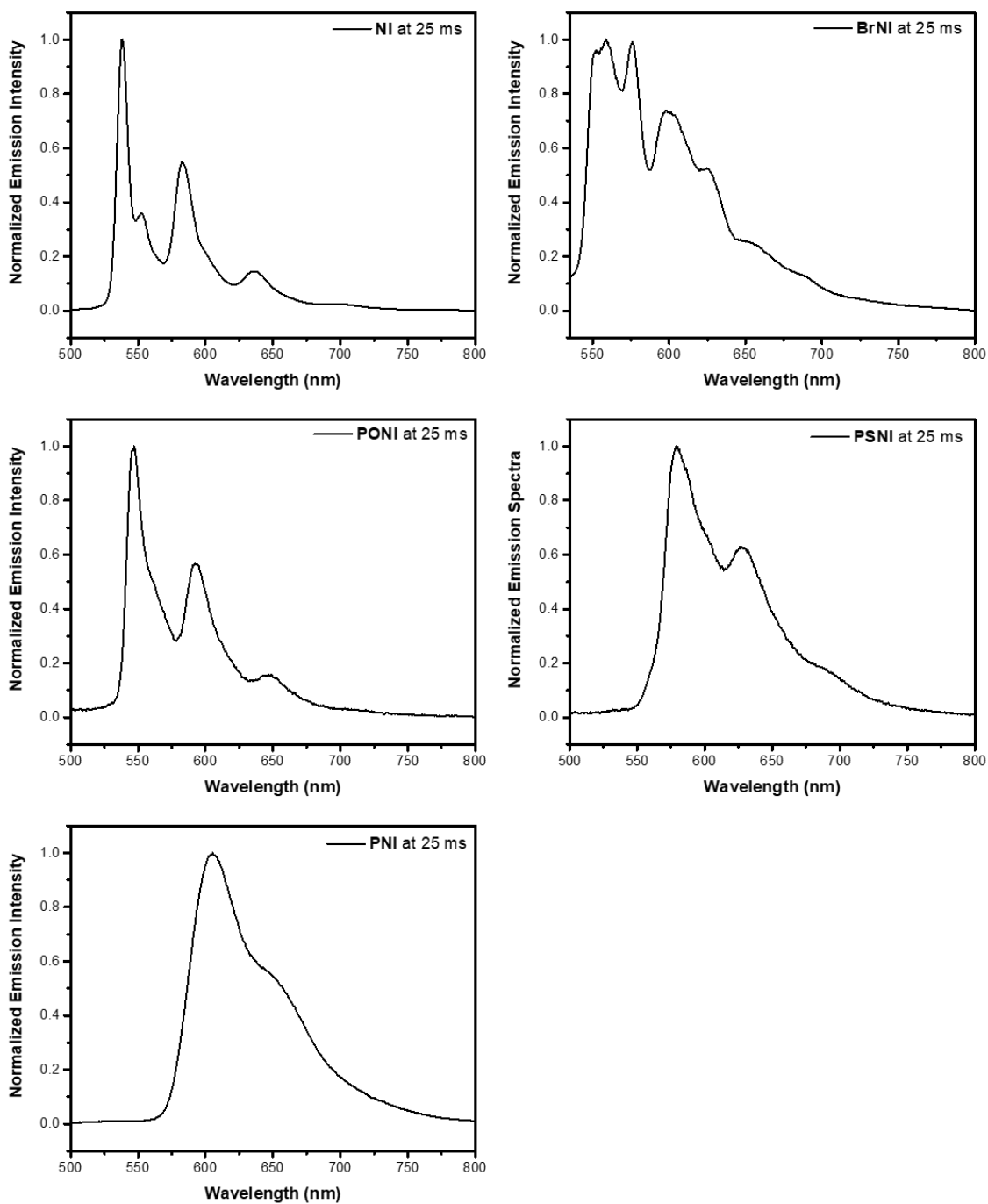


Figure A50. Time-resolved 77 K photoluminescence emission spectra of NI, BrNI, PONI, PSNI, and PNI at 25 ms after a 7 ns, 400 nm laser pulse in 2-methyl THF with 10% ethyl iodide.

A.3. Additional Transient Absorption Spectra

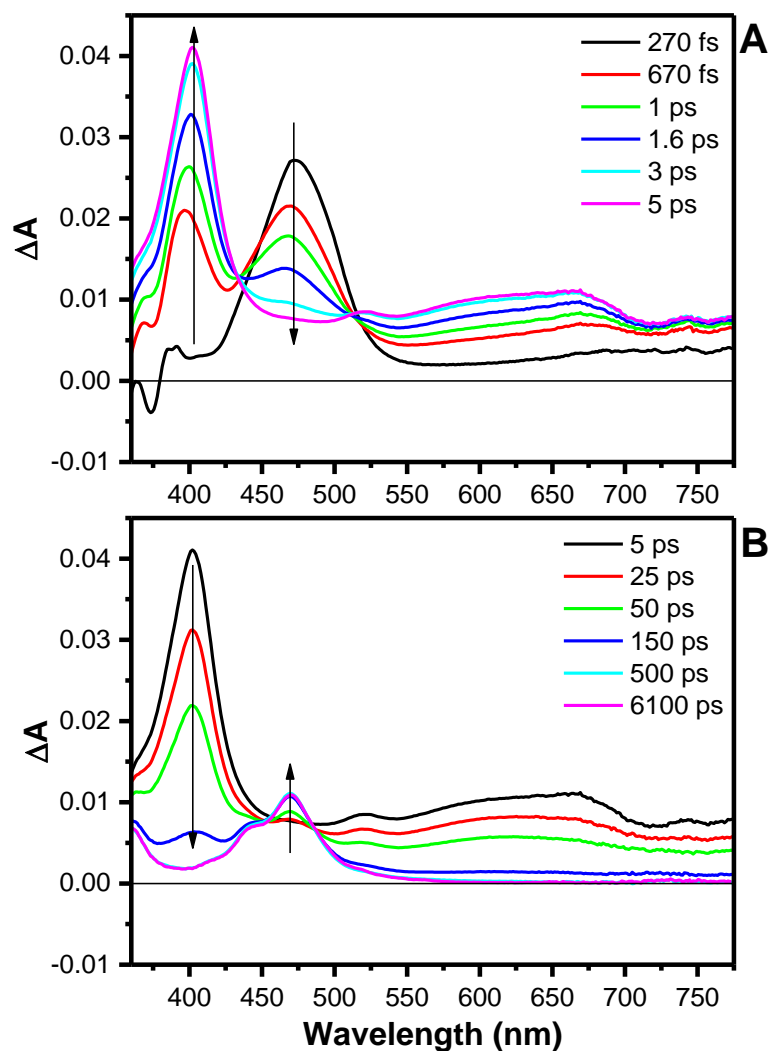


Figure A51. Excited-state absorption difference spectra of NI in ACN during short delay times (A) and long delay times (B) following 350 nm pulsed excitation (105 fs fwhm).

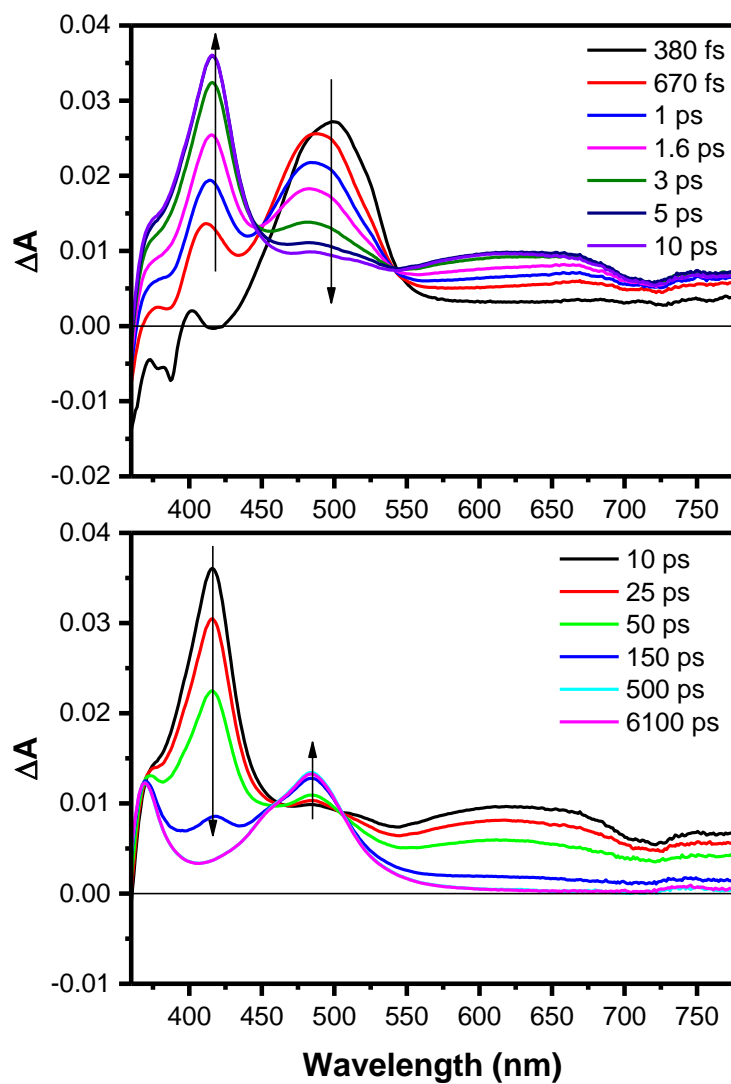


Figure A52. Excited-state absorption difference spectra of **BrNI** in ACN during short delay times (A) and long delay times (B) following 350 nm pulsed excitation (105 fs fwhm).

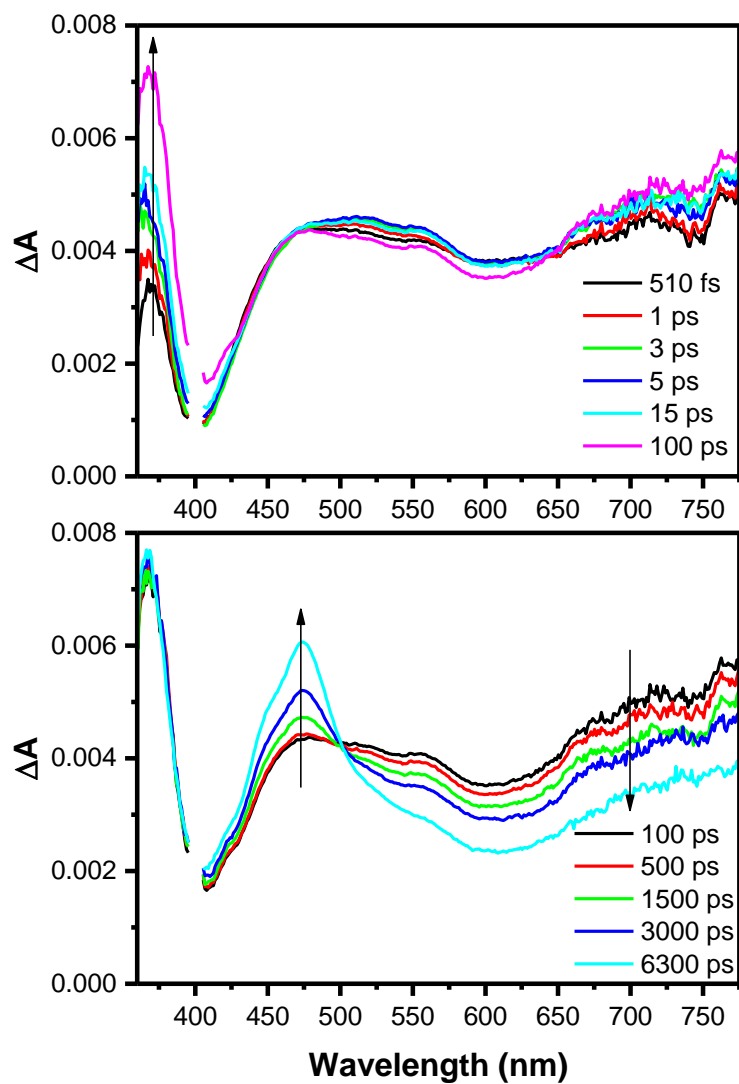


Figure A53. Excited-state absorption difference spectra of **Re1** in ACN during short delay times (A) and long delay times (B) following 400 nm pulsed excitation (105 fs fwhm).

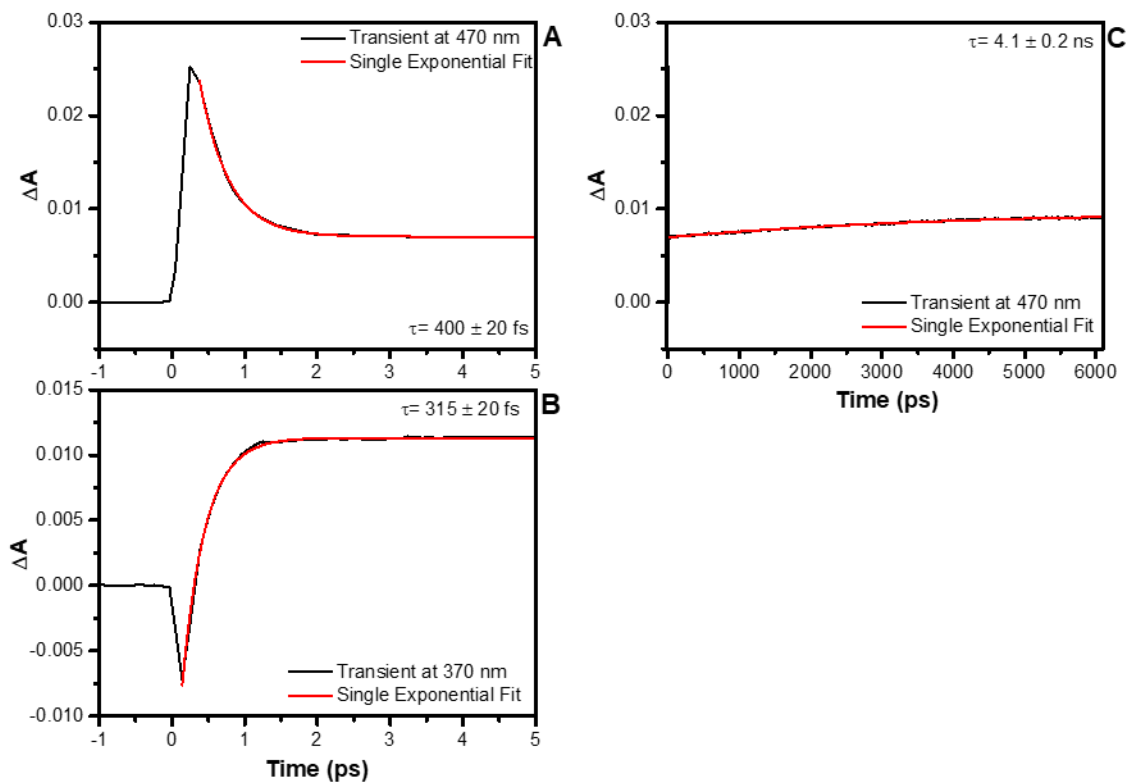


Figure A54. Ultrafast transient absorption kinetic data of **Re1** in ACN following 350 nm pulsed excitation. (A) Single wavelength kinetic analysis at 470 nm. (B) Single wavelength kinetic analysis at 370 nm. (C) Single wavelength kinetic analysis at 470 nm.

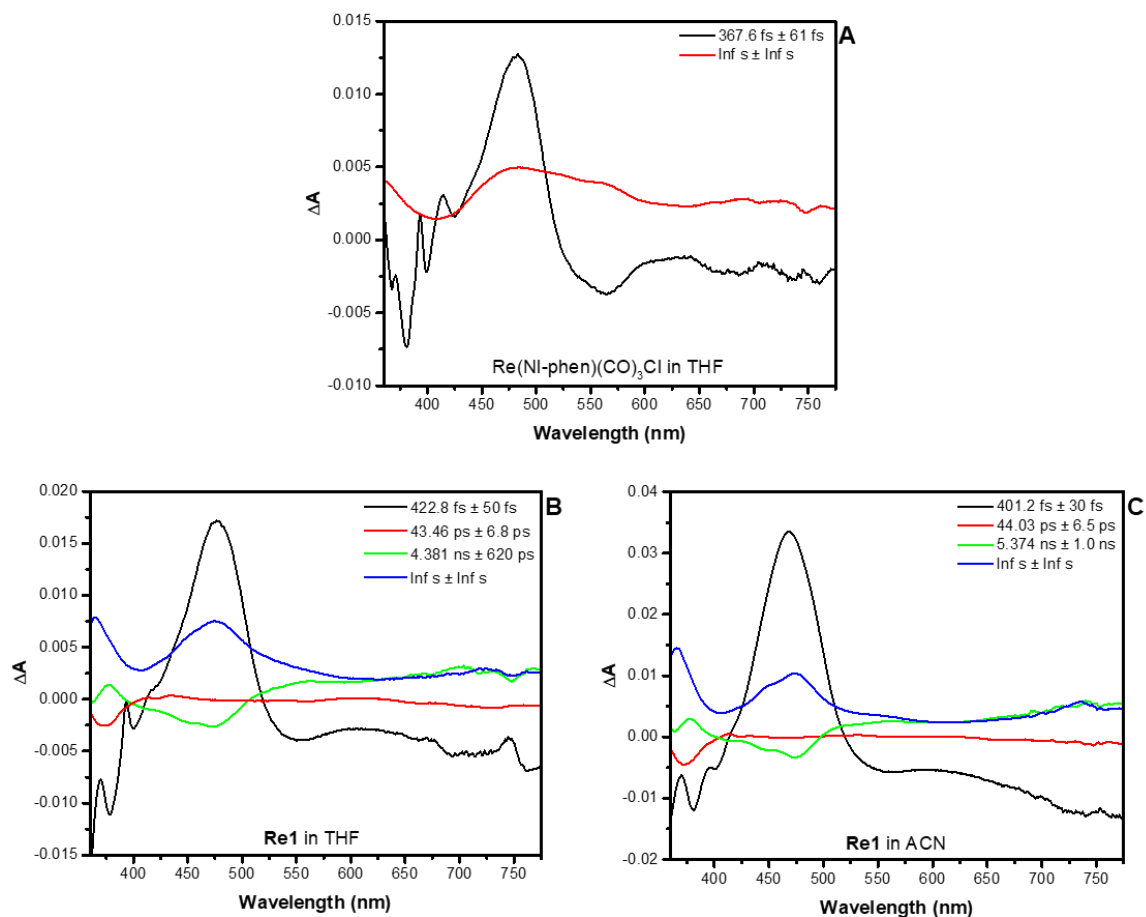


Figure A55. Global fit spectral analysis of ultrafast transient absorption data of Re(NI-phen)(CO)₃Cl in THF (A), **Re1** in THF (B), and **Re1** in ACN (C) following 350 nm pulsed excitation.

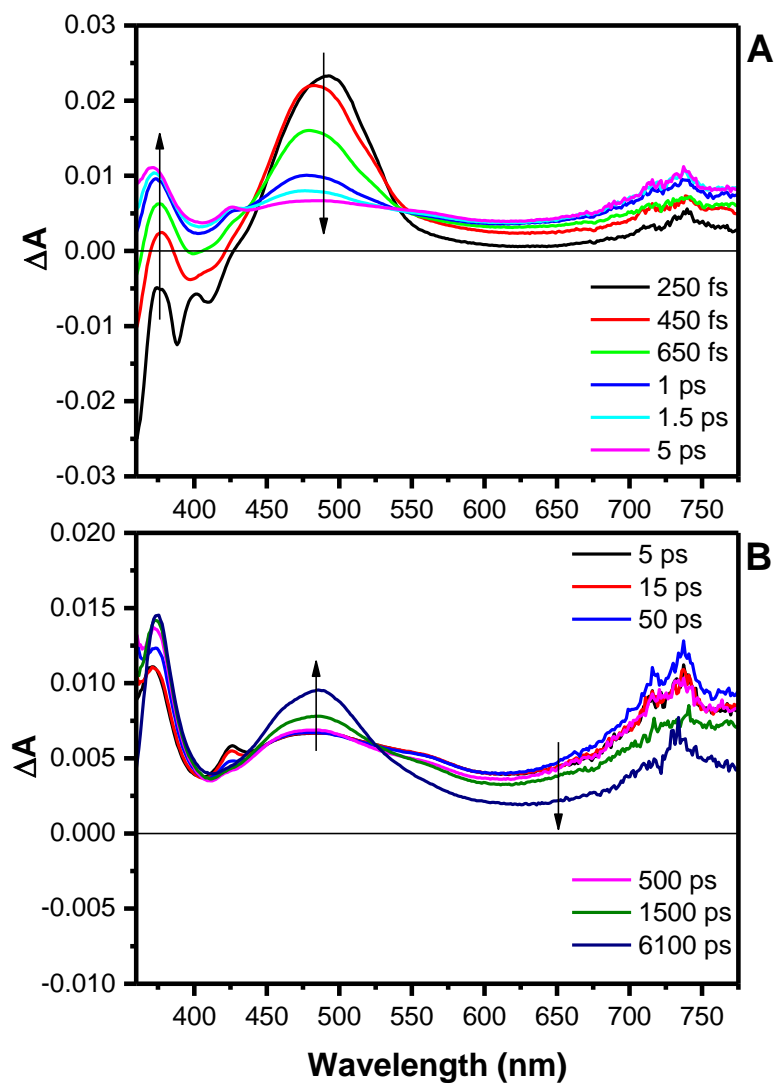


Figure A56. Excited-state absorption difference spectra of **Re2** in ACN during short delay times (A) and long delay times (B) following 350 nm pulsed excitation (105 fs fwhm).

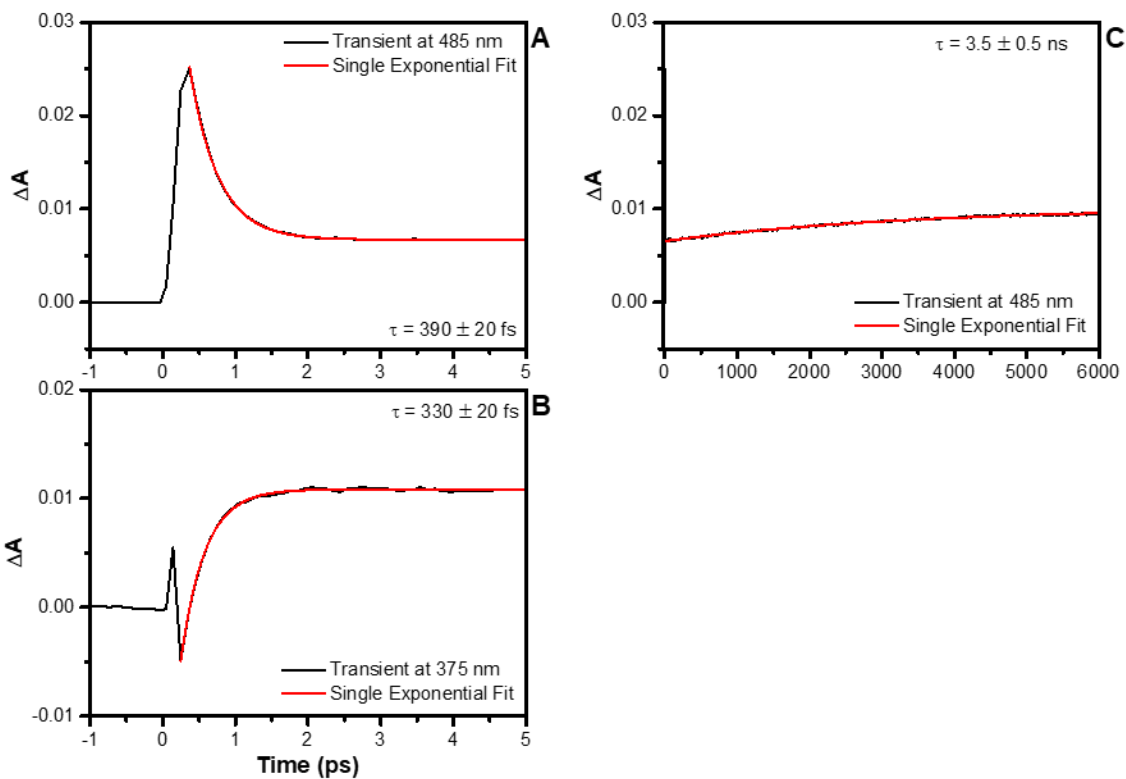


Figure A57. Ultrafast transient absorption kinetic data of **Re2** in ACN following 350 nm pulsed excitation. (A) Single wavelength kinetic analysis at 485 nm. (B) Single wavelength kinetic analysis at 375 nm. (C) Single wavelength kinetic analysis at 485 nm.

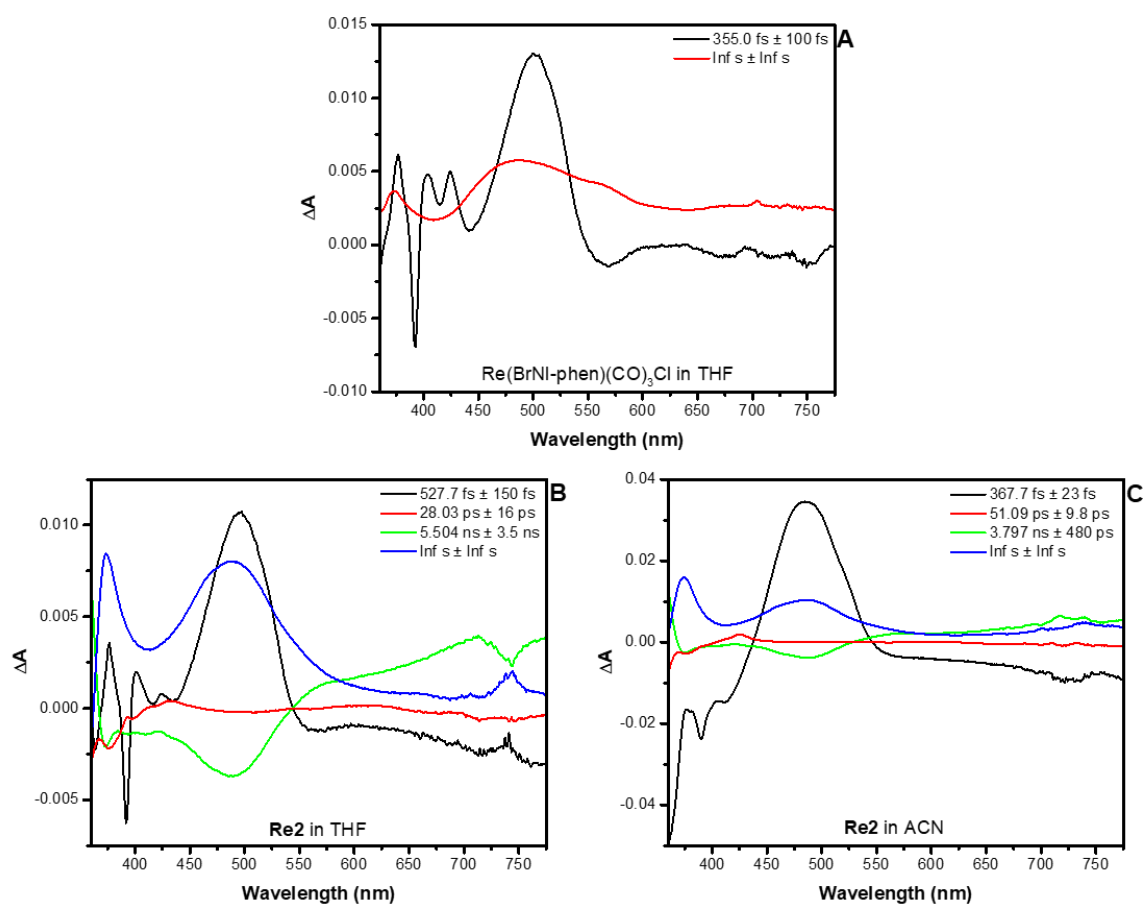


Figure A58. Global fit spectral analysis of ultrafast transient absorption data $\text{Re}(\text{BrNi-phen})(\text{CO})_3\text{Cl}$ in THF (A), Re_2 in THF (B), and Re_2 in ACN (C) following 350 nm pulsed excitation.

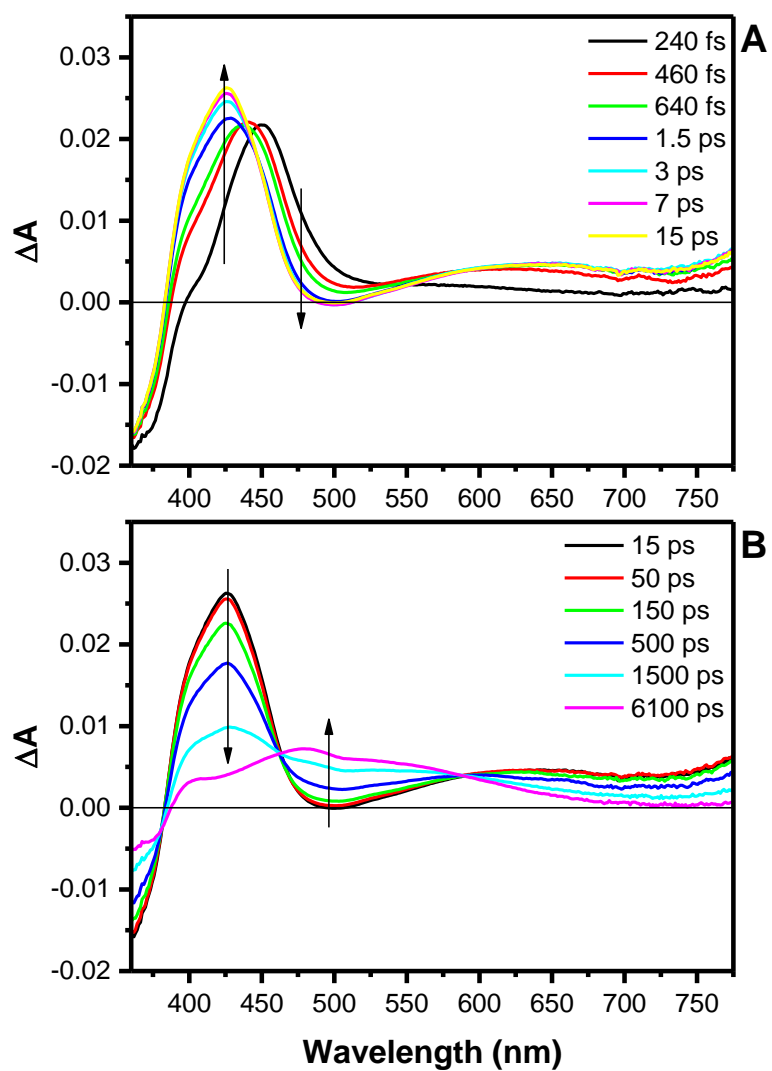


Figure A59. Excited-state absorption difference spectra of PONI in ACN during short delay times (A) and long delay times (B) following 350 nm pulsed excitation (105 fs fwhm).

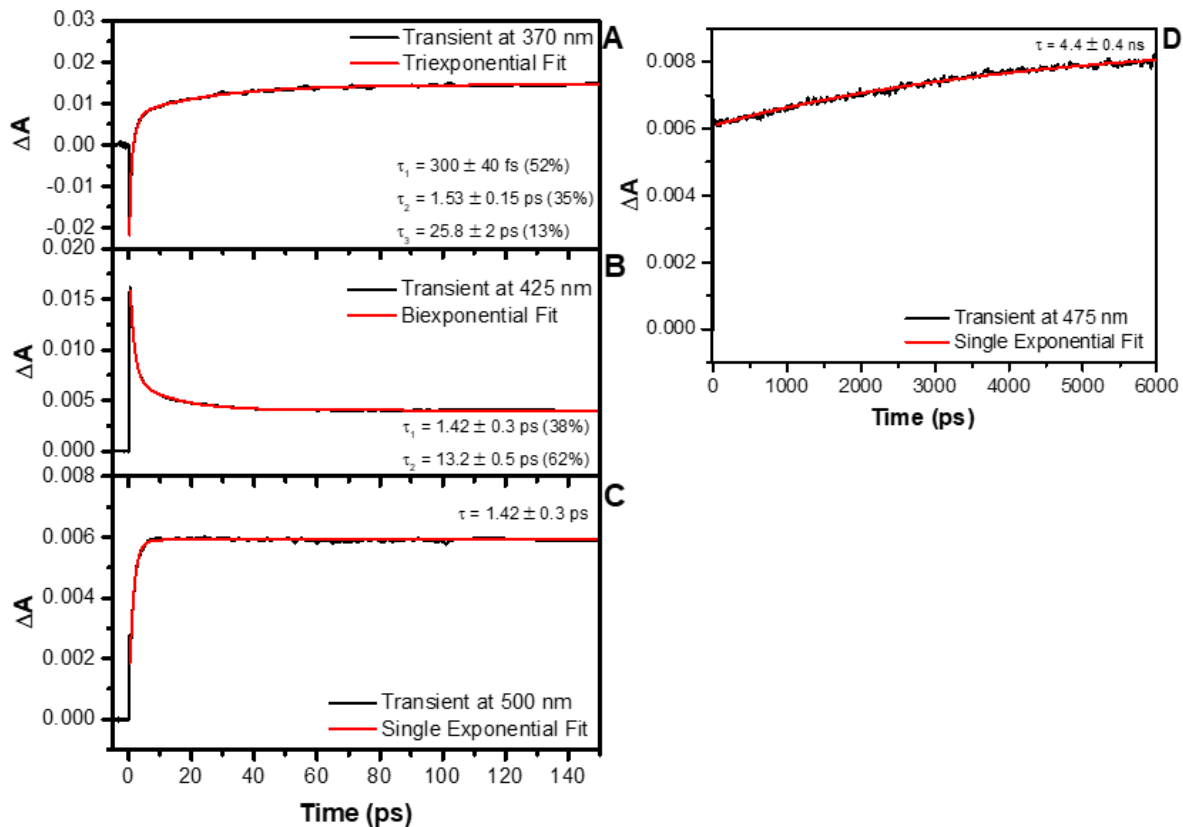


Figure A60. Ultrafast transient absorption kinetic data of **Re3** in ACN following 350 nm pulsed excitation. (A) Single wavelength kinetic analysis at 370 nm. (B) Single wavelength kinetic analysis at 425 nm. (C) Single wavelength kinetic analysis at 500 nm. (D) Single wavelength kinetic analysis at 475 nm.

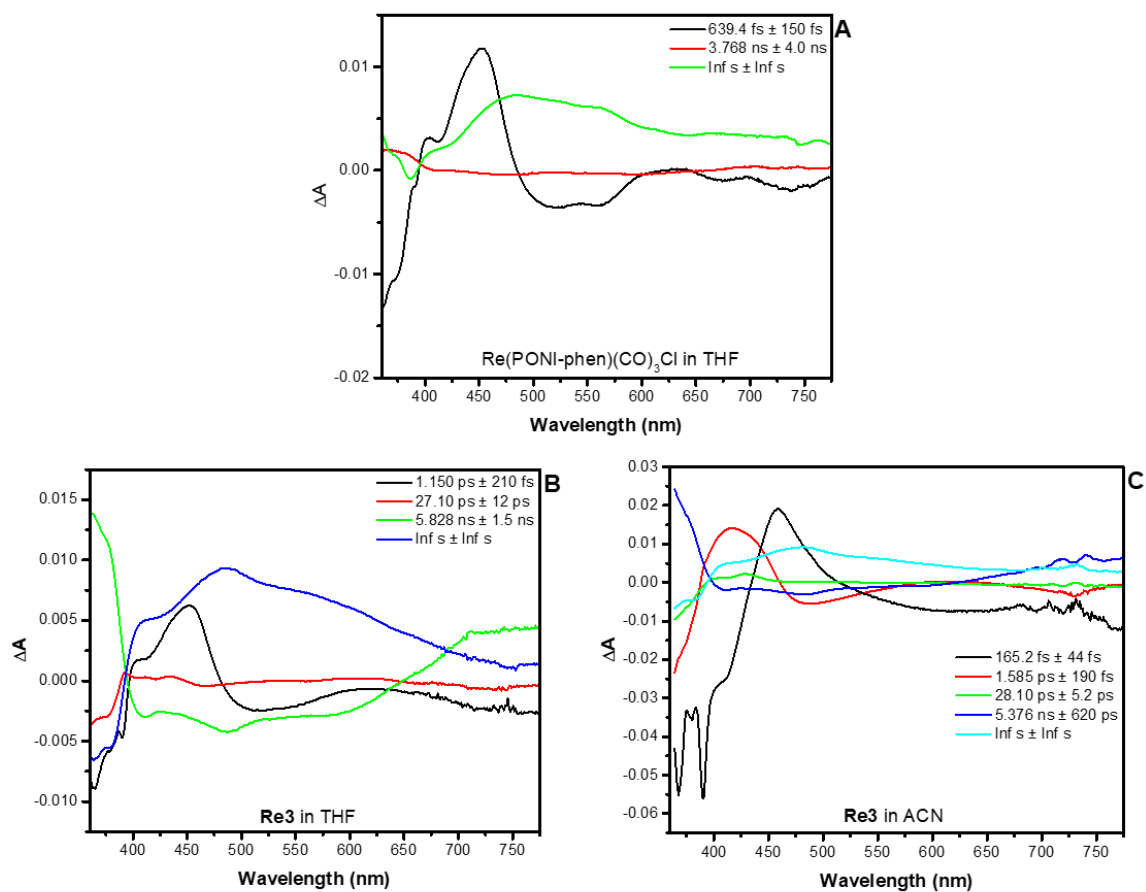


Figure A61. Global fit spectral analysis of ultrafast transient absorption data of Re(PONI-phen)(CO)₃Cl in THF (A), **Re₃** in THF (B), and **Re₃** in ACN (C) following 350 nm pulsed excitation.

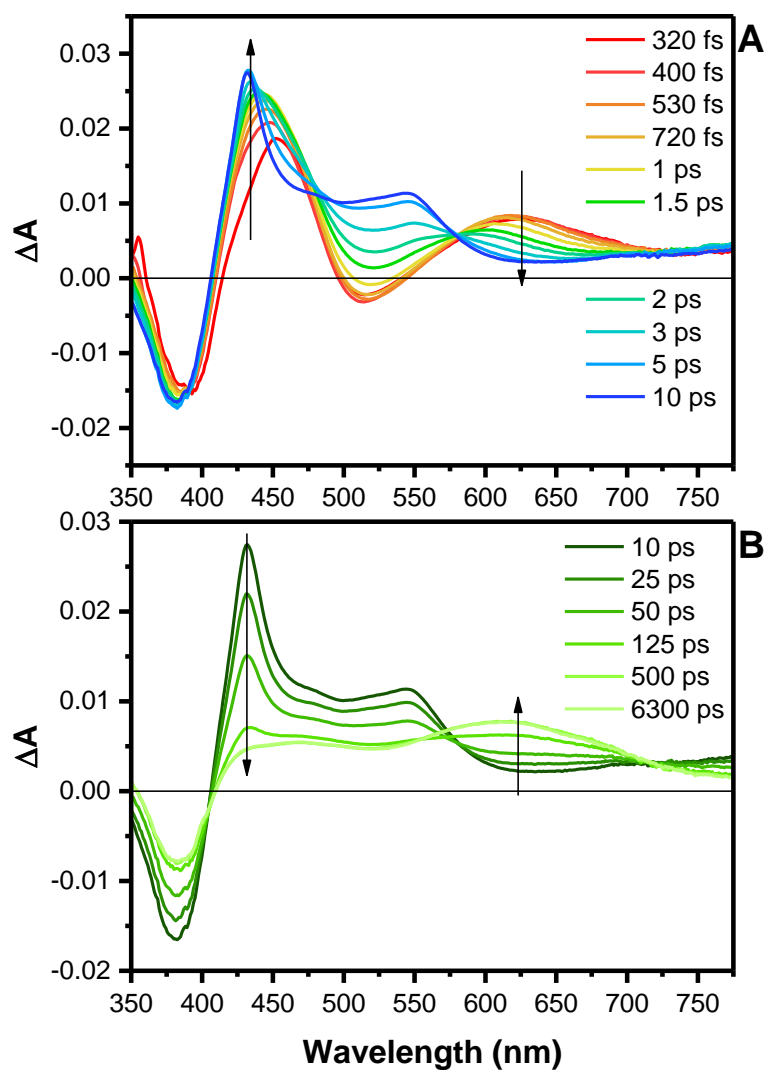


Figure A62. Excited-state absorption difference spectra of **PSNI** in ACN during short delay times (A) and long delay times (B) following 400 nm pulsed excitation (105 fs fwhm).

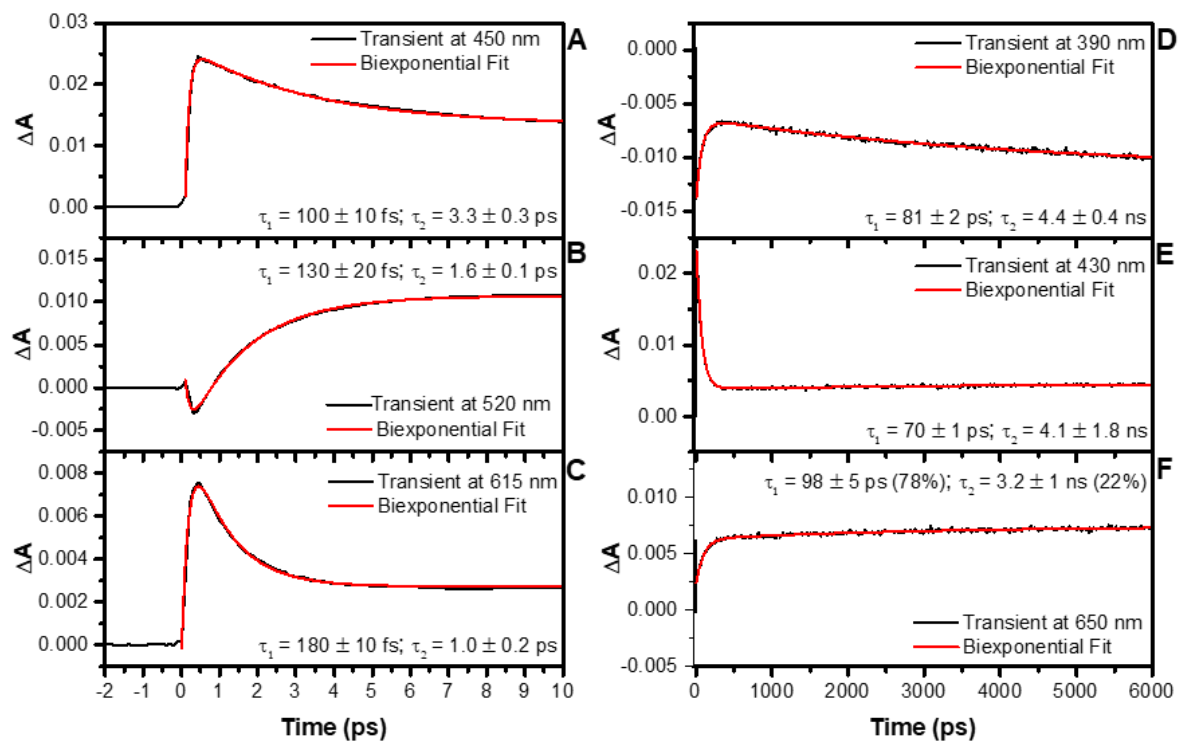


Figure A63. Ultrafast transient absorption kinetic data of **Re4** in ACN following 400 nm pulsed excitation. Single wavelength kinetic analysis at 450 nm (A), 520 nm (B), and 615 (C) at short time after the laser pulse. Single wavelength kinetic analysis at 390 nm (D), 430 nm (E), and 650 (F) at longer time after the laser pulse.

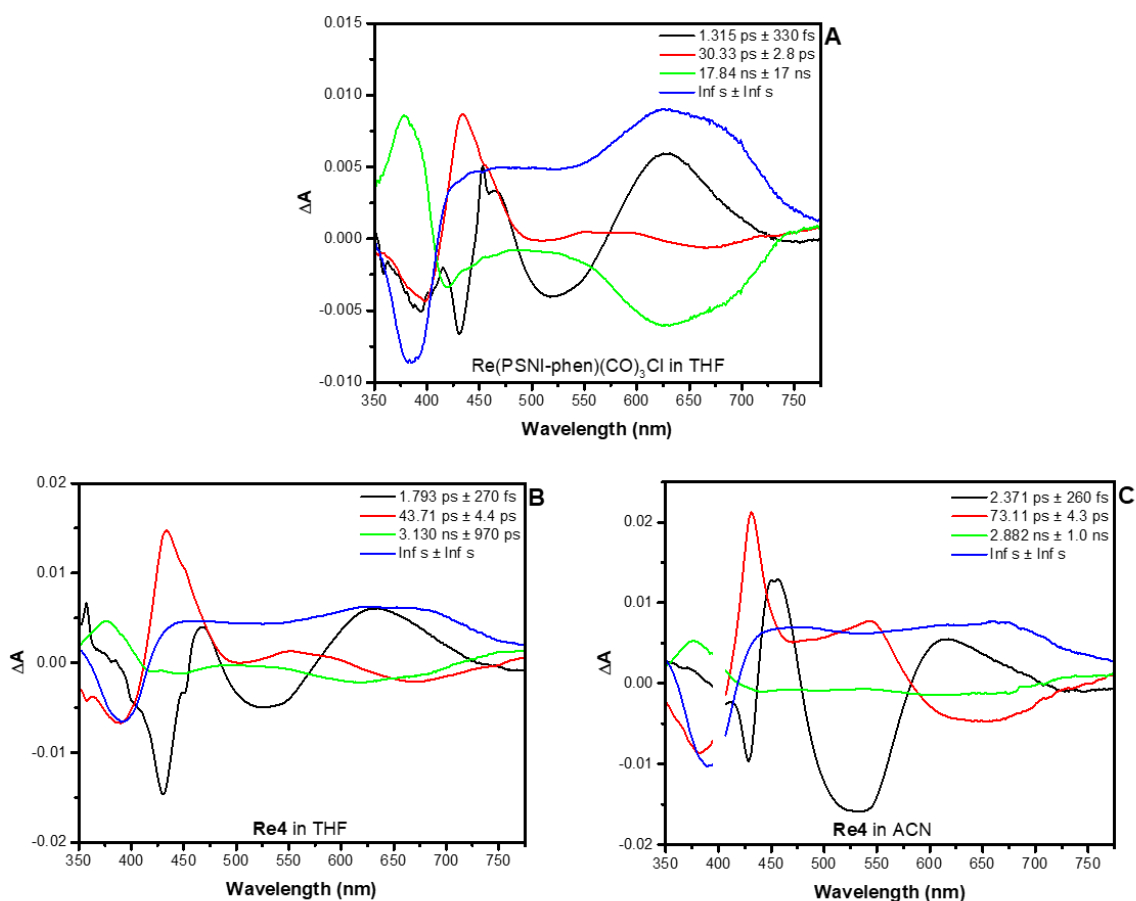


Figure A64. Global fit spectral analysis of ultrafast transient absorption data of Re(PSNI-phen)(CO)₃Cl in THF (A), **Re4** in THF (B), and **Re4** in ACN (C) following 400 nm pulsed excitation.

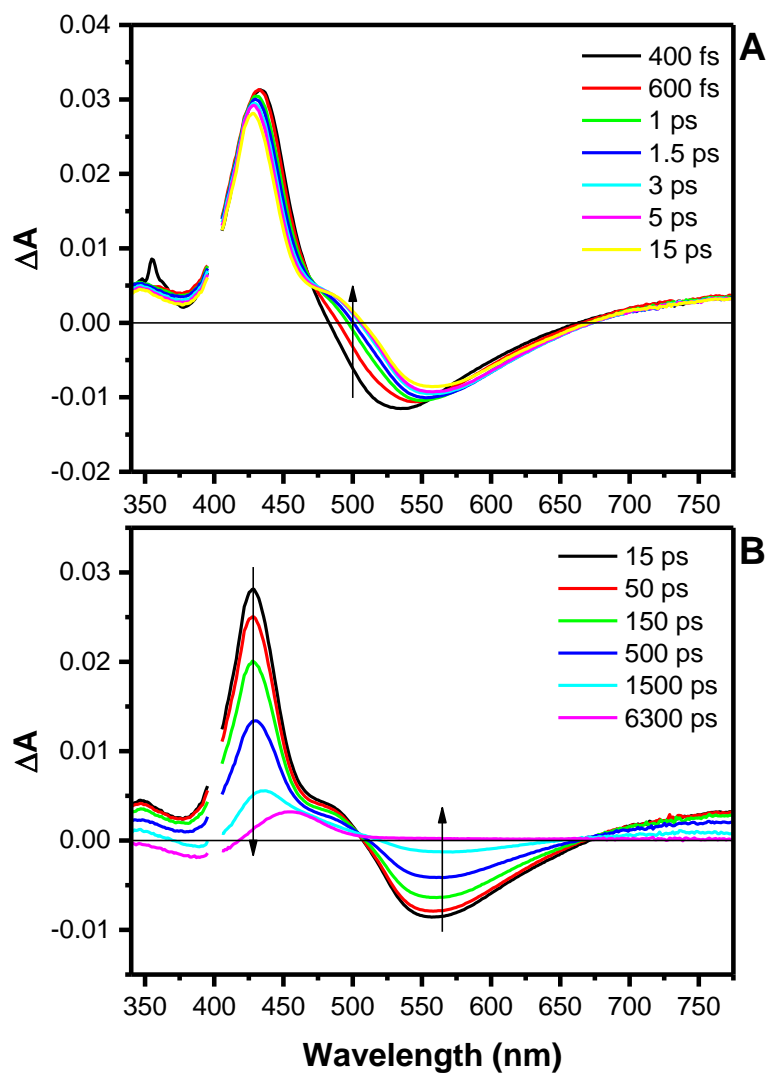


Figure A65. Excited-state absorption difference spectra of **PNI** in ACN during short delay times (A) and long delay times (B) following 400 nm pulsed excitation (105 fs fwhm).

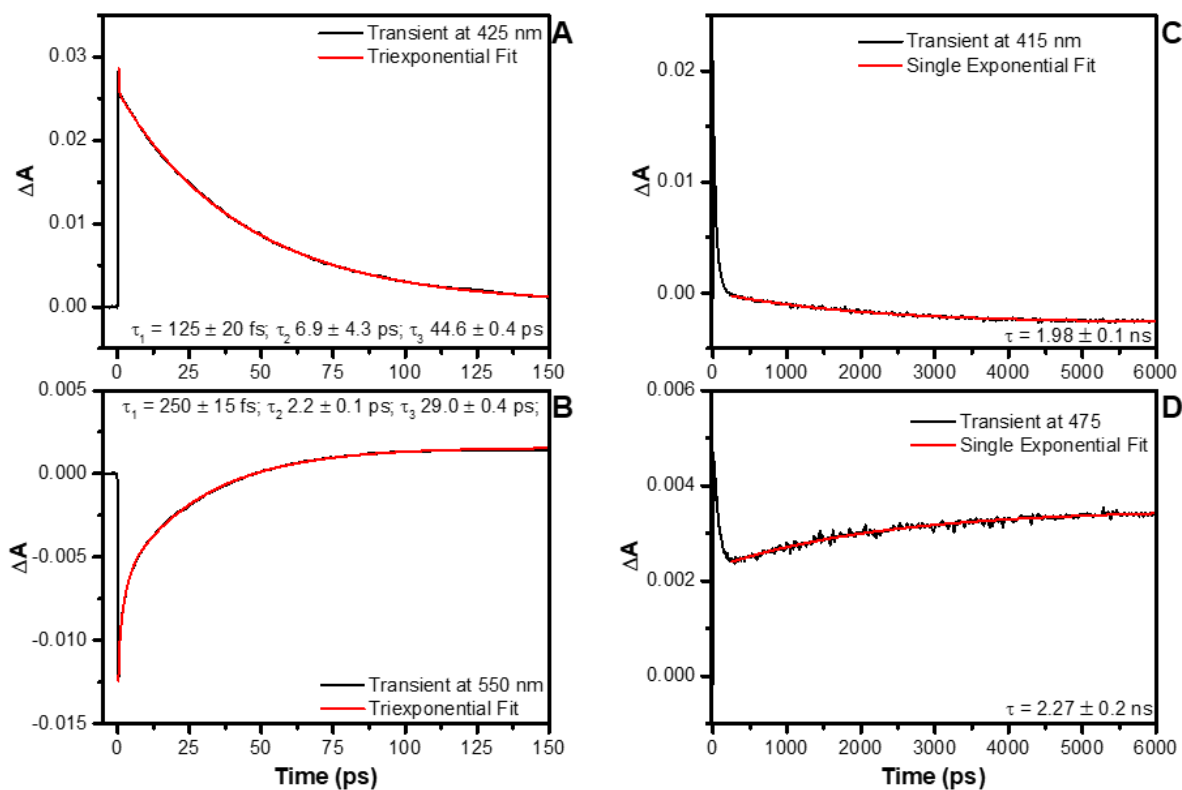


Figure A66. Ultrafast transient absorption kinetic data of **Re5** in ACN following 400 nm pulsed excitation. Single wavelength kinetic analysis at 425 nm (A) and 550 nm (B) at short time after the laser pulse. Single wavelength kinetic analysis at 415 nm (C) and 475 nm (D) at longer time after the laser pulse.

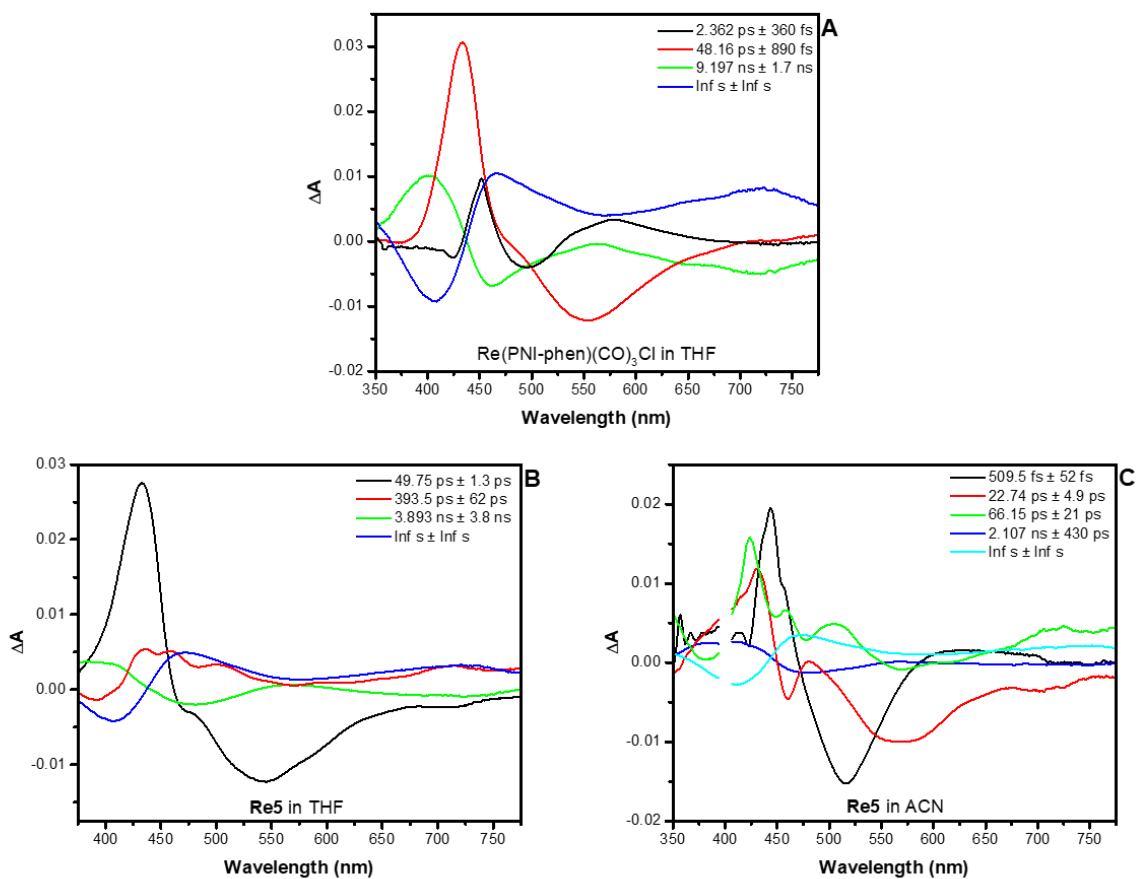


Figure A67. Global fit spectral analysis of ultrafast transient absorption data of Re(PNI-phen)(CO)₃Cl in THF (A), **Re5** in THF (B), and **Re5** in ACN (C) following 400 nm pulsed excitation.

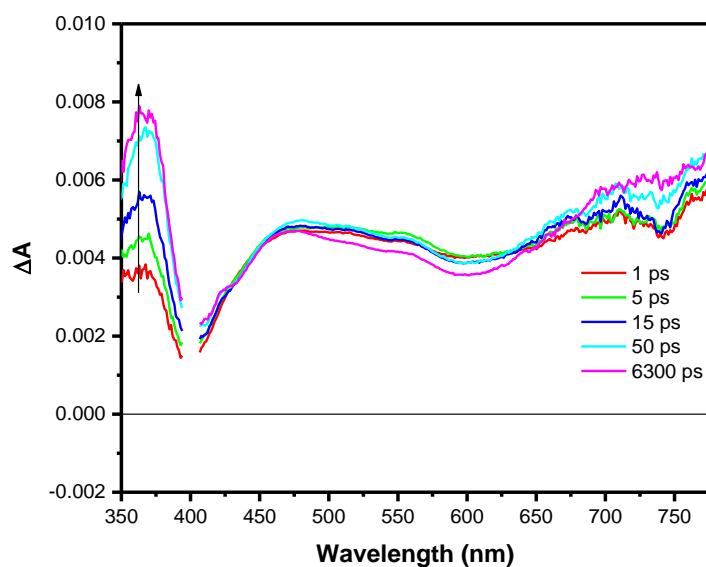


Figure A68. Excited-state absorption difference spectra of **Re6** in ACN following 400 nm pulsed excitation (105 fs fwhm).

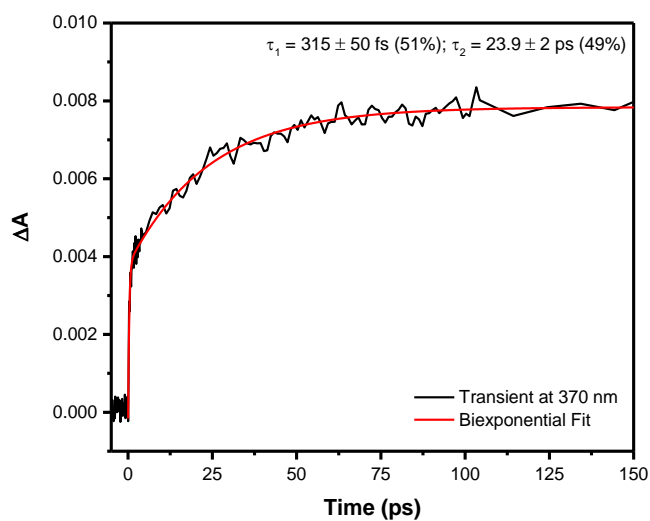


Figure A69. Ultrafast transient absorption kinetic data of **Re6** in ACN following 400 nm pulsed excitation.

Table A1. Summary of time constants from UFTA global fit analysis.

Molecule	Solvent	τ_1 (ps)	τ_2 (ps)	τ_3 (ps)	τ_4 (ns)
Re(NI-phen)(CO) ₃ Cl	THF	0.04 ± 0.05	0.37 ± 0.06		
[Re(NI-phen)(CO) ₃ (dmap)](PF ₆)	THF	0.07 ± 0.03	0.42 ± 0.05	43.5 ± 6.8	4.4 ± 0.6
	ACN	0.40 ± 0.03		44.0 ± 6.5	5.4 ± 1.0
Re(BrNI-phen)(CO) ₃ Cl	THF	0.36 ± 0.1			
[Re(BrNI-phen)(CO) ₃ (dmap)](PF ₆)	THF		0.53 ± 0.15	28 ± 16	5.5 ± 3.5
	ACN	0.37 ± 0.02		51.1 ± 9.8	3.8 ± 0.5
Re(PONI-phen)(CO) ₃ Cl	THF	0.64 ± 0.15			3.8 ± 4.0
[Re(PONI-phen)(CO) ₃ (dmap)](PF ₆)	THF		1.2 ± 0.2	27 ± 12	5.8 ± 1.5
	ACN	0.17 ± 0.04	1.6 ± 0.2	28.1 ± 5.2	5.4 ± 0.6
Re(PSNI-phen)(CO) ₃ Cl	THF	0.12 ± 0.05	1.3 ± 0.3	30.3 ± 2.8	17.8 ± 17
[Re(PSNI-phen)(CO) ₃ (dmap)](PF ₆)	THF		1.8 ± 0.3	43.7 ± 4.4	3.1 ± 1.0
	ACN		2.4 ± 0.3	73.1 ± 4.3	2.9 ± 1.0
Re(PNI-phen)(CO) ₃ Cl	THF	0.16 ± 0.05	2.4 ± 0.4	48.2 ± 0.9	9.2 ± 1.7
[Re(PNI-phen)(CO) ₃ (dmap)](PF ₆)	THF		49.8 ± 1.3	394 ± 62	3.9 ± 3.8
	ACN	0.51 ± 0.05	22.7 ± 4.9	66.2 ± 21	2.1 ± 0.4

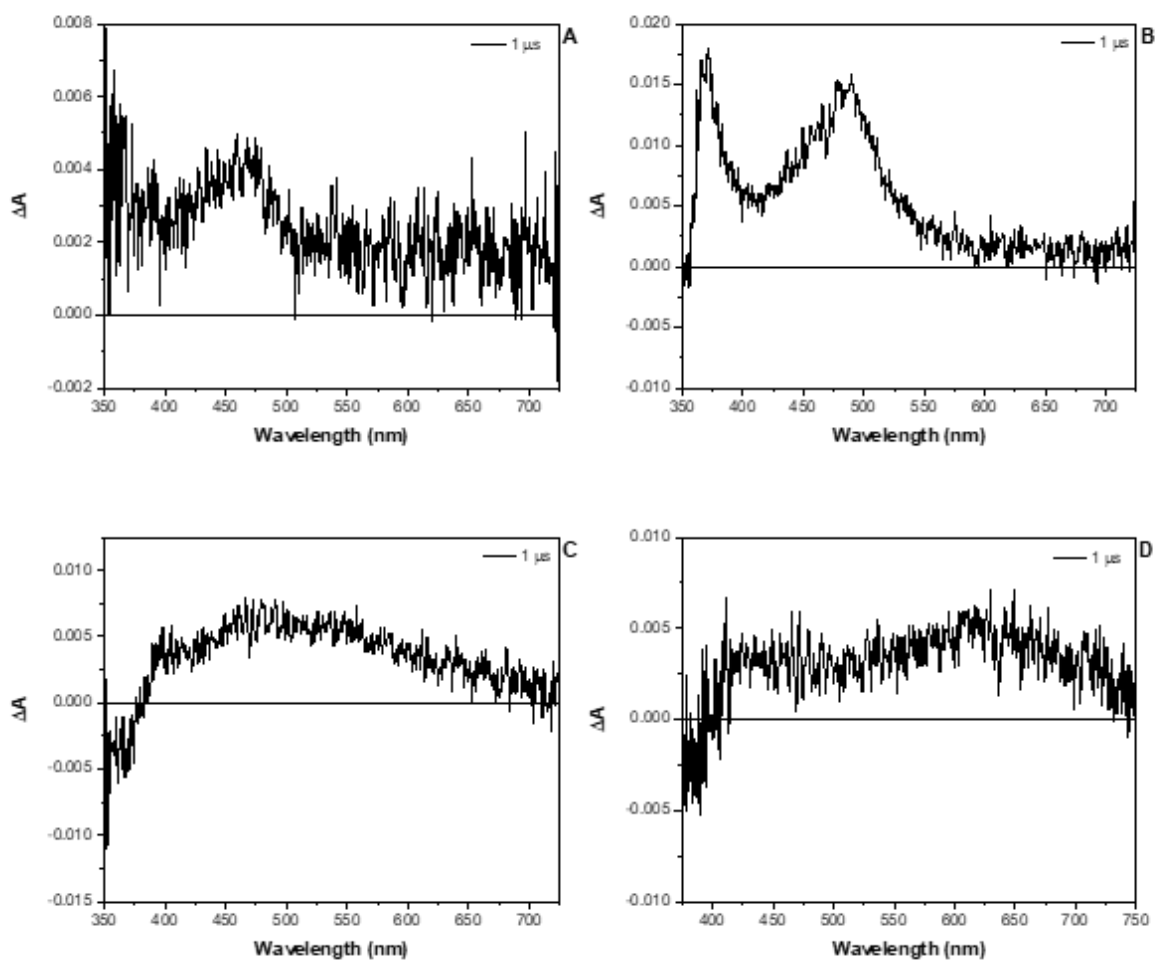


Figure A70. Excited-state absorption difference spectra of NI (A), BrNI (B), PONI (C), and PSNI (D) in ACN following 350 nm pulsed excitation (3 mJ/pulse, 7 ns fwhm).

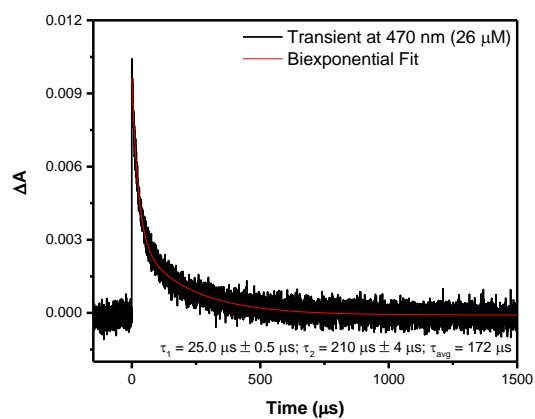


Figure A71. Transient absorption decay of **NI** in ACN. Excited at 355 nm (3 mJ/pulse).

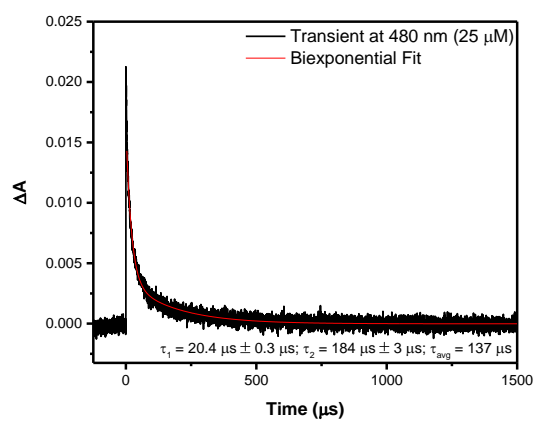


Figure A72. Transient absorption decay of **BrNI** in ACN. Excited at 355 nm (3 mJ/pulse).

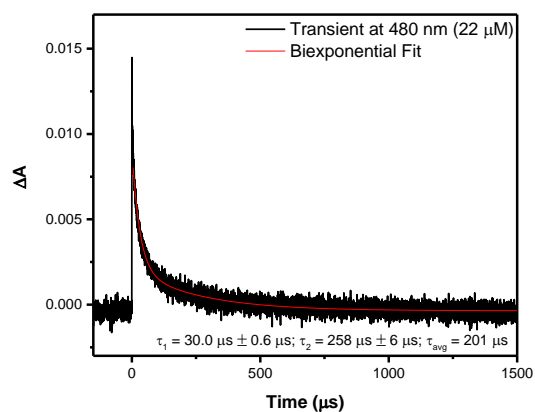


Figure A73. Transient absorption decay of **PONI** in ACN. Excited at 355 nm (3 mJ/pulse).

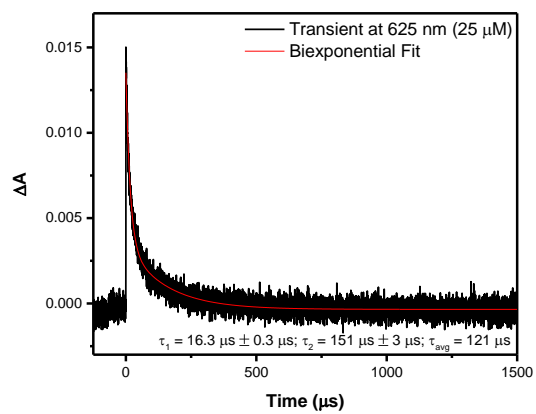


Figure A74. Transient absorption decay of **PSNI** in ACN. Excited at 355 nm (3 mJ/pulse).

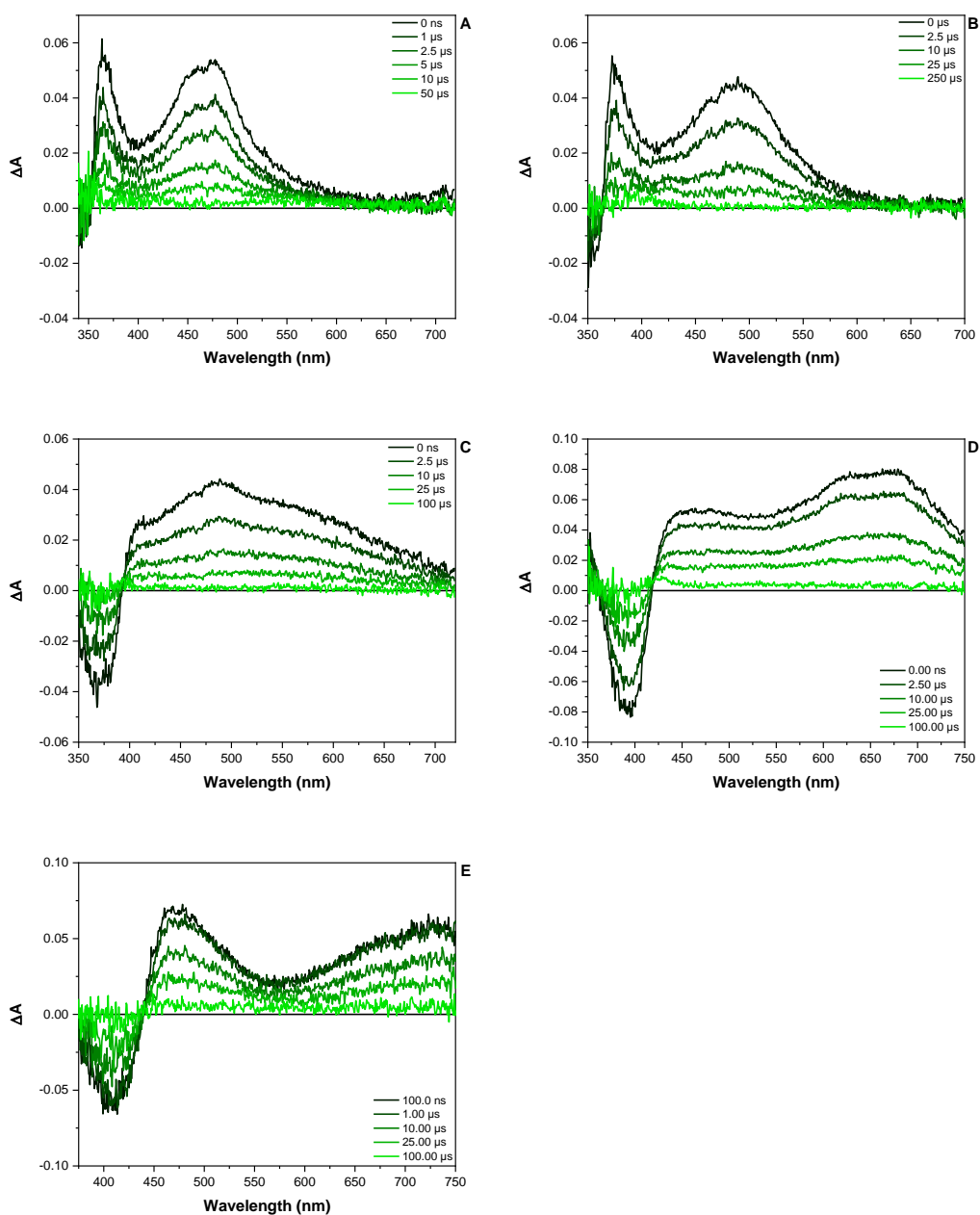


Figure A75. Excited-state absorption difference spectra of **Re1** (A), **Re2** (B), **Re3** (C), **Re4** (D), and **Re5** (E) in THF. **Re1-3** were excited using a Continuum Minilite with 355 nm pulsed excitation (3.4 mJ/pulse, 5 ns fwhm). **Re4-5** were excited using the OPOTEK with 410 nm pulsed excitation (3 mJ/pulse, 7 ns fwhm).

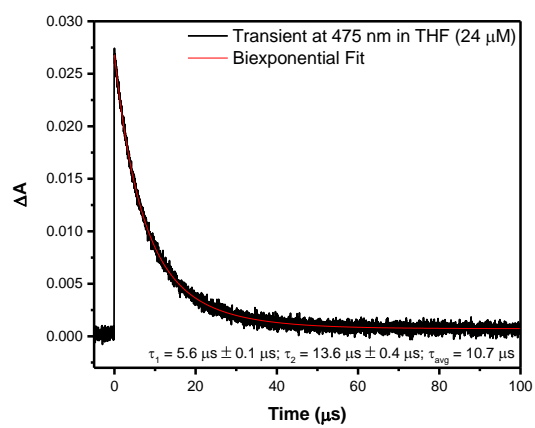
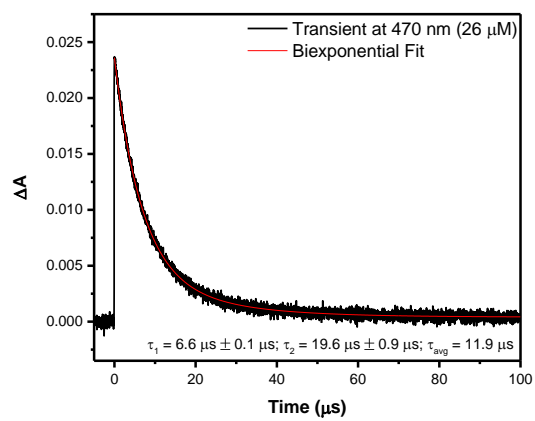


Figure A76. Transient absorption decay of **Re1** in ACN (top) and THF (bottom). Excited at 355 nm (3 mJ/pulse).

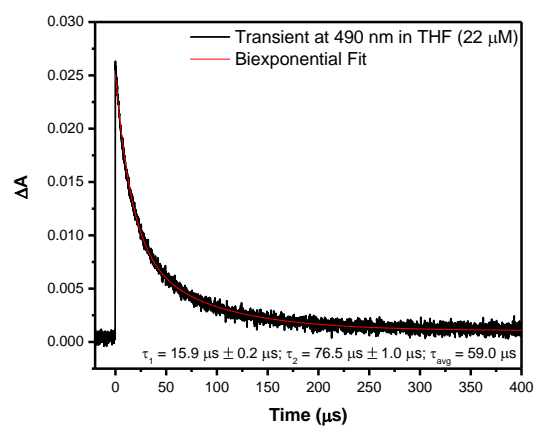
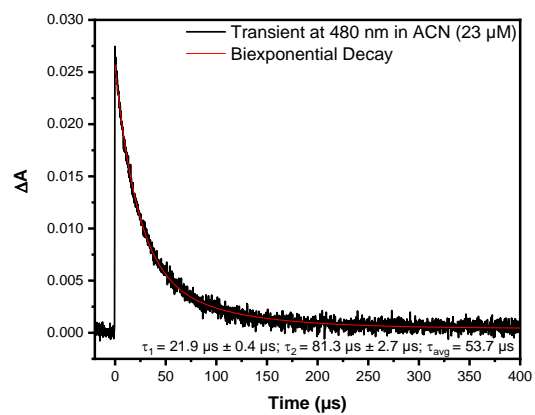


Figure A77. Transient absorption decay of **Re2** in ACN (top) and THF (bottom). Excited at 355 nm (3 mJ/pulse).

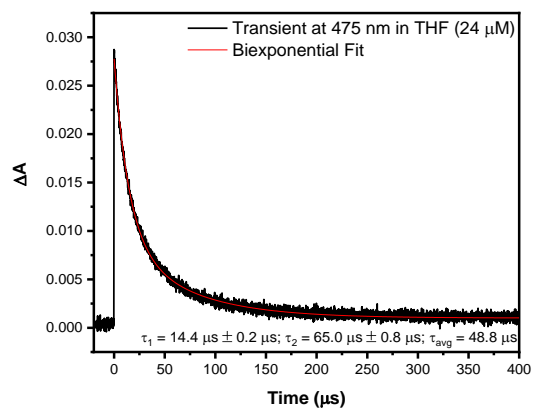
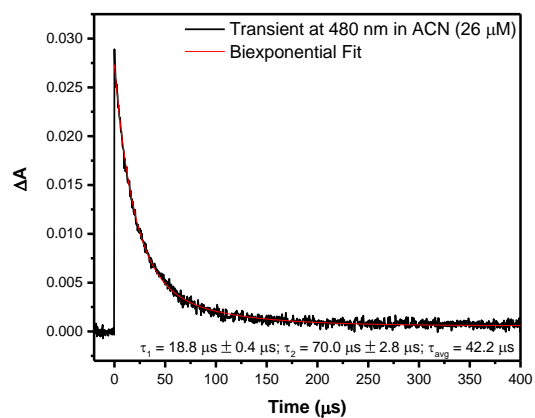


Figure A78. Transient absorption decay of **Re3** in ACN (top) and THF (bottom). Excited at 355 nm (3 mJ/pulse).

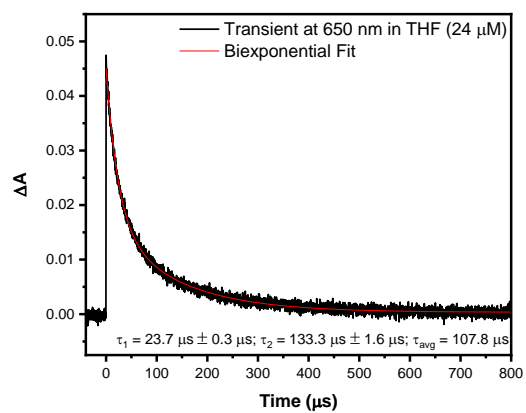
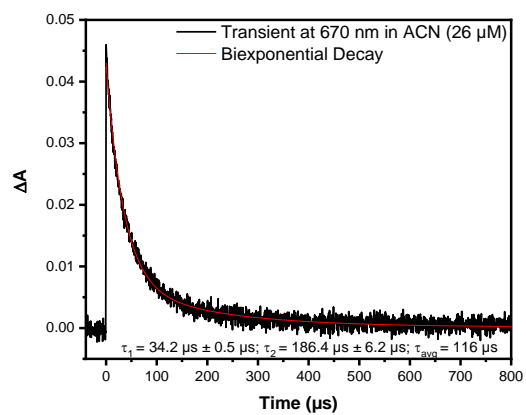


Figure A79. Transient absorption decay of **Re4** in ACN (top) and THF (bottom). Excited at 410 nm (3 mJ/pulse).

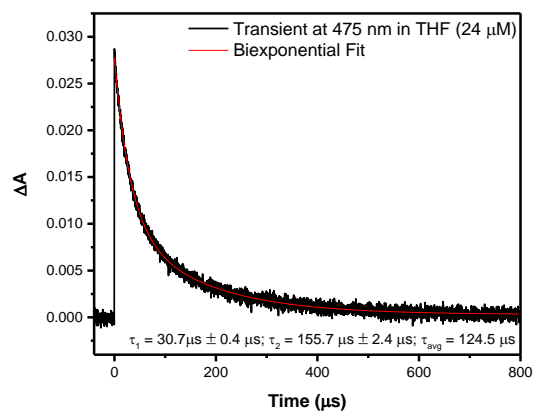
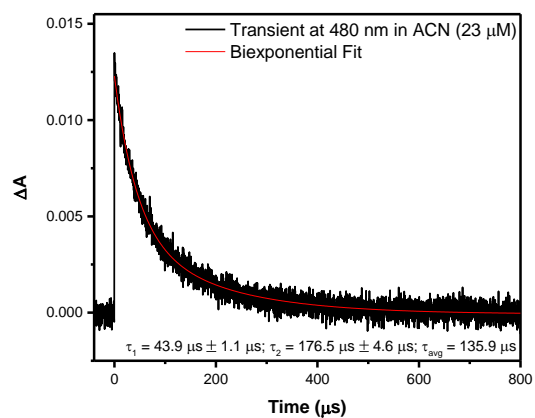


Figure A80. Transient absorption decay of **Re5** in ACN (top) and THF (bottom). Excited at 410 nm (3 mJ/pulse).

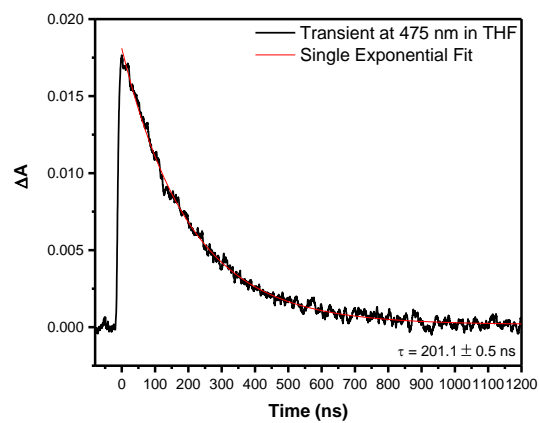
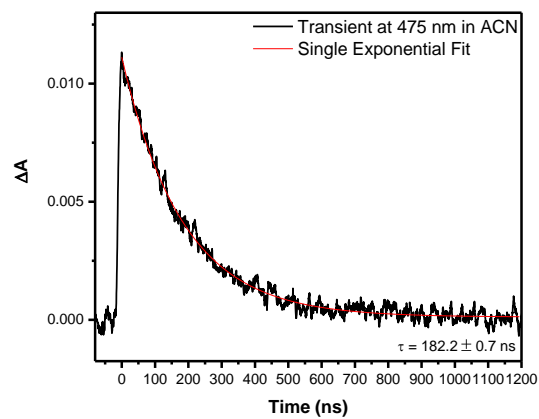


Figure A81. Transient absorption decay of **Re6** in ACN (top) and THF (bottom). Excited at 410 nm (3 mJ/pulse).

A.4. Additional DFT Results

Table A2. Wavelength, energies, and oscillator strength (f) for selected $S_0 \rightarrow S_n$ excitations as determined via TDDFT at the level of theory specified below. Experimental UV/Vis data obtained in acetonitrile at room temperature.

Molecules	$\lambda_{\text{abs max}}/\text{nm}$, eV ($\epsilon/\text{M}^{-1} \text{cm}^{-1}$)	B3LYP/Def2-SVP	M06/Def2-SVP	CAM-
		$S_0 \rightarrow S_1/\text{nm}$, eV (f) $S_0 \rightarrow S_2/\text{nm}$, eV (f)	$S_0 \rightarrow S_1/\text{nm}$, eV (f) $S_0 \rightarrow S_2/\text{nm}$, eV (f)	B3LYP/Def2-SVP $S_0 \rightarrow S_1/\text{nm}$, eV (f) $S_0 \rightarrow S_2/\text{nm}$, eV (f)
NI	332, 3.73 (14200)	342, 3.63 (0.0000) 337, 3.68 (0.2827)	334, 3.71 (0.2919) 325, 3.81 (0.0001)	304, 4.08 (0.3548) 285, 4.35 (0.0536)
BrNI	340, 3.65 (17100)	353, 3.51 (0.1169) 352, 3.52 (0.2273)	348, 3.56 (0.3620) 336, 3.69 (0.0011)	314, 3.95 (0.4364) 286, 4.34 (0.0417)
PONI	359, 3.45 (15601)	361, 3.43 (0.3693) 334, 3.71 (0.0000)	353, 3.51 (0.3891) 318, 3.90 (0.0013)	321, 3.86 (0.4912) 281, 4.41 (0.0097)
PSNI	384, 3.23 (14700)	445, 2.79 (0.0696) 355, 3.49 (0.0000)	426, 2.91 (0.1021) 339, 3.66 (0.2885)	340, 3.65 (0.2164) 302, 4.11 (0.2794)
PNI	407, 3.05 (11300)	423, 2.93 (0.3296) 331, 3.75 (0.0001)	403, 3.08 (0.3567) 316, 3.92 (0.0013)	359, 3.45 (0.4645) 288, 4.31 (0.0107)

Table A3. Wavelength and energies for selected $S_0 \rightarrow T_n$ excitations as determined via TDDFT at the level of theory specified below. Experimental photoluminescence data obtained in 2-methyltetrahydrofuran at 77 K.

Molecules	λ_{em}/nm , eV (at 77 K)	B3LYP/Def2-SVP	M06/Def2-SVP	CAM-B3LYP/Def2-SVP
		$S_0 \rightarrow T_1/nm$, eV $S_0 \rightarrow T_2/nm$, eV $S_0 \rightarrow T_3/nm$, eV	$S_0 \rightarrow T_1/nm$, eV $S_0 \rightarrow T_2/nm$, eV $S_0 \rightarrow T_n/nm$, eV	$S_0 \rightarrow T_1/nm$, eV $S_0 \rightarrow T_2/nm$, eV $S_0 \rightarrow T_n/nm$, eV
NI	538, 2.30	536, 2.31 372, 3.33 357, 3.47	535, 2.32 368, 3.37 T_4 : 333, 3.72	549, 2.26 355, 3.49 T_5 : 304, 4.08
BrNI	553, 2.24	554, 2.24 368, 3.37 365, 3.40	556, 2.23 365, 4.30 T_5 : 347, 3.57	567, 2.19 355, 3.49 T_5 : 307, 4.04
PONI	547, 2.27	546, 2.27 361, 3.43 350, 3.54	536, 2.31 356, 3.48 T_6 : 325, 3.81	550, 2.25 355, 3.49 T_6 : 299, 4.15
PSNI	579, 2.14	562, 2.21 447, 2.77 375, 3.31	568, 2.18 428, 2.90 T_3 : 370, 3.35	567, 2.19 369, 3.36 T_3 : 363, 3.42
PNI	605, 2.05	605, 2.05 403, 3.08 354, 3.50	577, 2.15 390, 3.18 T_3 : 351, 3.53	585, 2.12 376, 3.30 T_3 : 355, 3.49

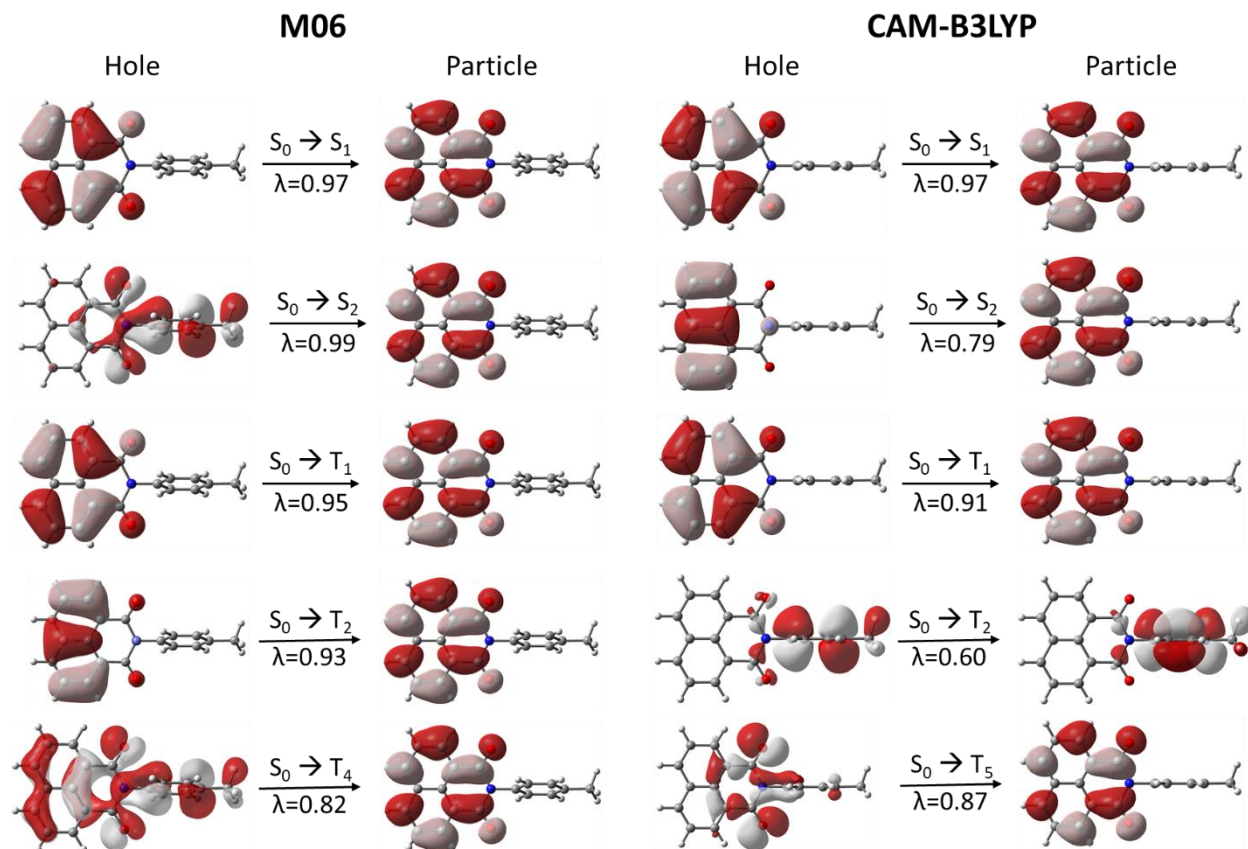


Figure A82. Natural transition orbitals for selected $S_0 \rightarrow S_n$ and $S_0 \rightarrow T_n$ excitations of **NI** determined at the M06/Def2-SVP (left) and CAM-B3LYP/Def2-SVP (right) levels of theory; λ is the fraction of the hole–particle contribution to the excitation.

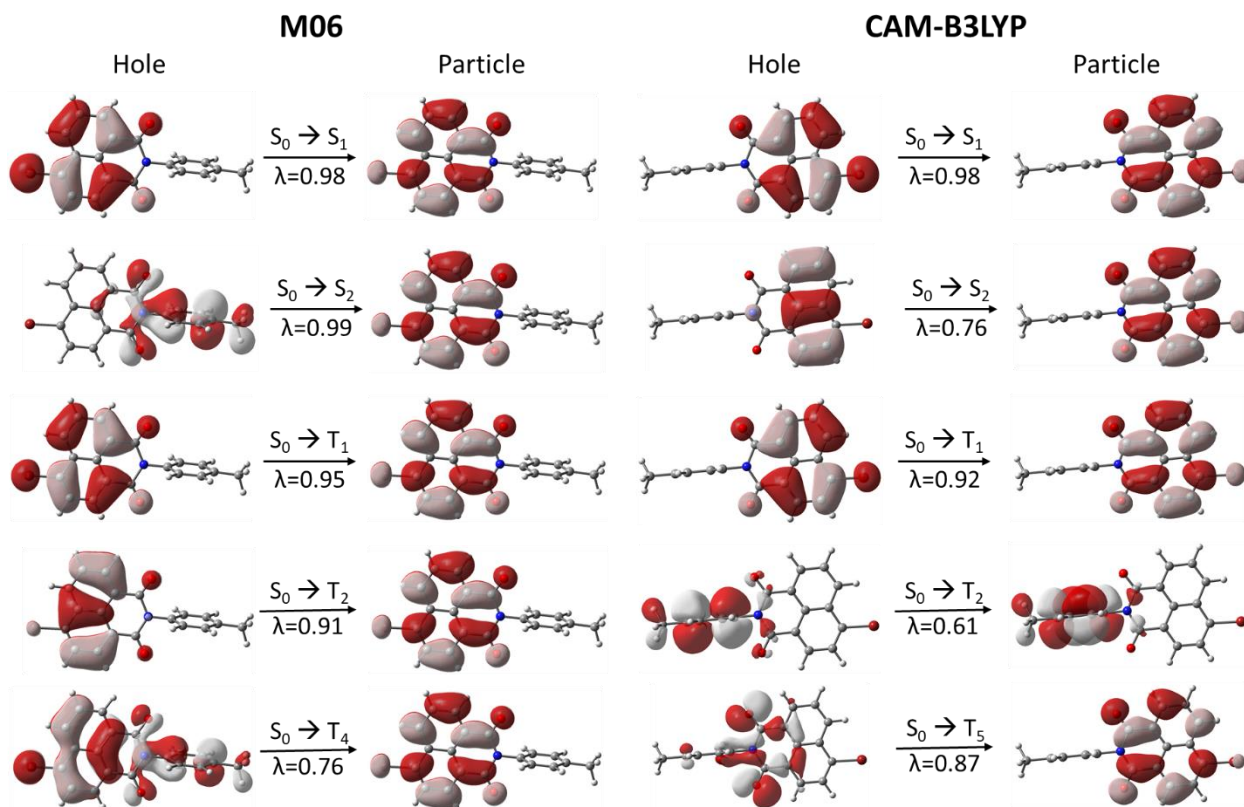


Figure A83. Natural transition orbitals for selected $S_0 \rightarrow S_n$ and $S_0 \rightarrow T_n$ excitations of **BrNI** determined at the M06/Def2-SVP (left) and CAM-B3LYP/Def2-SVP (right) levels of theory; λ is the fraction of the hole–particle contribution to the excitation.

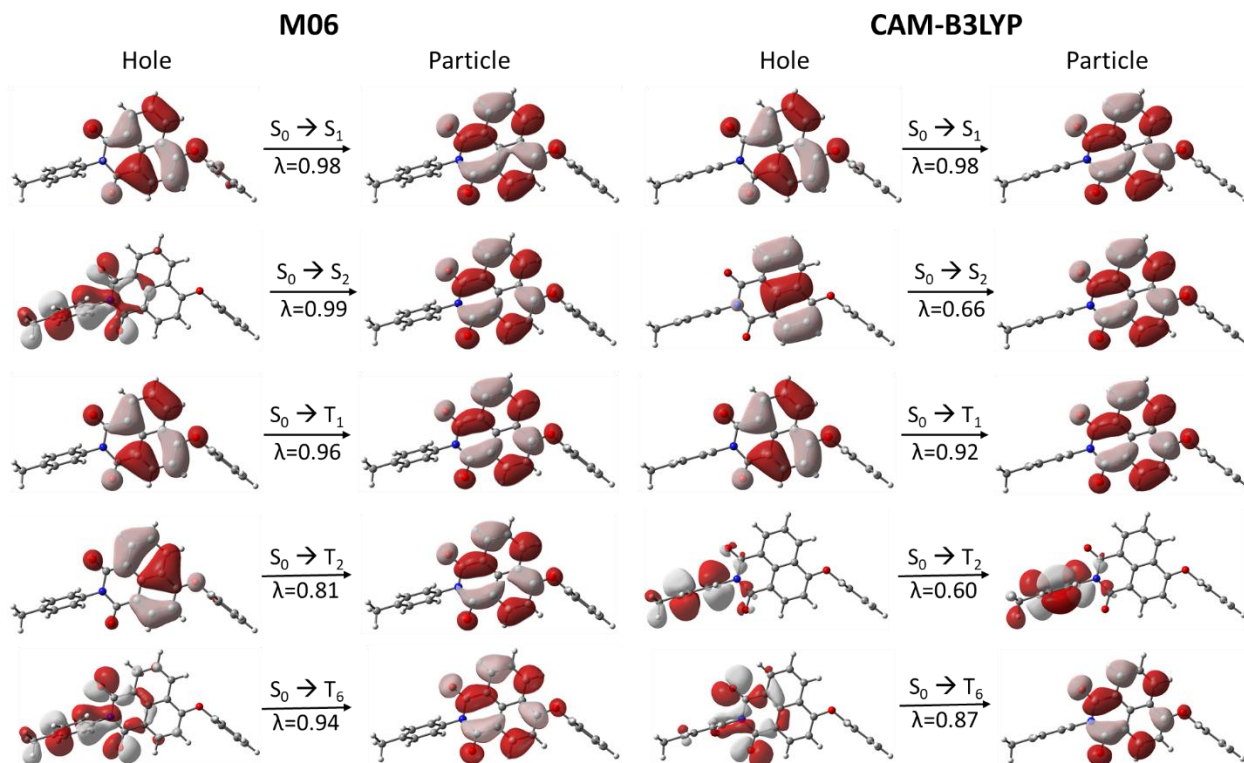


Figure A84. Natural transition orbitals for selected $S_0 \rightarrow S_n$ and $S_0 \rightarrow T_n$ excitations of **PONI** determined at the M06/Def2-SVP (left) and CAM-B3LYP/Def2-SVP (right) levels of theory; λ is the fraction of the hole–particle contribution to the excitation.

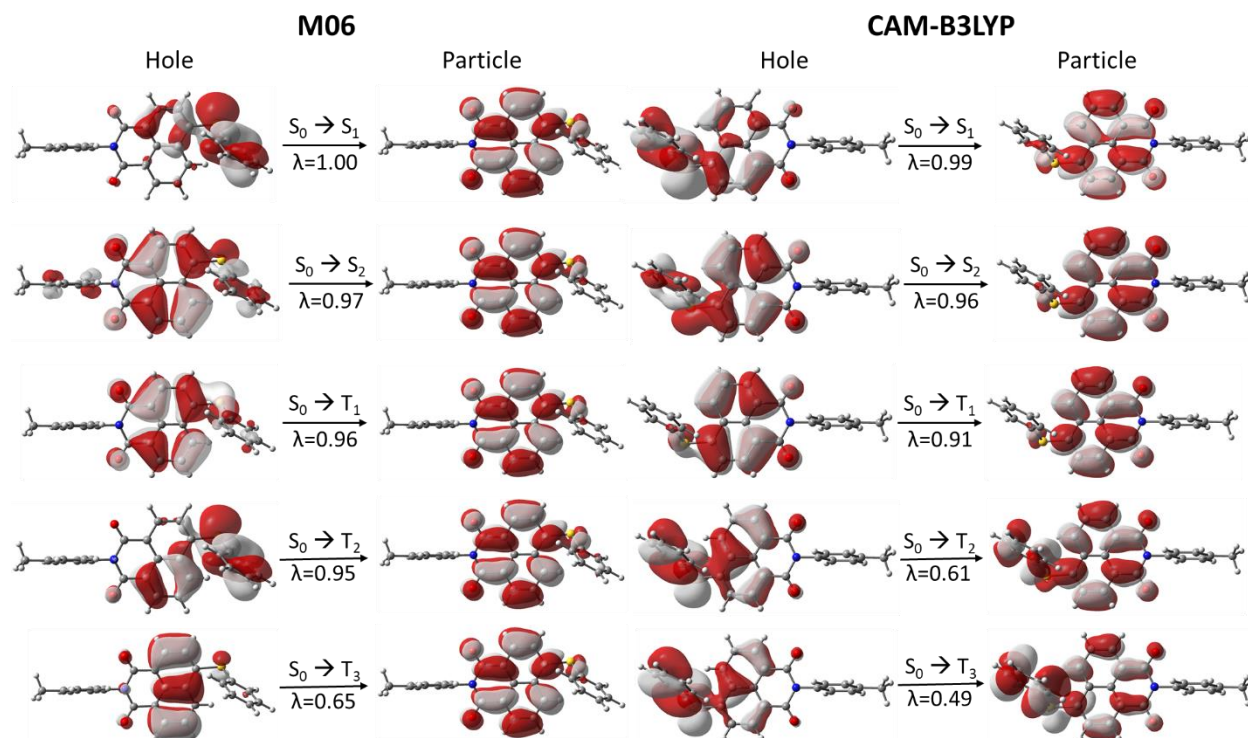


Figure A85. Natural transition orbitals for selected $S_0 \rightarrow S_n$ and $S_0 \rightarrow T_n$ excitations of **PSNI** determined at the M06/Def2-SVP (left) and CAM-B3LYP/Def2-SVP (right) levels of theory; λ is the fraction of the hole–particle contribution to the excitation.

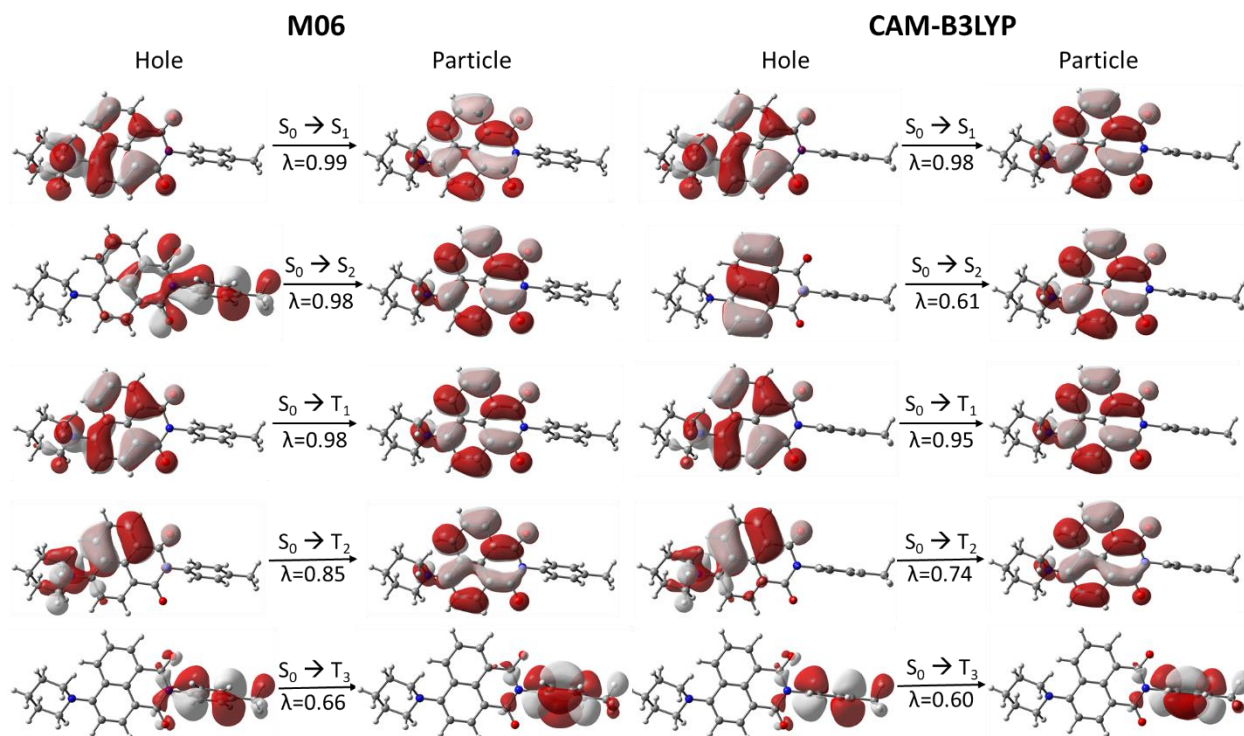


Figure A86. Natural transition orbitals for selected $S_0 \rightarrow S_n$ and $S_0 \rightarrow T_n$ excitations of **PNI** determined at the M06/Def2-SVP (left) and CAM-B3LYP/Def2-SVP (right) levels of theory; λ is the fraction of the hole–particle contribution to the excitation.

Table A4. Wavelength, energies, and oscillator strength (f) for selected $S_0 \rightarrow S_n$ excitations as determined via TDDFT at the level of theory specified below. Experimental UV/Vis data obtained in acetonitrile at room temperature.

Molecules	$\lambda_{\text{abs max}}/\text{nm}$, eV ($\epsilon/M^{-1} \text{ cm}^{-1}$)	B3LYP/Def2-SVP	M06/Def2-SVP	CAM- B3LYP/Def2-SVP
		$S_0 \rightarrow S_1/\text{nm}$, eV (f) $S_0 \rightarrow S_2/\text{nm}$, eV (f) $S_0 \rightarrow S_n/\text{nm}$, eV (f)	$S_0 \rightarrow S_1/\text{nm}$, eV (f) $S_0 \rightarrow S_2/\text{nm}$, eV (f) $S_0 \rightarrow S_n/\text{nm}$, eV (f)	$S_0 \rightarrow S_1/\text{nm}$, eV (f) $S_0 \rightarrow S_2/\text{nm}$, eV (f) $S_0 \rightarrow S_n/\text{nm}$, eV (f)
Re1	334, 3.71 (20400)	449, 2.76 (0.0412) 420, 2.95 (0.0056) S ₇ : 359, 3.45 (0.1384)	415, 2.99 (0.0615) 390, 3.44 (0.0013) S ₇ : 341, 3.64 (0.1967)	339, 3.66 (0.1305) 329, 3.77 (0.0021) S ₄ : 306, 4.05 (0.4089)
Re2	343, 3.61 (23200)	450, 2.76 (0.0424) 423, 2.93 (0.0038) S ₇ : 360, 3.44 (0.2752)	416, 2.98 (0.0646) 391, 3.17 (0.0011) S ₇ : 351, 3.53 (0.4580)	339, 3.66 (0.1437) 330, 3.76 (0.0034) S ₃ : 316, 3.92 (0.5027)
Re3	364, 3.41 (21600)	448, 2.77 (0.0442) 419, 2.96 (0.0054) S ₉ : 365, 3.40 (0.4800)	415, 2.99 (0.0663) 390, 3.44 (0.0020) S ₅ : 357, 3.47 (0.2083)	339, 3.66 (0.1735) 329, 3.77 (0.0060) S ₃ : 324, 3.83 (0.5314)
Re4	392, 3.16 (20700)	459, 2.70 (0.0946) 450, 2.76 (0.0329) S ₁₁ : 359, 3.45 (0.1158)	438, 2.83 (0.1282) 415, 2.99 (0.0574) S ₁₀ : 342, 3.63 (0.4100)	348, 3.56 (0.2763) 339, 3.66 (0.0918)
Re5	415, 2.99 (15800)	461, 2.69 (0.0004) 447, 2.77 (0.0666) S ₄ : 430, 2.88 (0.3384)	414, 2.99 (0.1843) 409, 3.03 (0.2391)	365, 3.40 (0.5691) 338, 3.67 (0.0901)
Re6	368, 3.37 (3160)	438, 2.83 (0.0359) 402, 3.08 (0.0050)	405, 3.06 (0.0536) 383, 3.24 (0.0011)	334, 3.71 (0.1037) 325, 3.81 (0.0015)

Table A5. Wavelength and energies for selected $S_0 \rightarrow T_n$ excitations as determined via TDDFT at the level of theory specified below. Experimental photoluminescence data obtained in 2-methyltetrahydrofuran at 77 K.

Molecules	λ_{em} /nm, eV (at 77 K) ^[a]	B3LYP/Def2-SVP	M06/Def2-SVP	CAM- B3LYP/Def2-SVP
		$S_0 \rightarrow T_1$ /nm, eV $S_0 \rightarrow T_2$ /nm, eV	$S_0 \rightarrow T_1$ /nm, eV $S_0 \rightarrow T_2$ /nm, eV	$S_0 \rightarrow T_1$ /nm, eV $S_0 \rightarrow T_2$ /nm, eV
Re1	536, 2.31	538, 2.30	536, 2.31	551, 2.25
	512, 2.42	470, 2.64	465, 2.67	466, 2.66
Re2	555, 2.23	557, 2.23	557, 2.23	568, 2.18
	516, 2.40	471, 2.63	464, 2.67	466, 2.66
Re3	546, 2.27	549, 2.26	536, 2.31	551, 2.25
	514, 2.41	470, 2.64	465, 2.67	467, 2.65
Re4	577, 2.15	570, 2.18	573, 2.16	570, 2.18
	516, 2.40	471, 2.63	465, 2.67	466, 2.66
Re5	595, 2.08	614, 2.02	581, 2.13	590, 2.10
	512, 2.42	469, 2.64	464, 2.67	466, 2.66
Re6	507, 2.45	459, 2.70	454, 2.73	460, 2.70

^[a] Two emission bands corresponding to the LC excited state localized on the NI chromophore (black) and MLCT excited state localized on the Re(I) chromophore (blue) were observed.

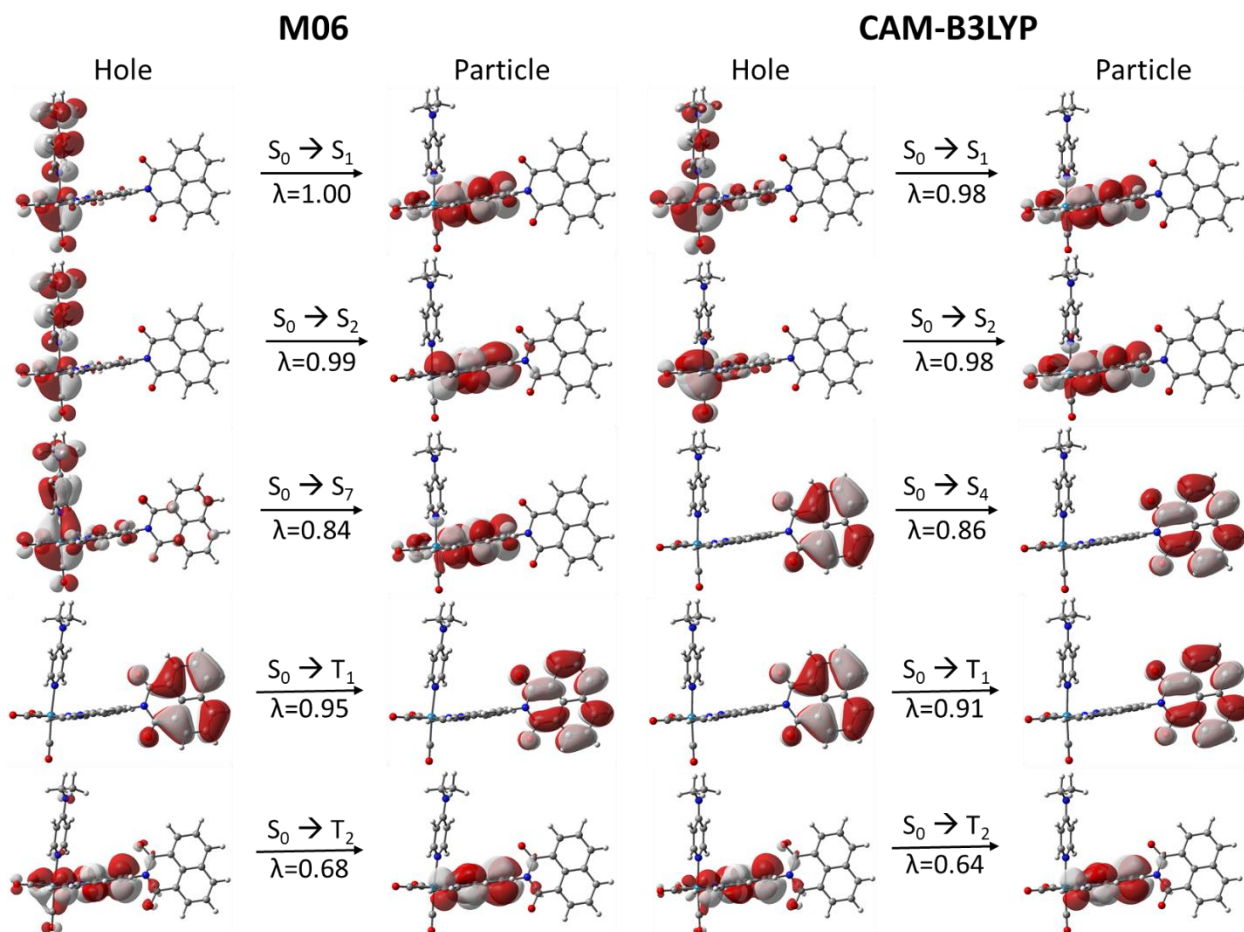


Figure A87. Natural transition orbitals for selected $S_0 \rightarrow S_n$ and $S_0 \rightarrow T_n$ excitations of **Re1** determined at the M06/Def2-SVP (left) and CAM-B3LYP/Def2-SVP (right) levels of theory; λ is the fraction of the hole–particle contribution to the excitation.

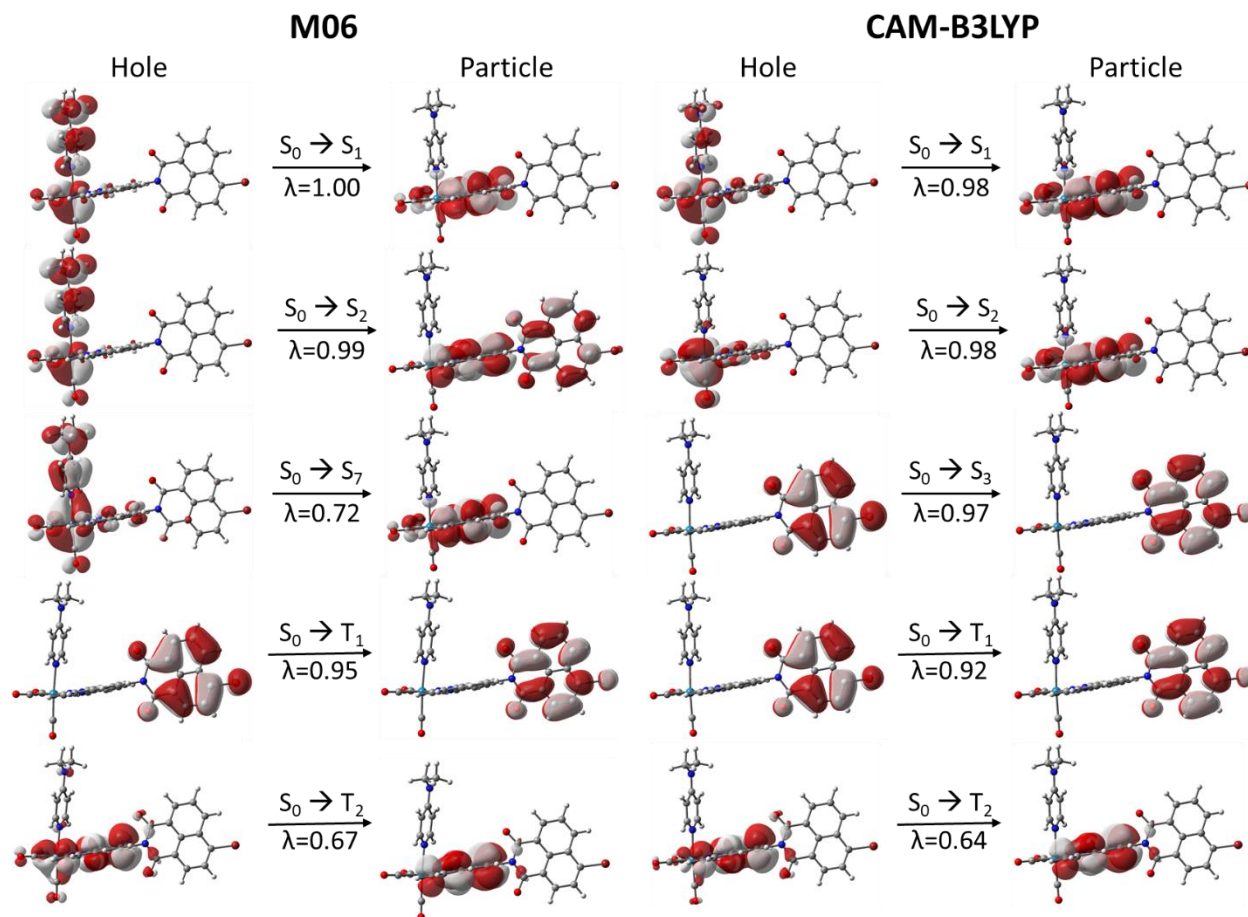


Figure A88. Natural transition orbitals for selected $S_0 \rightarrow S_n$ and $S_0 \rightarrow T_n$ excitations of **Re2** determined at the M06/Def2-SVP (left) and CAM-B3LYP/Def2-SVP (right) levels of theory; λ is the fraction of the hole–particle contribution to the excitation.

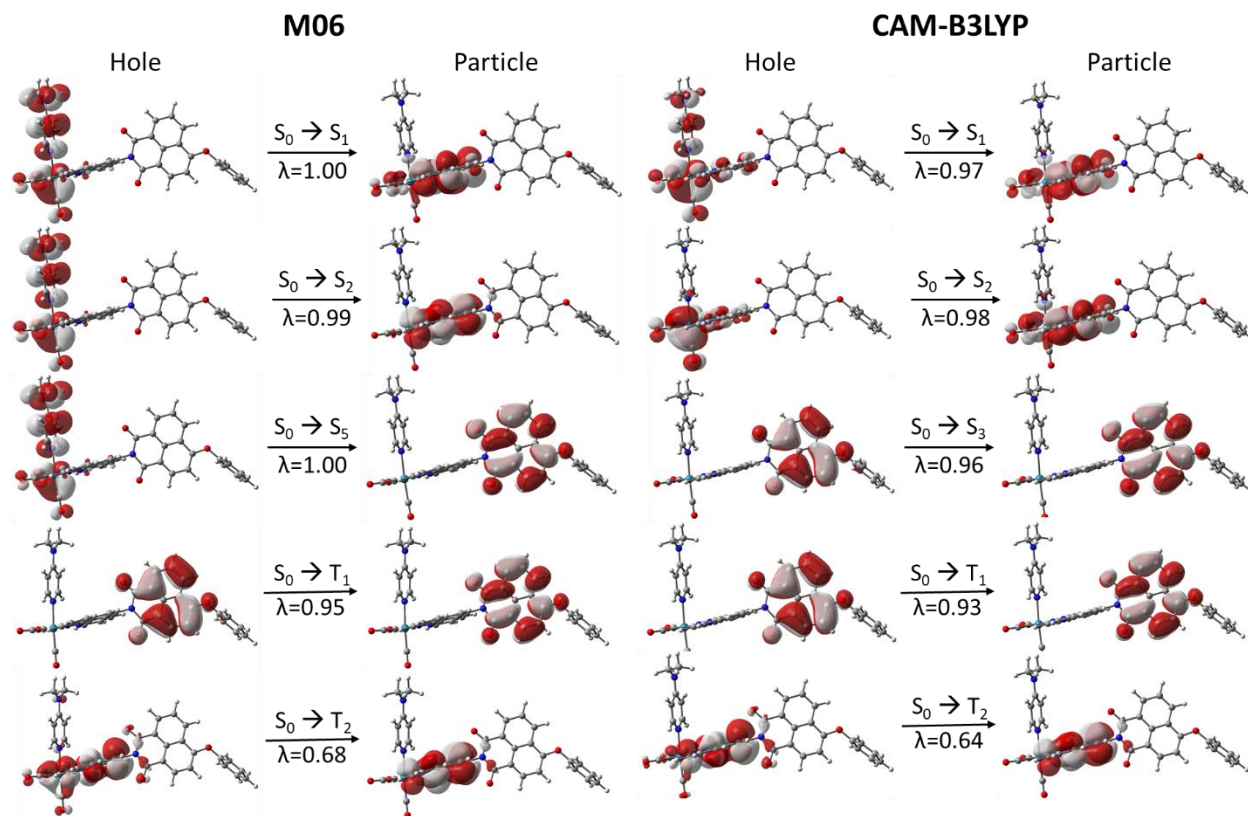


Figure A89. Natural transition orbitals for selected $S_0 \rightarrow S_n$ and $S_0 \rightarrow T_n$ excitations of **Re3** determined at the M06/Def2-SVP (left) and CAM-B3LYP/Def2-SVP (right) levels of theory; λ is the fraction of the hole–particle contribution to the excitation.

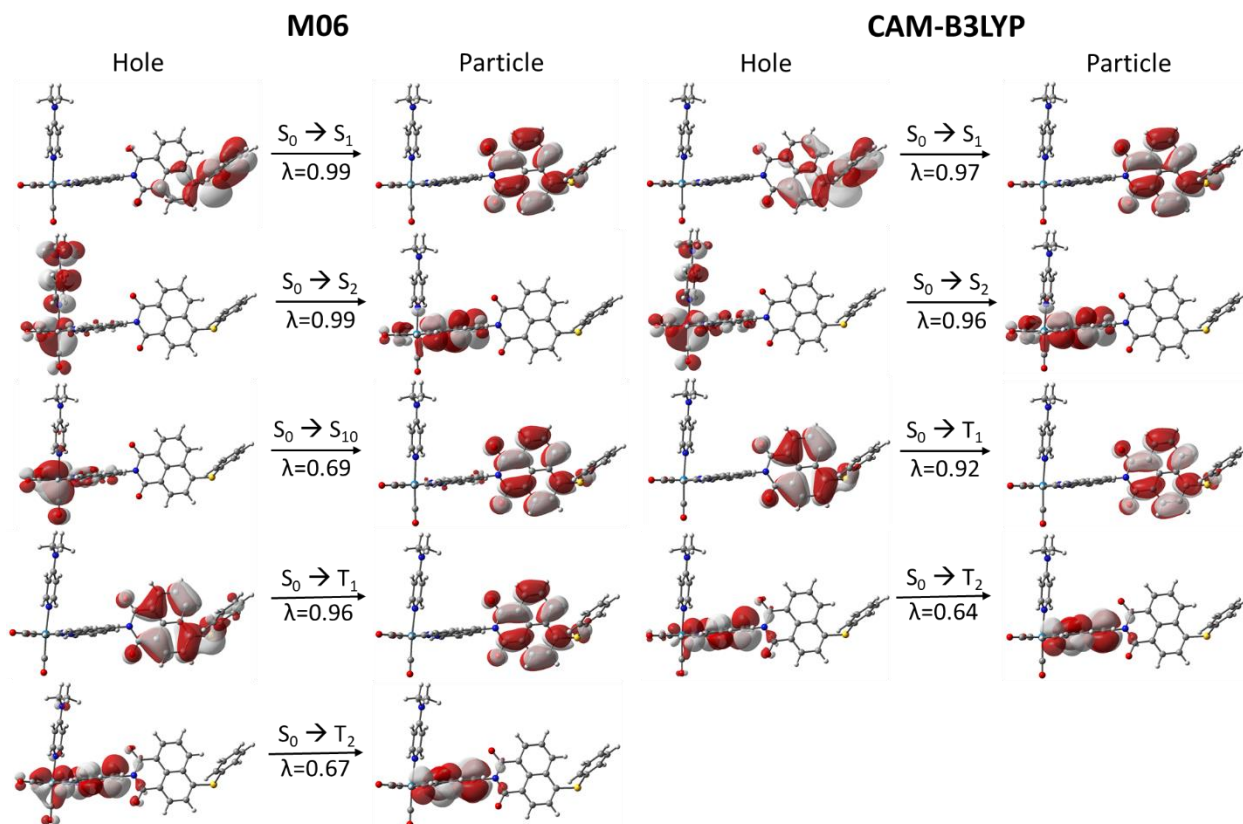


Figure A90. Natural transition orbitals for selected $S_0 \rightarrow S_n$ and $S_0 \rightarrow T_n$ excitations of **Re4** determined at the M06/Def2-SVP (left) and CAM-B3LYP/Def2-SVP (right) levels of theory; λ is the fraction of the hole–particle contribution to the excitation.

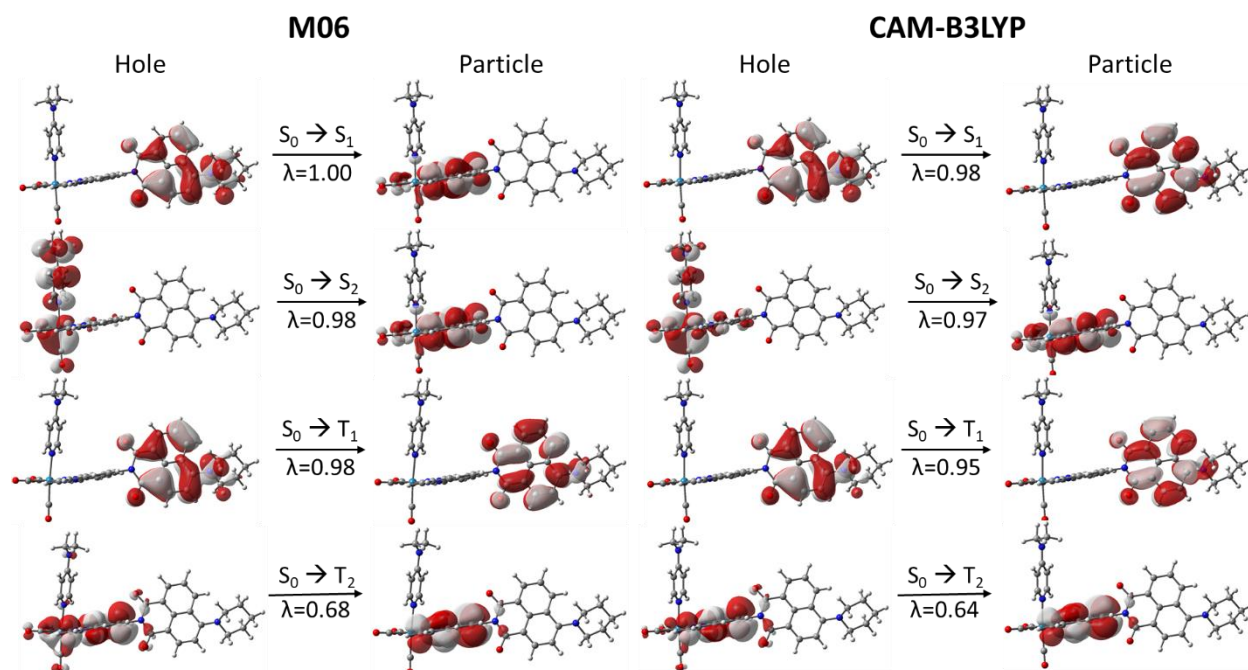


Figure A91. Natural transition orbitals for selected $S_0 \rightarrow S_n$ and $S_0 \rightarrow T_n$ excitations of **Re5** determined at the M06/Def2-SVP (left) and CAM-B3LYP/Def2-SVP (right) levels of theory; λ is the fraction of the hole–particle contribution to the excitation.

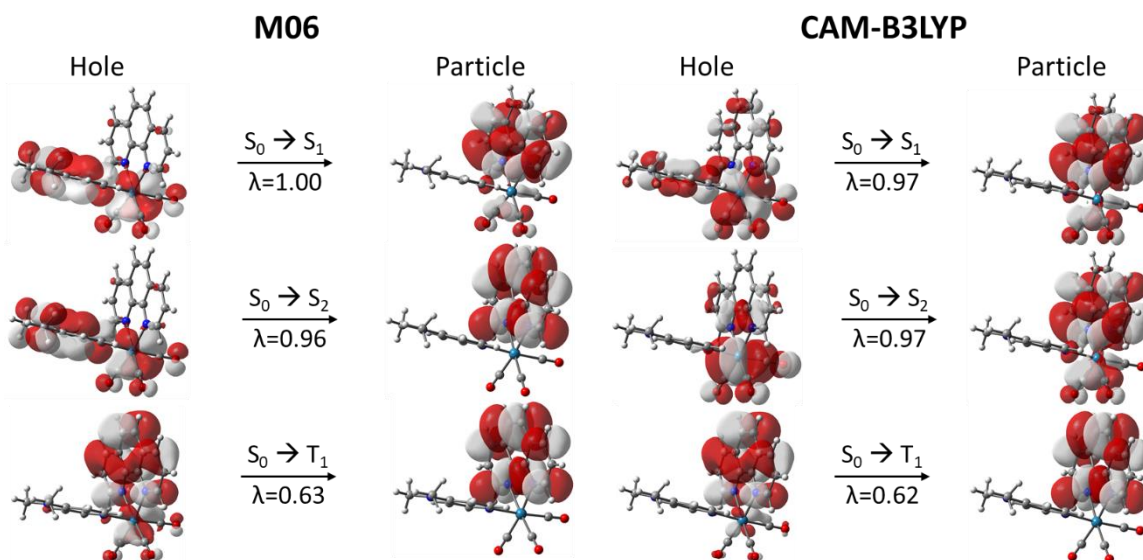


Figure A92. Natural transition orbitals for selected $S_0 \rightarrow S_n$ and $S_0 \rightarrow T_n$ excitations of **Re6** determined at the M06/Def2-SVP (left) and CAM-B3LYP/Def2-SVP (right) levels of theory; λ is the fraction of the hole–particle contribution to the excitation.

Appendix B

B.1. Synthetic Details and Structural Characterization

NNI-py.(NNI-py was prepared using the procedure from Kitchen and co-workers.¹ 4-nitro-1,8-naphthalic anhydride (3.005 g, 12.4 mmol), 4-aminopyridine (1.576 g, 16.7 mmol), and 3.36 mL of triethylamine were added to toluene (300 mL) and 3 Å sieves and refluxed for 3 days under an inert atmosphere. The resulting red/brown mixture was filtered hot through celite and was washed with warm toluene in 50 mL aliquots (repeated 4 times). The toluene was removed via rotary evaporation and then recrystallized using methanol. The solid was collected on a frit and was washed with methanol. The product was obtained in 44 % yield and used without further purification. ¹H NMR (400 MHz, Methylene Chloride-*d*₂) δ 8.88 (dt, *J* = 8.8, 1.0 Hz, 1H), 8.84 – 8.80 (m, 2H), 8.77 (dt, *J* = 7.3, 1.0 Hz, 1H), 8.73 (dd, *J* = 8.0, 0.9 Hz, 1H), 8.44 (dd, *J* = 8.0, 0.9 Hz, 1H), 8.09 – 8.02 (m, 1H), 7.36 – 7.29 (m, 2H).

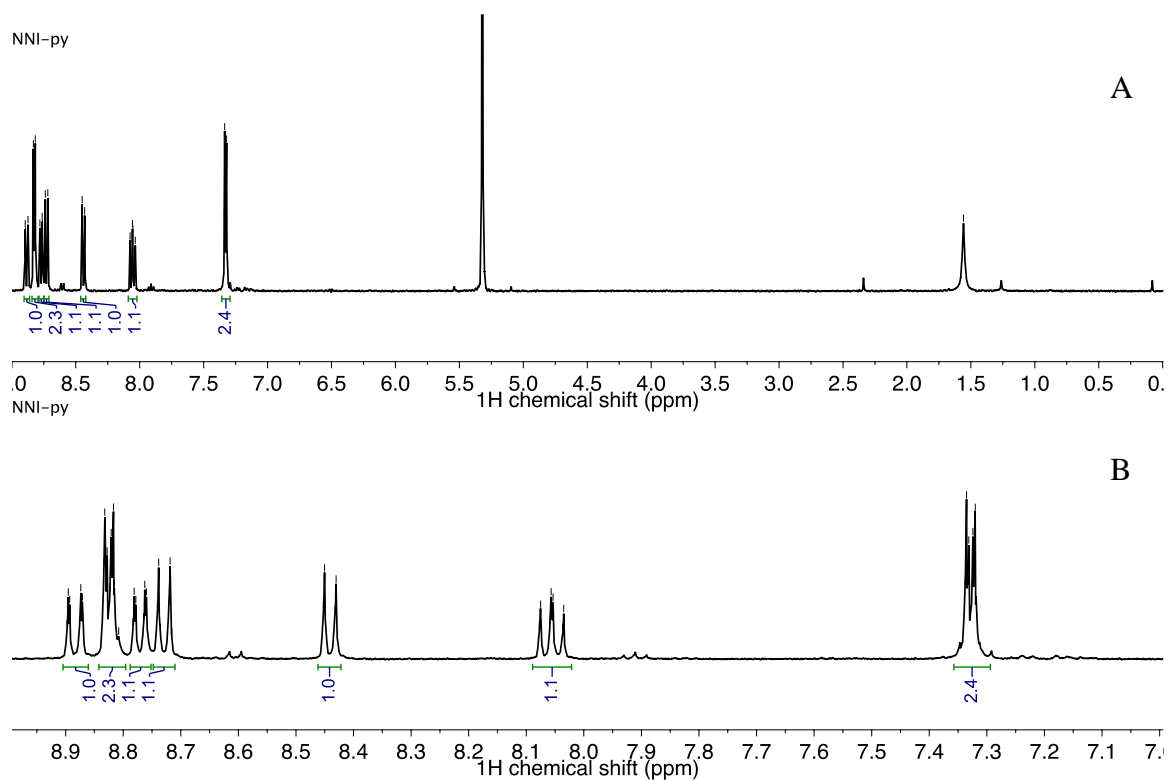
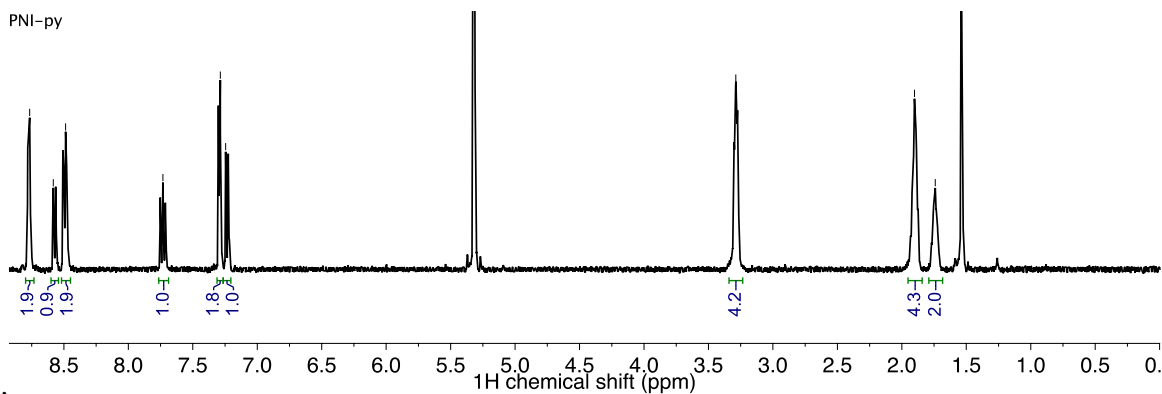


Figure B1. ¹H NMR spectrum of **NNI-py** in in CD₂Cl₂ (400 MHz). (A) Full spectrum and (B) Zoomed in aromatic region.

PNI-py. NNI-py (1.999 g, 6.25 mmol) and piperidine (3.00 mL, 30.4 mmol) were refluxed in dimethylformamide (65 mL) under inert atmosphere for 2 hours. Once cool, the reaction mixture was transferred to a separatory funnel along with 200 mL of dichloromethane and washed 4 times with water. The organic layer was collected and the dichloromethane was reduced via rotary evaporation. Pentanes were used to precipitate the red/orange solid out. The solid was then collected on a frit and washed with pentanes. The product was obtained in 84 % yield and used without further purification. ¹H NMR (400 MHz, Methylene Chloride-*d*₂) δ 8.84 – 8.70 (m, 2H), 8.57 (dt, *J* = 7.0, 1.6 Hz, 1H), 8.53 – 8.43 (m, 2H), 7.80 – 7.67 (m, 1H), 7.29 (dt, *J* = 4.4, 1.6 Hz, 2H), 7.24 (d, *J* = 8.2 Hz, 1H), 3.29 (t, *J* = 5.4 Hz, 4H), 1.90 (h, *J* = 5.8 Hz, 4H), 1.79 – 1.70 (m,



2H).

Figure B2. ^1H NMR spectrum of **PNI-py** in in CD_2Cl_2 (400 MHz).

***fac*-[Re(phen)(CO)₃(PNI-py)](PF₆) (Re1).** *fac*- [Re(phen)(CO)₃(PNI-py)](PF₆) was prepared using a modified synthetic procedure from Langdon-Jones and co-workers.² *fac*-Re(phen)(CO)₃Cl (0.243 g, 0.50 mmol) and AgBF₄ (0.096 g, 0.49 mmol) was refluxed in acetonitrile (30 mL) for 3-4 hours under inert atmosphere and shielded from light. Once cool, the solution mixture was filtered through celite and washed with acetonitrile. The acetonitrile was removed via rotary evaporation and the crude yellow product was used without purification. PNI-py (0.214 g, 0.60 mmol) was added to the crude product and refluxed in chloroform for 24 hours. Once cool, diethyl ether was added dropwise to the solution and the product was collected on a frit where it was washed with diethyl ether. The dried product was recrystallized using a methanol: acetone (1:1) mixture to dissolve the product and then precipitated out with concentrated NH₄PF₆ solution and water and collected on a frit. The product was then recrystallized with dichloromethane/hexanes as needed and was yellow in color. The product was obtained in 50 % yield. ^1H NMR (400 MHz, Methylene Chloride-*d*₂) δ 9.59 (dd, $J = 5.1, 1.4$ Hz, 2H), 8.84 (dd, $J = 8.3, 1.4$ Hz, 2H), 8.49 – 8.42 (m, 2H), 8.41 – 8.34 (m, 3H), 8.22 (d, $J = 1.6$ Hz, 2H), 8.17 (dd, $J = 8.3, 5.1$ Hz, 2H), 7.68 – 7.66 (t, $J = 8.5$ Hz, 1H), 7.35 – 7.30 (m, 2H), 7.18 – 7.16 (d, $J = 8.1$ Hz, 1H), 3.27 (t, $J = 5.3$ Hz, 4H), 1.91 – 1.83 (m, 4H), 1.76 – 1.68 (m, 2H).

MS [HR-ESI (CH₂Cl₂) m/z] 806.1512 [M—PF₆]⁺, calcd (C₃₇H₂₇N₅O₅¹⁸⁵Re) 806.1542. Anal.
Calcd (found) for C₃₇H₂₇N₅O₅Re·2H₂O: C, 44.94 (44.75); H, 3.16 (2.77); N, 7.08 (6.85).

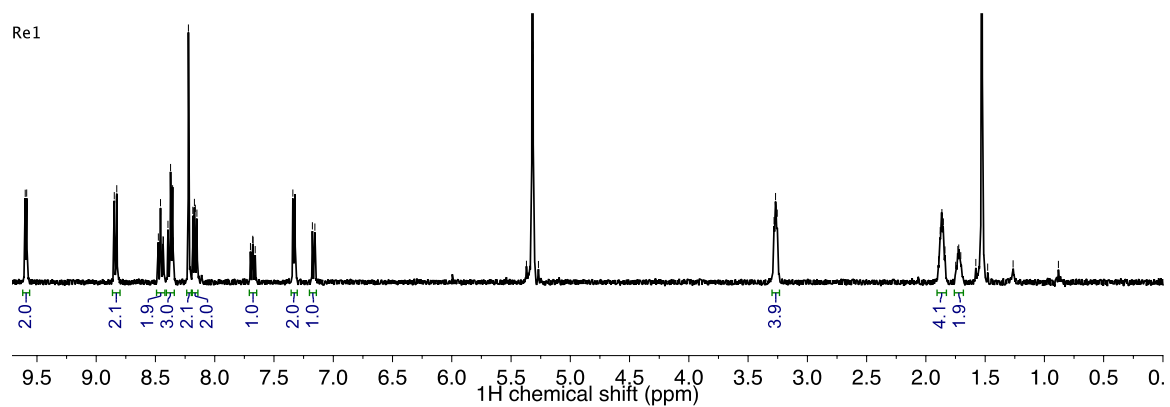


Figure B3. ¹H NMR spectrum of *fac*-[Re(phen)(CO)₃(PNI-py)](PF₆) (**Re1**) in CD₂Cl₂ (400 MHz).

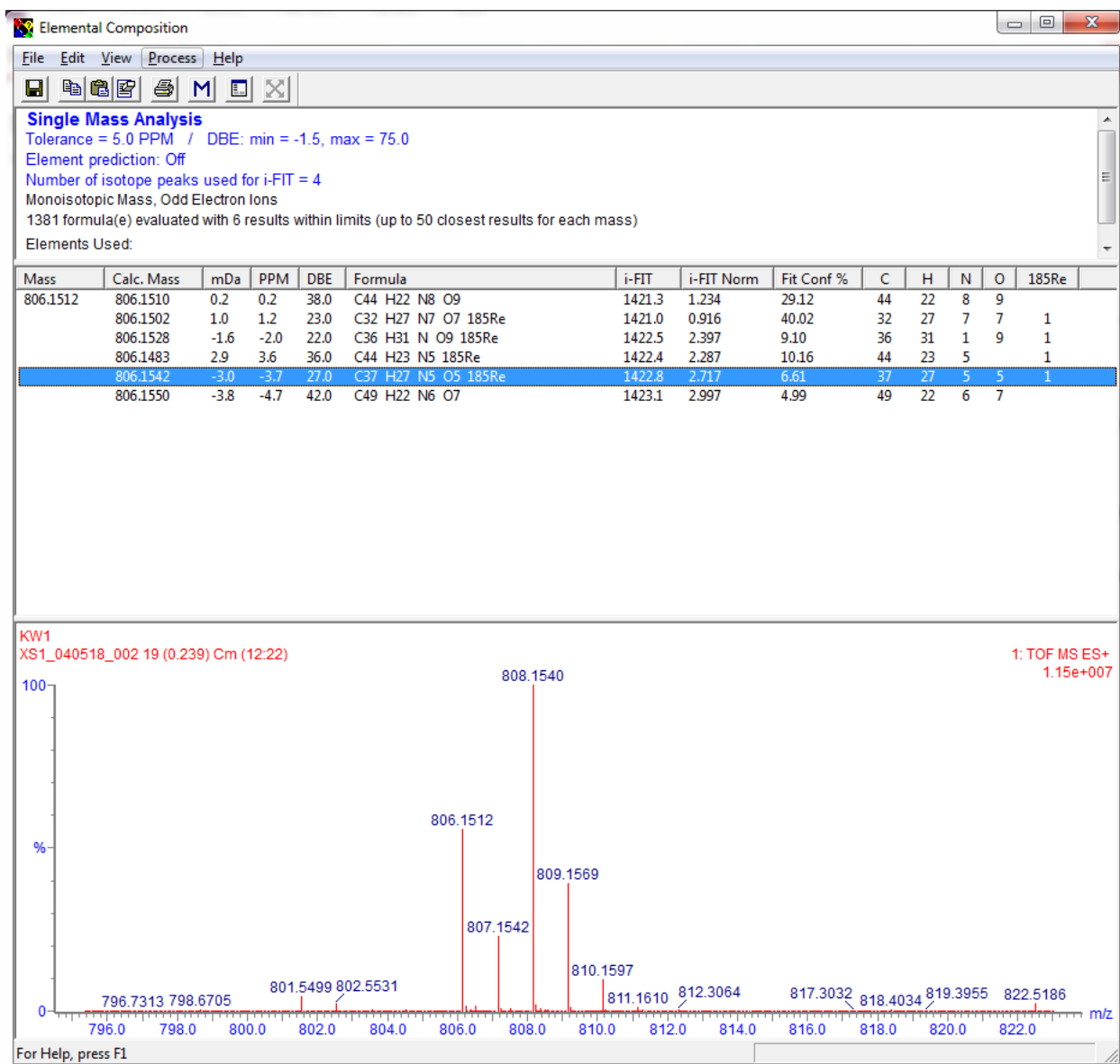


Figure B4. HRMS of *fac*-[Re(phen)(CO)₃(PNI-py)](PF₆) (**Re1**).

fac- [Re(bcp)(CO)₃(PNI-py)](PF₆) (**Re2**). *fac*- [Re(bcp)(CO)₃(PNI-py)](PF₆) was prepared as Re1 but with *fac*-Re(bcp)(CO)₃Cl (0.333 g, 0.50 mmol), AgBF₄ (0.099 g, 0.51 mmol) and PNI-py (0.213 g, 0.60 mmol) to give a yellow solid with a yield of 47 %. ¹H NMR (400 MHz, Methylene Chloride-*d*₂) δ 8.51 (dd, *J* = 7.3, 1.2 Hz, 1H), 8.47 (d, *J* = 8.5 Hz, 1H), 8.42 (d, *J* = 8.3 Hz, 1H), 8.17 (d, *J* = 6.3 Hz, 2H), 8.02 (s, 2H), 7.93 (s, 2H), 7.74 – 7.57 (m, 11H), 7.34 (d, *J* = 6.0 Hz, 2H), 7.19 (d, *J* = 8.3 Hz, 1H), 3.36 (s, 6H), 3.28 (t, *J* = 5.4 Hz, 4H), 1.88 (q, *J* = 9.9, 7.7 Hz, 4H), 1.73

(p, $J = 5.8$ Hz, 2H). MS [HR-ESI (CH_2Cl_2) m/z] 986.2449 [$\text{M}-\text{PF}_6$] $^+$, calcd ($\text{C}_{51}\text{H}_{39}\text{N}_5\text{O}_5^{185}\text{Re}$) 986.2481. Anal. Calcd (found) for $\text{C}_{51}\text{H}_{39}\text{N}_5\text{O}_5\text{Re}\cdot 0.75\text{H}_2\text{O}$: C, 53.42 (53.25); H, 3.56 (3.50); N, 6.11 (6.08).

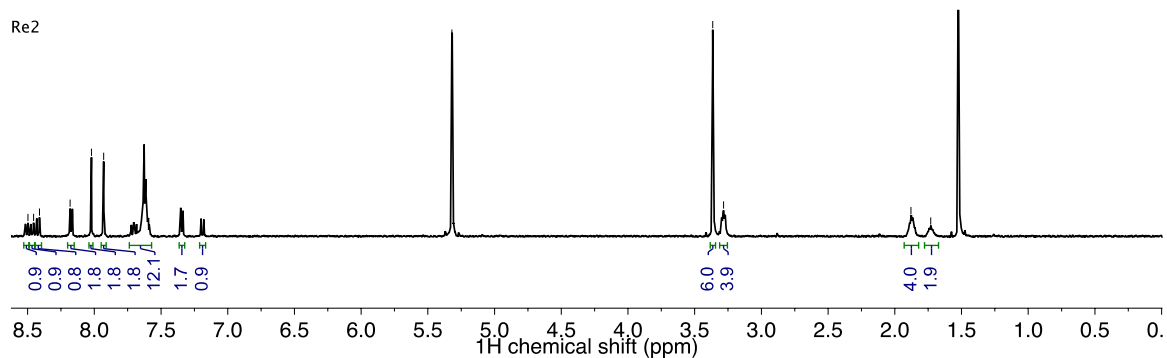


Figure B5. ^1H NMR spectrum of *fac*- $[\text{Re}(\text{bcp})(\text{CO})_3(\text{PNI-py})](\text{PF}_6)$ (**Re2**) in CD_2Cl_2 (400 MHz). Due to overlapping signals from the 10 protons of the phenyl rings on the bcp ligand and the single proton on the naphthalene ring in PNI that yields a triplet at 7.74-7.57 ppm, the program integrated that region to 12 when it should be 11.

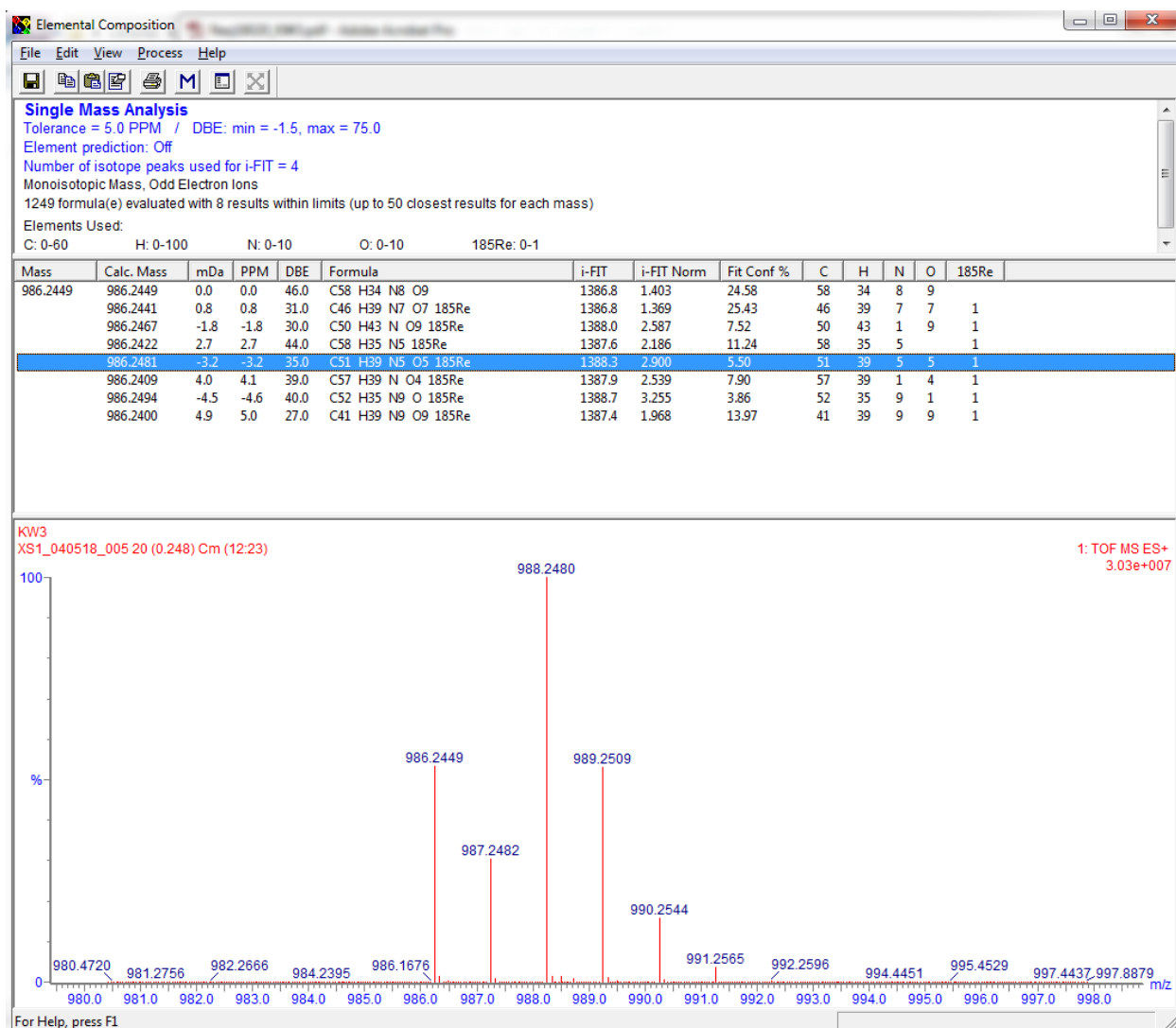


Figure B6. HRMS of *fac*-[Re(bcp)(CO)₃(PNI-py)](PF₆) (**Re2**).

fac- [Re(dtbb)(CO)₃(PNI-py)](PF₆) (**Re3**). *fac*- [Re(dtbb)(CO)₃(PNI-py)](PF₆) was prepared as Re1 but with *fac*-Re(dtbb)(CO)₃Cl (0.276 g, 0.48 mmol), AgBF₄ (0.093 g, 0.485 mmol) and PNI-py (0.174 g, 0.49 mmol) to give a yellow solid with a yield of 30 %. ¹H NMR (400 MHz, Methylene Chloride-*d*₂) δ 9.08 – 9.04 (m, 2H), 8.51 (dd, *J* = 7.4, 1.3 Hz, 1H), 8.49 – 8.45 (m, 1H), 8.43 (d, *J* = 8.2 Hz, 1H), 8.37 (d, *J* = 6.8 Hz, 2H), 8.26 (d, *J* = 1.9 Hz, 2H), 7.76 (dd, *J* = 5.9, 2.0 Hz, 2H), 7.70 (dd, *J* = 8.5, 7.3 Hz, 1H), 7.45 – 7.41 (m, 2H), 7.19 (d, *J* = 8.3 Hz, 1H), 3.31 – 3.26 (m, 4H), 1.92 – 1.84 (m, 4H), 1.77 – 1.71 (m, 1H), 1.48 (s, 19H). MS [HR-ESI (CH₂Cl₂) *m/z*] 894.2766

$[M-PF_6]^+$, calcd ($C_{43}H_{43}N_5O_5^{185}Re$) 894.2794. Anal. Calcd (found) for $C_{43}H_{43}N_5O_5Re \cdot H_2O$: C, 48.77 (48.54); H, 4.28 (4.15); N, 6.61 (6.66).

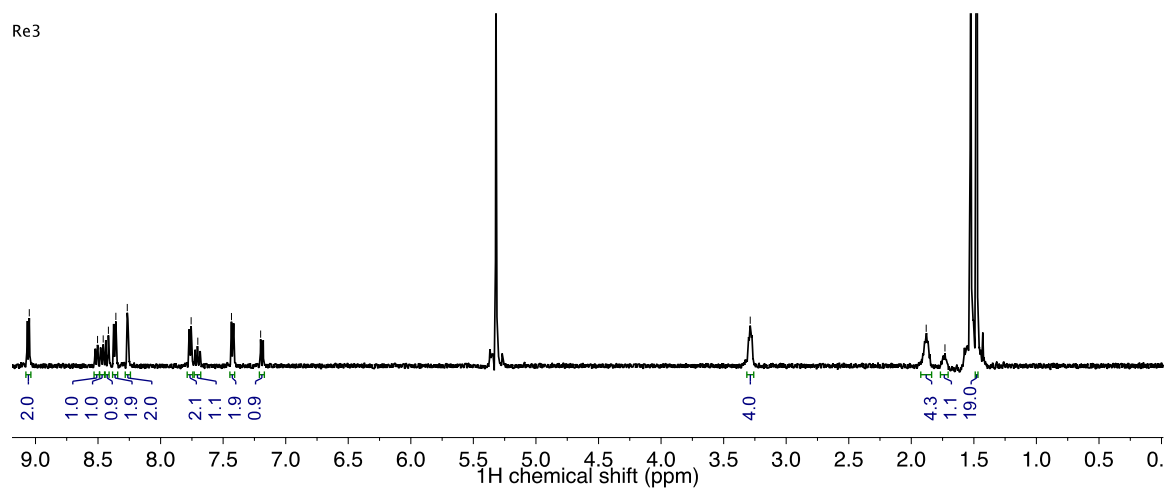


Figure B7. 1H NMR spectrum of *fac*- $[Re(dtbb)(CO)_3(PNI-py)](PF_6)$ (**Re3**) in CD_2Cl_2 (400 MHz).

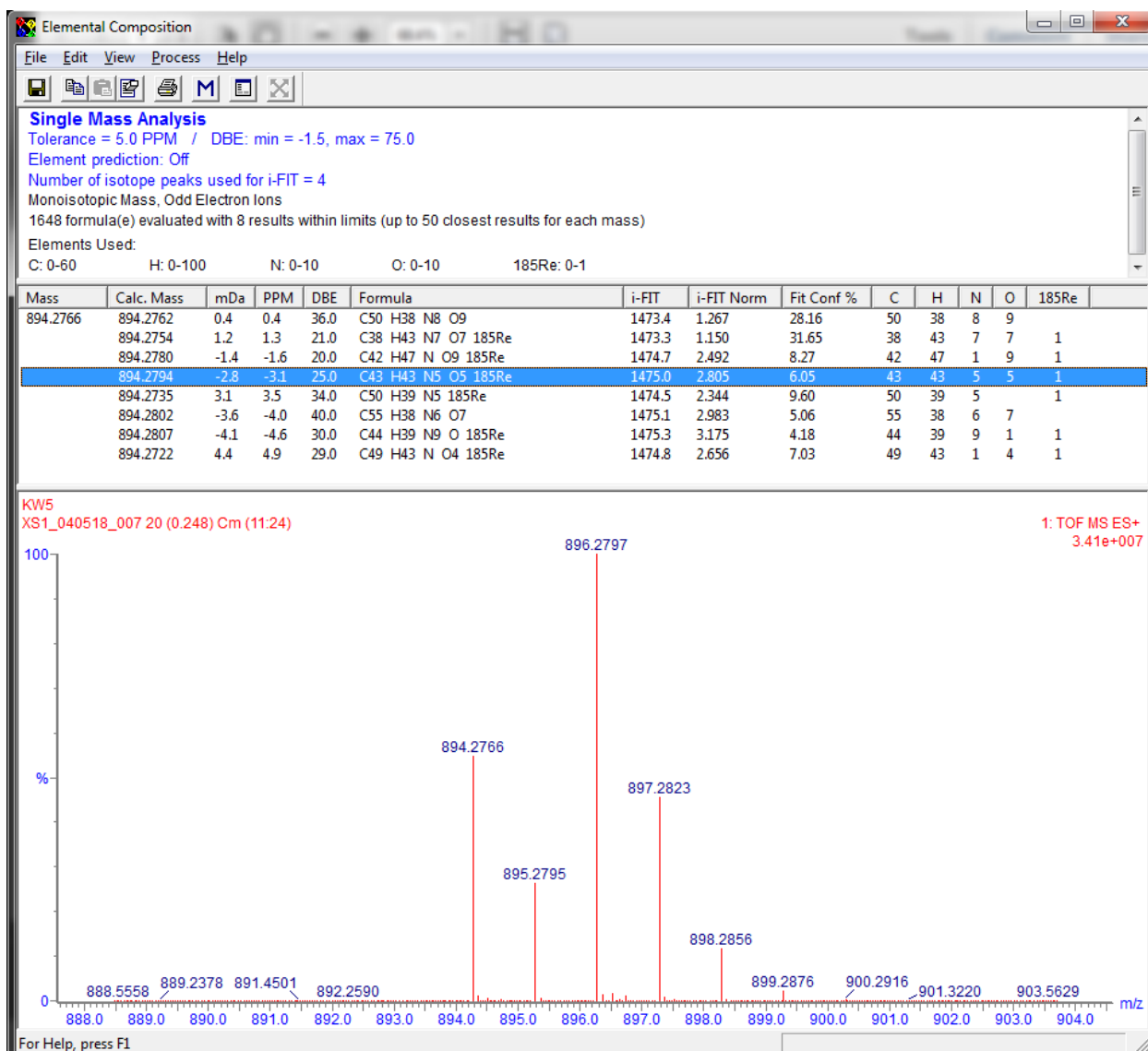


Figure B8. HRMS of *fac*-[Re(dtbb)(CO)₃(PNI-py)](PF₆) (**Re3**).

fac- [Re(deeb)(CO)₃(PNI-py)](PF₆) (**Re4**). *fac*- [Re(deeb)(CO)₃(PNI-py)](PF₆) was prepared as Re1 but with *fac*-Re(deeb)(CO)₃Cl (0.303 g, 0.50 mmol), AgBF₄ (0.099 g, 0.51 mmol) and PNI-py (0.215 g, 0.60 mmol) to give a yellow-orange solid with a yield of 40 %. ¹H NMR (400 MHz, Methylene Chloride-*d*₂) δ 9.39 (d, *J* = 5.6 Hz, 2H), 8.98 (s, 2H), 8.54 – 8.39 (m, 3H), 8.34 (t, *J* = 5.8 Hz, 4H), 7.70 (t, *J* = 7.8 Hz, 1H), 7.44 (d, *J* = 6.0 Hz, 2H), 7.19 (d, *J* = 8.2 Hz, 1H), 4.56 (q, *J* = 7.1 Hz, 4H), 3.29 (t, *J* = 5.4 Hz, 4H), 1.88 (m, 4H), 1.76 – 1.67 (m, 2H), 1.50 – 1.46 (m, 6H).

MS [HR-ESI (CH₂Cl₂) m/z] 926.1930 [M—PF₆]⁺, calcd (C₄₁H₃₅N₅O₉¹⁸⁵Re) 926.1964. Anal.
Calcd (found) for C₄₁H₃₅N₅O₉Re·3.1H₂O: C, 43.63 (43.46); H, 3.68 (3.34); N, 6.20 (5.99).

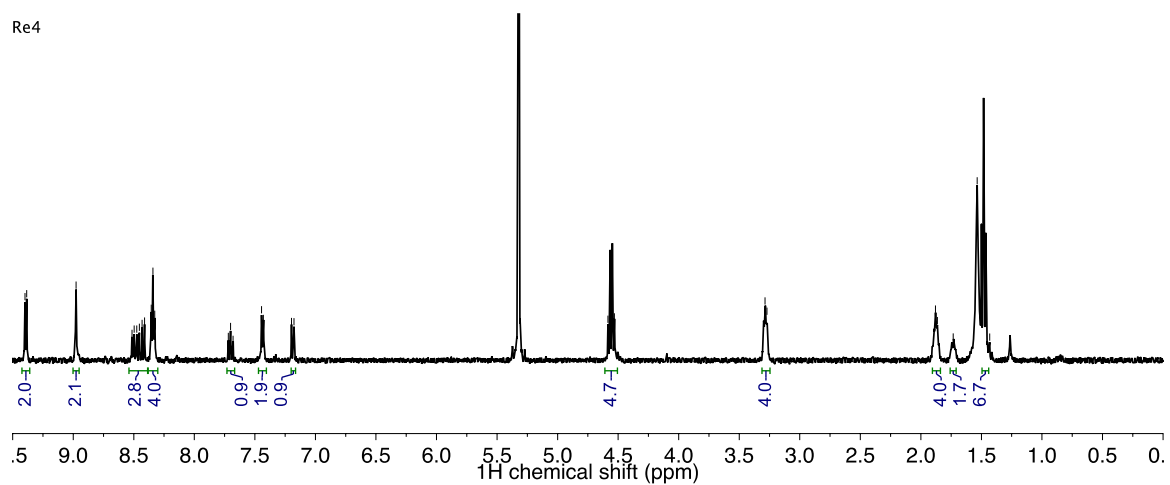


Figure B9. ¹H NMR spectrum of *fac*-[Re(deeb)(CO)₃(PNI-py)](PF₆) (**Re4**) in CD₂Cl₂ (400 MHz).

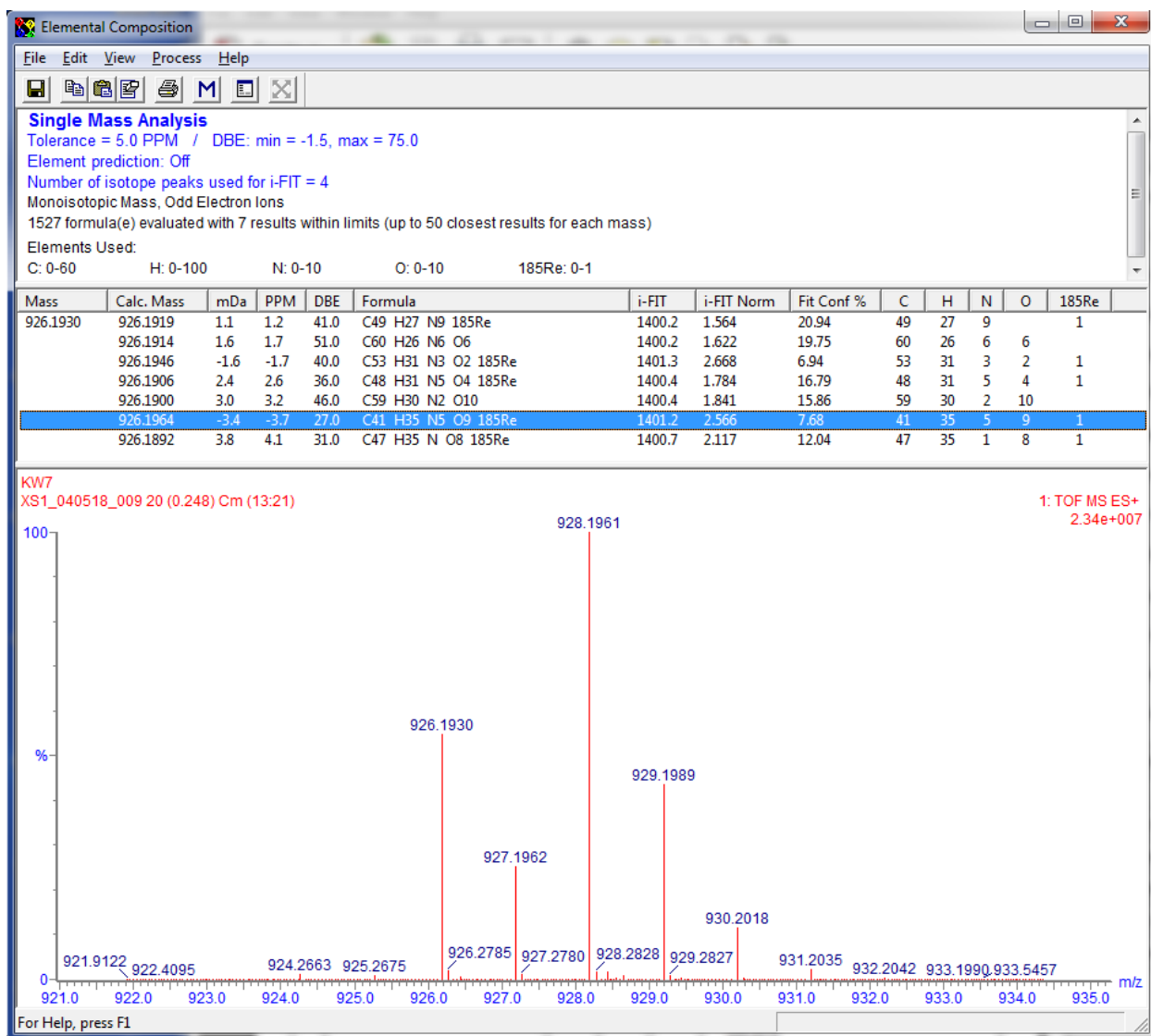


Figure B10. HRMS of *fac*-[Re(deeb)(CO)₃(PNI-py)](PF₆) (**Re4**).

fac-[Re(biq)(CO)₃(PNI-py)](PF₆) (**Re5**). *fac*-[Re(biq)(CO)₃(PNI-py)](PF₆) was prepared as **Re1** but with *fac*-Re(biq)(CO)₃Cl (0.278 g, 0.49 mmol), AgBF₄ (0.100 g, 0.51 mmol) and PNI-py (0.213 g, 0.60 mmol) to give an orange solid with a yield of 40%. ¹H NMR (400 MHz, Methylene Chloride-*d*₂) δ 9.00 – 8.95 (m, 2H), 8.85 (d, *J* = 8.6 Hz, 2H), 8.53 – 8.48 (m, 2H), 8.48 – 8.43 (m, 2H), 8.40 (dd, *J* = 8.3, 1.4 Hz, 1H), 8.26 – 8.18 (m, 4H), 8.01 – 7.96 (m, 2H), 7.69 (dd, *J* = 8.5, 7.3 Hz, 1H), 7.47 (dd, *J* = 6.8, 1.5 Hz, 2H), 7.18 (d, *J* = 8.3 Hz, 1H), 7.12 (dd, *J* = 6.8, 1.4 Hz, 2H), 3.30 – 3.24 (m, 4H), 1.91 – 1.82 (m, 4H), 1.76 – 1.68 (m, 2H). MS [HR-ESI (CH₂Cl₂) *m/z*]

882.1825 [M—PF₆]⁺, calcd (C₄₃H₃₁N₅O₅¹⁸⁵Re) 882.1855. Anal. Calcd (found) for C₄₃H₃₁N₅O₅Re·3.5H₂O: C, 47.30 (47.13); H, 3.51 (2.95); N, 6.41 (6.34).

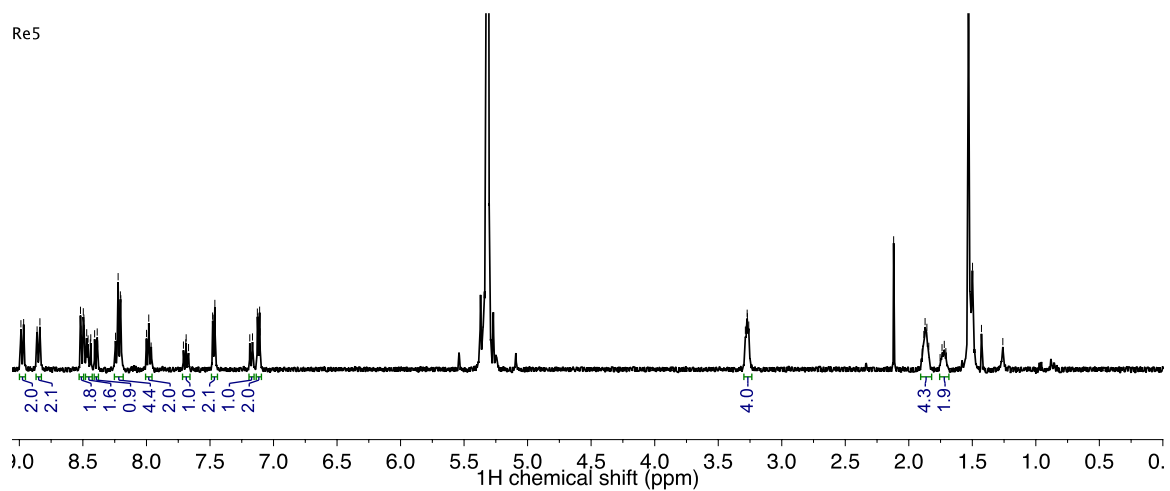


Figure B11. ¹H NMR spectrum of *fac*-[Re(biq)(CO)₃(PNI-py)](PF₆) (**Re5**) in CD₂Cl₂ (400 MHz).

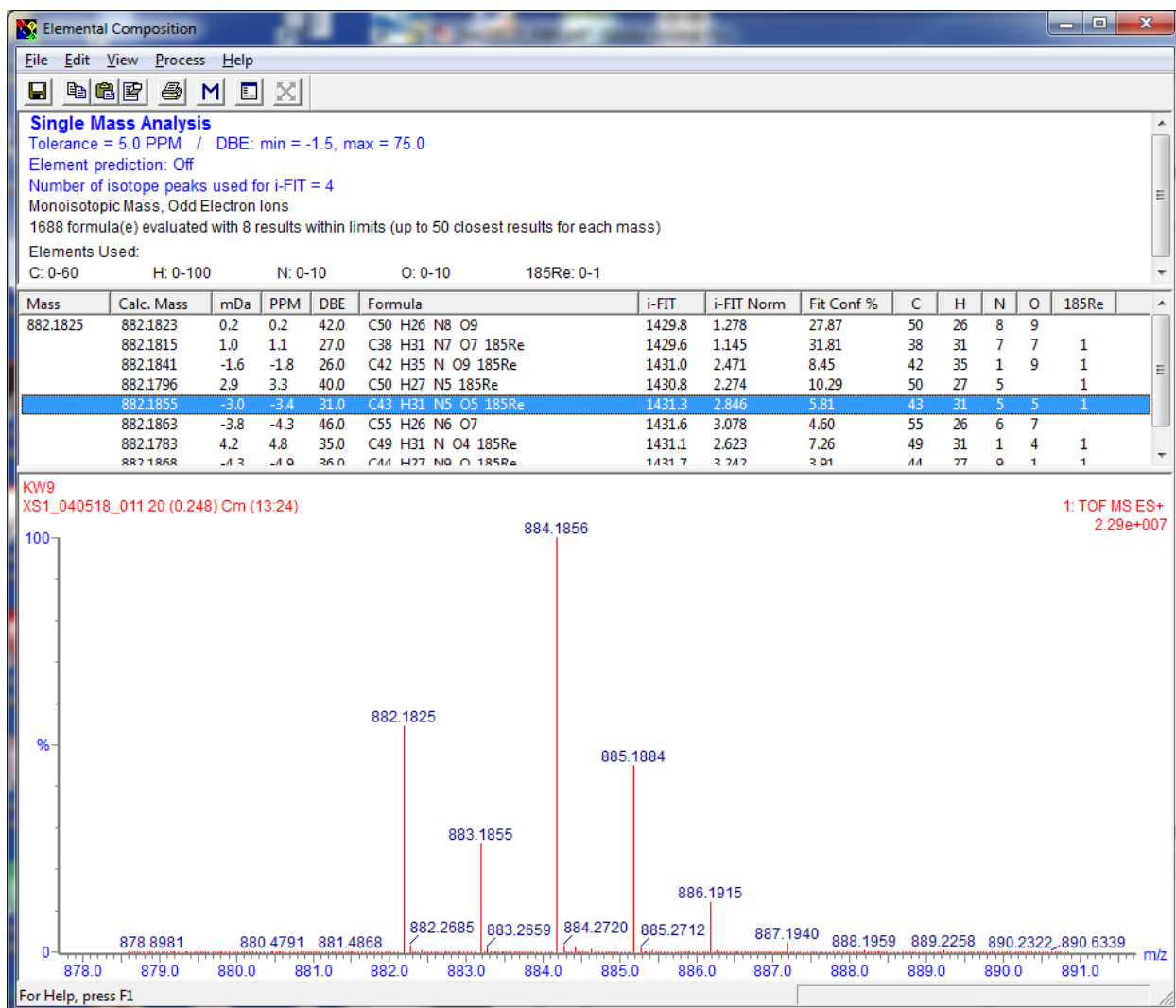


Figure B12. HRMS of *fac*-[Re(biq)(CO)₃(PNI-py)](PF₆) (**Re5**).

fac-[Re(phen)(CO)₃(4-etpy)](PF₆) (**Mod1**). *fac*-[Re(phen)(CO)₃(4-etpy)](PF₆) was prepared as Re1 but with *fac*-Re(phen)(CO)₃Cl (0.243 g, 0.50 mmol), AgBF₄ (0.101 g, 0.52 mmol) and 4-etpy (0.50 mL, 4.40 mmol). For initial precipitation of the solid from the chloroform solution, the solution was added dropwise to cold, stirring pentanes and filtered in small amounts to prevent the product to sticking to the beaker, flask, or wall of frit. All other precipitations, including the metathesis reaction from the BF₄⁻ anion to the PF₆⁻ anion are as stated in the synthesis for **Re1**. The final pale yellow solid was collected on a frit with a yield of 81 %. ¹H NMR (400 MHz, Methylene Chloride-*d*₂) δ 9.55 (dd, *J* = 5.1, 1.4 Hz, 2H), 8.80 (dd, *J* = 8.3, 1.4 Hz, 2H), 8.19 – 8.11

(m, 4H), 8.02 (d, $J = 5.9$ Hz, 2H), 7.04 (d, $J = 6.0$ Hz, 2H), 2.53 (q, $J = 7.6$ Hz, 2H), 1.08 (t, $J = 7.6$ Hz, 3H). MS [HR-ESI (CH_2Cl_2) m/z] 556.0785 [$\text{M} - \text{PF}_6$] $^+$, calcd ($\text{C}_{22}\text{H}_{17}\text{N}_3\text{O}_3^{185}\text{Re}$) 556.0785. Anal. Calcd (found) for $\text{C}_{22}\text{H}_{17}\text{N}_3\text{O}_3\text{Re}$: C, 37.61 (37.60); H, 2.44 (2.42); N, 5.98 (5.87).

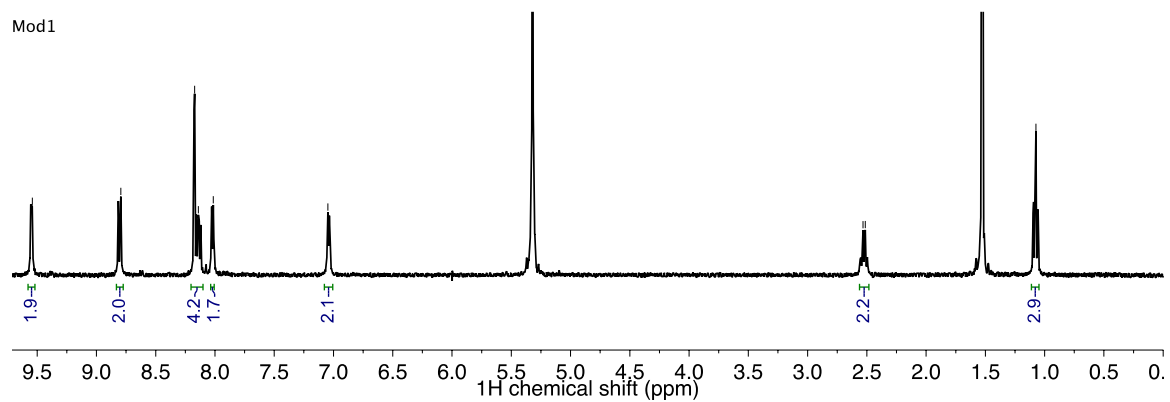


Figure B13. ^1H NMR spectrum of *fac*-[Re(phen)(CO) $_3$ (4-ety)](PF $_6$) (**Mod1**) in CD_2Cl_2 (400 MHz).

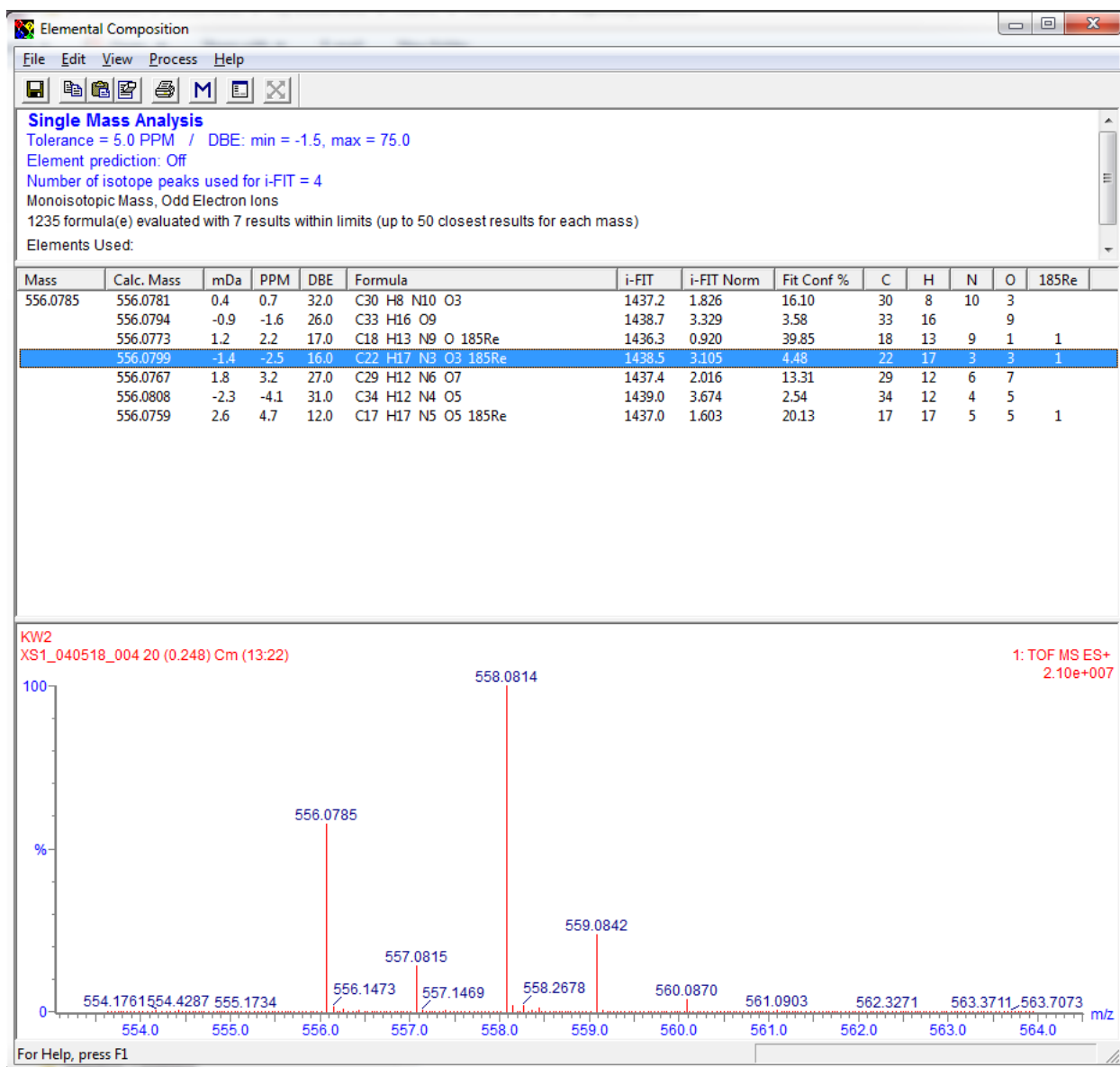


Figure B14. HRMS of *fac*-[Re(phen)(CO)₃(4-*etpy*)](PF₆) (**Mod1**).

fac- [Re(*bcp*)(CO)₃(4-*etpy*)](PF₆) (**Mod2**). *fac*- [Re(*bcp*)(CO)₃(4-*etpy*)](PF₆) was prepared as Mod1 but with *fac*-Re(*bcp*)(CO)₃Cl (0.333 g, 0.50 mmol), AgBF₄ (0.105 g, 0.54 mmol) and 4-*etpy* (0.50 mL, 4.40 mmol). The final pale yellow solid collected had a yield of 42 %. ¹H NMR (400 MHz, Methylene Chloride-*d*₂) δ 7.97 (d, *J* = 0.5 Hz, 2H), 7.90 (s, 2H), 7.85 (d, *J* = 5.8 Hz, 2H), 7.65 – 7.61 (m, 6H), 7.59 – 7.55 (m, 4H), 7.09 (d, *J* = 6.1 Hz, 2H), 3.31 (s, 6H), 2.59 (q, *J* = 7.5 Hz, 2H), 1.14 (t, *J* = 7.6 Hz, 3H). MS [HR-ESI (CH₂Cl₂) *m/z*] 736.1738 [M—PF₆]⁺, calcd

(C₃₆H₂₉N₃O₃¹⁸⁵Re) 736.1738. Anal. Calcd (found) for C₃₆H₂₉N₃O₃Re: C, 48.98 (48.70); H, 3.31 (3.38); N, 4.76 (4.67).

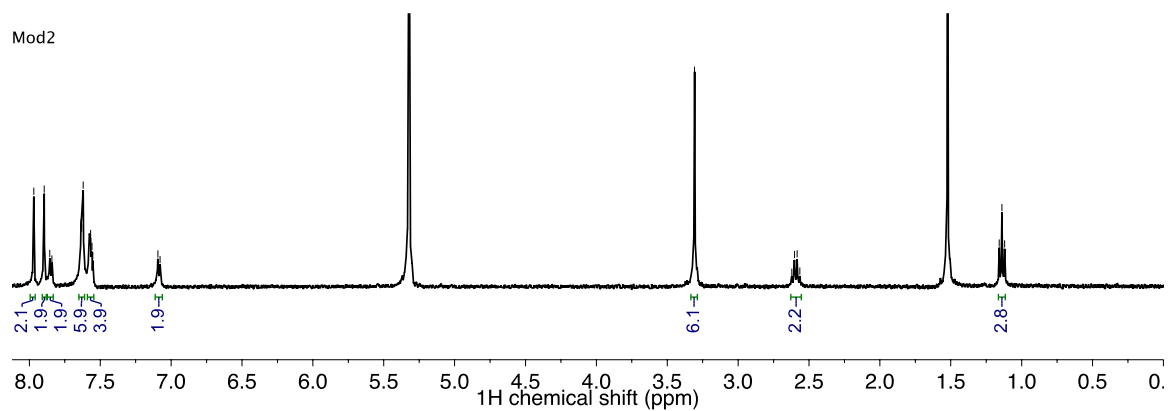


Figure B15. ¹H NMR spectrum of *fac*-[Re(bcp)(CO)₃(4-ety)](PF₆) (**Mod2**) in CD₂Cl₂ (400 MHz).

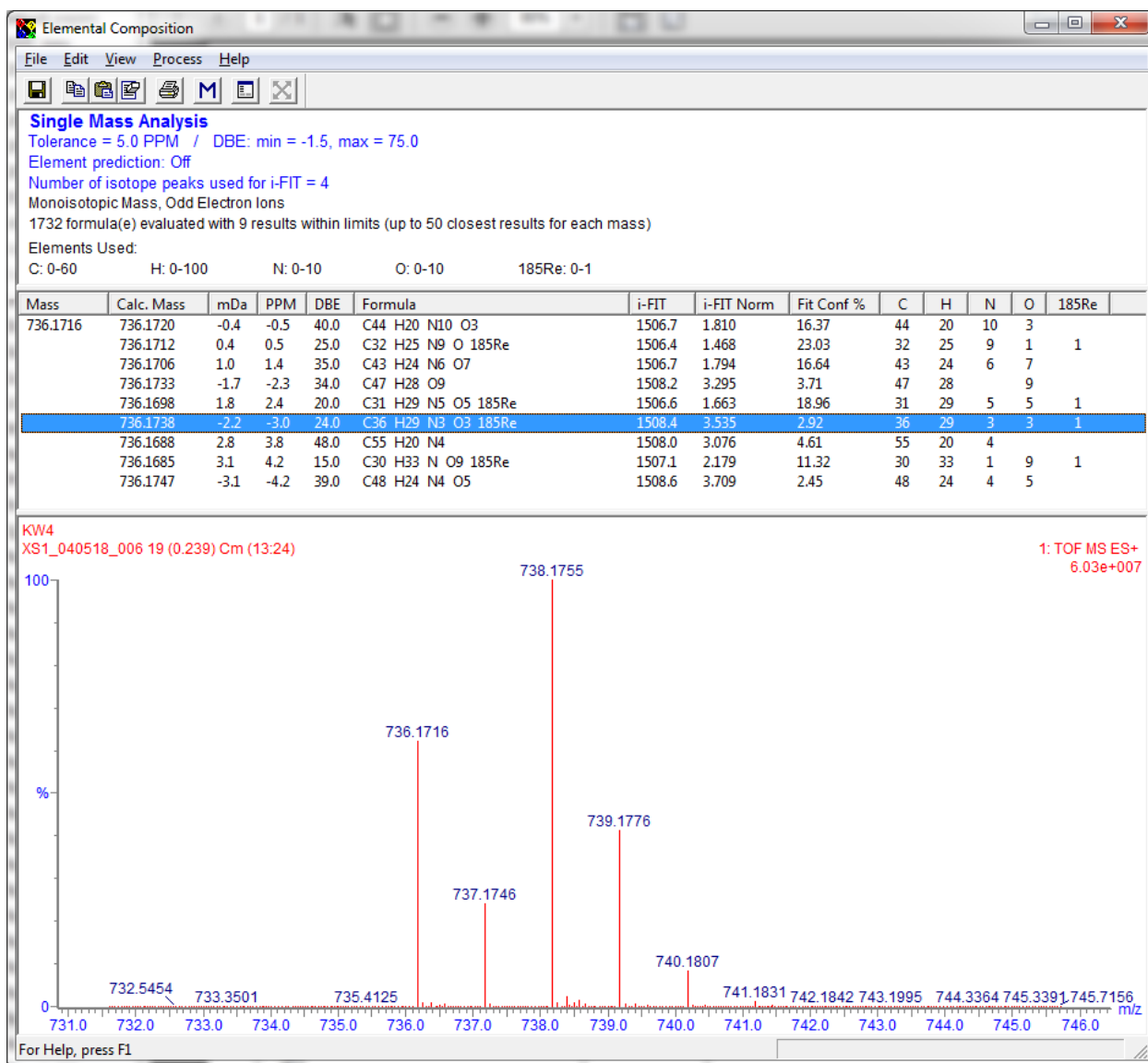


Figure B16. HRMS of *fac*-[Re(*bcp*)(CO)₃(4-*etpy*)](PF₆) (**Mod2**).

fac- [Re(*dtbb*)(CO)₃(4-*etpy*)](PF₆) (**Mod3**). *fac*- [Re(*dtbb*)(CO)₃(4-*etpy*)](PF₆) was prepared as Mod1 but with *fac*-Re(*dtbb*)(CO)₃Cl (0.285 g, 0.50 mmol), AgBF₄ (0.099 g, 0.51 mmol) and 4-*etpy* (0.50 mL, 4.40 mmol). The final pale yellow solid collected had a yield of 40 %. ¹H NMR (400 MHz, Methylene Chloride-*d*₂) δ 9.03 – 8.98 (m, 2H), 8.20 (d, *J* = 2.0 Hz, 2H), 8.04 – 7.99 (m, 2H), 7.75 – 7.70 (m, 2H), 7.16 (d, *J* = 5.7 Hz, 2H), 2.66 – 2.58 (m, 2H), 1.46 (m, 18H), 1.16 (td, *J* = 7.6, 3.0 Hz, 3H). MS [HR-ESI (CH₂Cl₂) m/z] 644.2036 [M—PF₆]⁺, calcd

(C₂₈H₃₃N₃O₃¹⁸⁵Re) 644.2051. Anal. Calcd (found) for C₂₈H₃₃N₃O₃Re: C, 42.53 (42.31); H, 4.21 (4.22); N, 5.31 (5.27).

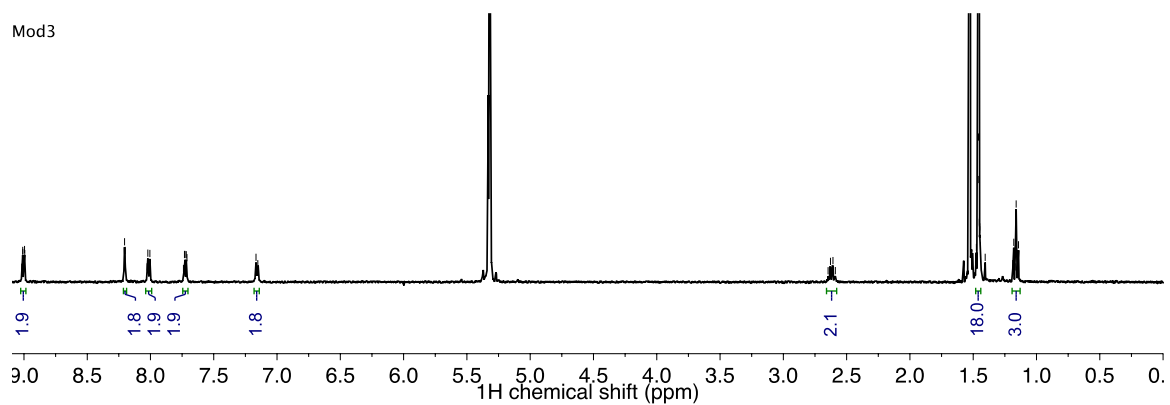


Figure B17. ¹H NMR spectrum of *fac*-[Re(dtbb)(CO)₃(4-etry)](PF₆) (**Mod3**) in CD₂Cl₂ (400 MHz).

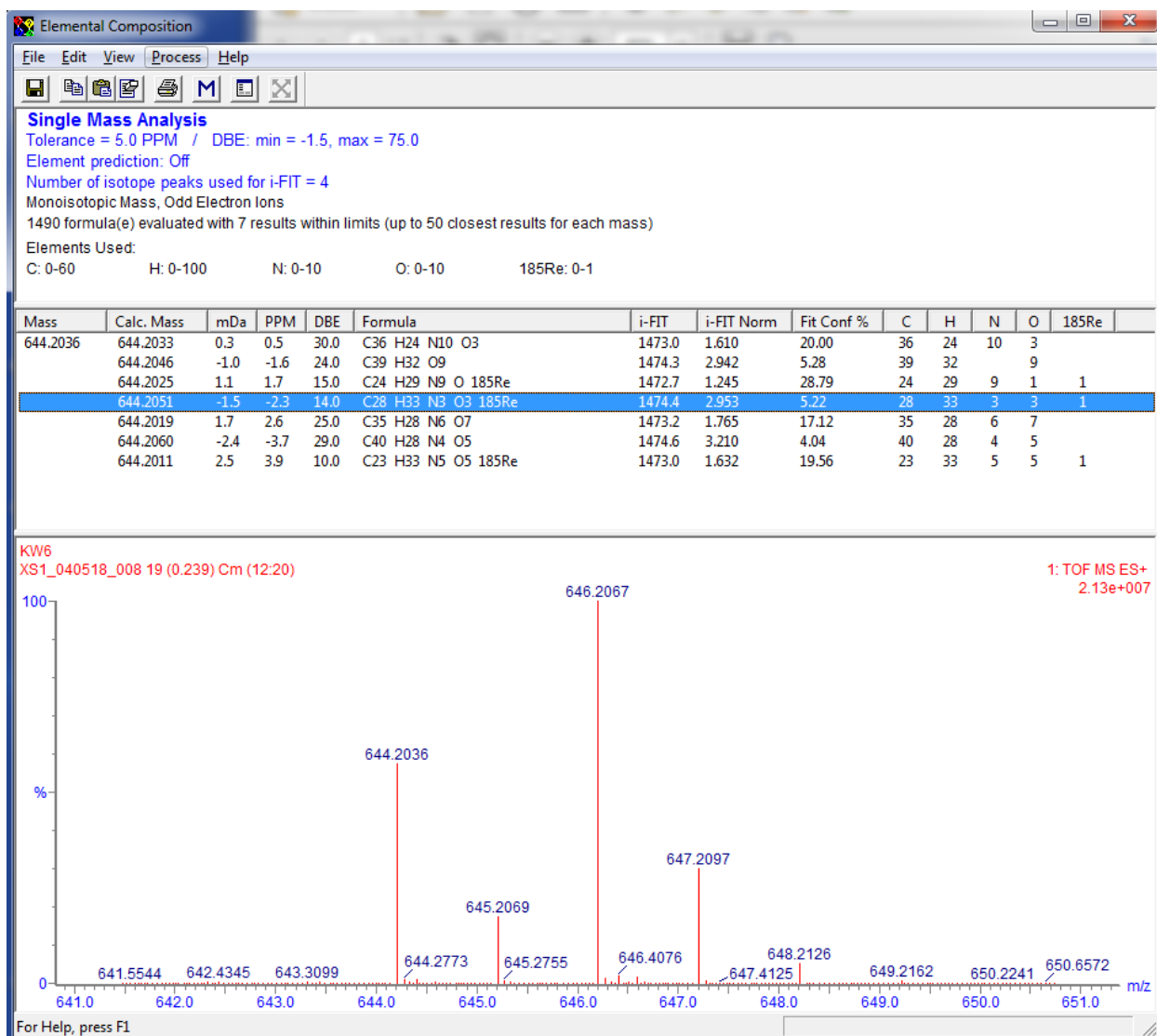


Figure B18. HRMS of *fac*-[Re(dtbb)(CO)₃(4-*etpy*)](PF₆) (**Mod3**).

fac- [Re(deeb)(CO)₃(4-*etpy*)](PF₆) (**Mod4**). *fac*- [Re(deeb)(CO)₃(4-*etpy*)](PF₆) was prepared as Mod1 but with *fac*-Re(deeb)(CO)₃Cl (0.333 g, 0.50 mmol), AgBF₄ (0.105 g, 0.54 mmol) and 4-*etpy* (0.50 mL, 4.40 mmol). The final yellow solid collected had a yield of 42 %. ¹H NMR (400 MHz, Methylene Chloride-*d*₂) δ 9.34 (dd, *J* = 5.6, 0.8 Hz, 2H), 8.90 (d, *J* = 1.6 Hz, 2H), 8.31 (dd, *J* = 5.7, 1.6 Hz, 2H), 7.98 (d, *J* = 6.6 Hz, 2H), 7.15 (d, *J* = 6.0 Hz, 2H), 4.57 – 4.52 (m, 4H), 2.60 (q, *J* = 7.5 Hz, 2H), 1.47 (t, *J* = 7.1 Hz, 6H), 1.14 (t, *J* = 7.5 Hz, 3H). MS [HR-ESI (CH₂Cl₂) *m/z*]

676.1208 [M—PF₆]⁺, calcd (C₂₆H₂₅N₃O₇¹⁸⁵Re) 676.1222. Anal. Calcd (found) for C₂₆H₂₅N₃O₇Re·2.5H₂O: C, 35.99 (25.67); H, 3.49 (2.79); N, 4.84 (4.73).

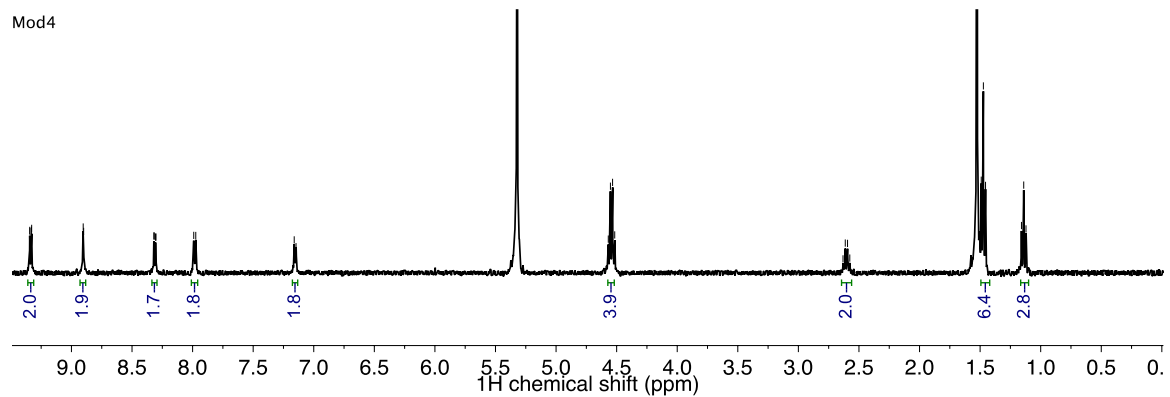


Figure B19. ¹H NMR spectrum of *fac*-[Re(deeb)(CO)₃(4-ety)](PF₆) (**Mod4**) in CD₂Cl₂ (400 MHz).

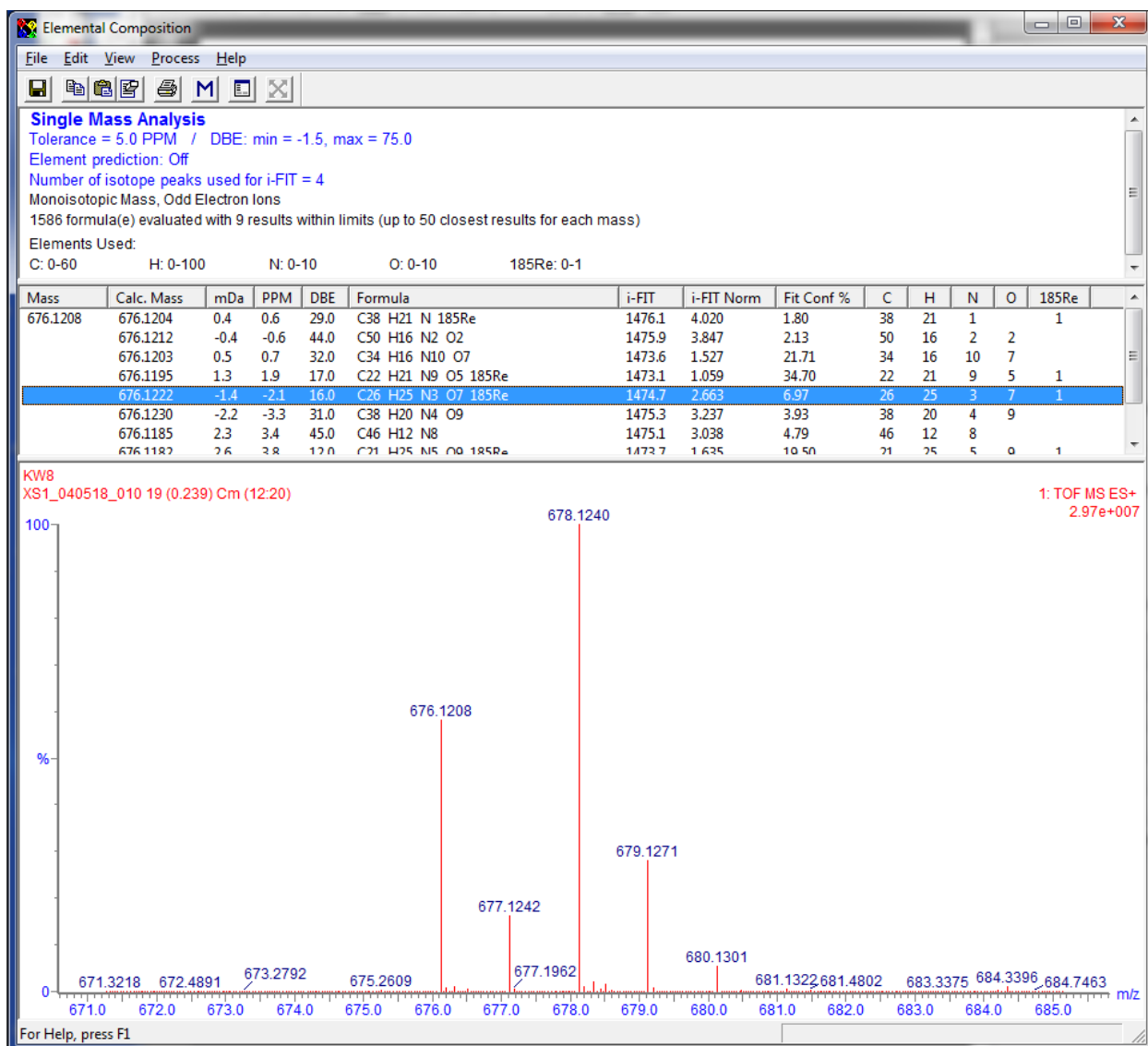


Figure B20. HRMS of *fac*-[Re(deeb)(CO)₃(4-*etpy*)](PF₆) (**Mod4**).

fac- [Re(biq)(CO)₃(4-*etpy*)](PF₆) (**Mod5**). *fac*- [Re(biq)(CO)₃(4-*etpy*)](PF₆) was prepared as Mod1 but with *fac*-Re(biq)(CO)₃Cl (0.164 g, 0.29 mmol), AgBF₄ (0.063 g, 0.32 mmol) and 4-*etpy* (0.50 mL, 4.40 mmol). The final orange solid collected had a yield of 54 %. ¹H NMR (400 MHz, Methylene Chloride-*d*₂) δ 8.95 (d, *J* = 9.0 Hz, 2H), 8.79 (d, *J* = 8.7 Hz, 2H), 8.40 (d, *J* = 8.7 Hz, 2H), 8.20 (m, 4H), 8.00 – 7.93 (m, 2H), 7.09 (d, *J* = 5.8 Hz, 2H), 6.83 (d, *J* = 5.8 Hz, 2H), 2.53 (q, *J* = 7.5 Hz, 2H), 1.08 (t, *J* = 7.6 Hz, 3H). MS [HR-ESI (CH₂Cl₂) m/z] 632.1099 [M—PF₆]⁺, calcd

(C₂₈H₂₁N₃O₃¹⁸⁵Re) 632.1112. Anal. Calcd (found) for C₂₈H₂₁N₃O₃Re·1.75H₂O: C, 41.51 (41.01); H, 3.05 (2.47); N, 5.19 (5.02).

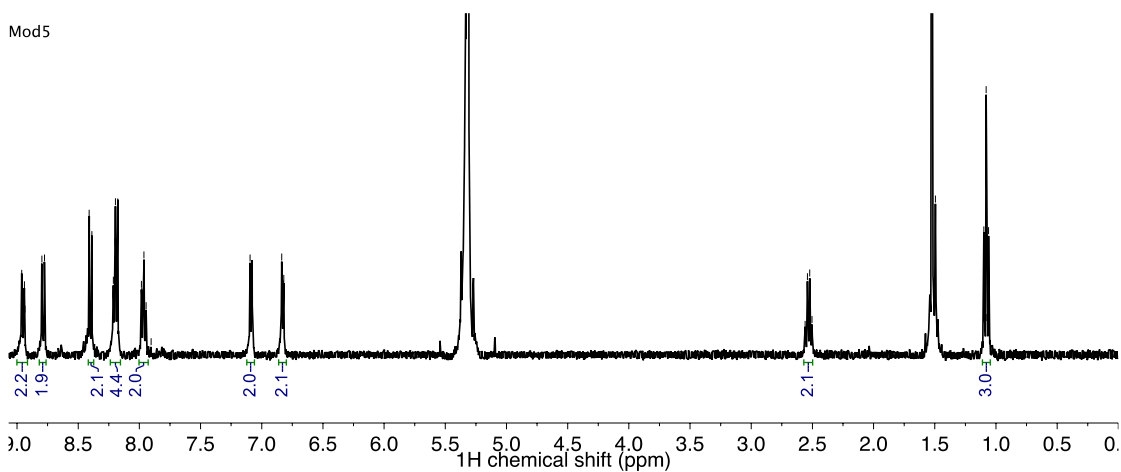


Figure B21. ¹H NMR spectrum of *fac*-[Re(biq)(CO)₃(4-ety)](PF₆) (**Mod5**) in CD₂Cl₂ (400 MHz).

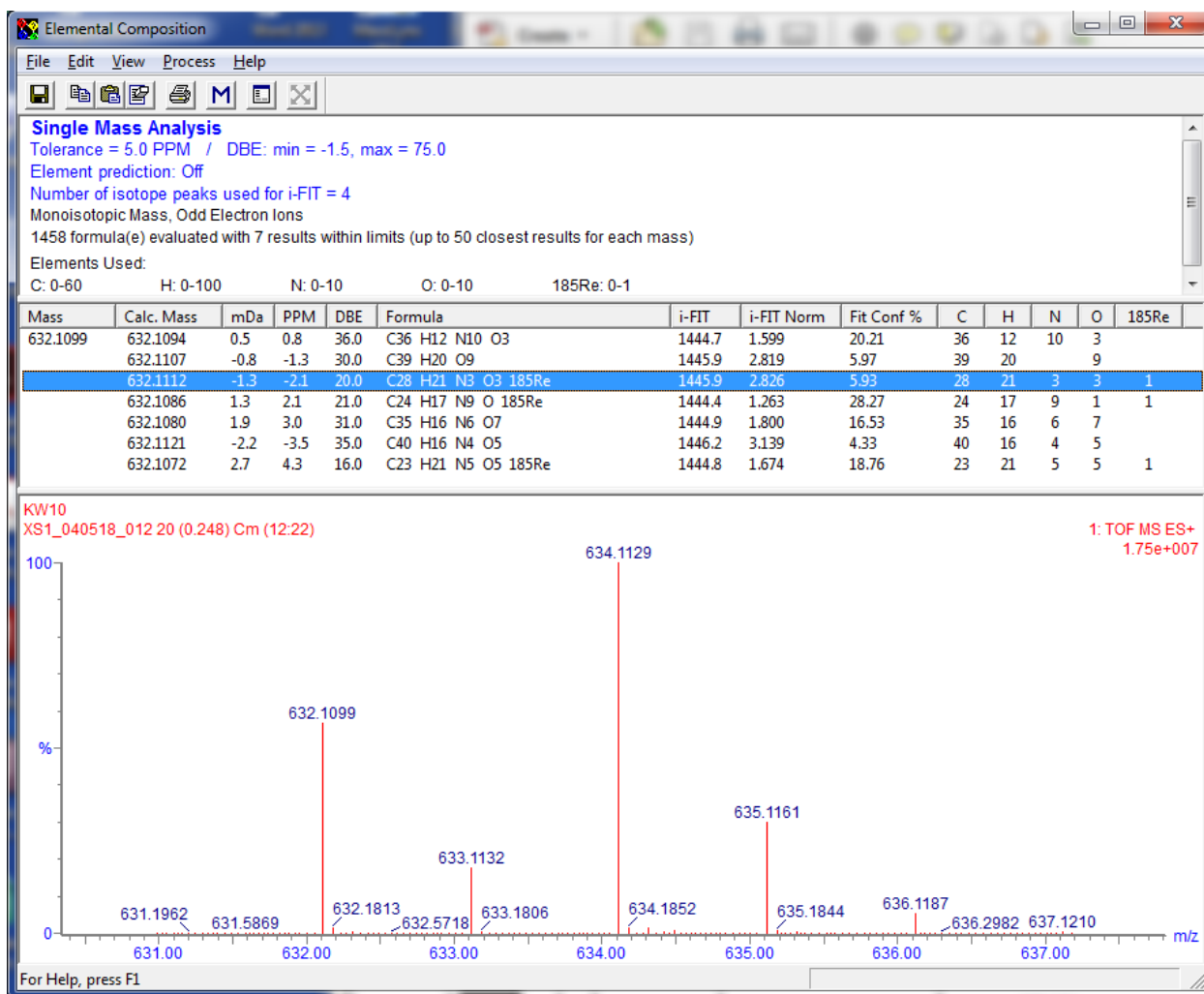


Figure B22. HRMS of *fac*-[Re(biq)(CO)₃(4-*etpy*)](PF₆) (Mod5).

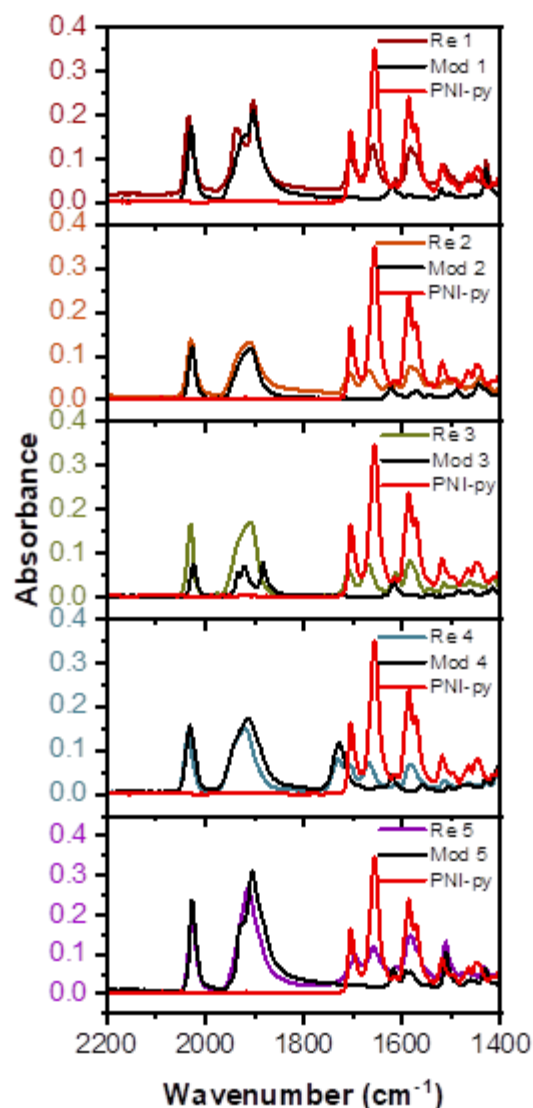


Figure B23. ATR-FTIR spectra of **Re1-5**, **Mod1-5**, and **PNI-py** overlaid.

Table B1. Reduction potentials of **Mod1-5** obtained from DPV experiments using a platinum disk as the working electrode, a platinum wire as the counter electrode, and Ag/AgNO₃ as the reference electrode.

	Reduction Potential (eV)
Mod1	-1.34
Mod2	-1.37
Mod3	-1.42
Mod4	-0.94
Mod5	-0.88

B.2. Electronic Structure Calculations

Optimized Singlet Geometries of **Re1-5** and **Mod1-5** (Table B2):

Optimized Geometry of **Re1**:

C	-3.73529235	2.98240126	-2.69194018
C	-3.53191834	3.90423533	-1.68696611
C	-3.57911634	3.48542329	-0.34194901
C	-3.82206736	2.11740220	-0.09450099
C	-3.96855437	1.64205116	-2.35343216
C	-3.40783033	4.37892236	0.76445807
C	-3.91953536	1.64580016	1.25537710
C	-3.77401936	2.55341123	2.32647118
C	-3.50197133	3.93145533	2.04603716
C	-3.92064737	2.04512119	3.63308227
H	-3.81432636	2.71926724	4.48810733
C	-4.20755739	0.70848810	3.81303829
C	-4.33144239	-0.12162096	2.68992621
H	-3.20907331	5.43345345	0.55375305
H	-3.71843235	3.27356828	-3.74383426
H	-3.34358732	4.95706840	-1.91678713
H	-4.13419638	0.89244711	-3.13469121
H	-3.38113233	4.61843238	2.88831522
H	-4.34044639	0.28353407	4.80971836
H	-4.55973941	-1.18630404	2.80848221
N	-4.00229637	1.21397513	-1.09476607
N	-4.18357839	0.32545707	1.44629912
Re	-4.25901839	-0.87811102	-0.41218402
C	-6.19570852	-0.79460501	-0.51687002
O	-7.34276159	-0.73018901	-0.57367303
C	-4.37200240	-2.61717914	0.42674804
C	-4.19412439	-1.71494708	-2.15408214
O	-4.12577138	-2.15550711	-3.21693422
O	-4.41601740	-3.62420421	0.98520008
C	-1.39322118	-1.20679804	0.88546108
C	-1.24998217	-0.45770099	-1.28096908
C	-0.01784708	-1.17344304	1.03866109
H	-2.02410723	-1.54429907	1.71397314
C	0.13049193	-0.39658498	-1.21789108
H	-1.76396521	-0.19369597	-2.21063515
C	0.77361297	-0.75309901	-0.03132599
H	0.42981095	-1.47941306	1.98412315
H	0.70001097	-0.07441696	-2.08987614
N	-2.01913023	-0.84723502	-0.24873501
N	2.18251408	-0.69236300	0.07436102
C	2.85438212	-1.84873809	0.55840305

C	2.81089712	0.53572208	-0.29706801
O	2.22418207	-2.83183616	0.87228808
O	2.13132107	1.47506615	-0.64983003
C	6.34499138	1.77106517	-0.49819602
C	7.10704641	0.65307109	-0.15012800
C	6.41785538	-0.53608499	0.28942403
C	4.99711328	-0.58139699	0.22471003
C	4.26715822	0.55454809	-0.20411800
C	4.95099828	1.71665517	-0.52870603
H	8.17472448	-1.57156707	1.01374108
H	6.84301241	2.68965624	-0.81417704
C	7.09478945	-1.63854707	0.86073507
C	4.32063623	-1.75709308	0.63211406
H	4.37015823	2.58697123	-0.84733505
C	5.02402628	-2.84162316	1.12926110
C	6.41704436	-2.77082016	1.26646010
H	4.46491024	-3.73021122	1.43458412
H	6.96441843	-3.60564822	1.71055413
C	9.18280158	-0.29292998	-1.05165606
C	9.17893959	1.95257018	-0.13555800
C	10.59858367	-0.54249599	-0.57318903
H	9.21323256	0.12328505	-2.08391214
H	8.60250153	-1.22447704	-1.11321607
C	10.60193167	1.76720117	0.36463704
H	9.19477660	2.43172022	-1.14162807
H	8.62435454	2.62515923	0.53780905
C	11.36500775	0.76813610	-0.48912902
H	11.09588974	-1.25177804	-1.25512608
H	10.56806469	-1.02348003	0.42315204
H	11.10972269	2.74547224	0.38251704
H	10.56186469	1.40865715	1.40975112
H	12.38047582	0.60794909	-0.09241299
H	11.49103676	1.17909013	-1.50975810
N	8.48905952	0.67065309	-0.18741300

Optimized Geometry of **Re2**:

C	-2.58501525	3.70476417	0.43531398
C	-1.54602317	3.23567014	1.21872803
C	-1.55974017	1.84901804	1.55439006
C	-2.55569825	1.04036699	0.96612502
C	-3.54758532	2.84298112	-0.12143806
C	-0.66069611	1.26503900	2.49657613
C	-2.64090825	-0.35276812	1.31098805
C	-1.73117319	-0.90085916	2.24075611
C	-0.74483312	-0.05171109	2.82789115

C	-1.88560820	-2.27580925	2.58747814
C	-2.98763228	-2.93718230	2.07787310
C	-3.85886634	-2.33063626	1.15383503
H	0.08075594	1.90445005	2.97987916
H	-2.63883525	4.76943225	0.18966296
H	-0.07429007	-0.46838112	3.58232421
H	-3.16703529	-3.98096238	2.35196812
Re	-4.41589338	-0.10729510	-1.12999213
N	-3.64104533	-1.08162417	0.72888500
N	-3.48518531	1.52317102	0.08705596
C	-6.21362450	0.16913592	-0.47083808
O	-7.28052759	0.33571493	-0.06913806
C	-4.81821941	0.87460897	-2.74189425
O	-5.02786342	1.45665502	-3.71576832
C	-4.98117942	-1.66821421	-2.11290320
O	-5.28954844	-2.60538428	-2.71131024
C	-0.49906910	4.16222721	1.68741907
C	0.85932000	3.85599719	1.51063106
C	-0.85655112	5.38991328	2.26213111
C	1.83292507	4.76858925	1.90583909
H	1.15255202	2.91285412	1.03553303
C	0.12308795	6.28933336	2.66949914
H	-1.91433320	5.62882331	2.41340412
C	1.46999805	5.98100633	2.48955213
H	2.88916014	4.53198724	1.74952707
H	-0.16702707	7.23683644	3.13116717
H	2.24003510	6.69088740	2.80359515
C	-0.93610313	-2.98990531	3.46195320
C	0.44167897	-2.96387730	3.19842618
C	-1.40769317	-3.75481436	4.53724427
C	1.32391303	-3.68602036	3.99513324
H	0.81937999	-2.39249527	2.34335612
C	-0.52081810	-4.46386441	5.34120833
H	-2.47989724	-3.77229036	4.75786429
C	0.84547500	-4.43246641	5.07069831
H	2.39409711	-3.67008636	3.77201422
H	-0.89978813	-5.04452745	6.18631742
H	1.54111105	-4.99436345	5.69962236
C	-4.61474539	3.41791416	-0.98819712
H	-4.32284738	3.39948115	-2.05214220
H	-5.55921544	2.86394411	-0.89381511
H	-4.79513741	4.46979623	-0.72591910
C	-5.00571242	-3.11845131	0.62019299
H	-5.88159647	-2.48316727	0.42696998
H	-4.74401040	-3.62036735	-0.32690807
H	-5.29191447	-3.90692537	1.33019405

C	2.62186113	-1.59721720	-2.33179822
C	4.08612523	-1.61552921	-2.18977221
C	4.74081128	-0.72009414	-1.30889514
C	3.98907122	0.16644392	-0.49724409
C	2.53454012	0.22855393	-0.58514709
C	4.80798028	-2.54360627	-2.92145126
C	6.16030640	-0.75008514	-1.21237914
C	6.85569145	-1.75326722	-1.92686419
C	6.19860137	-2.62799628	-2.76890125
C	6.82883142	0.17934792	-0.33298007
C	6.04482738	0.98398698	0.49963799
C	4.65315727	0.97740698	0.41187898
H	4.05928823	1.64634103	1.04150702
H	6.52548940	1.68023803	1.18924404
H	4.26456024	-3.21804832	-3.58880731
H	6.76037943	-3.39744334	-3.30376529
C	8.93499359	0.55251095	-1.54250216
C	8.87335556	0.76988297	0.87316401
C	10.34714970	0.00432791	-1.51006616
H	8.97530457	1.66033703	-1.64338317
H	8.37275652	0.18544192	-2.41254022
C	10.29228365	0.23433193	0.97111702
H	8.89342058	1.88341405	0.83877501
H	8.29778952	0.48047994	1.76652408
C	11.08715873	0.52921195	-0.28994407
H	10.86808073	0.28058193	-2.44151323
H	10.31002469	-1.10138117	-1.47951116
H	10.78078373	0.66591096	1.86006608
H	10.24362369	-0.85838815	1.13244103
H	12.09910481	0.09819992	-0.22515607
H	11.22133073	1.62373103	-0.39172708
N	8.20815054	0.23247193	-0.30640507
N	1.93460308	-0.64362114	-1.53221316
C	0.52350497	-0.58152113	-1.65712017
C	-0.27063008	-1.71259721	-1.47254015
C	-0.10503007	0.62342296	-1.97038919
C	-1.64819418	-1.57223920	-1.51587416
H	0.17443495	-2.68968228	-1.28073014
C	-1.48732617	0.67051296	-1.99549519
H	0.47734197	1.52382602	-2.17211321
H	-2.29360223	-2.44094227	-1.34717015
H	-2.00202220	1.61070103	-2.22031321
N	-2.26051123	-0.39403212	-1.72043617
O	1.83331207	0.95475698	0.09288096
O	2.00333408	-2.32347126	-3.07339727
H	7.93317750	-1.85648223	-1.77765218

Optimized Geometry of **Re3**:

C	-2.53379928	1.99184210	-3.14124318
C	-2.04942525	2.89405617	-2.19008612
C	-2.34471227	2.59866314	-0.85278302
C	-3.03954832	1.44671207	-0.50614199
C	-3.21084533	0.85104702	-2.73291315
C	-3.39746335	1.10501104	0.88564111
C	-3.23616233	1.98251410	1.95191518
C	-3.63407636	1.63178308	3.24810428
C	-4.19991940	0.36222799	3.39799529
C	-4.33110741	-0.47212707	2.29730421
H	-2.37878527	2.14993511	-4.20952826
H	-3.57384536	0.12769397	-3.47072321
H	-4.54945542	0.00282396	4.36693036
H	-4.77210845	-1.46855914	2.40565422
Re	-4.04720839	-1.43049014	-0.70529400
N	-3.93673438	-0.12387205	1.06631912
N	-3.43781535	0.55740300	-1.44773606
C	-5.95232053	-1.13751112	-0.91410602
O	-7.08156160	-0.94853011	-1.02990003
C	-4.00193639	-2.37804921	-2.38944913
O	-3.93850238	-2.88780425	-3.42229920
C	-4.38656842	-3.09666526	0.21730106
O	-4.56467643	-4.05797433	0.82816510
H	-2.80752930	2.97027317	1.76886117
H	-2.00809024	3.27490920	-0.06423596
C	-3.45832435	2.61118115	4.39868536
C	-1.97301624	2.96508917	4.52915437
C	-4.27117841	3.87547924	4.09782234
C	-3.93876638	2.02455411	5.72181648
H	-1.36432220	2.06841011	4.73310838
H	-1.57311321	3.45020321	3.62403230
H	-1.82927423	3.66687623	5.36682342
H	-5.34333848	3.64439522	3.98512433
H	-4.16643740	4.59243429	4.92843540
H	-3.93478138	4.38464428	3.18011627
H	-3.79087837	2.76109116	6.52704153
H	-5.01332346	1.77839009	5.70125747
H	-3.37699134	1.11804404	6.00255750
C	-1.25621219	4.14132626	-2.54621114
C	-2.08742625	5.37290335	-2.16827711
C	0.06152490	4.13861826	-1.76296508
C	-0.93913217	4.20248126	-4.03673324
H	-3.04301932	5.39578434	-2.71796215

H	-2.31448227	5.41086034	-1.09034804
H	-1.53080721	6.29032742	-2.42085713
H	0.65441695	3.23086519	-1.96288210
H	0.66595295	5.01309732	-2.05417911
H	-0.09496011	4.20372026	-0.67412400
H	-0.35245513	5.10929733	-4.25174926
H	-0.33917112	3.33784420	-4.36642827
H	-1.85017923	4.25436227	-4.65557129
C	3.03405812	-2.21653020	0.83207110
C	4.48756422	-2.03313319	0.96620211
C	5.13547727	-0.91575911	0.38557807
C	4.38277222	0.08505897	-0.27770898
C	2.93608611	-0.02667404	-0.43470699
C	5.20619427	-2.97102226	1.68864117
C	6.54690737	-0.78495010	0.51076908
C	7.23562743	-1.72830017	1.30840514
C	6.58418336	-2.80229724	1.88112818
C	7.20944342	0.33872798	-0.10648796
C	6.42124936	1.33407405	-0.69003600
C	5.03486426	1.20316705	-0.77584101
H	4.43757022	1.97064610	-1.27624005
H	6.89643841	2.20422812	-1.14663704
H	4.66903124	-3.81885432	2.12224220
H	7.13968839	-3.51257629	2.49813123
C	9.37137157	-0.64874809	-0.71472801
C	9.21975154	1.72484208	-0.23894497
C	10.76746170	-0.72982509	-0.13149797
H	9.44180157	-0.43040707	-1.80420409
H	8.83596151	-1.60469316	-0.62716900
C	10.61927164	1.71072308	0.35288407
H	9.27057759	2.00932510	-1.31525905
H	8.60049753	2.48053914	0.26977806
C	11.47088675	0.61195900	-0.26078597
H	11.33205572	-1.52669815	-0.64294600
H	10.70157569	-1.01759811	0.93519011
H	11.08263369	2.70066816	0.20977206
H	10.53666268	1.55126307	1.44383515
H	12.46868379	0.58222500	0.20577906
H	11.63560973	0.83168602	-1.33363005
N	8.58904354	0.42115299	-0.08156396
N	2.34366407	-1.20453713	0.10974105
C	0.94824297	-1.36425714	-0.06704496
C	0.09995691	-1.62135216	1.01055812
C	0.38032893	-1.27132713	-1.33843605
C	-1.26254319	-1.72640417	0.78199610
H	0.49159994	-1.73664216	2.02122819

C	-0.99054617	-1.39024914	-1.47369906
H	1.00043797	-1.10229712	-2.21921412
H	-1.94289624	-1.92215318	1.61727316
H	-1.44687321	-1.32514814	-2.46625013
N	-1.81913223	-1.58795515	-0.43292299
O	2.23702206	0.80369402	-0.97686203
O	2.42937907	-3.15995127	1.28563214
H	8.30092050	-1.57844916	1.50039515

Optimized Geometry of **Re4**:

C	-3.41181030	2.20848115	-2.68278120
C	-3.30618630	3.02067521	-1.55561912
C	-3.33988730	2.43088116	-0.29622602
C	-3.46971431	1.04946706	-0.18506702
C	-3.52756731	0.83759205	-2.49999718
C	-3.57525332	0.35755901	1.11201708
C	-3.56369331	1.03362106	2.33132416
C	-3.72395033	0.31562201	3.51226425
C	-3.90282334	-1.06485109	3.44261525
C	-3.89736234	-1.67360913	2.19756816
H	-3.40226930	2.63782718	-3.68607927
H	-3.61074132	0.16479700	-3.35936525
H	-4.04215135	-1.64205013	4.35978131
H	-4.03432935	-2.75526621	2.10192715
Re	-3.58940132	-1.91065915	-0.93816507
N	-3.72727833	-0.98616208	1.05709107
N	-3.54639731	0.26530101	-1.28694809
C	-5.51807043	-2.03093016	-1.13957608
O	-6.66092353	-2.08979316	-1.25273309
C	-3.35856030	-2.47500619	-2.77485020
O	-3.19814929	-2.74262521	-3.88432028
C	-3.52637931	-3.76031128	-0.36644003
O	-3.47196631	-4.83727836	0.03832800
H	-3.43712631	2.11632314	2.37817117
H	-3.26707129	3.08223321	0.57772404
C	-3.72022833	0.96478805	4.86476035
O	-3.84028233	0.33755601	5.88205844
O	-3.57114031	2.27836715	4.78174934
C	-3.16701929	4.51271231	-1.62323612
O	-3.07826628	5.19797836	-0.63895505
O	-3.15793829	4.95075834	-2.87067521
C	-3.55846331	3.00787720	6.02475643
C	-3.38684330	4.46356331	5.70723140
H	-2.74271026	2.60801417	6.65030649
H	-4.50039238	2.79576119	6.55790748

H	-3.37330530	5.05202535	6.63582746
H	-2.44080623	4.64628332	5.17547337
H	-4.21351636	4.83443933	5.08262936
C	-3.03521428	6.37445443	-3.05867322
C	-3.05934428	6.65128546	-4.53241533
H	-2.09978121	6.70543649	-2.57684519
H	-3.86220434	6.86511848	-2.51838918
H	-2.96802027	7.73173454	-4.71412234
H	-2.22536022	6.14861042	-5.04502836
H	-4.00205335	6.30918544	-4.98537136
C	3.54104619	-2.24253217	0.29859402
C	4.98683630	-2.01395916	0.44553703
C	5.55461033	-0.74632806	0.16968501
C	4.72787528	0.34744901	-0.18587302
C	3.28422618	0.19719000	-0.33480203
C	5.77933635	-3.06514023	0.87588606
C	6.96112245	-0.56959806	0.29328002
C	7.72673350	-1.64765813	0.79491506
C	7.15303345	-2.87161922	1.07561207
C	7.54125751	0.71475804	-0.01694900
C	6.68191340	1.78036212	-0.29658702
C	5.30172832	1.59466310	-0.38278903
H	4.64643428	2.42990516	-0.64601005
H	7.09402346	2.76735019	-0.51458404
H	5.30342635	-4.02807230	1.07989008
H	7.76679851	-3.68547128	1.46897210
C	9.72664165	0.05492499	-0.91505507
C	9.47242860	2.20209415	0.18315401
C	11.14538675	-0.09714602	-0.40533603
H	9.74641663	0.55998603	-1.90713114
H	9.24403861	-0.91943208	-1.07612408
C	10.89169971	2.11304514	0.71904005
H	9.46946764	2.76545818	-0.77841006
H	8.83452956	2.75725819	0.88898706
C	11.77502079	1.26929608	-0.18482502
H	11.73062478	-0.69426306	-1.12391308
H	11.13310376	-0.66225606	0.54620704
H	11.29873073	3.13077421	0.83625506
H	10.85732970	1.66437011	1.72895412
H	12.78927688	1.17448907	0.23528101
H	11.88950077	1.77631612	-1.16272108
N	8.91509256	0.86883705	-0.00090900
N	2.77004214	-1.11698709	-0.10640901
C	1.38046004	-1.30632210	-0.28514902
C	0.59875898	-1.93002815	0.68907505
C	0.74594000	-0.87724108	-1.45283511

C	-0.75817811	-2.08727116	0.46430903
H	1.03985102	-2.29912818	1.61470512
C	-0.61648810	-1.07077309	-1.59047212
H	1.30793004	-0.39620604	-2.25334617
H	-1.37811516	-2.58570920	1.21648108
H	-1.12088414	-0.74853307	-2.50702118
N	-1.37688516	-1.66092413	-0.65073005
O	2.52581912	1.09704306	-0.62368805
O	3.00597016	-3.30951725	0.49129903
H	8.78934158	-1.49046312	0.99576907

Optimized Geometry of **Re5**:

C	-3.20417927	3.68244318	1.33865708
C	-2.28435220	3.21337715	2.32564115
C	-2.13171119	1.87546205	2.52990217
C	-2.83257724	0.93947198	1.71894811
C	-3.88173131	2.71044711	0.54323202
C	-2.75386423	-0.47442912	1.92890512
C	-1.98250717	-1.05093516	2.97630420
C	-1.98412618	-2.39915226	3.17175021
C	-2.81586724	-3.23432432	2.36466216
C	-3.57396929	-2.61555827	1.32569308
Re	-3.94929732	-0.22079110	-0.81179007
N	-3.45990028	-1.26884217	1.06697606
N	-3.61388029	1.36749202	0.68088703
C	-5.86559547	-0.30067011	-0.62528706
O	-7.01543953	-0.34857711	-0.51507405
C	-4.10426633	0.88320498	-2.38765819
O	-4.15232234	1.54706803	-3.33557726
C	-3.96047832	-1.73488921	-2.00898416
O	-3.92365632	-2.64030328	-2.73051421
H	-1.38426013	-0.40790511	3.62362025
H	-1.45803214	1.51857102	3.31011422
H	-1.73334016	3.94110020	2.92921119
H	-1.38244814	-2.85431229	3.96465927
C	-4.44797835	-3.43310133	0.57541203
H	-5.08508740	-2.97010830	-0.18012103
C	-4.53391336	-4.79377243	0.81118905
H	-5.22683441	-5.39405547	0.21470900
C	-3.75698431	-5.40359547	1.80650011
H	-3.82831131	-6.48037354	1.98122113
C	-2.91556524	-4.62106442	2.57634117
H	-2.31405020	-5.06683745	3.37599623
C	-3.46108728	5.05152728	1.14436407
H	-2.91742024	5.77275233	1.76414311

C	-4.38179535	5.48009032	0.20565400
H	-4.57578836	6.54665336	0.06467599
C	-5.07894340	4.52682124	-0.55055906
H	-5.83189445	4.84903326	-1.27549511
C	-4.83767438	3.17425914	-0.38744604
H	-5.41280041	2.44525809	-0.96112008
C	2.92091718	0.95880799	0.69558304
C	4.38533328	1.06219899	0.86331105
C	5.26565134	0.36787594	-0.00167102
C	4.75321531	-0.39660111	-1.07747009
C	3.30759321	-0.52587912	-1.30296711
C	4.88087431	1.86642205	1.87302012
C	6.67072246	0.47190195	0.19694400
C	7.14027350	1.34726501	1.20464207
C	6.26680343	2.02605106	2.02901313
C	7.55767550	-0.25857110	-0.67036706
C	7.01456845	-0.95485315	-1.74656014
C	5.63000237	-1.02221716	-1.94437115
H	5.21205634	-1.59894520	-2.77455722
H	7.67040454	-1.50199719	-2.42700619
H	4.16832926	2.38787909	2.51792116
H	6.65353447	2.70327411	2.79480018
C	9.39690665	-0.83801515	0.82327005
C	9.83371569	-0.48919412	-1.53017112
C	10.76494773	-0.31178611	1.20855607
H	9.45203464	-1.94258622	0.68296303
H	8.65941158	-0.66566613	1.62093410
C	11.22003779	0.04791892	-1.21660010
H	9.90028767	-1.58298120	-1.74006014
H	9.43155765	-0.00921608	-2.43697419
C	11.75694880	-0.53872313	0.07874299
H	11.10053977	-0.80209814	2.13757714
H	10.68661072	0.77062897	1.42619709
H	11.89537781	-0.16840510	-2.06099716
H	11.15807478	1.14833300	-1.12843010
H	12.74292889	-0.11172009	0.32538001
H	11.91270885	-1.62774520	-0.05097902
N	8.92780763	-0.22620110	-0.42350205
N	2.47581014	0.17092093	-0.38845904
C	1.06695004	0.07015592	-0.58286906
C	0.30326099	1.20916300	-0.82058407
C	0.42882700	-1.16604017	-0.54160606
C	-1.06728811	1.07369299	-0.97039608
H	0.76575002	2.19609307	-0.87062008
C	-0.94689310	-1.21042017	-0.70467607
H	0.99267904	-2.08567124	-0.37905104

H	-1.69699116	1.95395906	-1.13937910
H	-1.47958214	-2.16647124	-0.65910807
N	-1.69217016	-0.11116009	-0.89466508
O	2.82036217	-1.16930517	-2.20327618
O	2.12973612	1.50383603	1.43051209
H	8.21748354	1.50708303	1.30084208

Optimized Geometry of **Mod1**:

C	-0.37722065	1.92632125	-3.45330676
C	0.06727366	3.06928936	-2.82395770
C	0.12282344	3.10924307	-1.41583996
C	-0.27452358	1.95054238	-0.71613486
C	-0.74958975	0.81938593	-2.67819970
C	0.54640484	4.26269864	-0.68034161
C	-0.27449298	1.95050920	0.71626844
C	0.12288119	3.10917801	1.41601121
C	0.54643243	4.26266756	0.68054886
C	0.06738601	3.06915964	2.82412929
H	0.36951319	3.94896575	3.39898105
C	-0.37708077	1.92616141	3.45344352
C	-0.74947448	0.81925972	2.67830064
H	0.86055115	5.14706236	-1.24107895
H	-0.44443459	1.86342955	-4.54041146
H	0.36938005	3.94912137	-3.39878075
H	-1.10426782	-0.09789143	-3.15864119
H	0.86060182	5.14700551	1.24131396
H	-0.44425220	1.86322027	4.54054796
H	-1.10412678	-0.09804283	3.15871301
Re	-1.14989676	-0.87286994	0.00002143
N	-0.69220764	0.82169939	1.34983564
N	-0.69226957	0.82176356	-1.34973711
C	-3.04900639	-0.51129655	0.00009377
O	-4.18115715	-0.28771960	0.00013535
C	-1.40935063	-2.22215780	-1.35529168
O	-1.54825835	-3.00705017	-2.19184342
C	-1.40925777	-2.22222253	1.35528924
O	-1.54809996	-3.00715541	2.19181336
C	1.77410267	-1.23482454	-1.14997048
C	1.77421506	-1.23478777	1.14977711
C	3.14813862	-1.40310406	-1.19097741
H	1.20189699	-1.17574573	-2.08125654
C	3.14825539	-1.40306514	1.19065387
H	1.20209936	-1.17567815	2.08111696
H	3.65230223	-1.47148044	-2.15907830
H	3.65251420	-1.47140745	2.15870775

N	1.08138241	-1.14780198	-0.00006425
C	3.87497330	-1.49424289	-0.00019589
C	5.36511439	-1.62116240	-0.00026449
C	6.03372646	-0.25132223	-0.00027292
H	5.68241082	-2.19540637	-0.88676916
H	5.68248871	-2.19543122	0.88619660
H	7.12958777	-0.34637526	-0.00032292
H	5.74365912	0.33115979	-0.88992612
H	5.74373823	0.33113252	0.88942406

Optimized Geometry of **Mod2**:

C	0.35858068	-3.41183227	-1.09361215
C	1.59832082	-2.82566735	-0.92045814
C	1.63926198	-1.40123125	-0.85070813
C	0.41058096	-0.70492907	-0.83540113
C	-0.83014233	-2.65924809	-1.08469215
C	2.85826614	-0.65711532	-0.87417214
C	0.40588211	0.73462003	-0.82103813
C	1.63008627	1.43905496	-0.82631113
C	2.85380928	0.70334678	-0.86344813
C	1.58001941	2.86412507	-0.87213313
C	0.33573438	3.44543223	-1.02832115
C	-0.84825578	2.68548230	-1.02710815
H	3.80308915	-1.20012846	-0.94806814
H	0.28356756	-4.49830633	-1.19611616
H	3.79495940	1.25373972	-0.92893514
H	0.25353649	4.53306132	-1.11080816
Re	-2.49149718	-0.00091572	-0.29054209
N	-0.81040192	1.35831420	-0.85608914
N	-0.80152719	-1.33569299	-0.88693914
C	-3.33824624	0.02019236	-2.03191222
O	-3.83267027	0.03282542	-3.07197629
C	-3.75354540	-1.31857369	0.33772195
O	-4.49585654	-2.10021967	0.74905798
C	-3.75912813	1.29356650	0.37396195
O	-4.50448311	2.06020663	0.80732698
C	-1.04343120	-1.18476896	2.26241409
C	-1.03083296	1.11378621	2.28862809
C	-0.31876115	-1.24370604	3.44139017
H	-1.36422831	-2.10616899	1.76400105
C	-0.30548990	1.13765413	3.46893417
H	-1.34120288	2.04981430	1.81106505
H	-0.06767623	-2.21769613	3.87189720
H	-0.04390978	2.09868018	3.92152821
N	-1.39447210	-0.02649084	1.67618504

C	0.07430800	-0.06223899	4.07816022
C	0.91401706	-0.08354408	5.31582931
C	2.39904516	-0.13086524	4.97285128
H	0.64066495	-0.95915512	5.92859736
H	0.69479614	0.81005301	5.92403034
H	3.01612220	-0.14768130	5.88301435
H	2.64277108	-1.03003233	4.38321124
H	2.69794627	0.74804079	4.37830324
C	2.80781283	-3.66555353	-0.83785113
C	3.72588691	-3.50144362	0.21039394
C	3.02527874	-4.68198363	-1.77813720
C	4.83499291	-4.33433579	0.31199795
H	3.55009098	-2.73214854	0.96990100
C	4.14367873	-5.50385678	-1.68190120
H	2.32193968	-4.81080256	-2.60716826
C	5.04884482	-5.33308187	-0.63655212
H	5.53604298	-4.20717085	1.14118801
H	4.31039767	-6.28296789	-2.43027025
H	5.92437680	-5.98304604	-0.55895212
C	2.78454059	3.71063500	-0.78361413
C	3.71038763	3.53721989	0.25619794
C	2.98929570	4.74232305	-1.71005920
C	4.81453080	4.37601484	0.36323395
H	3.54469054	2.75558685	1.00520800
C	4.10280387	5.57018799	-1.60871219
H	2.27981667	4.87868914	-2.53262826
C	5.01570892	5.39011490	-0.57168712
H	5.52162682	4.24131576	1.18607301
H	4.25953096	6.36138005	-2.34649424
H	5.88736402	6.04475684	-0.48992411
C	-2.12796650	-3.36891401	-1.26542816
H	-2.59670555	-3.60945697	-0.29622610
H	-2.84528249	-2.76554189	-1.83944421
H	-1.97256659	-4.32207109	-1.78944520
C	-2.15121080	3.39095349	-1.18564416
H	-2.86664292	2.79815352	-1.77287720
H	-2.61811182	3.60312155	-0.20896209
H	-2.00381369	4.35832854	-1.68528319

Optimized Geometry of **Mod3**:

C	1.12887720	-3.47905726	-0.51157209
C	2.34007528	-2.88800522	-0.14104506
C	2.35624229	-1.48797712	-0.10021106
C	1.22419921	-0.74158607	-0.40849708
C	0.02985712	-2.68321320	-0.80080010

C	1.21285620	0.73600104	-0.43812408
C	2.33110429	1.51178710	-0.15308606
C	2.29349128	2.90862720	-0.24979107
C	1.07648119	3.46529324	-0.65296109
C	-0.00833588	2.64143518	-0.91618211
H	1.01979519	-4.56207334	-0.58515609
H	-0.92067295	-3.13982724	-1.09597913
H	0.95173119	4.54264832	-0.77133710
H	-0.96377595	3.07090321	-1.23528614
Re	-1.67379600	-0.03901701	-1.13293213
N	0.04087312	1.30808909	-0.80574511
N	0.05939512	-1.34586111	-0.74611810
C	-1.41633899	-0.08174802	-3.05463627
O	-1.24721097	-0.10694602	-4.19227535
C	-3.02201410	-1.41800811	-1.27537114
O	-3.77927016	-2.28638417	-1.32331514
C	-3.04006910	1.31396709	-1.33833515
O	-3.80838115	2.16952114	-1.42532815
C	-1.93475002	-1.11855709	1.83461908
C	-1.94854802	1.17812007	1.77683608
C	-2.10412503	-1.12622709	3.20958218
H	-1.87365602	-2.06191216	1.28178604
C	-2.11828703	1.25330208	3.14958318
H	-1.89921702	2.09337814	1.17764404
H	-2.17209304	-2.08143016	3.73866922
H	-2.19792504	2.23309715	3.62980421
N	-1.85714602	0.01286299	1.11201103
C	-2.20745804	0.08128300	3.90712223
C	-2.34895505	0.11793500	5.39574434
C	-0.98786595	0.14469100	6.08236139
H	-2.92304709	-0.76278806	5.72972038
H	-2.93524509	1.00643207	5.68495537
H	-1.09734596	0.17163700	7.17626549
H	-0.39400991	-0.74745406	5.82489137
H	-0.40628191	1.03076706	5.77984838
H	3.25986235	1.02018006	0.14375896
H	3.27928536	-0.97043408	0.16912096
C	3.53112638	3.73591026	0.06228295
C	3.95755340	3.46435824	1.50911606
C	4.65388645	3.32689123	-0.89787111
C	3.27063836	5.22982837	-0.09857306
H	3.16056834	3.73977326	2.21983611
H	4.21853142	2.40751116	1.68143407
H	4.84854847	4.06507328	1.75404608
H	4.36457443	3.49715324	-1.94804719
H	5.55492752	3.92833227	-0.69504310

H	4.93649647	2.26713615	-0.78998211
H	4.18749342	5.79140842	0.13937196
H	2.98832833	5.49368536	-1.13123413
H	2.48272830	5.59024539	0.58364099
C	3.59315138	-3.68293727	0.19267496
C	4.70257946	-3.29262725	-0.79052411
C	4.02508341	-3.34995225	1.62498107
C	3.35622636	-5.18590338	0.09018196
H	4.40868243	-3.50633326	-1.83145018
H	4.96942848	-2.22541017	-0.72418710
H	5.61434053	-3.87212529	-0.57233509
H	3.23746735	-3.61048527	2.35157512
H	4.92718047	-3.92691829	1.88585609
H	4.27045643	-2.28337317	1.75510408
H	4.28380642	-5.72305444	0.34256097
H	2.57894031	-5.53319643	0.79112401
H	3.07174734	-5.49321942	-0.92978112

Optimized Geometry of **Mod4**:

C	1.53387216	-3.04486328	-0.61483035
C	2.56690504	-2.13717992	-0.39522462
C	2.27756657	-0.77658986	-0.38097745
C	0.96711819	-0.35039711	-0.57641917
C	0.24884256	-2.55186772	-0.79068309
C	0.58813728	1.07232358	-0.63424042
C	1.51587224	2.10440784	-0.51144860
C	1.08882512	3.42330929	-0.63098174
C	-0.25753760	3.67654843	-0.88061499
C	-1.12751245	2.60244941	-0.98536919
H	1.72093112	-4.11883640	-0.64542390
H	-0.58853760	-3.23430251	-0.96083123
H	-0.61539158	4.70201274	-0.98932450
H	-2.19116904	2.76437056	-1.18055418
Re	-2.07206305	-0.41131185	-0.90702301
N	-0.72158882	1.33054773	-0.85623864
N	-0.03483752	-1.24203447	-0.76222655
C	-2.09564412	-0.48179378	-2.84192096
O	-2.10364159	-0.52242173	-3.99438574
C	-3.05757486	-2.07176685	-0.83538983
O	-3.61208324	-3.08316467	-0.77820134
C	-3.75470895	0.53931998	-0.92483578
O	-4.74019537	1.14103026	-0.92491494
C	-1.58332751	-1.37652573	2.06211731
C	-2.14692476	0.85283378	1.98994531
C	-1.47393688	-1.34616471	3.44268397

H	-1.40843721	-2.31113831	1.51951518
C	-2.05763689	0.96184443	3.36702373
H	-2.42907220	1.72256422	1.38843533
H	-1.20823080	-2.26043391	3.98043471
H	-2.26610222	1.92360445	3.84434076
N	-1.91215763	-0.29671571	1.33035631
C	-1.71466673	-0.15584957	4.13460022
C	-1.55910986	-0.06171846	5.61908936
C	-0.17415644	0.44887098	5.99999792
H	-1.73416268	-1.05293299	6.06899761
H	-2.33157064	0.61517987	6.02181854
H	-0.06514212	0.51464208	7.09254727
H	0.61438992	-0.22082716	5.62010263
H	0.00877400	1.45204485	5.58143607
H	2.57067267	1.89585410	-0.33004472
H	3.09564856	-0.07216733	-0.21865465
C	2.02549721	4.58636029	-0.50973027
O	1.66153158	5.73066813	-0.60454727
O	3.27107104	4.19875573	-0.29036182
C	3.98867244	-2.55583973	-0.17575616
O	4.87835082	-1.76784452	0.02532359
O	4.13082306	-3.86838826	-0.22888388
C	4.26516157	5.23084256	-0.15905438
C	5.59117156	4.56866612	0.07083605
H	3.97149441	5.89048548	0.67459613
H	4.25126875	5.84387417	-1.07557349
H	6.37741888	5.32979737	0.17626319
H	5.57709793	3.96232920	0.98913810
H	5.85881406	3.91541491	-0.77336973
C	5.45602593	-4.39415351	-0.03344263
C	5.38044693	-5.88813101	-0.14266315
H	5.81947720	-4.05959027	0.95262785
H	6.12113310	-3.94759874	-0.79129531
H	6.37842485	-6.32597539	0.00176880
H	4.70905894	-6.30738248	0.62191071
H	5.01291136	-6.19387460	-1.13386836

Optimized Geometry of **Mod5**:

C	-3.50623231	0.32165176	1.87291925
C	-2.83258996	1.25274722	2.68930895
C	-1.46237028	1.30299160	2.68082546
C	-0.74584395	0.46398920	1.80154167
C	-2.72458831	-0.51636207	1.02077995
C	0.73182558	0.43344728	1.80206055
C	1.48444571	1.26825804	2.65440213

C	2.85134071	1.15893013	2.66636583
C	3.48321026	0.17018127	1.88489702
C	2.66568722	-0.65485902	1.05409202
Re	-0.02986020	-1.07807856	-0.68972292
N	1.31075769	-0.44939384	0.98056003
N	-1.36065639	-0.37310488	0.95837136
C	-0.10044495	-2.95137965	-0.21403433
O	-0.14373393	-4.07001427	0.06839319
C	-1.33600318	-1.34146336	-2.08239802
O	-2.11826333	-1.46387362	-2.92399758
C	1.28882970	-1.43820320	-2.04874779
O	2.08167300	-1.62278733	-2.86884747
C	-1.07762778	1.85101710	-1.25351361
C	1.22382166	1.76443599	-1.27236248
C	-1.06810674	3.21624850	-1.48444220
H	-2.02824620	1.31476315	-1.15637960
C	1.31358080	3.12695341	-1.50368886
H	2.13310462	1.15839547	-1.19047034
H	-2.01670724	3.75376051	-1.56954012
H	2.29857515	3.59138604	-1.60401024
N	0.04838648	1.12238865	-1.13993790
C	0.14878927	3.89248666	-1.61603764
C	0.20017720	5.37503123	-1.80572624
C	0.20699182	6.10142257	-0.46545315
H	-0.66964803	5.69650275	-2.40295282
H	1.10229169	5.63900934	-2.38239616
H	0.24678471	7.19145272	-0.60738996
H	-0.69960504	5.86842964	0.11661716
H	1.07875016	5.80640028	0.14108179
H	0.99114741	2.00369889	3.28830484
H	-0.93865233	1.98641901	3.34808004
H	-3.41143072	1.90933356	3.34472382
H	3.45833436	1.81475487	3.29672335
C	3.28686085	-1.69880851	0.32710164
H	2.67092662	-2.38333464	-0.25724435
C	4.64789539	-1.88353303	0.39586999
H	5.10447242	-2.70525975	-0.16152159
C	5.46089209	-1.03638099	1.18177544
H	6.54140768	-1.19473621	1.21227921
C	4.88470311	-0.03193324	1.91882303
H	5.48903717	0.62158673	2.55433567
C	-4.91598605	0.18650587	1.89597116
H	-5.49118759	0.85088697	2.54716725
C	-5.53637885	-0.76726147	1.12808650
H	-6.62338137	-0.87422507	1.15009756
C	-4.76090337	-1.62910569	0.32091350

H	-5.25319813	-2.41150576	-0.26210778
C	-3.39222023	-1.50766945	0.26194120
H	-2.80861256	-2.20368342	-0.34114453

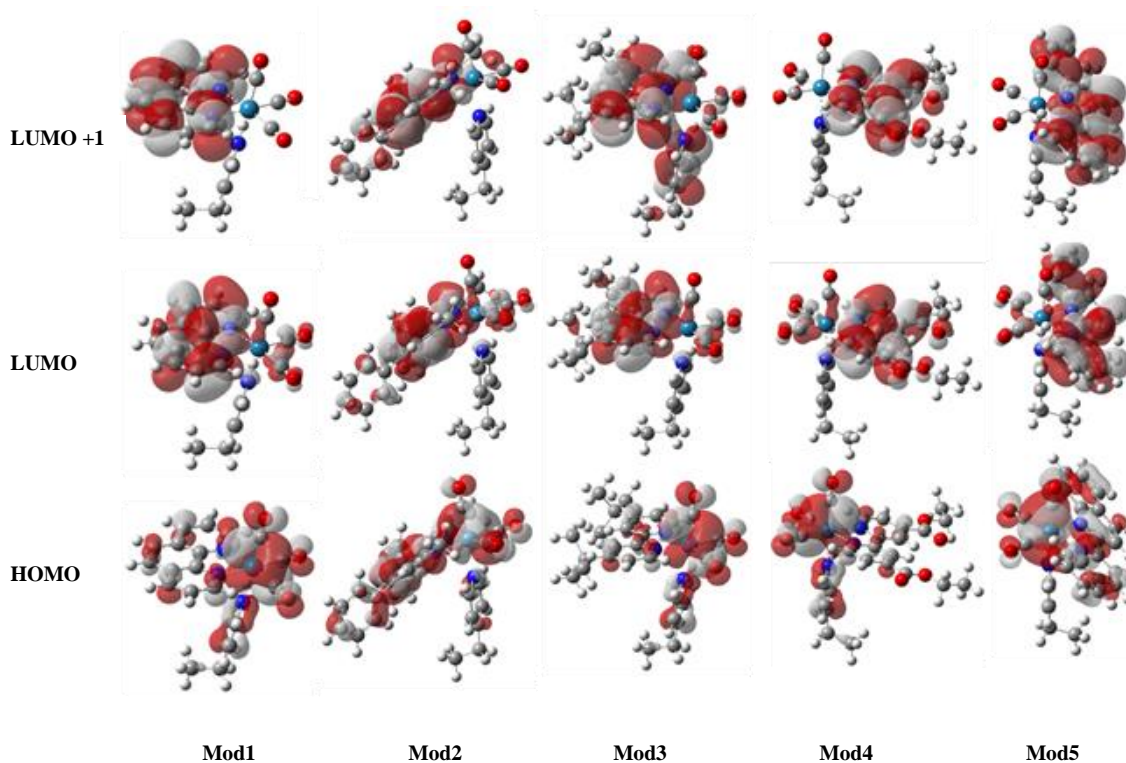


Figure B24. HOMO, LUMO, and LUMO + 1 of **Mod1-5**. M06//Def2-SVP/SDD PCM: THF.

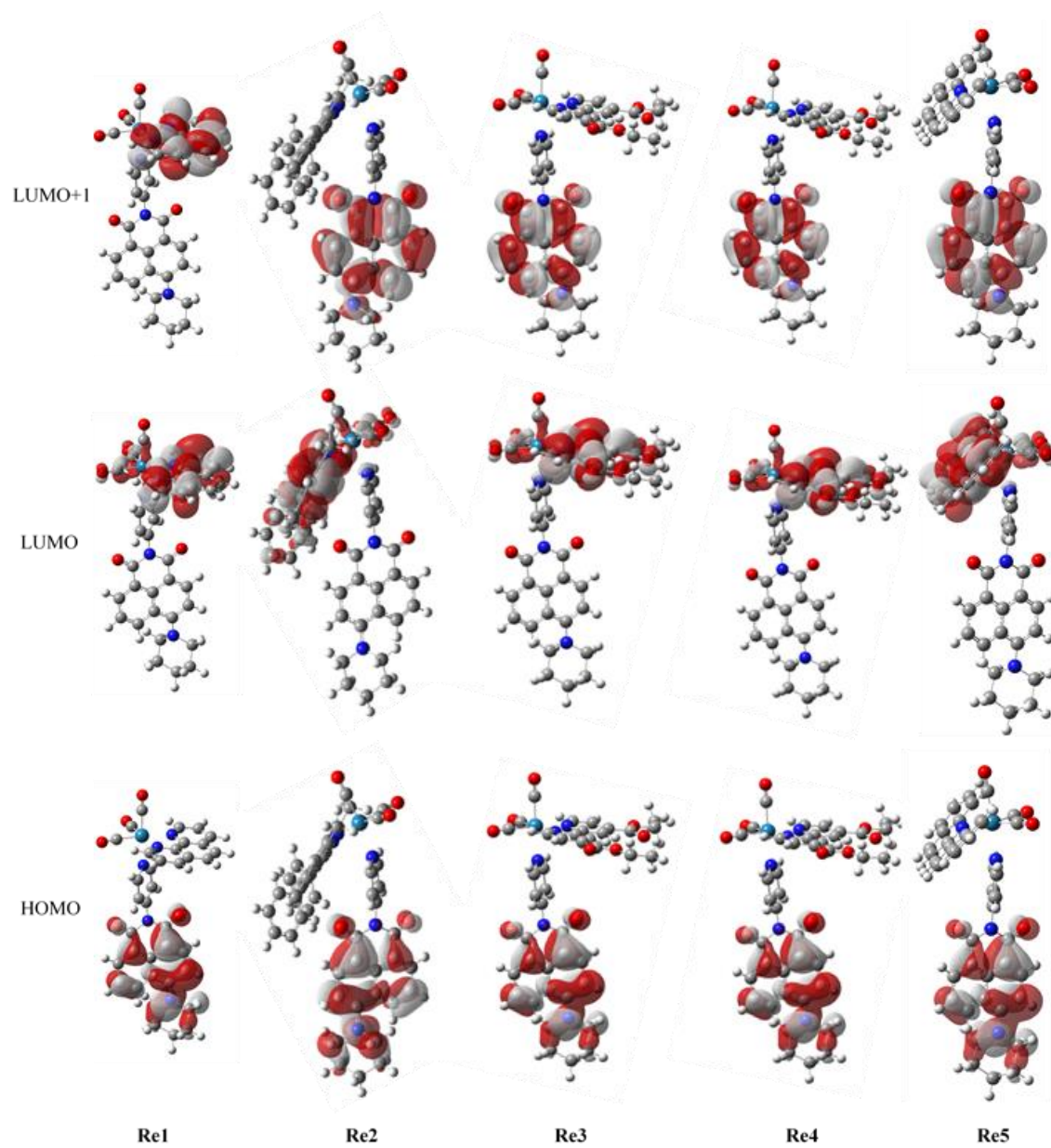


Figure B25. HOMO, LUMO, and LUMO + 1 of **Re1-5**. M06//Def2-SVP/SDD PCM: THF.

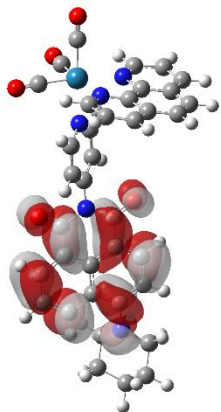


Figure B26. LUMO + 2 of **Re1**. M06//Def2-SVP/SDD PCM: THF.

Table B3. Experimental UV/Vis data obtained in THF at room temperature. Wavelength, energies, and oscillator strength (f) for selected $S_0 \rightarrow S_n$ excitations as determined via TDDFT at the level of theory specified below.

<i>Molecule</i>	<i>Experimental</i> $\lambda_{abs\ max}/nm, eV$ $(\epsilon/M\ cm^{-1})$	<i>M06/Def2-SVP</i> $S_0 \rightarrow S_1/nm, eV (f)$ $S_0 \rightarrow S_2/nm, eV (f)$ $S_0 \rightarrow S_n/nm, eV (f)$
Mod1	364, 3.41 (3950)	390, 3.18 (0.0017) 383, 3.24 (0.0941) S ₁₅ : 271, 4.51 (0.3626)
Mod2	377, 3.29 (5000)	391, 3.17 (0.1534) 385, 3.22 (0.0089) S ₄ : 351, 3.53 (0.2183)
Mod3	339, 3.66 (5000)	380, 3.27 (0.0054) 374, 3.31 (0.1164) S ₁₂ : 281, 4.41 (0.2527)
Mod4	385, 3.22 (5000)	440, 2.82 (0.0094) 424, 2.93 (0.1094) S ₉ : 304, 4.07 (0.3399)
Mod5	407, 3.04 (4200)	466, 2.66 (0.0001) 442, 2.81 (0.0731) S ₅ : 354, 3.50 (0.4860)
Re1	403, 3.08 (11500)	412, 3.01 (0.3949) 403, 3.07 (0.0012) S ₁₄ : 308, 4.02 (0.1212)
Re2	407, 3.04 (12500)	413, 3.00 (0.3954) 395, 3.14 (0.0003) S ₃ : 389, 3.18 (0.1416)
Re3	400, 3.10 (15900)	412, 3.01 (0.3991) 384, 3.23 (0.0014) S ₄ : 371, 3.35 (0.1047)
Re4	407, 3.04 (13200)	475, 2.61 (0.0004) 440, 2.82 (0.0092) S ₅ : 412, 3.01 (0.3865)
Re5	406, 3.05 (15400)	529, 2.35 (0.0001) 520, 2.38 (0.0018) S ₅ : 409, 3.03 (0.3825)

Table B4. Energies of the LUMO's of Re-CDI complexes with both ancillary ligands.

	4-etry LUMO (eV)	PNI-py LUMO (eV)
$[Re(phen)(CO)_3(L)](PF_6)$	-3.13	-3.09
$[Re(bcp)(CO)_3(L)](PF_6)$	-3.05	-3.00
$[Re(dtbb)(CO)_3(L)](PF_6)$	-2.87	-2.92
$[Re(deeb)(CO)_3(L)](PF_6)$	-3.60	-3.56
$[Re(biq)(CO)_3(L)](PF_6)$	-3.62	-3.86

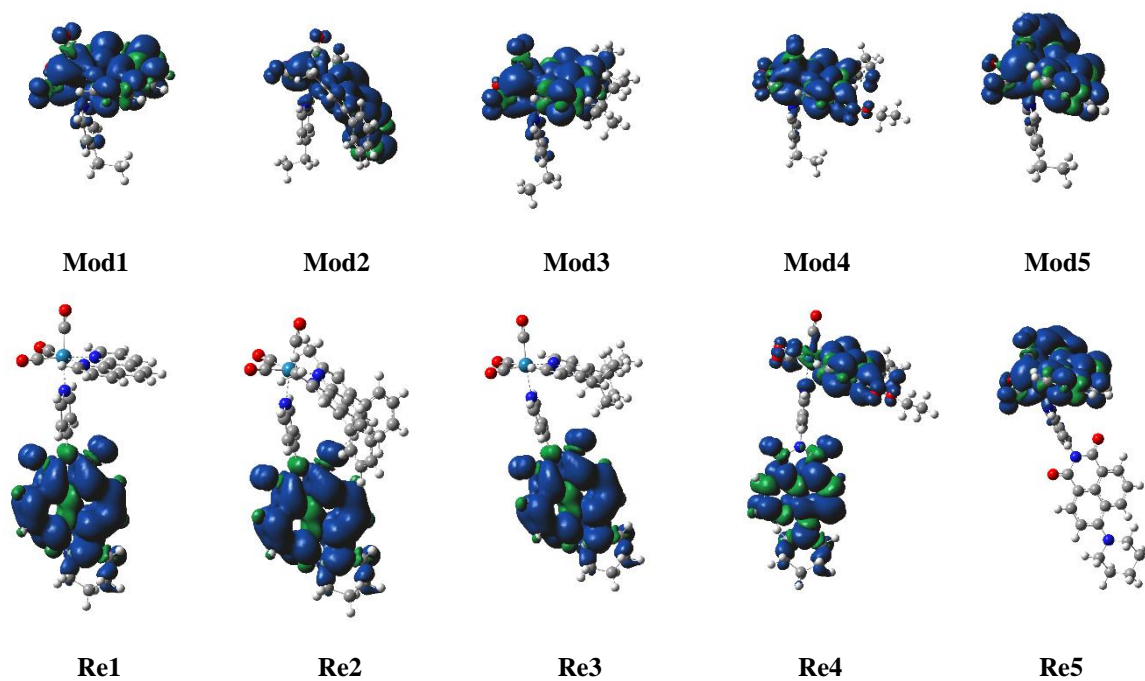


Figure B27. Triplet spin densities of **Mod1-5** and **Re1-5**. M06//Def2-SVP/SDD PCM: THF.

B.3. Additional Spectroscopic Information

Steady-state Spectroscopic Information:

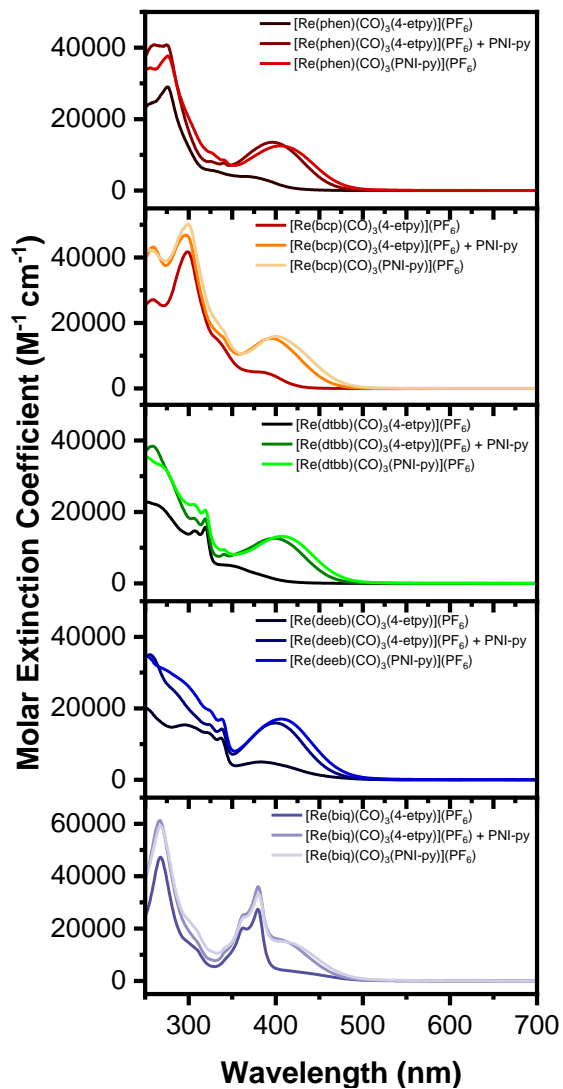


Figure B28. Additive combination of electronic spectra between PNI, Re(I) model and Re(I) complex in THF.

Time-Resolved Spectroscopic Information:

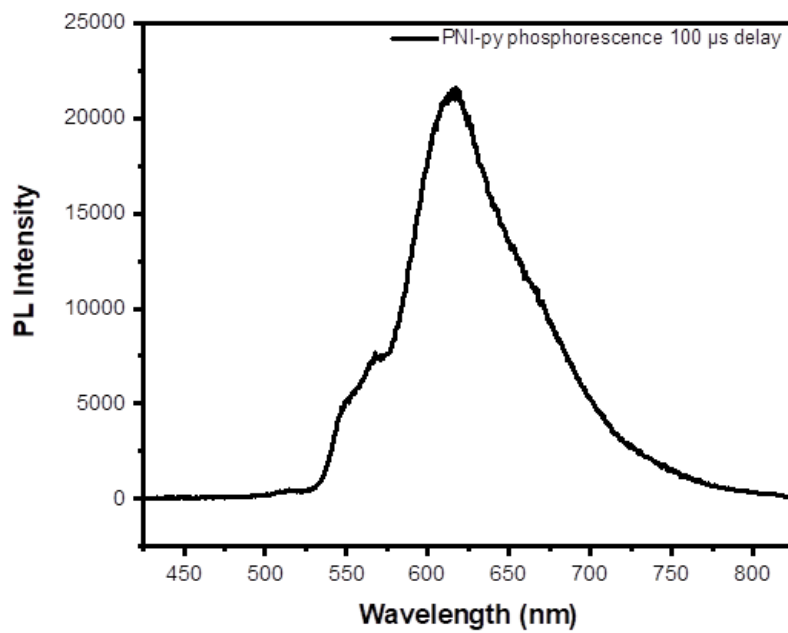


Figure B29. 77 K of PNI-py triplet sensitized using 10% EtI. Blue shoulder is residual fluorescence. Energy estimated by converting to wavenumbers and taking the peak maximum.

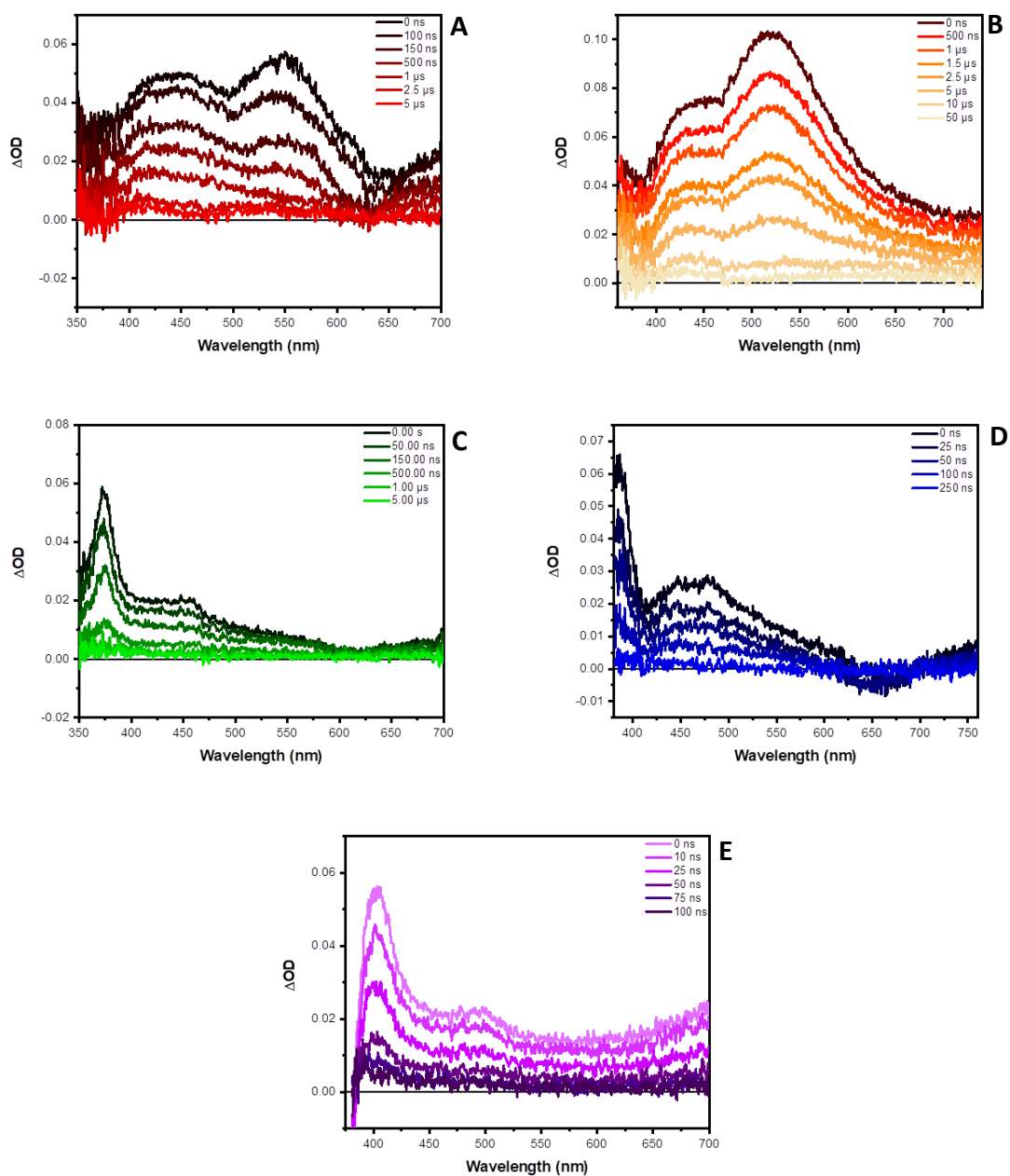


Figure B30. Excited-state absorption difference spectra of **Mod1** (A), **Mod2** (B), **Mod3** (C), **Mod4** (D), and **Mod5** (E) in THF. **Mod1-5** were excited using a Continuum Minilite with 355 nm pulsed excitation (5.0 mJ/pulse, 5 ns fwhm).

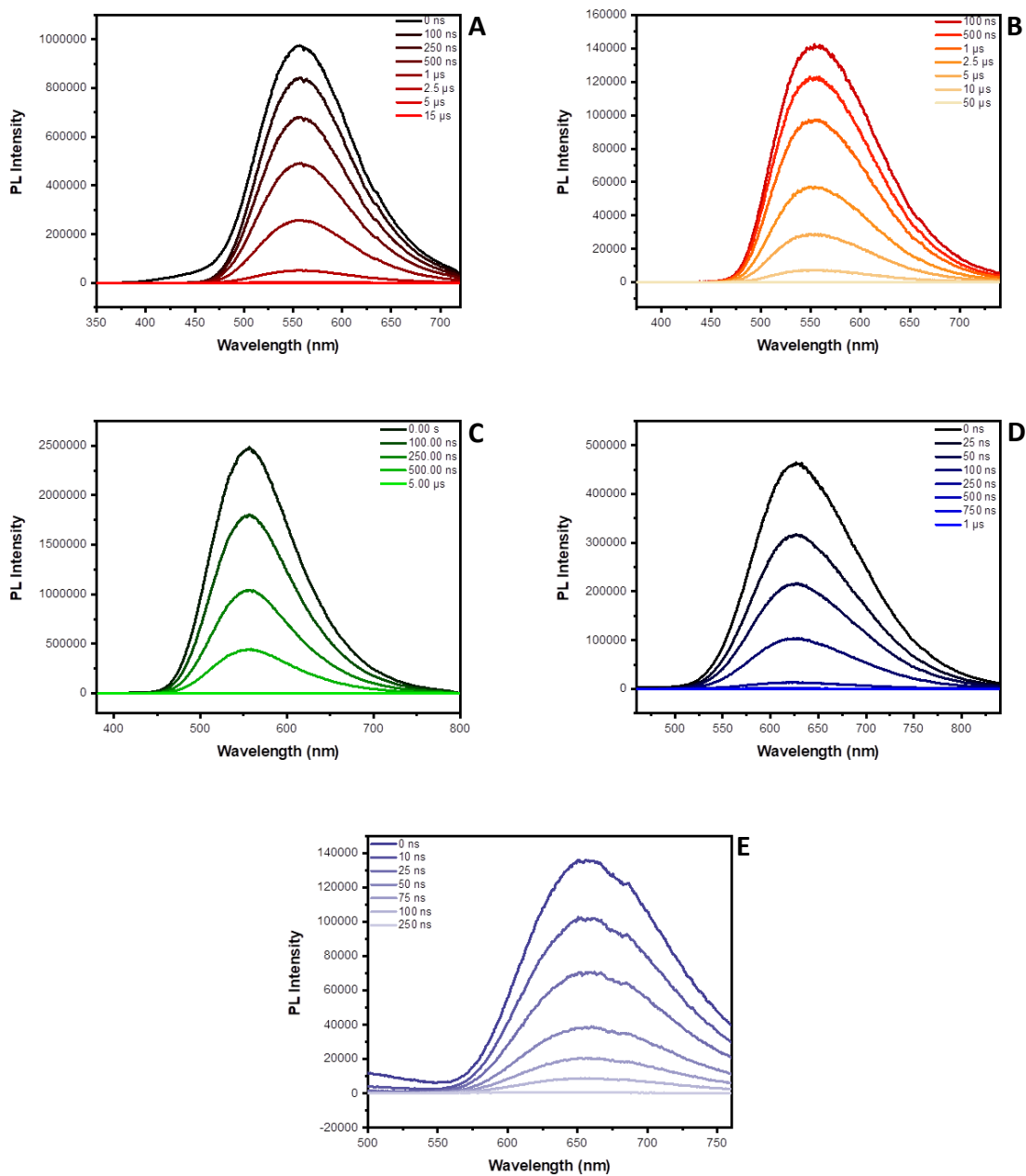


Figure B31. Time-resolved photoluminescence spectra of **Mod1** (A), **Mod2** (B), **Mod3** (C), **Mod4** (D), and **Mod5** (E) in THF. **Mod1-5** were excited using a Continuum Minilite with 355 nm pulsed excitation (5.0 mJ/pulse, 5 ns fwhm).

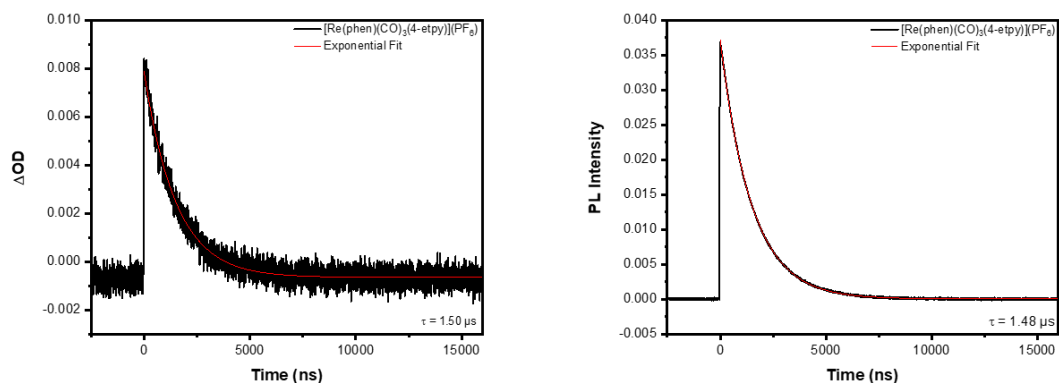


Figure B32. nsTA (left, 450 nm) and photoluminescence (right, 557 nm) decays of **Mod1**. Excited at 410 nm (2.0 mJ/pulse).

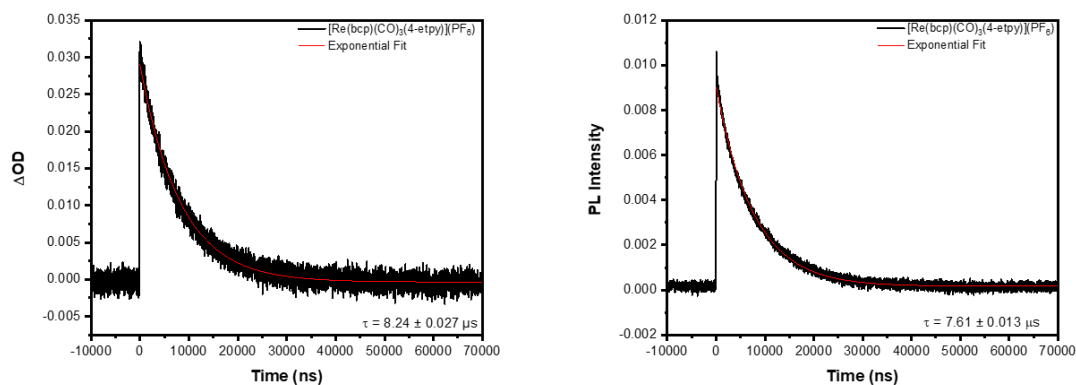


Figure B33. nsTA (left, 520 nm) and photoluminescence (right, 556 nm) decays of **Mod2**. Excited at 410 nm (2.0 mJ/pulse).

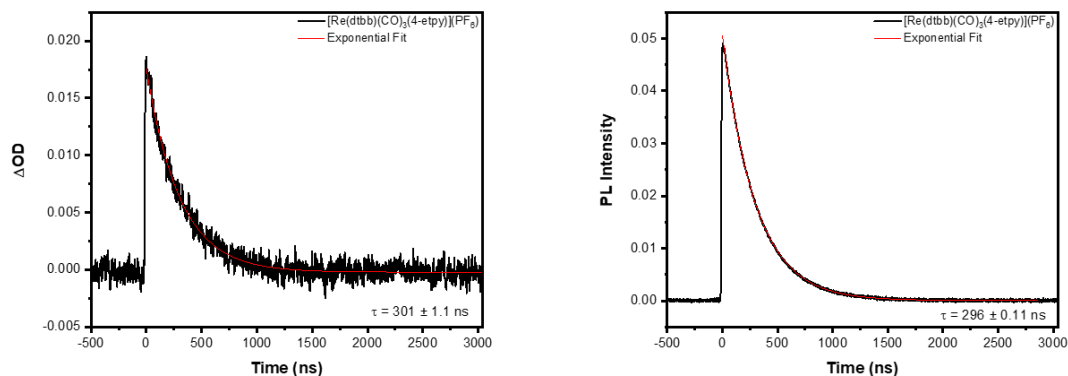


Figure B34. nsTA (left, 455 nm) and photoluminescence (right, 556 nm) decays of **Mod3**. Excited at 410 nm (2.0 mJ/pulse).

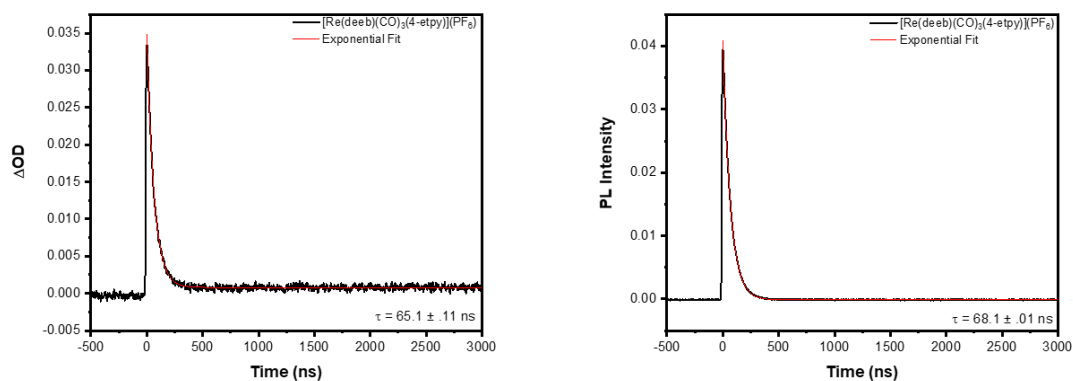


Figure B35. nsTA (left, 475 nm) and photoluminescence (right, 627 nm) decays of **Mod4**. Excited at 410 nm (2.0 mJ/pulse).

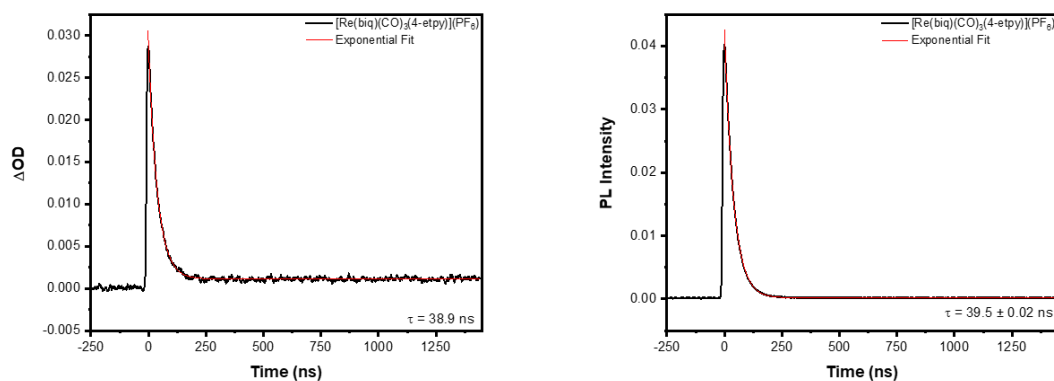


Figure B36. nsTA (left, 403 nm) and photoluminescence (right, 660 nm) decays of **Mod5**. Excited at 410 nm (2.0 mJ/pulse).

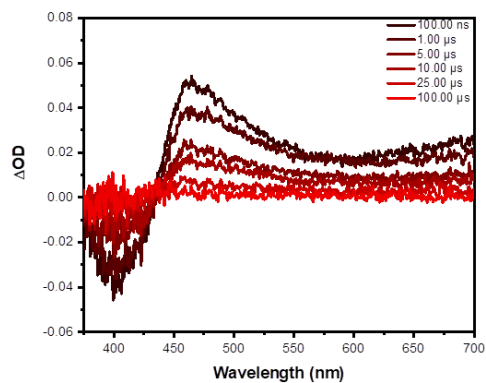


Figure B37. Excited-state absorption difference spectra of **Re1** (92.3 μM) in THF excited using a Continuum Minilite with 355 nm pulsed excitation (5.0 mJ/pulse, 5 ns fwhm).

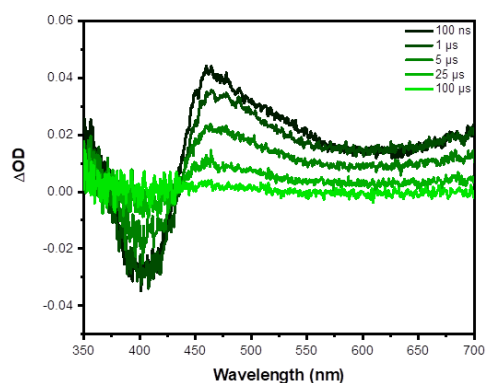


Figure B38. Excited-state absorption difference spectra of **Re3** (90.7 μM) in THF excited using a Continuum Minilite with 355 nm pulsed excitation (5.0 mJ/pulse, 5 ns fwhm).

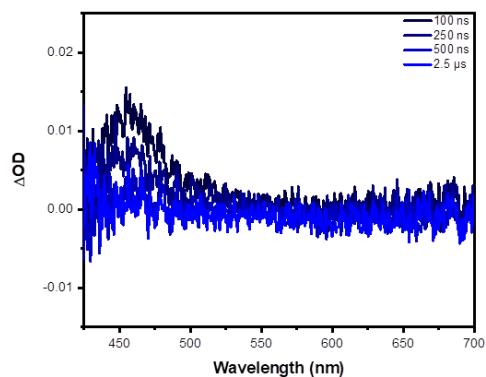


Figure B39. Excited-state absorption difference spectra of **Re4** (93.0 μM) in THF excited using a Continuum Minilite with 355 nm pulsed excitation (5.0 mJ/pulse, 5 ns fwhm).

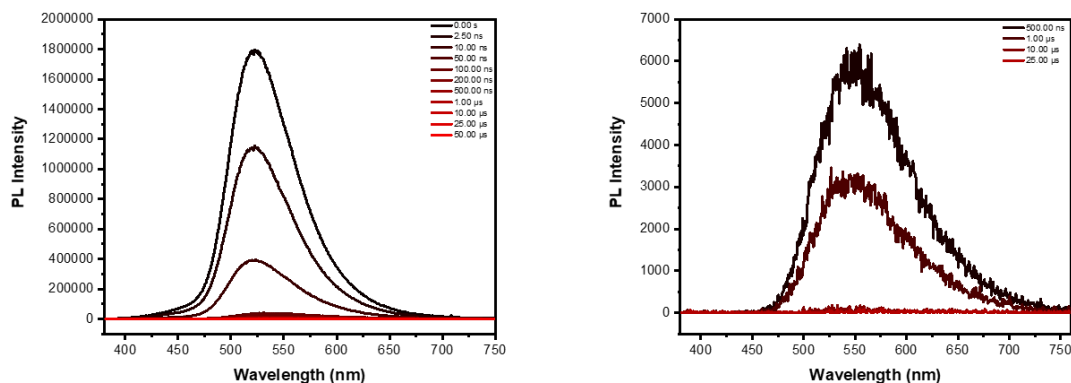


Figure B40. Time-resolved photoluminescence spectra of **Re1** at early times (left) and later times (right) after excitation using a Continuum Minilite with 355 nm pulsed excitation (5.0 mJ/pulse, 5 ns fwhm).

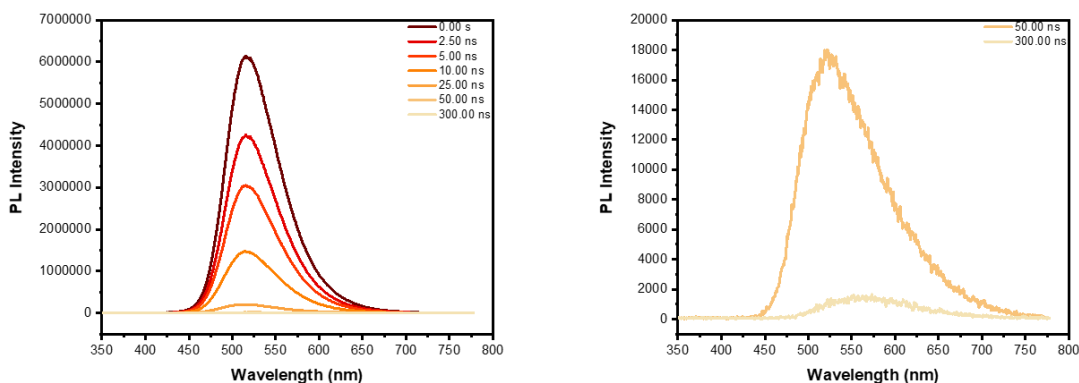


Figure B41. Time-resolved photoluminescence spectra of **Re2** at early times (left) and later times (right) after excitation using a Continuum Minilite with 355 nm pulsed excitation (5.0 mJ/pulse, 5 ns fwhm).

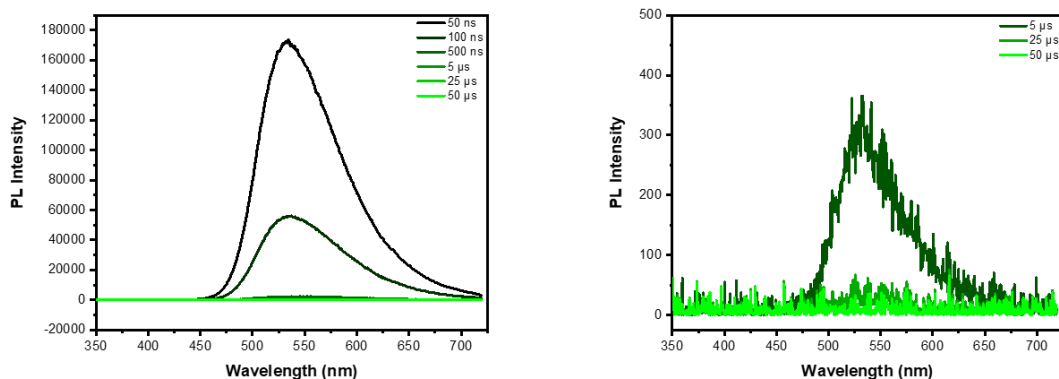


Figure B42. Time-resolved photoluminescence spectra of **Re3** at early times (left) and later times (right) after excitation using a Continuum Minilite with 355 nm pulsed excitation (5.0 mJ/pulse, 5 ns fwhm).

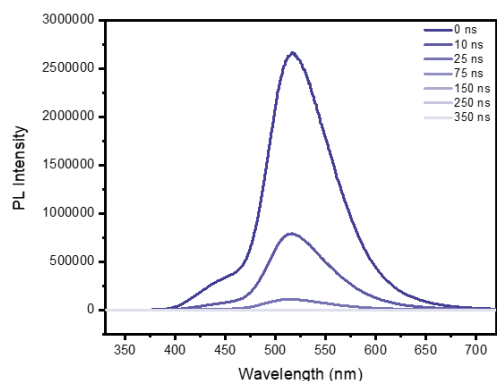


Figure B43. Time-resolved photoluminescence emission spectra of **Re5** at specified times after excitation using a Continuum Minilite with 355 nm pulsed excitation (5.0 mJ/pulse, 5 ns fwhm).

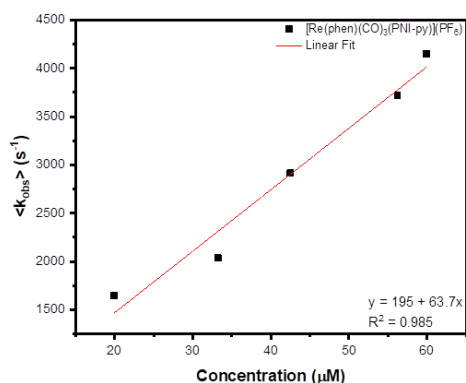


Figure B44. The concentration dependent study of **Re1** showing self-quenching behavior using the LP 920 laser flash photolysis system (Edinburgh Instruments) with a Vibrant 355 Nd:YAG/OPO system (OPOTEK) for pulsed laser excitation for single wavelength kinetics detection at 465 nm ($\lambda_{\text{ex}} = 410$ nm, 2.0 mJ/pulse).

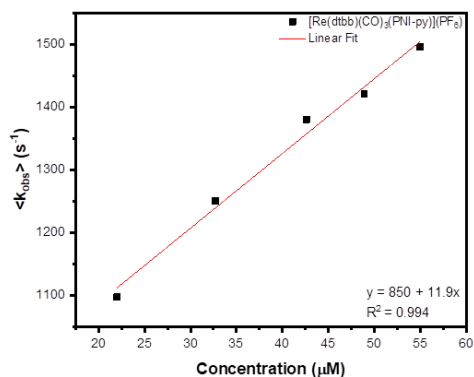


Figure B45. The concentration dependent study of **Re3** showing self-quenching behavior using the LP 920 laser flash photolysis system (Edinburgh Instruments) with a Vibrant 355

Nd:YAG/OPO system (OPOTEK) for pulsed laser excitation for single wavelength kinetics detection at 465 nm ($\lambda_{\text{ex}} = 410$ nm, 2.0 mJ/pulse).

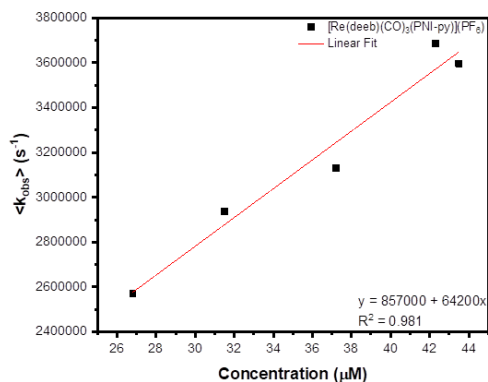


Figure B46. The concentration dependent study of **Re4** showing self-quenching behavior using the LP 920 laser flash photolysis system (Edinburgh Instruments) with a Vibrant 355 Nd:YAG/OPO system (OPOTEK) for pulsed laser excitation for single wavelength kinetics detection at 465 nm ($\lambda_{\text{ex}} = 410$ nm, 2.0 mJ/pulse).

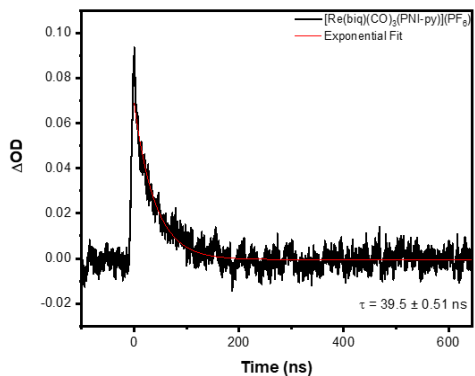


Figure B47. nsTA decay at 400 nm of **Re5**. Excited at 410 nm (2.0 mJ/pulse).

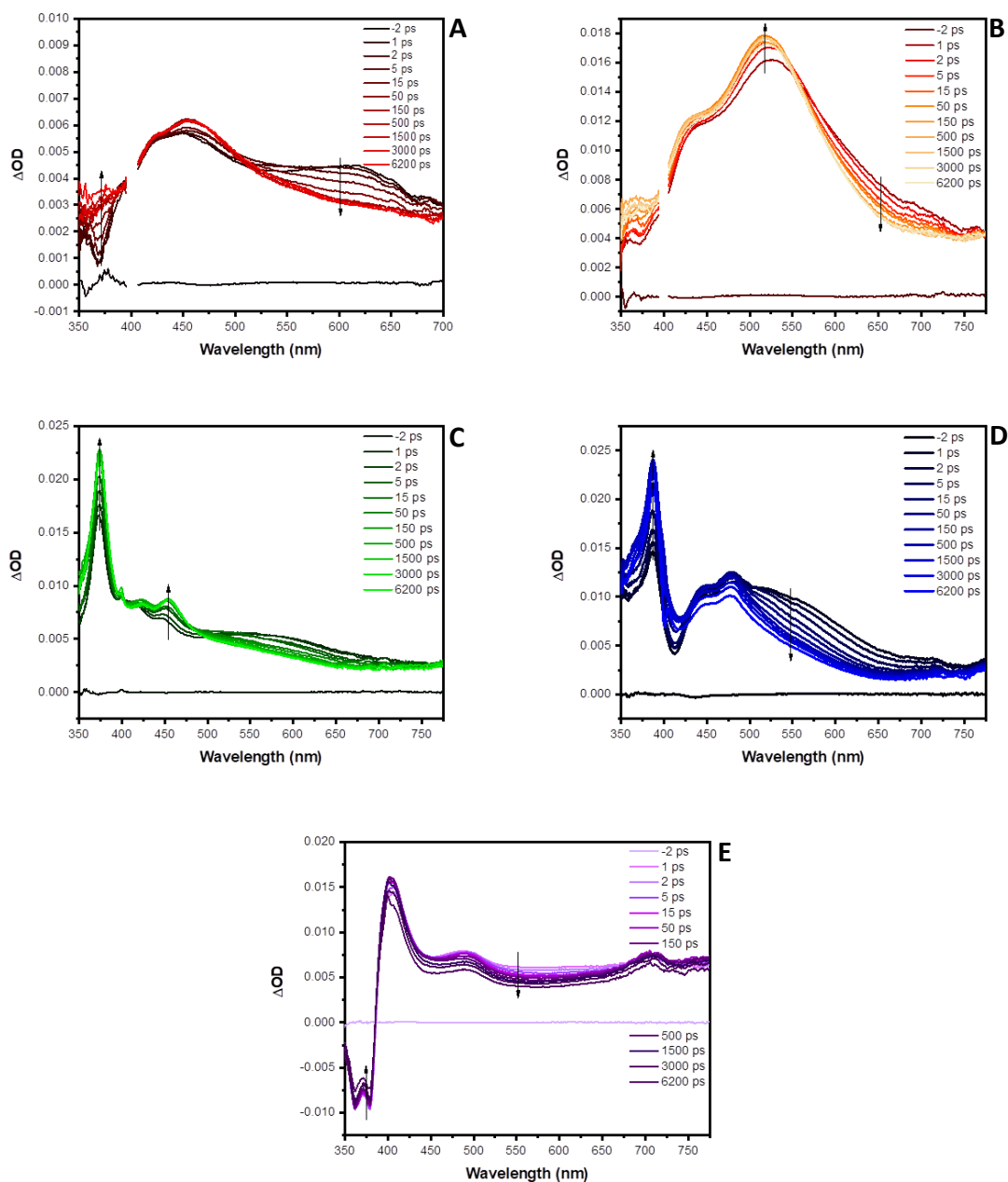


Figure B48. Excited-state absorption difference spectra of **Mod1** (A), **Mod2** (B), **Mod3** (C), **Mod4** (D), and **Mod5** (E) in THF following 400 nm pulsed excitation (105 fs fwhm, 0.7 $\mu\text{J}/\text{pulse}$).

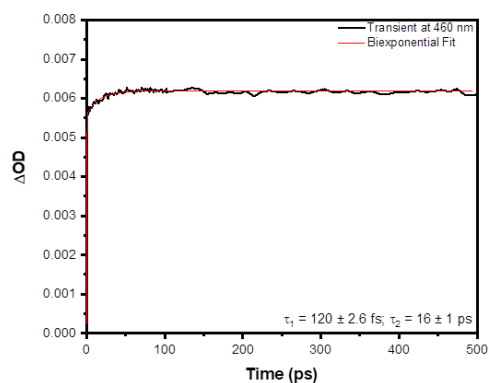


Figure B49. Ultrafast transient absorption kinetic data of **Mod1** in THF following 400 nm pulsed excitation. Single wavelength kinetic analysis at 460 nm.

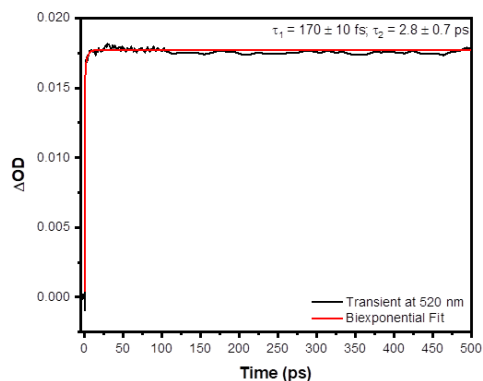


Figure B50. Ultrafast transient absorption kinetic data of **Mod2** in THF following 400 nm pulsed excitation. Single wavelength kinetic analysis at 520 nm.

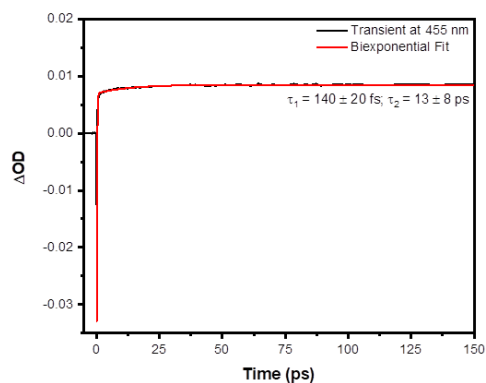


Figure B51. Ultrafast transient absorption kinetic data of **Mod3** in THF following 400 nm pulsed excitation. Single wavelength kinetic analysis at 455 nm.

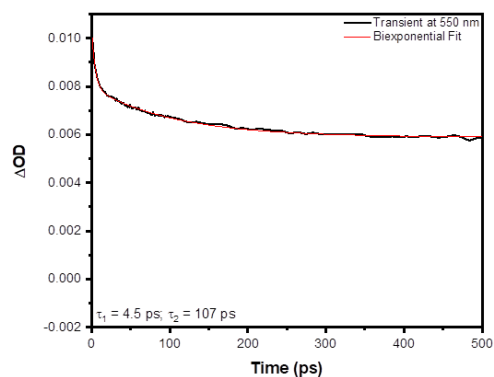


Figure B52. Ultrafast transient absorption kinetic data of **Mod4** in THF following 400 nm pulsed excitation. Single wavelength kinetic analysis at 550 nm.

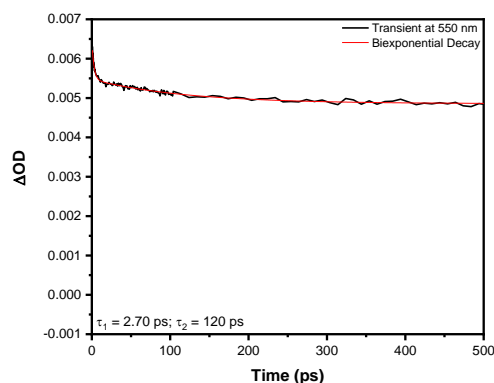


Figure B53. Ultrafast transient absorption kinetic data of **Mod5** in THF following 400 nm pulsed excitation. Single wavelength kinetic analysis at 550 nm.

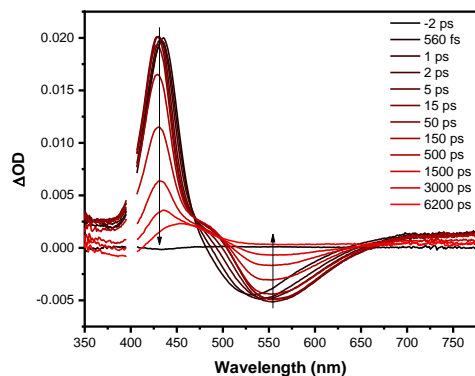


Figure B54. Excited-state absorption difference spectra of **Re1** in THF following 400 nm pulsed excitation (105 fs fwhm).

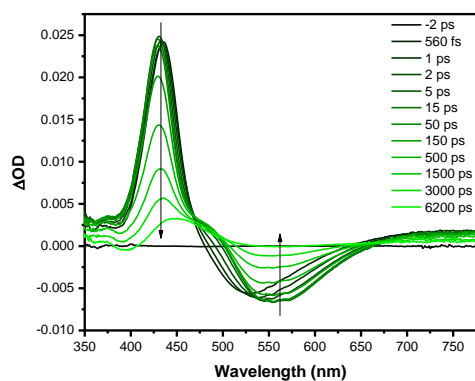


Figure B55. Excited-state absorption difference spectra of **Re3** in THF following 400 nm pulsed excitation (105 fs fwhm).

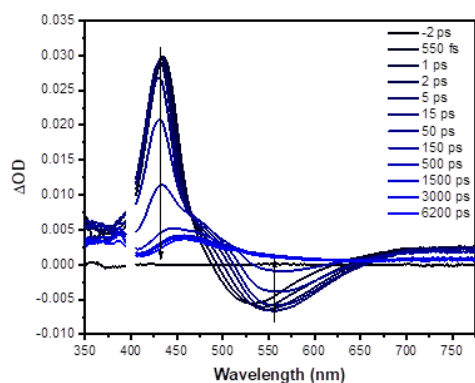


Figure B56. Excited state absorption difference spectra of **Re4** in THF excited following 400 nm pulsed laser excitation (105 fs fwhm).

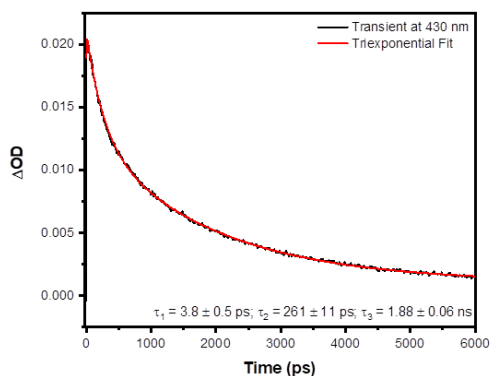


Figure B57. Ultrafast transient absorption kinetic data of **Re1** in THF following 400 nm pulsed excitation. Single wavelength kinetic analysis at 430 nm.

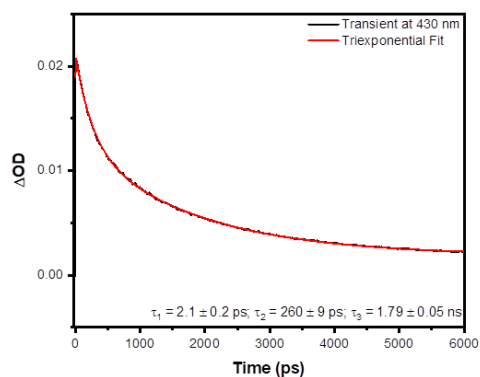


Figure B58. Ultrafast transient absorption kinetic data of **Re2** in THF following 400 nm pulsed excitation. Single wavelength kinetic analysis at 430 nm.

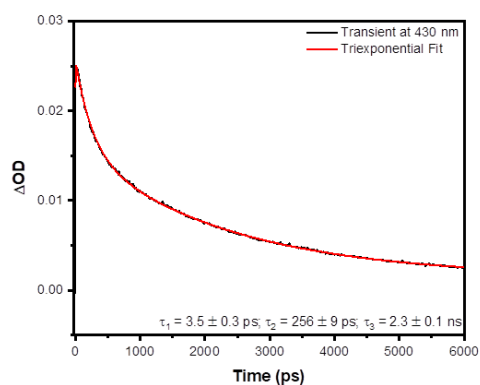


Figure B59. Ultrafast transient absorption kinetic data of **Re3** in THF following 400 nm pulsed excitation. Single wavelength kinetic analysis at 430 nm.

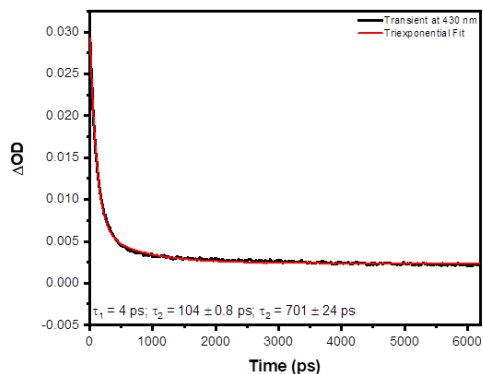


Figure B60. Ultrafast transient absorption kinetic data of **Re4** in THF following 400 nm pulsed excitation. Single wavelength kinetic analysis at 430 nm.

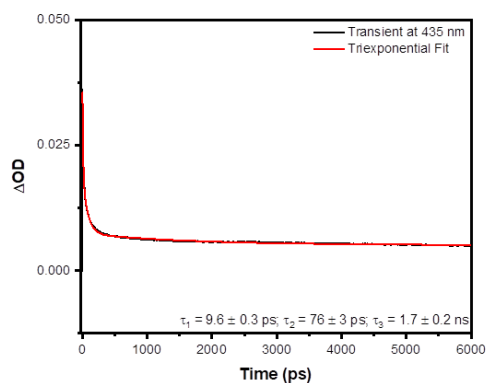


Figure B61. Ultrafast transient absorption kinetic data of **Re5** in THF following 400 nm pulsed excitation. Single wavelength kinetic analysis at 435 nm.

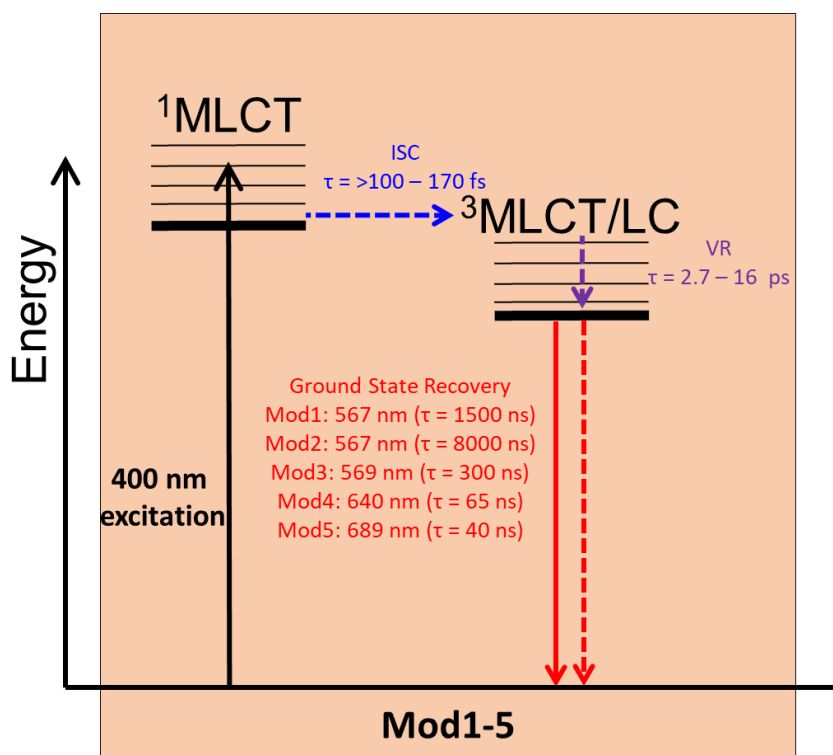


Figure B62. Energy level diagram of **Mod1-5**. The mixed $^3\text{MLCT}$ and LC is for **Mod1-2** only.

B.4. References

1. Kitchen, J. A.; Martinho, P. N.; Morgan, G. G.; Gunnlaugsson, T., Synthesis, crystal structure and EPR spectroscopic analysis of novel copper complexes formed from N-pyridyl-4-nitro-1,8-naphthalimide ligands. *Dalton Trans.* **2014**, 43 (17), 6468.
2. Langdon-Jones, E. E.; Williams, C. F.; Hayes, A. J.; Lloyd, D.; Coles, S. J.; Horton, P. N.; Groves, L. M.; Pope, S. J. A., Luminescent 1,8-Naphthalimide-Derived ReI Complexes: Syntheses, Spectroscopy, X-ray Structure and Preliminary Bioimaging in Fission Yeast Cells. *Eur. J. Inorg. Chem.* **2017**, 2017 (44), 5279-5287.

Appendix C

C.1. Synthetic Details and Structural Characterization

All chemicals and solvents were analytical grade, and they were used without further purification. Nuclear magnetic resonance (NMR) spectra were measured at 298 K with a Bruker® Avance NEO 700 MHz (^1H) and 176 MHz (^{13}C) and processed with MestreNova software (version 10.0.2), with the chemical shifts referenced to residual solvent signals. The chemical shifts (δ ppm) are referenced to the respective solvent and splitting patterns are designed as s (singlet), d (doublet), t (triplet), m (multiplet). High resolution electrospray ionization mass spectrometry (HR-ESI-MS) was measured by the Michigan State University Mass Spectrometry Core, East Lansing, MI. MS values are given as m/z.

Synthesis of 16H-benzo[4',5']isoquinolino[2',1':1,2]imidazo[4,5-f][1,10]phenanthroline-16-one (**NBI-phen**). **NBI-phen** was synthesized with modification to the previously reported procedure.¹ 5,6-Diamino-1,10-phenanthroline (1.46 mmol, 308 mg) and 1,8-naphthalic anhydride (2.01 mmol, 398 mg) were mixed in 30 mL of acetic acid which was degassed with nitrogen. This mixture was then heated for 24 hours at 140 °C. After addition of water and a saturated, aqueous solution of sodium carbonate the ligand began to precipitate and was then filtered off on a glass frit and washed with water, ethanol, and diethyl ether. The resulting dark yellow solid was recrystallized in hot ethanol to give **NBI-phen** (64 %). ^1H NMR (700 MHz, CDCl_3) δ 10.80 (d, $J = 8.7$ Hz, 1H), 9.56 (d, $J = 8.2$ Hz, 1H), 9.36 (t, $J = 5.3$ Hz, 2H), 9.23 (d, $J = 7.4$ Hz, 1H), 9.17 (d, $J = 7.4$ Hz, 1H), 8.66 (d, $J = 8.1$ Hz, 1H), 8.59 (d, $J = 8.2$ Hz, 1H), 8.45 – 8.42 (m, 1H), 8.33 – 8.30 (m, 1H), 8.14 (dd, $J = 11.4, 4.0$ Hz, 1H), 8.11 (t, $J = 7.8$ Hz, 1H) ppm. ^{13}C NMR (176 MHz, CDCl_3) δ 159.93, 151.64, 150.36, 144.93, 144.89, 139.16, 137.70, 137.44, 136.74, 135.76, 132.63, 132.25, 131.90,

129.08, 128.83, 128.02, 126.77, 126.29, 123.99, 121.76, 121.09, 120.94, 77.34, 77.16, 76.98, 21.26 ppm. MS [HR-ESI]: m/z calcd for C₂₄H₁₂N₄OH [M+H]⁺ 373.1089, found 373.1094.

Synthesis of Re(CO)₃(NBI-phen)Cl. Pentacarbonylchlororhenium(I) (1 mmol, 332 mg) was added to NBI-phen (1.1 mmol, 382 mg) and 80 mL of toluene in a 150 mL round bottom flask. The solution was degassed, put under N₂, and refluxed while mixing for 12 hours. After cooling, the yellow precipitate was filtered out on a glass frit and washed with 800 mL of toluene. The yellow solid was further purified using neutral alumina and eluted with dichloromethane and 10% acetonitrile to give Re(CO)₃(NBI-phen)Cl (89 %). ¹H-NMR (DMSO-d₆) δ 10.27 (d, J= 8.42 Hz, 1H), 9.53 (d, J= 4.45 Hz, 1H), 9.47 (d, J= 4.20 Hz, 1H), 9.39 (d, J= 6.96 Hz, 1H), 8.88 (d, J= 6.81 Hz, 1H), 8.84 (d, J= 6.65 Hz, 1H), 8.58 (d, J= 8.84 Hz, 1H), 8.41 (d, J= 8.25 Hz, 1H), 8.23 (m, 2H), 8.02-7.94 (m, 2H). MS [HR-ESI]: m/z calcd for [M-Cl]⁺ 643.04106, found 643.03910.

Synthesis of Re(CO)₃(NBI-phen)OTf. Re(CO)₃(NBI-phen)(Cl) (0.16 mmol, 109 mg) was added to 50 mL round bottom flask along with 20 mL of absolute ethanol. The solution was covered (dark), deaerated, put under N₂. Silver triflate (0.18 mmol, 47 mg) was added to the reaction mixture and refluxed for 6 hours. Once cool, the solution was filtered through celite on a glass frit to remove AgCl from solution. The yellow filtrate was dried under reduced pressure. The crude product was chromatographed using acidic alumina and eluted with acetonitrile to give Re(CO)₃(NBI-phen)OTf (80 %). MS [HR-ESI]: m/z calcd for [M-OTf]⁺ 643.04106, found 643.03964.

Synthesis of fac-[Re(NBI-phen)(CO)₃(PPh₃)](PF₆) (**Re1**). Re(CO)₃(NBI-phen)OTf (0.19 mmol, 150 mg) and PPh₃ (1.34 mmol, 350 mg) were added to 50mL round bottom flask along with 20mL

acetonitrile. This mixture was then refluxed for 12 hours. The solvent was removed under reduced pressure and the crude product was chromatographed on acidic alumina with dichloromethane and increasing amounts of acetonitrile. The collected fraction was dissolved in minimal amount of methanol and precipitated as the PF₆ salt using a dropwise addition of an ammonium hexafluorophosphate solution in water (1.0 g in 10 mL). The solid was collected on a glass frit and washed with 250 mL of distilled water. The solid was recrystallized in dichloromethane and diethyl ether. The yellow solid was dried under vacuum overnight to give fac-[Re(NBI-phen)(CO)₃(PPh₃)](PF₆) (**Re1**) (96 %). ¹H NMR (700 MHz, DMSO) δ 10.16 (d, J = 8.6 Hz, 1H), 9.41 (d, J = 5.0 Hz, 1H), 9.31 (t, J = 7.0 Hz, 2H), 8.97 (d, J = 7.1 Hz, 1H), 8.93 (d, J = 7.2 Hz, 1H), 8.69 (d, J = 8.0 Hz, 1H), 8.53 (d, J = 8.1 Hz, 1H), 8.09 (t, J = 7.6 Hz, 1H), 8.07 – 8.00 (m, 3H), 7.35 (t, J = 7.4 Hz, 3H), 7.25 (t, J = 6.7 Hz, 6H), 7.01 – 6.97 (m, 6H) ppm. ¹³C NMR (176 MHz, DMSO) δ 194.95, 160.86, 155.04, 153.32, 152.42, 144.99, 144.44, 138.65, 138.32, 136.42, 134.14, 132.98, 132.86, 132.26, 132.20, 131.67, 131.05, 129.93, 129.13, 129.07, 128.08, 128.00, 127.82, 127.59, 127.50, 126.12, 125.99, 124.97, 124.47, 122.94, 122.59, 120.12, 40.02, 39.88, 39.76, 39.64, 39.52, 39.40, 39.28, 39.16 ppm. MS [HR-ESI]: m/z calcd for C₄₅H₂₇N₄O₄Pre [M]⁺ 903.1299, found 903.1307.

Synthesis of fac-[Re(NBI-phen)(CO)₃(CH₃CN)](PF₆) (**Re2**). Re(CO)₃(NBI-phen)Cl (0.10 mmol, 69 mg) and silver triflate (0.10 mmol, 26 mg) were suspended in 50 mL of freshly distilled acetonitrile. The solution was covered (dark), deaerated, put under N₂, and refluxed for 12 hours. Once cool, the reaction contents were filtered over celite to remove AgCl from solution. The filtrate was dried under reduced pressure and then dissolved in a minimal amount of methanol and precipitated as the PF₆ salt using a dropwise addition of an ammonium hexafluorophosphate

solution in water (1.0 g in 10 mL). The solid was collected on a glass frit and washed with water and dried under vacuum to give fac-[Re(NBI-phen)(CO)₃(CH₃CN)](PF₆) (**Re2**) (71 %). ¹H NMR (700 MHz, CD₃CN) δ 10.48 (d, J = 8.6 Hz, 1H), 9.51 (t, J = 5.8 Hz, 2H), 9.47 (d, J = 4.8 Hz, 1H), 9.01 (d, J = 7.2 Hz, 1H), 8.96 (d, J = 7.2 Hz, 1H), 8.57 (d, J = 8.0 Hz, 1H), 8.42 (d, J = 8.1 Hz, 1H), 8.20 (ddd, J = 18.7, 8.4, 4.9 Hz, 2H), 8.01 (dt, J = 15.5, 7.7 Hz, 2H) ppm. ¹³C NMR (176 MHz, CD₃CN) δ 155.38, 153.88, 146.88, 140.41, 140.10, 137.58, 135.93, 134.30, 133.87, 132.96, 128.94, 128.82, 128.67, 128.11, 127.30, 127.00, 126.49, 126.28, 124.40, 123.87, 123.48, 121.29, 120.71, 118.26, 68.24, 26.20, 1.27, 1.15. MS [HR-ESI]: m/z calcd for C₂₉H₁₅N₅O₄Re [M]⁺ 682.0654, found 682.0661.

Synthesis of Re(CO)₃(phen)Cl. It was synthesized according to the previously reported procedure.² Pentacarbonylchlororhenium(I) (5.53 mmol, 2 g) was added to 1,10-phenanthroline (5.53 mmol, 1 g) and 30 mL of toluene in a 100 mL round bottom flask. The solution was degassed, put under N₂, and refluxed while mixing for 4 hours. After cooling, the yellow precipitate was filtered out on a glass frit and washed with 300 mL of toluene to give Re(CO)₃(phen)Cl (93 %). ¹H NMR (700 MHz, CD₂Cl₂) δ 9.42 – 9.36 (m, 1H), 8.62 (dd, J = 8.2, 0.8 Hz, 1H), 8.07 (s, 1H), 7.91 (dd, J = 8.2, 5.1 Hz, 1H). ¹³C NMR (176 MHz, CD₂Cl₂) δ 153.36, 147.35, 138.70, 131.28, 128.04, 126.25, 54.15, 53.99, 53.84, 53.68, 53.53. MS [HR-ESI]: m/z calcd for C₁₅H₈N₂O₃Re [M-Cl]⁺ 449.0064, found 449.0045.

Synthesis of Re(CO)₃(phen)OTf. Re(CO)₃(phen)(Cl) (3.1 mmol, 1.5 g) was added to 500 mL round bottom flask along with 300 mL of absolute ethanol. The solution was covered (dark), deaerated, put under N₂. Silver triflate (3.2 mmol, 0.82 g) was added to the reaction mixture and

refluxed for 6 hours. Once cool, the solution was filtered through celite on a glass frit to remove AgCl from solution. The yellow filtrate was dried under reduced pressure to give $\text{Re}(\text{CO})_3(\text{phen})\text{OTf}$ (90 %). MS [HR-ESI]: m/z calcd for $[\text{M}-\text{OTf}]^+$ 449.0064, found 449.0095.

Synthesis of fac- $[\text{Re}(\text{phen})(\text{CO})_3(\text{PPh}_3)](\text{PF}_6)$ (**Mod1**). $\text{Re}(\text{CO})_3(\text{phen})\text{OTf}$ (2.5 mmol, 1.5 g) and PPh_3 (25 mmol, 1 g) were added to 500 mL round bottom flask along with 300 mL tetrahydrofuran. This mixture was then refluxed for 12 hours. The solvent was removed to 90% under reduced pressure and product was precipitated as the PF_6 salt using a dropwise addition of an ammonium hexafluorophosphate solution in water (1.0 g in 10 mL). The solid was collected on a glass frit and washed with 250 mL of distilled water. The yellow solid was dried under vacuum overnight to give fac- $[\text{Re}(\text{phen})(\text{CO})_3(\text{PPh}_3)](\text{PF}_6)$ (**Mod1**) (98 %). ^1H NMR (700 MHz, CD_3CN) δ 9.11 (dd, $J = 5.1, 0.6$ Hz, 2H), 8.62 (d, $J = 8.2$ Hz, 2H), 8.05 (s, 2H), 7.73 (dd, $J = 8.2, 5.1$ Hz, 2H), 7.33 (dt, $J = 7.4, 3.7$ Hz, 3H), 7.20 (td, $J = 7.7, 2.1$ Hz, 6H), 7.04 – 7.00 (m, 6H) ppm. ^{13}C NMR (176 MHz, CD_3CN) δ 155.79, 147.18, 140.24, 133.51, 133.45, 131.95, 131.93, 129.94, 129.88, 129.65, 129.38, 128.87, 127.56, 118.26, 1.27 ppm. MS [HR-ESI]: m/z calcd for $\text{C}_{33}\text{H}_{23}\text{N}_2\text{O}_3\text{PRe} [\text{M}]^+$ 711.0976, found 711.0970.

Synthesis of fac- $[\text{Re}(\text{phen})(\text{CO})_3(\text{CH}_3\text{CN})](\text{PF}_6)$ (**Mod2**). $\text{Re}(\text{CO})_3(\text{phen})\text{Cl}$ (2.06 mmol, 1 g) were suspended in 300 mL of acetonitrile. The solution was covered (dark), deaerated, put under N_2 . Silver triflate (2.12 mmol, 0.545 g) was added to the reaction mixture and refluxed for 12 hours. Once cool, the reaction contents were filtered over celite to remove AgCl from solution. The filtrate was dried under reduced pressure and then dissolved in a minimal amount of methanol and precipitated as the PF_6 salt using a dropwise addition of an ammonium hexafluorophosphate

solution in water (1.0 g in 10 mL). The solid was collected on a glass frit and washed with water and dried under vacuum to give fac-[Re(phen)(CO)₃(CH₃CN)](PF₆) (**Mod2**) (91 %). ¹H NMR (400 MHz, CD₂Cl₂) δ 9.38 (dd, J = 5.1, 1.3 Hz, 2H), 8.80 (dd, J = 8.3, 1.3 Hz, 2H), 8.21 (s, 2H), 8.05 (dd, J = 8.3, 5.1 Hz, 2H), 2.06 (s, 3H), 1.54 (s, 3H) ppm. ¹³C NMR (176 MHz, CD₂Cl₂) δ 154.46, 147.24, 140.55, 131.72, 128.63, 127.13, 54.15, 54.00, 53.84, 53.69, 53.53, 3.70 ppm. MS [HR-ESI]: m/z calcd for C₁₇H₁₁N₃O₃Re [M]⁺ 490.0330, found 490.0339.

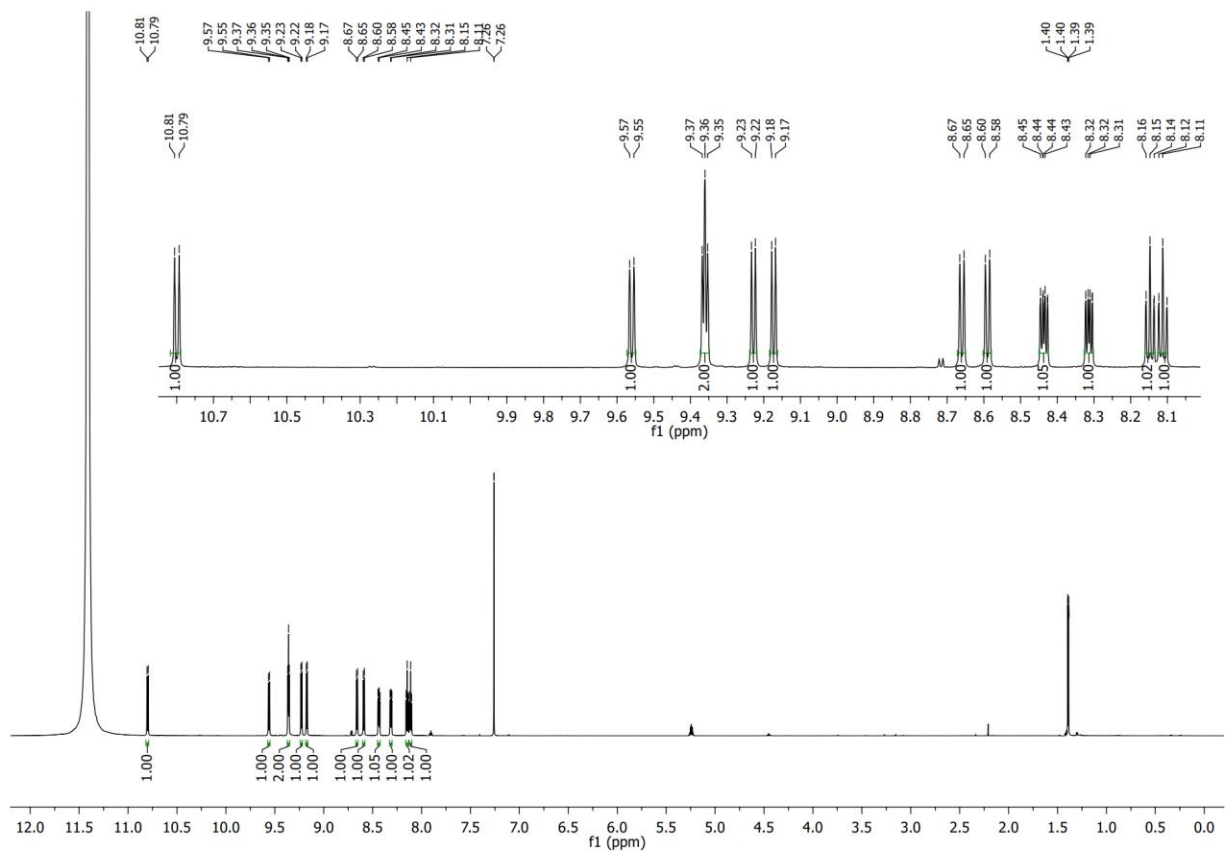


Figure C1. 700 MHz ^1H NMR of 16H-benzo[4',5']isoquinolino[2',1':1,2]imidazo[4,5-f][1,10]phenanthrolin-16-one (**NBI-phen**) in CDCl_3 at 300K.

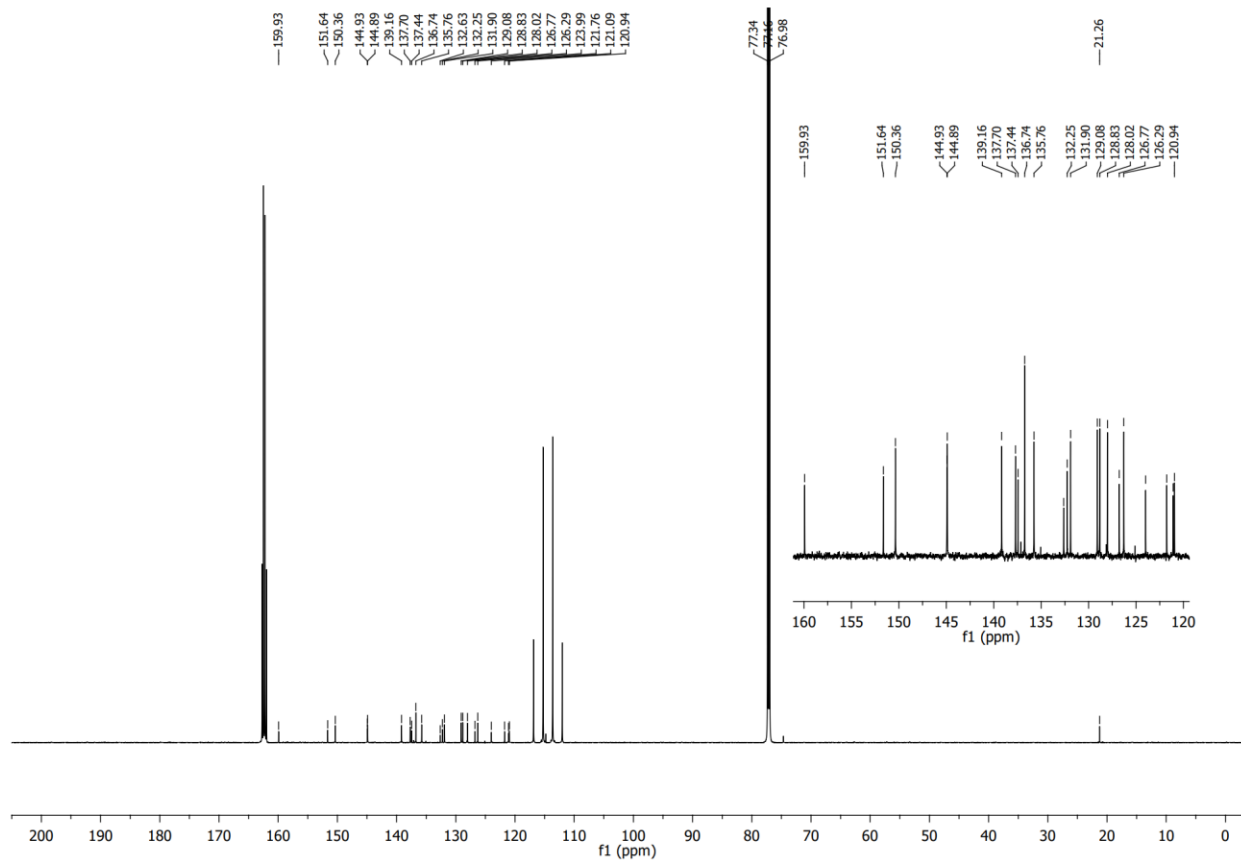


Figure C2. 176 MHz ^{13}C NMR of 16H-benzo[4,5']isoquinolino[2',1':1,2]imidazo[4,5-f][1,10]phenanthrolin-16-one (**NBI-phen**) in CDCl_3 at 300K.



Figure C3. HR-ESIMS of 16H-benzo[4',5']isoquinolino[2',1':1,2]imidazo[4,5-f][1,10]phenanthrolin-16-one (**NBI-phen**).

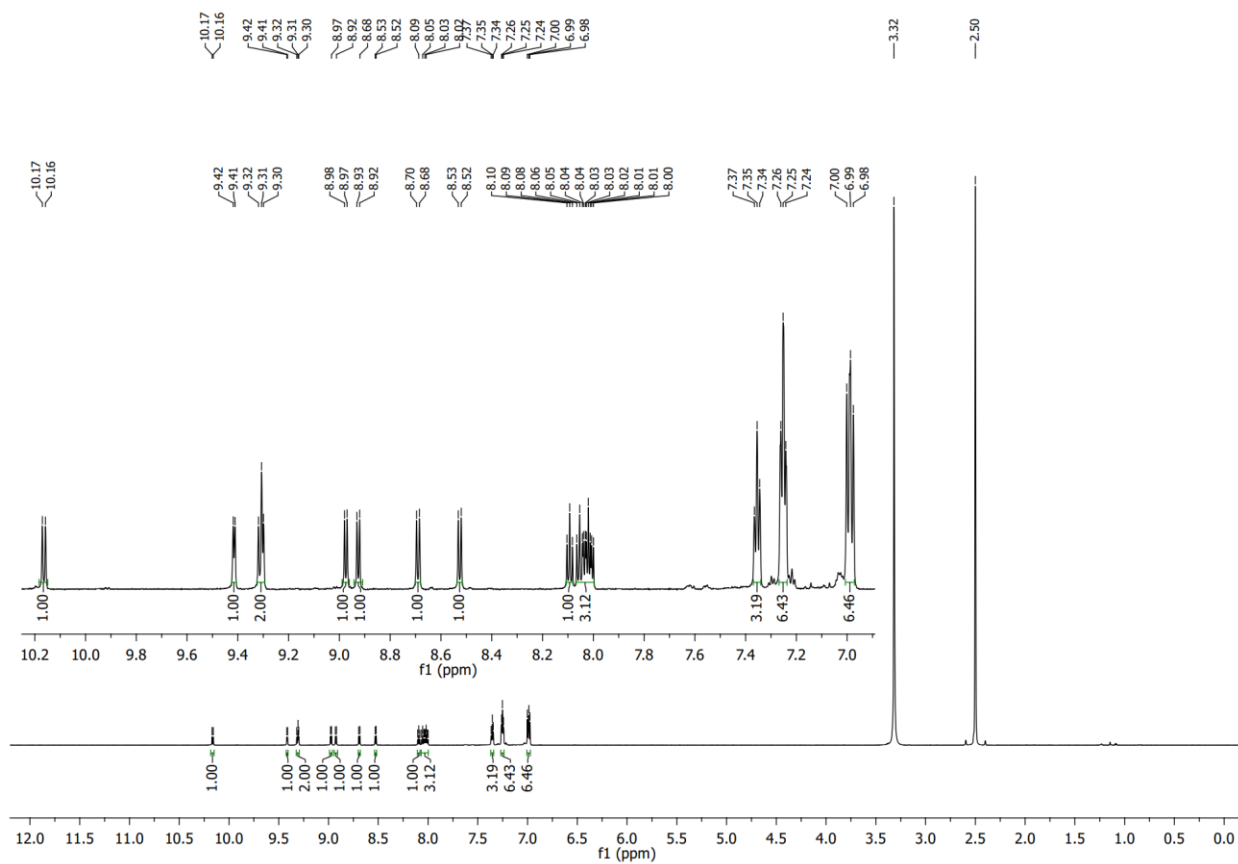


Figure C4. 700 MHz ^1H NMR of $\text{fac-}[\text{Re}(\text{NBI-phen})(\text{CO})_3(\text{PPh}_3)](\text{PF}_6)$ (**Re1**) in DMSO at 300K.

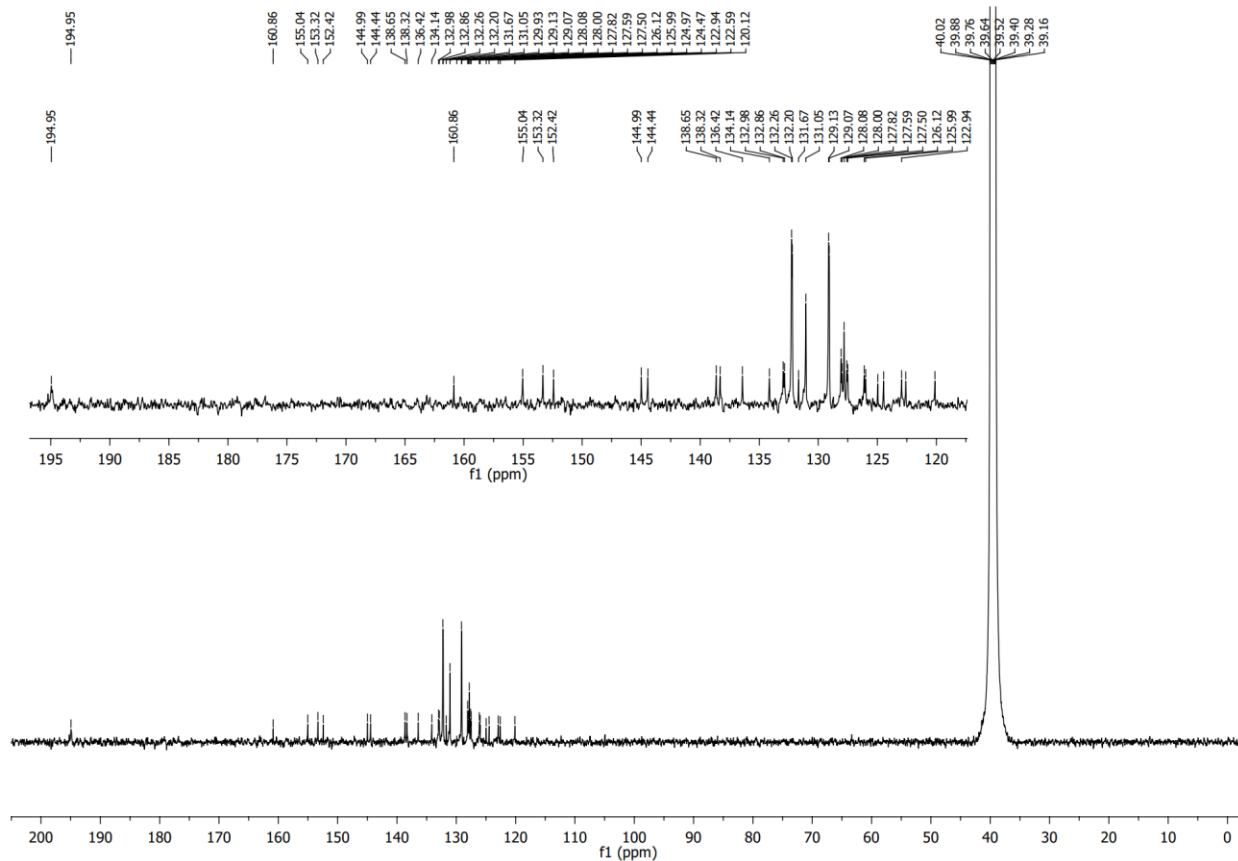


Figure C5. 176 MHz ^{13}C NMR of fac-[Re(NBI-phen)(CO) $_3$ (PPh $_3$)](PF $_6$) (**Re1**) in DMSO at 300K.



Figure C6. HR-ESIMS of fac-[Re(NBI-phen)(CO)₃(PPh₃)](PF₆) (**Re1**).

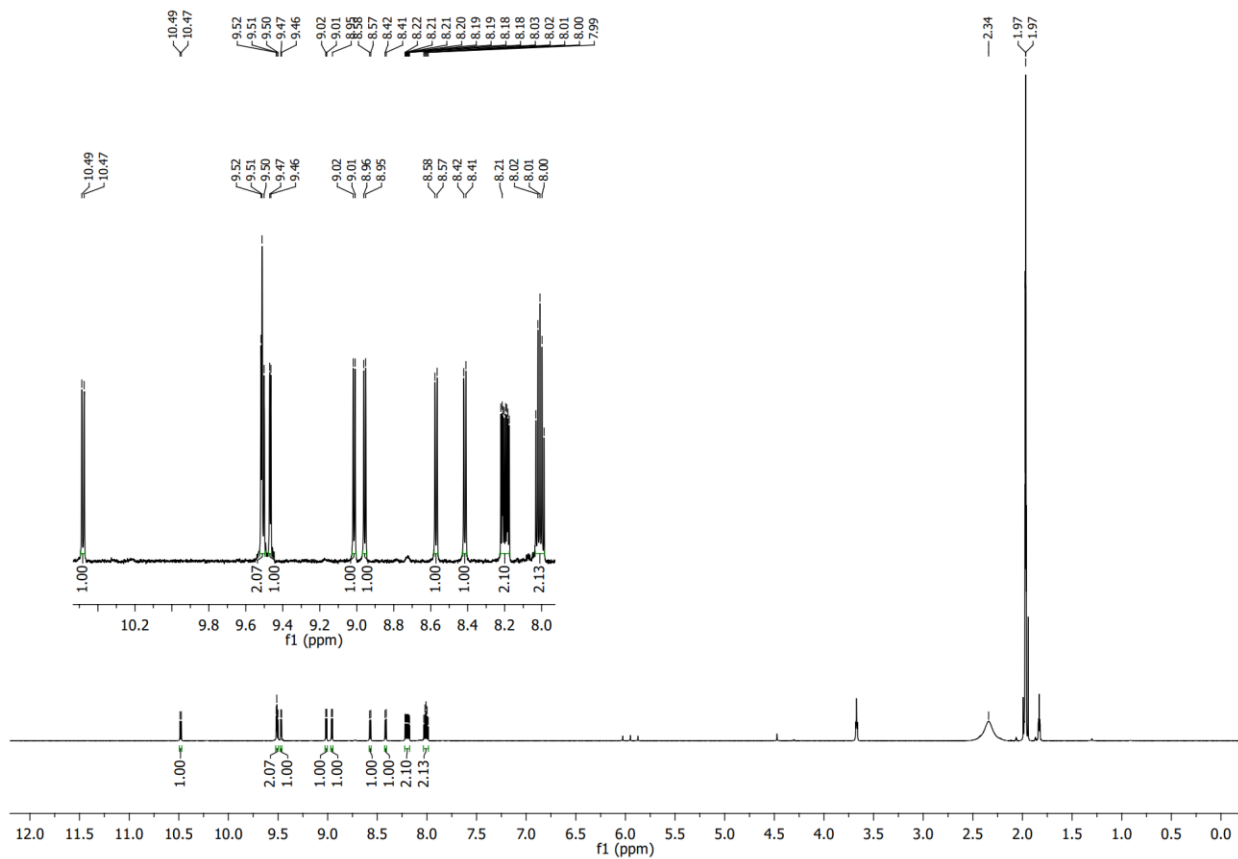


Figure C7. 700 MHz ¹H NMR of fac-[Re(NBI-phen)(CO)₃(CH₃CN)](PF₆) (**Re2**) in CD₃CN at 300K.

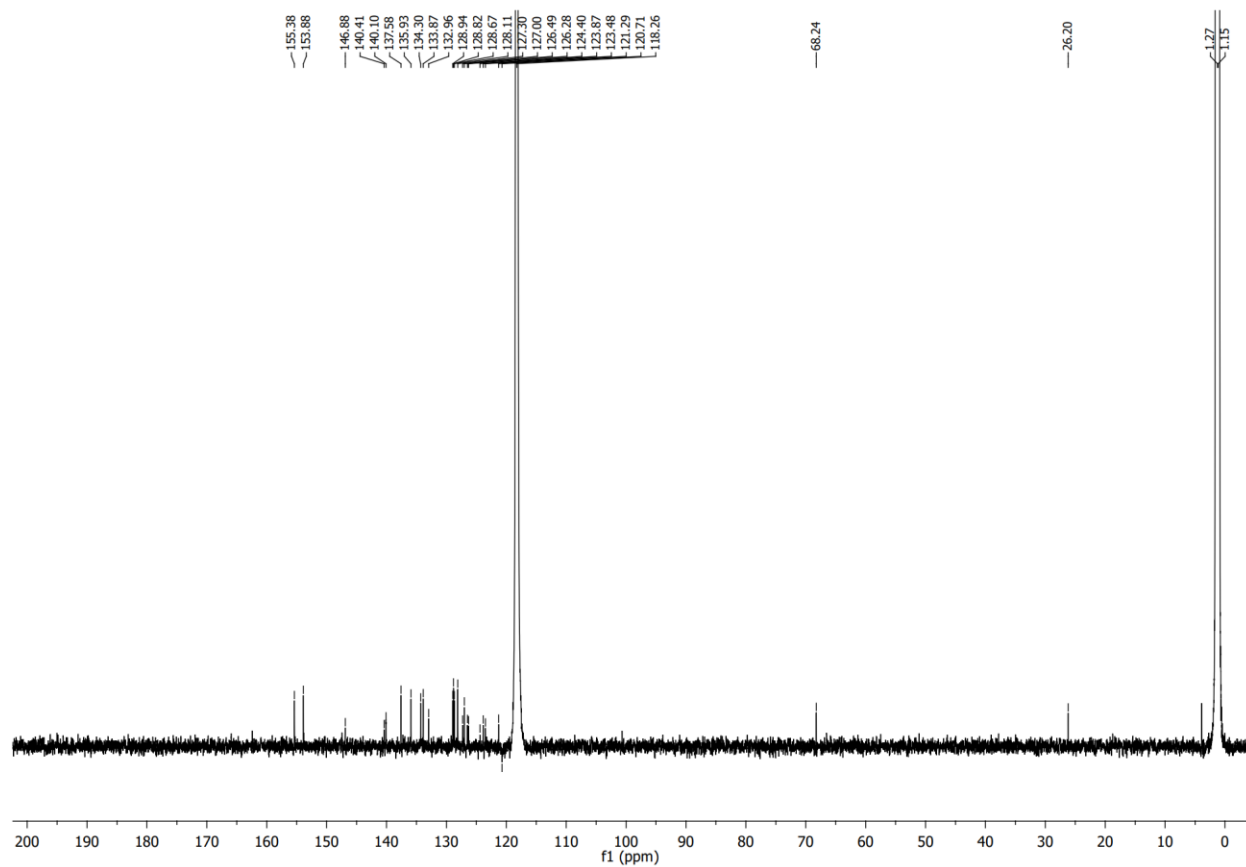


Figure C8. 176 MHz ^{13}C NMR of fac-[Re(NBI-phen)(CO) $_3$ (CH $_3$ CN)](PF $_6$) (**Re2**) in CH $_3$ CN at 300K.



Figure C9. HR-ESIMS of fac-[Re(NBI-phen)(CO)₃(CH₃CN)](PF₆) (**Re2**).

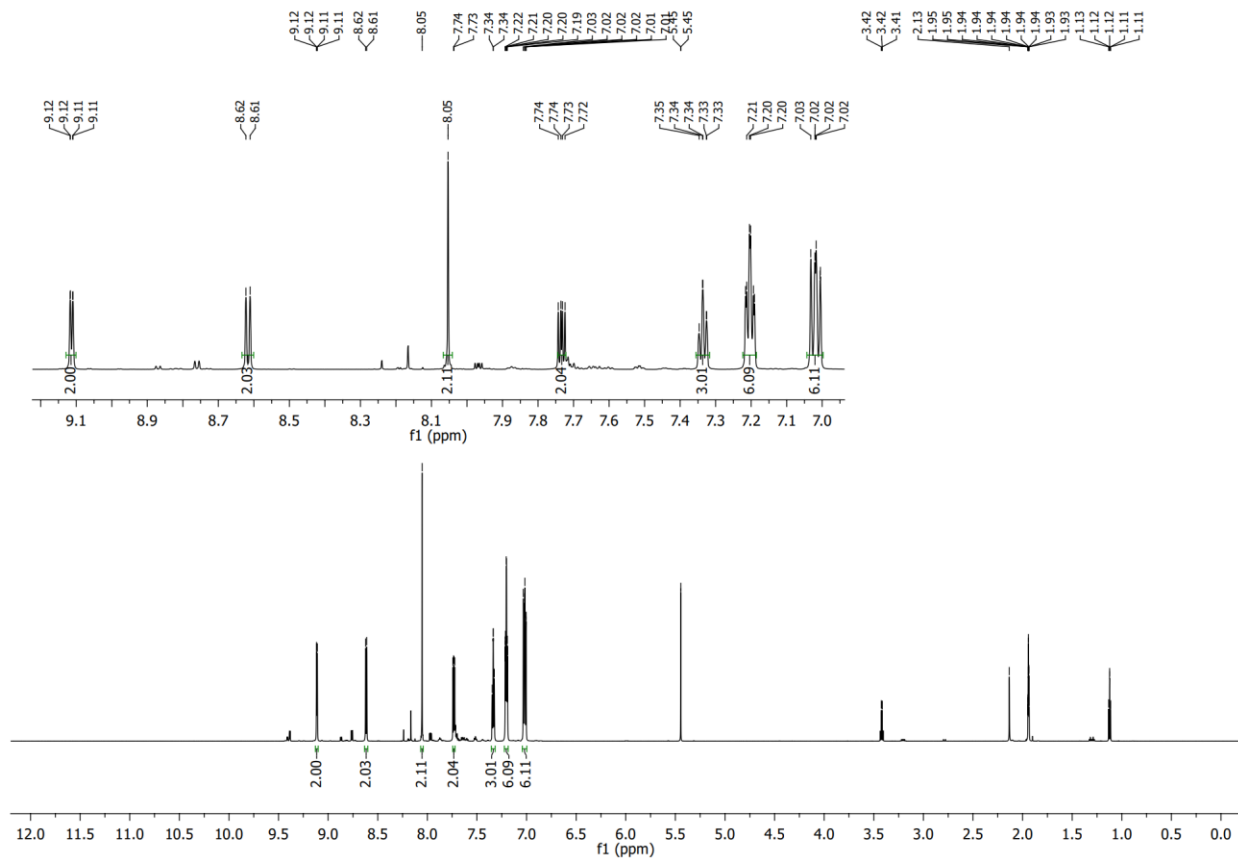


Figure C10. 700 MHz ¹H NMR of fac-[Re(phen)(CO)₃(PPh₃)](PF₆) (**Mod1**) in CD₃CN at 300K.

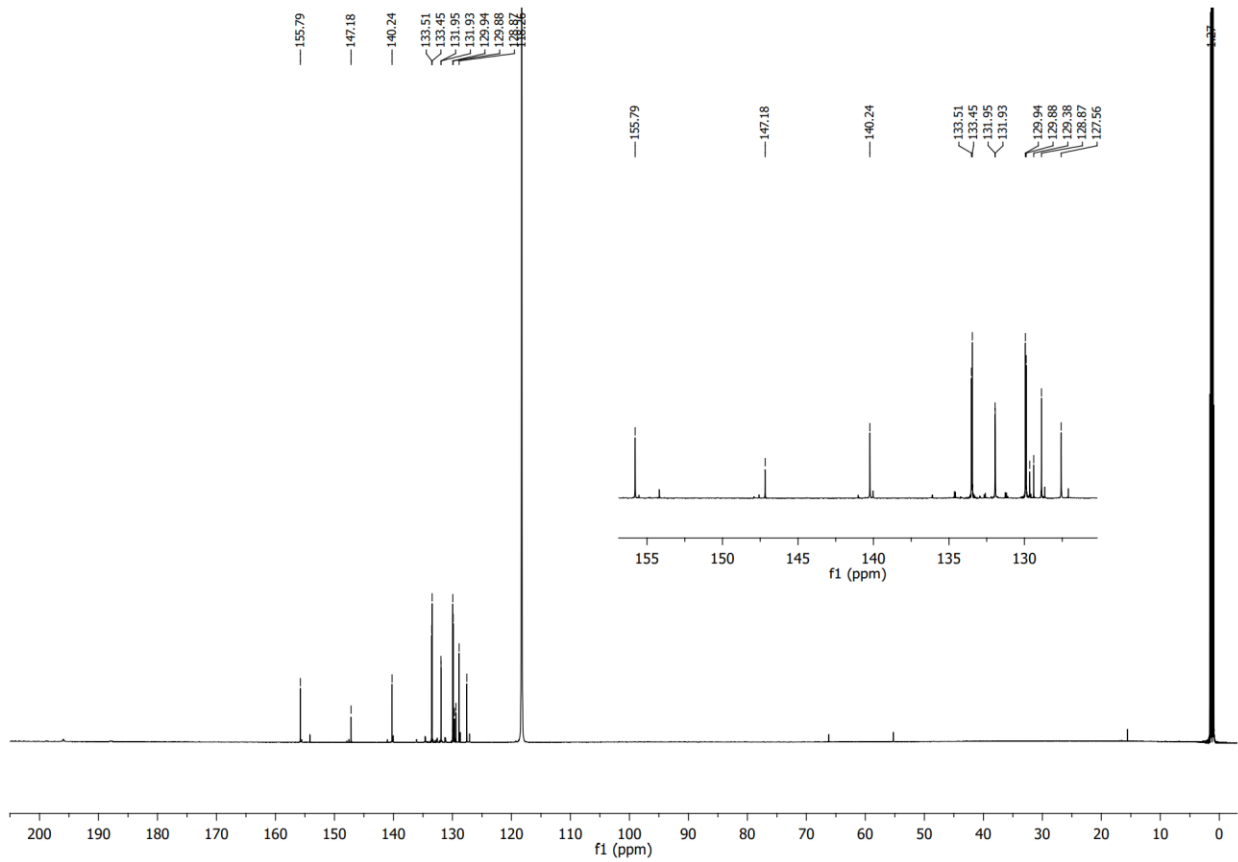


Figure C11. 176 MHz ^{13}C NMR of fac-[Re(phen)(CO) $_3$ (PPh $_3$)](PF $_6$) (**Mod1**) in CD $_3$ CN at 300K.



Figure C12. HR-ESIMS of fac-[Re(phen)(CO)₃(PPh₃)](PF₆) (**Mod1**).

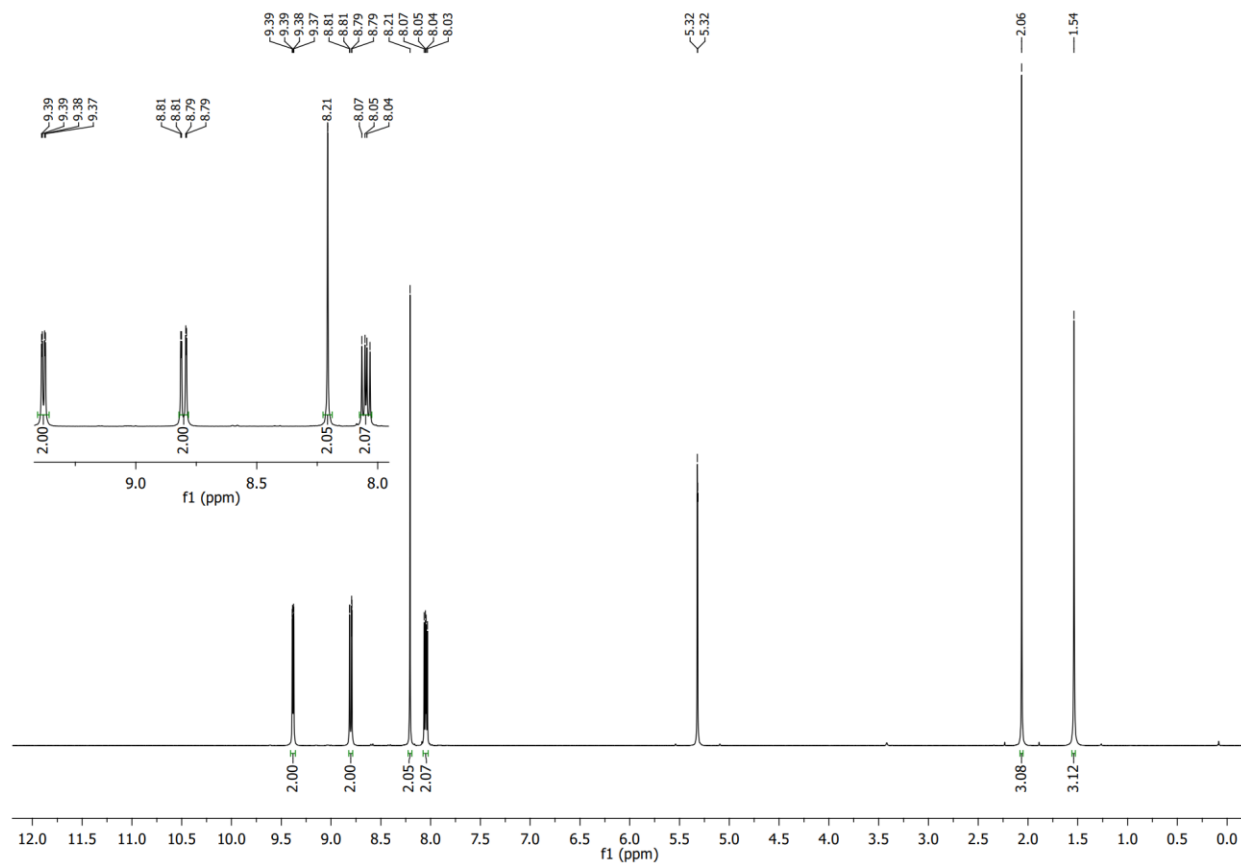


Figure C13. 700 MHz ¹H NMR of fac-[Re(phen)(CO)₃(CH₃CN)](PF₆) (**Mod2**) in CD₂Cl₂ at 300K.

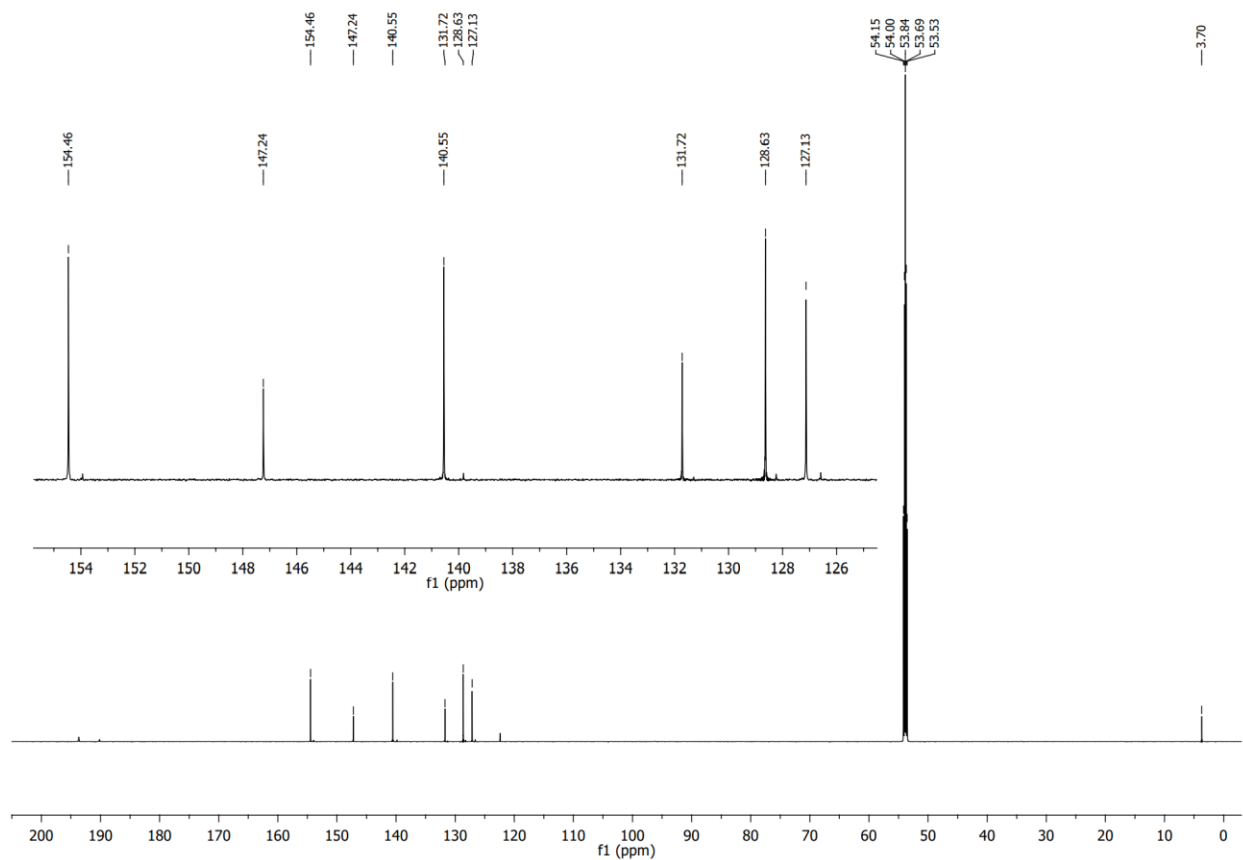


Figure C14. 176 MHz ^{13}C NMR of *fac*-[Re(phen)(CO) $_3$ (CH $_3$ CN)](PF $_6$) (**Mod2**) in CD $_2$ Cl $_2$ at 300K.



Figure C15. HR-ESIMS of fac-[Re(phen)(CO)₃(CH₃CN)](PF₆) (**Mod2**).

C.2. Additional Computational Data

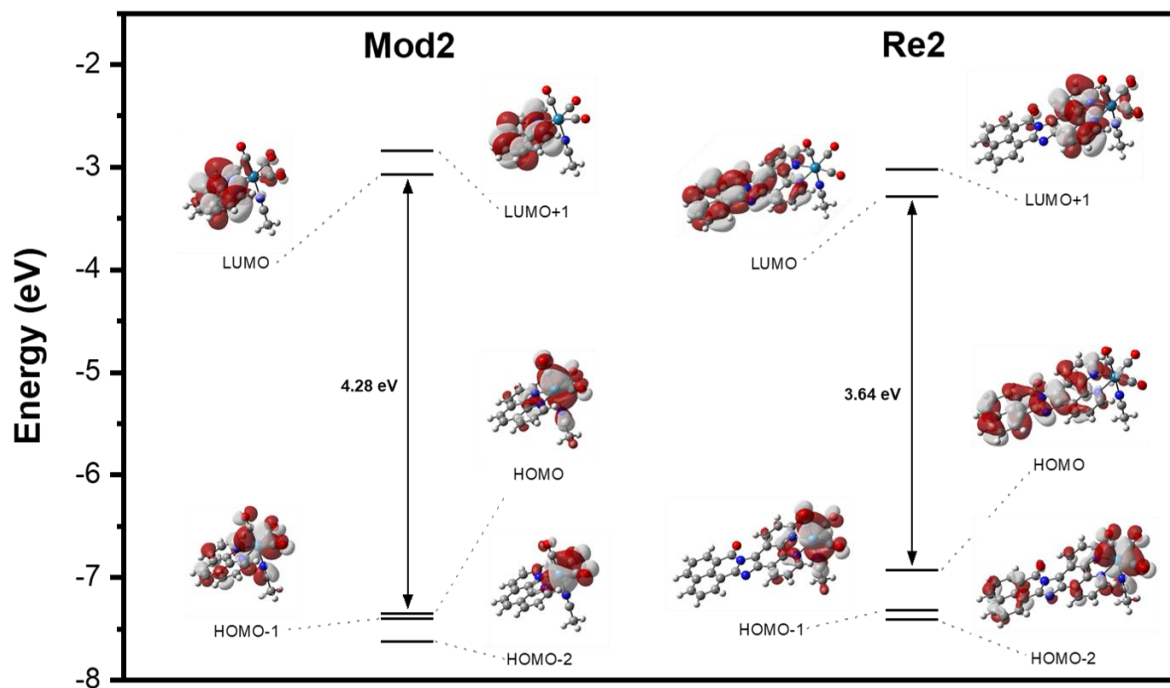


Figure C16. Frontier molecular orbital diagrams of the model Re(I)-CDI complex **Mod2** and corresponding NBI-phen complex **Re2**, where L = CH₃CN.

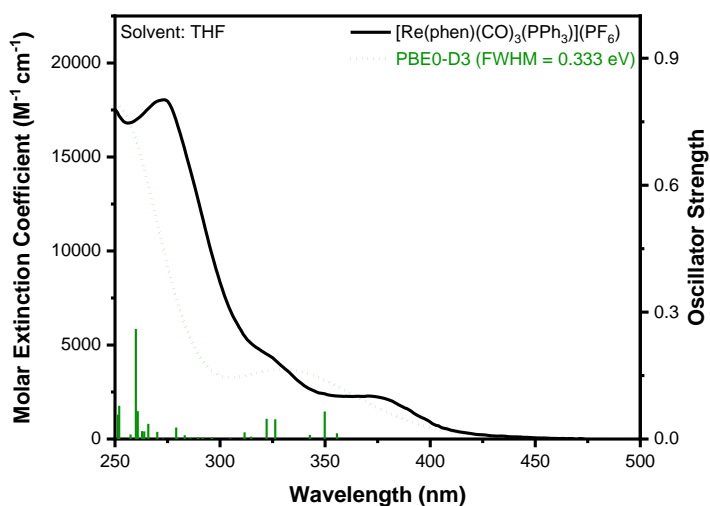


Figure C17. Experimental electronic absorption spectra overlay of **Mod1** with calculated singlet excited states.

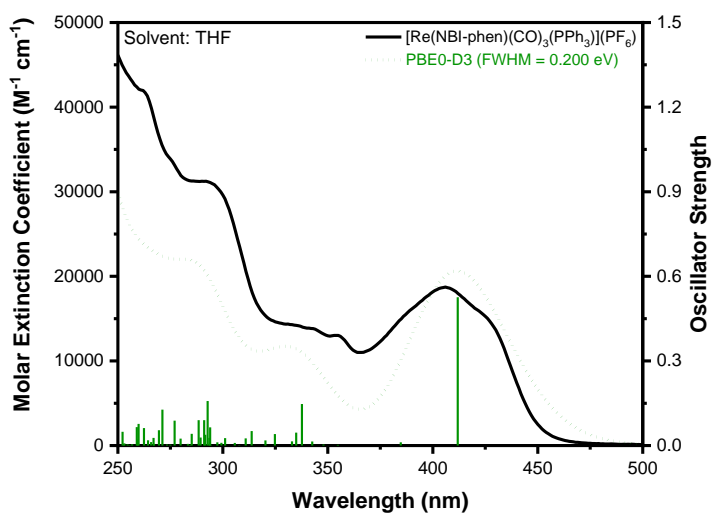


Figure C18. Experimental electronic absorption spectra overlay of **Re1** with calculated singlet excited states.

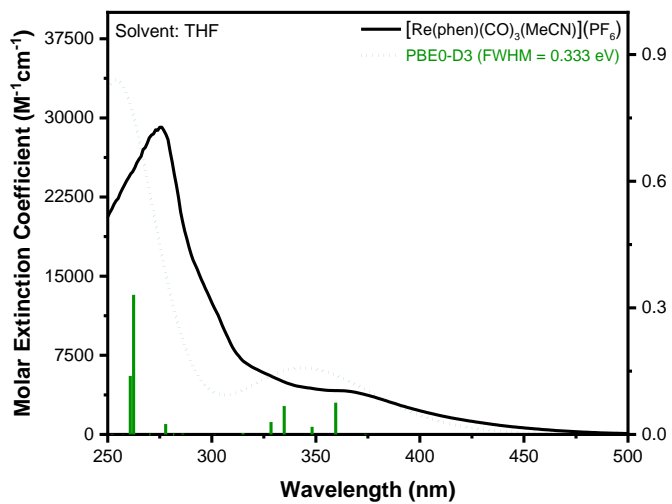


Figure C19. Experimental electronic absorption spectra overlay of **Mod2** with calculated singlet excited states.

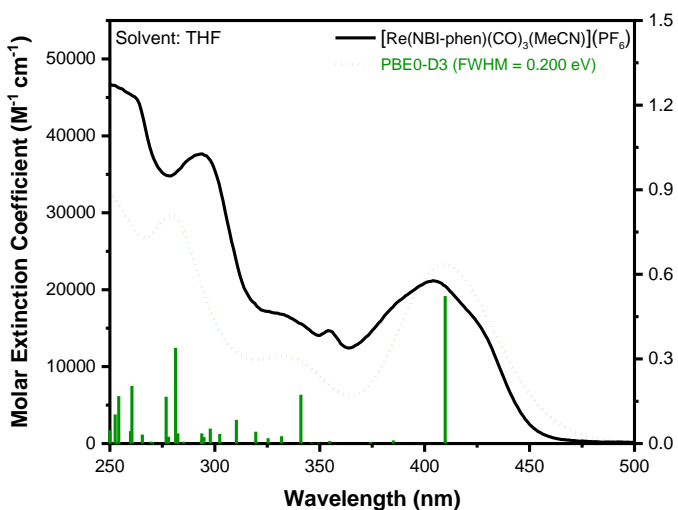


Figure C20. Experimental electronic absorption spectra overlay of **Re2** with calculated singlet excited states.

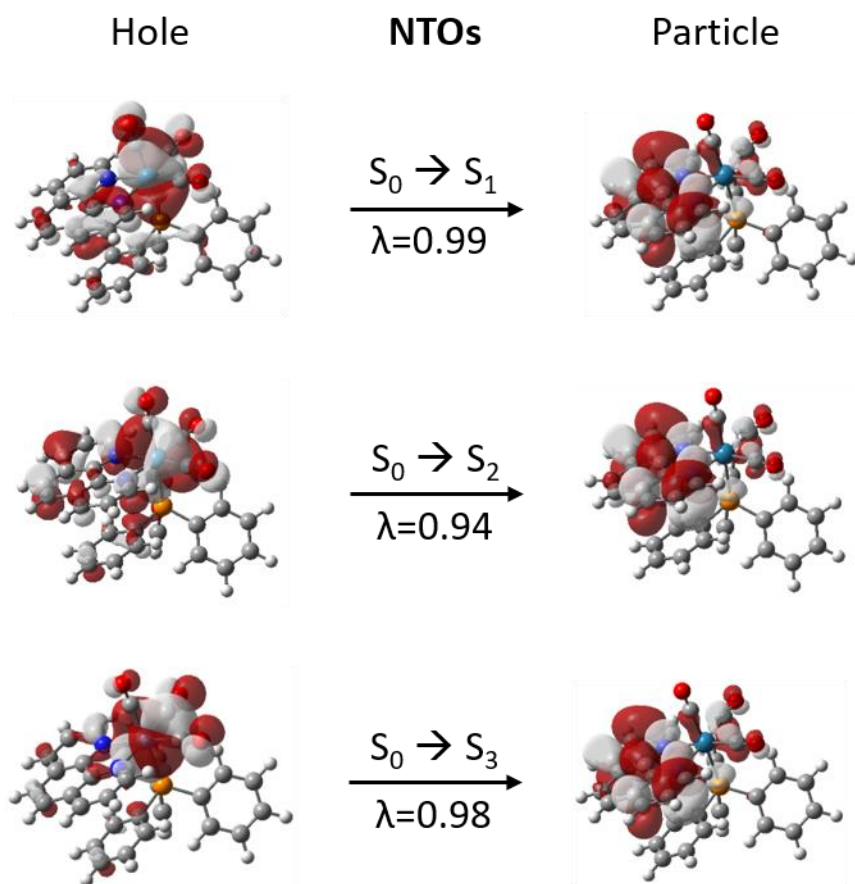


Figure C21. Natural transition orbitals for the three lowest transitions of **Mod1** predicted via TD-DFT at the PBE0-D3/Def2-SVP level of theory; λ is the fraction of the hole–particle contribution to the excitation.

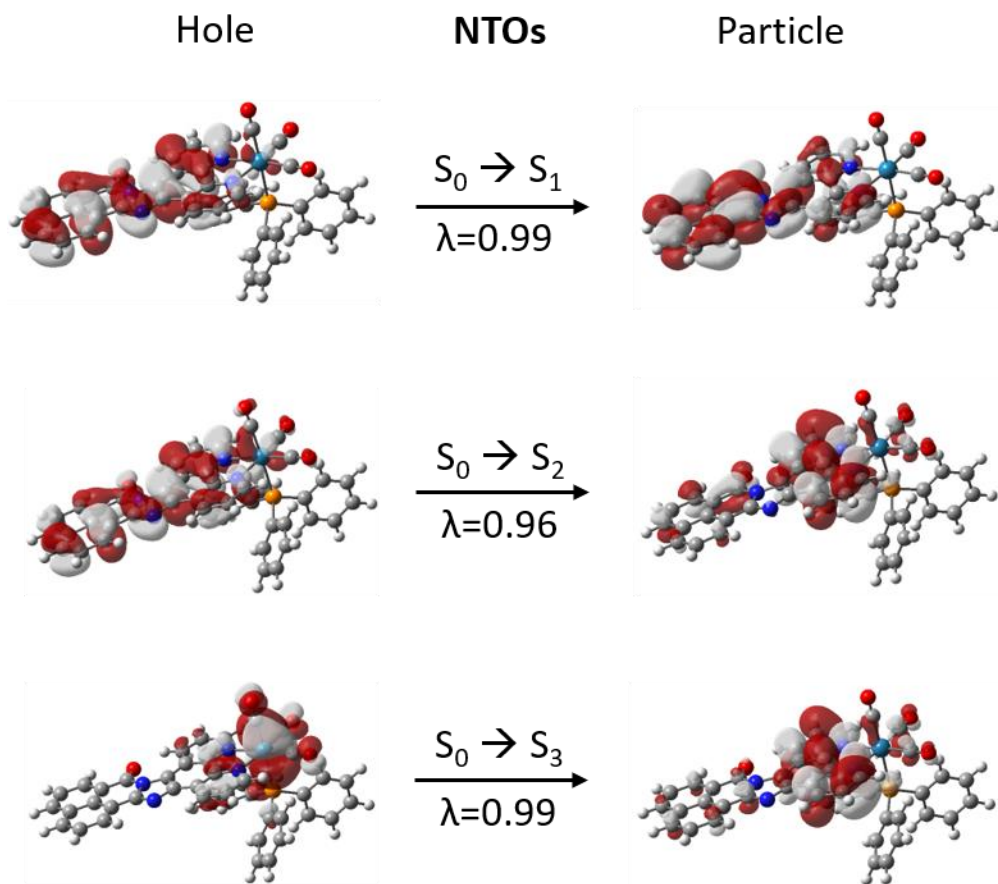


Figure C22. Natural transition orbitals for the three lowest transitions of **Re1** predicted via TD-DFT at the PBE0-D3/Def2-SVP level of theory; λ is the fraction of the hole–particle contribution to the excitation.

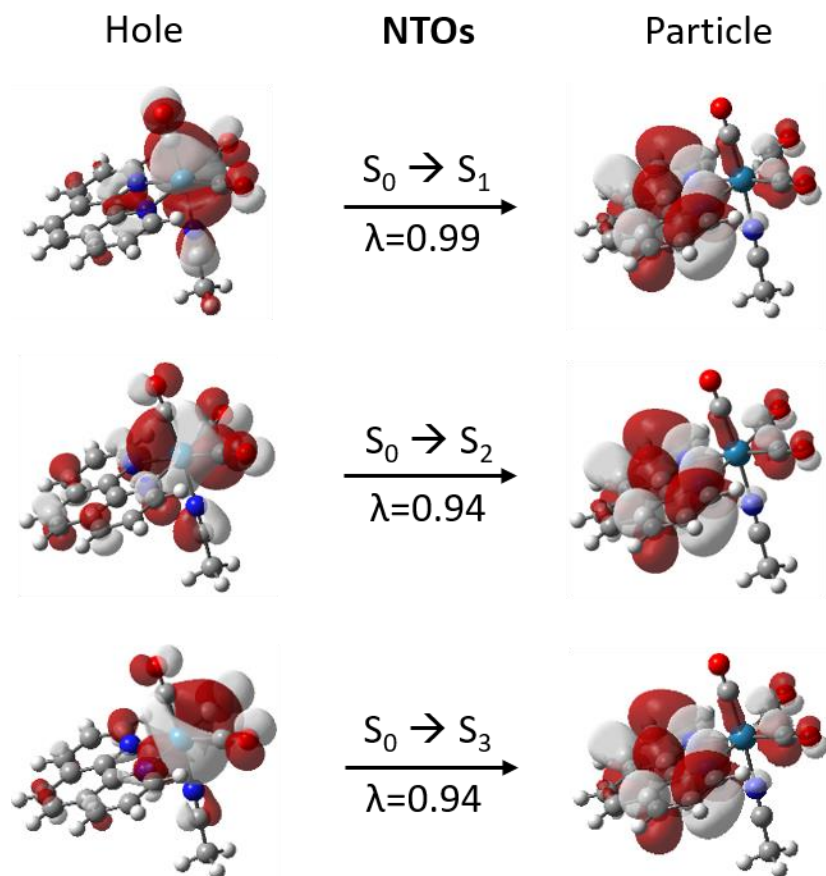


Figure C23. Natural transition orbitals for the three lowest transitions of **Mod2** predicted via TD-DFT at the PBE0-D3/Def2-SVP level of theory; λ is the fraction of the hole–particle contribution to the excitation.

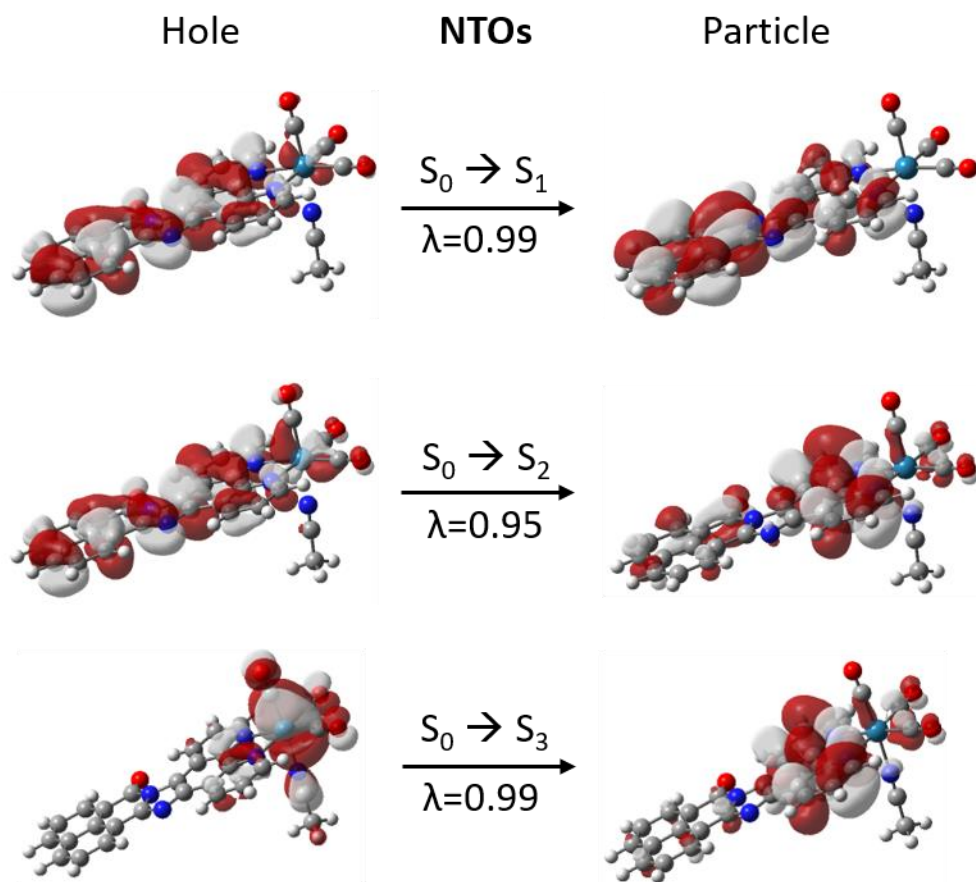
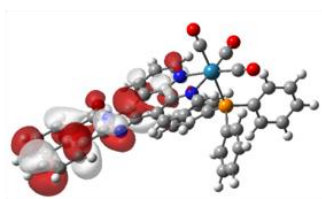


Figure C24. Natural transition orbitals for the three lowest transitions of **Re2** predicted via TD-DFT at the PBE0-D3/Def2-SVP level of theory PCM: THF; λ is the fraction of the hole–particle contribution to the excitation.

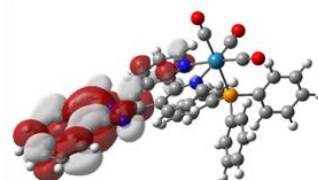
Table C1. Selected electronic excitation energies (nm) and corresponding oscillator strengths (f) of the low-lying singlet excited states of complexes **Mod1-2** and **Re1-2**.

molecule	S ₀ →S ₁ /nm (f)	S ₀ →S ₂ /nm (f)	S ₀ →S ₃ /nm (f)
Mod1	355.6 (0.0136)	349.8 (0.0650)	342.7 (0.0095)
Re1	411.9 (0.5259)	384.7 (0.0114)	354.8 (0.0026)
Mod2	373.9 (0.0016)	359.6 (0.0754)	348.2 (0.0179)
Re2	409.7 (0.5234)	385.1 (0.0107)	374.3 (0.0056)

Singly Occupied Ligand Natural Orbitals

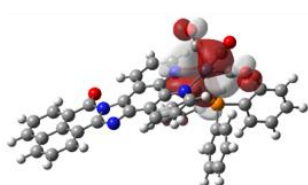


Occ. # = 1

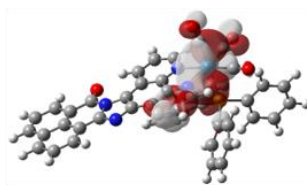


Occ. # = 1

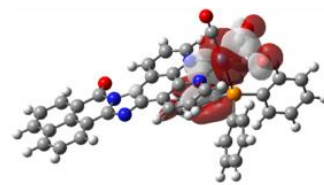
Doubly Occupied dπ Natural Orbitals



Occ. # = 2



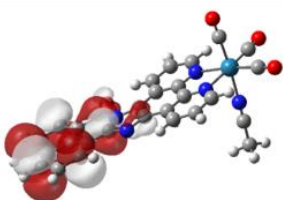
Occ. # = 2



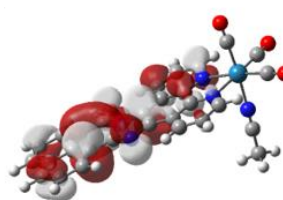
Occ. # = 2

Figure C25. Natural orbitals of **Re1**. PBE0-D3/Def2-SVP level of theory PCM: THF.

Singly Occupied Ligand Natural Orbitals

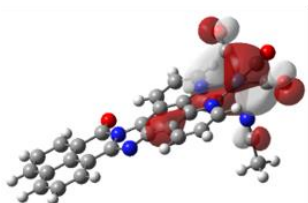


Occ. # = 1

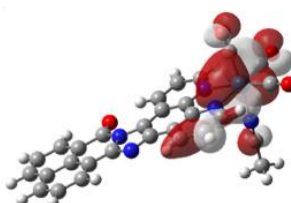


Occ. # = 1

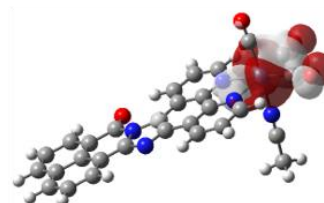
Doubly Occupied dπ Natural Orbitals



Occ. # = 2



Occ. # = 2



Occ. # = 2

Figure C26. Natural orbitals of **Re2**. PBE0-D3/Def2-SVP level of theory PCM: THF.

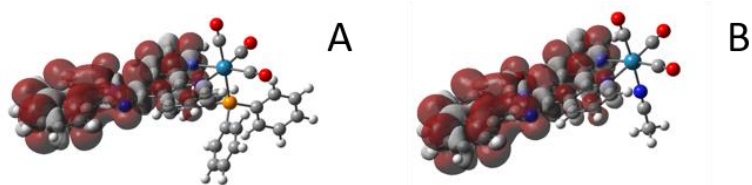


Figure C27. Triplet spin densities of (A) **Re1** and (B) **Re2**. PBE0-D3/Def2-SVP level of theory PCM: THF.

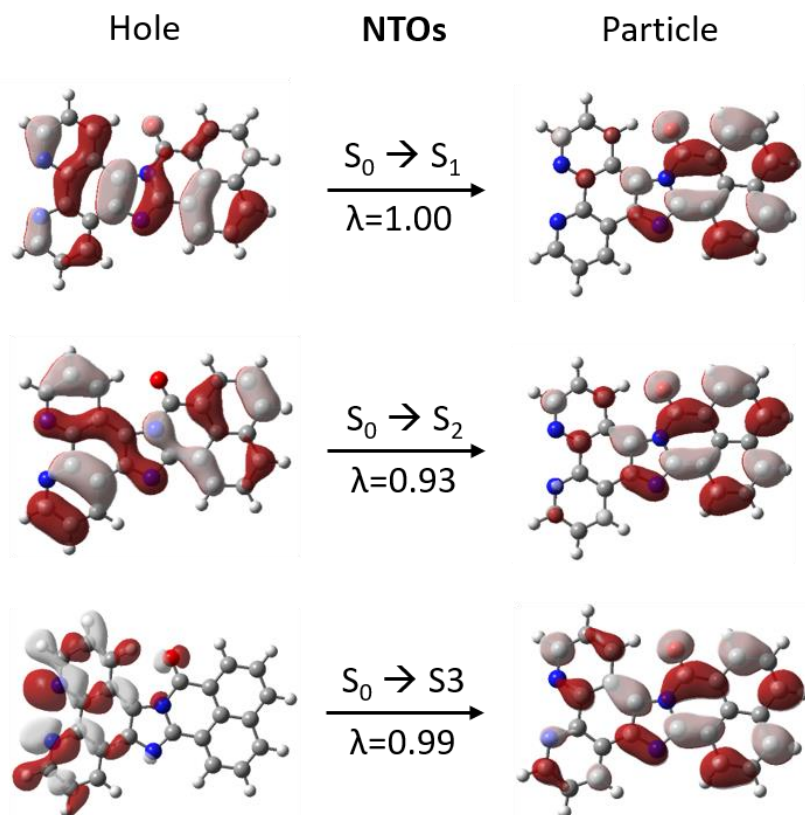


Figure C28. Natural transition orbitals for the three lowest transitions of **NBI-phen** predicted via TD-DFT at the PBE0-D3/Def2-SVP level of theory PCM: THF; λ is the fraction of the hole–particle contribution to the excitation.

Table C2. Optimized singlet geometries of **Re1-2** and **Mod1-2**:

Optimized geometry of **Re1**:

Re	-2.45645997	-0.20208138	-1.53399293
C	-2.17212009	-0.46227691	-3.45175425
O	-2.02594601	-0.61172225	-4.57897127
C	-3.93899404	-1.43045975	-1.59580505
O	-4.79768683	-2.20024091	-1.63383305
C	-3.63880734	1.27818846	-1.90622157
O	-4.30214052	2.19331246	-2.12960988
N	-0.60297767	0.97665377	-1.40605167

C	0.52659900	0.29161461	-1.09110719
C	-0.54554445	2.28954390	-1.60245351
C	1.79209057	0.93474938	-0.94906498
C	0.36289173	-1.12635400	-0.90257692
C	0.65488988	2.99378068	-1.51082495
H	-1.47915616	2.79905807	-1.84268125
C	1.81712197	2.32570552	-1.18763138
C	2.89660427	0.09019857	-0.57106029
C	1.46360135	-1.93362932	-0.56860550
N	-0.87904087	-1.65206793	-1.06902122
H	0.66003834	4.07000127	-1.68527036
H	2.76008352	2.85670189	-1.09108957
C	2.72648259	-1.28624483	-0.40466804
N	4.26227523	0.28941349	-0.31140836
C	1.27012861	-3.31776483	-0.41515648
C	-1.04358338	-2.96529029	-0.94075586
N	3.88624385	-1.91528238	-0.07794875
C	4.78980223	-0.97421542	-0.02709029
C	5.03736308	1.47350941	-0.24704255
H	2.11964275	-3.95045353	-0.15250228
C	0.00591234	-3.83317905	-0.61230653
H	-2.04841600	-3.35336234	-1.10939516
C	6.19092655	-1.15323595	0.27903931
C	6.46990467	1.28078362	0.04775129
O	4.54527267	2.56491221	-0.41796182
H	-0.19719912	-4.90020856	-0.51580187
C	7.01509287	-0.00255013	0.30337721
C	6.72862842	-2.40497673	0.53882432
C	7.28964410	2.39976062	0.07930209
C	8.40216566	-0.13710497	0.59343579
C	8.09920988	-2.53901691	0.82604534
H	6.07493402	-3.27885793	0.51480542
C	8.66106536	2.27162838	0.36031969
H	6.84939461	3.37886395	-0.11896604
C	9.20724333	1.02928899	0.61318381
C	8.92179327	-1.43096220	0.85277169
H	8.51034970	-3.53010540	1.02769740
H	9.29246658	3.16193488	0.37840379
H	10.27301753	0.92993101	0.83355744
H	9.98624542	-1.53723759	1.07541190
P	-2.74022222	0.19854449	0.94930748
C	-2.33306832	-1.22409856	2.03027645
C	-2.84972260	-2.47184375	1.65426307
C	-1.62696289	-1.11221507	3.23458008
C	-2.63992262	-3.59411460	2.45143389
H	-3.44124633	-2.56627490	0.74135155

C	-1.41313852	-2.23969254	4.02729947
H	-1.24443008	-0.14608866	3.56874642
C	-1.91134849	-3.48162875	3.63575329
H	-3.04937398	-4.55942830	2.14513281
H	-0.85670399	-2.14159676	4.96232347
H	-1.74025965	-4.36199955	4.25962442
C	-1.68175522	1.59306370	1.47434237
C	-2.20430397	2.89372523	1.46068780
C	-0.31609548	1.40704879	1.73461810
C	-1.37894900	3.98513455	1.72767129
H	-3.26192577	3.05866613	1.24105508
C	0.50376317	2.50143850	2.00129985
H	0.11943371	0.40540072	1.72727724
C	-0.02589807	3.79178968	2.00263787
H	-1.79943843	4.99329481	1.71904972
H	1.56614710	2.34246867	2.20090839
H	0.61945624	4.64812578	2.21122908
C	-4.40971393	0.65360273	1.54780826
C	-4.56110394	1.04610720	2.88704922
C	-5.53600218	0.56939723	0.72512111
C	-5.82048507	1.36151573	3.38591357
H	-3.68927459	1.10804946	3.54374814
C	-6.79906906	0.88260460	1.23010631
H	-5.43929652	0.25420342	-0.31369723
C	-6.94230935	1.28077341	2.55689660
H	-5.92860857	1.66984871	4.42832134
H	-7.67252596	0.81374621	0.57792031
H	-7.93118298	1.52754981	2.95061261

Optimized geometry of **Re2**:

Re	-2.45645997	-0.20208138	-1.53399293
C	-2.17212009	-0.46227691	-3.45175425
O	-2.02594601	-0.61172225	-4.57897127
C	-3.93899404	-1.43045975	-1.59580505
O	-4.79768683	-2.20024091	-1.63383305
C	-3.63880734	1.27818846	-1.90622157
O	-4.30214052	2.19331246	-2.12960988
N	-0.60297767	0.97665377	-1.40605167
C	0.52659900	0.29161461	-1.09110719
C	-0.54554445	2.28954390	-1.60245351
C	1.79209057	0.93474938	-0.94906498
C	0.36289173	-1.12635400	-0.90257692
C	0.65488988	2.99378068	-1.51082495
H	-1.47915616	2.79905807	-1.84268125
C	1.81712197	2.32570552	-1.18763138

C	2.89660427	0.09019857	-0.57106029
C	1.46360135	-1.93362932	-0.56860550
N	-0.87904087	-1.65206793	-1.06902122
H	0.66003834	4.07000127	-1.68527036
H	2.76008352	2.85670189	-1.09108957
C	2.72648259	-1.28624483	-0.40466804
N	4.26227523	0.28941349	-0.31140836
C	1.27012861	-3.31776483	-0.41515648
C	-1.04358338	-2.96529029	-0.94075586
N	3.88624385	-1.91528238	-0.07794875
C	4.78980223	-0.97421542	-0.02709029
C	5.03736308	1.47350941	-0.24704255
H	2.11964275	-3.95045353	-0.15250228
C	0.00591234	-3.83317905	-0.61230653
H	-2.04841600	-3.35336234	-1.10939516
C	6.19092655	-1.15323595	0.27903931
C	6.46990467	1.28078362	0.04775129
O	4.54527267	2.56491221	-0.41796182
H	-0.19719912	-4.90020856	-0.51580187
C	7.01509287	-0.00255013	0.30337721
C	6.72862842	-2.40497673	0.53882432
C	7.28964410	2.39976062	0.07930209
C	8.40216566	-0.13710497	0.59343579
C	8.09920988	-2.53901691	0.82604534
H	6.07493402	-3.27885793	0.51480542
C	8.66106536	2.27162838	0.36031969
H	6.84939461	3.37886395	-0.11896604
C	9.20724333	1.02928899	0.61318381
C	8.92179327	-1.43096220	0.85277169
H	8.51034970	-3.53010540	1.02769740
H	9.29246658	3.16193488	0.37840379
H	10.27301753	0.92993101	0.83355744
H	9.98624542	-1.53723759	1.07541190
P	-2.74022222	0.19854449	0.94930748
C	-2.33306832	-1.22409856	2.03027645
C	-2.84972260	-2.47184375	1.65426307
C	-1.62696289	-1.11221507	3.23458008
C	-2.63992262	-3.59411460	2.45143389
H	-3.44124633	-2.56627490	0.74135155
C	-1.41313852	-2.23969254	4.02729947
H	-1.24443008	-0.14608866	3.56874642
C	-1.91134849	-3.48162875	3.63575329
H	-3.04937398	-4.55942830	2.14513281
H	-0.85670399	-2.14159676	4.96232347
H	-1.74025965	-4.36199955	4.25962442
C	-1.68175522	1.59306370	1.47434237

C	-2.20430397	2.89372523	1.46068780
C	-0.31609548	1.40704879	1.73461810
C	-1.37894900	3.98513455	1.72767129
H	-3.26192577	3.05866613	1.24105508
C	0.50376317	2.50143850	2.00129985
H	0.11943371	0.40540072	1.72727724
C	-0.02589807	3.79178968	2.00263787
H	-1.79943843	4.99329481	1.71904972
H	1.56614710	2.34246867	2.20090839
H	0.61945624	4.64812578	2.21122908
C	-4.40971393	0.65360273	1.54780826
C	-4.56110394	1.04610720	2.88704922
C	-5.53600218	0.56939723	0.72512111
C	-5.82048507	1.36151573	3.38591357
H	-3.68927459	1.10804946	3.54374814
C	-6.79906906	0.88260460	1.23010631
H	-5.43929652	0.25420342	-0.31369723
C	-6.94230935	1.28077341	2.55689660
H	-5.92860857	1.66984871	4.42832134
H	-7.67252596	0.81374621	0.57792031
H	-7.93118298	1.52754981	2.95061261

Optimized geometry of **Mod1**:

Re	0.04581263	-1.55954082	-0.47377045
C	1.09334822	-3.11516865	-1.01408312
O	1.69763302	-4.03355411	-1.34035010
C	-0.95361345	-2.66494580	0.74973389
O	-1.50840994	-3.32126959	1.51632910
C	-1.22841805	-1.98581129	-1.85544675
O	-1.97299652	-2.27136083	-2.68914463
N	1.37448755	-0.17633249	-1.56600978
C	2.38888315	0.33864077	-0.82176428
C	1.25735145	0.20351250	-2.83461137
C	3.30364383	1.28416566	-1.33491391
C	2.52657806	-0.12562921	0.52541059
C	2.11600400	1.14040509	-3.42439829
H	0.45510533	-0.25451620	-3.41372324
C	3.13529725	1.69078399	-2.67431979
C	4.34799182	1.77646180	-0.48645306
C	3.58666172	0.34782574	1.32880566
N	1.62037804	-1.03091938	0.97169863
H	1.96331694	1.41745922	-4.46799741
H	3.81754616	2.42579471	-3.10702786
C	4.48607902	1.32419721	0.79111247
C	3.69981895	-0.18046643	2.63101290

C	1.75348842	-1.51817733	2.20141614
H	4.50657954	0.15858376	3.28453733
C	2.78837000	-1.12384120	3.05899421
H	1.00941303	-2.24715044	2.52663375
H	2.84659551	-1.55952643	4.05693863
H	5.03940303	2.51828408	-0.89134312
H	5.29028151	1.69700493	1.42851203
P	-1.19242632	0.55017993	0.23187240
C	-2.71499978	0.28583025	1.21237808
C	-3.56611048	-0.75858711	0.82891869
C	-3.10537448	1.14911062	2.24450971
C	-4.78380578	-0.94750778	1.47871497
H	-3.28300948	-1.42431920	0.01017999
C	-4.32133757	0.95153239	2.89650778
H	-2.46346349	1.97898141	2.54751867
C	-5.16039209	-0.09635296	2.51746891
H	-5.43881413	-1.76604745	1.17201717
H	-4.61478031	1.62515485	3.70499488
H	-6.11241835	-0.24819322	3.03150577
C	-1.78899955	1.69087523	-1.07493006
C	-2.20140372	2.98635680	-0.72469312
C	-1.91741155	1.27130305	-2.40152786
C	-2.70823663	3.84725307	-1.69317745
H	-2.12461050	3.32915279	0.31011424
C	-2.42769599	2.13513475	-3.37132666
H	-1.63891718	0.25863860	-2.68657138
C	-2.81841674	3.42484047	-3.02000371
H	-3.02293839	4.85418310	-1.40956168
H	-2.52150074	1.79184818	-4.40401886
H	-3.21688201	4.10273678	-3.77852251
C	-0.09372998	1.59180433	1.25423528
C	0.11303745	1.26999947	2.60334949
C	0.66404889	2.61714621	0.66997793
C	1.04083589	1.98224466	3.36003396
H	-0.45351839	0.45882701	3.06797573
C	1.59368595	3.32397490	1.43110284
H	0.52985669	2.87090784	-0.38404640
C	1.78071687	3.01136603	2.77676418
H	1.18932980	1.72657771	4.41156040
H	2.17585341	4.12213260	0.96550554
H	2.50877742	3.56692383	3.37222990

Optimized geometry of **Mod2**:

Re	1.15018878	0.00103779	-0.18968860
C	1.32370252	0.00576094	-2.11543094

O	1.41754390	0.00849101	-3.26103014
C	2.51830923	1.35954495	-0.07145149
O	3.30984207	2.19207453	0.00072312
C	2.51851938	-1.35785278	-0.07811421
O	3.31014769	-2.19063001	-0.00999425
N	0.80997841	-0.00505652	1.92496492
C	0.58809199	-0.01052184	3.05767531
C	0.32174367	-0.01902086	4.47630931
H	1.09666887	-0.60332559	4.99303344
H	0.32793567	1.01105259	4.86035494
H	-0.66167467	-0.47201487	4.66623848
N	-0.59239501	-1.34529677	-0.22584539
C	-1.79514433	-0.71557391	-0.20395117
C	-0.56173132	-2.67311838	-0.23745606
C	-3.01979681	-1.41813482	-0.19137527
C	-1.79521183	0.71719115	-0.20043293
C	-1.72792309	-3.45181017	-0.22708044
H	0.42306777	-3.14350485	-0.25651509
C	-2.95825066	-2.82774402	-0.20294537
C	-4.24851623	-0.68066123	-0.17107125
C	-3.01993301	1.41956357	-0.18445936
N	-0.59253426	1.34713076	-0.21924247
H	-1.64232961	-4.53898350	-0.23895387
H	-3.88214721	-3.41033341	-0.19468880
C	-4.24857921	0.68187828	-0.16774380
C	-2.95853085	2.82921650	-0.18916957
C	-0.56199765	2.67499386	-0.22436048
H	-3.88247710	3.41168083	-0.17819427
C	-1.72825948	3.45350968	-0.21019585
H	0.42276261	3.14554415	-0.24108727
H	-1.64277355	4.54073846	-0.21676301
H	-5.18881830	-1.23590853	-0.16101052
H	-5.18894006	1.23696829	-0.15497658

C.3. Additional Spectroscopic Data

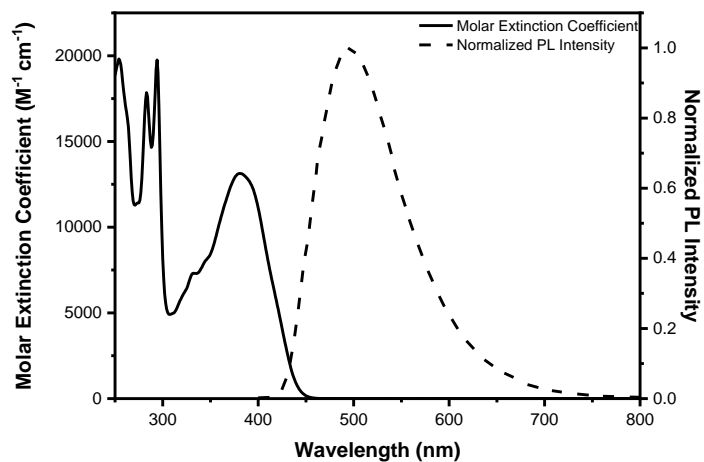


Figure C29. Electronic absorption spectra and PL of **NBI** in THF.

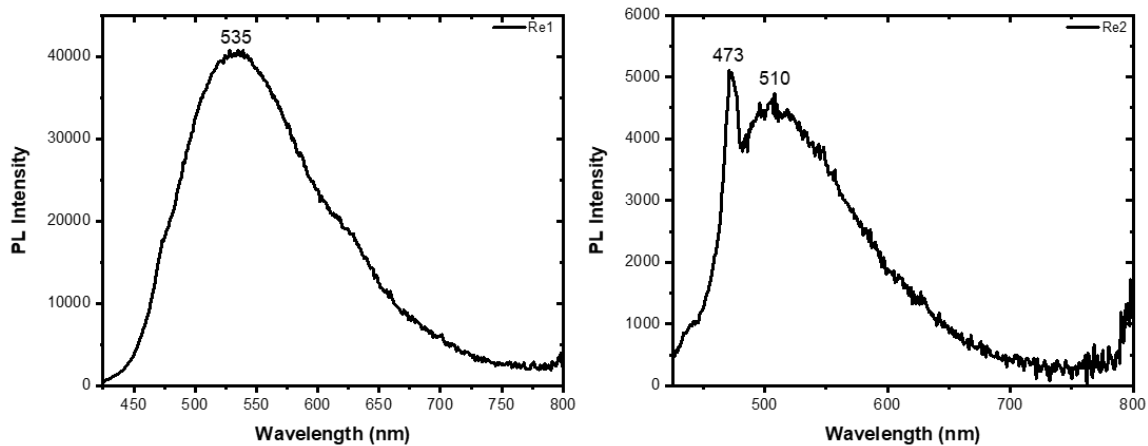


Figure C30. Aerated PL of **Re1** (left) and **Re2** (right). Feature at 473 nm is Raman band of THF excited at 415 nm.

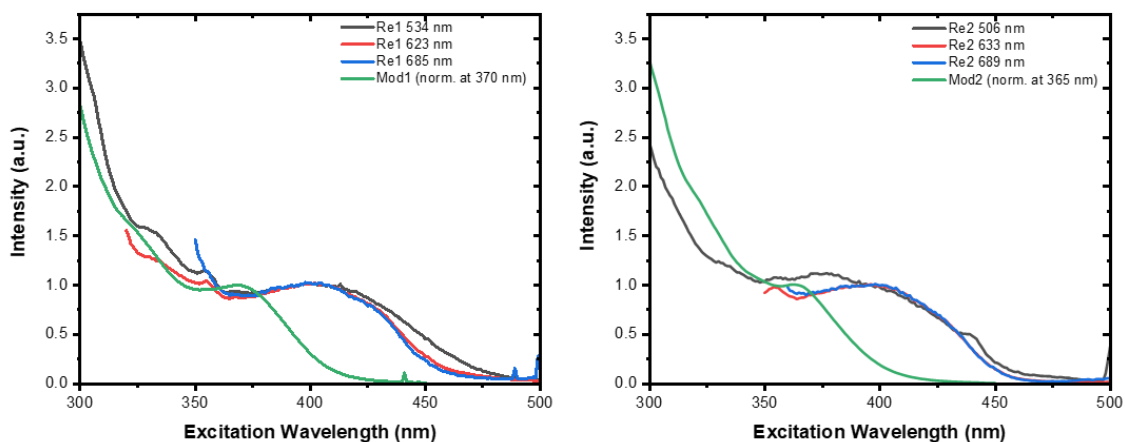


Figure C31. Excitation scans of **Re1**, **Mod1** (left) and **Re2**, **Mod2** (right). Monitored PL peak is denoted in the legend.

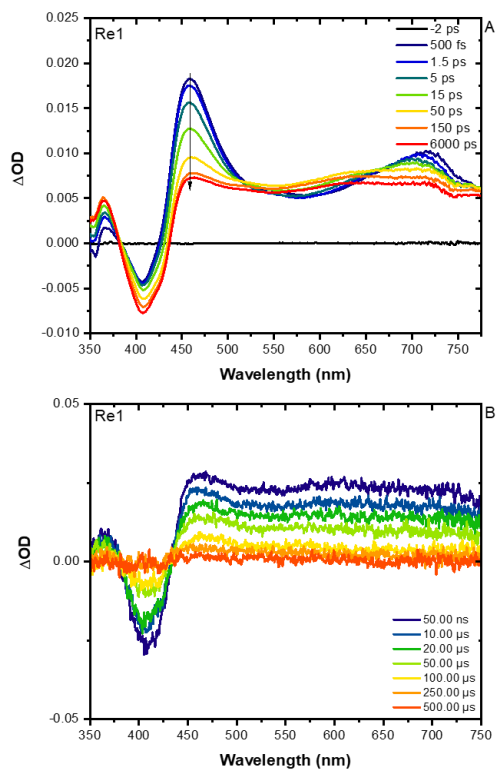


Figure C32. UFTA of (A) **Re1** in THF following 400 nm pulsed laser excitation (105 fs fwhm, 0.3 mJ/pulse) and (B) nsTA of **Re1** in deaerated THF following 415 nm excitation (1.8 mJ/pulse).

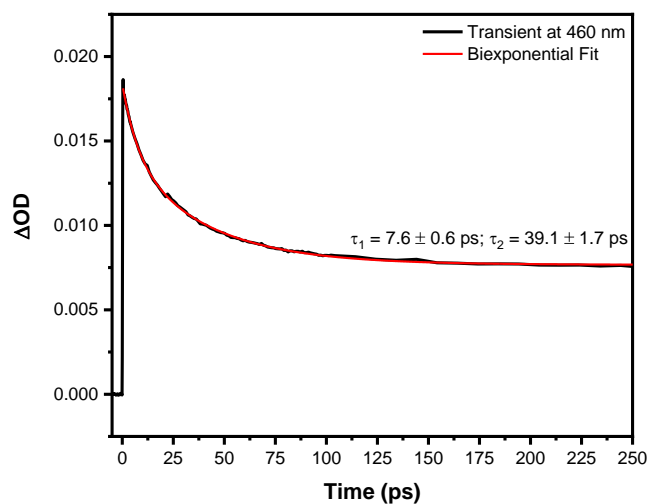


Figure C33. Ultrafast transient absorption kinetic data of **Re1** in THF following 400 nm pulsed excitation. Single wavelength kinetic analysis at 460 nm.

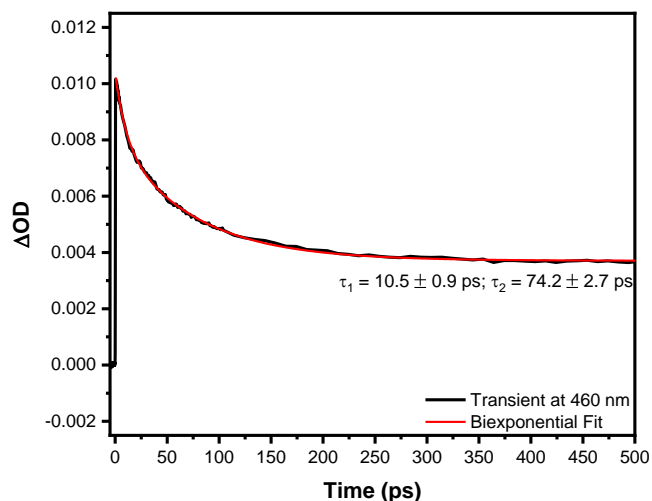


Figure C34. Ultrafast transient absorption kinetic data of **Re2** in THF following 400 nm pulsed excitation. Single wavelength kinetic analysis at 460 nm.

Table C3. Data table of **Re1** rate constants and beta values after fitting using the TTA fitting equation from Deng et. al.³ Experiments were carried out in deaerated THF ($\lambda_{\text{ex}} = 415 \text{ nm}$).

Power (mJ/pulse)	$k_T \text{ (ns}^{-1}\text{)}$	$k_T \text{ (s}^{-1}\text{)}$	β
2.0	1.34E-6	1.34E3	0.940
1.6	1.70E-6	1.70E3	0.909
1.2	1.95E-6	1.95E3	0.885
0.8	2.21E-6	2.21E3	0.834

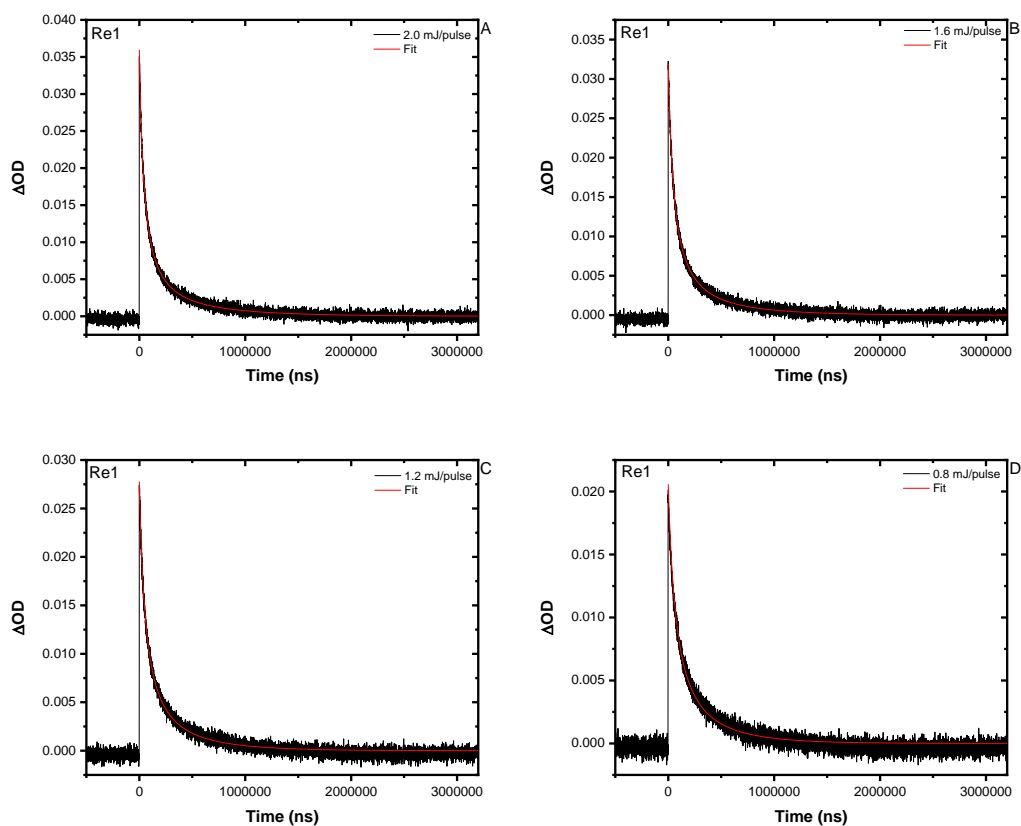


Figure C35. Kinetic traces and fits of **Re1** at 2.0 (A), 1.6 (B), 1.2 (C), and 0.8 (D) mJ/pulse in deaerated THF ($\lambda_{\text{ex}} = 415 \text{ nm}$).

Table C4. Data table of **Re2** rate constants and beta values after fitting using the TTA fitting equation from Deng et. al.³ Experiments were carried out in deaerated THF ($\lambda_{\text{ex}} = 415 \text{ nm}$).

Power (mJ/pulse)	$k_T \text{ (ns}^{-1}\text{)}$	$k_T \text{ (s}^{-1}\text{)}$	β
2.0	1.75E-6	1.75E3	0.956
1.7	2.18E-6	2.18E3	0.942
1.4	2.70E-6	2.70E3	0.923
1.0	3.14E-6	3.14E3	0.906

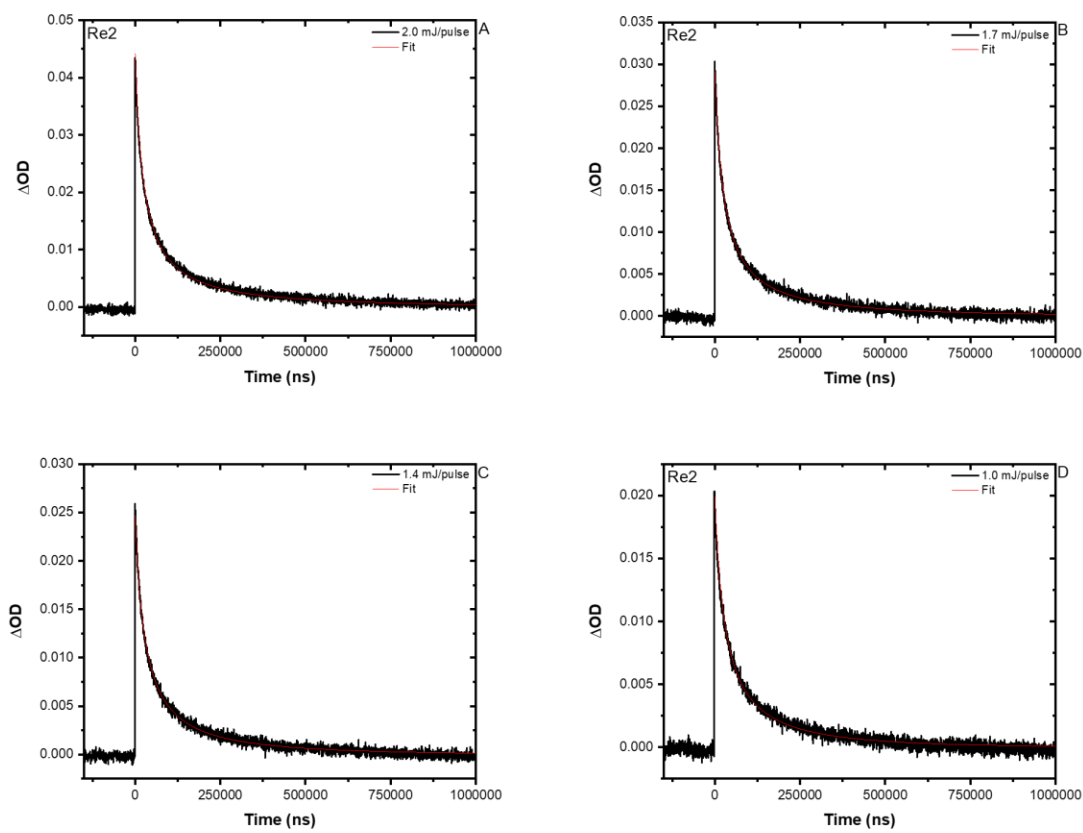


Figure C36. Kinetic traces and fits of **Re2** at 2.0 (A), 1.7 (B), 1.4 (C), and 1.0 (D) mJ/pulse in deaerated THF ($\lambda_{\text{ex}} = 415$ nm).

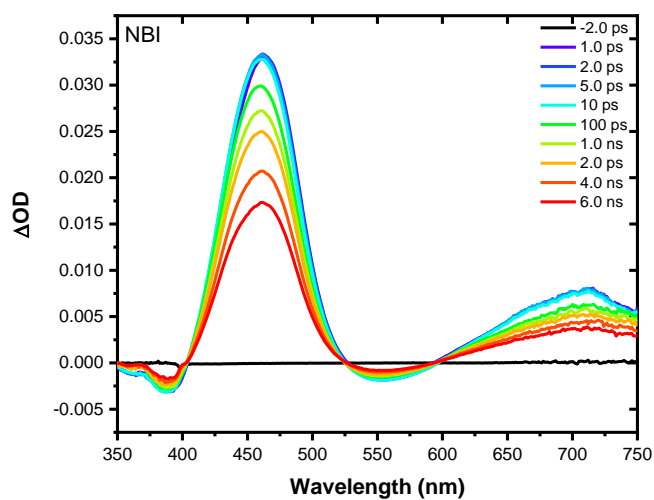


Figure C37. UFTA of **NBI** in THF following 400 nm pulsed laser excitation (105 fs fwhm, 0.5 mJ/pulse).

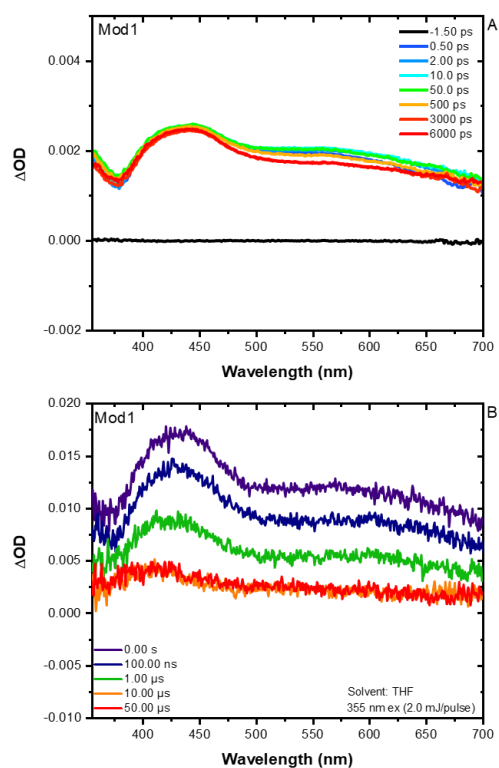


Figure C38. Nanosecond transient absorption spectra of (A) UFTA of **Mod1** following 350 nm excitation (105 fs fwhm, 50 μ J/pulse) in THF and (B) nsTA of **Mod1** following 355 nm excitation (1.8 mJ/pulse) in deaerated THF.

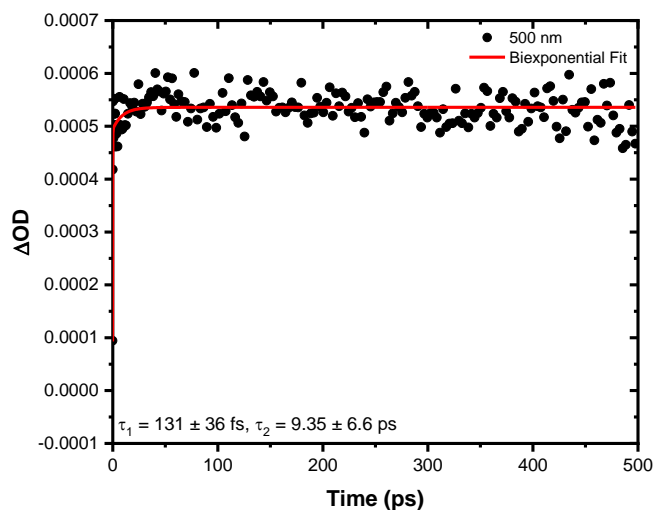


Figure C39. Ultrafast transient absorption kinetic data of **Mod1** following 350 nm excitation (105 fs fwhm, 50 μ J/pulse) in THF. Single wavelength kinetic analysis at 500 nm.

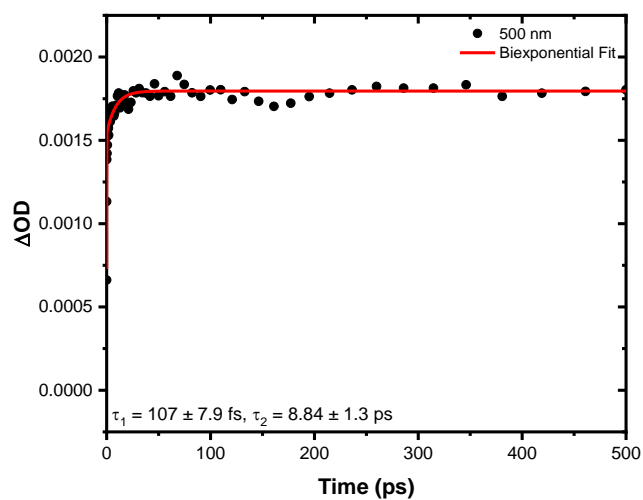


Figure C40. Ultrafast transient absorption kinetic data of **Mod2** following 350 nm excitation (105 fs fwhm, 50 $\mu\text{J}/\text{pulse}$) in THF. Single wavelength kinetic analysis at 500 nm.

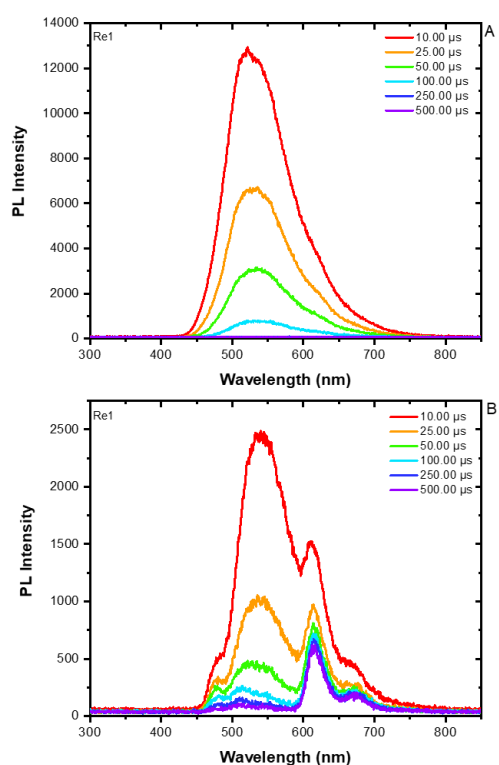


Figure C41. Time-resolved photoluminescence data of **Re1** at (A) room temperature in deaerated THF and (B) 77 K in 2-MeTHF following 415 nm excitation (1.8 mJ/pulse).

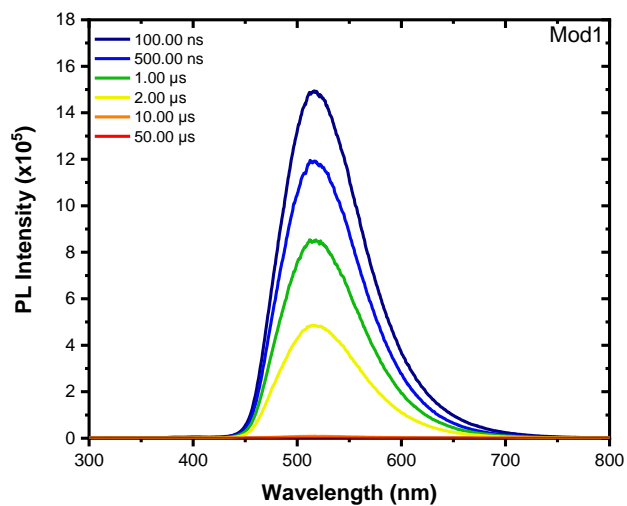


Figure C42. Time-resolved photoluminescence spectra of **Mod1** after excitation using a Continuum Minilite with 355 nm pulsed excitation (2.0 mJ/pulse, 5 ns fwhm).

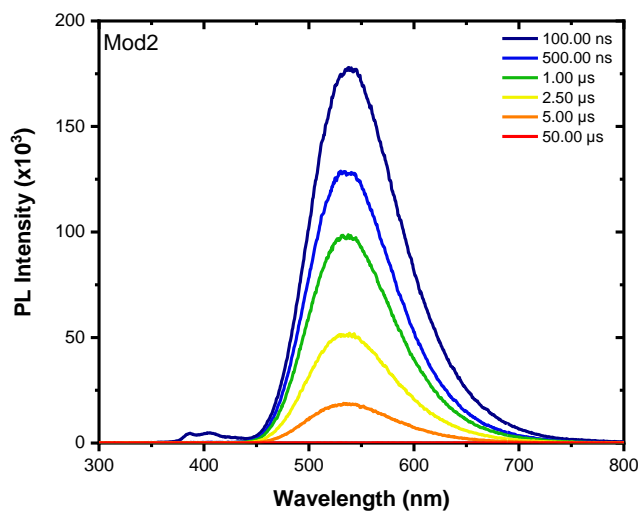


Figure C43. Time-resolved photoluminescence spectra of **Mod2** after excitation using a Continuum Minilite with 355 nm pulsed excitation (2.0 mJ/pulse, 5 ns fwhm).

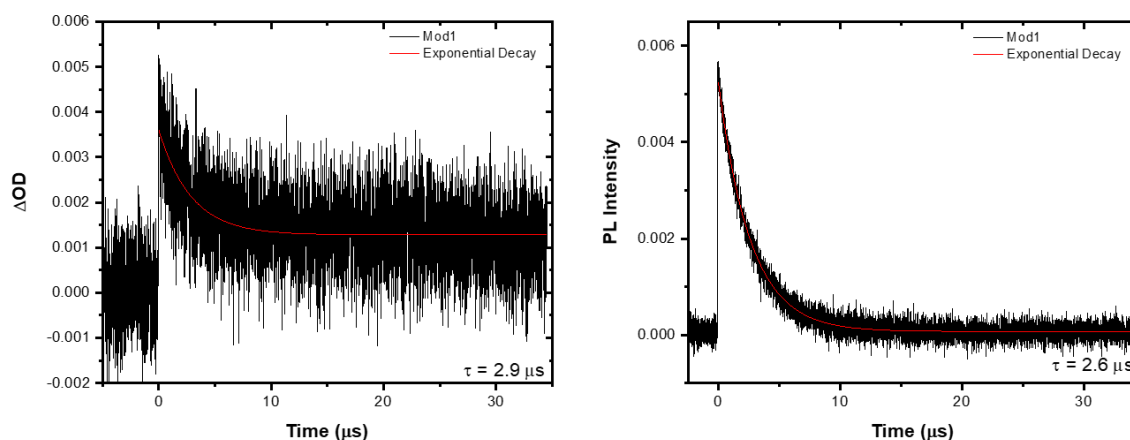


Figure C44. nsTA kinetics (left) and PL kinetics (right) of **Mod1** in THF after excitation using a Continuum Minilite with 355 nm pulsed excitation (2.0 mJ/pulse, 5 ns fwhm). Intense noise on nsTA kinetics due to a ND filter being placed in front of Xe arc lamp to reduce amount of decomposition of sample.

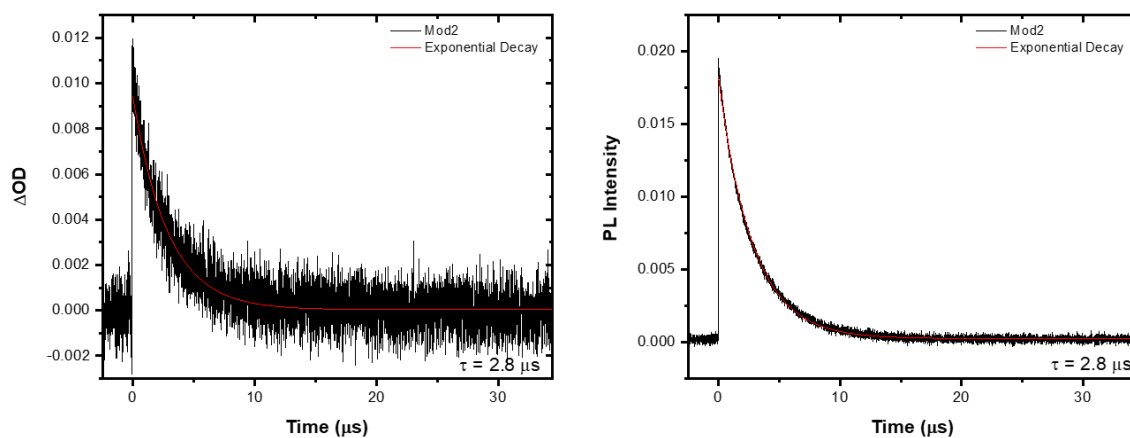


Figure C45. nsTA kinetics (left) and PL kinetics (right) of **Mod2** in THF after excitation using a Continuum Minilite with 355 nm pulsed excitation (2.0 mJ/pulse, 5 ns fwhm).

C.4. References

1. Yang, Y.; Brückmann, J.; Frey, W.; Rau, S.; Karnahl, M.; Tschierlei, S., Electron Storage Capability and Singlet Oxygen Productivity of a RuII Photosensitizer Containing a Fused Naphthaloylenebenzene Moiety at the 1,10-Phenanthroline Ligand. *Chem. Eur. J.* **2020**, *26* (71), 17027-17034.
2. Yarnell, J. E.; Wells, K. A.; Palmer, J. R.; Breaux, J. M.; Castellano, F. N., Excited-State Triplet Equilibria in a Series of Re(I)-Naphthalimide Bichromophores. *J. Phys. Chem. B* **2019**, *123* (35), 7611-7627.
3. Deng, F.; Blumhoff, J.; Castellano, F. N., Annihilation Limit of a Visible-to-UV Photon Upconversion Composition Ascertained from Transient Absorption Kinetics. *J. Phys. Chem. A* **2013**, *117* (21), 4412-4419.